NASA Technical Memorandum 102209

Proceedings of the Third Infrared Detector Technology Workshop

October 1989

NASA

National Aeronautics and
Space Administration

NASA Technical Memorandum 102209

Proceedings of the Third Infrared Detector Technology Workshop

Compiled by Craig R. McCreight, Ames Research Center, Moffett Field, California

October 1989

NASA

National Aeronautics and
Space Administration

Ames Research Center
Moffett Field, California 94035

FOREWORD

The dramatic technological and scientific progress achieved in the field of infrared (IR) detector and detector array development for astronomy is evident when one looks back to previous workshops in this series. In the initial July 1983 Workshop at Ames, we heard of promising concepts and some exploratory devices which we hoped would improve upon focal plane technology flown on the Infrared Astronomical Satellite (IRAS). There was an emphasis on plans, both for individual technology development projects and for future missions such as the Space Infrared Telescope Facility (SIRTF). At the second Ames workshop in August 1985, we learned that the feasibility and first-order characteristics of some of these ideas had been established, and that some initial technical data were becoming available. Arrays as large as 64 x 64 pixels were being tested in laboratories, and performance appeared to be good.

The outstanding workshop held in Hilo, Hawaii in March 1987 dramatically demonstrated that many scientists were able to do (as the title of the proceedings indicated) infrared astronomy with arrays. Devices were sufficiently sensitive, and data management and observing strategies were sufficiently mature, that important imaging and spectroscopic results were becoming available, and a revolution in ground-based IR instrumentation was at hand.

The February 1989 workshop at Ames showed that infrared detector and detector array technologies had continued to advance, and that important technological advances had been made. The papers indicated that the devices were more sensitive, were available in formats up to 256 x 256 pixels, and have been much more thoroughly characterized. In many cases, the performance levels met or exceeded the performance goals for major space missions such as SIRTF, the Infrared Space Observatory (ISO), and the second-generation Hubble Space Telescope. As a result of direct collaborations between industry and the scientific community, devices specifically tailored for astronomical applications had been developed and characterized, and unprecedented levels of performance had been achieved. The half-day session of recent ground-based results with arrays echoed the exciting progress reported at the Hilo meeting. A number of advance developments were discussed which promise to make future space astronomical systems even more powerful.

At the close of the workshop, summary comments were offered by R. Arentz, S. Willner, F. Low, R. Thompson, K. Shivanandan, E. Young, G. Rieke, T. Herter, and D. Allen. It was suggested that in addition to the more obvious challenges such as achieving larger formats and characterizing the effects of space radiation, the community needs to improve its overall detailed knowledge of array performance in the space environment, and to understand characteristics which may not appear on a conventional list of specifications. Continued cooperation and exchanges of test devices were felt to be essential, and improved definitions of key parameters such as read noise were needed. A wide range of challenges and possibilities are presented by the rapid pace of improvements in semiconductor science and processing.

We wish to thank the many people involved in the hosting of the workshop and the publication of its proceedings. The workshop was jointly sponsored by the SIRTF Study Office at Ames, and by the Offices of Aeronautics and Space Technology, and Space Science and Applications, at NASA Headquarters.

Craig R. McCreight
Ames Research Center

F. C. Gillett
NASA Headquarters

TABLE OF CONTENTS

TABLE OF CONTENTS (cont'd)

TABLE OF CONTENTS (cont'd)

TABLE OF CONTENTS (cont'd)

AGENDA

Infrared Detector Technology Workshop
Ames Research Center
Main Auditorium (Building 201)
Moffett Field, California 94035
Message Number: (415) 694-5256 or FTS 464-5256
February 7 - 9, 1989

Tuesday, February 7, 1989

9 AM	Introduction and Welcome	C. McCreight, Ames Research Center
	Requirements of IR Space Astronomy	F. J. Low, University of Arizona
9:45	**Current Developments in Discrete Detectors and Cryogenic Electronics**	C. McCreight, chair
	Stressed Ge:Ga Photoconductors for Space-Based Astronomy	J. W. Beeman, E. E. Haller, W. L. Hansen, P. N. Luke, Lawrence Berkeley Laboratory; P. L. Richards, University of California, Berkeley
	Near Contact Phenomena and Transient Effects in Far-Infrared Photoconductors	N. M. Haegel, University of California, Los Angeles
10:35	Break	
10:50	A 100 mK Bolometer System for SIRTF	G. M. Bernstein, P. T. Timbie, P. L. Richards, University of California, Berkeley
	A Progress Report on Using Bolometers Cooled by Adiabatic Demagnetization Refrigeration	L. Lesyna, Grumman Corporate Research Center; T. Roellig, Ames Research Center; M. Savage, Sterling Software; M. Werner, Ames Research Center
12:30	Lunch	
1:30	The Potential for High Performance HgCdTe Arrays at 4 Microns	G. H. Rieke, A. Sarfaraz, E. T. Young, M. J. Rieke, University of Arizona

Tuesday, February 7, 1989 (cont'd)

	Germanium Blocked Impurity Band (BIB) Detectors	E. E. Haller, H. Baumann, J. W. Beeman, W. L. Hansen, P. N. Luke, M. Lutz, C. S. Rossington, I. C. Wu, Lawrence Berkeley Laboratory
	Extrinsic Germanium Blocked Impurity Band Detectors	T. N. Krabach, Jet Propulsion Laboratory; J. E. Huffman, Rockwell International; D. M. Watson, University of Rochester
3:15	Break	
3:30	**Current Developments in IR Array Technology I**	K. Matthews, chair
	Ga:Ge Array Development	E. Young, G. Rieke, F. Low, University of Arizona; E. Haller, J. Beeman, Lawrence Berkeley Laboratory
	Common Source Cascode Amplifiers for Integrating IR-FPA Applications	J. Woolaway, Amber Engineering; E. Young, University of Arizona
	Study of Advanced InSb Arrays for SIRTF	A. W. Hoffman, R. Feitt, Santa Barbara Research Center
	InSb DRO Array Characteristics	W. J. Forrest, J. L. Pipher, Z. Ninkov, J. D. Garnett, University of Rochester
5:00	Adjourn	

Wednesday, February 8, 1989

9 AM	**Recent Results from Ground-Based Observations with IR Arrays**	A. Tokunaga, chair
	Experience with the UKIRT InSb Array Camera	I. S. McLean, M. M. Casali, G. S. Wright, C. Aspin, Joint Astronomy Centre
	Reduction and Analysis Techniques for Infrared Imaging Data	M. McCaughrean, Goddard Space Flight Center

Wednesday, February 8, 1989 (cont'd)

	Discovery of Low Mass Objects in Taurus	W. J. Forrest, Z. Ninkov, J. L. Pipher, University of Rochester; M. F. Skrutskie, University of Massachusetts; M. Shure, University of Hawaii; J. D. Garnett, University of Rochester
10:25	Break	
10:40	High Resolution Imaging of the Venus Night Side Using a Rockwell 128 × 128 HgCdTe Array	K.-W. Hodapp, W. Sinton, University of Hawaii; B. Ragent, Ames Research Center; D. Allen, Anglo Australian Observatory
	Infrared Ground-Based Astronomy with the Hughes 256 × 256 PtSi Array	A. Fowler, R. Joyce, R. Probst, I. Gatley, National Optical Astronomy Observatories
	Stressed Detector Arrays for Airborne Astronomy	G. Stacey, J. Beeman, E. Haller, University of California, Berkeley; R. Genzel, Max-Planck Institut für Extraterrestrische Physik; C. Townes, University of California, Berkeley
	AFGL Ten Micron Mosaic Array Spectrometer– Recent Results	P. D. LeVan, Air Force Geophysics Laboratory
	Initial Astronomical Results with the New 5 - 14 μm Si:Ga 58 × 62 DRO Array Camera	D. Gezari, W. Folz, L. Woods, Goddard Space Flight Center
	Preliminary Results on 2-Dimensional Interferometry of HL Tau	E. V. Tollestrup and P. M. Harvey, University of Texas
12:15	Lunch	
1:15	**Current Developments in IR Array Technology II – Hubble Space Telescope**	J. Pipher, chair
	Short Wavelength HgCdTe Staring Focal Plane for Low Background Astronomy Applications	J. Stobie, N. Hartle, D. Lacroix, K. Maschhoff, Honeywell Electro-Optics Division

Wednesday, February 8, 1989 (cont'd)

	Low Noise HgCdTe 128 × 128 SWIR FPA for Hubble Space Telescope	M. Blessinger, K. Vural, Rockwell International; W. Kleinhans, Valley Oak Semiconductor; M. Rieke, R. Thompson, R. Rasche, University of Arizona
	Laboratory and Telescope Use of the NICMOS2 128 × 128 HgCdTe Array	M. J. Rieke, E. F. Montgomery, G. H. Rieke, University of Arizona; K. Vural, and M. Blessinger, Rockwell International Science Center; W. Kleinhans, Valley Oak Semiconductor
	Future Directions for NICMOS Arrays	R. Thompson, M. Rieke, F. Low, E. Young, D. McCarthy, R. Rasche, University of Arizona; M. Blessinger, K. Vural, Rockwell International; W. Kleinhans, Valley Oak Semiconductor
3:05	Break	
3:20	**Current Status of Infrared Space Observatory (ISO) Detector Developments**	J. Wolf, chair
3:20	Introduction to the Infrared Space Observatory (ISO)	F. Sibille, Observatoire de Lyon; M. F. Kessler, European Space Research and Technology Centre
	Design and Status of the Detector Block for the ISO-SWS	W. Luinge, D. A. Beintema, Space Research Institute Groningen; L. Haser, R. Katterloher, Max-Planck Institut für Extraterrestrische Physik; G. Ploeger, Space Research Institute Groningen
	Status of the ISOPHOT Detector Development	J. Wolf, D. Lemke, M. Burgdorf, U. Grözinger, Ch. Hajduk, Max-Planck Institut für Astronomie
4:30	Adjourn	
6:45	Dinner	

Thursday, February 9, 1989

9 AM	**Current Status of ISO Detector Developments (cont'd)**	
	ISO/LWS: Detector Status	C. Le Naour, University of Toulouse
	ISO Camera Array Development Status	F. Sibille, Observatoire de Lyon; C. Cesarsky, CEN Saclay; D. Rouan, Observatoire de Meudon; P. Agnese, CEN Saclay
10:00	**Current Status of the Space Telescope Facility (SIRTF) and the Stratospheric Observatory for Infrared Astronomy (SOFIA)**	
	SIRTF in High Earth Orbit	M. W. Werner, Ames Research Center
	Stratospheric Observatory for Infrared Astronomy	E. F. Erickson, Ames Research Center
10:45	Break	
11:00	**Current Developments in IR Array Technology III**	R. Capps, chair
	Laboratory Characterization of Direct Readout Si:Sb and Si:Ga Infrared Detector Arrays	M. E. McKelvey, N. N. Moss, R. E. McMurray, Jr., J. A. Estrada, J. H. Goebel, C. R. McCreight, Ames Research Center; M. L. Savage, Sterling Software; F. Junga, T. Whittemore, Lockheed Research Laboratory
	HgCdTe 256 × 256 MWIR FPA	K. Vural, M. Blessinger, J. Chen, Rockwell International; W. Kleinhans, Valley Oak Semiconductor
	High Speed, Low Read Noise Electronics for Astronomy Detector Arrays	J. F. Arens, J. G. Jernigen, M. C. Peck, University of California, Berkeley
12:30	Lunch	

Thursday, February 9, 1989 (cont'd)

1:30	Improved Si:As BIBIB Hybrid Arrays	T. Herter, N. Rowlands, S. Beckwith, G. Gull, Cornell University; D. B. Reynolds, D. H. Seib, S. B. Stetson, Rockwell International
	Tests of the Rockwell Si:As Back-Illuminated Blocked-Impurity Band (BIBIB) Detectors	J. Wolf, U. Gröziṅger, M. Burgdorf, A. Salama, D. Lemke, Max-Planck Institut für Astronomie
3:10	Break	
3:25	**Summary, Conclusions, and Wrap-up**	
4:30	Adjourn	

ATTENDEES–INFRARED DETECTOR TECHNOLOGY WORKSHOP

David Allen
Anglo-Australian Observatory
P.O. Box 296
Epping NSW 2121
Australia
(2) 868-1666

Eric Arens
University of California
Space Sciences Laboratory
Berkeley, CA 94720
(415) 642-7287

Robert F. Arentz
Ball Aerospace Systems Group
P.O. Box 1062, T-2
Boulder, CO 80306
(303) 939-5780

P. Bahrami
NASA Ames Research Center
Mail Stop 260-1
Moffett Field, CA 94035
(415) 694-4964

Gary Bailey
Jet Propulsion Laboratory
4800 Oak Grove Drive
Mail Stop 11-116
Pasadena, CA 91109
(818) 354-5786

Robert Baron
Hughes Research Labs
Mail Station RL63
3011 Malibu Canyon Rd.
Malibu, CA 90265
(213) 317-5392

James Baukus
Hughes Research Labs
Mail Station RL63
3011 Malibu Canyon Rd.
Malibu, CA 90265
(213) 317-5336

Eric E. Becklin
Institute for Astronomy
2680 Woodlawn Drive
University of Hawaii
Honolulu, HI 96822
(808) 948-6666

Jeffrey Beeman
Lawrence Berkeley Laboratory
Bldg. 70A, Rm. 3363
One Cyclotron Road
Berkeley, CA 94720
(415) 486-5632

Gary M. Bernstein
Department of Physics
University of California
Berkeley, CA 94720
(415) 642-5721

Paul Besser
Rockwell International Science Center
3370 Miraloma Drive
Anaheim, CA 92803
(714) 762-8751

Giancarlo Bonazzola
Dipartimento Fisica Sperimentale
Via P. Giuria 1
10125 Torino
Italy
39-11-6527373

Mary Bothwell
Jet Propulsion Laboratory
Mail Stop 183-501
4800 Oak Grove Drive
Pasadena, CA 91109
(818) 354-5420

Jesse Bregman
Ames Research Center
Mail Stop 245-6
Moffett Field, CA 94035
(415) 694-6136

George Brims
Joint Astronomy Centre
665 Komohana Street
Hilo, HI 96720
(808) 961-3756

Kenneth Brown
The Aerospace Corporation
P.O. Box 9045
Albuquerque, NM 87119
(505) 844-9963

Michael Burton
NASA Ames Research Center
Mail Stop 245-6
Moffett Field, CA 94035
(415) 694-3118

Richard W. Capps
Jet Propulsion Laboratory
4800 Oak Grove Drive
Mail Stop 303-210
Pasadena, CA 91109
(818) 354-6080

Hao Chen
Department of Physics & Astronomy
University of Rochester
Rochester, NY 14627
(716) 275-5549

Lim Cheung
Grumman Corporate Research Center
Mail Stop A01-026
Bethpage, NY 11714-3580
(516) 346-6565

Vincent Chimelis
5600 Minton Road N.W.
Palm Bay, FL 37907
(407) 723-3100

Y.C. Cho
NASA Ames Research Center
Mail Stop 260-1
Moffett Field, CA 94035
(415) 694-4139

Phil Cizdziel
EG&G Reticon
345 Potrero Avenue
Sunnyvale, CA 94086-4197
(408) 738-4266

Jacqueline Davidson
NASA Ames Research Center
Mail Stop 245-6
Moffett Field, CA 94035
(415) 694-5531

Rudolf Decher
Marshall Space Flight Center
ES-61
Huntsville, AL 35812
(205) 544-7751

Lynne Deutsch
Smithsonian Astrophysical Obs.
60 Garden Street
Mail Stop 10
Cambridge, MA 02138
(617) 495-7158

David Dorn
Ball Aerospace Systems Group
P.O. Box 1062, T-2
Boulder, CO 80306
(303) 939-6739

Lionel Duband
Department of Physics
University of California
Berkeley, CA 94720
(415) 642-6189

W.L. Eisenman
2415 Lozana Road
Del Mar, CA 92014
(619) 481-3586

H. Benton Ellis, Jr.
Ball Aerospace Systems Group
P.O. Box 1062, CO-10B
Boulder, CO 80306
(303) 939-6755

Edwin Erickson
Ames Research Center
Mail Stop 245-6
Moffett Field, CA 94035
(415) 694-5508

John Estrada
NASA Ames Research Center
Mail Stop 244-10
Moffett Field, CA 94035
(415) 694-3192

Audrey J. Ewin
Goddard Space Flight Center
Code 724.3
Greenbelt, MD 20771
(301) 286-5374

Jam Farhoomand
NASA Ames Research Center
Mail Stop 244-10
Moffett Field, CA 94035
(415) 694-3412

Giovanni Fazio
Smithsonian Astrophysical Obs.
60 Garden Street
Mail Stop 65
Cambridge, MA 02138
(617) 495-7458

Robert F. Feitt
Santa Barbara Research Center
75 Coromar Drive
Goleta, CA 93117
(805) 562-4669

Attilio Ferrari
Istituto Fisica Generale
Via P. Giuria 1
I-10125 Torino
Italy
(39) 11-6527457

Richard A. Florence
Rockwell International Science Center
3370 Miraloma Ave.
Anaheim, CA 92803-3105
(714) 762-4553

Fred F. Forbes
NOAO
P.O. Box 26732
Tucson, AZ 85726-6732
(602) 325-9318

W. J. Forrest
Department of Physics & Astronomy
Rochester, NY 14627
(716) 275-4343

A.M. Fowler
NOAO
P.O. Box 26732
Tucson, AZ 85726
(602) 325-9339

Rognvald P. Garden
Department of Physics
University of California, Irvine
Irvine, CA 92717
(714) 856-6280

James D. Garnett
Department of Physics & Astronomy
University of Rochester
Rochester, NY 14627
(716) 275-4389

Rick Gerson
Institute for Space and Terrestrial Science
York University Campus
4759 Keele Street
North York, Ontario M3J lP3 1P3
Canada
(416) 736-5659

F. C. Gillett
National Aeronautics and Space Administration
Code EZ
Washington, DC 20546
(202) 453-1469

David A. Glenar
Goddard Space Flight Center
Code 693.1
Greenbelt, MD 20771
(301) 286-3354

John Goebel
NASA Ames Research Center
Mail Stop 244-10
Moffett Field, CA 94035
(415) 694-3188

Paula Grunthaner
Jet Propulsion Laboratory
Mail Stop 302/231
4800 Oak Grove Drive
Pasadena, CA 91109
(818) 354-0360

Michael R. Haas
NASA Ames Research Center
Mail Stop 245-6
Moffett Field, CA 94035
(415) 694-5511

John A. Hackwell
The Aerospace Corporation M2-266
Box 92957
Los Angeles, CA 90009
(213) 336-6041

Nancy M. Haegel
University of California
Dept. of Materials Science & Eng.
Los Angeles, CA 90024
(213) 825-8590

Donald N.B. Hall
Institute for Astronomy
2680 Woodlawn Drive
Honolulu, HI 96822
(808) 948-8566

Eugene Haller
Lawrence Berkeley Laboratory
University of California
70A/3363
Berkeley, CA 94720
(415) 486-5294

William L. Hansen
Lawrence Berkeley Laboratory
University of California
Berkeley, CA 94720
(415) 486-5632

Lothar Haser
Max-Planck-Institut für Extraterrestrische Physik
8046 Garching
Federal Republic of Germany
089 32 99 1

S. Roland Hawkins
Lockheed Palo Alto Research Lab
3251 Hanover Street
Palo Alto, CA 94304
(415) 424-2230

Kenneth M. Hays
Rockwell International Science Center
3370 Miraloma Ave.
Anaheim, CA 92803
(714) 762-6821

Mark Hereld
University of Chicago
Astronomy and Astrophysics
5640 S. Ellis Ave.
Chicago, IL 60637
(312) 702-9746

Terry L. Herter
Department of Astronomy
Space Sciences Building
Ithaca, NY 14853
(607) 255-5898

Michele Hinnrichs
Pacific Advanced Systems
P.O. Box 679
Solvang, CA 93463
(805) 688-2088

Klaus W. Hodapp
Institute for Astronomy
2680 Woodlawn Drive
Honolulu, HI 96822
(808) 948-8968

Alan W. Hoffman
Santa Barbara Research Center
75 Coromar Drive
Goleta, CA 93117
(805) 562-2230

A. Hollinger
Institute for Space and Terrestrial Science
4850 Keele Street
North York, Ontario, Canada
M3J 1P3
(416) 736-5305

William J. Hornaday
Jet Propulsion Laboratory 300-149
4800 Oak Grove Drive
Pasadena, CA 91109
(818) 354-4964

William B. Hornback
Grumman Space Systems
2852 Kelvin Avenue
Irvine, CA 92714
(714) 756-7011

J.E. Huffman
Rockwell International Science Center
3370 Miraloma Ave.
Anaheim, CA 92803
(714) 762-4011

Garth Illingworth
Lick Observatory
University of California
Santa Cruz, CA 95064
(408) 429-2843

Ev Irwin
Institute for Astronomy
2680 Woodlawn Drive
Honolulu, HI 96822
(808) 948-8580

Ken B. Jarratt
Calspan Corporation
AEDC Operations/640
Arnold AFB, TN 37389
(615) 454-3739

T.S. (Jay) Jayadev
Lockheed Research Labs
3251 Hanover Street
Palo Alto, CA 94304-1191
(415) 424-2278

Richard Joyce
NOAO/Kitt Peak National Observatory
Box 26732
Tucson, AZ 85726-6732
(602) 325-9323

Frank A. Junga
Lockheed Research Lab
MS 97/40-2
3251 Hanover Street
Palo Alto, CA 94304
(415) 424-2227

Reinhard Katterloher
Max-Planck-Institut für Extraterrestrische Physik
8046 Garching
Federal Republic of Germany
089 32 99 1

Peter Kittel
NASA Ames Research Center
Mail Stop 244-10
Moffett Field, CA 94035
(415) 694-4297

Michael K. Kiya
SKW, Inc.
1901 N. Moore St., Suite 1204
Arlington, VA 22209
(703) 243-3888

William Kleinhans
Valley Oak Semiconductor, Inc.
31255 Cedar Valley Drive
Westlake Village, CA 91362
(818) 707-4223

David C. Koo
Lick Observatory, NS2
University of California
Santa Cruz, CA 95064
(408) 429-2130

Dennis Korte
Hughes Aircraft Co.
6155 El Camino Real
B743/630
Carlsbad, CA 92009
(619) 931-3052

Timothy Krabach
Jet Propulsion Laboratory
300-149
4800 Oak Grove Drive
Pasadena, CA 91109
(818) 354-0884

G. Kuhr
Hughes Aircraft Co.
P.O. Box 902
E55/G222
El Segundo, CA 90245
(213) 616-8926

Richard Landee
Hughes Aircraft Company
P.O. Box 902
Mail Station E1/F148
El Segundo, CA 90245
(213) 616-6778

Andrew Lange
Department of Physics
University of California
Berkeley, CA 94720
(415) 642-6577

George Lee
NASA Ames Research Center
Mail Stop 227-5
Moffett Field, CA 94035
(415) 694-5877

Lewis Leibowitz
Lockheed Missiles & Space Co.
O51-9, B554
1111 Lockheed Way
Sunnyvale, CA 94088
(408) 742-4229

Claire LeNaour
Laboratoire de Physique des Solides
I.N.S.A.
Avenue de Rangueil
31077 Toulouse-Cedex
France
61 55 95 13

Jean Léotin
Laboratoire de Physique des Solides
I.N.S.A.
Avenue de Rangueil
31077 Toulouse-Cedex
France
61 55 95 13

Larry Lesyna
Grumman Corporate Research Center
Mail Stop A01-26
Bethpage, NY 11714
(516) 575-0806

Paul LeVan
OPC
Air Force Geophysics Laboratory
Hanscom AFB, MA 01731
(617) 377-4550

Franco Lisi
Osservatorio Astrofisico di Arcetri
Largo E. Fermi 5
50125 Firenze
Italy
001 39 55 2752289

J.K. Little
NOAO
P.O. Box 26732
Tucson, AZ 85726
(602) 325-9239

Larry Lloyd
Nichols Research Corporation
2201 Buena Vista S.E.
Suite 203
Albuquerque, NM 87106
(505) 843-7364

F. J. Low
Steward Observatory
University of Arizona
Tucson, AZ 85721
(602) 621-2727

John B. Lugten
Institute for Astronomy
2680 Woodlawn Drive
Honolulu, HI 96822
(808) 948-6795

Willem Luinge
Laboratory for Space Research
P.O. Box 800
9700 AV Groningen
The Netherlands
(31) 50634022

Paul N. Luke
Lawrence Berkeley Lab
University of California
70A/3363
Berkeley, CA 94720
(415) 486-5632

Joseph Maserjian
Jet Propulsion Laboratory
Mail Stop 302/306
4800 Oak Grove Drive
Pasadena, CA 91109
(818) 354-3801

Keith Matthews
CalTech
Mail Stop 320-47
Pasadena, CA 91125
(818) 356-4261

Mark McCaughrean
Goddard Space Flight Center
Code 685.0
Greenbelt, MD 20771
(301) 286-5801

Craig McCreight
NASA Ames Research Center
Mail Stop 244-10
Moffett Field, CA 94035
(415) 694-6549

Donald G. McDonald
National Institute of Standards and Technology
325 S. Broadway
Boulder, CO 80303-3328
(303) 497-5113

Mark McKelvey
NASA Ames Research Center
Mail Stop 244-10
Moffett Field, CA 94035
(415) 694-3196

Darrell McKibbin
NASA Ames Research Center
Mail Stop 244-10
Moffett Field, CA 94035
(415) 694-3173

Ian S. McLean
Joint Astronomy Centre
665 Komohana St.
Hilo, HI 96720
(808) 961-3756

Robert E. McMurray, Jr.
NASA Ames Research Center
Mail Stop 244-10
Moffett Field, CA 94035
(415) 694-3179

Leo Metcalfe
ESA/ESTEC
Postbus 299
2200 AG Noordwijk
The Netherlands
31 1719 83623

David Morrison
Ames Research Center
Mail Stop 245-1
Moffett Field, CA 94035
(415) 694-5028

David Murphy
Departement de Physique
C.P. 6128, Succ. A.
Université de Montréal
Montréal, Québec, Canada H3C 3J7
(514) 343-5927

Daniel Nadeau
Departement de Physique
C.P. 6128, Succ. A.
Université de Montréal
Montréal, Québec, Canada H3C 3J7
(514) 343-6676

P.S. Nayar
Hughes Aircraft, EDSG
E54/F255
P.O. Box 902
El Segundo, CA 90245
(213) 607-7689

Curtiss A. Niblack
Cincinnati Electronics Corp.
7500 Innovation Way
Mason, OH 45040
(513) 573-6238

Zoran Ninkov
S. R. L.
Box 1650
Salisbury, S.A. 5108
Australia
61 8 2595555

Ira G. Nolt
Langley Research Center
Mail Stop 474
Hampton, VA 23665
(804) 865-3761

Michael C. Peck
University of California
Space Sciences Laboratory
Berkeley, CA 94720
(415) 642-8494

J. L. Pipher
Department of Physics & Astronomy
University of Rochester
Rochester, NY 14627
(716) 275-4343

Richard Puetter
C-011, CASS
University of California
San Diego, CA 92093
(619) 535-4945

James V. Radostitz
Langley Research Center
Mail Stop 474
Hampton, VA 23665
(804) 865-3761

Boris Ragent
NASA Ames Research Center
Mail Stop 245-1
Moffett Field, CA 94035
(415) 694-5514

Rodolfo Ramos
HQ AFSTC/SWS
Kirtland AFB, NM 87117-6008
(505) 846-4964

David M. Randall
Santa Barbara Research Center
Goleta, CA 93117
(805) 562-2816

Robert W. Rasche
Steward Observatory
University of Arizona
Tucson, AZ 85721
(602) 621-6617

John Rayner
Institute for Astronomy
2680 Woodlawn Drive
Honolulu, HI 96822
(808) 948-6235

Harold Reitsema
Ball Aerospace Systems Group
Box 1062
Boulder, CO 80306-1062
(303) 939-5026

Dennis C. Reuter
Goddard Space Flight Center
Code 693.1
Greenbelt, MD 20771
(301) 286-2042

Paul L. Richards
Department of Physics
University of California
Berkeley, CA 94720
(415) 642-3027

Marcia J. Rieke
Steward Observatory
University of Arizona
Tucson, AZ 85721
(602) 621-2731

George Rieke
Steward Observatory
University of Arizona
Tucson, AZ 85721
(602) 621-2832

Donald W. Ritchie
Jet Propulsion Laboratory
Mail Stop 303-210H
4800 Oak Grove Drive
Pasadena, CA 91109
(818) 393-6204

Lloyd Robinson
Lick Observatory
University of California
Santa Cruz, CA 95064
(408) 429-2790

Thomas L. Roellig
Ames Research Center
Mail Stop 245-6
Moffett Field, CA 94035
(415) 694-6426

Neil Rowlands
Cornell University
206 Space Sciences Building
Ithaca, NY 14853
(607) 255-4083

Ray W. Russell
The Aerospace Corporation
Mail Stop M2-266
P.O. Box 92957
Los Angeles, CA 90009
(213) 336-5528

Richard L. Ryan
Ryan Associates, Inc.
516 Edgewater Drive
Wakefield, MA 01880
(617) 245-3910

Alberto Salama
ESA/ESTEC
Postbus 299
2200 AG Noordwijk
The Netherlands
31 1719 83623

Virendra Sarohia
Jet Propulsion Laboratory
180-604
4800 Oak Grove Drive
Pasadena, CA 91109
(818) 354-6758

Shinju Sato
Department of Physics
Nagoya University
Chikusa-Ku
Nagoya 464 Japan

Joseph E. Sauvageau
National Institute of Standards and Technology
325 Broadway
Boulder, CO 80303-3328
(303) 497-3770

Maureen Savage
NASA Ames Research Center
Mail Stop 245-6
Moffett Field, CA 94035
(415) 694-5537

Kirk Seaman
Jet Propulsion Laboratory
4800 Oak Grove Drive
Pasadena, CA 91109
(818) 354-9655

D. H. Scib
Rockwell International Science Center
3370 Miraloma Avenue
P.O. Box 3105
Anaheim, CA 92803
(714) 762-0953

Carol E. Selvey
The Aerospace Corporation
P.O. Box 92957
Mail Station M1-109
Los Angeles, CA 90009-2957
(213) 336-4199

Kandiah Shivanandan
Naval Research Laboratory
Space Science Division
Code 4138S
Washington, DC 20375
(202) 767-2749

Mark Shure
Institute for Astronomy
2680 Woodlawn Drive
Honolulu, HI 96822
(808) 948-6173

François Sibille
Observatoire de Lyon
69230 Saint Genis Laval
France
(33) 72399092

Robert G. Smith
Department of Physics
University of California
Irvine, CA 92717
(714) 856-8480

Christopher E. Solan
HQ AFSTC/SWS
Kirkland AFB, NM 87117
(505) 846-4964

Gordon J. Stacey
Department of Physics
University of California
Berkeley, CA 94720
(415) 642-0375

Craig Staller
Jet Propulsion Laboratory
Mail Stop 300-149
4800 Oak Grove Drive
Pasadena, CA 91109
(818) 354-0149

Maryn G. Stapelbroek
Rockwell International Science Center
3370 Miraloma Avenue
Anaheim, CA 92803-3105
(714) 762-4528

James Stobie
Honeywell Electro-Optics Division
2 Forbes Rd.
Lexington, MA 02173
(617) 863-3075

Donald Strecker
Ball Aerospace Systems Group
Box 1062
Boulder, CO 80306-1062
(303) 939-4346

Richard S. Taylor
Smithsonian Astrophysical Obs.
60 Garden Street
Mail Stop 65
Cambridge, MA 02138
(617) 495-7246

Rodger I. Thompson
Steward Observatory
University of Arizona
Tucson, AZ 85721
(602) 621-6527

Peter Timbie
Department of Physics
University of California
Berkeley, CA 94720
(415) 642-8923

Harold A. Timlin
Cincinatti Electronics Corp.
7500 Innovation Way
Mason, OH 45040
(513) 573-6269

Alan T. Tokunaga
Institute for Astronomy
2680 Woodlawn Drive
Honolulu, HI 96822
(808) 948-6691

Eric Tollestrup
Department of Astronomy
University of Texas
Austin, TX 78712
(512) 471-1496

Douglas Toomey
Institute for Astronomy
University of Hawaii
2680 Woodlawn Drive
Honolulu, HI 96822
(808) 948-8534

G. Wayne Van Citters
Division of Astronomical Sciences
National Science Foundation
1800 G. Street N.W.
Washington, DC 20550
(202) 357-9793

John Venzon
Hughes Aircraft Company
6155 El Camino Real
Carlsbad, CA 92009
(619) 931-3075

Kadri Vural
Rockwell International Science Center
1049 Camino Dos Rios
Thousand Oaks, CA 91360
(805) 373-4448

Richard Wade
Royal Observatory
Blackford Hill
Edinburgh EH16 3HJ
Scotland
031 667 3321

Richard Wainscoat
NASA Ames Reserach Center
Mail Stop 245-6
Moffett Field, CA 94035
(415) 694-4217

Russell G. Walker
Jamieson Science and Engineering
5321 Scotts Valley Drive
Suite 204
Scotts Valley, CA 95066
(408) 438-7233

Robert E. Warren
Hughes Aircraft Company
2000 E. El Segundo Blvd.
EO E54 F204
El Segundo, CA 90245
(213) 616-9530

D. M. Watson
Department of Physics & Astronomy
University of Rochester
Rochester, NY 14627
(716) 275-8576

Ted Weber
NASA Ames Research Center
Mail Stop 244-10
Moffett Field, CA 94035
(415) 694-3189

Daniel Weedman
Pennsylvania State University
525 Davey Lab
University Park, PA 16802
(814) 865-0418

Michael Werner
NASA Ames Research Center
Mail Stop 245-6
Moffett Field, CA 94035
(415) 694-5101

Raymond L. Whitney
Lockheed Palo Alto Research Labs
O/97-40 B202
3251 Hanover Street
Palo Alto, CA 94304
(415) 354-5594

Thomas E. Whittemore
Lockheed Palo Alto Research Labs
O/97-40 B202
3251 Hanover Street
Palo Alto, CA 94302
(415) 354-5266

Thor Wilbanks
Physics Department
University of California
Berkeley, CA 94720
(415) 642-6189

George M. Williams
Photon Research Associates, Inc.
1033 Massachusetts Avenue
Cambridge, MA 02138
(617) 354-1522

Steven P. Willner
Smithsonian Astrophysical Obs.
60 Garden Street
Cambridge, MA 02138
(617) 495-7123

James T. Wimmers
Cincinatti Electronics Corp.
7500 Innovation Way
Mason, OH 45040
(513) 573-6230

Warren Winovich
NASA Ames Research Center
Mail Stop 229-4
Moffett Field, CA 94035
(415) 694-5268

Fred C. Witteborn
Ames Research Center
Mail Stop 245-6
Moffett Field, CA 94035
(415) 694-5520

Jürgen Wolf
Max-Planck-Institut für Astronomie
Königstuhl 17
6900 Heidelberg
Federal Republic of Germany
49 6221 528 262

Diane Wooden
Ames Research Center
Mail Stop 245-6
Moffett Field, CA 94035
(415) 694-6151

James Woolaway
Amber Engineering, Inc.
5756 Thornwood Drive
Goleta, CA 93117-3802
(805) 683-6621

Helen Yang
Nichols Research Corp.
1901 Dove Street
Newport Beach, CA 92660
(714) 476-0800

James F. Yee
Aerojet ElectroSystems Company
P.O. Box 296
Azusa, CA 91702
(818) 812-2839

Erick T. Young
Steward Observatory
University of Arizona
Tucson, AZ 85721
(602) 621-4119

N90-21314

REQUIREMENTS OF IR SPACE ASTRONOMY

Frank J. Low
University of Arizona

The requirements of Infrared Space Astronomy, like the science itself, are rapidly evolving. This series of Infrared Detector Technology Workshops at the NASA Ames Research Center allows us to trace a critical part of this evolutionary process, by creating a written record, and, at the same time, give us an invaluable opportunity to exchange knowledge, results and new ideas in a timely manner so that progress can occur even more rapidly. In this spirit, the following comments are directed as much at the goals as at establishing requirements. Of course, we all know the difference between the two: when we meet our requirements we are justifiably satisfied, when we meet our goals we are elated.

One way to establish new requirements and goals is to examine those of the past. Indeed, there is now a record of past, present and future IR Space Astronomy missions and it is instructive to examine them in this respect, as in the following table.

Table 1. DETECTORS USED IN IR SPACE MISSIONS

MISSION	DATE	DETECTOR TYPES	SPECTRAL COVERAGE	NUMBER DETECTORS
IRAS	1983	Si,Ge	8-120 um	62
COBE	1989	InSb,Si,Ge, Bolometers	3->1000 um	>50
ISO	1993	InSb,Si,Ge, Stressed Ge	2-200 um	>2K
NICMOS	1995	HgCdTe	1-3 um	500K
SIRTF	1998	*.*	2-750 um	?

At the time of this workshop, the first three major missions listed above are past the stage of reaching for goals and have well established requirements. The fourth mission, NICMOS, is relatively new but is operating on a fast schedule since it is part of an ongoing project, the Hubble Space Telescope; therefore, NICMOS too has well established, though ambitious, requirements. It is the last mission on this list, SIRTF, that is far enough in the future that we can still realistically consider what the goals are and how they will lead to the mission requirements. It is for this reason that much of this workshop will be devoted to topics most closely related to the SIRTF mission.

The top level goals of SIRTF for its imaging arrays are easily stated, given that the wavelength coverage is established at 2 to 750 um and the unvignetted field of view is 7 arcmin.

- **The field should be fully utilized at each wavelength.**
- **Diffraction should be critically sampled.**
- **Each detector should be background limited.**

The sources of natural background emission in the vicinity of Earth are now reasonably well established and can be used to make useful predictions of photon fluxes for each detector type. This task is beyond the scope of this brief introduction, however, Figure 1 shows the four principle sources of cosmic background sources that limit the performance of the SIRTF instruments. Of special note are the two deep minima in the background levels near 4 and 300 microns. These two "cosmic windows" offer exciting opportunities to explore the early universe since the expansion of the universe redshifts much of the radiation into these parts of the spectrum and because the highest sensitivity is possible within spectral bands centered on these wavelengths. Clearly, detector technologies that allow this great potential of space based telescopes to be realized are those that will be pursued most eagerly.

Finally, it is imperative that very large arrays be developed that meet these sensitivity goals so

that the first two goals may also be satisfied. Of course there is no overriding reason why both of these goals must be met at every wavelength simultaneously; in some cases it may be necessary to use smaller arrays of diffraction limited pixels to sample only part of the available field of view while designing the instrument so that larger arrays, with less sensitivity, can be used to cover the entire field. In this case, the instrument is more complicated and the science return may suffer by some acceptable amount. One of the many benefits of this workshop will be that new results will be presented in a timely manner so that better informed judgments on issues of this type will be possible.

Table 2 is included here to stimulate discussion along these lines. For each octave of the spectrum, the number of pixels required to span the SIRTF field-of-view, assuming a square array geometry, is given in the second column. Arrays of this size would meet the first two goals. In the last column, the results in the second column are translated into a set of requirements for array dimensions that approximate these goals. As a result of this workshop it will be possible to judge which technologies will soon emerge to satisfy these requirements.

Table 2. SIRTF ARRAY DIMENSIONS

LAMBDA (um)	LAMBDA/2D (pixels)	5X5 ARCMIN ARRAY
2	1200	
4	600	512x512
8	300	256x256
16	150	
32	75	64x64
64	36	32x32
128	18	
256	9	8x8
512	5	4x4

COSMIC BACKGROUND

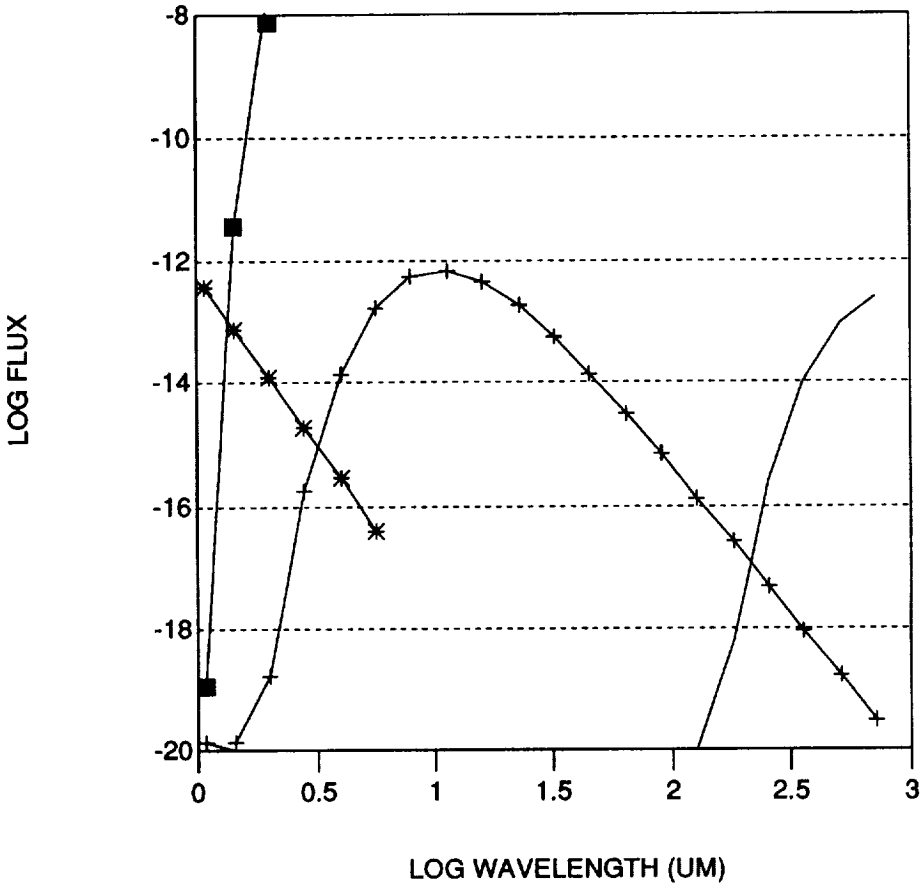

Figure 1. The 4 sources of IR background are: (1) solid squares, ambient temperature emission at an emissivity of 0.05 characteristic of uncooled telescopes such as HST, (2) asterisks, zodiacal light, (3) plus signs, zodiacal emission and (4) solid line, the 2.7 K cosmic background from the early universe. Note the 2 deep minima at 4 and 300 microns.

IR Detector Technology Workshop
Feb. 7 – 9, 1989
NASA Ames Research Center

Stressed Ge:Ga Photoconductors for Space–Based Astronomy

(Is There Life Beyond 120 μm?)

J.W. Beeman	Lawrence Berkeley Laboratory
E.E. Haller	U. C. Berkeley and Lawrence Berkeley Laboratory
W.L. Hansen	Lawrence Berkeley Laboratory
P.N. Luke	Lawrence Berkeley Laboratory
P.L. Richards	U. C. Berkeley and Lawrence Berkeley Laboratory

INTRODUCTION

- material changes & wavelength shift

- stress aparatus considerations

AMOUNT OF STRESS

- measurement of applied stress

- determining the correct amount

STRESSED DETECTORS IN SPACE

- materials for low dark currents

- responsivity and NEP

- remaining problems

CONCLUSIONS

STRESSED Ge:Ga

- stress along [100] axis strains chemical bonds in lattice
- reduces binding energy of holes
- detector becomes sensitive to lower energy photons

STRESS CAVITY

CROSS SECTION

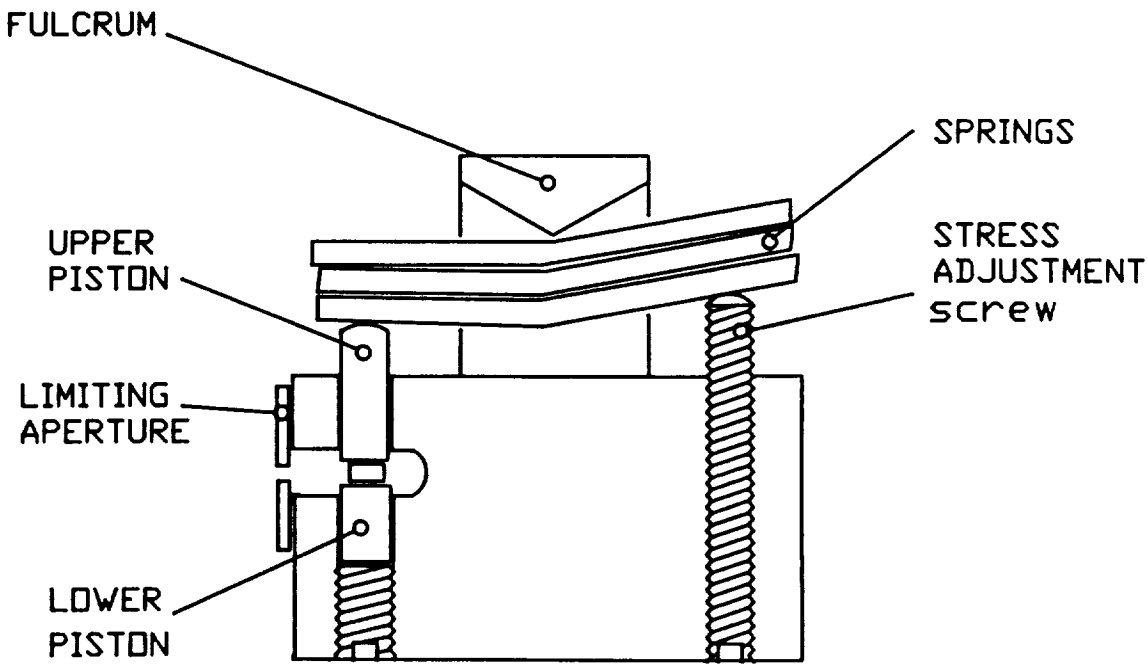

STRESSED DETECTOR

MOUNTING DETAILS

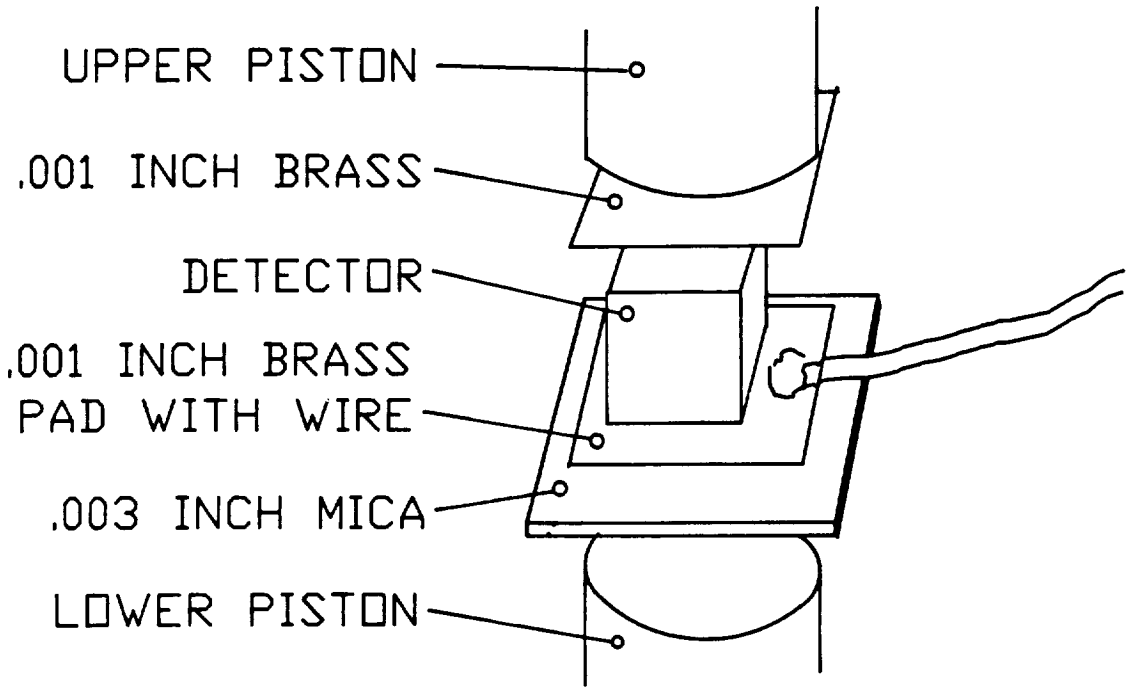

SPRING-TYPE STRESS CAVITY

- a "large" spring deflection minimizes stress changes on cooling

- no torque is applied to chip... all stress is on-axis

- reflecting cavity with limiting aperture accommodates easy photon flux calculations

MOUNTING HARDWARE

- brass pads deform to aid in stress uniformity, but do not over-extrude

- mica pad ensures electrical isolation from cavity

    * high compressional resilience, does not deform

    * highly planar: keeps stress on-axis

AMOUNT OF STRESS

- the mobility of carriers increases with stress, therefore we need only monitor the detector's room temperature resistance to measure the applied stress

- the hole binding energy is an inverse function of stress. The minimum binding energy is approached asymptotically

- when the detector's room temperature resistance is reduced to 40% of its unstressed value, we have attained >90% of the possible binding energy reduction

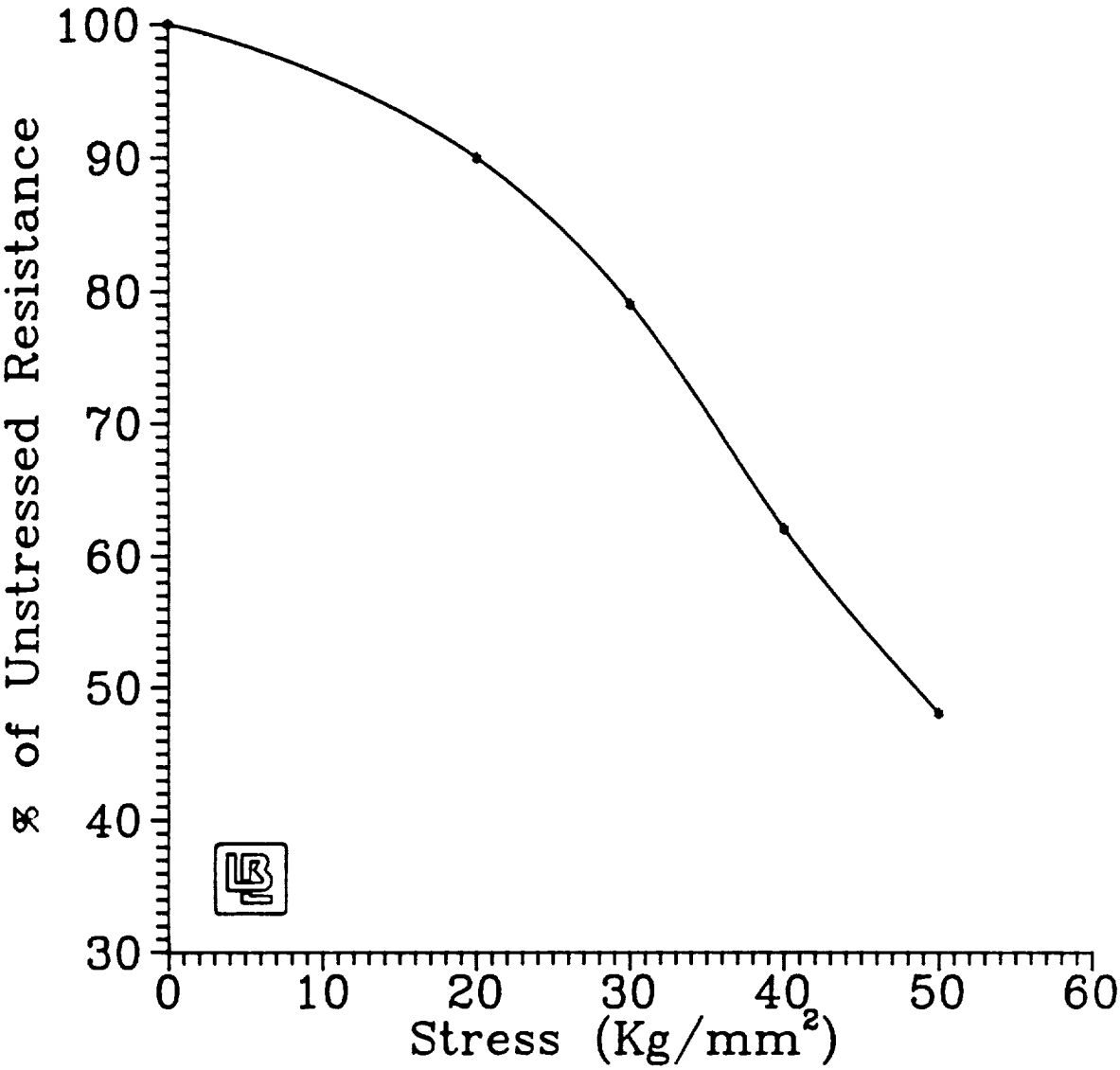

The change in resistance of Ge:Ga (100) as a function of stress (room temperature)

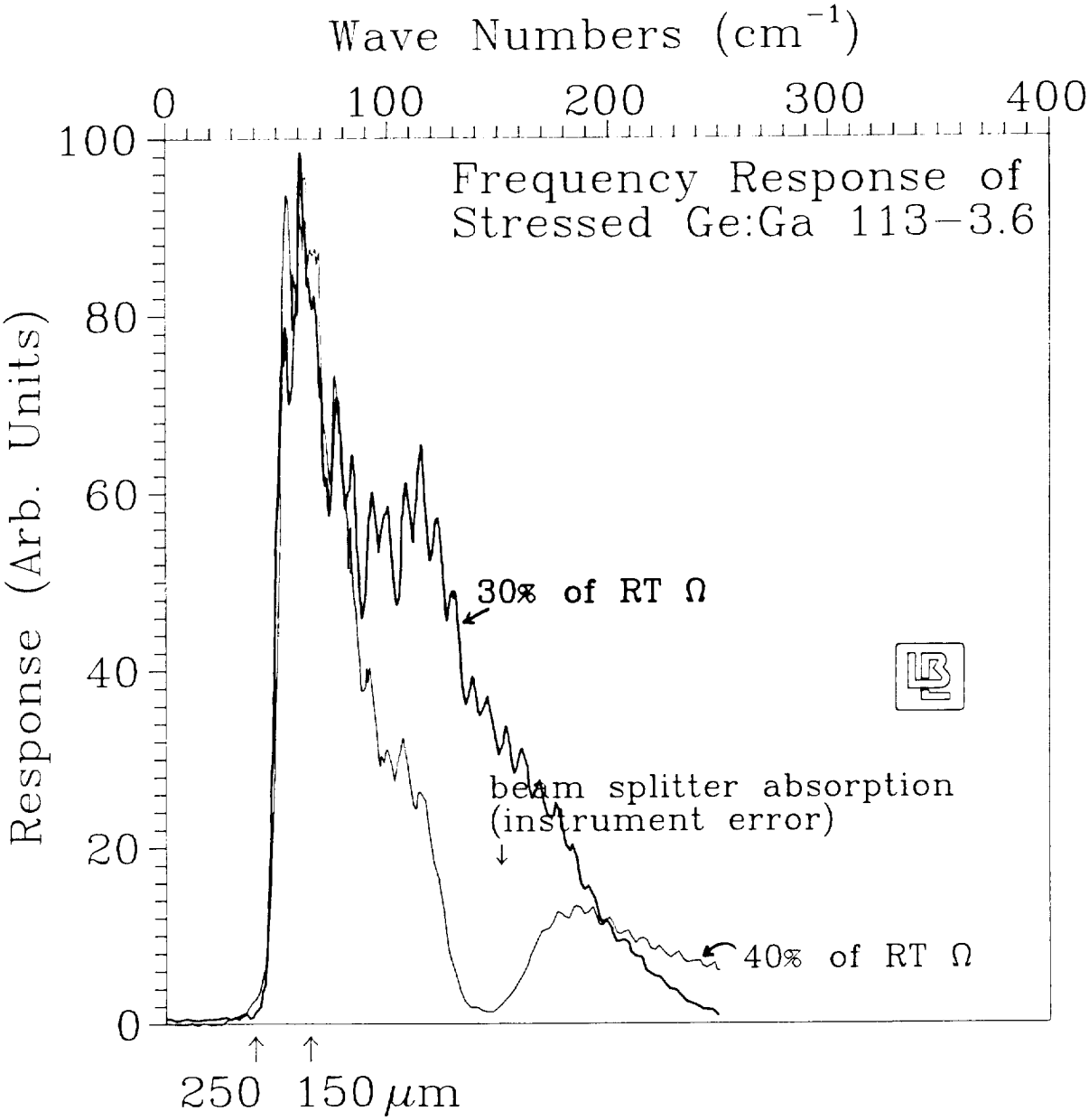

Detector response as a function of wavelength. Long wavelength extension saturates at 40% RT Ω. Additional stress (30% curve) does not further extend long wavelength response.

MATERIALS PARAMETERS AFFECTING DARK CURRENT

- higher compensation material has more hole traps which reduces carrier lifetime, and should, in turn, lead to devices with lower dark current
  this is not observed

- detectors exhibiting low dark currents were made from boules with a low occurrence of crystalline imperfections (dislocations)

- we have grown a series of dislocation-free materials to further study this correlation

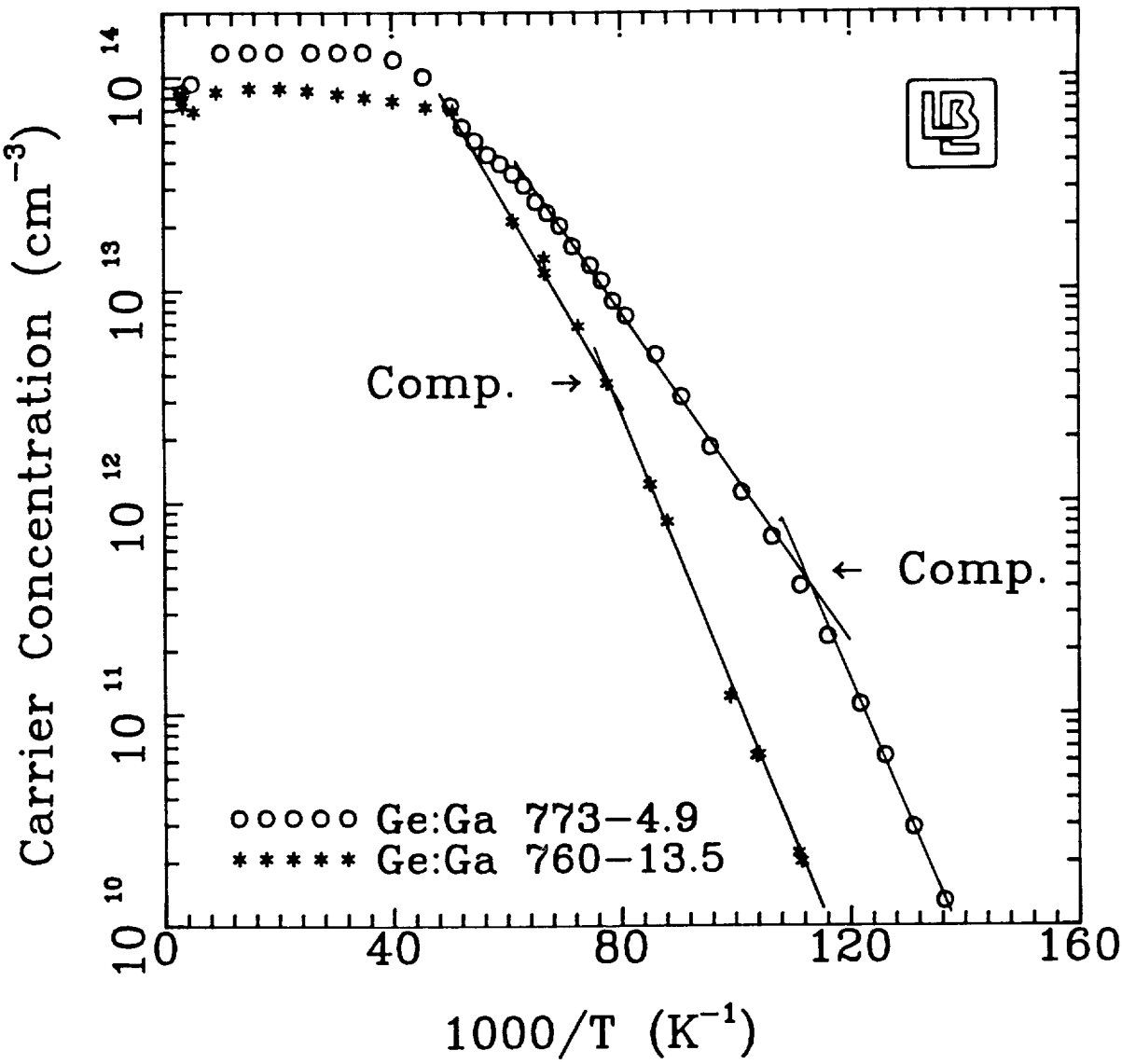

Hall effect of two Ge:Ga samples.
The 760 material is much more highly compensated than the 773 material

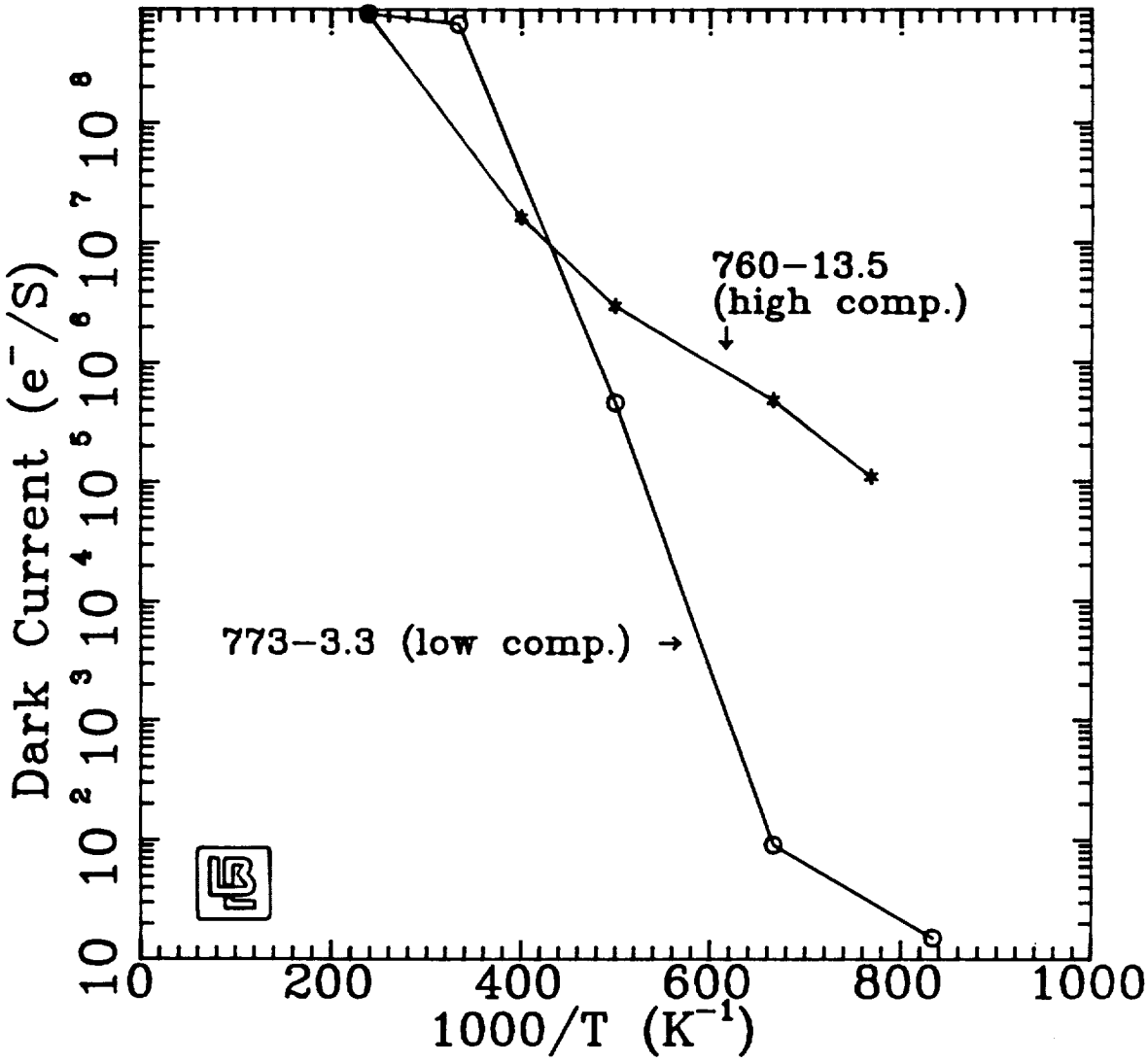

Freeze–out of two stressed detectors. Unlike unstressed Ge:Ga, high compensation does not necessarily reduce dark current.

BEHAVIOR OF LOW DARK CURRENT STRESSED Ge:Ga

- dislocation-free device 773-3.3 shows favorable responsivity and NEP when tested with transimpedance amplifiers

- detective quantum efficiency is approximately 9%

- should be able to reach background-limited performance with integrating amplifiers

- low operating bias voltage: breakdown field is approximately 50 mV/mm

- dark current is a strong function of bias

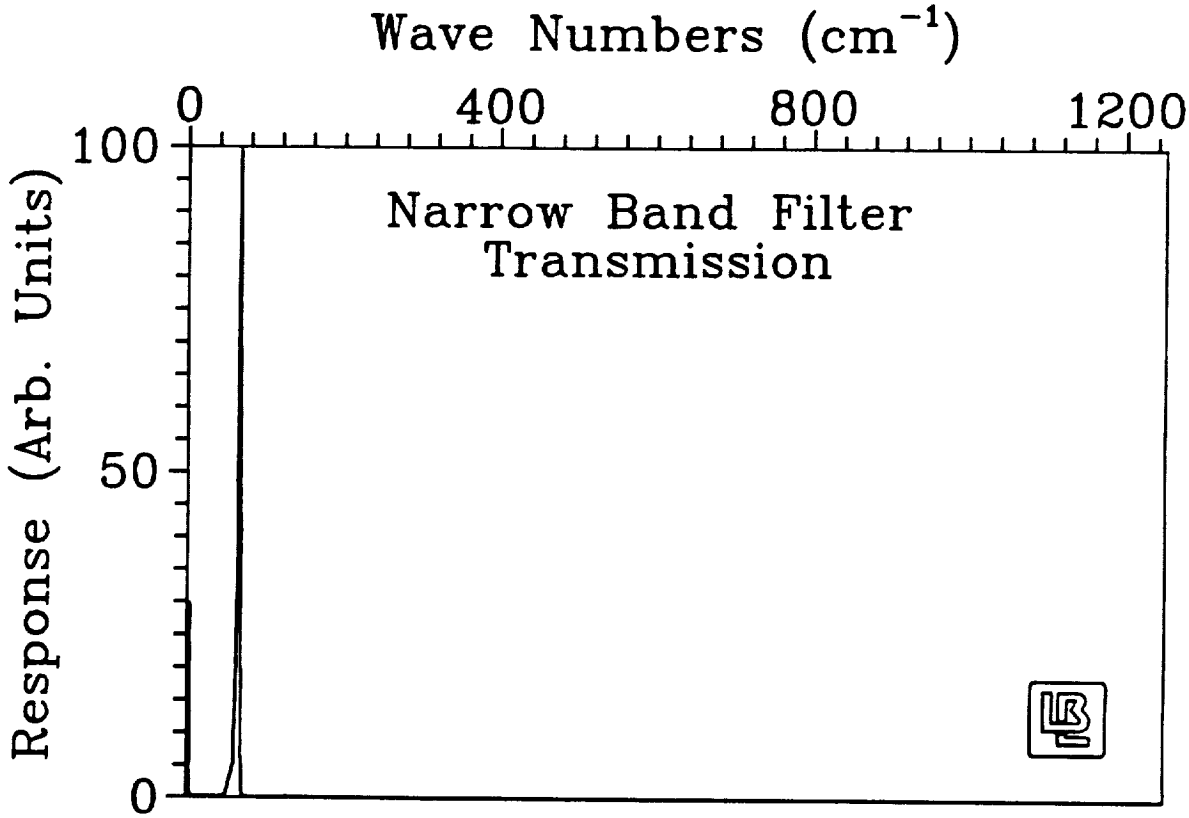

- 163 μm Peak Transmission
- 5.84 X 10^{-14} W Peak to Peak Signal
  (4.81 X 10^{7} Photons/Sec.)
- 2.66 X 10^{-14} W RMS Signal

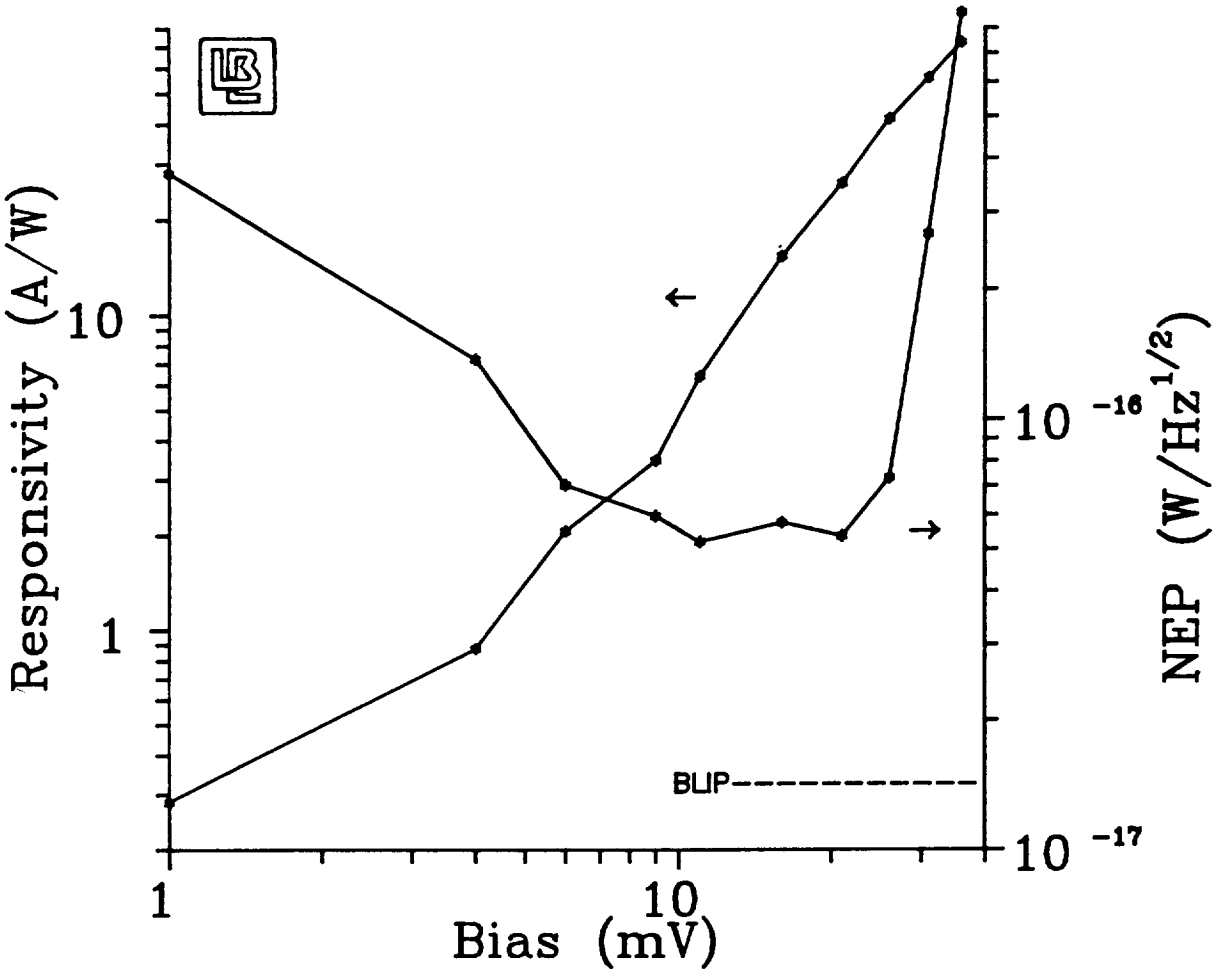

Responsivity and NEP of 773–3.3, dislocation–free Ge:Ga stressed detector. Conditions = TIA mode, $f_{chopper}$ = 23 Hz, 1.3K, stressed to 40% of room temperature resistance.

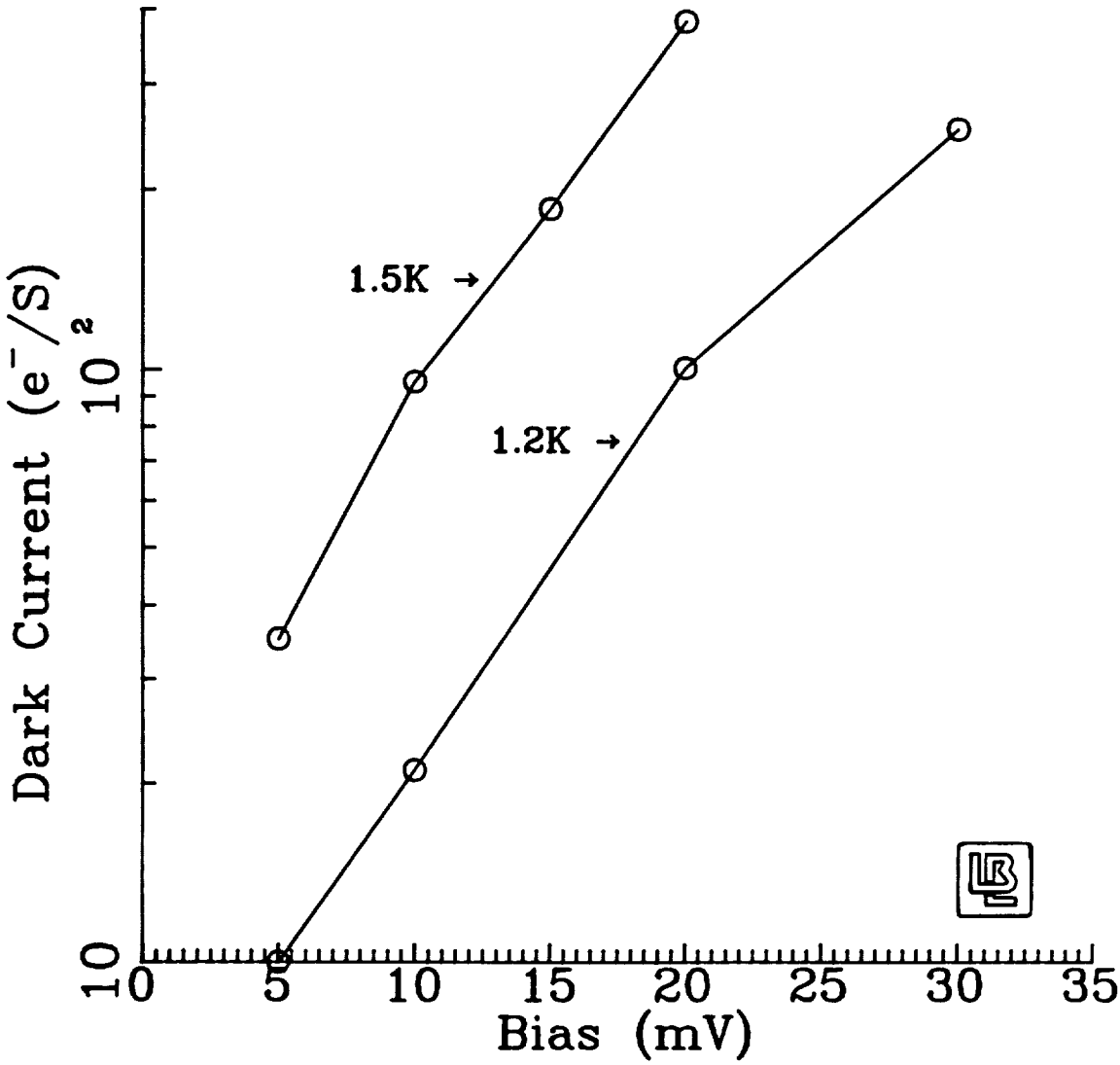

Dark current vs Bias for stressed Ge:Ga 773–3.3. Conditions = 0.5 X 1 X 1 mm chip, (1 mm interelectrode distance), results are the average of two independant tests.

PROBLEMS

- "cold" operation (1.5K or less) is required
- array construction is more complicated than with unstressed detectors
- low bias voltage may result in greater frequency of integrating amp resets
- ionizing radiation effects are similar to other photoconductor materials

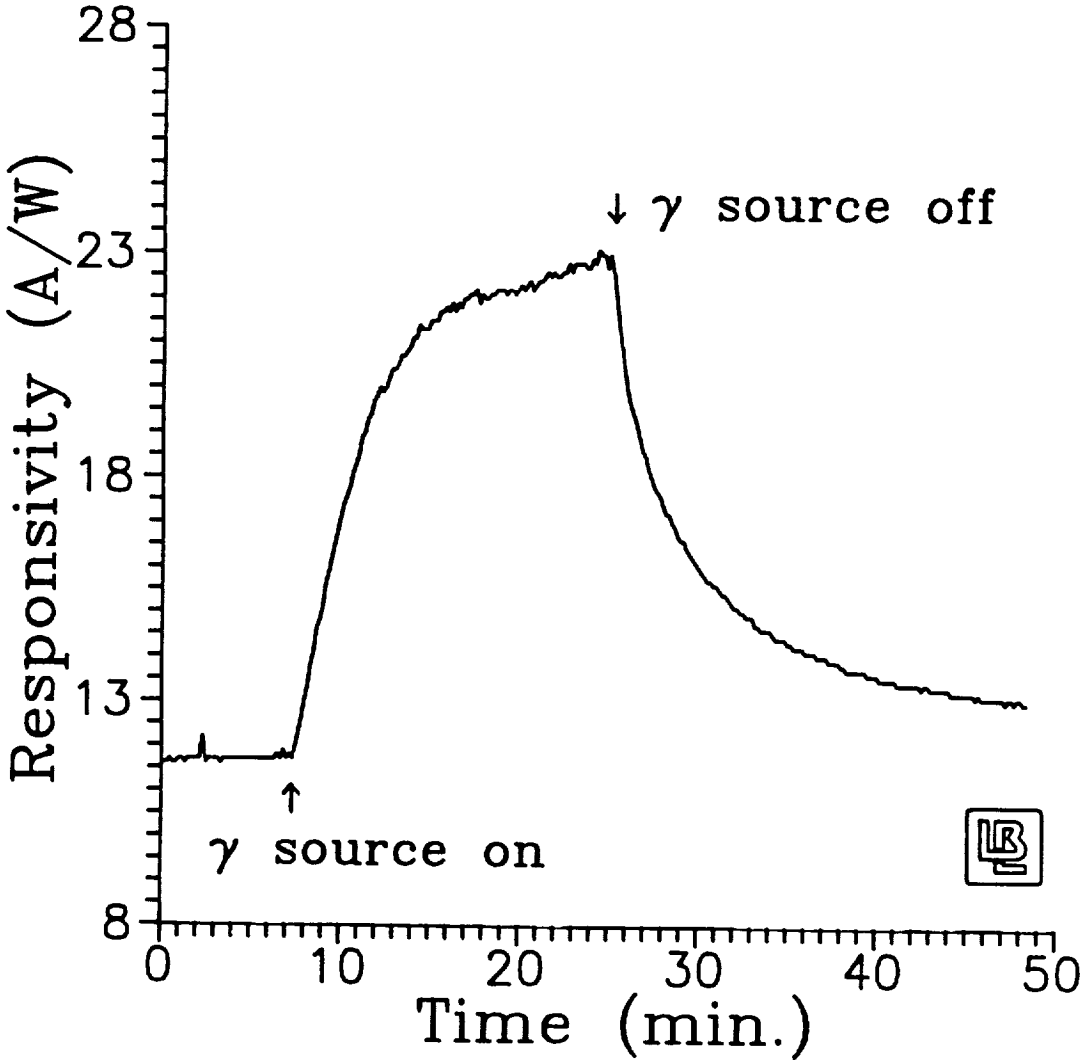

Effect of ionizing radiation on stressed Ge:Ga 773–3.3 (approx. 40 counts/sec. 60 KV γ)

CONCLUSIONS

- detectors exist today for background-limited detection at 200 microns

- we are "narrowing in" on the significant parameters that effect dark current in stressed photoconductors. These findings may apply to other photoconductor materials

- need some "creative problem solving" for an ionizing radiation effect reset mechanism

Near Contact Phenomena and Transient Effects in Far Infrared Photoconductors

Nancy M. Haegel

Department of Materials Science and Engineering
School of Engineering and Applied Science
University of California, Los Angeles

Abstract

This presentation summarizes a combination of experimental and modeling work in two areas: first, the calculation of excess free carrier and space charge distributions near contacts and their effects on device resistivity, and second, the characterization of a slow transient response ($\tau \sim 1$ sec) in Ge:Be detectors which is due to trapping associated with Be^+ formation. In both cases, analytical models, based on continuity and rate equations, have been developed to enable the application of these findings to a wide variety of photoconductor materials.

I. Near-contact Behavior

The goal of this work was to model the distribution of excess free carriers and space charge in the bulk material immediately adjacent to a heavily doped contact region. Figure 1 shows schematically the distribution of free holes (p), ionized acceptors (N_A^-), electric field (E) and potential (V) that might be expected as a result of the diffusion of carriers due to the concentration gradient and the resultant space charge. The object of the modeling was to determine the exact extent and shape of the space charge region, as a function of material parameters such as doping, compensation and mobility. Several attempts have previously been made to solve this problem using numerical modeling, but diffusion in both cases was neglected in the space charge region (1,2). This is not a good assumption, because the diffusion current plays a significant role in the near-contact region.

A complete numerical solution, including both diffusion and drift components to the current, has recently been completed (3), and this presentation is a summary of that work. Readers are referred to the publication for a complete discussion of the problem. The distributions of free holes (for p-type material), ionized acceptors and electric field are calculated by combining the continuity equation, Poisson's equation and the current equation. The continuity equation, for the steady state, can be expressed as

$$\mu pE' + \mu p'E + D\,p'' = 0 \qquad (1)$$

where μ is the mobility of the free carriers, D is the diffusion coefficient and the derivatives represent spatial derivatives in one dimension. Since Poisson's equation and the current equation can be used to express E and E' as a function of p, the final equation to be solved is a second order differential equation in p. This has been solved using a finite difference technique (4). In this work, we have used low field approximations and have not included the dependence of capture cross section on electric field or the effects of velocity saturation. These are valid assumptions for the low fields at which Ge detectors are usually operated.

The modeling parameters for this work are those appropriate for p-type Ge:Ga photoconductors operated under low photon backgrounds at 3.0 K. The boundary condition on both sides was taken as a thin region (L = 0.25 μm) with an excess hole concentration of 10^{16}-10^{18} cm^{-3}.

Solutions as a function of device thickness are shown in Figure 2 for a 10 μm and 25 μm thick layer of material with a contact at either side. In Figure 3, the effect of bias, on a 100 μm thick layer, is shown. The results are for material with a Ga concentration of 2 x 10^{14} cm^{-3}, with a compensating donor concentration of 10^{11} cm^{-3}. One sees that for the very thin layers, the resistivity of the device would be dominated by contact effects, since the hole concentration is determined by diffusion from the contact. Bulk resistivity values would not be obtained in an I-V measurement of this type of structure. For the common thicknesses for current detectors, however, ($t \geq 0.5$ mm) the contact should not have a significant effect on the I-V characteristic.

In Figure 4, the effect of varying the compensating donor concentration is seen. The space charge region will extend much farther as the compensation ratio is decreased. Thus, one would predict a contact effect on measured resistivity for thickness less than 200 μm for lightly compensated material with $N_D = 10$ cm^{-3}. The critical thicknesses will be even less for donor concentrations in the ranges of 10^{11}-10^{12} cm^{-3}, which are more common for Ge:Ga.

We have developed analytical expressions for the extent of the space charge region and the excess carrier concentrations and have verified them with the numerical results. These expressions are given in Figure 5. With these results, one can determine the effect of the contact in any extrinsic photoconductor.

The calculation of the steady state space charge distributions near the contacts is a necessary first step for further investigation of the transient response of the space charge region. Experimental work is in progress in order to verify the modeling predictions. We will measure the I-V characteristics and study the fundamental transport behavior of thin devices in the contact-dominated regime.

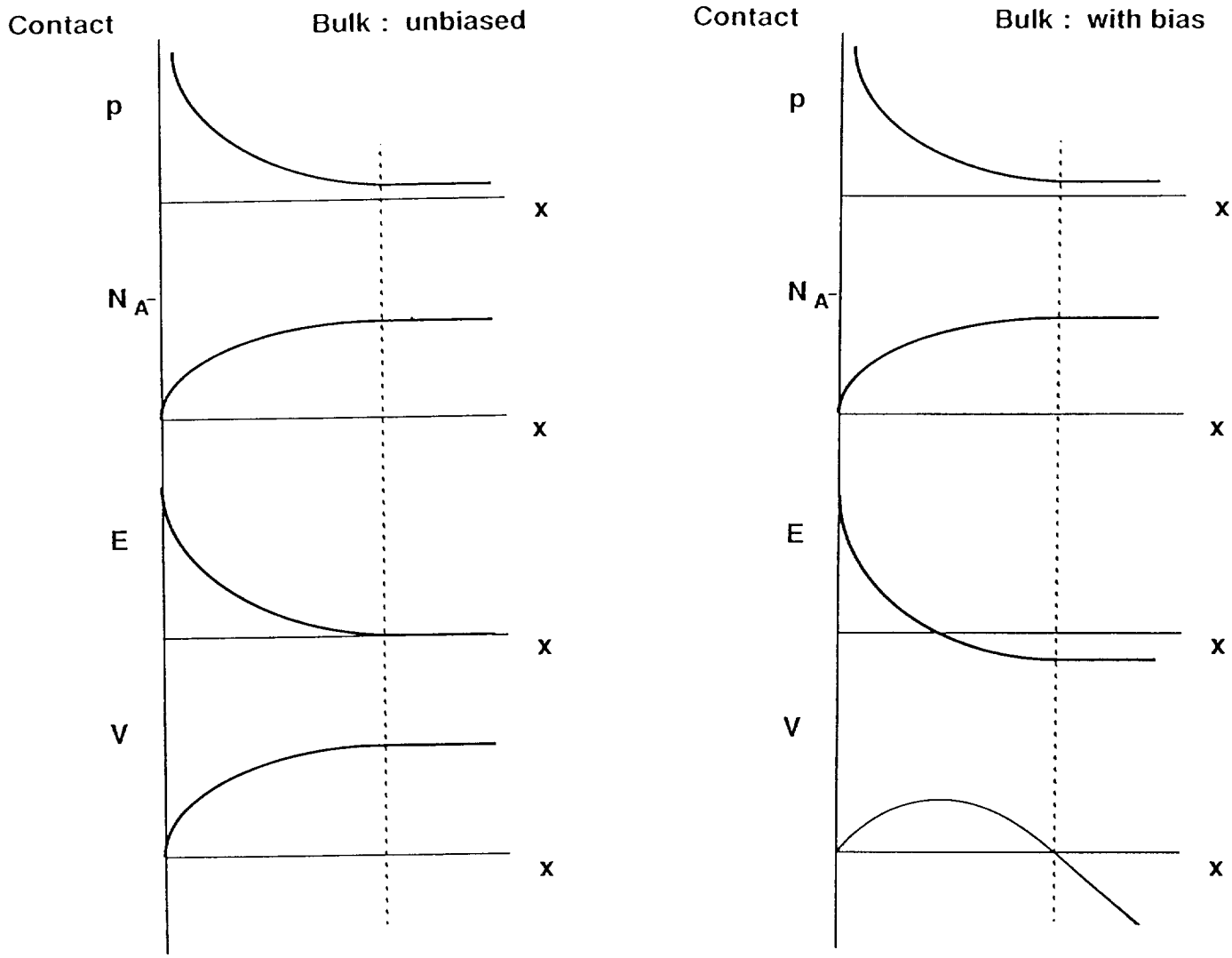
Contact
Bulk : unbiased
p
x
N A⁻
x
E
x
V
x
Contact
Bulk : with bias
p
x
N A⁻
x
E
x
V
x

Figure 1

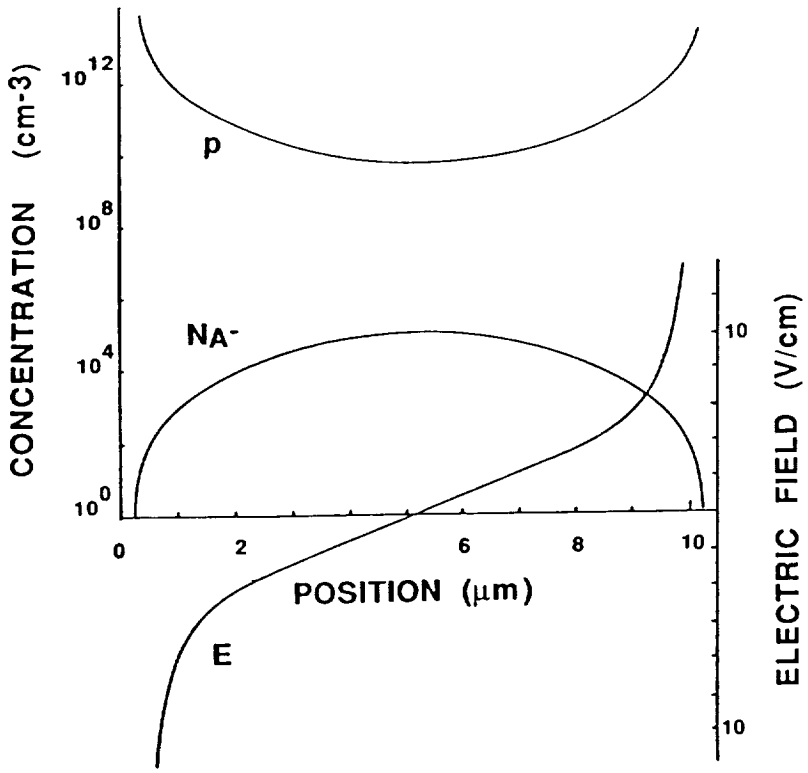
CONCENTRATION (cm-3)
10^12
10^8
10^4
10^0
p
NA-
E
0
2
6
8
10
POSITION (μm)
10
10
ELECTRIC FIELD (V/cm)

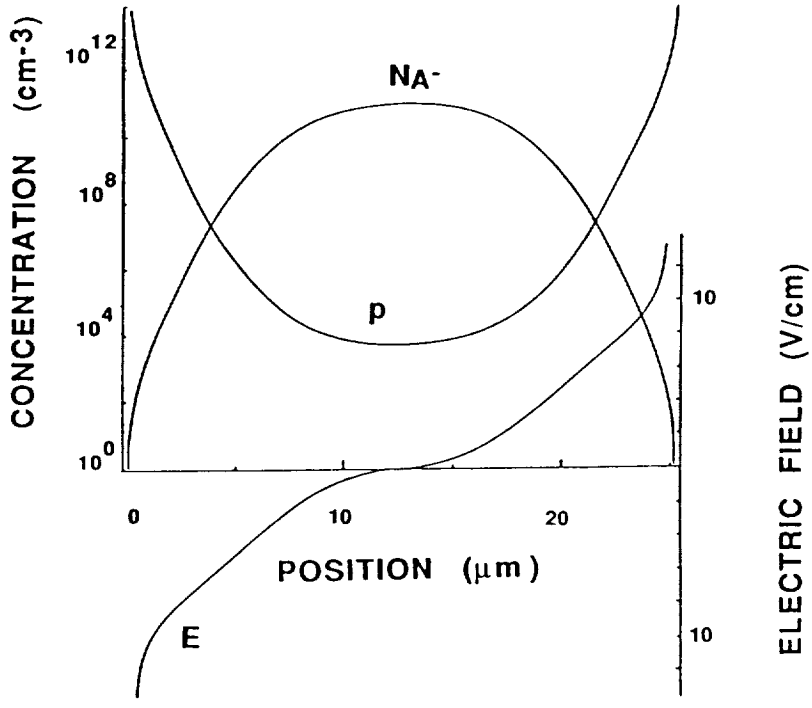
CONCENTRATION (cm-3)
10^12
10^8
10^4
10^0
NA-
p
E
0
10
20
POSITION (μm)
10
10
ELECTRIC FIELD (V/cm)

Figure 2

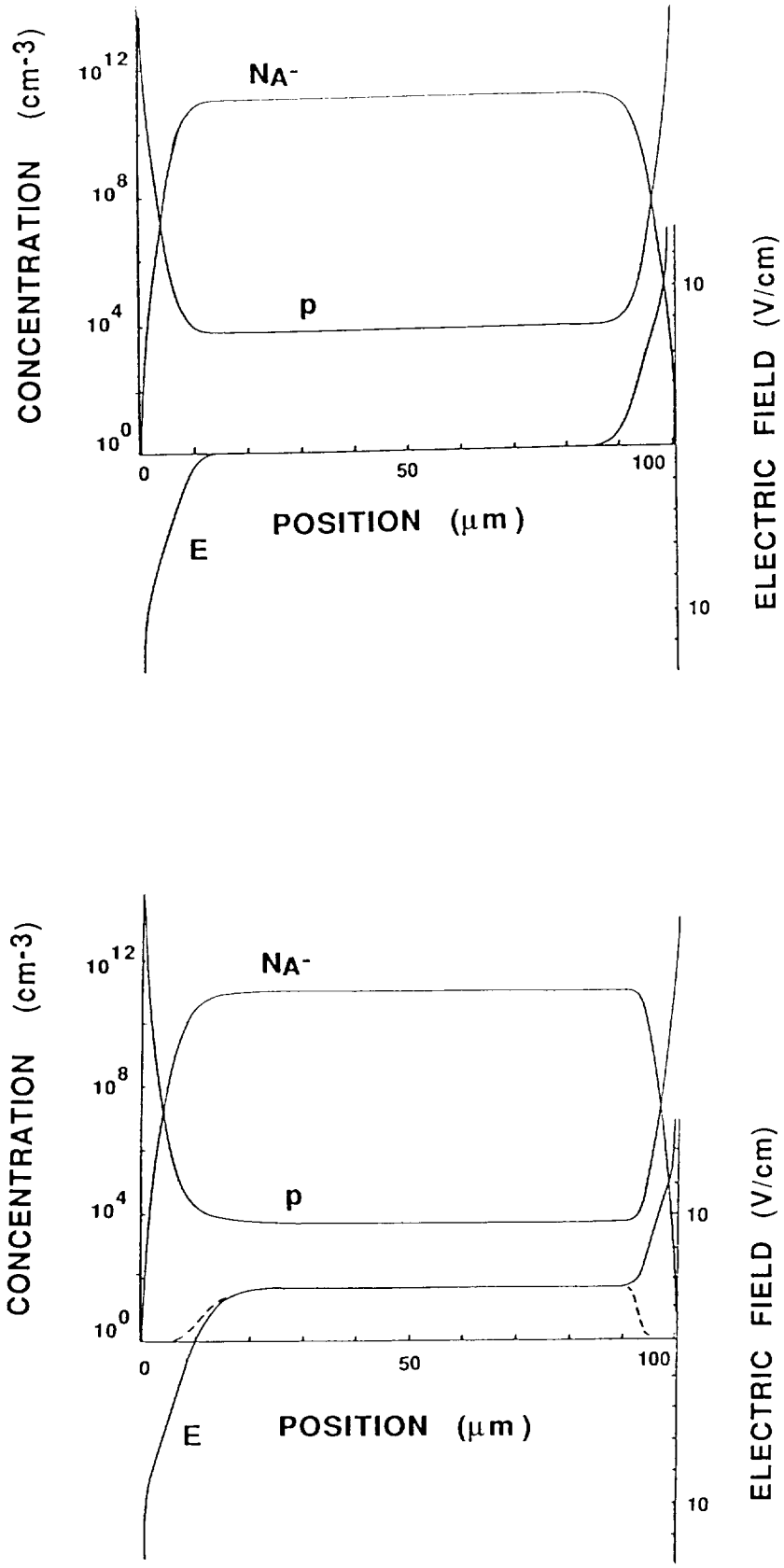
CONCENTRATION (cm-3)
10^12
10^8
10^4
10^0
NA-
p
E
0
50
100
POSITION (μm)
10
10
ELECTRIC FIELD (V/cm)
CONCENTRATION (cm-3)
10^12
10^8
10^4
10^0
NA-
p
E
0
50
100
POSITION (μm)
10
10
ELECTRIC FIELD (V/cm)

Figure 3

(a) $N_D = 10^{12}\ cm^{-3}$

(b) $N_D = 10^{11}\ cm^{-3}$

(c) $N_D = 10^{10}\ cm^{-3}$

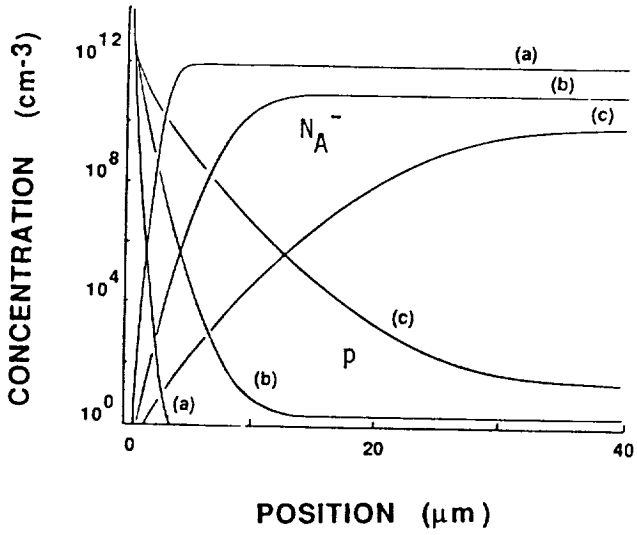

Figure 4

General Analytical Solutions: Si:X, GaAs:X, . . .

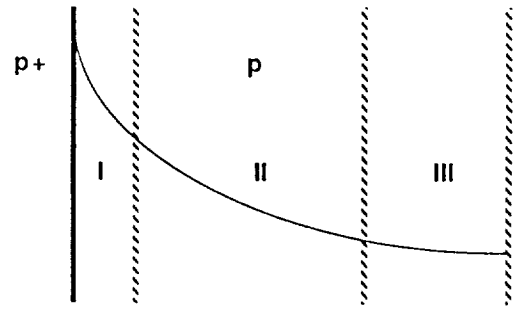

Distance of zones

I. $\Delta x = \lambda_i \left(\sqrt{\frac{N_{imp}}{10\ N_D}} - 1 \right)$

II. $\Delta x = \sqrt{\frac{2\varepsilon_s V}{e\ N_d}}$ $\qquad V = \frac{\varepsilon_A}{e} + kT\ \ell n \left(\frac{N_D^2}{N_v N_A} \right)$

III. $\Delta x = \sqrt{\frac{2kT\varepsilon_s}{e^2 N_D}}$

Figure 5

II. Transient Phenomenon due to A^+ Formation in Ge:Be Photoconductors

A slow transient response to step function increases in photon flux, with a time constant on the order of 0.1 - 1.0 sec, has previously been identified and documented in Ge:Be photoconductors operation under low photon backgrounds at temperatures of 2-3 K (5). A combination of modeling and experimental work has shown that the transient response is due to the effect of the formation of the overcharged Be acceptor center Be^+. This presentation summarizes a study of this phenomenon which has recently been published (6), and the reader should consult this reference for a complete description of the work.

The photoconductive response to a step function in photon signal as a function of temperature is shown in Figure 6. The transient response has a time constant which is significantly longer than would be expected due to either the free carrier lifetime or the dielectric relaxation time in the material. We believe that the slow transient response is due to hole trapping by neutral Be atoms to form the overcharged acceptor Be^+. Be can bind three or even four holes because of the four-fold degeneracy of the top of the valence band, and the existence of Be^+ has been clearly established experimentally (7).

The mechanism for the trapping phenomenon is shown in Figure 7. Development of the rate equations for the process results in an equation for the time constant τ' associated with Be^+ trapping and equilibration of

$$\tau' = \tau_o \left[\frac{Be}{N_V} e^{E/kT} \right] \qquad (2)$$

where τ^o is the free carrier lifetime, Be is the Be concentration, N_V is the valence band density of states and E is the Be^+ binding energy.

A plot of $[\tau'/\tau^o \times T^{3/2}]$ will have a slope proportional to the binding energy of the Be^+ center. This is shown in Figure 8. The value of 4.3 meV which is obtained from the data is in excellent agreement with the 4.5 meV binding energy of Be^+. The application of uniaxial stress, which breaks the degeneracy of the top of the valence band and eliminates Be^+ formation, also eliminates the slow transient response, as shown in Figure 9. This gives additional support to the assignment of the mechanism as associated with Be^+ formation.

Equation 2 can be adapted and used to estimate the time constant for A^+ or D^- trapping in any photoconductor material as a function of temperature. Overcharged acceptor and donor centers have been identified in a variety of photoconductor materials, including Ge:Ga, Ge:Be, Si:P, Si:B and Si:As.

In summary, a slow transient response, with a time constant on the order of 0.1 to 1.0 sec. between 2 and 3 K, has been observed in the photocurrent of Ge:Be extrinsic photoconductors. The activation energy of the transient phenomenon (4.3 meV) and its behavior under applied uniaxial stress indicate that trapping due to the formation of Be^+ centers is responsible for the dynamics of the photoresponse. An analytical model of transient photoconductivity in a unipolar system, where the trapping mechanism is associated with $Be^0 \rightarrow Be^+$, gives good agreement with the experimental results.

References

1. J. E. Ludman and J. Silverman, Infrared Physics 17, 177 (1977).

2. R. M. Westervelt and S. W. Teitsworth, J. Appl. Phys. 57, 5457 (1985).

3. N. M. Haegel and A. M. White, Infrared Physics, in press, 1989.

4. A. M. White, Infrared Physics 25, 729 (1985).

5. N. M. Haegel and E. E. Haller, Infrared Physics 26, 247 (1986).

6. N. M. Haegel, J. W. Beeman, P. N. Luke and E. E. Haller, Phys. Rev. B., 39, 3677 (1989).

7. E. E. Haller, R. E. MacMurray Jr., L. M. Falicov, N. M. Haegel and W. L. Hansen, Phys. Rev. Lett. 50, 612 (1983).

Acknowledgements

The author gratefully acknowledges the collaboration of A. M. White, of RSRE in Malvern, England, in the modeling work for near-contact space charge. J. W. Beeman, P.N. Luke and E. E. Haller of Lawrence Berkeley Laboratory have contributed to the characterization of the Be^+ transient response, and their work and interest are also acknowledged. This work has been supported in part by NSF Grant DMR -8809298. I am also pleased to acknowledge the generous support of my research program by a Fellowship in Science and Engineering from the David and Lucile Packard Foundation.

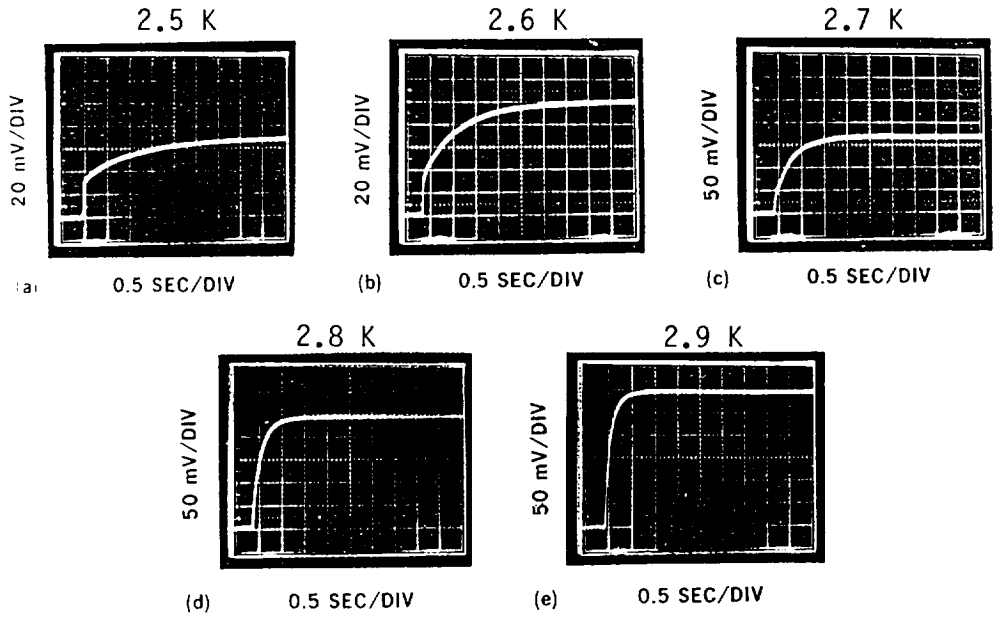

Figure 6

PROPOSED MECHANISM:

Hole trapping by Be^{o} to form Be^{+}

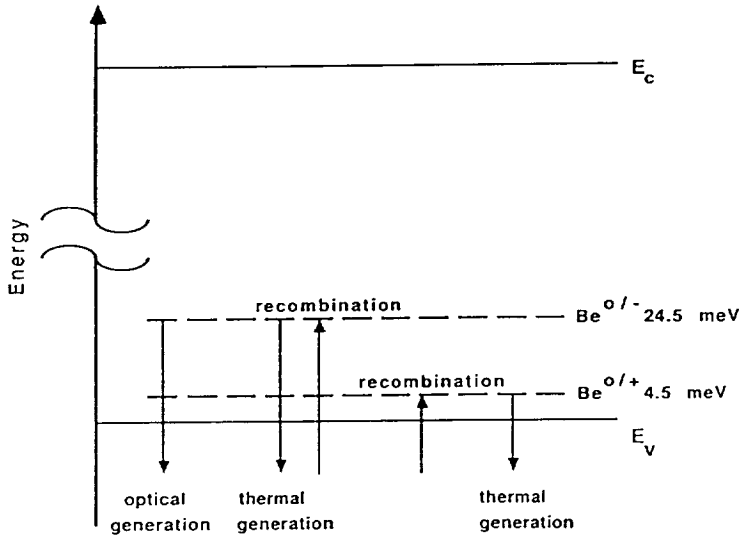

Haegel, Beeman, Luke and Haller, Phys. Rev. B., (in press) Feb. 15, 1989.

Figure 7

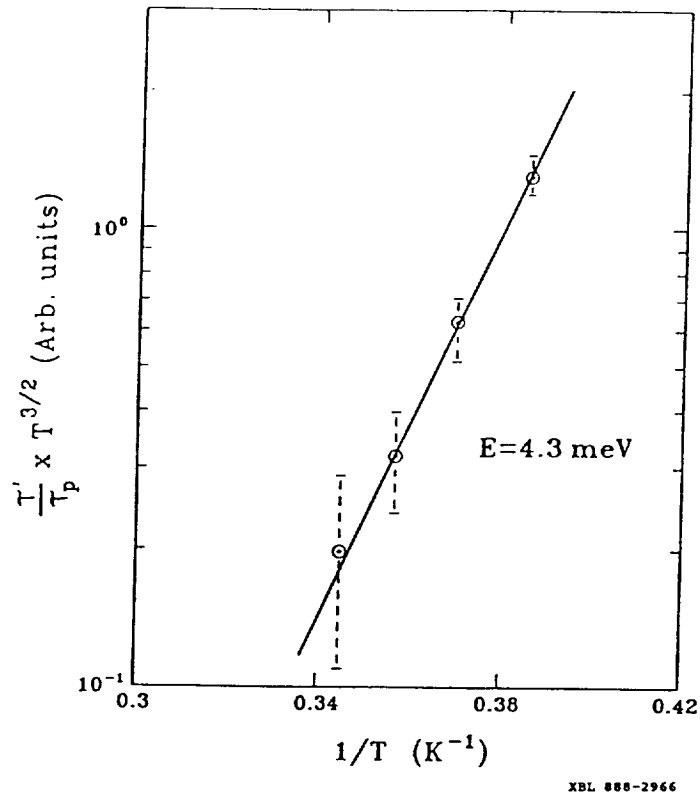

Figure 8

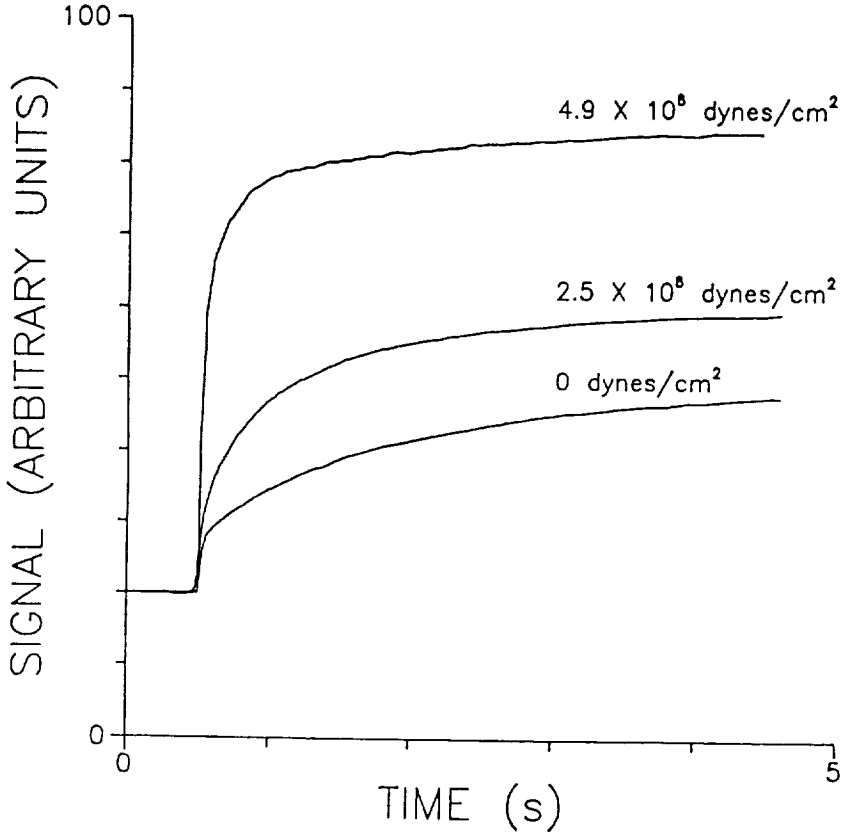

Figure 9

A 100 mK BOLOMETER SYSTEM FOR SIRTF

G.M. Bernstein, P.T. Timbie, and P.L. Richards
Department of Physics, University of California
Berkeley, California 94720

Abstract

Progress toward a prototype 100 mK bolometric detection system for SIRTF is described. Two adiabatic demagnetization refrigerators (ADR's) have been constructed, and used to investigate the capabilities necessary for orbital operation. The first, a laboratory ADR, has demonstrated a hold time at 0.1 K of over 12 hours, with temperature stability ~3 μK RMS achieved by controlling the magnetic field. A durable salt pill and an efficient support system have been demonstrated. A second ADR, the SIRTF flight prototype, has been built and will be flown on a balloon. Techniques for magnetic shielding, low heat leak current leads, and a mechanical heat switch are being developed in this ADR. Plans for construction of 100 mK bolometers are discussed. Three important cosmological investigations which will be carried out by these longest wavelength SIRTF detectors are described.

Introduction

The Space Infrared Telescope Facility (SIRTF) will require detectors in the 200 μm - 700 μm range with NEP's of order $10^{-17} W/\sqrt{Hz}$ for background limited or confusion limited observations [1]. To meet these specifications, bolometers must be cooled below temperatures attainable with He^3 refrigerators. The Multiband Imaging Photometer (MIPS) will use bolometers cooled to 0.1 K by an adiabatic demagnetization refrigerator (ADR). Although ADR's have been in use for over 50 years [2], only in the past few years has rapid progress been made toward implementation of ADR cooled detectors in astronomical observations. Ground-based observations have been made at mountain top observatories [3] and at the South Pole [4]. Balloon-borne ADR's will be flown this year, and both the SIRTF and AXAF satellites are planned to include ADR's. The focus of this report will be recent work at Berkeley on construction of a prototype for the SIRTF refrigerator; its design addresses all of the relevant issues for operation in the orbital environment. This prototype will be used on a balloon-borne telescope.

We will also discuss the progress towards construction of high performance 100 mK bolometers, and three exciting cosmological observations which are possible using such bolometers on SIRTF. These observations would benefit greatly from an extension of the SIRTF capability to 1500 μm.

Principles of Adiabatic Demagnetization

The refrigeration cycle of an ADR exploits the interaction between the atomic magnetic moments in a paramagnetic salt and an externally applied magnetic field. This process is fully discussed elsewhere [5,6]. The cycle can be described in terms of the entropy of the paramagnetic salt, S(T,H), where T is its temperature and H is the applied field. Fig. 1 displays the dependence of the entropy on temperature and field for the paramagnetic salt, ferric ammonium alum ($Fe(NH_4)(SO_4)_2 \cdot 12H_2O$), which is used in this work. The refrigeration cycle begins at point A; the entropy is reduced by increasing the magnetic field, thus ordering the spins. At point B, thermal contact to the helium bath is broken, and as the

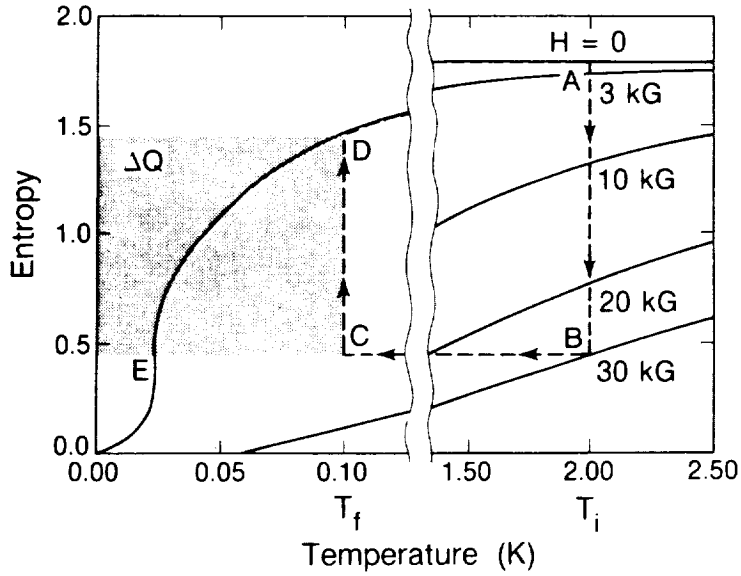

Figure 1. Entropy vs. temperature for ferric ammonium alum for several different applied magnetic fields (kG). The vertical axis is in units of R=8.31 J/moleK. The refrigeration cycle follows the path A-B-C-D (see text). Starting from T_i=2K and H=30 kG, the temperature of the salt pill is reduced to T_f=0.1K when H is reduced to ~1.5 kG. The shaded area is equal to the energy the salt can absorb at 0.1K.

field is reduced the temperature drops, until point E is reached at zero field. As heat leaks into the salt, the system follows the H=0 line to point D; during this time, the bolometers may be maintained at 100 mK by a heater.

A more efficient cycle, called isothermal demagnetization, halts demagnetization at point C, with T=0.1 K. The field H is gradually reduced to compensate for the heat leak, maintaining T=0.1 K along path CD. In this case, the cooling power of the refrigerator is nearly doubled - the total heat absorbed per cycle is proportional to the shaded area in Figure 1, rather than just the area to the left of curve ED. Our ADR's take this approach, regulating the cold stage to 100 mK by controlling the magnetic field on the salt.

Apparatus

Two ADRs are discussed in this paper. One is a complete operating refrigerator designed for testing bolometers in the laboratory. The second, which will serve as a prototype for the SIRTF flight refrigerator, is being tested. It is designed to cool bolometers on a balloon-borne astronomical telescope.

The laboratory refrigerator is shown in Fig. 2. The paramagnetic salt pill is suspended inside a vacuum space by Kevlar cords from walls cooled to ~1.4K by a pumped He^4 bath. The magnetic field is provided by a superconducting magnet immersed in this bath. Thermal contact between the salt pill and the 1.4K walls is achieved by a He^4 exchange gas heat switch. The bolometers being tested and the thermometer that is used for temperature regulation are mounted on a cold stage connected to the salt pill.

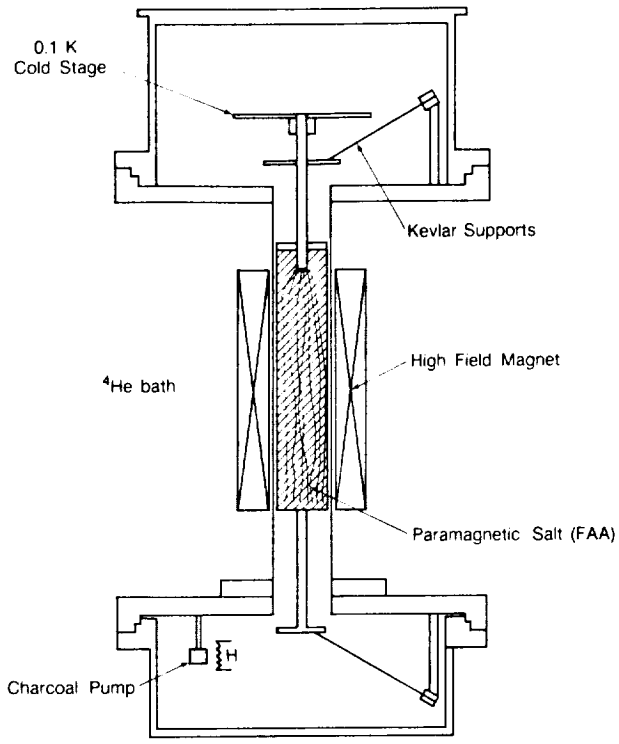

Figure 2. The laboratory adiabatic demagnetization refrigerator. The entire assembly is surrounded by a He^4 bath. The charcoal pump is part of the He^4 gas heat switch.

The flight refrigerator shown in Fig. 3 is similar to the laboratory refrigerator in the design of the salt pill, suspension system, and the cold stage. It uses a pumped He^4 bath as a 2K reservoir, but the entire refrigerator, including the superconducting magnet, is conduction-cooled through a thermal bus that is attached to the cold plate of a liquid He dewar [7]. It has a magnetic shield and an electro-mechanical heat switch. The flight prototype refrigerator is a compact structure that will bolt to a cold plate. The total mass of 3.4 kg is dominated by the 1.9 kg magnetic shield. Both of these refrigerators will be discussed further in terms of the issues of concern for use on balloons and in space.

Space Flight Issues

Several critical issues must be addressed in designing an ADR for operation in a satellite [8]. SIRTF will have three major instruments which share the cooled telescope and the liquid He^4 reservoir. The ADR is used for the longest wavelength detectors of one instrument, the MIPS. The length of the SIRTF mission is determined by the lifetime of the cryogen and is planned to be ≈5 years. The ADR must be reliable, must not interfere with the other instruments, and must not place excessive demands on the cryogen. The specific issues addressed below are:

- paramagnetic salt pill reliability
- salt pill suspension and hold time
- cold stage temperature stability
- magnetic shielding

- low heat load magnet leads
- reliable heat switch
- low mass, compact size

Paramagnetic Salt Pill

For space applications there are several concerns about the salt pill. First, commonly used paramagnetic salts like ferric ammonium alum (FAA) and chromic potassium alum (CPA) are mildly corrosive. Secondly, they dehydrate when exposed to air or vacuum. Finally, they decompose at moderate temperatures: 40°C for FAA and 89°C for CPA.

To establish good thermal contact between the paramagnetic salt and the cold stage and to prevent corrosion the salt is grown directly onto gold wires. The wires are silver-soldered to a copper post that in turn is bolted to a copper cold stage. The solder joint is gold-plated. The salt pill is 2.2 cm in diameter × 10 cm long and contains ≈40 grams of ferric ammonium alum and 200 gold wires. The wires are 250 μm in diameter. This salt pill is sealed in a stainless steel can to

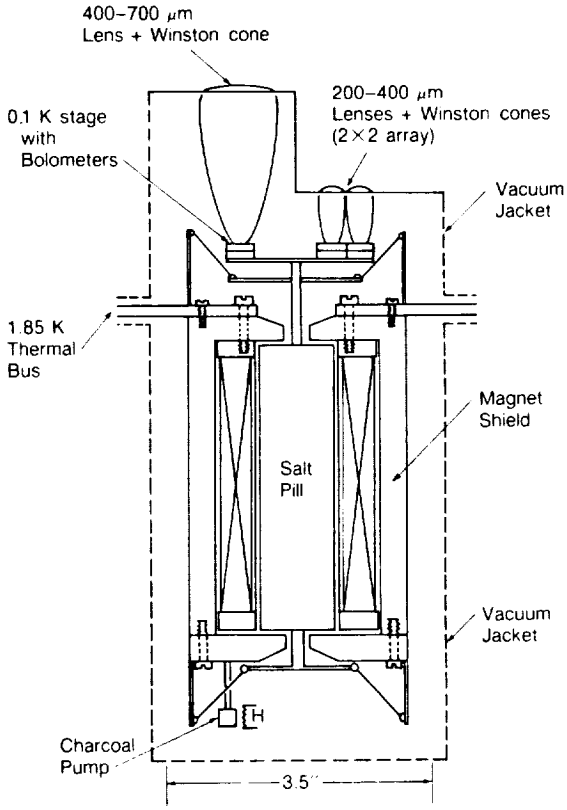

Figure 3. The flight prototype refrigerator now being tested. The refrigerator and superconducting magnet are cooled by conduction through the thermal bus. The He^4 gas heat switch may be replaced by a mechanical heat switch; the vacuum jacket then becomes unnecessary. The magnetic shield is to prevent stray magnetic fields from disturbing the bolometers or other instruments, both during normal operation and in the event of a magnet quench.

prevent the salt from dehydrating. Stainless steel end caps are sealed in place with epoxy [9].

The FAA salt pills made in this manner show no degradation in performance, even when stored at room temperature for several months. CPA salt pills will be used for SIRTF because their higher decomposition temperature is more compatible with the expected bake-out temperatures of the cryostat. A shake test of a CPA salt pill is planned to check the effects of launch vibrations on the salt pill.

Salt Pill Suspension

The salt pill and cold stage of the flight ADR are suspended from 2 K walls by 50 lb. test Kevlar cords as illustrated in Figure 4. A miniature pulley at each vertex of the star configuration allows for convenient and uniform tensioning. A drop of oil on each pulley freezes at liquid helium temperatures, locking the suspension into place. The lowest resonant frequency of the system, with the support warm, is measured to be 240 Hz, whereas the signal frequencies and the bulk of the launch vibrational energy will be below 100 Hz. The support should withstand a static load of over 150 g's. A complete vibration test of the system will be conducted shortly.

In the laboratory ADR, the heat leak from 1.4 K to 0.1 K for this support has been measured to be ~0.25μW. This will scale roughly as the cube of the temperature at the hot end; the hold time is inversely proportional to the heat leak.

Hold Time

The hold time of the laboratory ADR stage at 0.1 K easily exceeds the 12 hour hold time of the He^4 dewar. The achieved cooling power of the laboratory ADR is 50-70% of its theoretical capacity; this shortfall is probably attributable to the fact that the field in the solenoid achieves its rated 3 T only near the center of

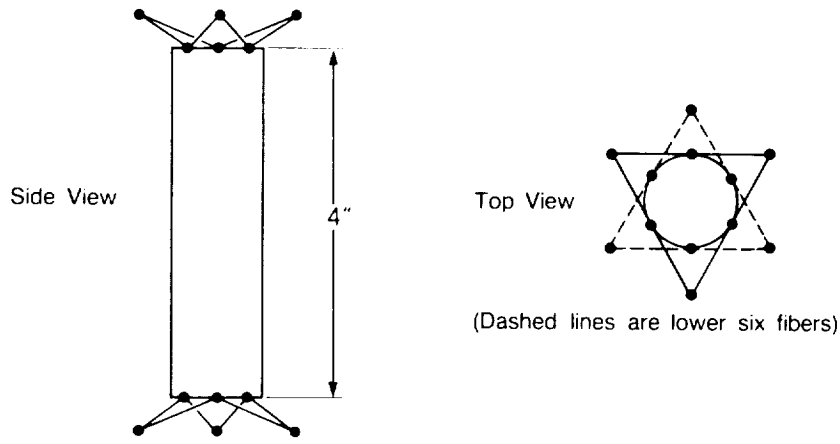

Figure 4. Schematic diagram of the suspension of the salt pill. The fibers are Kevlar cord. The black dots represent small pulleys which ensure uniform tension in the fibers.

the bore, whereas the salt fills the bore. The magnetic shield in the SIRTF prototype acts as a flux return which makes the field uniform over the entire salt pill. We project a hold time of order 24 hours for the SIRTF ADR, using a CPA salt pill and a 2.0 K helium bath. Since the time required to recycle is less than 30 minutes, the duty cycle of the ADR will be 98%, which is more than sufficient for proposed modes of observation.

Temperature Stability

In order to operate thermal detectors such as bolometers on the cold stage, the temperature must be very carefully regulated. For ideal refrigeration efficiency, one would like to regulate the temperature solely by controlling the magnetic field, following the vertical line CD in Figure 1 as closely as possible. In our laboratory ADR, the temperature is read out with commercial equipment - a Lakeshore Cryotronics GR-200A-30 thermistor [10] and a BTI Model 1000 potentiometric conductance bridge [11]. A personal computer reads the bridge and determines the desired magnet current, which is implemented by a custom built, digitally controlled, 16 bit, low ripple current supply. The system stabilizes the temperature readout to 2.8 μK RMS for several hours.

This level of stability is sufficient for our current work; a firm determination of the SIRTF requirement must await measurements on actual bolometers. The stability requirement also is dependent upon the observing mode of the SIRTF bolometers. Since the 2.8 μK variance is consistent with the noise specification of the BTI bridge, a lower noise bridge preamp is the obvious first step to obtain higher stability, should it be required.

A smaller and lighter version of all of the electronics necessary to operate the laboratory ADR is under construction for use on the balloon flight of the SIRTF prototype ADR.

Magnetic Shield

We have constructed and tested a ferromagnetic shield, necessary to avoid disturbing other SIRTF instruments, especially in the event of a magnet quench. The shield also improves the uniformity of the magnetic field inside the salt pill, and thus the efficiency of the refrigerator. The shield was designed using a computer program described elsewhere [12]. The shield is made of vanadium permendur, an alloy of iron, cobalt and vanadium with a high saturation induction.

Tests of this shield show that with the magnetic field inside the shield at its maximum value of 30 kG, the field more than 3 cm outside the shield is <1 G. Since the time constant for the decay of the field after a quench of the superconducting magnet is ~0.2s, the rate of change of the magnetic field outside the shield will be less than 5 G/s. The largest e.m.f. that could be induced in any single loop of wire in SIRTF would be less than 15 μV.

Magnet Leads

The superconducting solenoid [13] selected for the flight prototype requires 6 A to develop 30 kG. The magnet is quite compact; it has a 2.5 cm diameter bore, 5.7 cm outside diameter, and a 10 cm length and uses 140 μm diameter NbTi windings. Finer wire could be used to build a 3 A, 30 kG magnet [13] with the same dimensions. Copper leads can carry 6 A in typical cryogenic systems with modest loading (Joule

heating and thermal conduction) on the cryogens. In SIRTF the combination of thermal conduction and Joule heating from 6 A leads would give an average dissipation of ~10 mW in the 2K cryogen. The thermal and electrical properties of superconductors can be used to minimize this dissipation. Leads of Nb_3Sn from 2 K to ~12 K would almost eliminate the dissipation in the 2 K cryogen. The new high-T_c superconductors can potentially be used up to ~60 K.

Heat Switch

The He^4 gas heat switch used in the laboratory refrigerator is reliable and dissipates little heat (~30 mW when the charcoal heater is on). The duty cycle is <1% but requires a gas tight container around the ADR to isolate it from the thermal vacuum of the rest of the satellite. In particular, a vacuum window is required in the optical path (see Fig. 3). The solenoid-actuated heat switch shown in Fig. 5 has been developed to avoid these complications. The switch uses a commercial solenoid [14] to squeeze together a pair of copper jaws which contact a copper tab attached to the salt pill. The contacts are gold plated. The switch has a thermal conductivity of 0.015 W/K at 1.7 K when activated with 100 mA of current. This conductivity is sufficient to allow the isothermal magnetization step in the refrigeration cycle to occur in less than 5 minutes. When the solenoid current is off, the contacts fully disengage so the thermal conductivity is zero. The energy imparted to the salt pill when the jaws release the tab is ~3×10^{-3}J. This energy is

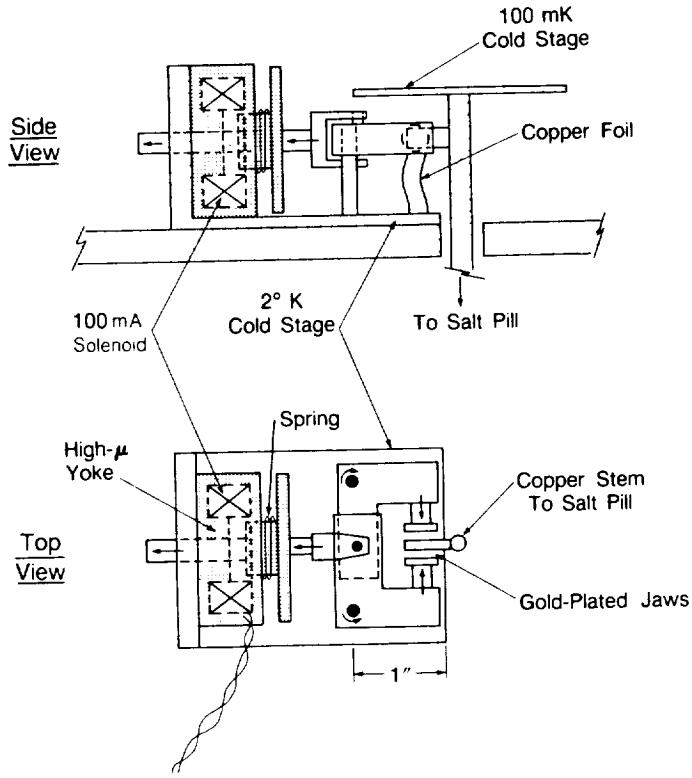

Figure 5. The solenoid-actuated heat switch. When activated with 100 mA, the solenoid forces the jaws together with ≈230 N of force. The spring pulls the jaws apart again when the current is off. The thermal conduction in the "off" state is zero.

small compared to the heat capacity of the salt pill at 2 K (~1 J), so its temperature will rise only slightly upon release. The switch was tested for reliability; in 4000 cycles over 2 days the "on" thermal conductivity remained stable to ≈5% and the jaws always released the contact to the salt pill in the "off" condition. This number of cycles is equivalent to one 5-year flight of SIRTF with the refrigerator cycled every 12 hours. A new heat switch is being developed that employs a superconducting solenoid.

100 mK Bolometers

We do not expect bolometers for use at 100 mK to look very different from those in use at 300 mK. We have measured the temperature dependence of the resistance R(T) for several samples of neutron transmutation doped germanium provided by Prof. Eugene Haller. These thermistors, as well as ion-implanted silicon thermistors, exhibit large non-thermal electrical non-linearities, perhaps due to an electric field dependent resistance or a hot electron effect. These non-linearities complicate the prediction and measurement of bolometer performance; we wish to have a satisfactory model, even if only phenomenological, of this behavior before attempting to optimize the SIRTF bolometers. Bolometers which are not optimal may of course be fabricated; we will do this shortly, and other groups have done so already, in order to gain information on the behavior of thermal links, absorbers, etc. Our laboratory ADR and regulation system are capable of attaining any temperature from 50 mK to 2 K within minutes, allowing rapid measurements of these properties.

Observations with SIRTF Bolometers

The bolometric channels on the MIPS will be able to observe numerous sources of submillimeter radiation, including the cosmic microwave background radiation (CBR) and the recently discovered submillimeter excess [15]. The MIPS will be ideally

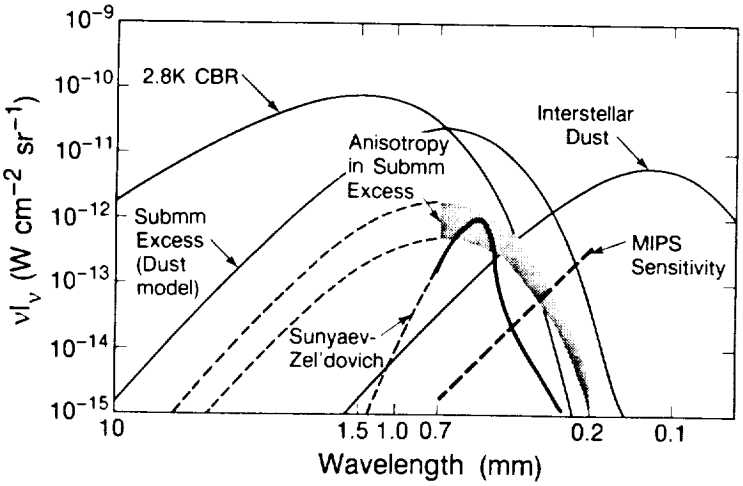

Figure 6. Sensitivity of the MIPS bolometer channels to submillimeter sources. The spectrum of the submillimeter excess is a fit to a dust model [16]. The predicted anisotropy in this excess is from Bond et al. 1986 [17]. The plotted signal from the Sunyaev-Zel'dovich effect is the expected enhancement in the CBR signal when viewed through the Coma cluster. The MIPS sensitivity is for a 500-second integration and includes detector and photon noise and confusion from galaxies and IR cirrus.

suited for searching for small scale (~arc minutes) anisotropy in the CBR and the submillimeter excess and for observing the Sunyaev-Zel'dovich effect (see Fig. 6). The possibility exists of extending the longest wavelength response of the bolometric channels beyond 700 μm; SIRTF would then have an even greater ability to detect these sources and to distinguish them from each other.

Acknowledgments

This work was supported by NASA Contract #NAS2-12578.

References

[1] G.H. Rieke, C. Lada, M. Lebofsky, F. Low, P. Strittmatter, E. Young, J. Arens, E. Haller, P. Richards, C. Beichman, T.N. Gautier, J. Mould, G. Neugebauer, S. Gaalema, and M. Werner, "MIPS: The Multiband Imaging Photometer for SIRTF," SPIE, vol. 589, pp. 242-248, November 1985.

[2] W.F. Giauque and D.P. MacDougall, "Attainment of Temperatures Below 1° Absolute by Demagnetization of $Gd_2(SO_4)_3 \cdot 8H_2O$," Physical Review, vol. 43, no. 9, p.768, May 1, 1933.

[3] L. Lesyna, T. Roellig, M. Werner, and P. Kittel, "An Adiabatic Demagnetization Cooled Bolometer System," Advances in Cryogenic Engineering, vol. 33, pp. 955-961, 1988.

[4] J.B. Peterson, private communication.

[5] R.D. Britt and P.L. Richards, "An Adiabatic Demagnetization Refrigerator for Infrared Bolometers," Int. J. Infrared and Millimeter Waves, vol. 2, no. 6, pp. 1083-1096, 1981.

[6] G.K. White, Experimental Techniques in Low Temperature Physics, 3rd ed., Oxford: Clarendon Press, 1979, ch. IX, pp. 219-254.

[7] HD-3(10) dewar, Infrared Laboratories, Inc., Tucson, AZ 85719.

[8] P. Kittel, "Magnetic Refrigeration in Space-Practical Considerations," Journal of Energy, vol. 4, no. 6, pp.266-272, Nov.-Dec. 1980.

[9] Stycast 2850 FT, Emerson and Cuming, Canton, MA 02021.

[10] Lakeshore Cryotronics, Westerville, Ohio 43081.

[11] Biomagnetic Technologies, Inc., San Diego, CA 92121.

[12] A.M. Winslow, "Numerical Solution to the Quasilinear Poisson Equation in a Nonuniform Triangle Mesh," Journal of Computational Physics, vol. 2, pp. 149-172, 1967.

[13] Cryomagnetics Incorporated, Oak Ridge, TN 37831.

[14] Ledex, Inc., Part #129450-035, Vandalia, OH 45377.

[15] T. Matsumoto, S. Hayakawa, H. Matsuo, H. Murakami, S. Sato, A.E. Lange, P.L. Richards, "The Submillimeter Spectrum of the Cosmic Background Radiation," Astrophysical Journal, vol. 329, pp. 567-571, 1988.

[16] S. Hayakawa, T. Matsumoto, H. Matsuo, H. Murakami, S. Sato, A.E. Lange, P.L. Richards, "Cosmological Implications of a New Measurement of the Submillimeter Background," Publ. Astron. Soc. Japan, vol. 39, pp. 941-948 (1987).

[17] J.R. Bond, B.J. Carr, and C.J. Hogan, "Spectrum and Anisotropy of the Cosmic Infrared Background," Astrophysical Journal, vol. 306, pp.428-450, 1986.

A Progress Report on using Bolometers Cooled by Adiabatic Demagnetization Refrigeration

L. Lesyna (Stanford*), T. Roellig (NASA-Ames), M. Savage (Sterling Software), M. Werner (NASA-Ames)

*Present address: Grumman Corporate Research Center

For sensitive detection of astronomical continuum radiation in the 200 μm - 3 mm wavelength range, bolometers are presently the detectors of choice. In order to approach the limits imposed by photon noise in a cryogenically cooled telescope in space, bolometers must be operated at temperatures near 0.1 K. We report our progress in building and using bolometers that operate at these temperatures. Our most sensitive bolometer had an estimated NEP of 7×10^{-17} W $Hz^{-1/2}$. We also briefly discuss the durability of paramagnetic salts used to cool our bolometers.

Theory

The noise equivalent power ($NEP_{optical}$) of a bolometer will be the quadrature sum of noise due to absorbed photons and noise components intrinsic to the detector. The $NEP_{optical}$ of a bolometer limited by photon induced noise from a thermal background is given by the following expression [1]:

$$NEP^2_{photon} = \frac{4\,A\,\Omega\,(kT_b)^5\,\varepsilon\,f}{\eta\,c^2\,h^3} \int \frac{x^4}{e^x - 1}\left(1 + \frac{\eta\,\varepsilon\,f}{e^x - 1}\right) dx$$

The corresponding expression for the absorbed background power is:

$$Q = \frac{2 A \Omega T_b^4 k^4}{c^2 h^3} \int \frac{x^3}{e^x - 1} \eta \varepsilon f dx$$

$$x \equiv \frac{h \nu}{k T_b}$$

where $A\Omega$ is the optical throughput, T_b is the background temperature, ε is the background emissivity, f is the optical system transmission, η is the bolometer absorptivity, k is the Boltzmann constant, c is the speed of light, and h is the Planck constant.

Bolometer optimization depends strongly upon the character of the background radiation [2]. For a bolometer exposed only to T_b = 2.7 K cosmic background in the 400 μm - 700 μm wavelength range by a diffraction limited telescope, and assuming that ε=1, f=0.5, η=1, we find $NEP_{photon} = 5 \times 10^{-18}$ W $Hz^{-1/2}$ and Q = 44 fW. The contribution of other astrophysical backgrounds [3], and telescope self-emission will raise both NEP_{photon} and Q. The Multiband Imaging Photometer for SIRTF (MIPS) has a sensitivity goal of $NEP_{optical} = 5 \times 10^{-17}$ W $Hz^{-1/2}$ in the 200 μm - 700 μm wavelength range [4]. As another example, ground based observations in the 1.0 - 1.4 mm range (assuming ε = 0.5 and T_b = 273 K) imply $NEP_{photon} = 1.4 \times 10^{-15}$ W $Hz^{-1/2}$ and Q = 870 pW.

Detector induced noise cannot be less than the noise due to thermal fluctuations; its contribution to $NEP_{optical}$ is $NEP_{thermal} = \eta^{-1}(4kT^2G)^{1/2}$, where G is the thermal conductance, and T is the bolometer temperature. We desire $NEP_{photon} >> NEP_{thermal}$ for background limited performance. Most bolometers heat up, and become slower and less sensitive as the background power is increased from zero. It becomes a bolometer design challenge to maintain the above inequality, while the bolometer absorbs the appropriate background power. The best bolometers operating at 0.3 K have $NEP_{optical}$ of about 4×10^{-16} W $Hz^{-1/2}$ [5]; to reach lower NEPs, a bolometer operating at 0.1 K is required.

Experiment

Useful materials for bolometers operating at 0.1 K that meet the more stringent low background requirements appear to exist. We have adopted a design shown in Figure 1. Our bolometer component selections were motivated by our desire to keep the total heat capacity, C, as low as possible. For our bolometers, the astronomical radiation is absorbed by a 120 nm Bi film [6] deposited onto a sapphire substrate. The temperature change induced by the heating of the Bi film is measured with a Ge:Ga thermistor [7]. The thermistor is maintained near 0.1 K by 25 μm brass wires, which also serve to provide electronic conduction paths to measure the induced impedance changes.

The bolometer is mounted on the work surface of our adiabatic demagnetization refrigerator (ADR). Our ADR system can reach temperatures of less than 0.05 K, and can maintain temperatures of 0.1 K to within 14 μK, for periods of time in excess of 12 hours. Additional details of the refrigerator system and its performance are described in detail elsewhere [8,9].

We digress to discuss an important issue affecting the reliability of ADRs used for cooling detectors: the lifetime of the magnetic refrigerant. Paramagnetic salts useful for cooling bolometers in ADRs are often chemically active and can deteriorate when stored at room temperature. Chemical reactions may occur that alter their low temperature magnetic properties and degrade or render them useless for ADR applications. We have achieved considerable success using chromic potassium sulfate (CPS) as our working paramagnetic salt. We encapsulate the CPS within a brass cylinder, with epoxy end caps to hermetically seal the CPS from the atmosphere. We have used one such salt pill over a period of three years without noticeable degradation of refrigeration performance. This result suggests that CPS is a very suitable magnetic refrigerant for reliable long-term use in ADRs.

Returning to our discussion of detectors, we designed our bolometers to have a thermal conductance, G equal to 2×10^{-8} W/K, so that they could effectively function in the presence of background power up to 400 pW. Thermodynamic induced noise places a minimum contribution to $NEP_{optical}$ of $\eta^{-1}(4kT^2G)^{1/2}$, hence $NEP_{optical} > 1 \times 10^{-16}$ W $Hz^{-1/2}$. This value is higher than that required for

a cosmic background limited bolometer, but is less than NEP_{photon} for the ground-based application mentioned above. In order for the bolometer to respond to modulated power at chopping frequencies of 10 Hz and higher, we desired a bolometer heat capacity $C < 10^{-10}$ J/K. This requirement was achieved, and the estimated contributions to the heat capacity of the materials we used are listed in Table 1.

We estimated $NEP_{optical}$ of our bolometer by measuring the current, I, and voltage noise v_n, as a function of electrical bias across the bolometer, to infer an electrically determined value of the bolometer NEP (NEP_{elec}). We then applied the relation $NEP_{optical} = \eta^{-1}\ NEP_{elec}$ [1], assuming a value of $\eta=1$, as is appropriate for a bolometer in an integrating cavity. Our bolometers were biased through a Eltek Model 106 metal film resistor, having an impedance of 250 MΩ at 2 K. A cold J230 JFET source-follower circuit was coupled to the bolometer, to match the bolometer impedance and to minimize microphonic and electrical interference. The current-voltage relationship for our most sensitive bolometer is shown in Figure 2. Our measured electrical parameters are listed in Table 2. From these data, we estimate a responsivity of 6.4×10^8 V/W and $NEP_{optical}$ of 6.7×10^{-17} W $Hz^{-1/2}$ at the bias point marked by an arrow in Figure 2. This value of the NEP is the lowest recorded for infrared and submillimeter bolometers, and represents a significant advance in sensitivity.

We have measured the optical response of our bolometer, to modulated power variations (Figure 3), to infer a time constant of 3 ms for the detector. This value provides useful, fast response for chopping radiometric applications. Further description of the bolometer and measurements made of it are reported elsewhere [9].

The bias point was selected to be such that the electrical power dissipated in the bolometer is greater than that of a hypothetical background power for 44 fW (as may be appropriate for a low background spacecraft application). This choice of electrical bias is close to optimal for this radiometric application [2]. In Table 3, we list the theoretical contributions to the NEP; the total contribution is equal to our measured NEP_{elec} to within experimental error.

However, we have observed a discrepancy in the value of the thermal conductance of our bolometer and the value we expected. An independent measurement of the thermistor yields a resistance-temperature relation, $R = 2.87\ \Omega \cdot \exp(4.58\ K^{1/2}\ T^{-1/2})$; we use this expression to calibrate the temperature of the bolometer, as a function of bias from Figure 2. From this temperature and bias power data, we infer a thermal conductance of our bolometer, $G = 1.6 \times 10^{-9}$ W/K, which is one order of magnitude lower than the value we would expect from published brass thermal conductivity data [10]. It is possible that boundary resistance effects induced by the electrical contacts, and compositional differences in the brass wire [11] used account for the differences in measured values; we do not fully understand the origin of this discrepancy. The low G value does not affect the accuracy of the electrical self-calibration procedure to estimate NEP_{elec}, but does limit the maximum background power the bolometer can accept.

It has been suggested that non-ohmic behavior of bulk thermistor material may be partially responsible for the nonlinearity shown in Figure 2, and may affect the accuracy of the self-calibration procedure we used to infer NEP_{elec} [12]. We do not believe this to be the case for our bolometers. The amount of bias power per unit volume necessary to reduce the resistance in 0.1 K Ge by 30% is 4×10^{-2} W/m^3 [13]. For our 0.1 K bolometer, the bias power density was 4×10^{-4} W/m^3, which suggests that non-ohmic behavior is a less than 1% effect, and has a negligible effect on NEP_{elec}.

Observational Tests

We have used our adiabatic demagnetization refrigerator system to perform one millimeter continuum observations using the Hale 5 m telescope at Palomar Mountain. During our observing run during November 1985, we used an unoptimized bolometer operating at 0.2 K. Construction materials were similar to our 0.1 K bolometer described earlier, except that thermistor material was selected with a lower dopant density, to provide a bolometer resistance of 1 MΩ at 0.2 K. In addition, brass wire of diameter 50 μm was used, to design this bolometer for the high background expected for our ground-based observing

location. A non-optimal Bi film thickness of 30 nm was applied to the sapphire substrate. NEP_{elec} of this bolometer was estimated to be 2×10^{-15} W $Hz^{-1/2}$.

We estimated a noise equivalent flux density (NEFD) of 10 Jy $Hz^{-1/2}$ for our ADR bolometer system, based upon one millimeter wavelength measurements of the planet Jupiter and the radio galaxy 3C84. The ADR system NEFD was higher than the 6 Jy $Hz^{-1/2}$ of an optimized helium-three cooled system [14], which was placed onto the telescope after the ADR. The relatively high NEP_{elec} , low absorptivity of the detector, and optical mismatch to atmospheric transmission windows precluded the ultimate in NEFD to be realized with the ADR system. We expect that bolometer optimization, and improved optical filtering will lower the ADR NEFD substantially.

As bolometers are thermal detectors, we expect them to be affected by temperature variations in the refrigeration system. In order to investigate the magnitude of this effect, we monitored the NEFD during temperature regulation of the ADR at the telescope. Regulation effects did not introduce significant amounts of excess noise into our radiometric observations. This result is consistent with our expectations, as the effect on the responsivity induced by bolometer heat sink temperature variations is given by the following expressions [9]:

$$\frac{\Delta S}{S} = \frac{1}{1 - l^2 \alpha} \frac{\Delta \alpha}{\alpha}$$

$$\alpha \equiv \frac{1}{G} \frac{dR}{dT}$$

where S is the responsivity, and $\Delta\alpha$ is calculated over the regulated temperature range. For our 0.2 K bolometer operated at Palomar, responsivity variations were calculated from the above equations to be less than 1%. For our 0.1 K bolometer, we estimate $\Delta S / S = 0.2\%$, for 14 μK temperature variations. Thus, temperature regulation effects would not be expected to degrade the bolometer system sensitivity to a significant degree.

Conclusions

We have successfully constructed and used bolometers cooled by ADR at an astronomical observatory to perform sensitive radiometric measurements. We have achieved NEP_{elec} as low as 7×10^{-17} W $Hz^{-1/2}$, for bolometers operating at 0.1 K . We expect that bolometers can be made more sensitive by decreasing the thermal conductance further and by cooling the load resistor below 2 K; such changes should readily achieve $NEP_{optical}$ of less than 5×10^{-17} W $Hz^{-1/2}$ as required for SIRTF and other low background applications.

This work was supported by a NASA Cryogenics RTOP and NASA-Ames Director Discretionary Funds.

REFERENCES AND NOTES

1. Mather, J.C. 1982, *Appl. Opt.* 21, 1125.

2. Griffin, M.J., and Holland, W.S. 1988, *Int. J. Infrared and Millimeter Waves*, 9, 1988.

3. Matsumoto, T., Hayakawa, S., Matsuo, H., Murakami, H., Sato, S., Lange, A.E., Richards, P.L. 1988, *Ap. J.* 329, 567.

4. Ramos, R., Hing, S.M., Leidich, C.A., Fazio, G., Houck, J.R., Rieke, G. 1988, *SPIE* 973.

5. Downey, P.M., Jeffries, A.D., Meyer, S.S., Weiss, R., Bachner, F.J., Donnelly, J.P., Lindley, W.T., Mountain, R.W., Silversmith, O.J. 1984, *Appl. Opt.* 23, 910.

6. Clarke, J., Hoffer, G.I., Richards, P.L., Yeh, N.-H. 1977, *J. Appl. Phys.* 48, 4865.

7. Lesyna, L., Roellig, T.L., Kittel, P. 1984, *Int. J. Infrared and Millimeter Waves* 5, 755.

8. Lesyna, L., Roellig, T., Werner, M., Kittel, P. in Advances in Cryogenic Engineering, 33, 955 (R. W. Fast, ed., Plenum Press, 1988).

9. Lesyna, L. , Ph.D. Dissertation 1987, Stanford University (unpublished).

10.Lounasmaa, O.V., Experimental Principles and Methods Below 1 K (Academic Press, 1974) p. 246.

11. Brass wire was purchased from California Fine Wire Company, and has a 70% Cu - 30% Zn composition.

12. Mather, J.C. 1984, *Appl. Opt.* 23, 3181.

13. McCammon, D. 1989, private communication.

14. Roellig, T.L., and Houck, J.R. 1983, *Int J. Infrared and Millimeter Waves* 4, 299.

15. Collan H.K., Krusius M., Pickett, G.R. 1970, *Phys. Rev. B* 1, 2888.

16. Nishioka, N.S., Richards, P.L., Woody, D.P. 1978, *Appl. Opt.* 17, 1562.

17. Specific Heat – Metallic Elements and Alloys, 4 (Y. S. Touloukian, ed., Plenum Press, 1970).

Table 1

Bolometer Thermal Data at 0.1 K

Material	Volume	Est. Heat Capacity, C	Ref.
Bismuth Film	1.1×10^{-3} mm^3	1.3×10^{-13} J/K	[15]
Sapphire Substrate	2.2 mm^3	8.4×10^{-13} J/K	[16]
Ge:Ga Thermistor	1.0 mm^3	3.5×10^{-12} J/K	[16]
Epoxy	0.01 mm^3	7.0×10^{-12} J/K	[16]
Brass Wires	3.0×10^{-3} mm^3	$1/3 \times 3.4 \times 10^{-11}$ J/K	[17]
In Solder	4.2×10^{-3} mm^3	5.5×10^{-13} J/K	[16]

	Theoretical	Experimental
Total heat capacity	2.3×10^{-11} J/K	6×10^{-12} J/K
Thermal conductance of brass wire	2.0×10^{-8} W/K	2×10^{-9} W/K
Time constant	1.1 ms	3 ms

Table 2

Measured bolometer electrical parameters

(Using notation of reference [1])

Z, dynamic impedance	36 MΩ
R, resistance	42 MΩ
I, current	9.8×10^{-11} A
v_n, voltage noise	43 nV $Hz^{-1/2}$ at 20 Hz
T_s, bolometer sink temperature	0.0725 K
R_L, load resistance	250 MΩ
T_L, load resistor temperature	2 K
S, responsivity	6.4×10^{8} V/W
NEP_{elec}	6.7×10^{-17} W $Hz^{-1/2}$

Table 3

Theoretical Estimates of Bolometer NEP_{elec} contributions [1]

$NEP_{thermal}$	2.3×10^{-17} W $Hz^{-1/2}$
$NEP_{Johnson,\ R}$	1.6×10^{-17} W $Hz^{-1/2}$
$NEP_{Johnson,\ load}$	3.3×10^{-17} W $Hz^{-1/2}$
$NEP_{amplifier}$	2.3×10^{-17} W $Hz^{-1/2}$
NEP_{elec}	4.9×10^{-17} W $Hz^{-1/2}$

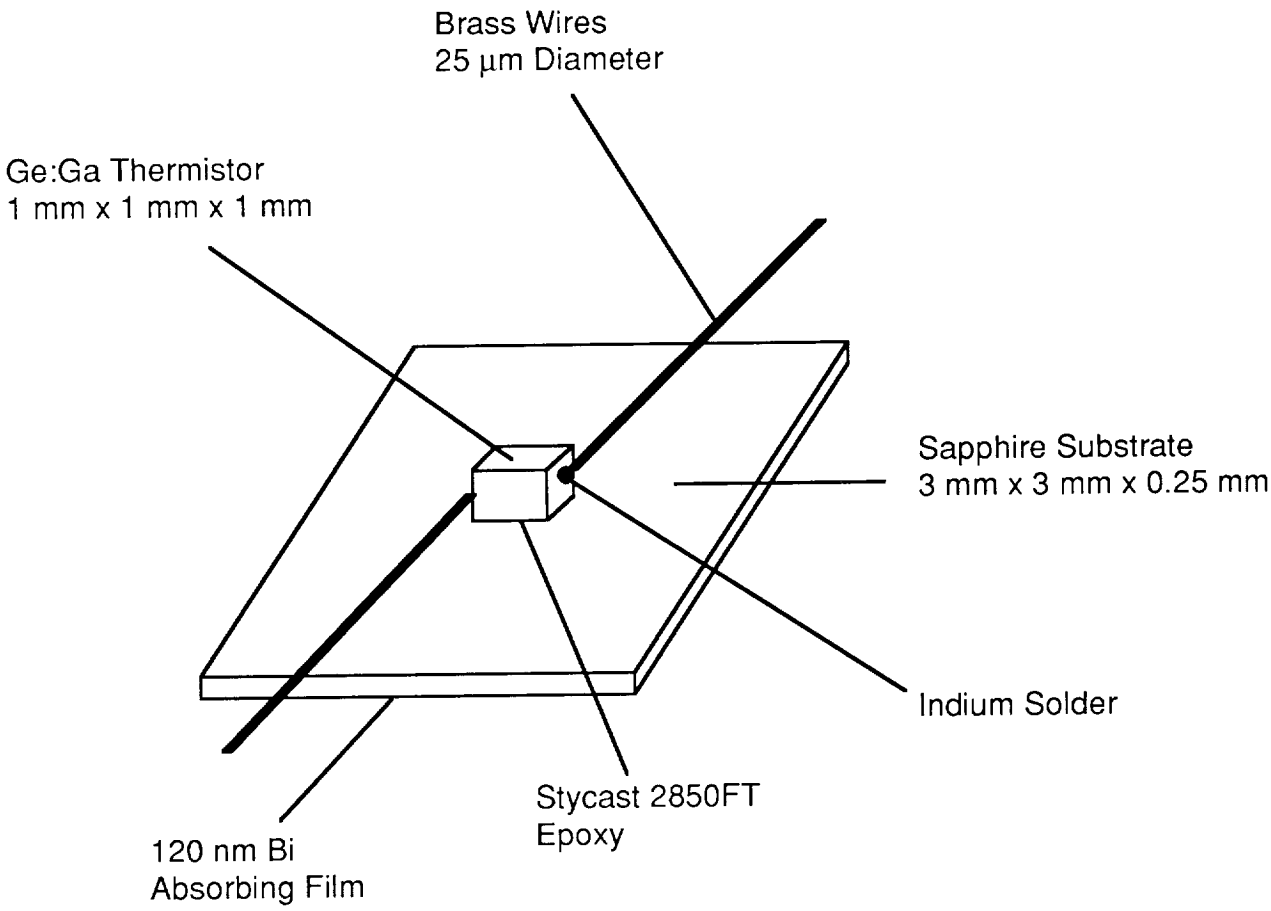

Figure 1

Bolometer Materials and Dimensions

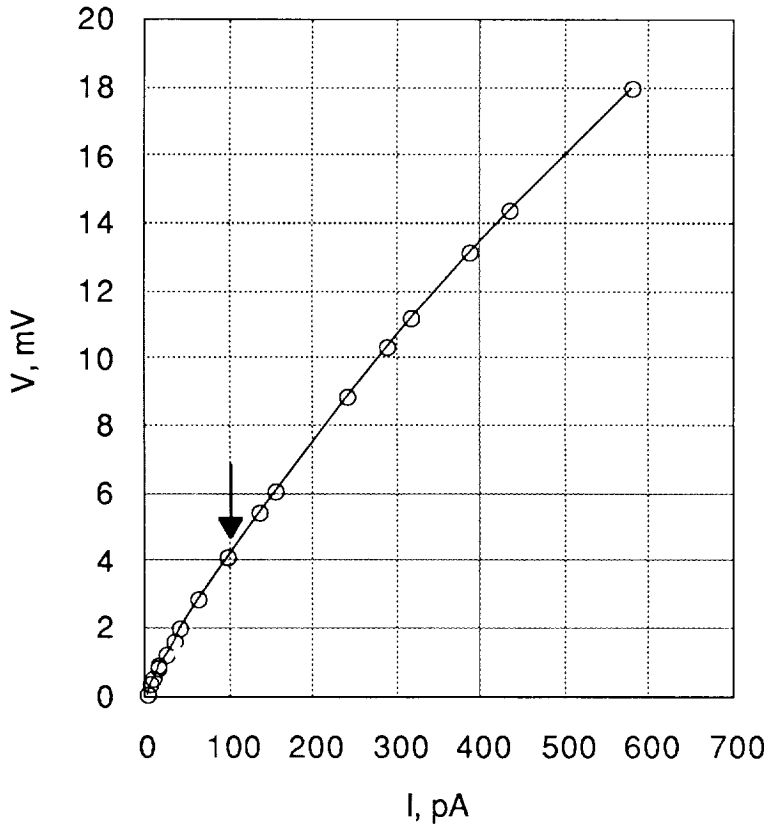

Figure 2

Bolometer Load Curve

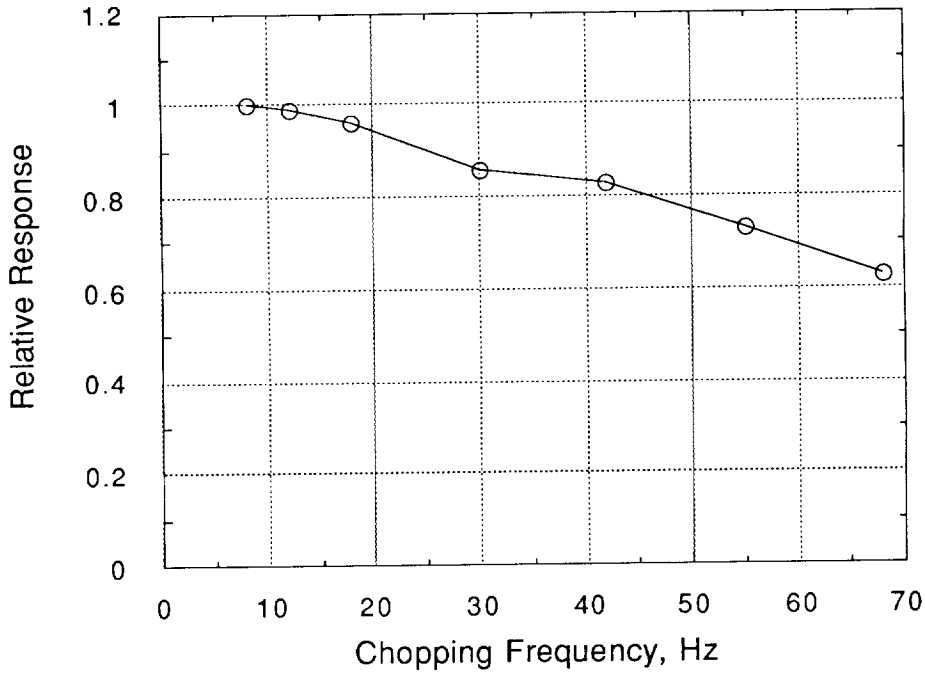

Figure 3

Bolometer Response to Modulated Radiation

A PRESENTATION ON

THE SOLID STATE PHOTOMULTIPLIER - STATUS OF PHOTON COUNTING BEYOND THE NEAR-INFRARED

TO

THE THIRD INFRARED DETECTOR TECHNOLOGY WORKSHOP
NASA-AMES RESEARCH CENTER
MOFFETT FIELD, CALIFORNIA

FEBRUARY 7-9, 1989

BY

K. M. HAYS, R. A. LaVIOLETTE, M. G. STAPELBROEK, AND M. D. PETROFF

ROCKWELL INTERNATIONAL
SCIENCE CENTER
ANAHEIM, CALIFORNIA

The Solid State Photomultiplier - Status of Photon Counting Beyond the Near-Infrared*

Rockwell International Science Center

Anaheim, CA 92803

Rockwell International's Solid State Photomultiplier (SSPM)[1] is an impurity-band avalanche device which can count individual photons with wavelengths between 0.4 and 28 micrometers.[2] Its response to a photon is a pulse of between 10^4 and 10^5 conduction electrons, making it an important device for use in phenomenology.

The characteristics of the SSPM make it a potentially important device for use in astronomical applications. Contract NAS2-12400 was initiated in June 1986 to conduct modeling and characterization studies of the SSPM to provide a basis for assessing its use in astronomical systems. This paper discusses some SSPM models and results of measurements which characterize the group of SSPMs recently fabricated on this contract.

*K. M. Hays, R. A. LaViolette, M. G. Stapelbroek and M. D. Petroff, Third Infrared Detector Technology Workshop, NASA-Ames Research Center, February 7-9, 1989.

1. M. D. Petroff, M. G. Stapelbroek and W. A. Kleinhans, U. S. Patent Number 4,586,068, Filed Oct. 7, 1983, Granted Apr. 29, 1986.

2. M. D. Petroff, M. G. Stapelbroek and W. A. Kleinhans, Appl. Phys. Lett. **51** (1987) 406.

STRUCTURE OF IMPURITY BAND CONDUCTION IR DETECTORS

The Solid-State Photomultiplier (SSPM) is the only device known which can continuously count single photons in the 1 to 28 μm wavelength range. The detector is a Si:As impurity band conduction device. SSPMs are fabricated by growing doped and undoped epitaxial layers on silicon substrates and then defining the detectors using established silicon processing techniques.

Area and line arrays of SSPMs, as well as discrete detectors, have been fabricated. Epitaxy for back-illuminated detectors must be grown on intrinsic silicon substrates. Arrays of this type can be connected to multiplexers or other signal processors with indium columns to form hybrids. An etch to the buried contact is required as a common detector biasing lead.

Front illuminated SSPMs have also been fabricated. Heavily-doped substrates can be used for front-illuminated devices to reduce optical crosstalk and to eliminate the need for a transparent buried contact.

STRUCTURE OF IMPURITY BAND CONDUCTION IR DETECTORS

- DEVICE SCHEMATIC CROSS-SECTION (NOT TO SCALE)

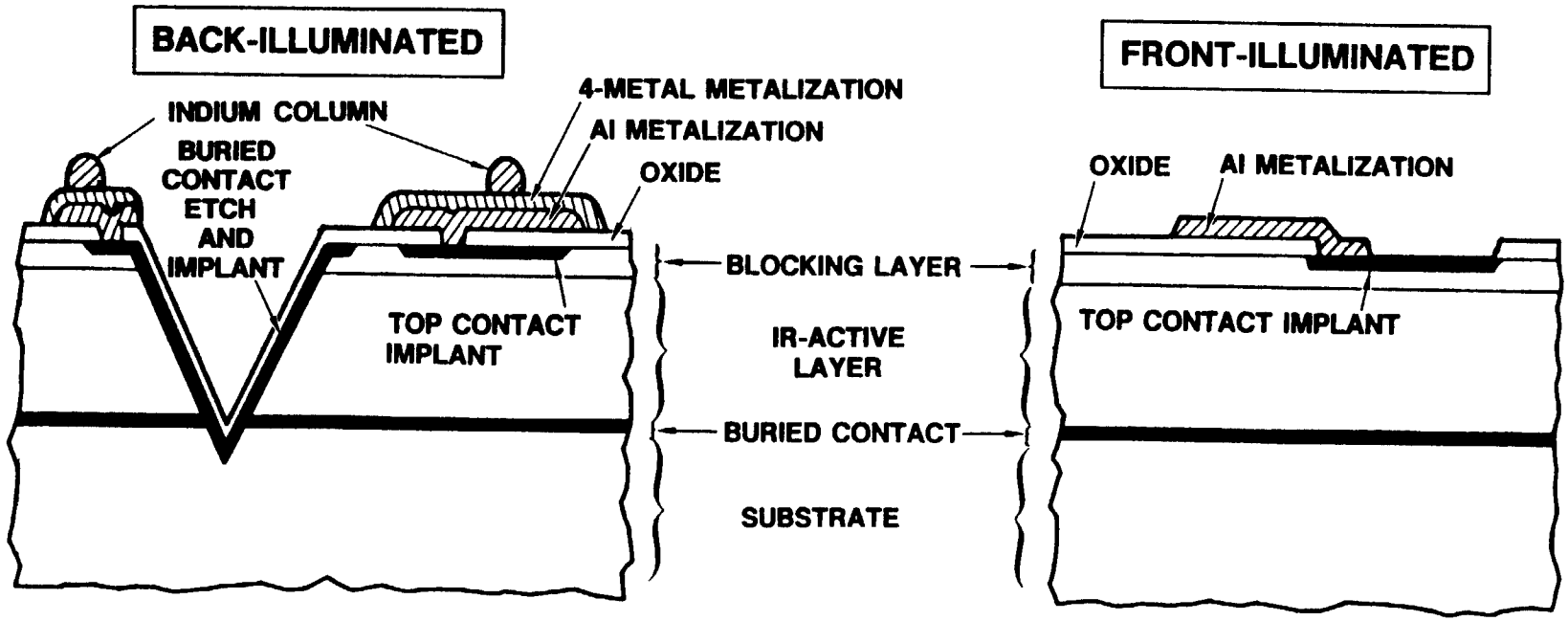

MATERIALS REQUIREMENTS

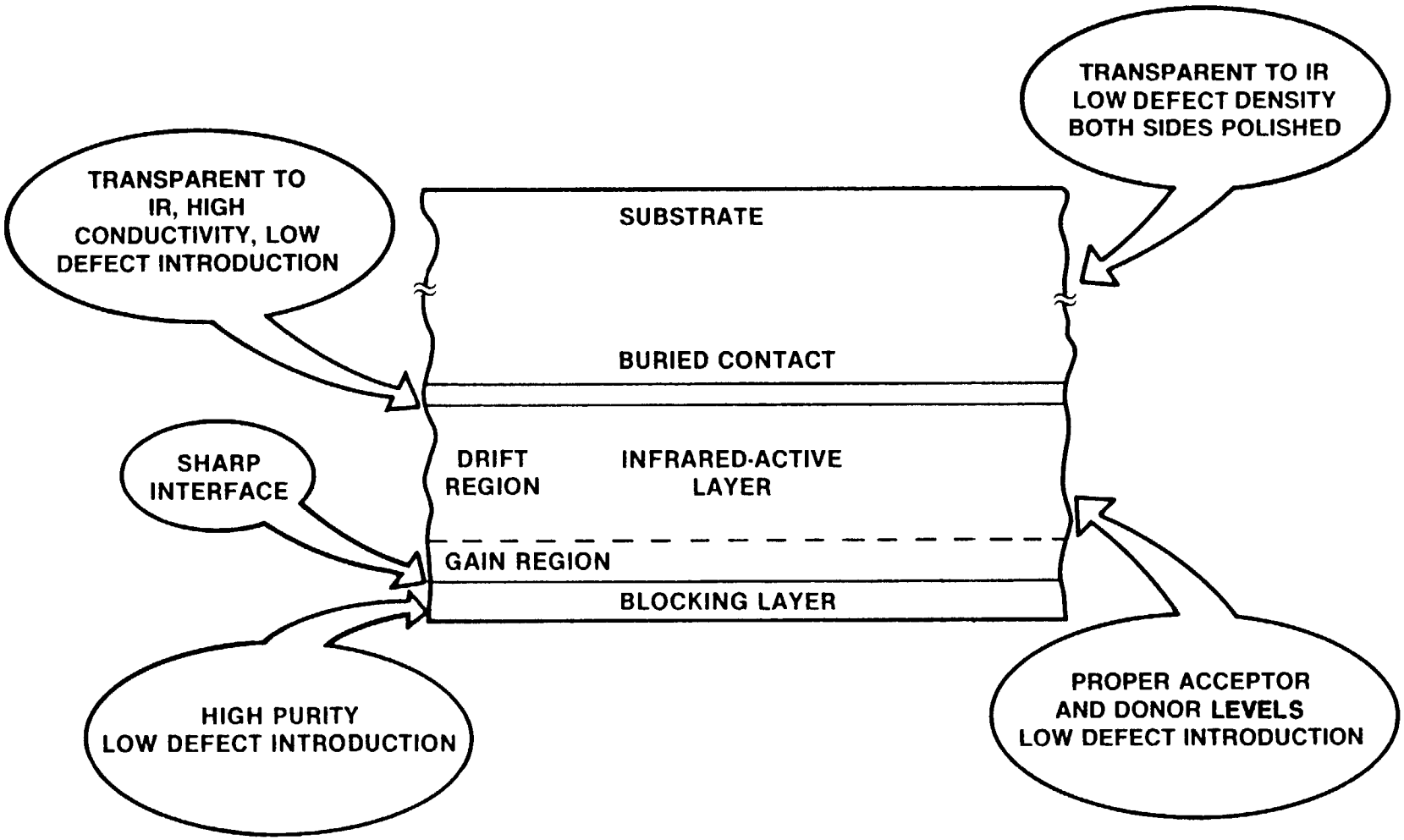

SOLID STATE PHOTOMULTIPLIER OPERATING PRINCIPLE

The Solid State Photomultiplier is a unique device in that it can continuously count single photons of wavelengths up to 28 μm. A pulse of about 40,000 electrons is the immediate and direct consequence of the absorption of a single photon.

An electric field profile through the SSPM is shown in (b), with the blocking layer on the left side of the cross-section. The slope of the field in the (depleted) gain region is proportional to the acceptor concentration. The higher fields toward the left end of the gain region produce most of the dc bias current by field-assisted thermal ionization (Poole-Frenkel effect). The dc bias current is responsible for the non-zero field throughout the undepleted part of the IR-active layer.

The detection of a single photon is shown schematically in (a). The photon ionizes a neutral donor in the drift region. The resultant ionized donor charge travels toward the substrate, while the conduction electron moves more quickly toward the gain region. At some point in the gain region the electric field is strong enough for impact ionization to occur. The primary photo-electron then ionizes additional neutral donors which, in turn, ionize other neutral donors, causing an avalanche. The produced pulse is a few nanoseconds wide and contains an average of about 4×10^4 electrons. The ionized donor charges produced in the avalanche move slowly and contribute a low tail to the pulse.

SOLID STATE PHOTOMULTIPLIER OPERATING PRINCIPLE

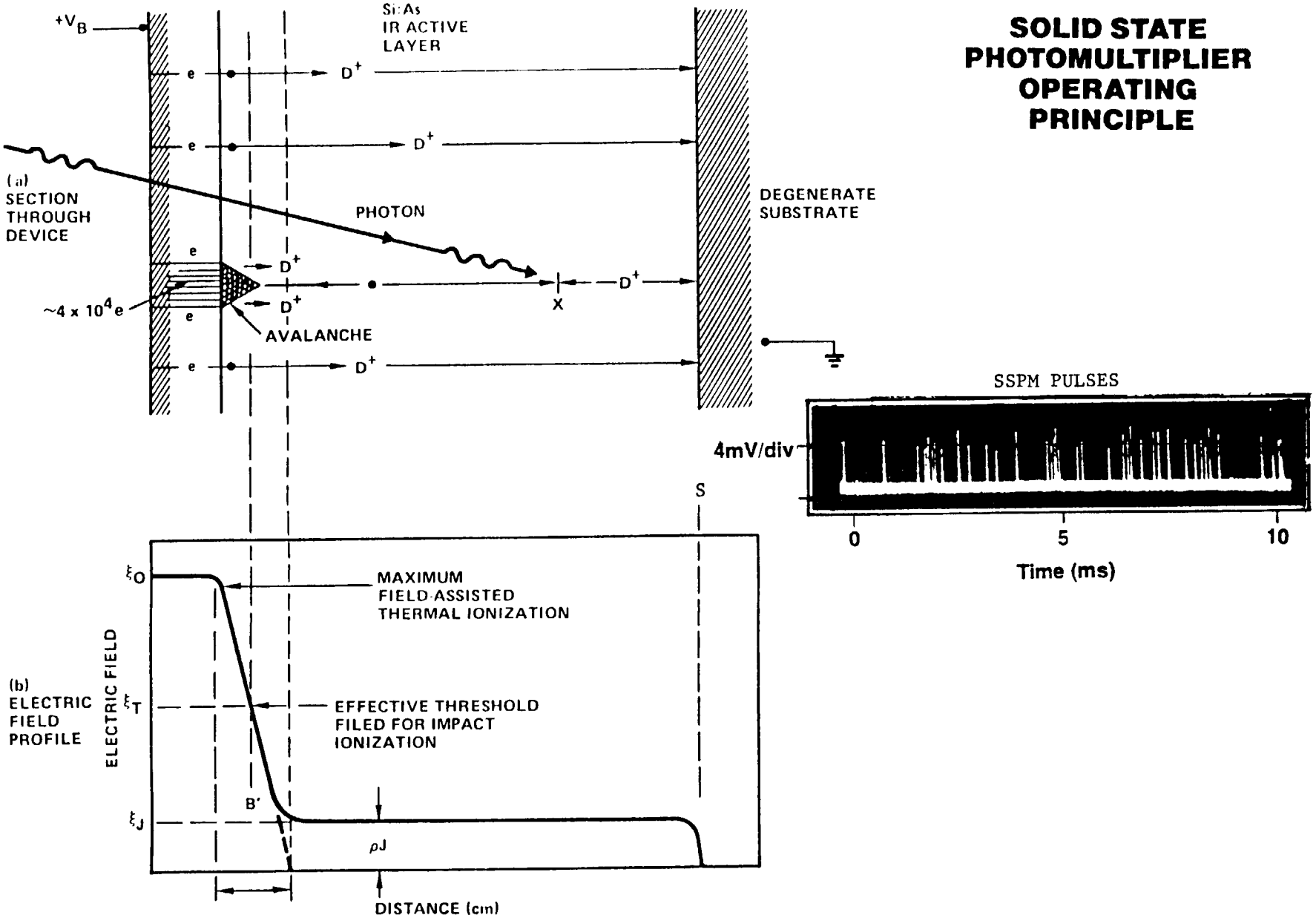

THEORY OF SSPM PULSE AMPLITUDE DISTRIBUTION

The SSPM pulse amplitude distribution is strikingly narrow, a feature which cannot be predicted with conventional avalanche photodiode (APD) theory.[3] A new phenomenological theory of the SSPM avalanche successfully predicts the shape of the observed pulse amplitude distribution by including the history-dependent effects present in the electron transport.[4] These effects appear as the presence of a finite mean distance $\hat{x}$ in the threshold distribution.[5] In conventional APDs, the mean distance-to-threshold is so small (i.e. $\hat{x}<0.05\mu m$) that its neglect is justified. For a simplified SSPM model, Monte-Carlo calculations show that $\hat{x}\approx 0.15-0.25\mu m$.[4] Although such distances are only about 5 percent of the SSPM gain region thickness, they are not negligible. The magnitude of the distance is due to the low (relative to the APD) electric field in the SSPM gain region; the variations are strongly correlated with variations in the field. As the accompanying figures show, for the SSPM model employed in Ref. 4, the theory provides pulse-amplitude distributions which are both realistic and dramatically different from the history-independent prediction.

3. G. E. Stillman and C. M. Wolfe, in *Semiconductors and Semimetals*, edited by R. K. Willardson and A. C. Beer, Vol. 12 (Academic Press, NY, 1977) .

4. R. A. LaViolette and M. G. Stapelbroek, J. Appl. Phys. **65** (1989) 830-6.

5. The threshold distribution is the distribution of distances between the birth of an electron via impact ionization and its subsequent achievement of the threshold energy required for impact ionization.

THEORY OF SSPM PULSE AMPLITUDE DISTRIBUTION

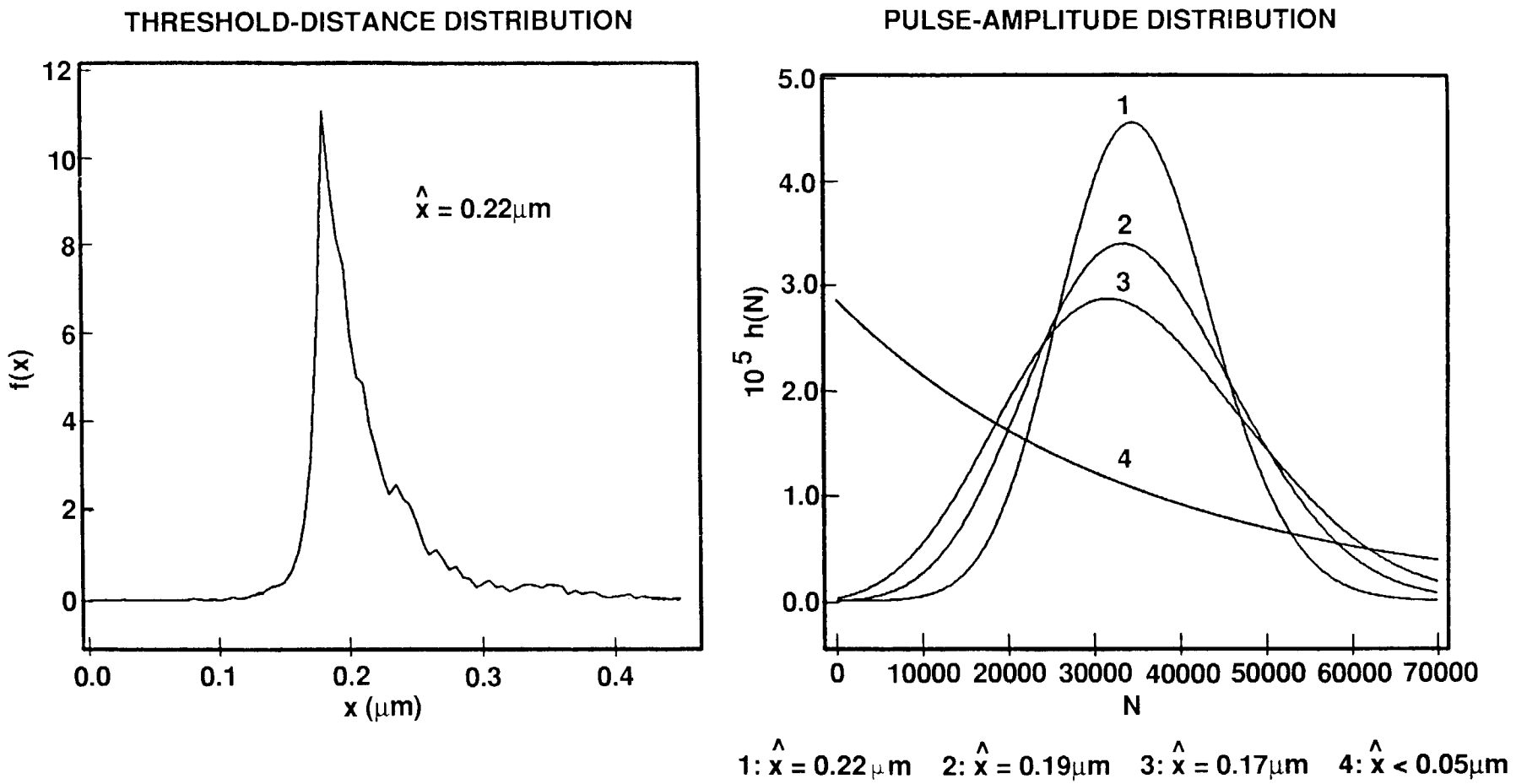

SSPM PROVIDES HIGH QUANTUM EFFICIENCY FROM 0.4 TO 28 MICROMETERS

The photon-counting quantum efficiency of an SSPM is affected by illuminating different faces of the device. The quantum efficiency changes because of differences in optical path lengths and the absorption coefficients of various layers.

Back-illuminated SSPMs make high-efficiency photon detectors in the infrared wavelength ranges, out to 28 μm. Photons that pass once through the active region of the SSPM without being absorbed are reflected at the front surface of the detector by an aluminum layer, so that the active thickness of the device is effectively doubled. Back-illumination is also the best approach for building hybrid focal plane arrays.

Front-illuminated SSPMs make high-efficiency photon counters in the visible and infrared wavelengths. The quantum efficiency in the visible range is extremely high, due to the generation of electron-hole pairs in the blocking layer and the subsequent impact-ionization of neutral donors in the IR-active layer by holes moving toward the substrate.

Finally, edge-illumination offers a significant advantage over front- or back-illumination in the near-to-mid IR wavelength ranges. With edge-illumination, the optical path length is no longer limited by the thickness of the IR-layer epitaxy, so that the probability of detecting these IR wavelengths, with their long attenuation lengths, can be greatly increased.

SSPM PROVIDES HIGH QUANTUM EFFICIENCY FROM 0.4 TO 28 MICROMETERS

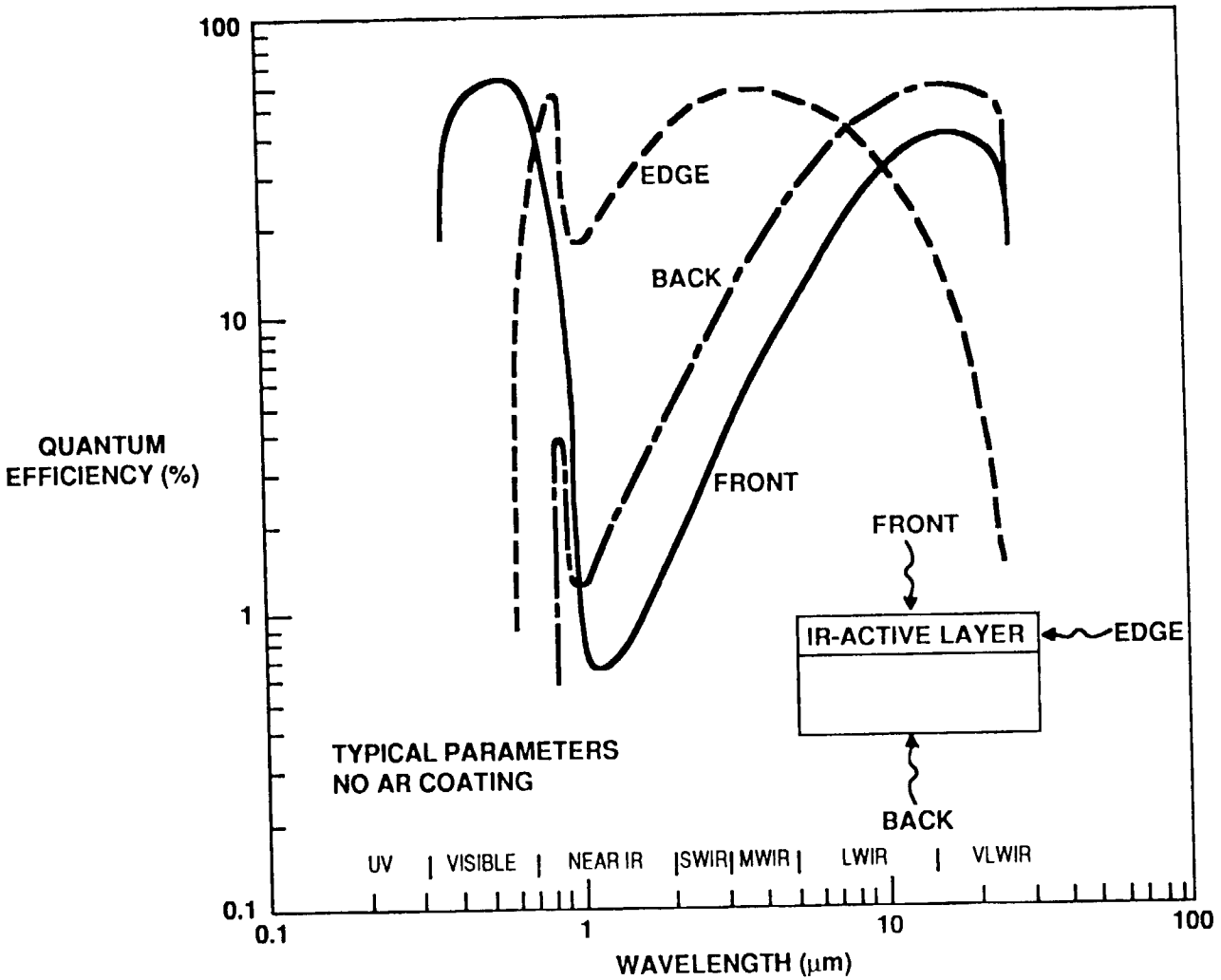

DETECTORS ARE TESTED IN VERSATILE CRYOGENIC DEWARS

SSPMs are characterized in custom-built low background test dewars. The extremely high sensitivity of these detectors requires that the flux be at or below 1×10^{6} photons/cm^{2}-s for accurate dark pulse rate measurements. Flux levels can be measured using an integral calibrated arsenic-doped extrinsic photoconductor mounted in close proximity to the detector cold stage. The temperature of the cold stage can be regulated between 4.3 and 20K.

The dewar contains a 3.2μm LED which can be used continuously or pulsed for intervals shorter than 1 microsecond. Other available illumination sources include pinhole shutter and hot resistor sources which are filtered by an interchangeable bandpass filter. Finally, a plastic optical fiber which transmits visible light and IR up to about 1.0μm wavelength is included for flood illumination studies of spectral response in the short wavelength range.

DETECTORS ARE TESTED IN VERSATILE CRYOGENIC DEWARS

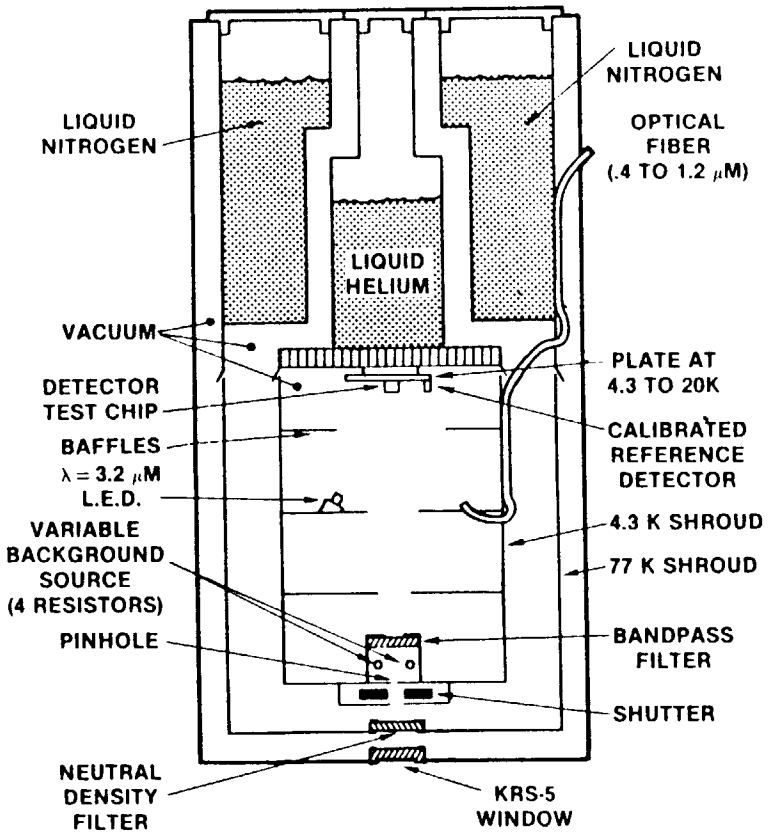

- BACKGROUNDS TO $< 10^6$ PHOTONS/CM^2-s
- PULSED 3.2μm LIGHT AT $>$ 1MHz
- CONTINUOUS VARIATION THROUGH VISIBLE SPECTRUM VIA OPTICAL FIBER
- UNIFORM FLOOD ILLUMINATION VIA FIBER, PINHOLE OR RESISTORS
- FILTERS EASILY INTERCHANGED
- TEMPERATURES RANGE FROM 4.3-20K
- INTEGRAL CALIBRATED DETECTOR

QUANTUM EFFICIENCY OF SSPMs FABRICATED FOR NASA-AMES

A fabrication lot of SSPMs was fabricated for NASA-Ames under contract NAS2-12400. One epitaxy set of wafers contained devices which showed quantum efficiencies of over 60 percent at λ = 20 μm.

The figures show photon counting quantum efficiencies gathered as a function of bias voltage and operating temperature. The quantum efficiencies were calculated using:

$$\eta = \frac{\nu_{illum} - \nu_{dark}}{\Phi A_{det}}$$

where ν was the average number of SSPM pulses counted per second and A_{det} = 150×150 μm^2 was the detector surface area. The incident flux density, Φ, was on the order of 10^8 photons/cm^2-s at both wavelengths.

The improvements in η with higher bias voltages and temperatures were due, in part, to increases in the drift region's electric field. Field-assisted thermal ionization near the high-field end of the gain region causes the bias current to increase at higher temperatures, resulting in a higher drift-region field.

At 11K, the maximum quantum efficiencies were lower than those measured at 10K. This was due to the high ν_{dark}, which was strongly temperature dependent. The recommended operating temperature for these SSPMs was 10K.

QUANTUM EFFICIENCY OF SSPMs FABRICATED FOR NASA-AMES

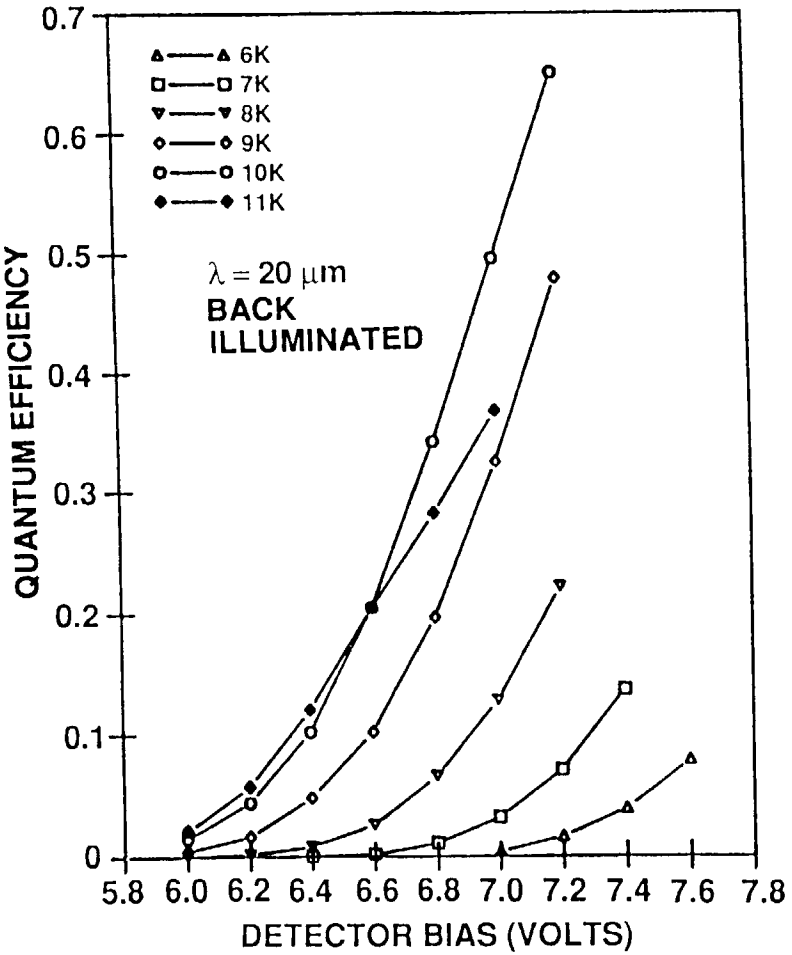

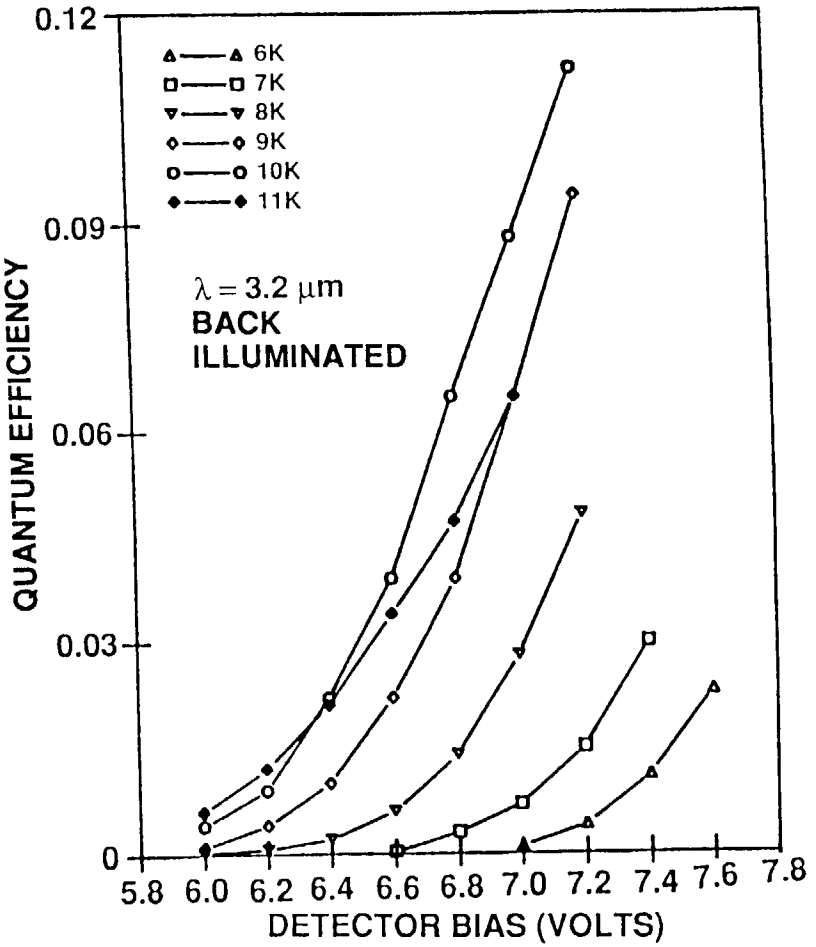

BIAS CURRENT OF SSPMs FABRICATED FOR NASA-AMES

The bias currents of the SSPMs whose quantum efficiencies appeared on the previous chart were measured as a function of temperature and bias voltage. It is important to characterize and minimize bias current for applications in which SSPM output current is integrated on a capacitor and periodically read out.

The bias currents were approximately given by:

$$I_{bias}(V_{bias}, T) = C_1 A_{det} e^{(C_2 V + C_3 / T)}$$

where A_{det} is the SSPM's area and C_1, C_2, and C_3 are constants which depend on the doping levels used in a particular device. The effect of field-assisted thermal ionization and the doping levels can cause changes in the detector's electric field profiles at different biases. This can result in a departure from the exponential dependence at lower bias voltages.

BIAS CURRENT OF SSPMs FABRICATED FOR NASA-AMES

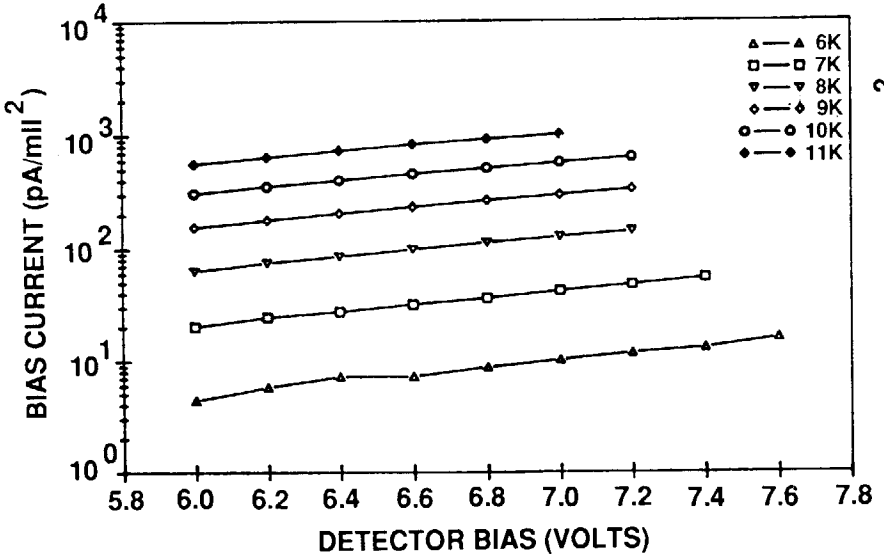

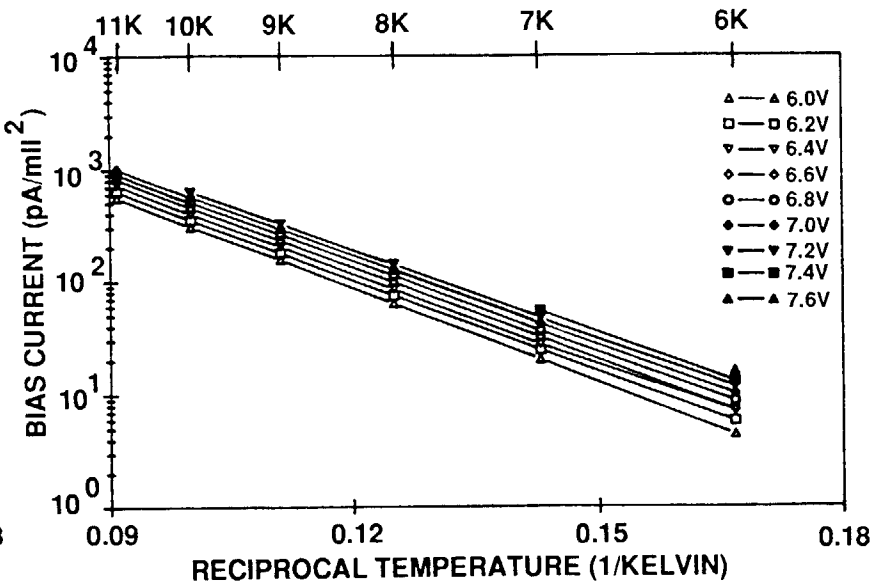

UNSURPASSED RESULTS OBTAINED FROM RECENT DEVICES

Efforts to produce SSPMs with lower dark count rates and higher operating temperatures have been successful. Since their invention, SSPM dark count rates at 10K have been reduced by almost two orders of magnitude. The success was due, in part, to improvements in epitaxy control and characterization. Lot PM-79 was produced under contract NAS2-12400 with NASA-Ames for Dr. C. McCreight. At their operating temperature, devices from lot PM-79 have higher quantum efficiencies and lower dark count rates than any previously produced SSPMs.

Further improvements in materials control are expected to result in further improvements in SSPM performance. The goal is a level of understanding and control sufficient to design SSPMs with gain, gain dispersion, dark count rates and operating temperatures matched to the needs of specific applications.

UNSURPASSED RESULTS OBTAINED FROM RECENT DEVICES

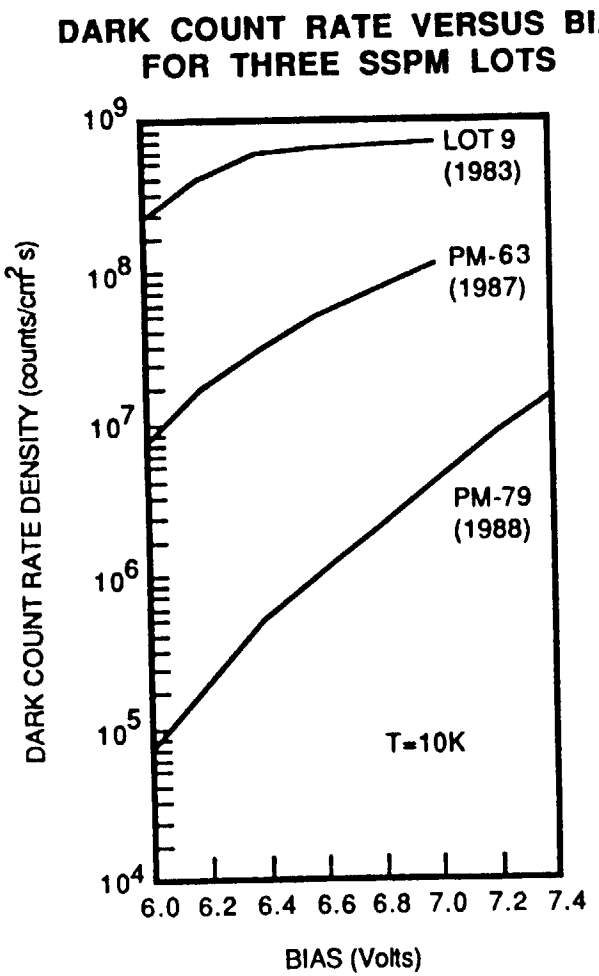

- DARK NOISE IS PROPORTIONAL TO THE SQUARE ROOT OF THE NUMBER OF DARK COUNTS
- THE PHOTON COUNTING QUANTUM EFFICIENCY OF AN SSPM IS MAXIMUM AT HIGH BIAS
- THE BEST GROUP OF SSPMs FROM LOT PM–79 HAS A LOWER DARK COUNT RATE AT ITS OPERATING BIAS THAN ANY PREVIOUSLY PRODUCED DEVICE GROUP

SSPM HAS UNPRECEDENTED SENSITIVITY AND SPEED

Due to its high gain, low gain dispersion and high speed, the SSPM does not require an ultra-low noise amplifier in order to resolve pulses due to single photons. As a result, SSPM performance is not limited by amplifier noise, even at extremely low flux levels. When it is used as a photon counter at low flux densities, the noise is given by:

$$\sigma_n = (n_{dark}+n_{signal})^{1/2}$$

where σ_n is the uncertainty in the number of counts, and n_{dark} and n_{signal} are the numbers of dark and signal counts, respectively. If the best illumination approach (e.g. front, back, or edge-illumination) is used at each wavelength, the low dark count rate and sensitivity of the SSPM result in a noise equivalent power that is orders of magnitude better than what is typically obtained from other common infrared detectors.

SSPM HAS UNPRECEDENTED SENSITIVITY AND SPEED

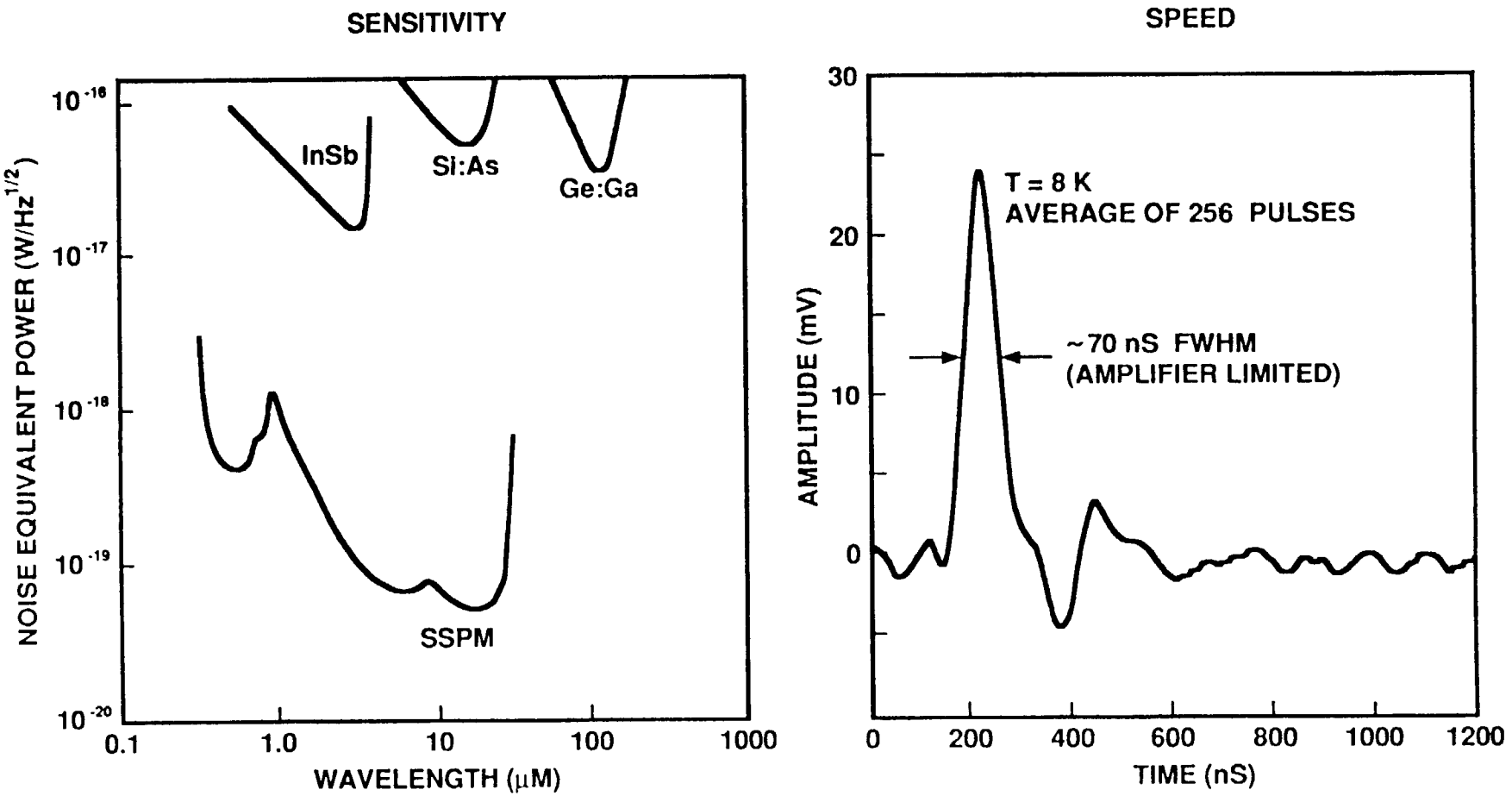

SUMMARY

- ROCKWELL'S SOLID-STATE PHOTOMULTIPLIER OUTPUTS A FAST PULSE OF ELECTRONS IN RESPONSE TO THE ABSORPTION OF A SINGLE 0.4-28 μm PHOTON
- MATHEMATICAL MODELS TO BETTER PARAMETERIZE THE SSPM AVALANCHE GAIN MECHANISM IN TERMS OF MATERIALS CHARACTERISTICS ARE CURRENTLY BEING DEVELOPED AND REFINED
- DRAMATIC IMPROVEMENTS IN PERFORMANCE HAVE RECENTLY BEEN REALIZED
- FURTHER OPTIMIZATION OF THE DEVICES IS BEING FUNDED BY NASA-AMES* AND OTHER AGENCIES

The Potential for High Performance HgCdTe Arrays at 4 Microns

G. H. Rieke, M. A. Sarfaraz, M. J. Rieke, and E. T. Young
Steward Observatory, University of Arizona

I. Introduction

The 3 to 4.5 micron spectral interval is of great interest for astronomy. In this interval, there is a minimum in background from earth orbit between the spectrum of solar light reflected by zodiacal dust grains (which dominates toward shorter wavelengths) and the thermal emission of these same grains (which dominates toward longer wavelengths). Coincidentally, the emission of stars in the galaxies as they first formed is likely to be redshifted into this wavelength interval. As a result, observations of great depth can be made with space borne infrared telescopes such as SIRTF that could extend to realms in the early Universe that are presently unobservable and that would provide entirely new insights on the formation of our galaxy and its environment.

There is also substantial interest in infrared spectroscopy over the same interval. Shortward of 1 micron, atomic lines dominate the spectra of astronomical sources; increasingly with longer wavelength, however, molecules become observable. Molecules exist in dense, cool regions of space where, for example, star and planet formation occur. Particularly for groundbased instrumentation, the thermal background emission of the telescope and atmosphere rises steeply toward 10 microns and atmospheric opacity increases dramatically longward of 15 microns, making sensitive molecular detections very difficult beyond 5 microns. Thus, the 3 to 4.5 micron region is very significant in understanding the origins of the solar system and of stars and planets.

Both of these applications are in part of interest because of the low backgrounds that make high sensitivity observations possible. To exploit these possibilities requires detectors and readouts of very high sensitivity. In the following, we have evaluated the potential of existing technology at Rockwell International in terms of the goals for astronomical detector arrays in the 3 to 5 micron interval.

II. Measurement Technique

A test system was built to allow operation of individual detectors over a temperature range of 5 K to 100 K. An integrating JFET amplifier allowed measurement of the current through the diode with an accuracy of a few electrons/sec or better. The diodes viewed a a variable infrared source through a fixed filter at 3.4 microns to measure the relative response.

The tests were conducted in a liquid helium dewar. The detector chip carrier is mounted in a connector on an aluminum block that is mounted to the work surface of the dewar through four fiberglass stalks that provide thermal isolation. A gold-plated copper bar screws to the aluminum block and presses the chip carrier into the connector, providing a large surface area for uniform cooling of the chip carrier; a hole in the bar allows introduction of infrared radiation to the test sample. This copper bar is attached by a gold-plated copper foil to a heat switch that allows sinking the copper to the

helium work surface or disconnecting this thermal path through an external actuator. A thermometer on the bottom of the aluminum block monitors the temperature; a heater is also provided in this location. Over the top of the copper bar and chip carrier there is a baffle that carries the infrared filter, which for all these tests had a bandpass of 0.1 microns centered at 3.4 microns. A second baffle box encloses the entire thermal stage and carries a filament from a small light bulb as a source of infrared radiation.

The JFET integrating amplifier was supplied by Infrared Laboratories, Inc. The amplifier is mounted on a header using insulating rods of polyamide and is provided with a heater. The header is cold sunk to the liquid helium work surface of the dewar and the heater current was adjusted to bring the amplifier to its optimum operating temperature. The output of the amplifier passes through a number of stages of gain and a low pass filter, and is then digitized and fed into a Compaq computer. The computer controlls the data-taking cycle by resetting the amplifier and collecting data as charge accumulates on the gate of the amplifier. The resulting voltage ramp is fitted with a straight line to estimate the current flowing onto the gate. The system was calibrated by measurement of the various gains and of the input capacitance of the amplifier (5 pf). A nominal allowance of 1 pf was made for the additional capacitance of the detector and wiring; because of the large capacitance of the amplifier, small variations in the detector capacitances will have little effect on the currents deduced. Errors in the current measurement are estimated from the repeatability of a series of measurements, each of which is 10 to 15 seconds in length. In cases where large currents were to be measured, the computer is replaced with a storage oscilloscope and the voltage slopes are estimated from the oscilloscope display.

An important aspect of the apparatus is that only the temperature of the detector (and infrared filter) were varied during the measurements, not the infrared stimulator or the output amplifier. As a result, any temperature-dependent changes could be attributed confidently to the detector.

Measurements were also made on the temperature dependence of the operation of a Rockwell-supplied NICMOS 2 switched FET readout. These tests were conducted with a dewar and control system designed and constructed by R. Rasche, G. Winters, and R. Schnurr of the NICMOS project. The NICMOS 2 MUX (without detector material) was attached to a copper block mounted on the work surface of the dewar. A thermometer and heater were embedded in the same copper block. The dewar work surface was cooled with liquid helium to ~ 10 K, and then allowed to warm up; the temperature of the detector mounting block increased roughly at the rate of 0.3 K/min, so measurements were always in a state of pseudo-equilibrium.

III. Results

Measurements have been obtained for a number of samples of HgCdTe diodes manufactured by Rockwell International. All the diodes reported on here had cutoff wavelengths at high temperatures of 4.6 to 4.7 microns. Although no confirming measurements were made, the cutoff wavelength is expected to move to 5 microns or beyond at the low temperatures of our tests. Diode sizes ranged from 20 to 150 microns. The test program yielded full diode curves and relative response at 3.4 microns for the sample diodes as a function of temperature. Dark currents are quoted below as the current passing through the diode with a back bias of 50 mV.

The various diode types showed a wide range of behavior, both with regard to dark current and responsivity. The test results for one of the best diode types are illustrated in more detail in Figure 1. This detector has a size of 148 microns and a cutoff wavelength of 4.61 microns.

The behavior in Figure 1 is fairly typical of the other good diodes. For all of these detectors, responsivity fell with decreasing temperature with most of the change occurring between 45 and 25 K. Little further change was observed below 25 K. At low temperatures, the responsivity was 40 to 50% of that observed at 60 to 70 K. Assuming the quantum efficiency at these higher temperatures is ~ 60% (K. Vural, private communication), the diodes operated with quantum efficiencies of 25 to 30% even at the lowest temperatures encountered in these tests (~ 5 K). The dark currents fell rapidly with decreasing temperature to 30 to 35 K. Below this temperature, the currents were constant, at values as low as 30 to 60 electrons/second.

The NICMOS 2 MUX functioned correctly above 36 K. Below 36 K, a shift register on the output failed and only two rows of the array could be read out. The MUX resumed full operation between 21 and 24 K, below which it was again inoperative. Under the assumption that the input capacitance is 0.05 pf (the value measured at 77 K) at all temperatures, the read noise is as in Table 1. The entries at 37 and 24 K should be interpreted as upper limits, since the results may be affected by the lack of complete temperature stability. In addition, the optimization of the voltage levels and other operating parameters had not been completed at 77 K, and no attempt was made to re-optimize for the lower temperatures. It is possible that further adjustment of operating parameters would both improve the read noise and extend the temperature regions of operability.

IV. Conclusion

Although none of the components we have tested was developed for the low temperature operation required for ultimate faint signal performance at 4 microns, it appears that judicious selection of diode type and MUX operating conditions would produce an array at or beyond the current state of the art. It is to be hoped that further improvements could be achieved by further development, for example by using a multiplexer design that would operate solidly below 30 K and perhaps by modifications in the diode architecture to enhance the response and reduce dark current at very low temperatures.

Acknowledgements

We appreciate the contributions of R. Rasche, R. Schnurr, and G. Winters to our measurements of the NICMOS 2 MUX. K. Vural provided helpful advice regarding these tests. This work was supported by NASA and is part of the technology development for the Multiband Imaging Photometer for SIRTF.

Table 1. Read Noise for NICMOS 2 MUX

T (^{o}K)	Noise (electrons rms)
77	42
37	$\leq$ 78
24	$\leq$ 92

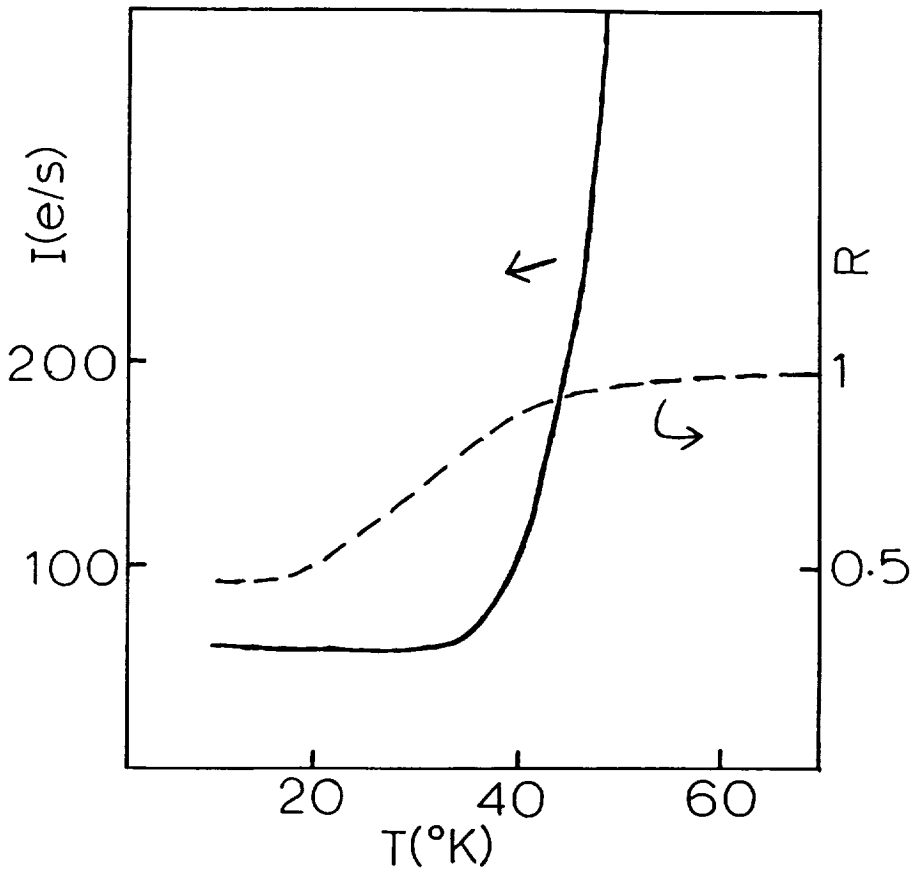

Figure 1. Dark Current and Relative Response for a HgCdTe Diode. Response is measured at 3.4 microns and is referred to 1.00 at 70 K, as indicated on the right scale. Dark current is measured under 50 mV back bias and is given in electrons/sec on the left scale. The diode is 148 microns in size and has a nominal response cutoff at 4.61 microns.

IR Detector Technology Workshop
Feb. 7 - 9, 1989
NASA Ames Research Center

GERMANIUM BLOCKED IMPURITY BAND (BIB) DETECTORS

E. E. Haller[1,2]
H. Baumann[1,2]
J. Beeman[2]
W. L. Hansen[2]
P. N.Luke[2]
M. Lutz[1,2]
C. S. Rossington[1,2,3]
I. C. Wu[1,2]

[1]University of California at Berkeley
[2]Lawrence Berkeley Laboratory, UCB
[3]Present address: Hewlett-Packard, Opto-Electronic Division, 350 W. Trimble Rd., San Jose, CA 95131

CONTENTS

1. INTRODUCTION

- Extrinsic, photoconductive semiconductor detectors cover the infrared spectrum from a few μm up to 250 μm.

- Photoconductors exhibit high responsivity and low noise equivalent power.

- The Si blocked impurity band (BIB) detector invented by M. D. Petroff and M. G. Stapelbroek has a number of advantages over standard bulk photoconductors. These include:

  - smaller detection volume leading to a reduction of cosmic ray interference

  - extended wavelength response because of dopant wavefunction overlap

  - photoconductive gain of unity

2. Ge BIB

- The success of Si BIB detectors has been a strong incentive for the development of Ge BIB detectors.
- The advantages of Si BIB detectors stated above should, in principle, be realizable for Ge BIB detectors.
- If Ge BIB detectors can be made to work out to 250 μm with high responsivity and sufficiently low dark current, they could replace stressed Ge:Ga photoconductors.
- Can the dark current be reduced to acceptable levels?

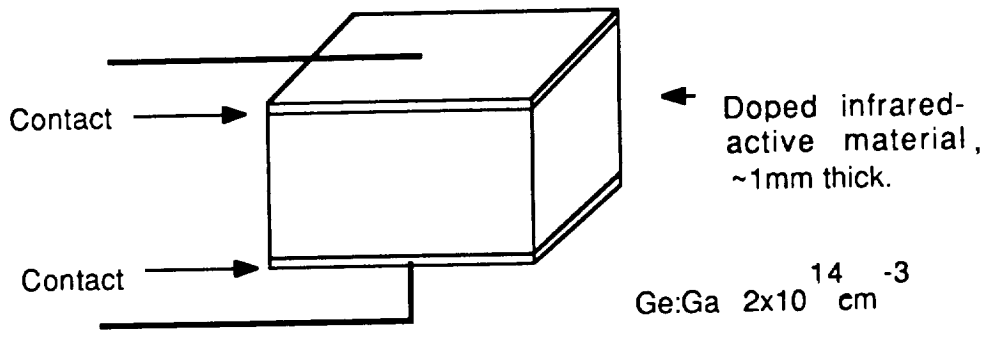

Figure 1(a). Schematic of conventional detector.

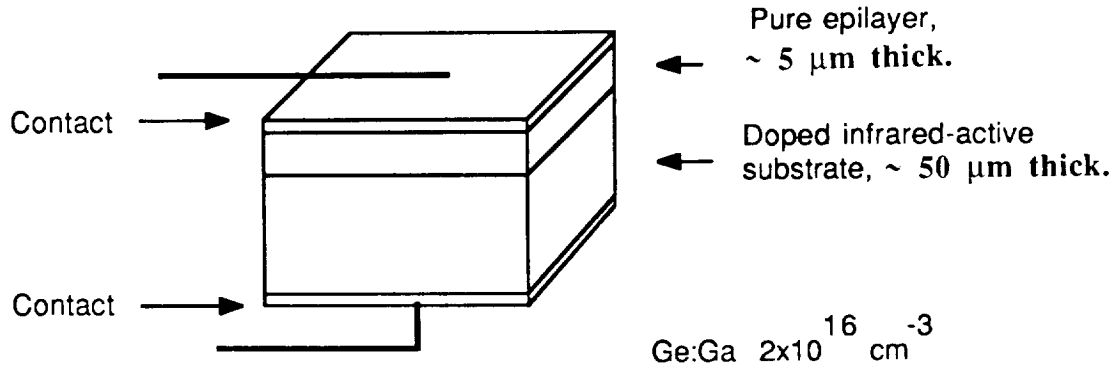

Figure 1(b). Schematic of BIB detector.

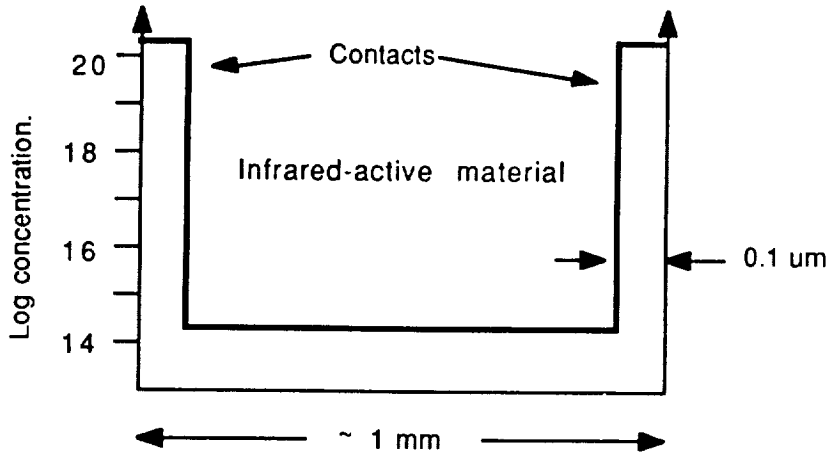

Figure 2(a). Doping levels in a conventional Ge detector.

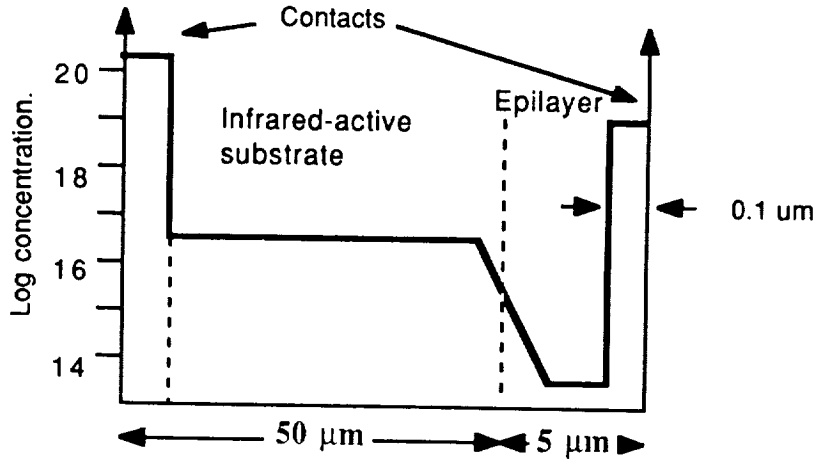

Figure 2 (b). Doping levels in a Ge BIB detector.

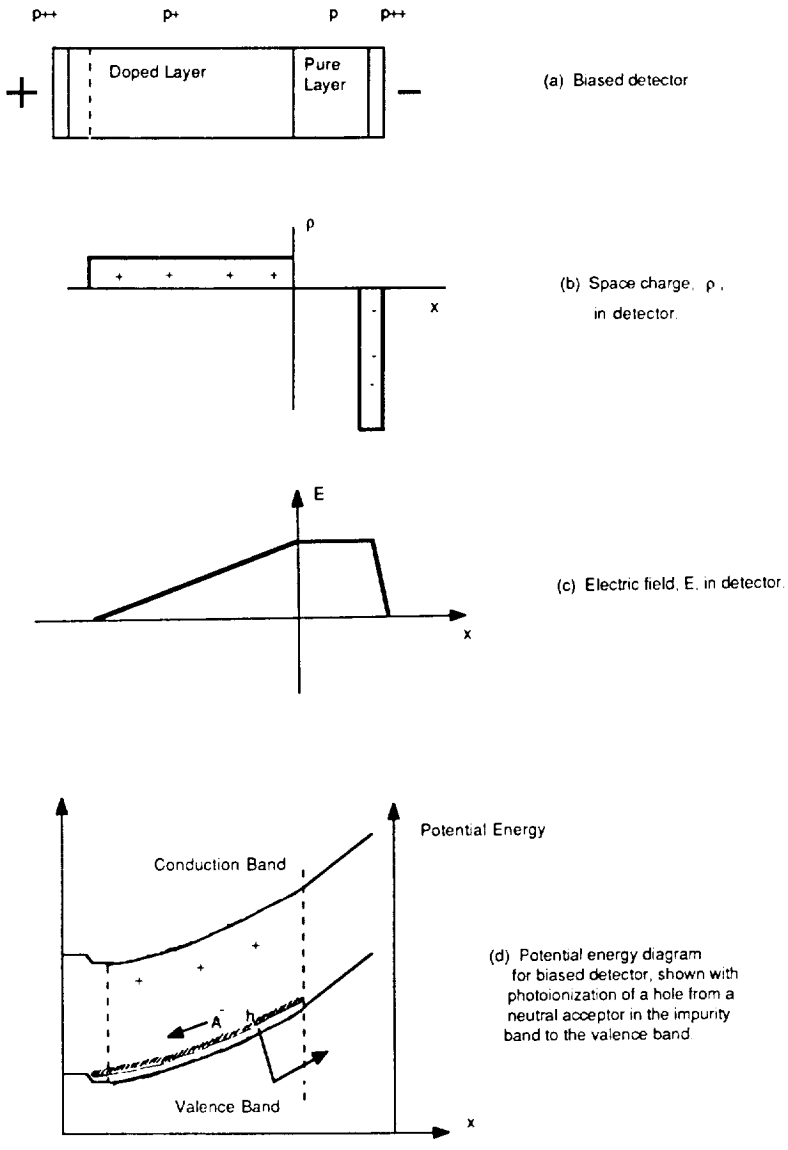

Fig. 3. Schematics of space charge, electric field and potential energy for a reverse biased p-type BIB detector.

3. Ge BIB DETECTOR DEVELOPMENT

3.1. Epitaxial Blocking Layer Devices

3.1.1. Ge epitaxy

- Whereas Si epitaxy techniques have been developed to a very high degree of perfection, Ge epitaxy has been attempted only on a few occasions.

- Ge chemistry is very different from Si chemistry.

- Ultra-pure Ge compounds [$Ge(CH_3)_4$, $Ge(C_2H_5)_4$] are being developed for III-V semiconductor technology. They may be useful to Ge epitaxy.

Substrate choice and preparation

- We have used a number of different crystals with various crystallographic orientations in the development of Ge epitaxy:
  - n-type wafers (~10^{11} cm^{-3}) are used for the electrical characterization of the epitaxial layers which are typically p-type because of residual copper contamination (junction isolation).
  - p-type wafers (~10^{15} cm^{-3}) are used for I-V comparison tests with conventional photoconductors.
  - p-type wafers (~2 x 10^{16} cm^{-3}, low compensation) are used for Ge BIB detectors.

- Wafer polishing process:
  - mechanical planar lapping with alumina slurry.
  - mechano-chemical polishing with syton containing H_2O_2.
  - brief etch in HNO_3:HF (3:1) followed by soak in HF (1% in H_2O) to remove oxides.

- Epitaxy:
  - first experiments with atmospheric pressure vapor phase epitaxy (VPE). Disadvantage: high substrate temperature, H_2 diluted feed gas (contamination, diffusion of dopants into the blocking layer).
  - current experiments are performed with low pressure VPE. Advantage: low substrate temperature.

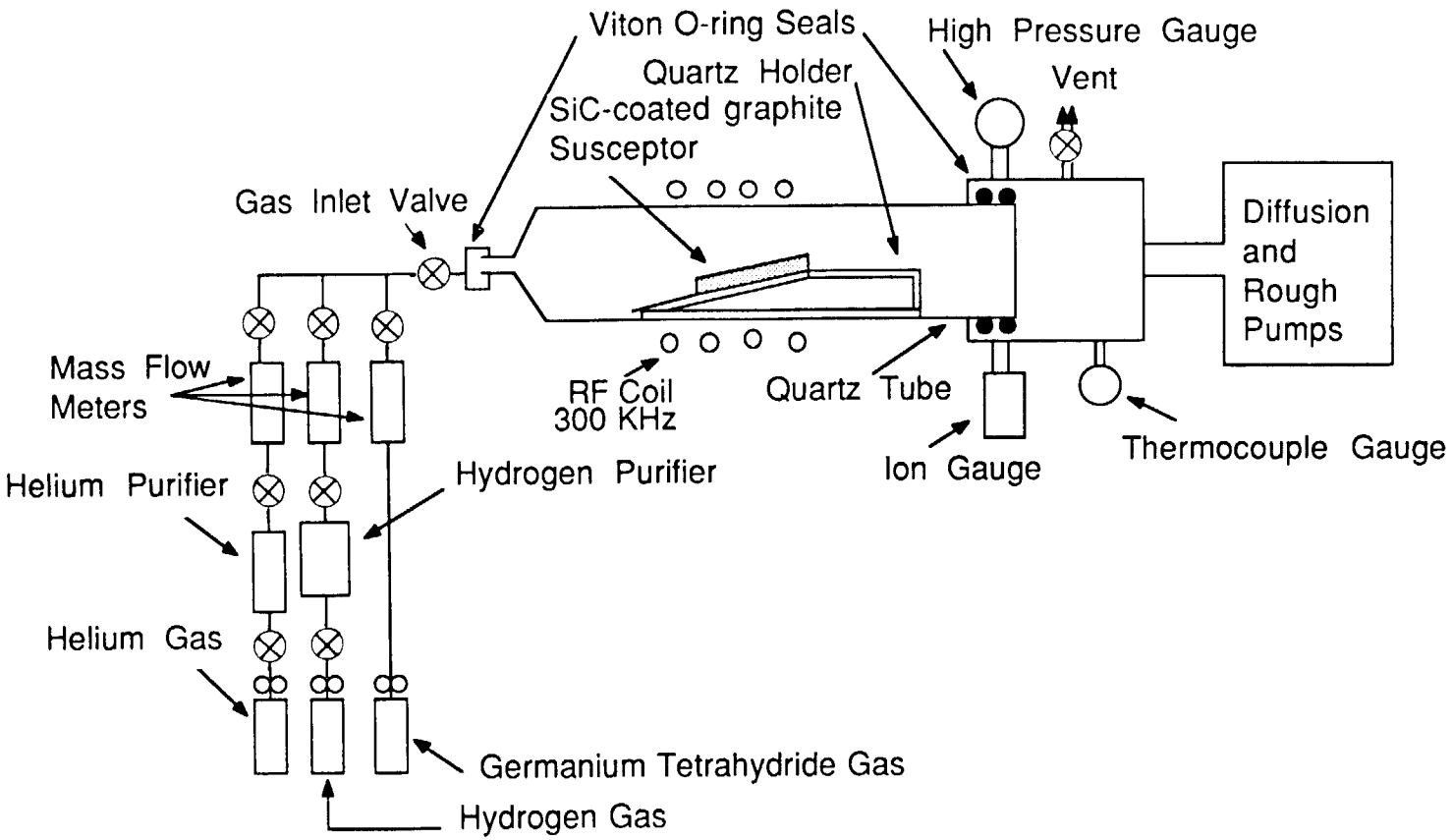

Fig. 4. Schematic of horizontal VPE apparatus. Quartz tube is 5.7 cm O.D. x 75 cm long.

3.1.2. Characterization of epi layers

- Optical micrographs
- Variable temperature Hall effect and resistivity
- Rutherford backscattering (channeling) spectrometry (RBS)
- Secondary ion spectrometry (SIMS)
- Spreading resistance measurements

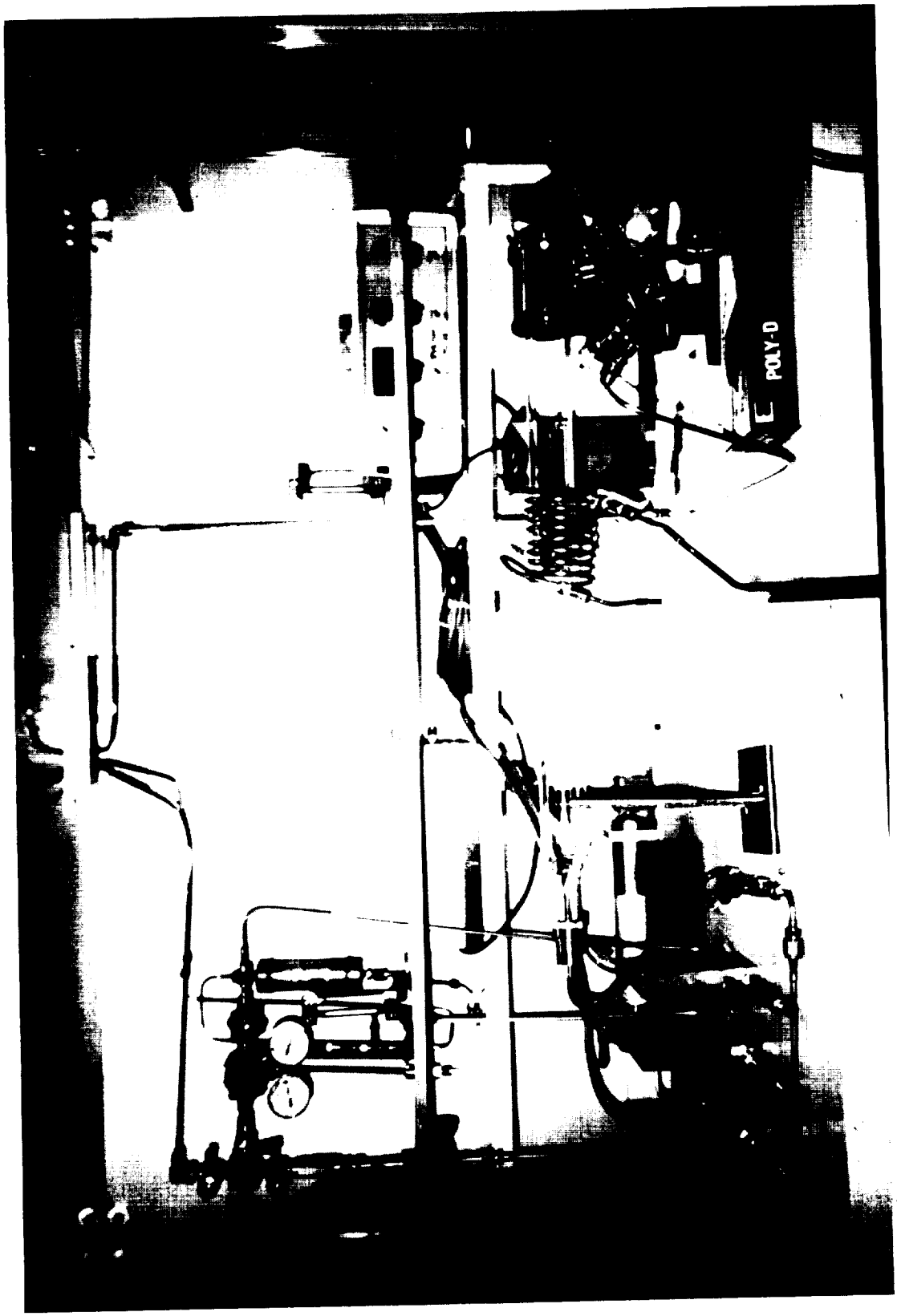

Fig. 5. Photograph of the horizontal VPE chamber.

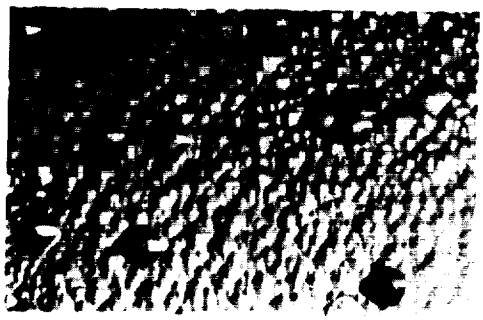

(100) $N_D - N_A = 1 \times 10^{14} / cm^3$
580 °C; 5 sccm GeH_4,
with H_2 reduction step,
polycrystalline deposition

(113) $N_D - N_A = 2 \times 10^{14} / cm^3$
580 °C; 5sccm GeH_4,
with H_2 reduction step,
no growth (etching)

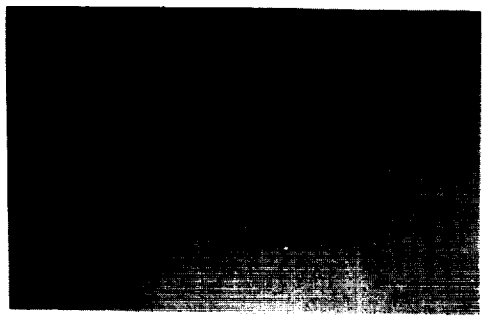

(113) $N_D - N_A = 5 \times 10^{11} / cm^3$
550 °C; 10sccm GeH_4,
no H_2 reduction step,
single crystal deposition

Fig. 6. Optical micrographs of Ge epi layers.

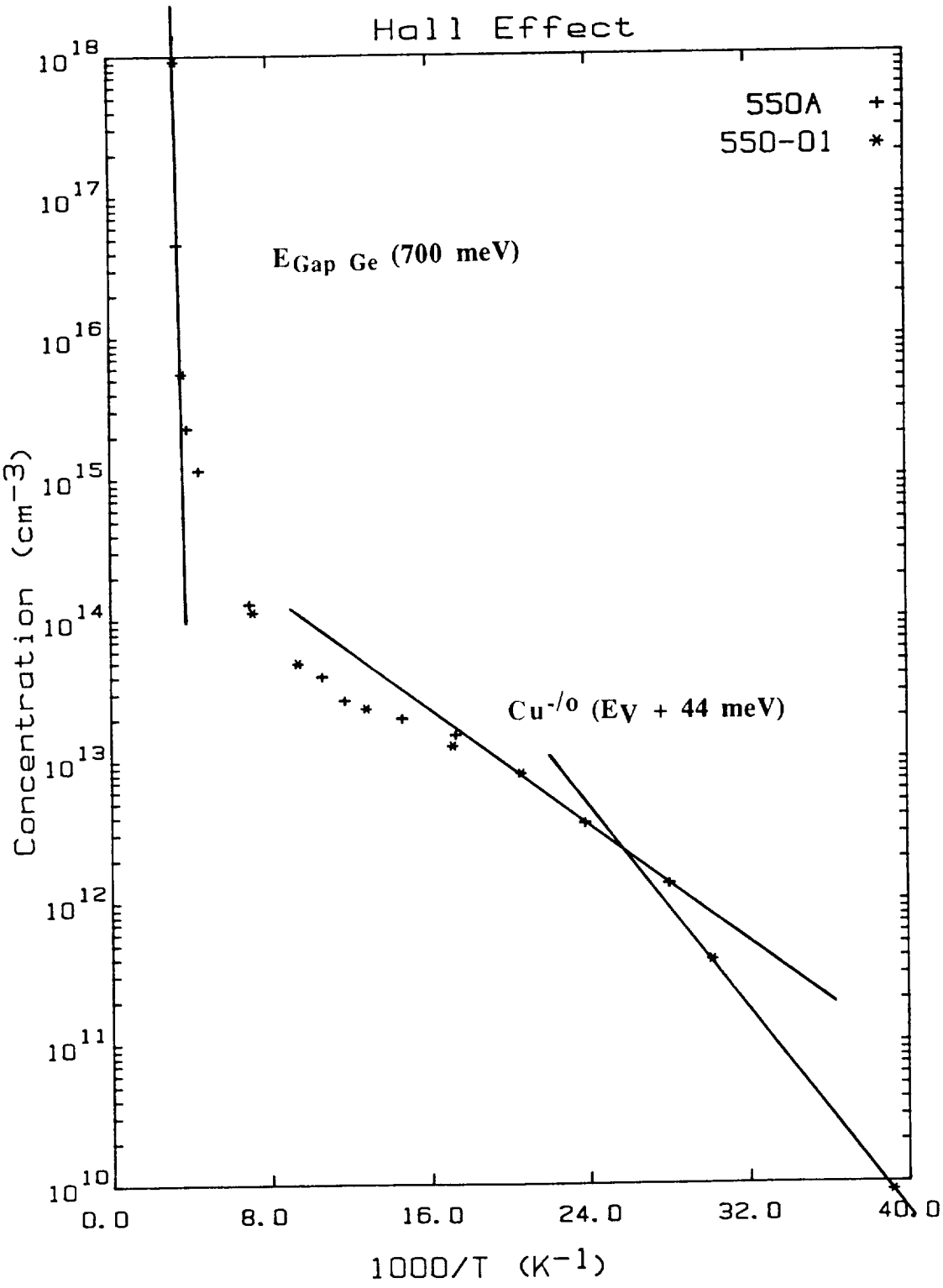

Fig. 7. Variable temperature Hall effect measurements of a Ge epilayer on an n-type [113] substrate. The hole freeze-out curves indicate a light copper contamination. The two curves (+, *) are measurements of the same sample and demonstrate reproducibility.

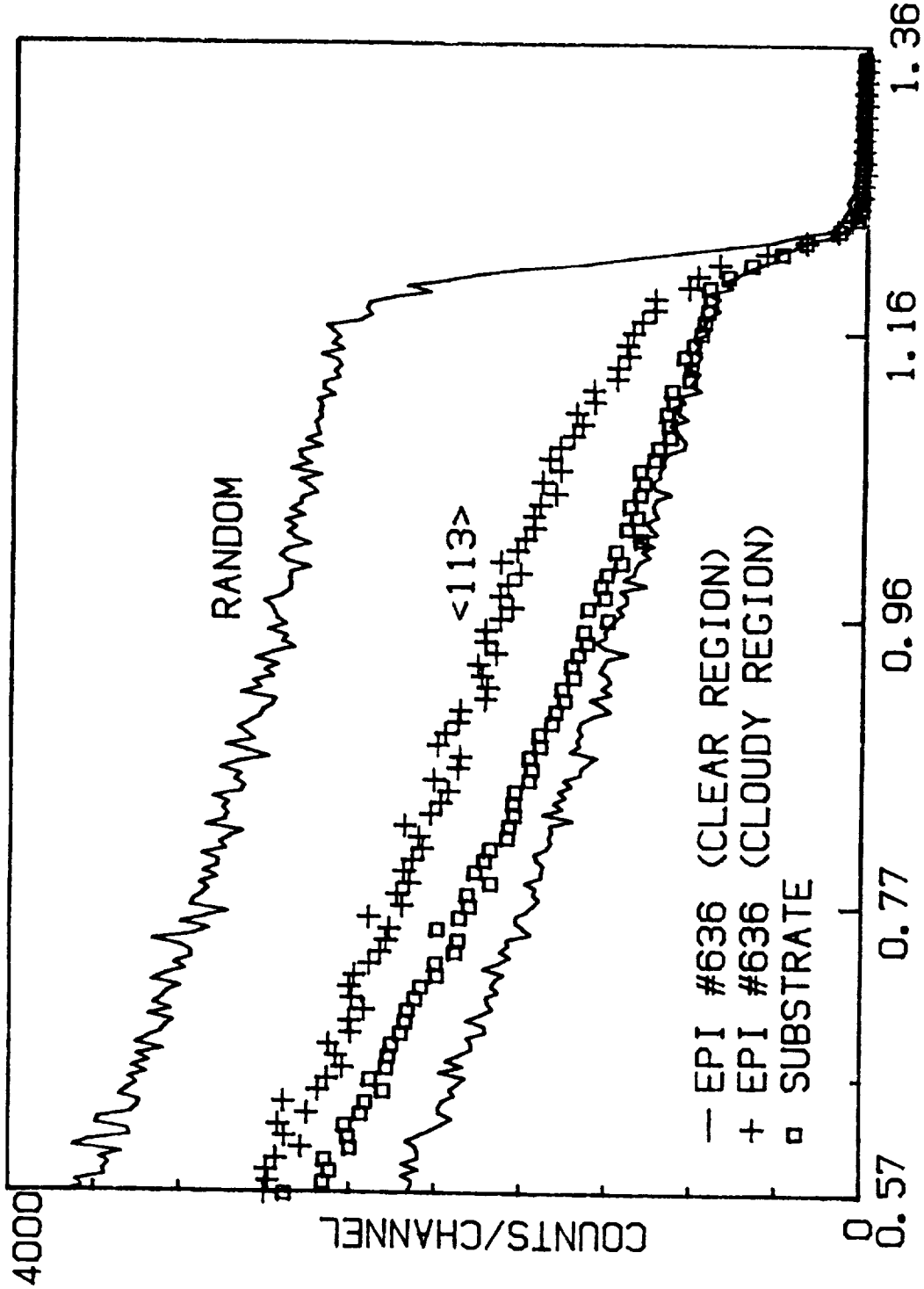

Fig. 8. RBS channeling spectra of a Ge epi film (#636). The "cloudy" region shows significant dechanneling indicating a high defect concentration.

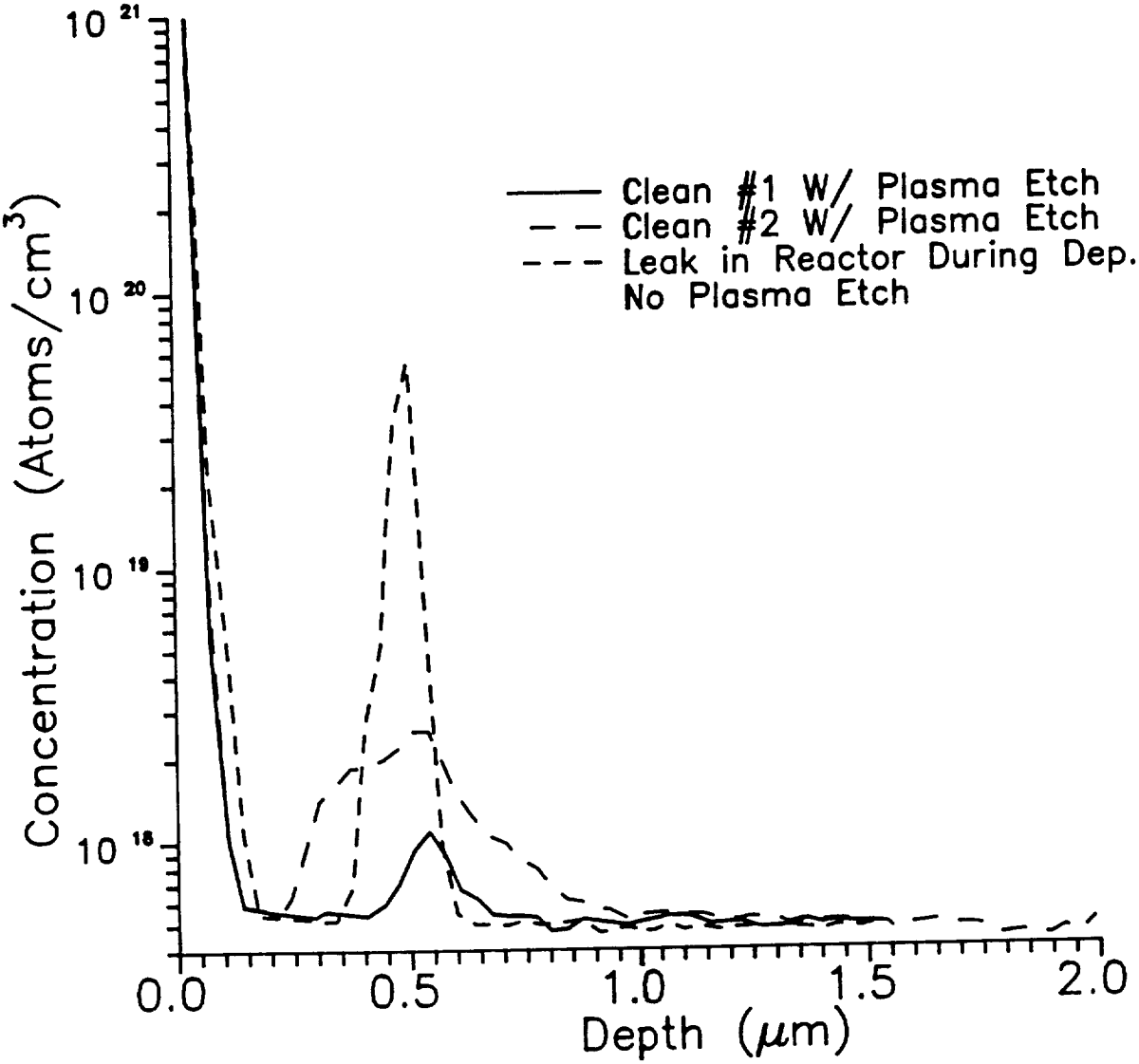

Fig. 9. SIMS of LPVPE Epi Films: Oxygen Concentration

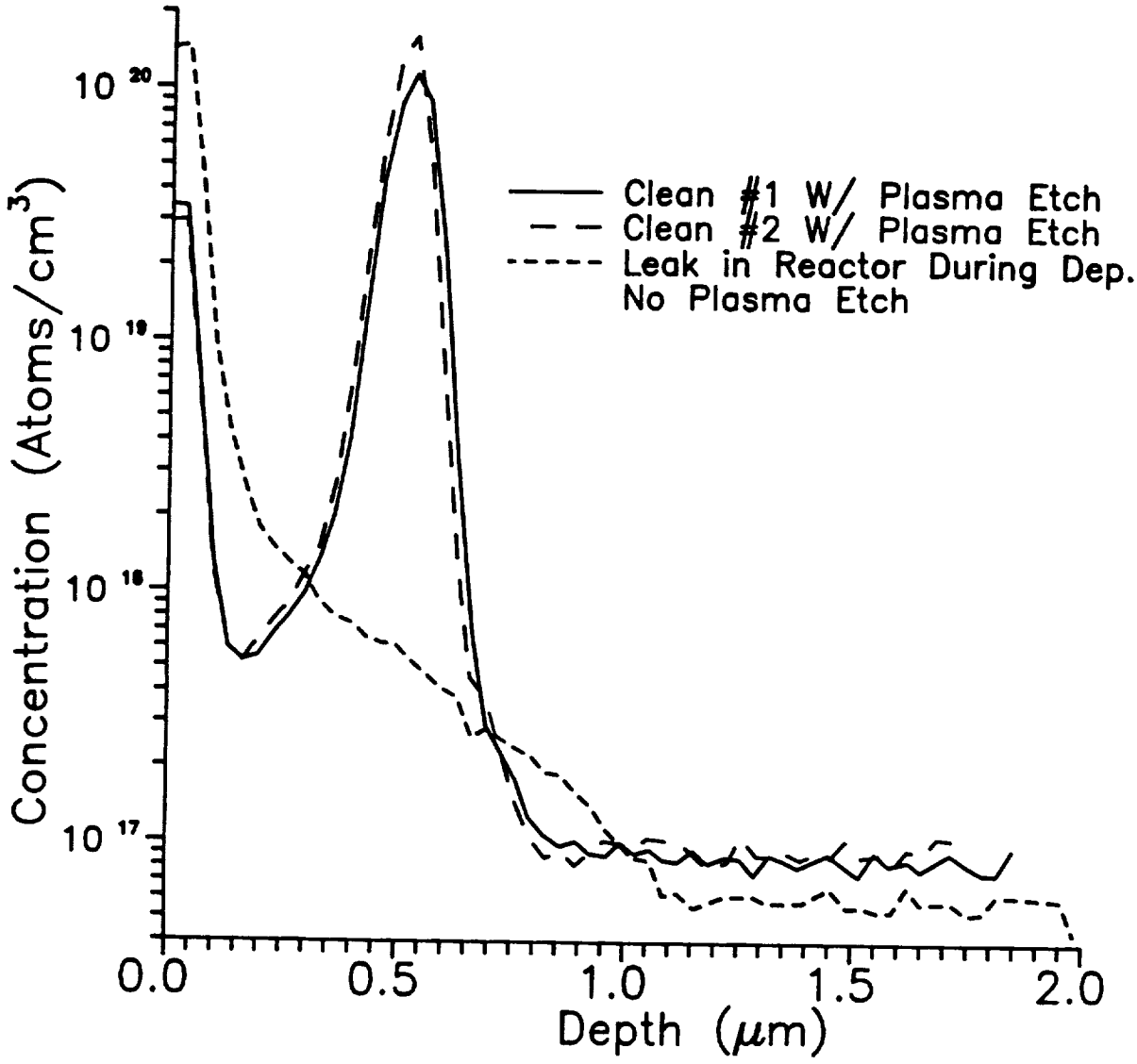

Fig. 10. SIMS of LPVPE Epi Films: Carbon Concentration

3.1.3. Preliminary detector test results

- **Responsivity**
- **Dark current**

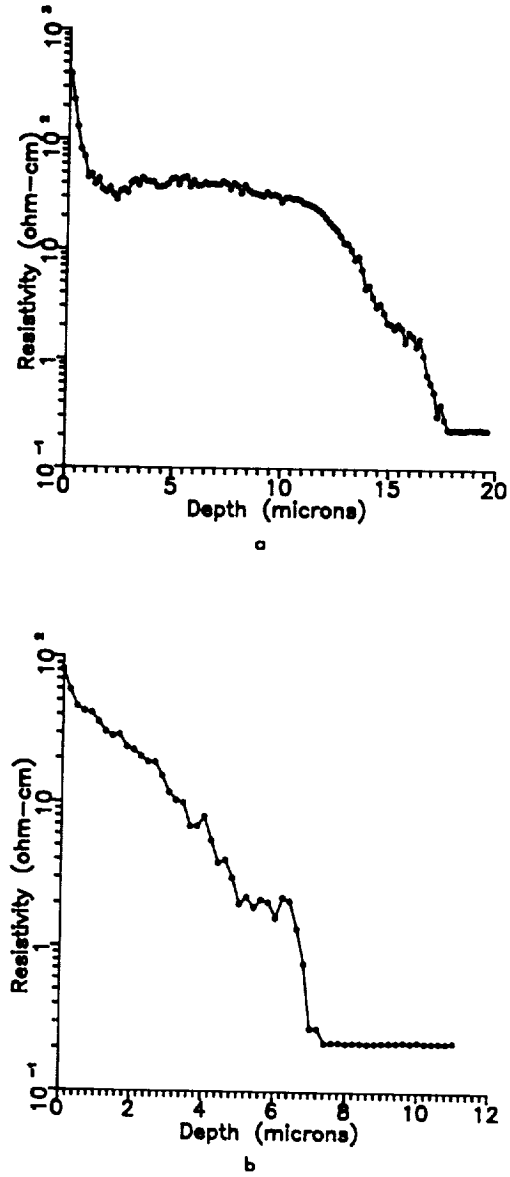

Fig. 11. Spreading resistance as a function of depth from the epilayer surface for: (a) an area of epilayer close to the leading edge of the wafer in II-16 where the growth rate was ~ 0.06 $\mu m min^{-1}$, and (b) an area of epilayer farthest from the leading edge of the same wafer where the growth rate was ~ 0.02 $\mu m min^{-1}$. The slight rise in resistivity at the very surface is due to the native oxide.

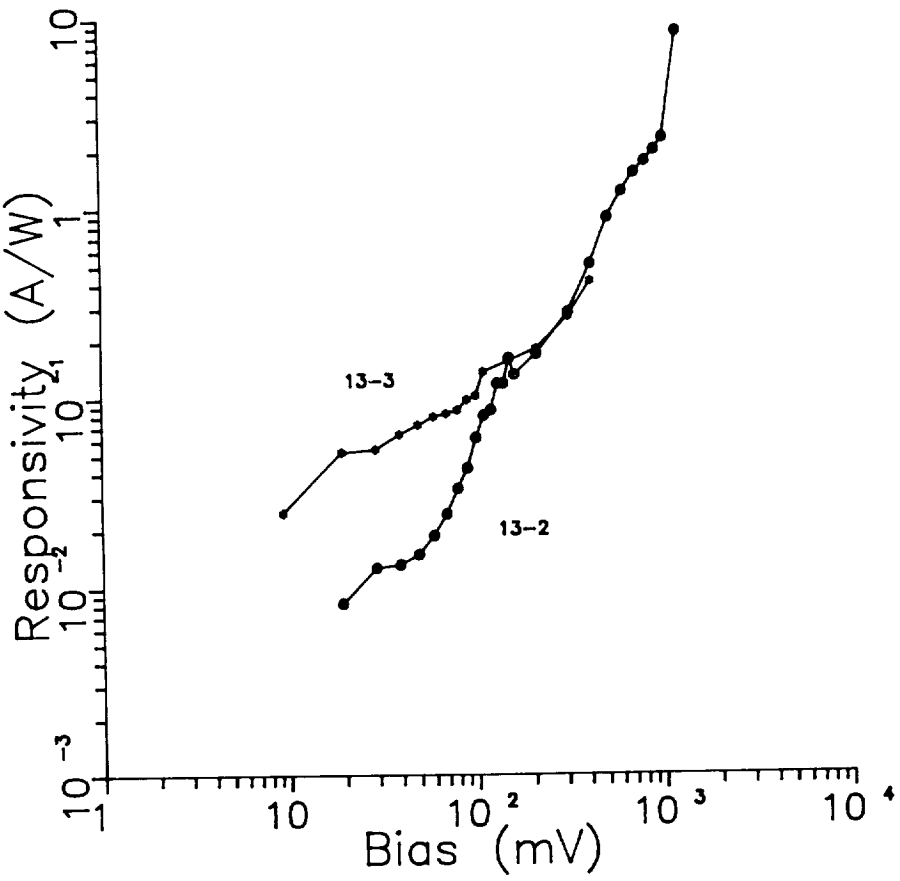

Fig. 12. Responsivity as a function of bias for detectors 13-2 and 13-3 at 2.3 K under reverse bias. The substrate material is moderately doped (5×10^{15} cm^{-3}). Such material exhibits hopping conduction but does not have extended wavelength spectral response. Tests were performed with a narrow band filter at $\lambda = 98.9$ μm.

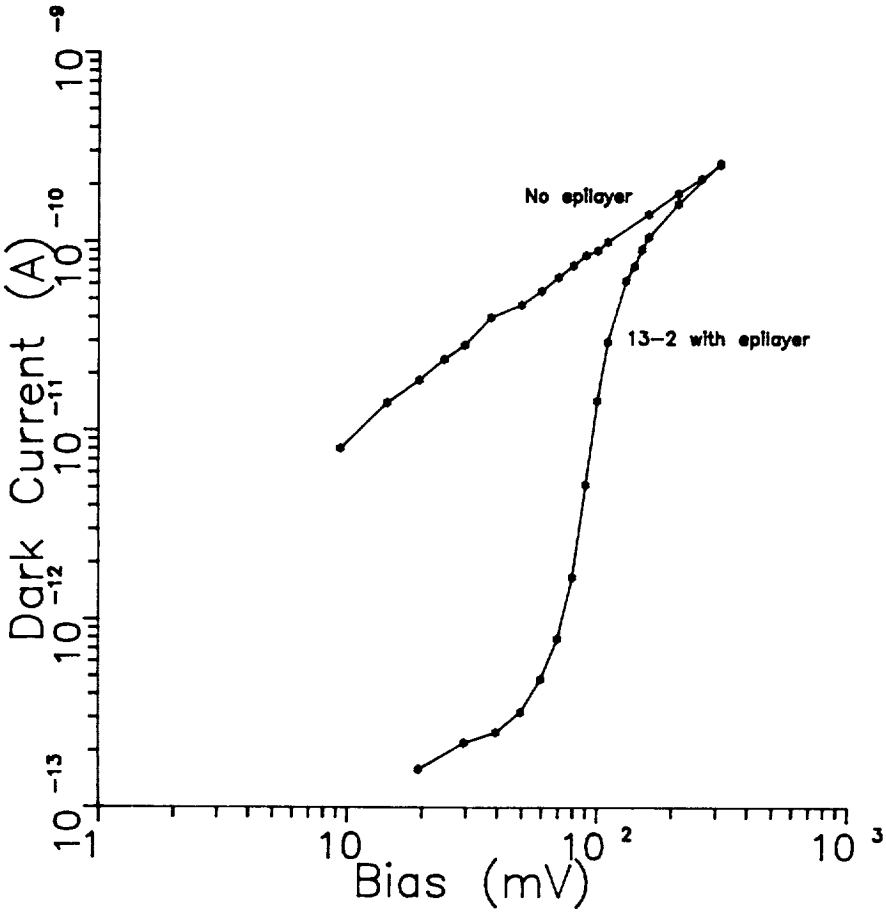

Fig. 13. Dark current as a function of detector bias for detector 13-2 with an epilayer and for the same "detector" without an epilayer at 2.3 K under reverse bias. Below a bias of ~ 100 mV, the blocking layer effectively reduces hopping conduction in this moderately doped material ($N_A - N_D = 5 \times 10^{15}$ cm^{-3}).

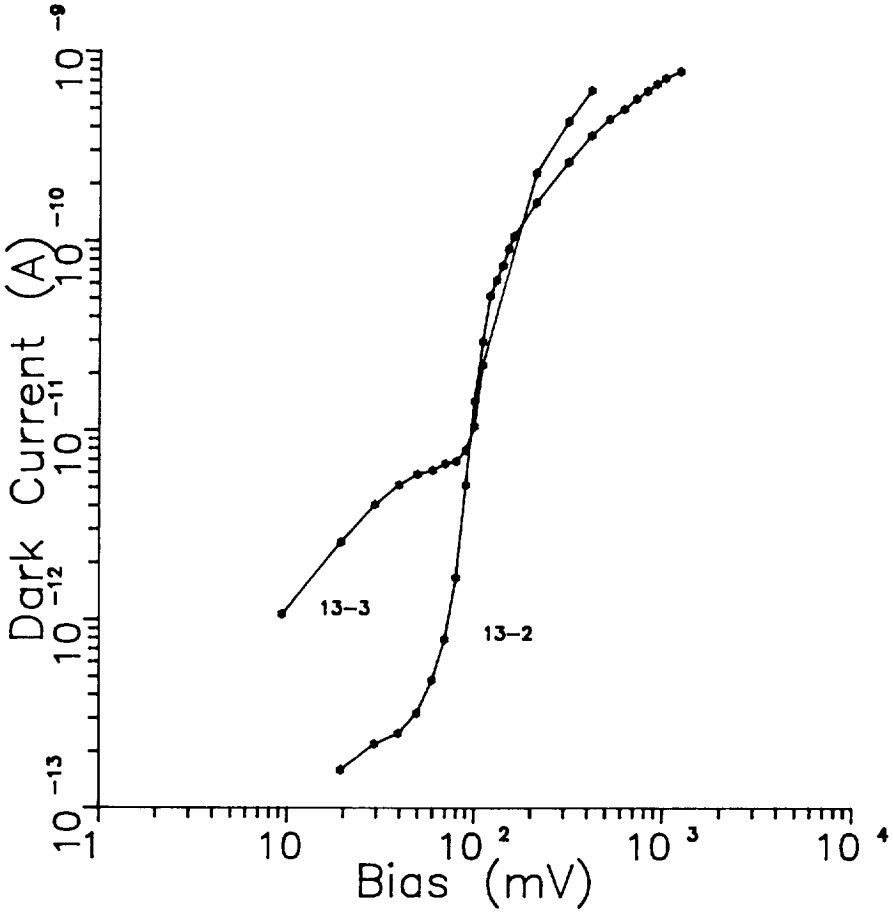

Fig. 14. Dark current as a function of bias for detectors 13-2 and 13-3 at 2.3 K under reverse bias.

3.2. Ion Implanted BIB Detectors

- Concept:
  - In case pure and structurally perfect epitaxial layers are hard to produce, we can resort to implantation of dopants into an ultra-pure crystal.
- Low energy B^+-implantation tests:
  - three B^+ energies: 150 keV, 95 keV, 50 keV form a 0.4 μm thick layer with $N_A = 3.5 \times 10^{16}$ cm^{-3}.
  - annealing at 400°C for one hour in argon.
  - extended wavelength response.
  - responsivity = 0.5 A/W, dark current $< 10^{-14}$ A, at bias = 100 mV and T = 2.0 K. NEP $\approx 4 \times 10^{-16}$ $W/\sqrt{Hz}$.

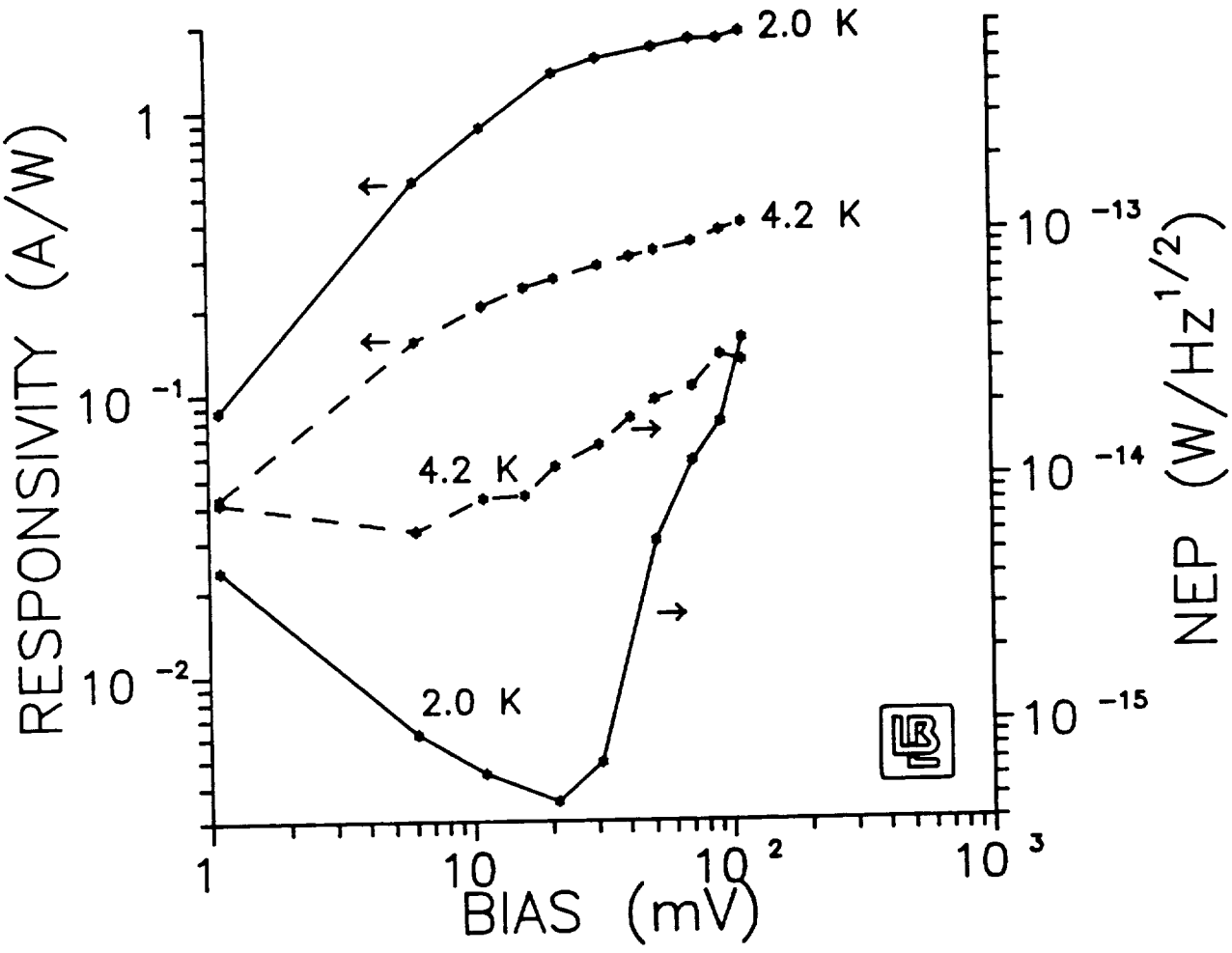

Fig. 15. Responsivity of a Ge BIB detector, low energy B^+-implant type. Active layer depth = 0.6 μm, [B] = 1 X 10^{16} cm^{-3}, λ_{filter} = 98.9 μm, $f_{chopper}$ = 23 Hz

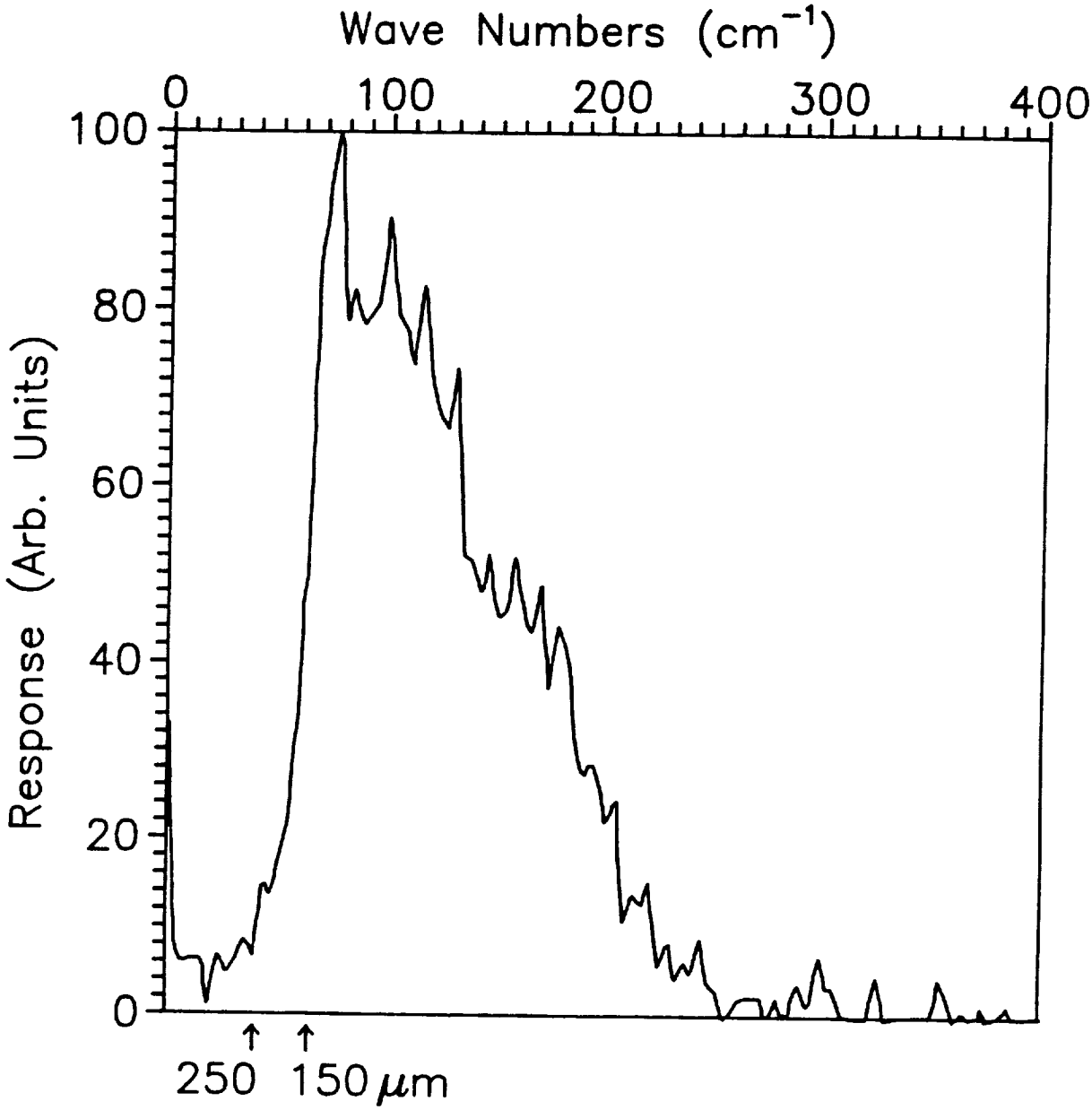

Fig. 16. Spectral response of Ge BIB detector, low energy B^+—implantation type.

- High energy B^+-implantation tests:
  - 14 implant energies up to 4 MeV doubly charged boron ions lead to a 5 μm thick layer with N_A = 1×10^{16} cm^{-3}.
  - Variable temperature Hall effect and resistivity measurements indicate full activation of shallow acceptor dopant B. No deep levels are detectable after annealing. Below 15 K, hopping conduction becomes dominant.
  - Infrared transmission measurements and device tests are in progress.

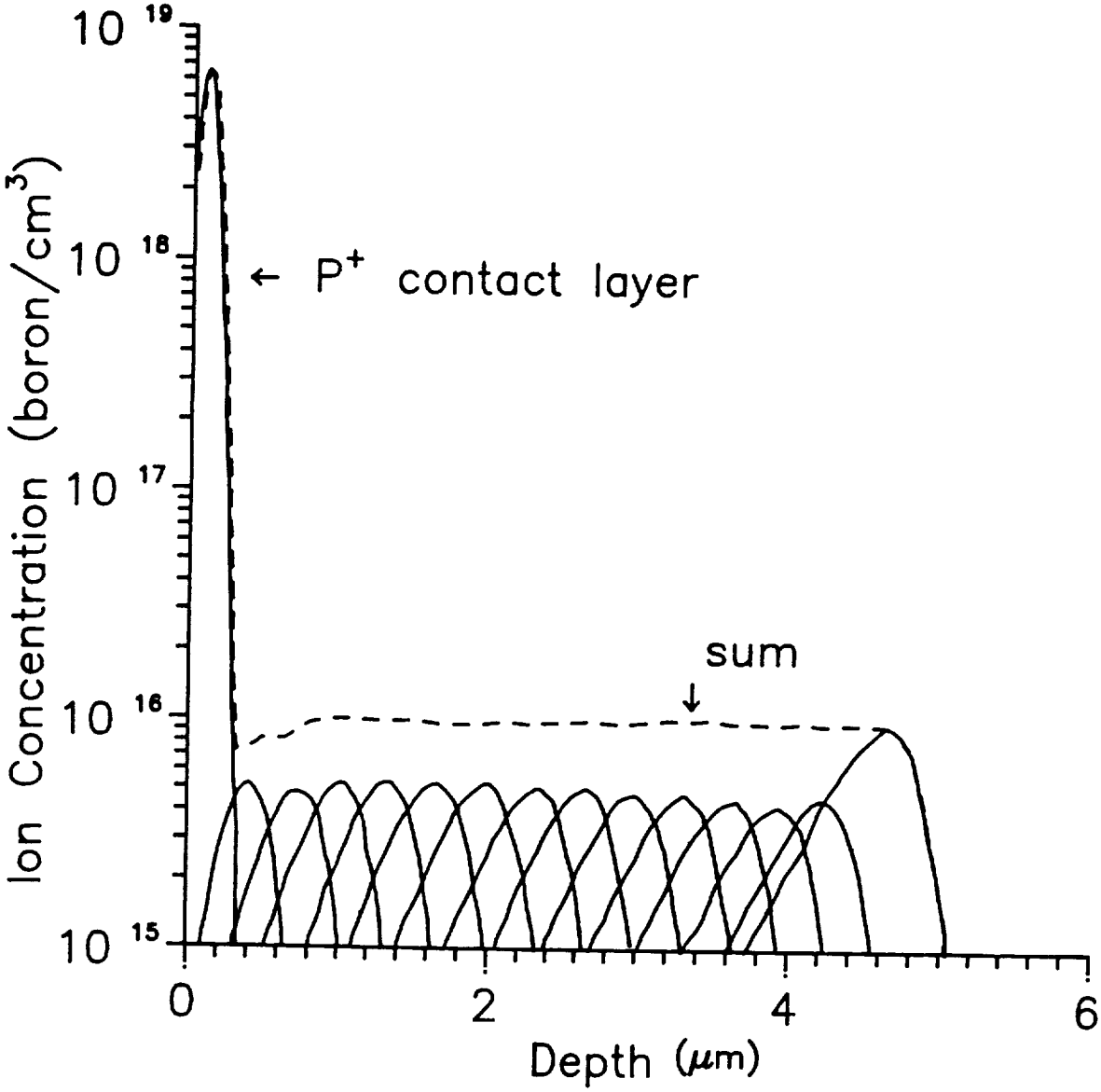

Fig. 17. Ge BIB, high energy ion implant profile

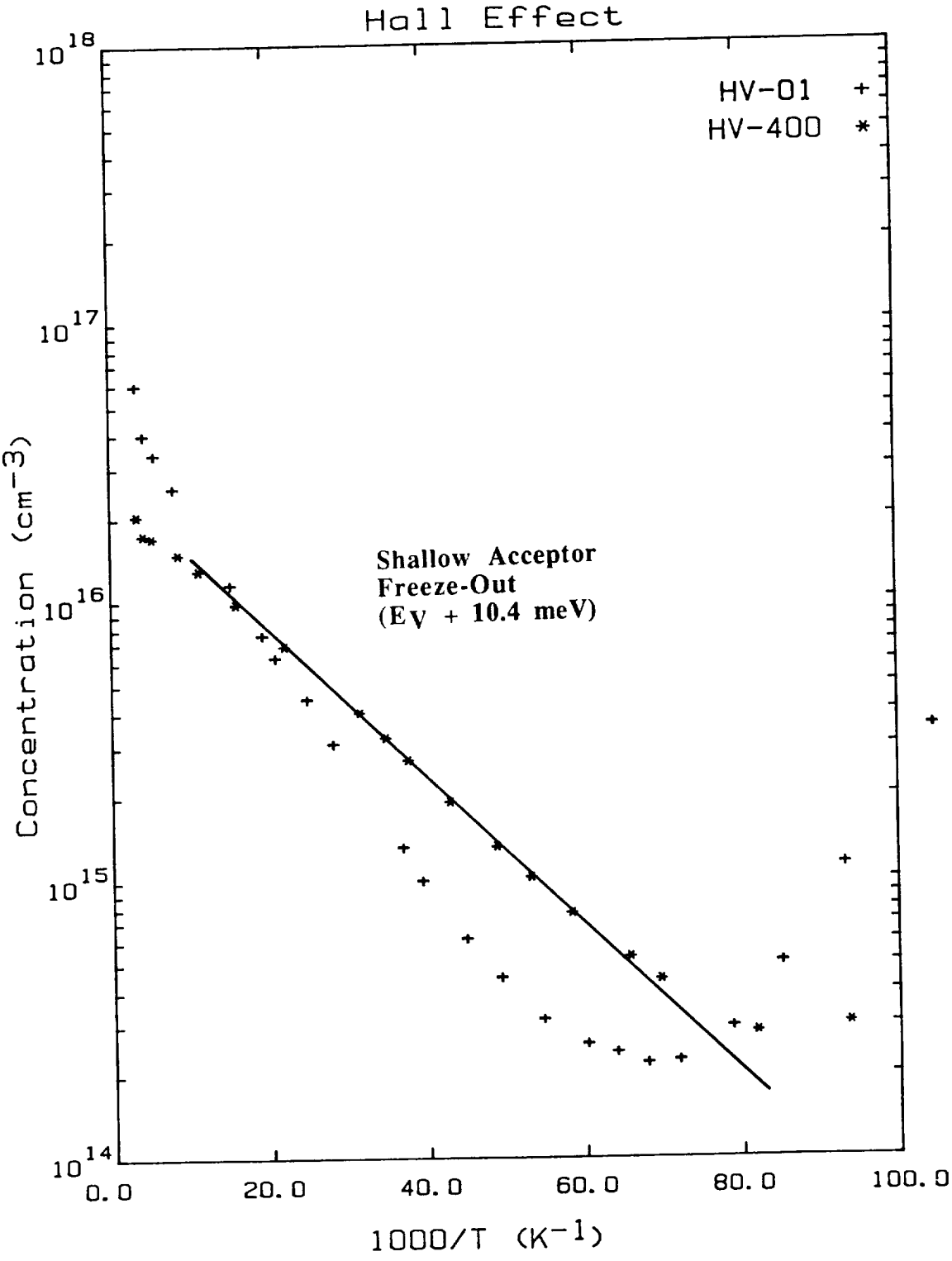

Fig. 18. Free carrier freeze-out of high energy B^+-implanted layer. Before annealing (+), the slope of the freeze-out curve is steeper than after annealing (*). The latter slope corresponds to ~ 10.4 meV, the binding energy of shallow boron acceptors. Below 15 K, hopping conduction becomes dominant.

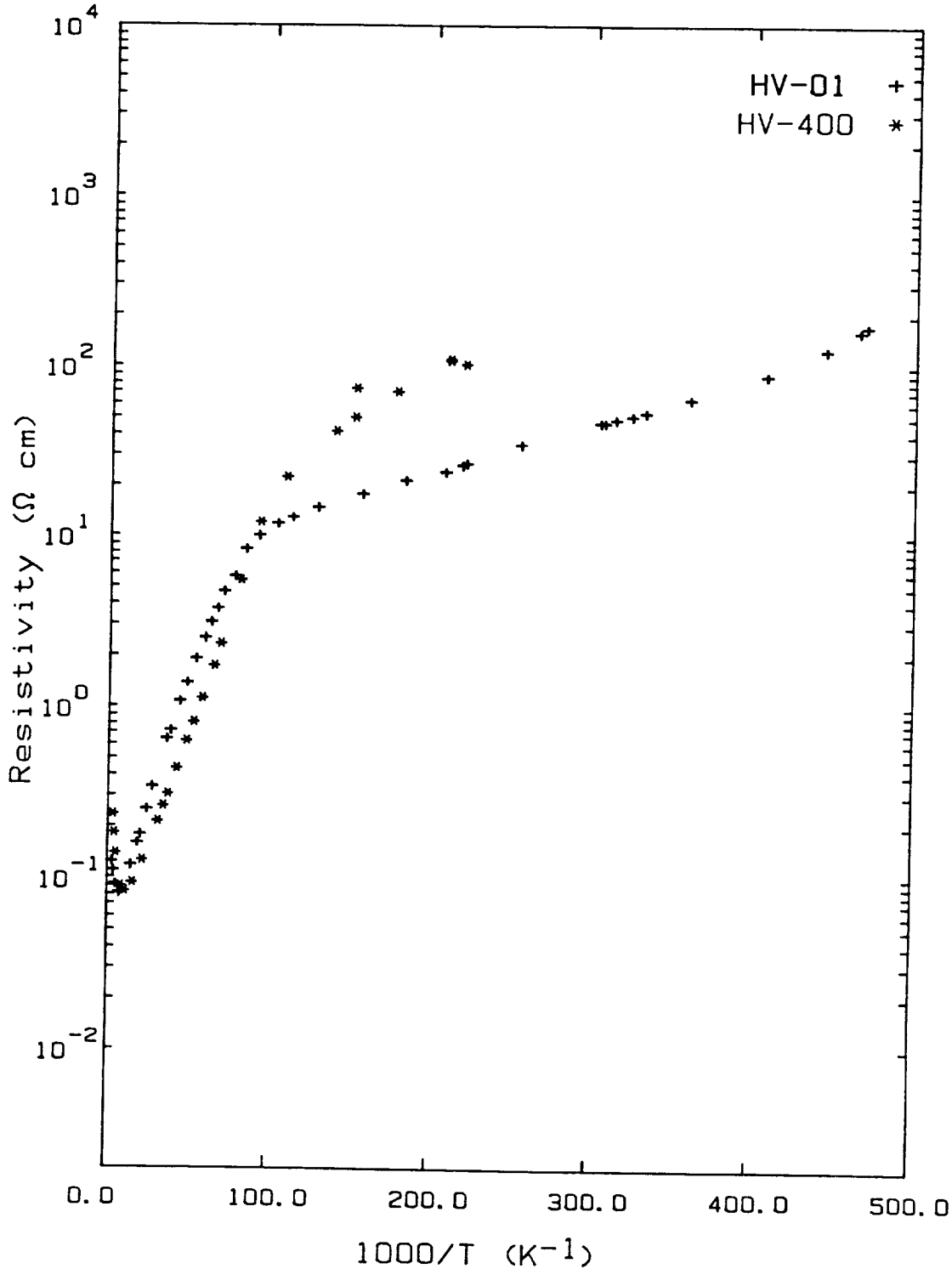

Fig. 19. Resistivity as a function of inverse temperature of the high energy B^+-implant layer before (+) and after (∗) annealing. Hopping conduction becomes dominant below 15 K.

4. CONCLUSIONS

- A LPVPE technique for the low temperature growth of epitaxial Ge layers has been developed.
- Hall effect and resistivity measurements indicate that the epi layers are lightly p-type due to residual copper contamination.
- First generation Ge BIB detectors made with moderately doped substrates (5×10^{15} cm^{-3}) exhibit effective blocking of the hopping current.
- First generation Ge BIB detectors exhibit responsivities around 1 A/W.
- Second generation devices using low pressure VPE are being processed.
- Ion implanted active layers are tested.
- It is currently not known what temperatures will be required to reduce the dark current down to levels which are acceptable for SIRTF applications.

EXTRINSIC GERMANIUM BLOCKED IMPURITY BAND DETECTORS

Timothy N. Krabach
Jet Propulsion Laboratory
Pasadena, California

James E. Huffman
Rockwell International Science Center
Anaheim, California

Dan M. Watson
University of Rochester
Rochester, New York

Ge:Ga blocked-impurity-band (BIB) detectors with long wavelength thresholds greater than 190 μm and peak quantum efficiencies of 4%, at an operating temperature of 1.8K, have been fabricated. These proof of concept devices consist of a high purity germanium blocking layer epitaxially grown on a Ga-doped Ge substrate. This demonstration of BIB behavior in germanium enables the development of far infrared detector arrays similar to the current silicon-based devices. Present efforts are focussed on improving the chemical vapor deposition process used to create the blocking layer and on the lithographic processing required to produce monolithic detector arrays in germanium. Approaches to test the impurity levels in both the blocking and active layers are considered.

For missions such as the Space Infrared Telescope Facility (SIRTF), a need exists for sensor arrays capable of background limited detection in the far infrared, from 30 to 300 μm. The state of the art for discrete FIR detectors are extrinsic germanium photoconductors, which have the combination of high responsivity and low noise required to reach the background noise limit.[1] Gallium, boron, and antimony have all been successfully used as dopants in germanium PC's, with Ge:Ga the most highly developed: it has a threshold wavelength of 120 μm, which can be extended out to 220 μm with the application of a large uniaxial stress. However, the incorporation of extrinsic germanium photoconductors into

focal plane arrays presents great difficulties. The low doping densities used, ~ 10^{14} cm^{-3}, leads to long absorption lengths of about 1 cm. The large detector volume leads to two problems: it makes these detectors vulnerable to saturation and long-lasting responsivity variations from cosmic-ray particle encounters, and the long distance between electrodes would lead to large crosstalk in monolithic array formats. Finally, the necessity of mechanical stress to extend the wavelength response would greatly complicate the creation of large format arrays.

Many of these same difficulties are found in shorter wavelength silicon PC's. Recently, the development of silicon-based blocked impurity band detectors (BIBs) has resulted in large format monolithic arrays that are free of these problems, offering high quantum efficiencies and radiation hardness.[2] The success of silicon BIBs has encouraged a similar effort to be undertaken in germanium, with the goal of producing monolithic, high performance arrays working in the 30 - 250 μm range.

The advantages of the BIB concept are many.[2,3] The active region of the device is thin because the high doping concentration provides a small absorption length; in silicon BIBs the active region is roughly 20 μm thick. This gives the detector high radiation hardness: the smaller detector volume presents less of a target, and the higher number of recombination centers allows a faster recovery. Arrays benefit from less crosstalk. At low bias voltages the BIB operates much like a reverse-biased photodiode. With no recombination noise, in the background photon noise limit BIBs have a $\sqrt{2}$ sensitivity advantage over PC's. Finally, BIBs respond at longer wavelengths than corresponding extrinsic photoconductors. The origin of this is due to both the impurity banding at these concentrations,[4] and the effects of the high electric fields on the impurities (Poole-Frenkel effect).

The first working demonstration of a germanium BIB detector was made by Watson and Huffman.[5] Simple detectors were fabricated by growing an intrinsic Ge epitaxial blocking layer on a Ga-doped Ge substrate (N_A from 3-6 × 10^{16} cm^{-3}) acquired from Eagle-Picher. Spreading resistance analysis (SRA) was used to determine the thickness of the blocking layer. The wafer was cut up by a diamond saw into 2 mm^2 individual detectors. A summary of the device characteristics is provided below, along with results obtained from a high performance Ge:Ga photoconductor in a cylindrical integrating cavity. The extension of the threshold wavelength to ~ 200 μm *without* mechanical stress being applied shows the fruitfulness of developing GeBIBs. The highest bias that could be applied before breakdown was only 40 mV. It is anticipated that further development will result in higher purity blocking layers and therefore higher breakdown voltages. The one large negative found in testing these detectors was a high dark current (> 10^6 electrons/sec), which could be due to several factors. It might represent a poor blocking layer, or it might be due to leakage around the edges. Because the detector region is extremely thin, saw damage cannot be easily eliminated by etching the sides of the detector, as is done for PC's.

Table I. Summary of detector characteristics

	Ge:Ga BIB (1.7K)	Ge:Ga PC (4.2K)
Gallium density (cm^{-3})	3×10^{16}	2×10^{14}
Donor density (cm^{-3})	4×10^{12}	$< 10^{12}$
Highest bias (mV)	40	200
Threshold wavelength	192	120
Peak current responsivity (A / W)	5	39
Peak quantum efficiency	4%	16%
Photoconductive gain	1	3

The present GeBIB program at JPL is focussed on using metal halide chemical vapor deposition (CVD) for the creation of ultrapure germanium blocking layers, and later on in the program, the doped active layer as well. The requirements for a good BIB detector are: high purity ($<10^{12}$ cm^{-3} impurities), adjustable thickness of the blocking and active layers, control of majority impurity concentrations, abrupt profile between the blocking and active layers, and good crystalline quality. CVD has already proven all of these characteristics in silicon, and some in Ge. This approach also offers the possibility of testing different impurities in Ge. Gallium is the dopant being used since it has the highest absorption cross-section. Given a background donor level in the active layer, a Ge:Ga active layer will offer the highest absorption length, and thus highest Q.E. Another factor in the concentration on gallium is the availability of ultrahigh purity $GeCl_4$ as a precursor. In an effort to further extend the wavelength response of GeBIBs, another dopant that will tested as part of the program will be antimony, which possesses a cutoff wavelength of 138 μm.

Another focus of the program is the immediate development of the processing techniques needed for photolithography on ultrapure Ge wafers. One reason for the jump into this instead of working more on single detectors is the need for reproducibility in creating detectors. The large variability from detector to detector can be traced in part to the saw processing; this provides little information for trying improvements in the growth process. The second reason for this is to investigate the cause of the high dark currents observed in the original devices. Only by creating lithographically patterned detectors of different areas, and avoiding entirely

the question of edge damage, can the true low-background performance of GeBIBs be found. A third reason lies in the pressing need for arrays from projects such as SIRTF. By making small linear and area arrays performance parameters such as crosstalk and uniformity can be measured. Finally, an optimized GeBIB detector, with the highest radiation hardness, will need a back-illuminated geometry such as that employed in silicon BIB arrays. This geometry requires photolithographic techniques to produce. The performance goals set out by the GeBIB program, designed to meet the needs for FIR focal planes in the SIRTF and LDR missions, are listed in Table II.

Table II. Performance Goals for GeBIB detector arrays.

threshold wavelength	250 μm
operating temperature	<2K
background conditions	$>10^5$ (SIRTF), $>10^{10}$ (LDR)
dark current	< 100 (SIRTF), $< 10^5$ (LDR)
quantum efficiency	> 20 %
breakdown voltage	200 mV
photoconductive gain	≥ 1
uniformity of responsivity	± 5%
crosstalk	± 2%

The major difficulty in the development of GeBIB detectors is in the inadequacy of the material testing techniques that have been used so successfully in the silicon BIB program. Beyond the standard tests for checking the crystallinity of the epitaxial layer, particularly near the interface with the doped substrate, the most important parameters to be measured are the acceptor concentration N_A in the doped layer, the residual donor concentration N_D in the doped layer, and the impurity concentration N_{BL} in the blocking layer. It is also important to identify what the impurities are in the blocking layer, to help eliminate those materials from the growth process. Of these parameters N_A is easy to determine by the resistivity of the substrate, N_D can be found after a device is fabricated, but N_{BL} cannot be measured with the presently available tools.

One measurement technique that does carry over from the silicon BIB development effort is cryogenic C-V testing, which gives the donor concentration N_D in the active region. With the sample device at its operating temperature, the device capacitance is obtained by applying a small, slow (<10 Hz), ac signal in addition to the dc bias, then measuring the amplitude and phase of the detector current. The capacitance is then derived from the complex impedance. One important point is that because of the low mobility of the A^- carriers, this testing must be done at low frequencies. The width of the depletion region can be calculated from the relation

$$C = \varepsilon\varepsilon_0 A / (d + w)$$

where C is the capacitance, A is the detector area, d is the blocking layer thickness, $\varepsilon = 15.4$ is the relative dielectric constant in germanium, and w is the depletion layer thickness. The donor concentration within the depleted layer is then found via

$$w = \sqrt{2\varepsilon\varepsilon_0 V / N_D e + d^2} - d$$

where V is the bias voltage. In the test devices the donor concentration was derived to be $N_D = 3 \times 10^{12}$ cm^{-3}. A powerful extension of this method is to measure the depletion layer thickness versus bias voltage; this differential C-V technique allows one to determine the depth profile of N_D.

The standard test to determine N_{BL} in Si BIBs is spreading resistance analysis (SRA). Due to germanium's smaller bandgap, at room temperature the intrinsic carrier concentration is ~ 2×10^{13} cm^{-3}. SRA is therefore of limited use in germanium, though it still is used to find the blocking layer thickness. However, a simple calculation reveals upon cooling the sample down to <240K, the intrinsic carrier concentration is reduced by a factor of 100. It should be possible to modify existing SRA apparatus to cool the sample and the test probes. By undertaking the SRA measurements cold, the true blocking layer impurity concentration can be found. An effort along these lines has been started.

Another possibility is the use of photothermal ionization spectroscopy (PTIS) to reveal the composition of the impurities in the blocking layer. PTIS is already used to measure the concentration of specific, shallow, hydrogenic impurities in bulk semiconductor crystals. Through the use of interdigitated electrodes implanted on the surface, the electric field would be confined to the blocking layer, and the heavily doped active region would not contribute to the photothermal signal. Though this technique could not be used on actual devices, it would provide information vital to the crystal grower to help in modifying the growth process to produce cleaner blocking layers.

The initial efforts in the GeBIB program have been in improving the epitaxial growth process and in identifying lithographic processing steps compatible with the BIB structure. A diagram of the device structure is shown in figure 1. The initial detectors produced all failed. The reasons for the devices not working were poor metal step coverage over the oxide down to the pixel, and disappearance of the boron ohmic implant. Both of these problems have now been traced back to the use of H_2O_2, utilized as a cleaning agent and a metal etch, which was found to be an excellent germanium etch as well. A new metallization scheme has been evaluated and found to produce good step coverage, and the corresponding metal etch has been verified not to harm the germanium or the boron implant. With a processing sequence now hopefully in place, both Ga and Sb-doped wafers are now being processed into detectors.

---

[1] J.-Q. Wang, P.L. Richards, J. W. Beeman, N. M. Haegel, and E.E. Haller, Appl. Opt **25,** 4127 (1986).

[2] M.D. Petroff and M.G. Stapelbroek, U.S. Patent No. 4-568-960 (4 February 1986).

[3] F. Szmulowicz and F.L. Madaraz, J. Appl. Phys. **62,** 2533 (1987).

[4] B.I. Shklovskii and A.L. Efros, *Electronic Properties of Doped Semiconductors* (Springer Verlag, Berlin) 1984.

[5] Dan M. Watson and James E. Huffman, Appl. Phys. Lett. **52,** 1602 (1988).

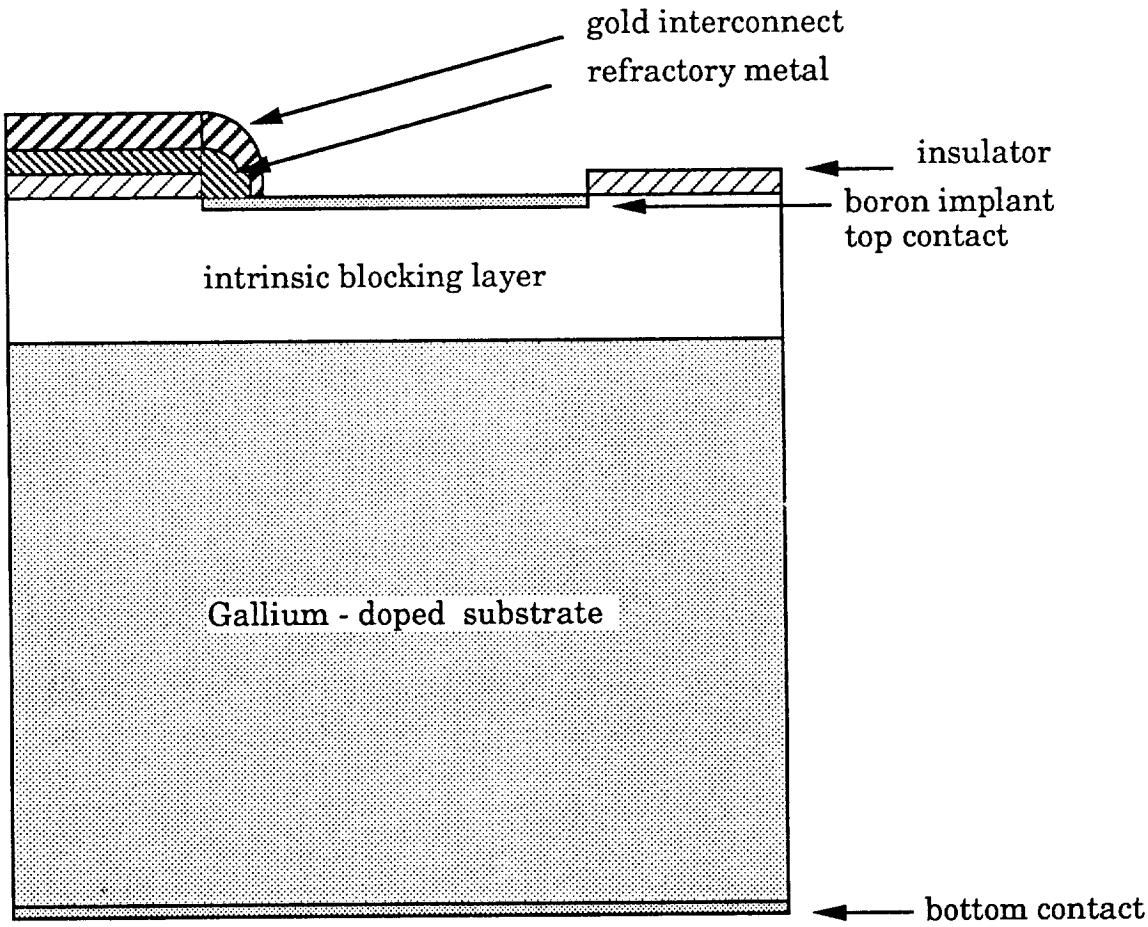

Figure 1. Outline of the first lithographically patterned GeBIB detectors. The detector is front-side illuminated, with the Ge blocking layer grown by CVD onto a commercial Ga-doped Ge substrate. Pixels range in size from 2 to 64 mils square.

Ga:Ge ARRAY DEVELOPMENT

E.T. Young, G.H. Rieke, and F.J. Low
Steward Observatory
University of Arizona

E.E. Haller and J.W. Beeman
Lawrence Berkeley Laboratory
University of California, Berkeley

Abstract

We describe work at the University of Arizona and at Lawrence Berkeley Laboratory on the development of a far infrared array camera for the Multiband Imaging Photometer on SIRTF. The camera design uses stacked linear arrays of Ge:Ga photoconductors to make a full two-dimensional array. Initial results from a 1 x 16 array using a thermally isolated J-FET readout are presented. Dark currents below 300 electrons s^{-1} and readout noises of 60 electrons have been attained. Operation of these types of detectors in an ionizing radiation environment are discussed We present results of radiation testing using both low energy gamma rays and protons. We also describe work on advanced C-MOS cascode readouts that promise lower temperature operation and higher levels of performance than the current J-FET based devices.

I. INTRODUCTION

SIRTF will be the premier infrared facility in the late 1990's and will represent a dramatic increase in the sensitivity attainable in infrared astronomy. An important part of this capability will be a far infrared camera being developed by the Multiband Imaging Photometer for SIRTF (MIPS) team. The basic goal for this camera is to provide diffraction limited imaging between 60-120 μm at a sensitivity limited only by the natural backgrounds. Of equal importance in a real system are the requirements of good stability, ability for precise calibration, and low power dissipation. We describe our development efforts for this camera. This paper is divided into discussions of detector development, J-FET-based readout arrays, and C-MOS readout technology.

With the change in the SIRTF orbit from a 900 km to a 100,000 km high earth orbit baseline, there is now an increased premium for very low power dissipation, resistance to ionizing radiation, and stable photometric performance. The far infrared array development for MIPS has evolved to reflect these changes.

II. DETECTOR DEVELOPMENT

Ionizing radiation effects can greatly complicate the operation of infrared detectors in space. Two general problems have been identified that can make sensitive observations with photoconductors difficult. First, individual particles (primarily high energy protons) generate a large number of hole-electron pairs in the detector. Since all the new systems under development will use integrating amplifiers because of their much higher sensitivity, the result will be a large step in the input voltage of the amplifier until a reset occurs. The Ge:Ga detectors planned for the far infrared camera operate at a relatively low bias voltage (~50 mV), and this voltage step can represent a significant bias change for the detector. Since some photoconductors exhibit long time constant relaxation effects after bias changes (Young and Speed 1985), and we have devoted some effort in characterizing the single hit behavior of the proposed Ge:Ga detector material. The second radiation effect is the change in responsivity after an exposure to ionizing radiation. During the IRAS mission, changes in excess of a factor of 5 were observed after a passage through the South Atlantic Anomaly (IRAS Explanatory Supplement 1988). Since, a SIRTF goal is to do photometry to the 1 to 2% level, it will be important to be able to understand and correct for these changes. In general, it has been observed that these effects are more serious at lower infrared backgrounds, so we have begun a program of radiation characterization at the very low backgrounds appropriate to SIRTF.

The bulk of the radiation testing has been done at Steward Observatory using a 10 mCi Americium^{241} gamma ray source. This isotope primarily produces 60 keV radiation. Because of the low energy of the gamma rays, the radiation is easily shielded and collimated with simple brass fixtures. The test apparatus also includes a photon-tight dewar with an internal infrared source and an integrating J-FET amplifier capable of measuring currents below 1 electron s^{-1}. Backgrounds in the dewar below 10^3 photons cm^{-2} s^{-1} at 100 μm have been observed. With the internal stimulator, changes in responsivity can be observed even at ultra-low background levels, while changes in the dark current can be determined with the stimulator turned off.

Figure 1 shows the radiation induced responsivity change in a Ge:Ga detector made from boule LBL 113 at two different infrared background levels. This material is characteristic of the best currently available Ge:Ga photoconductors. At the high background, the increase in responsivity appears to saturate at a factor of 5-6, while the saturation value for the low background case is twice as high. Additionally, the dose required for a given responsivity increase is significantly lower for the low background case. These two effects are consistent with a self-annealling rate that is dependent on the infrared background flux.

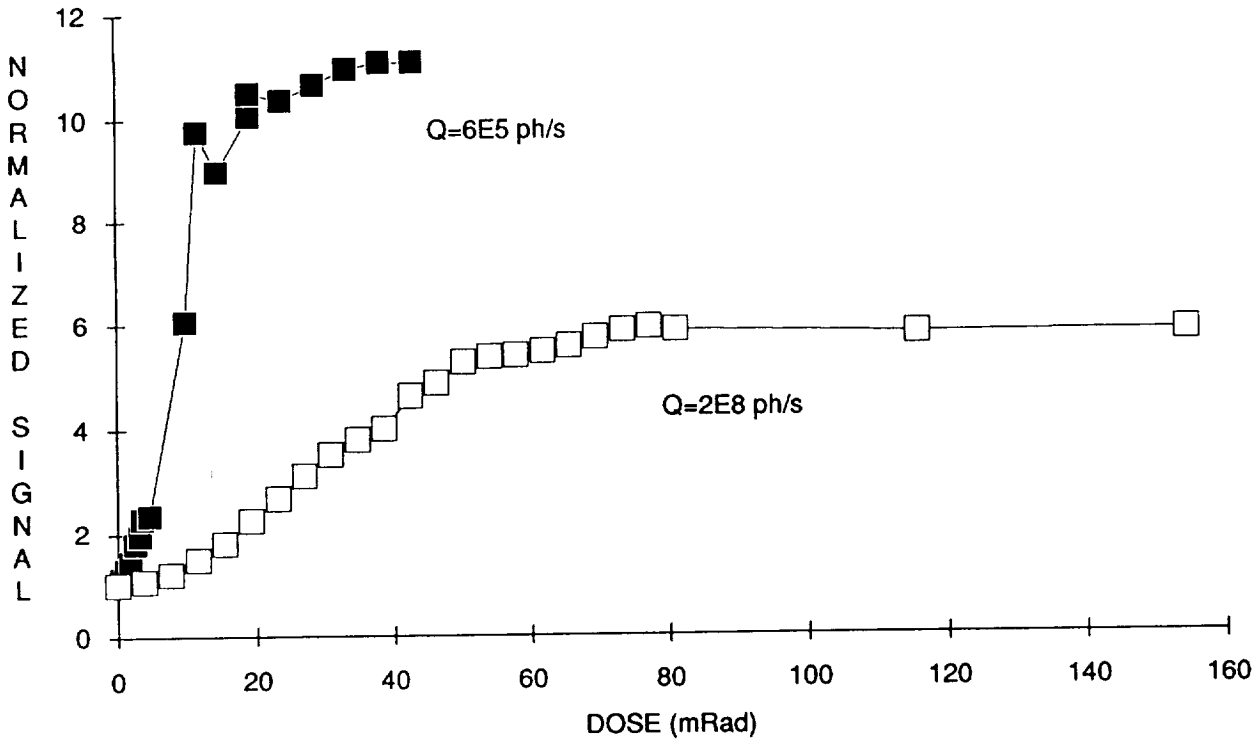

Figure 1. Responsivity change in LBL 113 Ge:Ga detector with gamma ray exposure.

The very low thresholds for significant responsivity changes in Ge:Ga suggests that the normal cosmic ray proton background may be enough to induce troublesome effects in a SIRTF application. To investigate these effects, we have extended the radiation measurements to lower infrared backgrounds (10^3 ph/s) and lower ionizing dose rates (<10^{-6} rad/s). We have found a complicated behavior under these conditions. There appears to be a persistent 2x responsivity increase with a very long time constant and another component that decays with a background dependent rate.

We have also investigated the efficacy of various correction schemes for these radiation effects. The methods we have considered are the bias boost as used in IRAS, thermal anneal, and photon flooding. In general, the thermal anneal technique, where the detector temperature is raised for a few seconds to ~8K appears to be the most effective and rapid method.

Since the ionizing flux for SIRTF will primarily be high energy protons rather than gamma rays, it is important to understand the differences due to proton irradiation. In particular, it is important to define the effects of the much larger energy per interaction for the protons. Initial investigation of proton effects was made in January 1989 at the Crocker Nuclear Laboratory cyclotron at the University of California, Davis. This facility can produce 60 MeV protons at fluxes ranging from a few tens of

protons s^{-1} cm^{-2} to many orders of magnitude higher. The bulk of the run was spent simulating a SIRTF-like cosmic ray flux to investigate the gradual increase in responsivity. The cyclotron output was adjusted to 60 MeV energy and an initial flux of approximately one hit per 5 seconds in the 1 mm^3 detector. Figure 2 shows an averaged plot of the Ge:Ga detector current over nearly 12,000 seconds of exposure. Each point represents the median average of three five-second integrations, with time given in seconds after midnight. The initial photocurrent from the detector is approximately 2000 e/s due to the background in the dewar and is typical of the expected SIRTF conditions. The lower envelope of the curve is a measure of the responsivity of the detector, while samples well above the envelope are contaminated by particle hits. The gradual increase in responsivity is evident as dose accumulates. The most dramatic increase, however, only occurs after t=50500 seconds when the proton flux is increased by a factor of 300 over the initial rate. At 52300 s and 52600 s, the detector is thermally annealled dropping the responsivity to nearly the original level. For this run, however, the anneal temperature only reached 5.9K, and the recovery is not complete. The responsivity drifts upward even though the proton exposure was stopped at t=51,000 s. Clearly much additional work is needed to come up with an optimal radiation recovery strategy.

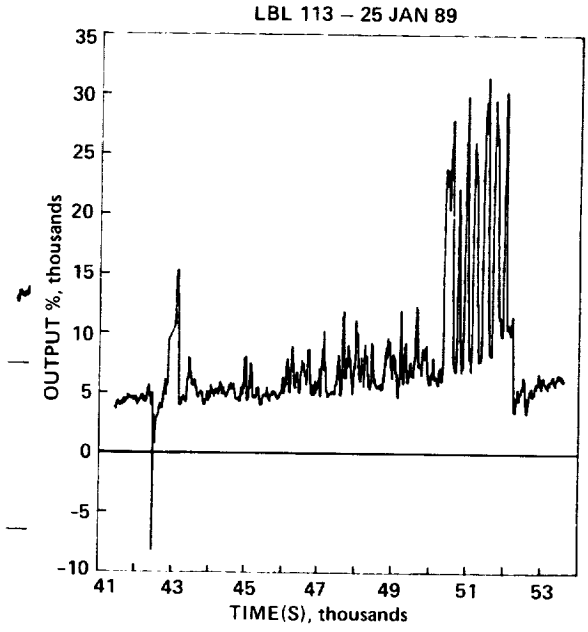

Figure 2. Photocurrent from Ge:Ga detector with low infrared background and proton irradiation. Points are median averages of three 5-second integrations. Thermal anneal cycles were initiated at 52300 and 52600 s.

To summarize these radiation tests, the change in responsivity due to the cosmic ray background is slow and predictable. Precise photometry should be possible with a careful calibration strategy involving regular use of an internal reference source. The single hit effects for this detector do not appear to be serious. LBL 113 recovers from single particle hits rapidly and does not seem to have significant long time constants. Moreover, the charge collection efficiency at the low bias voltages typical for these detectors is less than 10% for both gamma ray and proton events.

III. J-FET DEMONSTRATION ARRAY

The design for the demonstration linear array must satisfy a number of conflicting requirements. First, the design must isolate the J-FET integrators both thermally and optically from the Ge:Ga detectors. Since the electronics must operate at a temperature of 50 K while the detectors must operate below 2 K, a large temperature gradient must be supported by the mount. At the same time, the support must have a very low thermal conductivity to minimize the power dissipation in the unit. It is also desirable, however, to have the first stage electronics as close as possible to the detectors to minimize spurious pickup and microphonics. Finally, the design must be stackable into a two-dimensional configuration with a high filling factor.

Figure 3 shows the basic configuration of the demonstration linear array. The 16-channel J-FET integrator integrated circuit from Burr Brown/Infrared Laboratories and an RCA CD4067 multiplexer are mounted on a metallized sapphire substrate using flip-chip techniques. This substrate is physically suspended and thermally isolated by thinwall 125 μm diameter polyimide tubes. These tubes also provide the electrical connection to the J-FETs since they are metallized with 200 A of chromium and 2000 A of gold. The Ge:Ga detectors are also thermally isolated from the J-FET module using an additional set of polyimide conductors. We have found that even though the frame for the J-FET modules is nominally operating at 2K, this extra degree of isolation is important for minimizing thermal interference. The aluminum frame and the detectors are thermally sunk to the 2K heat station. To insure against photon leaks from the "hot" J-FET electronics, we have made liberal use of indium gaskets and black Stycast epoxy in the joints.

We have found the polyimide support system to have the desired combination of ruggedness and low thermal conductivity. Previous versions of the module used glass fibers or glass sheets for the suspension system. Although the glass fibers potentially have a lower thermal conductivity, the polyimide support is superior due to its much greater resistance to breakage.

We have demonstrated functional operation of several of these arrays, and the latest tests show that the design meets the basic noise and dark current needs of a SIRTF far-infrared imager. Table 1 summarizes some of the module characteristics. The low dark current demonstrates the success of the thermal and optical isolation. It is important to note that these performance figures are for fully multiplexed operation with a computerized data acquisition system and any contribution due to digital noise is included in the total noise. This array would be background noise limited in less than 10 seconds of integration if used in the SIRTF diffraction limited imager.

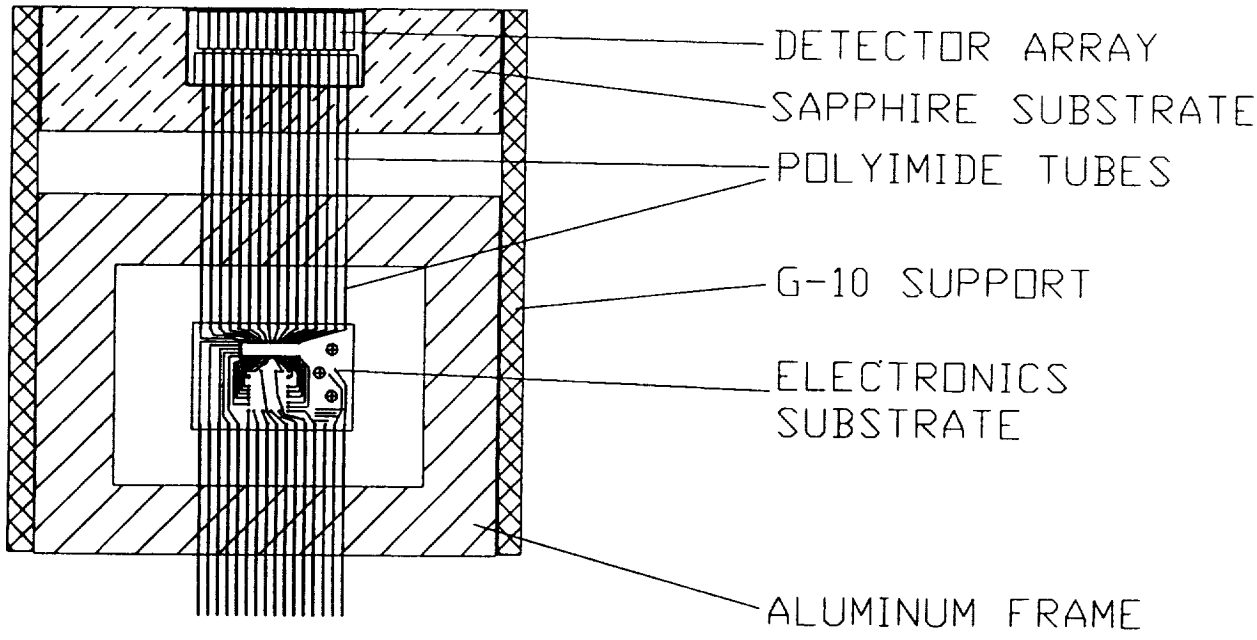

Figure 3. Demonstration Array Sub-module Top View

Table 1. Demonstration Array Module Characteristics

Detector Material	Ge:Ga
Number of Channels	16
Detector Active Area	500 μm x 500 μm
Detector Style	Transverse contact
Module Thickness	0.5 mm
Ambient Operating Temperature	2.0 K
J-FET Operating Temperature	50 K
Power Dissipation	0.5 mW/module
Detector Responsivity	5 A/W
Dark Current	<300 e^-/s @ 50 mV bias
Read Noise	<60 e^- for 32 s integration, 0 bias

With the current array design, the detector filling factor is lower than desired. Using the 500x500 μm detector size with 750 micron pixel spacing, the net filling factor is only 44%. To improve on this situation, we are investigating a number of optical concentration methods. One promising technology involves the anisotropic etching of silicon (Kaminsky 1987). We have experimented with an etch of pyrocatechol and ethylene diamine (P-ED). The etch rate for the 111 orientation is at least one hundred times greater than for the 100 orientation. By using appropriate masks aligned to the crystal orientation in 100 wafers, we have produced arrays of pyramid-shaped solid cones that could act as solid concentrators. We are doing analysis to determine whether the opening angle (which is fixed by the crystal planes in silicon) is appropriate for this application.

IV. C-MOS READOUT DEVELOPMENT

Although the basic requirements of a SIRTF far infrared camera could be met with stacked J-FET based modules, we have been exploring possible enhancements both in the size of the array and performance of the readout. Significant advances in the noise performance of C-MOS analog circuits have been made in the past few years. In particular, the noise now seen for a new 1.25 μm process is only 200 nV $Hz^{-1/2}$ at 1 Hz (1000 square μm gate area). This noise level is about a factor of five better than devices made with the older 3 μm technology, and with this level of performance, C-MOS readouts can be competitive with J-FETs.

C-MOS circuit technology has a number of additional advantages over J-FET technology. C-MOS fabrication has a density advantage of J-FET designs. For the SIRTF imager application, for example, it is possible to produce at least a 32-channel readout with multiplexer using very relaxed design rules. In fact, additional circuitry to do simple signal processing such as baseline correction can be incorporated directly on the integrated circuit. Finally, CMOS circuits can operate at lower temperatures than their J-FET counterparts. For a far infrared camera, the thermal and photon isolation of the amplifier from the detectors is a significant complication. By running the readout at lower temperatures, this problems diminishes greatly.

To explore the applicability of these new technologies to high performance infrared focal plane arrays, this program has funded the fabrication of test circuits at Amber Engineering. Four input circuits were considered to cover a range of possibilities. Because of the flexibility of C-MOS fabrication processing, all four test circuits were placed on a single die. The test circuits consisted of p- and n-channel versions of the source follower and common source cascode amplifier. The use of the common cascode circuit for infrared array readouts is discussed in more detail in the accompanying paper by Woolaway and Young (1989). The most important difference between the cascode and source follower configurations is that the cascode provides a factor of 20-30 gain. Although the cascode should theoretically have no noise advantage over the source follower, the extra gain makes it significantly easier from a systems standpoint to meet the noise potential of the MOSFETs. Table 2 gives some of the measured performance values for the test circuits at a temperature of 77K. Even though the input capacitance is

relatively large, the noise level for the cascode circuits is excellent. We have also carried the testing to lower temperatures. For the p-channel cascode, the noise performance holds down to 30K, below which there is a gradual increase in low frequency noise. At the lowest temperature measured (2 K) the circuit continues to function but with a readout noise of 30 e^-.

Table 2. Performance of AE133-2A Test Circuits

Circuit	Voltage Gain	Input Capacitance (pF)	RMS Noise (e^- $Hz^{-1/2}$)
n-channel Cascode	27.6	0.68	7
p-channel Cascode	26.9	0.66	8
p-channel Follower	0.84	0.43	38
n-channel Follower	0.75	0.44	*

Temperature = 77K
Power Dissipation = 114 μW
* Not measured due to excessive leakage current in input test diode.

The excellent performance of the common source cascode circuits gave us the confidence to go ahead with the fabrication of a 32-channel readout based on these circuit concepts. If the performance of these parts attains the predicted levels, the task of fabricating full far-infrared arrays will be greatly simplified. The integrated circuit is being fabricated using a 2 μm design rule p-channel process. P-channel is used for its superior low temperature operation. In addition to the cascode input stages, the circuit includes an AC-coupled driver stage and a serial multiplexer. The purpose of the AC-coupling is to remove any offset voltages in the input stage and results in an improved dynamic range for the circuit. The multiplexer is a shift register-transmission gate configuration that features break-before-make operation. Table 3 gives some of the predicted characteristics of the circuit.

One of the more challenging constraints on the design was the desire to minimize the power dissipation in the circuit. Minimizing the power dissipation is especially important in the SIRTF high orbit context since parasitic and aperture heat loads are very low. We were able to meet the power dissipation goals by maintaining only a minimal continuous current in the input cascode stage. The subsequent driver and logic stages are operated in the switched mode, drawing current only when a given channel is being read out. With this power management strategy, the total power dissipation for a 32 x 32 array would be only 5 mW.

Table 3. Design Characteristics of 1x32 Readout

Input configuration	p-channel common-source cascode
Reset accuracy	limited by kTC
Multiplexing	serial shift register
	break before make
Sample rate	up to 32 x 10 Hz
Output circuit	current-mode
Input stage gain	15-20
Maximum input excursion	20 mV
Full well capacity	1.2 x 10^6 electrons
Power dissipation	156 μW
Input capacitance	9 pF
Read noise	50 e^-, 0.01-100 Hz
Operating Temperature	<30 K

The expected performance of this readout should demonstrate the usefulness of custom circuits for infrared astronomical applications and extends the application of MOS readouts to high input capacitance applications. The benefits of low noise, low power dissipation and higher levels of integration should enable us to more fully exploit the power of SIRTF with a large format far-infrared camera.

Acknowledgements

This work has been partially supported by NASA grants NASW-3703 and NAGW-1285. We acknowledge the efforts of P. Hubbard, J. Davis, and M. Alwardi in the array development.

References

IRAS Explanatory Supplement, 1988 C.A. Beichman, G. Neugebauer, H.J. Habing, P.E.Clegg, and T.J. Chester, editors. NASA RP-1190.

Kaminsky, G. 1987 "Micromachining of Silicon Mechanical Structures" in ***Science and Technology of Microfabrication,*** ed. R.E. Howard, E.L. Hu, S. Namba, and S. Pang, (Pittsburgh: Materials Research Society) p. 111.

Woolaway, J.T., and Young, E.T. 1989 "Common Source Cascode Amplifiers for Integrating IR-FPA Applications" this volume.

Young, E.T. and Speed, D. 1985, ***Proceedings NASA Infrared Detector Workshop, Ames Research Center***, NASA Technical Memorandum.

COMMON SOURCE CASCODE AMPLIFIERS FOR INTEGRATING IR-FPA APPLICATIONS

James T. Woolaway

Amber Engineering Inc.

Santa Barbara, California

Erick T. Young

Steward Observatory

University of Arizona

Tuscon, Arizona

* Work sponsored in part through NASA contract NAS2-12578.

ABSTRACT

Space based astronomical infrared measurements present stringent performance requirements on the infrared detector arrays and their associated readout circuitry. To evaluate the usefulness of commercial CMOS technology for astronomical readout applications a theoretical and experimental evaluation has been performed on source follower and common-source cascode integrating amplifiers. Theoretical analysis indicate that for conditions where the input amplifier integration capacitance is limited by the detectors capacitance the input referred rms noise electrons of each amplifier should be equivalent. For conditions of input gate limited capacitance the source follower should provide lower noise. Measurements of test circuits containing both source follower and common source cascode circuits showed substantially lower input referred noise for the common-source cascode input circuits. Noise measurements yielded 4.8 input referred rms noise electrons for an 8.5 minute integration. The signal and noise gain of the common-source cascode amplifier appears to offer substantial advantages in acheiving predicted noise levels.

INTRODUCTION

An attempt has been made to correlate the theoretical and experimental noise performance for CMOS source follower and common-source cascode integrating amplifiers operating with temperature and bandwidth consistent with astronomical infrared measurement applications. Several CMOS process technologies were evaluated for low temperature noise performance. Theoretical performance predictions were made using the measured noise performance of each process and models developed for the Source Follower (SF) and Common Source Cascode (CSC) amplifiers. A test circuit was designed and fabricated using an advanced commercial 1.25um CMOS technology that contained both P & N channel amplifiers of the SF and CSC configurations. Measurements of the circuits were performed at Amber Engineering and the University of Arizona. The CSC circuits showed excellent noise performance and agreed well with theory. The SF circuits, however, exhibited much higher noise than was predicted.

PROCESS MEASUREMENTS

Three processes were evaluated for low temperature operability and noise. These were CMOS 3um, 2um, and 1.25um analog processes. Noise was evaluated for the P & N-channel MOSFETs of each process with the MOSFETs in a common source configuration. A HP-3582A spectrum analyzer was used to measure the output noise spectrum of each device. The gain of each circuit was also measured. Input referred noise voltage spectral density curves were obtained by dividing the output noise spectrum by the measured AC transfer function of the circuit.

The input referred noise spectra exhibited a classical behavior with the low frequency behaving as 1/f and the high frequency as thermal white noise. The measured 1/f and thermal noise voltage spectra were numerically fit. In addition to measurements of several processes, devices of differing sizes were measured for each process. For these devices the 1/f noise scaled as the inverse of the square root of the gate area as expected. The 1/f measurement results have been normalized to 1000um^2 gate at 1Hz and are presented in Table 1 below. Thermal noise levels were measured at about 1.5X of what was predicted by sqrt(8/3KT/Gm).

TABLE 1. (CMOS, 77 KELVIN, 1000UM^2, VOLTS/RTHZ)

Device	P-channel	N-channel
Process		
3um	1uV/rtHz	2uV/rtHz
2um	800nV/rt/Hz	1.2uV/rtHz
1.25um	200nv/rtHz	200nv/rtHz

INTEGRATED NOISE

The input referred noise voltage spectral density can be expressed as

$en^2 = en^2(1/f) + en^2(thermal)$

The RMS or integrated noise is then

$$Vn2 = \int_{f1}^{f2} (en(1/f)^2/f)df + \int_{f1}^{f2} en^2(thermal)\, df$$

This reduces to $Vnrms = \{en^2(1/f)[\ln(f2/f1)] + en^2(thermal)[f2-f1]\}^{1/2}$. For the 1.25um CMOS process a $1000um^2$ gate area would measure at about 600nV rms for integrated 1/f for a bandwidth of .01Hz to 100Hz. The 1/f voltage noise spectra measured (0.1Hz to 100Hz) was also integrated directly and was found to agree reasonably well with the theoretical expression above.

SOURCE FOLLOWER AND COMMON SOURCE AMPLIFIER THEORY [1,2]

The principle difference between the CSC and SF circuits is that the CSC circuit has a gain of approximately Rload*GM (20-50V/V) where the SF circuit gain is less then unity, typically .7V/V. Figure 1 shows the schematic diagrams for these circuits. The voltage gain of the SF amplifier is:

$Av = Vout/Vin = Gm1/(Gds1+Gds2+gm1(1+n)$ where $n=Gmbs/Gm1$

which approximately equals $1/(1+n)$ or 0.75 to 0.95 for bulk effect and no bulk effect, respectively. Similarly the voltage gain of the CSC ampfifier is:

$Av = Vout.Vin = -Gm1(Gds2+gm2+gmbs2)/[Gds1Gds2+Gds1Gds3+Gds2Gds3+Gds3(Gm2+Gmbs2)]$

which is approximately $-Gm1/Gds3$ or about -10 to -50. It is important to note the effectiveness of the cascode in reducing the gain to the drain of M1. The gain to M1 or Miller gain is:

$Av(Miller) = Vd(m1)/Vin = -2Gm1/(Gm2+gmbs2)$ or about -2 to -3.

The cascode reduces the Miller gain to from -10 to -50 to -2 to -3. This is significant as the Miller gain multiplies the parasitic capacitance between the gate and drain of the input transistor.

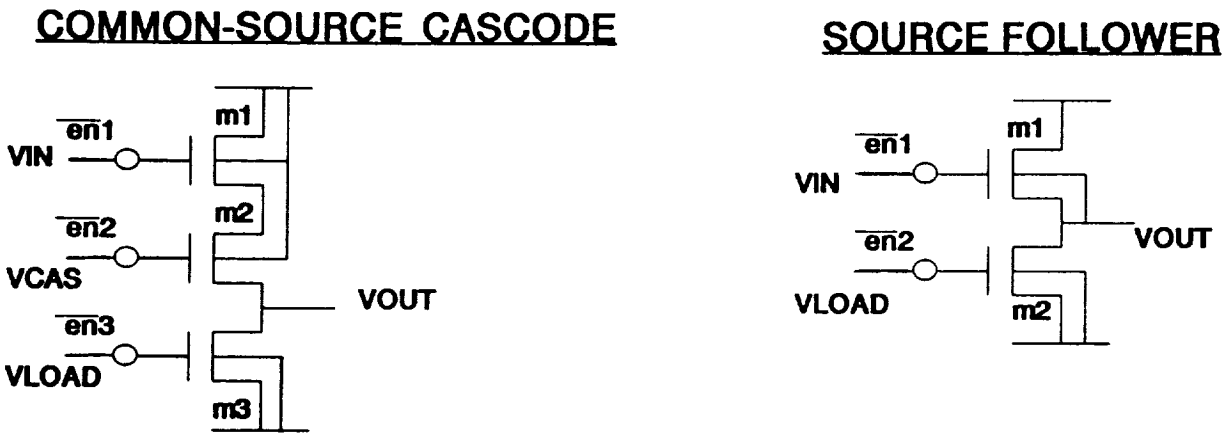

FIGURE 1. COMMON SOURCE CASCODE AND SOURCE FOLLOWER CIRCUIT CONFIGURATIONS

PREDICTED NOISE PERFORMANCE

The measured MOS noise characteristics showed classical behavior with 1/f and thermal noise characteristics. These noise sources appeared as noise voltage sources at the input or gate of the MOSFET. The noise performance of the MOS integrating amplifier can be expressed in terms of the integrators input referred noise voltage and the total integration node capacitance (including detector capacitance and Miller). This relationship is drawn from:

$$Q = nq = C*V = Ctotal*Vn(rms)$$

The input referred rms noise electrons can be expressed as:

$$e\text{-}(rms) = Ctotal*Vn(rms)/q$$

The total capacitance of the integration node is composed of the capacitance of the detector, the detector to input circuit interconnect, the source or drain diffusion to bulk capacitance of the reset transistor, the capacitance of the gate of the input MOSFET, and other similar components. For simplicity this analysis assumes all stray capacitance with the exception of the gate capacitance is lumped into the detector capacitance term.

$$Ctotal = Cgate + Cdetector$$

It is also useful to limit this analysis to the condition where the SF and CSC circuits are operating in saturation. In saturation SF gate capacitance is approximately equal to one minus the SF gain multiplied by the gate to source capacitance (0.1(Cgs) to 0.3(Cgs)) and the CSC configuration gate capacitance is approximately equal to the gate to source capacitance. Where Cgs is Approximately equal to CoxWL (Cox

= [EE0/Tox], and E & E0 are the Dielectric constant for SiO2 Permittivity in a vacuum and Tox is the thickness of the oxide).

Technology	Gate Capacitance
1.25um technology	[1.53ff/um^2]
3.0um technology	[0.6ff/um^2]

The input referred rms noise electrons for the SF and CSC circuits can be expressed as

e-(rms,SF) = (*Cdet*+*COX*WL*0.1)*Vn*(rms)*/q

e-(rms,CSC) = (*Cdet*+*COX*WL)*Vn*(rms)*/q

The input referred noise of the MOSFET is proportional to one over the square root of the gate area. The input referred noise voltage for a MOSFET of arbitrary size can be expressed in terms of the input referred noise of a MOSFET with gate area of 1000umsq:

$En^2(1/f) = en^2(1/f\ 1000umsq)$*sqrt(1000*umsq*/GateArea *squm*)

for 1/f dominated noise performance

$Vn(rms) = [En^2(1/f)*\text{sqrt}(\ln(f2/f1))]^{1/2}$

where En is the 1/f noise voltage per rtHz at 1Hz and f1 and f2 define the sampling band width. Combining we can express the input referred rms noise electrons for the SF and CSC as

$e\text{-}(rms,SF) = (Cdet+COXWL*0.1)(1/q)(en(1/f1000um^2))(\text{sqrt}(1000um^2/WLum^2)^{1/2}(\ln(f2/f1))^{1/2}$

$e\text{-}(rms,CSC) = (Cdet+COXWL)(1/q)(en(1/f1000um^2))(\text{sqrt}(1000um^2/WLum^2)^{1/2}(\ln(f2/f1))^{1/2}$

Figures 2 and 3 show the calculated input referred rms noise electrons of the SF and CSC circuits fabricated in 1.25um CMOS for varying gate area and stepped Cparasitic. These figures are based on calculations using the measurements of gate referred voltage noise and the expression derived above. The Cdet term in Figure 2 is stepped from 0 to 1.0pF by 0.2pf where Figure 3 Cdet is stepped from 0 to 10pF by 2.0pf. These calculations show a low in the rms input referred noise electrons for each value of parasitic capacitance with the minimum moving to larger gate areas with increased Cparasitic. The calculations were based on the following:

f1 = .01Hz
f2 = 100Hz
En*(1/f 1000umsq)* = 1uV/rtHz at 1Hz for 3um technology
En*(1/f 1000umsq)* = 200nV/rtHz at 1Hz for 1.25um technology
Gate Capacitance = 0.69ff/um for 3um technology
Gate Capacitance = 1.53ff/um for 1.25um technology

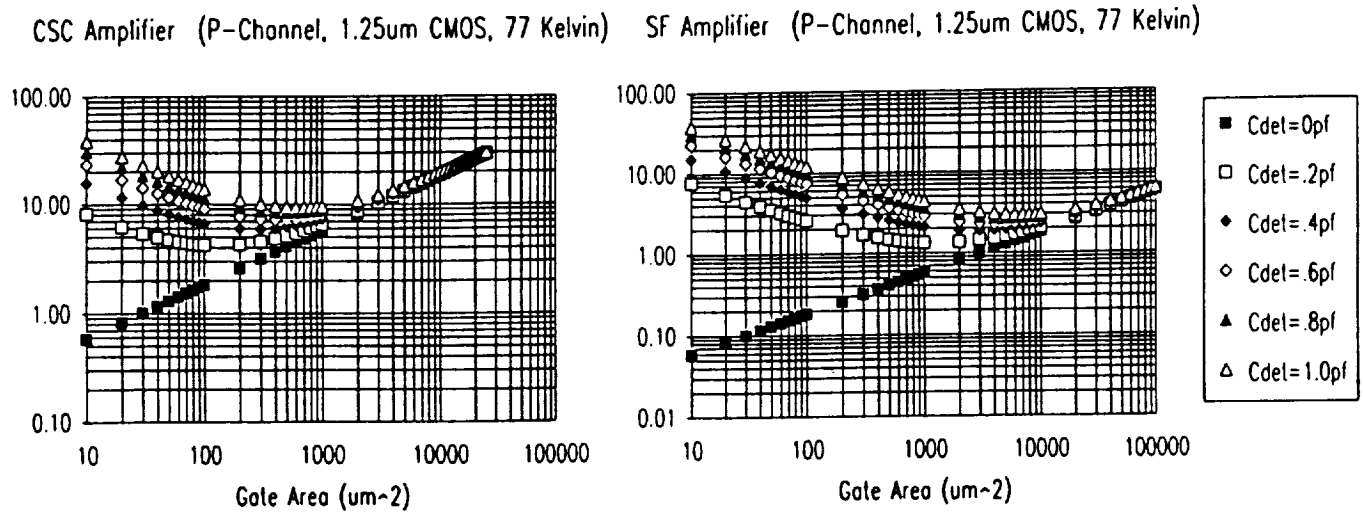

FIGURE 2. COMMON SOURCE CASCODE AND SOURCE FOLLOWER NOISE PREDICTIONS

(RMS E- VS. INPUT CAPACITANCE [0.2PF STEPS] & GATE AREA)

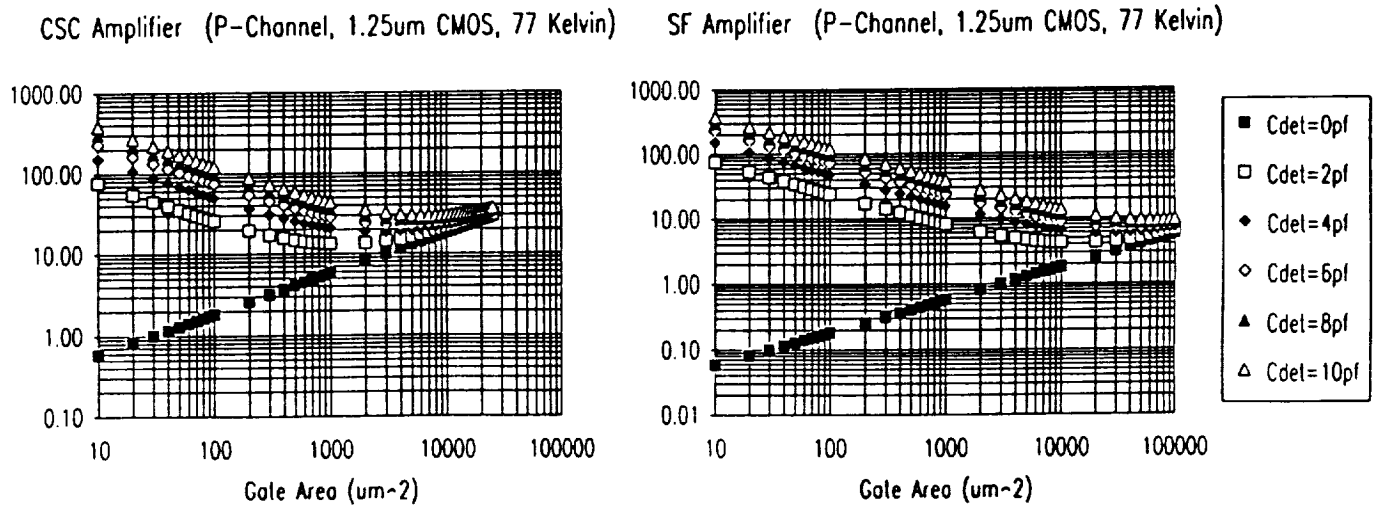

FIGURE 3. COMMON SOURCE CASCODE AND SOURCE FOLLOWER NOISE PREDICTIONS

(RMS E- VS. INPUT CAPACITANCE [2.0PF STEPS] & GATE AREA)

TEST CIRCUIT DESCRIPTION

A test circuit containing four reset integrator circuits was designed and fabricated in 1.25um CMOS. The four versions of the input circuit consist of SF and CSC designs implemented in both P and N type MOSFET's. These circuits are shown in Figure 4.

The operation of the reset intergator test circuits is based on the integration of the detector current on a capacitive node. The change in potential on the capacitive node is used to modulate the potential of the gate of the input MOSFET. The MOSFET output voltage is sensed non-destructively to measure the total integrated detector current.

Two means of determining the input node capacitance were incorporated into the design for each circuit. The first was a p/n photo diode connected to the input of each amplifier to allow the optical stimulation of input current. An additional photo diode was provided with direct connection to the test set to provide a reference for the test input current source. The photo diode current would cause a change in the input node potential $I = CdV/dT$. Since the input to output voltage transfer function can be measured directly, the input capacitance can be determined. The input node is also connected to two small switch MOSFET's with gates PHI1 and PHI2. The additional reset MOSFET to the input node of the circuit was provided to allow a switched capacitor resistor measurement of the input node capacitance.

All four circuits are laid out with the input MOSFET W/L at 50/10. The sum of the estimated capacitance of the reversed biased 10 x 10 um test input diode and 85 x 85 um input pad is 250 fF. The input gate capacitance is estimated to be 750 fF. The effective gate capacitance is expected to be lower than this depending upon the circuit operation. For the SF configuration, most of the capacitance is between the gate and source. However, since the source varies in phase with the gate, the effective capacitance is reduced by one minus the SF gain.

With the CSC circuit the MOSFET is in saturation and the depletion region is increased reducing the effective gate capacitance. The gate to drain capacitance is kept low by using the cascode MOSFET which reduces the Miller capacitance between the gate and drain. The total input node capacitance of the CSC amplifier is expected to be somewhat less than the sum of the input pad, diode, and input gate. The SF total input node capacitance is expected to be about half of the above sum or about 500fF.

All four circuit versions have static protection devices on all pads except for the small internal input pads. Diodes to VDD and VSS with resistive input routing on the pads are used for the static protection.

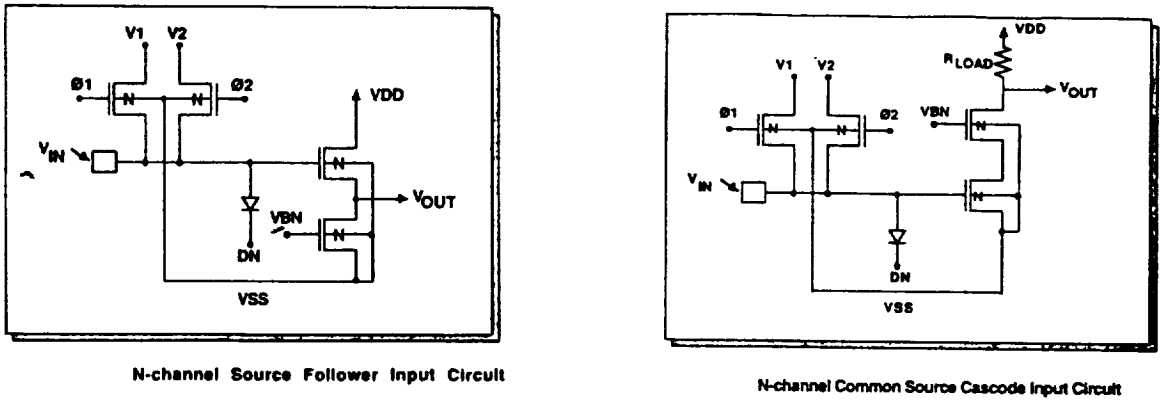

FIGURE 4. COMMON SOURCE CASCODE & SOURCE FOLLOWER TEST CIRCUIT

TEST MEASUREMENT RESULTS

Measurements of the test circuits were performed at Amber Engineering and at the Steward Observatory Detector Laboratory at the University of Arizona. Measurements at Amber were performed at 77 Kelvin for a bandwidth of 0.1Hz to 100Hz. Steward Observatory measurements were made at 28 Kelvin with a bandwidth of 620 micro-Hertz to 10 Hertz.

MEASUREMENT TECHNIQUES

Three basic measurements were performed at Amber and the University of Arizona on the reset integrator test circuits. These measurements were transfer function, input node capacitance, and input referred noise spectral density. These measurements were all performed using the measurement techniques described below.

TRANSFER FUNCTION

The voltage transfer function (TF) relates the circuit output voltage to the circuit input voltage. The TF is measured with the test device operating at nominal bias conditions. A 220K ohm resistor was used to load the CSC circuits. The on chip current source was used for the SF circuits. These measurements were performed using the HP4145A Parameter Analyzer to supply the DC and ramped voltages and to measure the output voltages. The AC gain was verified by connecting the input to a sine wave source and then measuring the amplitude response of the circuit output.

CAPACITOR MEASUREMENT

The input node capacitance was measured while the circuit is in operation by using a switch capacitor technique with switches PHI1 and PHI2. The circuit is biased in its dynamic range as in the transfer function measurement with the exception of PHI1, PHI2 and V2. V2 is set to produce a mid-scale output when PHI2 is turned on and PHI1 is turned off. V1 is swept from V2-delta to V2+delta where delta is about .1 volt for the CSC circuits and 1 volt for the SF circuits. As V1 is slowly swept, PHI1 and PHI2 are clocked with non-overlapping 30% duty cycle pulses with a period T. The current (I) from V1 to V2 is measured.

The input node capacitance can be calculated from:

$$I = C (V1-V2) / T$$

The period T was made short enough to produce a measurable current but also must be long enough that the input node capacitance can be fully charged through PHI1 to V1 and discharged through PHI2 to V2. A value of 5 to 100 microseconds is appropriate for the period T.

NOISE MEASUREMENTS

For the noise spectral density measurement the circuit is biased as in the transfer function measurement above with the addition that V1 is biased to produce a mid_scale output(input diode reversed biased). PHI1 is turned off, ending the reset process isolating the input node potential near V1.

Measurements performed at Amber utilized a HP3561A Dynamic Signal Analyzer to measure output noise spectral density in the bandwidth of 0.1Hz to 100Hz. Steward Observatory laboratory measurements were made using a successive differencing apparatus capable of measuring noise over integration times of 20 minutes. In both facilities the measurements were made after the reset process, so the KTC reset noise is correlated during the measurement procedure and dose not contribute to the measurement noise.

The output noise spectral density is then divided by the voltage gain of the input circuit to yield the input referred noise spectral density. The input referred rms voltage noise can be expressed as rms noise electrons by multiplying the noise voltage by the capacitance and dividing by the electronic charge.

MEASURED PERFORMANCE

The results of the gain, capacitance, and noise measurements taken on the reset integrator test circuit are summarized in Table 2 and Table 3.

	Gain	Cap.	Noise	A1/f@1Hz	Predicted	
	v/v	pf	uv rms	e rms	uv/rt(Hz)	e rms
NCS	27.6	0.68	1.6	6.8	0.44	3.6
PCS	26.9	0.66	1.9	7.7	0.44	3.6
PSF	0.84	0.43	14	38	3.0	3.0
NSF	0.75	0.44	n/a	n/a	n/a	n/a

TABLE 2. SUMMARY OF AMBER MEASURED GAIN, CAPACITANCE, AND NOISE RESULTS FROM RESET INTEGRATOR TEST CHIP.

Temp Kelvin(Start)		28.86	28.62	28.62	29.8	
Temp Kelvin(Stop)		28.64	28.62	28.62	29.03	
Bandwidth(f1,f2)		(Noise data in rms e-)				Predicted
40mHz	10Hz	5.4	5.2	5.4	5.2	2.9
20mHz	10Hz	4.4	4.7	5.1	6.1	3.0
10mHz	10Hz	4.0	5.1	4.8	9.2	3.1
5mHz	10Hz	4.8	4.3	4.8	16.2	3.3
2.5mHz	10Hz	5.4	5.1	5.7	29.8	3.5
1.2mHz	10Hz	10.0	5.8	4.8	55.7	3.6
620uHz	10Hz	n/a	n/a	n/a	89.6	3.7

TABLE 3. SUMMARY OF STEWARD OBSERVATORY TEST RESULTS.

The SF circuits tested at Amber measured about 30 to 40 rms e-. Steward Observatory measurements were similarly above 25 rms e-.

The data in Tables 2 and 3 show a potential advantage that the CSC circuit has over the SF circuits for noise performance. Here the voltage gain in the front end of the CSC circuits elevates both the signal and the noise voltages to levels 20 to 30 times that of the SF circuits. This may allow the input cell and signal path to be less susceptible to interface electronics and post chip noise sources and more importantly it may reduce the noise sensitivity of the input circuit to the switching and multiplexing electronics on chip.

1X32 ELEMENT COMMON SOURCE DEVELOPMENT FOR SIRTF

An array of 32 CSC input amplifiers is in development for the SIRTF high capacitance long wave length detectors. Figure 5 shows the layout for a single channel of the 1 x 32 readout. The performance perditions for this array are about 60 and 30 rms electrons for 2um and 1.25um CMOS technologies for a 10pF total input capacitance and a bandwidth of 0.1Hz to 100Hz.

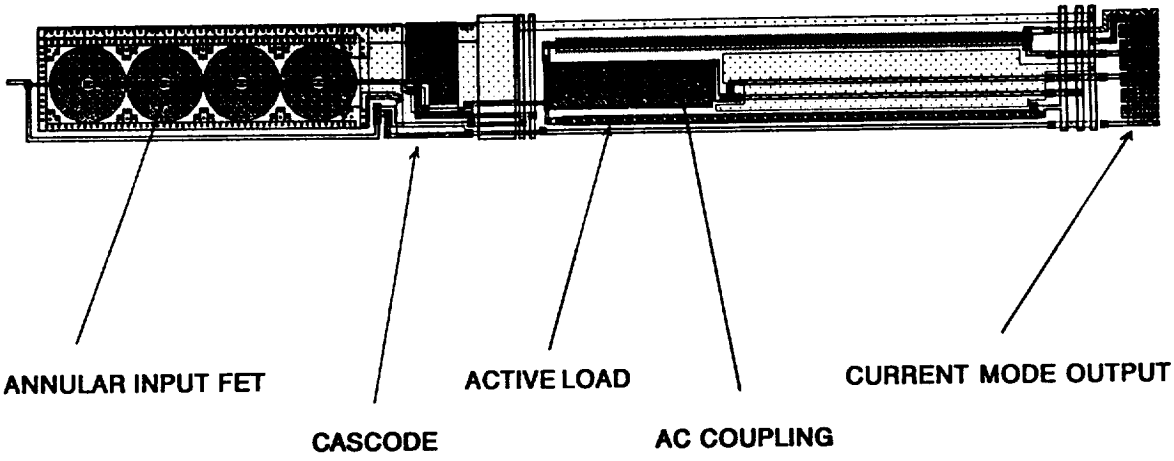

FIGURE 5. SINGLE CHANNEL COMMON SOURCE CASCODE AMPLIFIER CELL FOR 1 X 32 SIRTF HIGH CAPACITANCE DETECTOR ARRAY

SUMMARY

Measurement and theoretical performance perditions based on CMOS process performance measurements agreed extremely well for the CSC input amplifiers. The SF configuration, however, showed much higher noise than predicted. Both input circuit configurations should provide excellent noise performance for low detector and input stray capacitance focal plane arrays.

In the case where the input capacitance is dominated by the detector capacitance, input referred noise performance for the CSC and SF circuits should be identical. The SF should achieve low noise for gate capacitance limited conditions. This was not seen in our measurements of the SF test circuit.

For the bandwidth discussed of .01Hz to 100Hz with a total parasitic detector and stray capacitance at 0.5pF input referred RMS noise electrons should be around 27e- and 8e- for 3um and 1.25um CMOS technology. The availability of CMOS processes is abundant with competitive commercial sources. Processing is relatively low cost and yields are high. Readout processing capabilities and input cell sizes and power requirements should be compatible with large starring arrays for formats to greater then 128x128 elements. The size limitations will be imposed by hybridization and detector yield and not readout fabrication.

The key to realizing this performance will be in the multiplexer architecture and the careful shielding of on and off chip noise sources from the input cell and signal path.

ACKNOWLEDGEMENTS

We acknowledge the important contributions of Chris Fletcher for the layout of the SF and CSC test circuit, Glenn Kincaid for layout of the 1 x 32 CSC array for SIRTF, John Blackwell for noise and test circuit performance testing, and Dr. William Parrish for technical discussions. Work sponsored in part through NASA contract NAS2-12578 through a University of Arizona subcontract.

REFERENCES

1. P. Gray and R. Meyer, "Analysis and Design of Analog Integrated Circuits", John Wiley & Sons, 1984

2. P. Allen and D. Holberg, "CMOS Analog Circuit Design", Holt Rinehart and Winston Inc., 1987

N90-21325

STUDY OF ADVANCED InSb ARRAYS FOR SIRTF

Alan Hoffman and Robert Feitt
Santa Barbara Research Center
Goleta, CA 93117

ABSTRACT

The Santa Barbara Research Center has completed a study leading to the development of advanced Indium Antimonide detector arrays for the Space Infrared Telescope Facility (SIRTF) Focal Plane Array Detector (FPAD) Subsystem of the Infrared Array Camera (IRAC) Band 1. The overall goal of the study was to perform design tradeoff studies, analysis and research to develop a Direct Readout Integrated Circuit to be hybridized to an advanced, high performance InSb detector array that would satisfy the technical requirements for Band 1 as specified in the IRAC Instrument Requirements Document (IRD), IRAC-202. The overall goal of the study was divided into both a near-term goal and a far-term goal. The near-term goal identifies current technology available that approaches, and in some cases meets the program technological goals as specified in IRAC-202. The far-term goal identifies technology development required to completely achieve SIRTF program goals.

Analyses of potential detector materials indicates that InSb presently meets all Band 1 requirements and is considered to be the baseline approach due to technical maturity. The major issue with regard to photovoltaic detectors such as InSb and HgCdTe is to achieve a reduction in detector capacitance. An analysis of Capacitive Transimpedance Amplifiers (CTIAs), Source-Follower per Detector (SFD), and Modified Source-Follower per Detector (MSFD) amplifiers is performed. The baseline approach is the use of a PMOS SFD. An assessment of radiation effects anticipated during the SIRTF mission indicates that orbit-to-orbit performance shifts are negligible, and detector total-dose effects are expected to be negligible for a period of ten years.

INTRODUCTION

The study of Advanced InSb Arrays for SIRTF was performed at the Santa Barbara Research Center, Goleta, California, a wholly-owned subsidiary of GM-Hughes Electronics, for the Harvard-Smithsonian Astrophysical Observatory of Cambridge, Massachusetts. This work is to be utilized by the Smithsonian Astrophysical Observatory (SAO) on its Wide Field and Diffraction Limited Infrared Array Camera (IRAC) Program.

The interim technical goals of the SIRTF IRAC Program are given in Figure 1.

BAND 1 DETECTOR DEVELOPMENT

The selection of Indium Antimonide detectors as the baseline approach for Band 1 of the IRAC was made primarily due to the maturity of InSb technology and the fact that InSb presently meets all SIRTF Band 1 requirements. Mercury Cadmium Telluride (HgCdTe) detector technology could demonstrate performance equivalent to InSb at 10 Kelvins in the future; however, higher quantum efficiencies in the 1 to 5 μm band must be demonstrated and the technology be allowed to mature to be considered for the SIRTF IRAC Band 1 mission. Another alternative to InSb is Gallium doped Silicon (Si:Ga) Impurity Band Conduction (IBC) technology, however, higher quantum efficiencies in the 1 to 5 μm band must also be demonstrated before consideration will be given to this technology. As previously stated, InSb technology presently meets all SIRTF Band 1 requirements and is technically mature.

The major issue that remains with photovoltaic detectors such as InSb and HgCdTe is the reduction of detector capacitance, which is necessary due to circuits in the readout unit cell. Given the fact that Noise Equivalent Power (NEP) increases almost linearly with detector capacitance, and SIRTF mission low-background, long integration time requirements the reduction of detector capacitance is an important goal in the development of SIRTF flight focal plane array detector assemblies.

Several techniques exist that achieve reductions in detector capacitance.

Since the detector gate overlap with the implanted region results in a capacitance that is proportional to that overlap, a reduction in overall detector capacitance can be realized by minimizing the gate overlap or employing gateless detectors, which totally eliminates the gate capacitance contribution. In addition, increasing the depletion width via lower doping and/or a "graded junction" will also serve to decrease capacitance.

Another method of capacitance reduction is the reduction of detector junction size. Figure 2 illustrates the exponential relationship and trade between capacitance and detector size. Obviously, the smaller detectors have lower values of capacitance and therefore, generate lower noise.

λ RANGE (μm)	DETECTOR MATERIAL	DETECTOR FORMAT - PIXEL FOV (ARCSEC) WF/DL	READOUT NOISE	DETECTOR QUANTUM EFFICIENCY η/Gη	DETECTOR RESPONSIVITY	DETECTOR DARK CURRENT	WELL CAPACITY (e^-)	POWER (MW) 1 frame/sec	READOUT
1.4-5.3	InSb (Si:In) (HgCdTe)	128 x 128 2.35/0.59	$\leq 10e^{-*}$	0.6/0.6	2.4 A/W @ 5μm	$\leq 10e^{-1}$/sec per pixel	$>5x10^5$	≤12	Direct Readout Random Access Non-Destructable
5.3-14	Si:Ga (Si:As)	64 x 64 4.7/1.17	$\leq 100e^-$	0.3/0.15	2.2 A/W @ 18μm	$\leq 10e^-$/sec per pixel	$>5x10^5$	≤3	" "
14-30	Si:Sb (Si:As)	64 x 64 4.7/1.17	$\leq 100e^-$	0.3/0.15	3.4 A/W @ 30μm	$\leq 10e^-$/sec per pixel	$>5x10^5$	≤3	" "

* Design goal, present projected performance ~ 60-80e^-

Figure 1. IRAC array interim performance goals

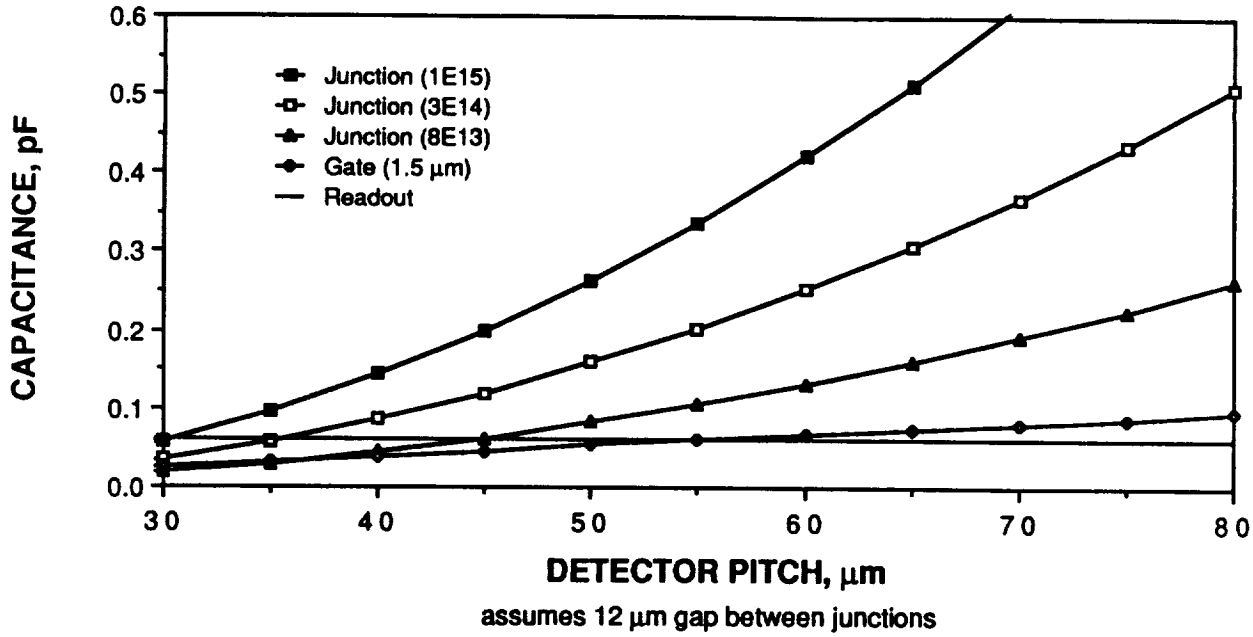

Figure 2. Capacitance as a function of detector size for InSb detectors

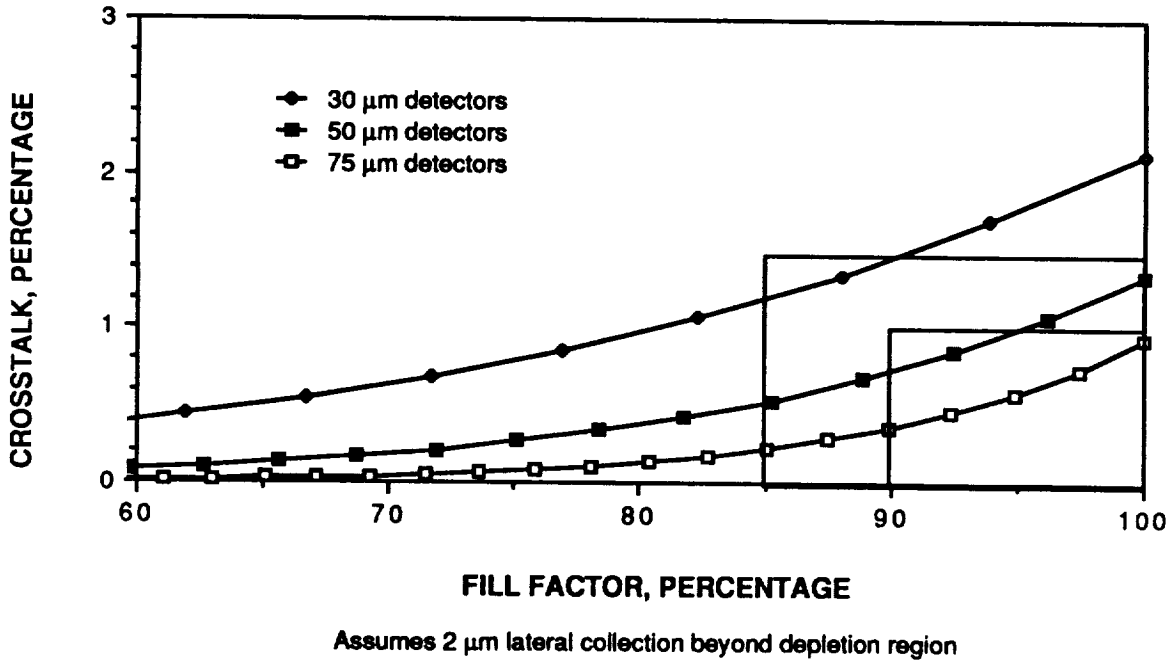

Figure 3. Trade between crosstalk and optical fill factor

The reduction of detector junction size as a capacitance reduction technique must also consider the effect on fill factor and crosstalk. As shown in Figure 3 the tradeoff between crosstalk and fill factor indicates that crosstalk increases with an increase in fill factor. The larger area diodes can experience higher percentages of fill factor (up to 100%) and still have values of crosstalk equal to or less than 1%. As diode area decreases values of crosstalk increase for constant percentages of fill factor. At 100% fill factor a 30 μm x 30 μm diode exhibits 2% crosstalk. The tradeoff between detector capacitance and fill factor must be optimized with consideration given mission performance. In addition, a decrease in the size of the optical image of the focal plane will be experienced when a reduction is made in detector junction area, and must also be considered when evaluating this trade.

READOUT INTEGRATED CIRCUIT DEVELOPMENT

The second thrust of the Advanced InSb Array Study for SIRTF was to evaluate SIRTF mission signal processing requirements versus readout integrated circuit device performance, and define the technology(ies) that would meet SIRTF IRAC specified performance goals.

The first step in determining an appropriate readout circuit for SIRTF is a thorough understanding of the performance requirements. Important performance requirements included noise, power dissipation, pixel sizes, integration time and background. By far the most demanding requirement for the SIRTF focal plane is the low-noise floor of <10 electrons. A summary of the SIRTF Band 1 specification is shown in Figure 4.

Requirement	Specification
Wavelength	2 to 5 μm
Array Size	128 × 128 nominal
Pixel Size	50 to 100 μm
Fill Factor	>90%
Readout Modes	Nondestructive, random access
Pixel Operability	≥98% array, ≥98.5% central 32 × 64
Signal/Noise	BLIP, 10 e^-
Integration Time	≤1000 sec
Background (Average)	10 photons/pixel/sec
Latent Image	Discharge in ≤1 sec
Uniformity	±5% of responsivity
Charged Particle Events	Complete recovery in ≤10 ms
Power Dissipation	≤5 mW
Pixel Access Time	≤75 μs
Array Read Time	≤300 ms

Figure 4. Band 1 specification

Based upon the SIRTF requirements, the possible number of candidate readout circuits was narrowed to two candidates; the source follower per detector (SFD), and the capacitive transimpedance

amplifier (CTIA). A noise analysis was performed for both circuits as well as power dissipation and a basic point design.

The SFD circuit is being considered for this program because of its simplicity and low power dissipation. Simplicity of design enables a 128^2 or 256^2 array to be fabricated with high yield. Low power dissipation not only increases focal plane lifetime during a space flight but also reduces the possibility of IR emission from the readout chip itself.

However, there are several advantages to the CTIA circuit. The circuit designer can choose to enhance either the sensitivity or the bucket capacity by the adjusting the size of the feedback capacitor. In addition, the CTIA inherently has better linearity than the SFD (although this may not be of paramount importance to astronomy) and the detector bias remains constant at all times. For other applications, the CTIA may be the circuit of choice, but for SIRTF the SFD appears to have an advantage.

As a part of the SIRTF study, readout excess noise was investigated. Transients induced by clock transitions on the array were found to not have an effect on noise. However, a FET that is switched off/on has excess noise due to the switching itself. The noise is increased to as much as 3 times the unswitched noise. This effect needs to be addressed in future readout designs to help achieve SIRTF noise goals.

Another direction for future readouts in astronomy applications is to use PMOS rather than NMOS FETs for all critical transistors. At the relatively low data rates of most astronomy readouts, 1/f noise dominates, and 1/f noise of NMOS FETs is typically 3 times that for comparable PMOS FETs. During the SIRTF study, measurements of 1/f noise as a function of temperature were performed. One result, shown in Figure 5, is that the 1/f noise of some PMOS FETs increases around 10 Kelvins. The presence and magnitude of this effect depends on the readout processing but the cause is not understood.

RADIATION EFFECTS

Radiation effects on the detector have been studied to determine what degradation in the data, if any, could be expected during a SIRTF mission.

The dominant ionizing radiation is high energy protons. Figure 6 shows the number of events over the proton energy spectrum for different detector areas (Figure 6a) and different detector thickness (Figure 6b). For InSb the number of events is nearly proportional to the detector area but there is little change with thickness. For a 50 by 50 μm detector, the expected number of proton events is 1 per second within the South Atlantic Anomaly (SAA) and 1 every 7 hrs. outside the SAA. For a high orbit only the lower rate is applicable. Gamma events are an order of magnitude less frequent: 1 every 2 days.

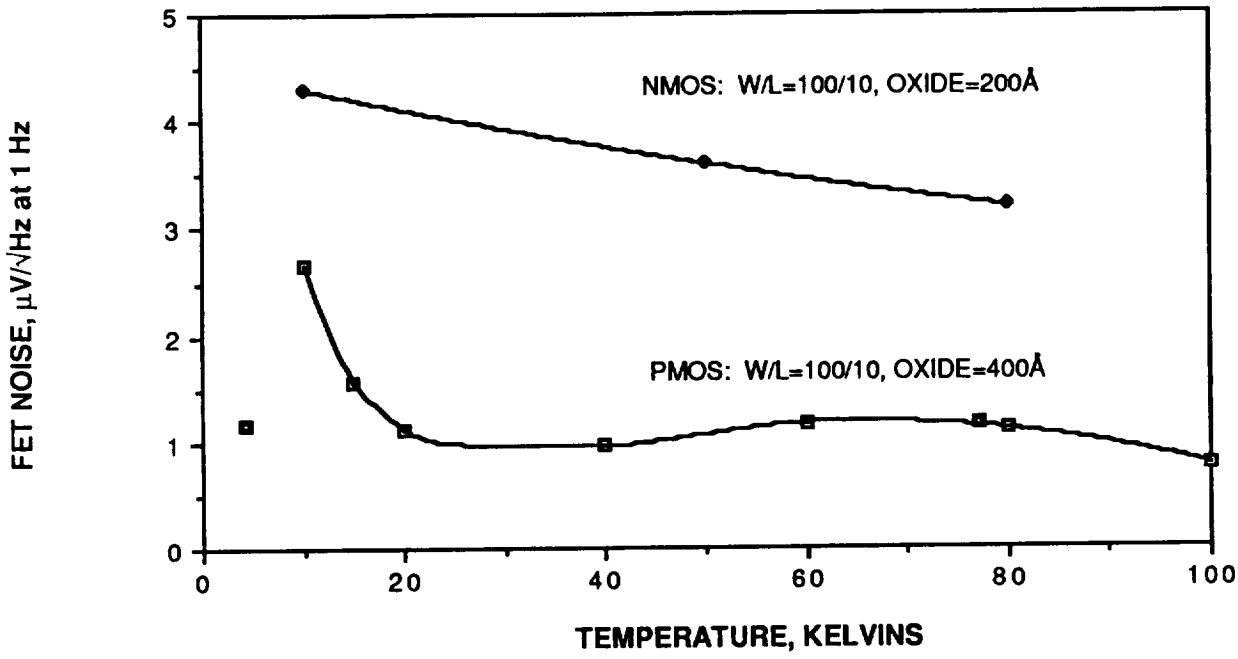

Figure 5. 1/f noise versus temperature for an NMOS and PMOS FET

The pulse amplitude for each proton event is determined by the proton energy, as shown in Figure 7. The amplitude depends less on detector area (Figure 7a) than on thickness (Figure 7b). The amplitudes are large enough that they can be easily discriminated from the infrared signal.

Total dose requirements for SIRTF are not severe for either InSb detector material or silicon MOSFET readouts. Even for a low orbit that includes transiting the SAA, the total dose is just 750 rad(Si) per year. SBRC InSb detector arrays have been irradiated with up to 10^4 rad(Si) without any degradation in quantum efficiency or leakage current. Recently another detector surface passivation has been developed and tested out to 6 x 10^5 rad(Si) without degradation.

Typical CMOS devices with 200 to 300 Å oxides exhibit a 0.1 volt shift in threshold after irradiation with 10^4 rad(Si). Readout circuits can easily accept this much shift without performance degradation.

CONCLUSIONS

Most SIRTF IRAC requirements have been demonstrated on test devices. In particular, InSb detector dark current and radiation hardness measurements meet SIRTF goals.

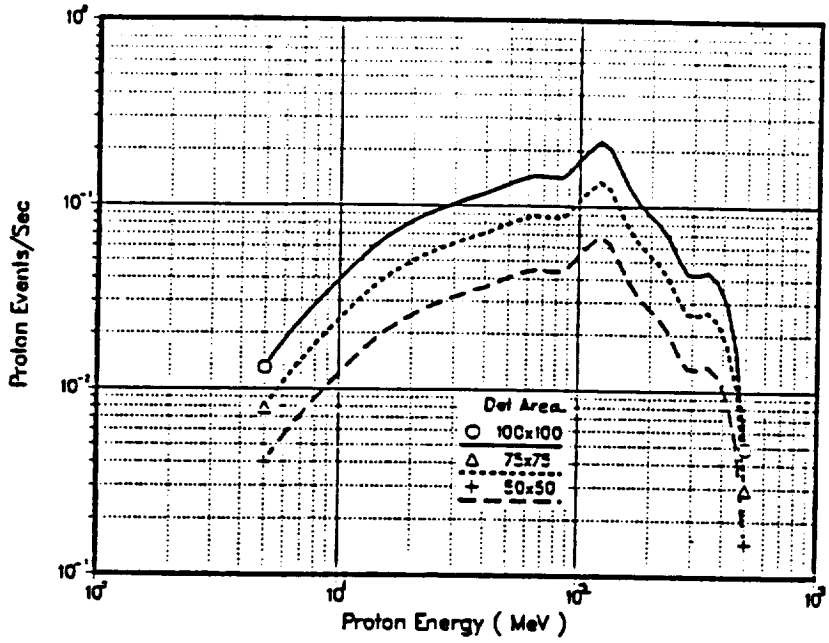

a. Proton events for 15 μm thick detectors of different areas

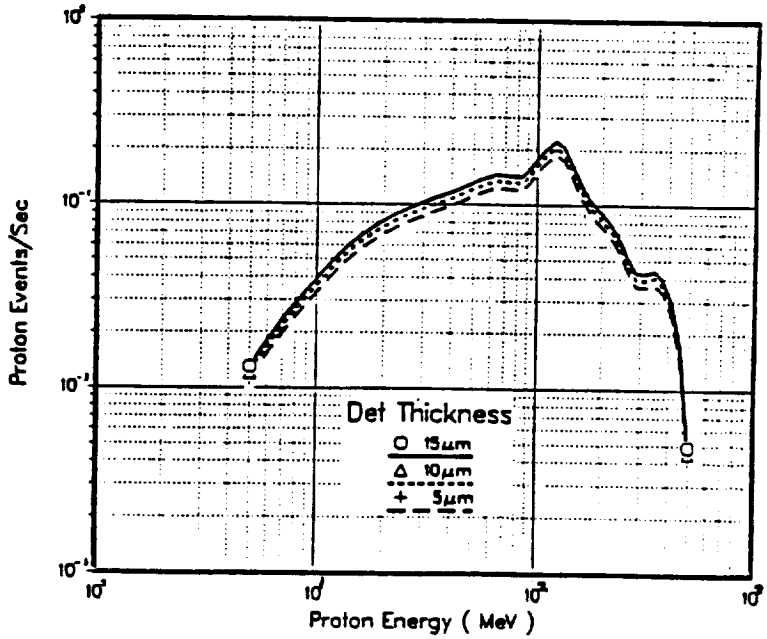

b. Proton events for (100 μm)^2 detectors of different thicknesses

Figure 6. Proton event rate in the SAA for InSb detectors as a function of proton energy

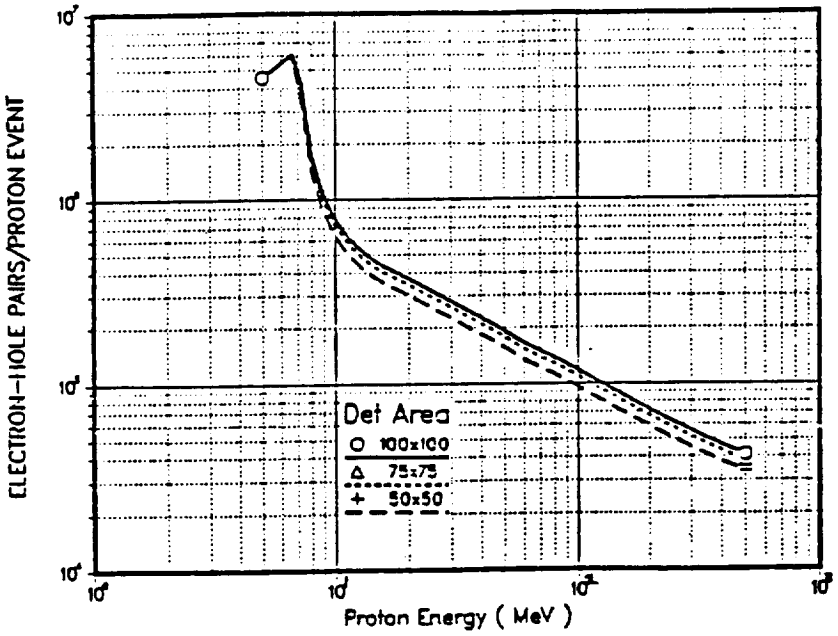

a. Pulse amplitudes for 15 μm thick detectors with different areas

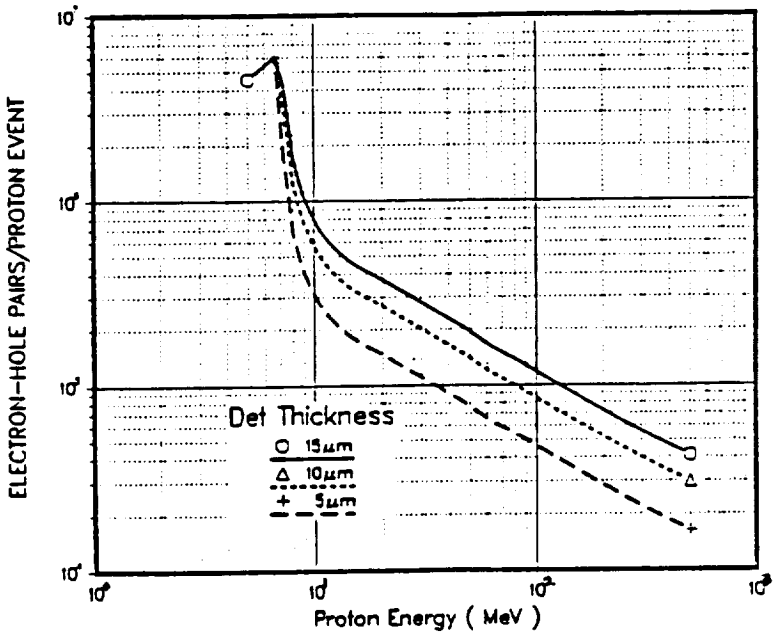

b. Pulse amplitudes for $(100\ \mu m)^2$ detectors of different thicknesses

Figure 7. Pulse amplitude per proton event as a function of proton energy

One major issue, excess noise, still needs to be addressed to insure optimum performance of the flight instrument. The noise goal can be approached from two sides: reduce detector capacitance and improve readout noise. Noise associated with FET switching needs to be addressed in future SIRTF research and development. Many of the capacitance reduction techniques discussed above will be investigated this year. The excess 10 Kelvin PMOS noise will be examined both analytically and experimentally to determine its origin. A PMOS 256^2 readout will also be developed this year to demonstrate the performance and producibility of this type of array.

ACKNOWLEDGMENTS

We wish to thank the entire SIRTF IRAC team for their support and guidance during this project. Difficult readout noise measurements supplied by groups at NARC (C. McCreight and M. McKelvey) and the University of Rochester (J. Pipher and W. Forrest) were especially valuable.

N90-21326

InSb DRO Array Characteristics

W. J. Forrest, J. L. Pipher, Z. Ninkov, J. D. Garnett
Department of Physics and Astronomy
University of Rochester, Rochester, NY 14627

Abstract: We have tested 58×62 low-doped InSb diode arrays bonded to MOSFET readouts for their performance potential in a low background space environment. The arrays were constructed by SBRC under a contract from NASA. Of primary concern were the quantum efficiency, dark current and read noise. The quantum efficiency (45% at 3.3μm) and dark current ($< 2.4e^-/s$) were found to be adequate for the SIRTF experiments, while the read noise (200 e^- RMS) was found to be wanting. More subtle concerns, such as image quality, linearity/calibratibility and flat fielding were also investigated. In these respects the arrays appear to be well suited for the high sensitivity, photometric accuracy, and image clarity demanded by the SIRTF experiments.

Introduction

The Infrared Array Camera (IRAC) and Infrared Spectrometer (IRS) on NASA's Space Infrared Telescope Facility (SIRTF) experiment require high quality, large format detector arrays for the 2 to 5 μm spectral region. Under contract from NASA, the IRAC team approached Santa Barbara Research Center (SBRC) to produce the first generation arrays, optimized for space. InSb photovoltaic material was selected, being the most mature technology with the best immediate prospects for high performance. Low doping ($2 \times 10^{14}/\mathrm{cm}^3$, rather than the standard $1-2 \times 10^{15}/\mathrm{cm}^3$) was chosen in order to reduce the dark current at low temperatures and reduce the detector capacitance, leading to reduced read noise. The goals for these detectors were high quantum efficiency ($> 50\%$), low dark current ($< 2e^-/\mathrm{sec}$), low read noise ($< 100e^- RMS$), excellent imaging qualities, stable (calibratible) output, and resilience to the SIRTF radiation environment. The research team at the University of Rochester has been responsible for the test and evaluation of these arrays, described below. The 58×62 InSb detectors and CRC 228 MOSFET direct readout have been described in detail by Fowler *et al.* (1987) and Orias *et al.* (1986). A brief description of our detector test station has been given by Ninkov *et al.* (1987).

Quantum Efficiency/Detector Thickness

The first array tested, SCA 1, displayed a common fault with these detectors, loss of quantum efficiency (QE) as temperature is lowered. In fig. 1 is shown a comparison of the 3.3μm QE at 8K and 31K. In fig. 2 this data is shown as a histogram. It can be seen

that at 31K, the QE is quite respectable, about 45%, with a relatively narrow distribution about the mean. However at 8K, the average QE drops to 20%, with a severe loss of QE on the left side of the array. Since the dark current was too high, about 6 aA ($38e^-/s$) at 31K, we consider this particular array unsuitable for SIRTF.

Figure 3 compares the QE of SCA 2 to SCA 1 at low temperatures. It can be seen that SCA 2 is much superior at maintaining QE at low temperatures. From the histogram in fig. 4, the average QE is 32% using -1.5V on the detector gates (VGATE, see Fowler *et al.* (1987) and Orias *et al.* (1987) for a description) and 43% with -2.3V at 10K. Figure 5 shows the ratio of a 10K flat field to a 7K flat field at 3.3μm. It can be seen that there is some die-off of QE with lowered temperature, and it is concentrated in the lower right corner, where the QE is lowest. For this array, there is a temperature, around 10K, where the quantum efficiency is acceptably high, yet the dark current (next section) remains acceptably low.

The loss of quantum efficiency with decreased temperature is evidently due to a decrease in the mean free path of the charge carriers in the InSb. Either the mobility and/or the lifetime of the carriers is too small. We suspect low temperature traps, either crystal defects or impurities, may cause this. If the mean free path is less than the distance the carriers have to travel before collection by the pn junction, then the charge may never show up in the external circuit. Since the absorption depth for 2-5 μm photons is only 1-2 μm in InSb (Sze, 1981, p.751), the carriers have to traverse nearly the full thickness of InSb, about 10μm for these detectors, before reaching the depletion region at the pn junction (which is only about a few μm deep).

We have discovered an interesting interference phenomenon which, we believe, allows us to measure the InSb thickness directly, and test the above ideas. Figure 6 shows data on SCA 2 detector, showing interference effects. The flat field through the narrow 4.67μm filter (4% resolution) shows a subtle pattern of light and dark ridges, most noticeable at the left of the array. The 22% resolution 3.75μm flat field, on the top left, shows no such effect. (We have looked for the effect using a 3.75μm 1% filter and don't see it - so it is primarily a wavelength dependent phenomenon). Dividing the 4.67μm image by the 3.75μm image removes the large gradient and other structure in the flat field and accentuates the interference pattern. At least 8 fringes may be seen, most prominent and closer together on the left side. We interpret these fringes as interference between incident and reflected radiation at the top surface of the InSb. A maximum in intensity will be observed whenever the thickness t is an integral (m) multiple of the quantity $\lambda/2n = 0.6\mu$m, where λ is the wavelength and $n = 3.8$ is the index of refraction of InSb. $m = 1, 2, 3, \ldots$ is the order of the interference:

$$t = m\frac{\lambda}{2n} \tag{1}$$

We interpret the fringes as indicating a wedge in the InSb thickness, with each fringe indicating an increase in thickness of about $0.6\mu m$. For SCA 2, we believe the thin side is on the left, where the fringes can be seen most easily. Since the penetration depth of 4.67μm photons is only about 2μm, fringes can only be seen clearly in fairly thin material. This is also the side with the best quantum efficiency, which we expect for thinner material. By counting fringes, we conclude that this detector has at least 5μm of wedge from the

left side to the right. We draw attention to the curve of the fringes at the upper and lower left corners, indicating "turned down corners", which is what one might expect from the mechanical thinning method used by SBRC.

This interpretation is strengthened and extended by measurements made on the FPA 72 detector. Here we used our 1% resolution CVF (circular variable filter) to investigate the fringing as a function of wavelength. In fig. 7, the data at 4.5μm and 3.3μm is compared. The fringes are not as pronounced as for SCA 2, probably at least partly due to the AR coating on this array, as well as the shorter wavelength employed. However, they can still be seen in the 4.5μm/3.3μm ratio image; again we point out the curvature of the fringes in the upper and lower left corners, indicating "turned down corners". Also we interpret the left side as being thinner, since the fringes are much more visible there. By repeating this at 4.4μm (figure 8), we learn a lot. First, we note that the fringes move to the right as we increase wavelength from 4.4 to 4.5μm. This means the thickness increases toward the right, confirming the speculations made above. The amount of fringe shift for a given wavelength change compared to the fringe spacing gives the order m and hence the thickness through:

$t_1 = m\lambda_1/2n$	thickness at fringe peak of wavelength λ_1
$t_2 = m\lambda_2/2n$	thickness at fringe peak of wavelength λ_2
$t_3 = (m+1)\lambda_1/2n$	thickness at next fringe peak, wavelength λ_1

These can be combined to give:

$$m = \frac{\lambda_1}{\lambda_1 - \lambda_2}\frac{t_1 - t_2}{t_1 - t_3} \tag{2}$$

and assuming a linear wedge, the thicknesses can be replaced by the x displacement on the array:

$$m = \frac{\lambda_1}{\lambda_1 - \lambda_2}\frac{x_1 - x_2}{x_1 - x_3} \tag{3}$$

Using the following data for the first three bright fringes named a, b, and c on the left side of the array approximately half way down at row 30, where the fringes are nearly vertical):

Table. Fringes Crossing Row 30

$\lambda(\mu m)$	Fringe peak (column # = x)		
	a	b	c
4.4	8	16	25
4.5	10	17.5	28

gives an average fringe shift of $< x_1 - x_2 >$ of 2.17 pixels, for a wavelength difference $(\lambda_2 - \lambda_1)$ of $0.1\mu m$. The average fringe spacing normalized by the wavelength $< x_3 - x_1 > /\lambda$ is 1.97 pixels/μm. Inserting these values in equation (3) gives m=11.02 for the fringe crossing row 30, column 16 at 4.4μm (fringe b above). The very small deviation of the

calculated m value from an integer is taken as further support for the assumptions used here. (Our convention is rows 1 through 58 starting at the top and columns 1 through 62 starting at the left of all the images shown). From the order $m = 11$ at row 30 column 16, the thickness is determined to be 6.4μm at that position. All the other fringes can now be interpreted as iso-thickness contours, each separated by 0.6 μm, as shown in fig. 8. From this figure, it can be seen that the good side of the array (upper left corner), which maintains high QE at low temperatures, is about 5μm thick, while the poorer side (lower right corner) is about 10μm thick. Thus we conclude that even if the carrier mean free path at low temperatures can't be improved in future generations of InSb arrays, good QE performance can be achieved if the thickness is tightly controlled to $5 \pm 1\mu$m everywhere.

"Tree Rings" in Flat Fields

In all of the low and high doped InSb arrays we have tested, there is a regular pattern of bright and dark markings in the flat fields, reminding one of tree rings with the center of the tree off the array. Examples can be seen in figs. 1 and 3. We have been informed by the manufacturer of the InSb starting material that the Czochralski growth method they employ will lead to doping variations in swirling circular patterns, called by them "beach lines." It is not immediately obvious, however, how doping variations can lead to flat-field variations, since the QE should be only weakly dependent on doping (InSb is an intrinsic semiconductor). We now believe the tree rings do not represent QE variations, but rather responsivity variations caused by capacitance variations. The capacitance C of an InSb diode varies as $\sqrt{n}$, where n is the doping concentration. Since the output voltage V will be roughly given by:

$$V = Q/C \tag{4}$$

where Q is the charge collected, a variation in C will cause a variation in the output voltage, leading to tree rings. The bright rings are lower doped, lower capacitance regions and vice-versa.

For four of the more prominent tree rings on SCA 2, the peak-to-peak variation is about 25%. The total dynamic capacitance is about 0.5 pF at the 350mV of back-bias that we employed, and we estimate the fixed contribution of 0.23 pF from the detector gate and MOSFET gate. To get this much signal variation requires a detector capacitance variation from 0.21 to 0.33 pF. Taking the nominal doping level as $2 \times 10^{14}/\mathrm{cm}^3$, from the manufacturer, this implies the doping varies from 1.2 to $3.0 \times 10^{14}/\mathrm{cm}^3$, rather than the much more modest variation of $1.7 - 2.3 \times 10^{14}/\mathrm{cm}^3$ or less we had originally been told by the vendor.

Fortunately, the tree rings are very stable and hence easy to calibrate out (see fig. 5 for instance). They represent primarily a nuisance, and not a fundamental limit for SIRTF applications. We do recommend that in the future generations, the doping variations be kept to $\pm 15\%$ peak to peak rather than the present $\pm 50\%$.

Effect of VGATE on QE

The following table gives a summary of QE measurements on various low- doped arrays as a function of VGATE and temperature. We report the average QE of the working pixels, always > 90% of the total. The wavelength is 3.3μm, near the center of IRAC Band I and the short wavelength spectrometer of the IRS:

SCA 01 (non AR coated)

55% at 31K, detector gate = -0.2V
27% at 8 K, detector gate = -0.5V

SCA 02 (non AR coated)

gate:		-1.5V	-2.3V
T=	10K	32%	43%
	7K	25%	

FPA 72 (AR coated)

gate:		-2.0V	-2.3V	-2.4V	-2.5V
T=	13K		52%		
	10K				52%
	9K	36%	47%	50%	

The FPA 72 data, which were all taken on 6 July 1988, show the trend with detector gate most clearly. The data at 9 and 10K are plotted in fig. 9. The SCA 02 data for the different gate voltages were taken in Aug. 1987 (-1.5Vgate) and May 1988 (-2.3Vgate).

This is not the whole story, as we have attempted to reproduce the variation seen with FPA 72 and saw little or no variation of QE with VGATE. Re-checking the 6 July 1988 data indicates little doubt that the effect was real at that time, though a little less pronounced than shown in the figure. We conclude that the QE variation with VGATE depends also on the history of the VGATE setting, i.e. whether the gate voltages were -2.0, -2.3, -2.4, -2.5 or cycled -2.0, +2.0, -2.3, +2.0, -2.4, +2.0, -2.5. The +2.0 intermediate VGATEs are sometimes used to reset the array.

Dark Current

The extremely low backgrounds anticipated for SIRTF require correspondingly low dark currents, in order to achieve background limited performance. A key element of our development of InSb detectors was the desire to minimize the dark current. The following tables show typical backgrounds in space and backgrounds we have seen at the telescope:

TABLE 1: TYPICAL BACKGROUNDS IN SPACE (ZODIACAL LIGHT)

SIRTF Effective Area $4.9 \times 10^3 \mathrm{cm}^2$, Pixel diameter $= 2.4\lambda/D$

Wavelength (μm)	$\Delta\lambda$ (μm)	Background (photons/sec)	pixel diameter (arc sec)
2.1	0.6	6.8	1.2
3.54	1.1	12.8	2.0
4.6	1.4	85.2	2.6
12.6	3.8	1.4×10^4	7.0
26.9	8.1	1.1×10^6	15

TABLE 2: BACKGROUNDS SEEN ON MAUNA KEA

(f/14, 76 μm pixels, 1 airmass)

Filter	Wavelength (μm)	$\Delta\lambda$ (μm)	Background (electrons/sec)	Primary Source
J	1.23	0.23	80-800	OH emission
H	1.65	0.32	500-5000	OH emission
K	2.23	0.41	2500-3000	telescope thermal emission
1% CVF	2.08	0.02	60	OH emission
1% CVF	2.12	0.02	100	OH emission

It can be seen that backgrounds approaching those anticipated in space are occasionally reached in the near IR at a ground based telescope, especially when observing through our 1% resolution CVF. The OH emission is highly variable on short time scales, as indicated for the J and H bands above. The actual photon background, incident on the telescope, is probably about a factor of 4-8 higher than the electrons/sec seen at the detectors.

From table 1, we conclude a dark current less than a few e^-/s is desirable. For SCA 2, the dark current is very low. In fact, we have not been able to detect it convincingly at 7K or 10K. The dark charge collected in 500 sec is given in fig. 10. The data were generated by subtracting a 500 sec integration from a 0.1 sec integration. The dark charge was actually negative, i.e. less, apparently, in the 500 sec than the 0.1 sec. This is attributed to a small offset in the whole output of the array (about -400 electrons). Taking 3 times this value as a conservative limit on the true dark charge gives a limit of $< 2.4e^-$/ s (0.4 aA) for the dark current. The spread in dark charge shown in the figure corresponds to an RMS noise of about 300 e^- for this data.

A grey scale image of dark current at 10K is shown in fig. 11. No true dark current could be detected in the central 95% of the array. Since the integration time was shorter, 167 sec., the upper limit on dark current is somewhat higher, $< 6e^-$/sec, here. There is considerable dark current in row 1 and, especially, column 62 at this temperature. Also noticeable is a glow in the lower right corner of the array, amounting to some 100's of e^- /sec. This is the region where the output amplifiers are located. We have eliminated this glow recently by reducing VGGUC and VDD.

Read Noise

A read noise of $< 100e^-$ RMS is required for SIRTF, and, in fact, $< 10e^-$ RMS would be highly desirable. It is here that the present InSb arrays and MOSFET readout are lacking. We have been able to achieve a reproducable $200e^-$ RMS (corresponding to 63 μV at the InSb input) read noise in the lab and at the telescope, but efforts to reduce this further have not been succesful to date.

In what follows we will only discuss our results using the correlated triple sampling method which is appropriate for the source-follower amplifier per detector, direct readout (DRO) multiplexer which has been used for these tests. A measurement of signal begins by resetting the integration node to its starting value. The output voltage with the reset switch closed is called the reset or "R" level. We label this reset level R_1, corresponding to the first read cycle. Then the reset switch is opened and the integration begins. There is typically a small (few mV) jump in output voltage when the switch is opened; the new output voltage, at the beginning of the integration, is called the pedestal or "P_1" level. During the integration, the nodal capacitance, which is composed of the InSb diode capacitance plus the detector gate and MOSFET gate capacitances, is discharged by the photocurrent and dark current. At the end of integration, the output is read again. This level is called the signal or "S_2" level. Then the cycle is repeated. If succesive cycles are labelled 1, 2, 3 etc., then a good first approximation of the net signal due to photocurrent and dark current during the integration time is $S_2 - P_1$. This differential measurement eliminates DC offsets and the noise incurred when resetting the node (a minimum of $\sqrt{kTC}$). However, since the time between 1 and 2 can be very long, say 500 sec. for a deep SIRTF integration, this measurement is prone to $1/f$ drifts in the various circuit elements. We monitor this drift by also measuring the reset levels at the beginning and end of the integration. The quantity $(S_2 - P_1) - (R_2 - R_1) = (S_2 - R_2) - (P_1 - R_1)$ is formed, which should also eliminate the $1/f$ drift in the amplifier chain. This is called correlated-triple-sampling, though it probably should be called quadruple sampling. A factor of 2 increase in noise, compared to only sampling the signal levels, is accepted in order to remove the $1/f$ and resetting noises. Using this technique, we have found no increase in read noise going from 0.1 sec to 500 sec. integrations (with a constant pixel sampling time).

One source of $1/f$ drift which is not eliminated by this technique is variation in the DET SUB and VRSTUC supplies, which determine the bias across the detector after resetting. Drifts in these supplies will come through with full force. However, since all 58 × 62 detectors use the same DET SUB and VRSTUC supplies, this will result in an overall level shift of all the pixels on the array, rather than pixel to pixel noise. This probably explains the anomalous negative dark currents seen, as described previously. The negative 400 electron dark charge seen corresponds to a drift of 0.1 mV in the supplies during the 500 sec. integration. For SIRTF, the supplies should be made more stable than this.

We have compared our observed read noise to the theoretically expected read noise. We use the theory presented by Janesick *et al.* (1984), extended for correlated triple sampling. The theory takes as input the voltage noise spectrum of the MOSFET amplifiers. For our arrays we have measured a white noise floor of $76nV/\sqrt{(Hz)}$ and a $1/f$ noise of

$4\mu V/\sqrt{(Hz)}$ at 1 Hz at low temperatures $(6-10K)$. These were measured at the array output. The DC gain of the array MOSFETs is measured to be 0.8 at low temperatures. For optimal signal-to-noise ratio, a bandwith limiting RC filter of time constant $\tau = t/2$, where t is the "clamp-to-sample" time, is called for (Janesick *et al.* 1984). In our case t is the duration of the signal, reset, and pedestal levels. Thus for a 36 μsec/pixel read period, $t = 10.7\mu$sec is used (the extra 4 μsec are due to overhead). The voltage sampling function H(f) for an integration time T is given by:

$$H(f) = 2\frac{(1-\cos(2\pi ft))}{1+(2\pi f\tau)^2}2[1-\cos(2\pi fT)]$$

Because in all case T is at least 6000 times t (there being 1798 pixels to read out on each of the 2 outputs), the last term is a very rapidly oscillating function which averages to 2, giving effectively:

$$H(f) = 4\frac{1-\cos(2\pi ft)}{1+(2\pi f\tau)^2}$$

This function is multiplied by the square of the MOSFET voltage noise and integrated over all frequencies. The square root of this latter quantity gives the predicted RMS read noise at the array output. Dividing by the DC gain of 0.8 and the gain of the RC filter (0.86) gives the noise referred to the InSb input, δV. By operating our arrays at 350-400 mV of back bias, we reduce the nodal capacitance (dynamic) to $C' = 0.5$pF. The read noise in electrons will be:

$$\delta Q = C'\delta V \tag{5}$$

READ NOISES AT InSb INPUT

pixel time (μsec)	t (μsec)	f_{peak} (kHz)	RMS read noise Theory δV (μv)	Theory δQ (e^-)	Observed δV (μV)	Observed δQ (e^-)
36	10.7	33	46	146	79	250
$\geq$576	$\geq$171	≤ 2	12	38	63	200

The quantity f_{peak} is the frequency where the largest contribution to the read noise occurs. At fast pixel read times, i.e. 36μsec/pixel, the theoretical read noise is limited by the white noise floor near 33kHz. The observed read noise is somewhat less than a factor of 2 above this. At slow pixel read times, i.e. $\geq$ 576 μsec/pixel, The MOSFET $1/f$ noise results in a minimum read noise of $12\mu V$ RMS; however, the best observed read noise is about 5 times higher than this. We have not been able to determine the origin of this excess read noise. In the absence of a solution to this problem, we recommend employing lower capcitance pixels to reduce the read noise in electrons as given by equation (5).

Non-Linearity/Calibratibility

It is important that the output of the array be calibratible to achieve a high level of photometric accuracy. We anticipate observing using a wide range of integration times and signal levels and wish to calibrate these data based on measurements of objects of known brightness. Our system permits selection of a large number of different data taking modes: correlated double sampling ($S_2 - R_1$) and correlated triple sampling with pixel read times ranging from 18μsec/pixel to 1152μsec/pixel, operating under both high background ($\lambda > 3\mu m$) and low background ($\lambda < 2.5\mu m$) conditions.

The output of our array is inherently non-linear primarily because of the voltage dependent capacitance of the InSb diodes. The dynamic capactance of an abrupt-junction, low temperature InSb diode is given by

$$C'_{InSb} = \frac{dq}{dV} = \frac{C'_0}{\sqrt{1 + V/V_{bi}}} \tag{6}$$

where q is the stored charge, V is the back bias, $V_{bi} \approx 0.24$V is the built-in junction voltage. For our pixels (62μm square junctions, $2 \times 10^{14}/cm^3$ doping) we estimate the zero-bias dynamic capacitance $C'_0 = 0.41pF$. The total capacitance of the integrating node will be the sum of this plus the fixed capactance due to the MOSFET gate, detector gate, and In bump bonds. We estimate this at:

$$C'_{fixed} = C_{fixed} \simeq 0.23pF$$

The total dynamic capacitance will be

$$C'_{tot} = C'_{fixed} + C'_{InSb}$$

This dynamic capacitance immediately gives the noise in electrons from the measured voltage noise δV through equation (5).

For estimates of the QE, we need the effective <u>*static*</u> capacitance, defined through

$$q(v) = q_o + \int_o^v C'_{tot} dV \tag{7}$$

where q_o is the charge stored on the InSb junction at zero bias. Defining Q as the difference in charge:

$$Q \equiv q - q_o \tag{8}$$

and C as the effective static capacitance:

$$C \equiv \frac{1}{V} \int_o^v C'_{tot} dV \tag{9}$$

We recover the familiar:

$$Q = CV \tag{10}$$

Q versus back-bias V is plotted in figure 12. This shows the slight non- linearity expected. The total effective capacitance versus V is plotted in figure 13. The dynamic capacitance C' is given in figure 14 and compared to the static capacitance. At zero detector bias, the dynamic and effective static capacitance are equal. Figure 14 shows that read noise (equation (5)) can be reduced by employing a large back bias to reduce the dynamic capacitance. We typically employ 350-400 mV of back bias which reduces C' to 0.5 pF from its zero bias value of 0.64 pF.

We have had three observing runs, in June 1988, July 1988, and September 1988, where data was taken to calibrate the system non-linearity. In order to emphasize the deviations from linearity, we plot the signal divided by integration time (ITIME). According to the capacitance model above, we expected to see a constant value for this at short ITIME's, and a droop downward as the InSb diode becomes discharged, increasing its capacitance, at longer ITIME's. A sampling of the actual data is given in figure 15. We analyze the 62 pixels in row 52, which has about a factor of 2 variations in QE from one end to the other. In the plots, full scale is $\sim 10 - 20\%$ variation in signal/ITIME.

From these graphs, an anomalous increase of a few percent in signal/ITIME is seen for the first few ITIME's in many of the time series. (ITIME = 60 for a one second integration). This has happened at pixel read times ranging from 18 μsec (2 Rate, 2/60 sec. to read out the array) to 288 μsec (32 rate, 32/60 sec to read out the array), using both correlated double and triple sampling. Apparently, the array takes a little (integration) time to get up to speed. We are currently studying this effect further, but have no bright ideas yet. This effect could introduce a few percent uncertainty in calibrated fluxes.

At longer ITIME's, the plots show the droop expected, from capacitance increase. In order to be able to use a large number of pixels, each with different signal levels, to generate a non-linearity calibration curve, we form the logaritmic derivative:

$$\frac{dlog(signal)}{dlog(ITIME)} = \frac{dlogS}{dlogt} \tag{11}$$

and plot it versus signal S. A signal of 16,500 counts here corresponds to capacitance discharge of $10^6 e^-$. The logarithmic derivative has the property of being 1 if the output is exactly linear. It basically gives the slope on a log-log plot of S *vs* t. Figure 16 gives a typical result. Values near 1 are seen at low signals and a drop down to 0.8 is seen near 16,500 counts of signal. The data has been fit with a quadratic function:

$$\frac{dlogt}{dlogS} = 1 + 0.08(\frac{S}{10^4})^2 \tag{12}$$

which is also shown in the plot. Equation (12) can be immediately integrated to give a "linearized" signal Q which is proportional to the charge accummulated:

$$Q = Se^{0.04(S/10^4)^2} \tag{13}$$

This is plotted in figure 17. About 10% droop in S/Q occurs at 16,500 counts ($\sim 10^6 e^-$).

The capacitance model described above has been compared to this data. We estimate the initial detector back bias is $\simeq$400 mV when we have applied 300 mV of back-bias

through the CRC 228 readout (the source of this offset is not understood at this time). Using this value, the expected logarithmic derivative and linearization factor S/Q are given in figure 18, compared to the data and the numerical fit. Only fair agreement is seen. Some of the effects which could contribrute to such a discrepancy are:

a. Back-bias really lower than the 400 mV assumed.

b. The fixed capacitance is lower than the 0.23 pF assumed

c. The gain of the signal chain is off by several percent.

In addition, a non-abrupt InSb junction may exhibit different non-linearity characteristics.

We estimate that the uncertainty in fluxes introduced by our incomplete knowledge of the hybrid array and associated electronics is a few percent. Flat-fielding, described below, is potentially more limiting.

Flat Fielding

The images obtained when observing a uniformly bright screen (figs 1 & 3) show large variations. There are prominent "tree rings" as well as an overall gradient from left to right. In order to calibrate these effects out of our images, we obtain images of candidate flat fields, which we will (after linearization) divide into our astronomical images. In addition, we desire the flat fields to represent as nearly as possible the same optical illumination of the array as the astronomical images. In the past, we have used the moon as a candidate flat field. With the current array, the moon is too bright at most wavelengths. Therefore, the 1.25-2.5μm region we have taken images of the evening or morning blue sky and the inside of the dome illuminated by 5000 W of incandescent lamps. For the thermal infrared ($\lambda > 2.5\mu m$), we image the inside of the dome and subtract the image of blank sky. The last step eliminates the thermal emission from the mirrors, etc., which does not represent the same optical illumination of the array as our astronomical images.

In order to test our candidate flat fields for photometric accuracy, we have imaged two calibration stars at 25 different positions on the array. Figure 19 summarizes the photometric results at $2.23\mu m$. With no flat field correction, there is a large standard deviation of 21% of the mean, due primarily to the gradient in QE. Using a flat field composed of comparable parts of dome plus blue sky (they were very similar in appearance) improves the standard deviation to 4.5%. With this data, a systematic pattern can be seen. A minimum in counts is seen near the center of the array (x's) and a maximum is seen near the peripheries (+'s). We attribute this to the effects of plate scale distortion caused by our re-imaging optics. These optics give a small amount of pincushion distortion. This means the arcsec/pixel plate scale is *smaller* near the peripheries than on the optic axis. This *reduces* the signal from the flat field near the peripheries. However, the signal from the star is not reduced because a large aperture ($\sim$ 9 pixel square box) is used to include all the star's signal. Therefore the flat field for stellar photometry differs from a flat field appropriate for extended emission (such as the dome and blue sky). In order to account for this distortion effect in stellar photometry, the flat field was divided by an optics correction

factor f:

$$f = 1 - \epsilon\rho_{41}^2 \tag{12}$$

This being the simplest function of the nature suggested by the optics distortion. ρ_{41} is the distance from the optic axis at row R_o, column C_o normalized to a distance of 41 pixels (i.e. the corner of the array). ϵ is the magnitude of flat field correction. By varying the three parameters ϵ, R_o, and C_o a minimum of 2.6% in the standard deviation of the stellar signals was achieved. The optic axis was found to be at row 42 ± 4, column 26 ± 5 which is believable. This is displaced 14 pixels or 1.06mm from the array center. The magnitude ϵ was 0.10, i.e., a 10% effect 41 pixels away from the optic axis (the array corner). Ray tracing of the optics gives a plate scale distortion resulting in a flat-field correction function nearly identical to equation (12), but with a 10% smaller ϵ. This supports the interpretation offered above.

We estimate a net uncertainty in stellar photometry of about 3.5% due to flat fielding and linearization uncertainities. For typical ground based observing, a net accuracy of 5-10% should be achievable.

For SIRTF, more study (or better-behaved detector and optics) would be necessary to surpass 3.5% photometric accuracy.

References

Fowler, A. M., Probst, R. G., Britt, J. P. Joyce, R. R., and Gillett, F. C., 1987 "Evaluation of an Indium Antiminide Hybrid Focal Plane Array for Ground- Based Astronomy", Opt. Eng. **26**, #3, p. 232 (March 1987)

Orias, G., Hoffman, A. W. and Gasselman, M. F., 1986, "58 × 62 InSb Focal Plane Array for Infrared Astronomy" Proc. S.P.I.E, **627**, p. 608 (March 1986)

Ninkov, Z., Forrest, W. J., and Pipher, J. L., 1987, "Testing of a 58× 62 InSb Engineering Array" in Infrared Astronomy with Arrays ed. C. G. Wynn-Williams and E. E. Becklin (U. Hawaii, Institute for Astronomy, Honolulu, Hawaii)

Janesick, J. R., Elliott, T., Collins, S., Marsh, H., Blouke, M., and Freeman, J., 1984, "The Future Scientific CCD", S.P.I.E. Proc. Vol. 501, p.2.

Sze, S. M. 1981 "Physics of Semiconductor Devices, 2nd Ed." (John Wiley & Sons, NY).

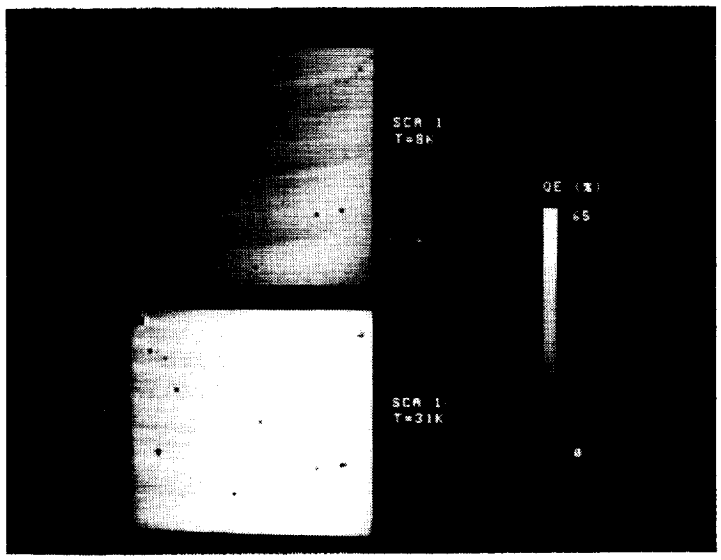

Fig. 1 - Gray Scale representation of Quantum efficiency measurement of SCA 01 at 31 K and 8 K.

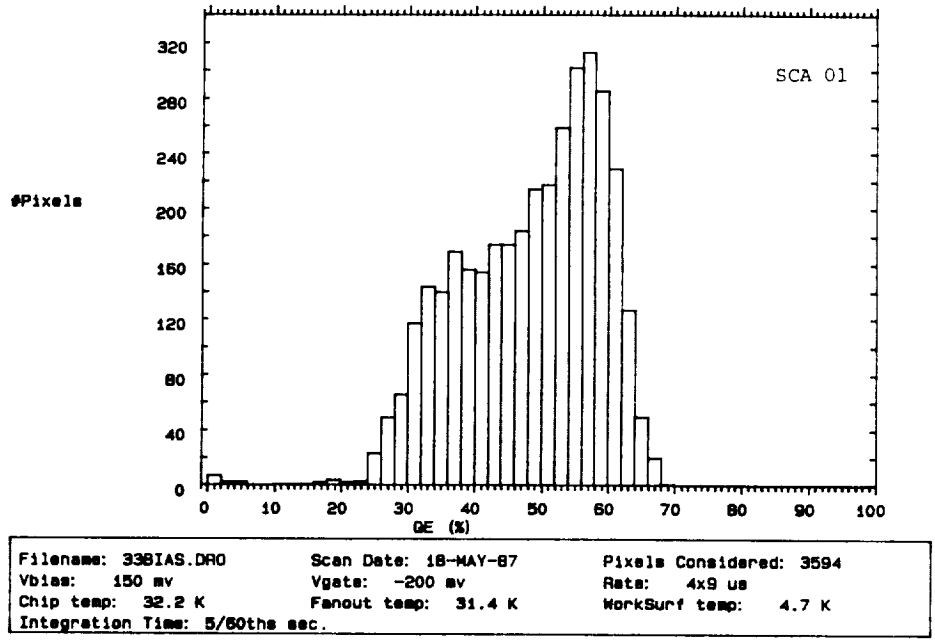

Fig. 2a - Histogram of Quantum Efficiency measurements at 31 K. Assumed zero-bias capacitance was 0.63 pF. Illumination through narrowband 3.3 micron filter; room irradiance.

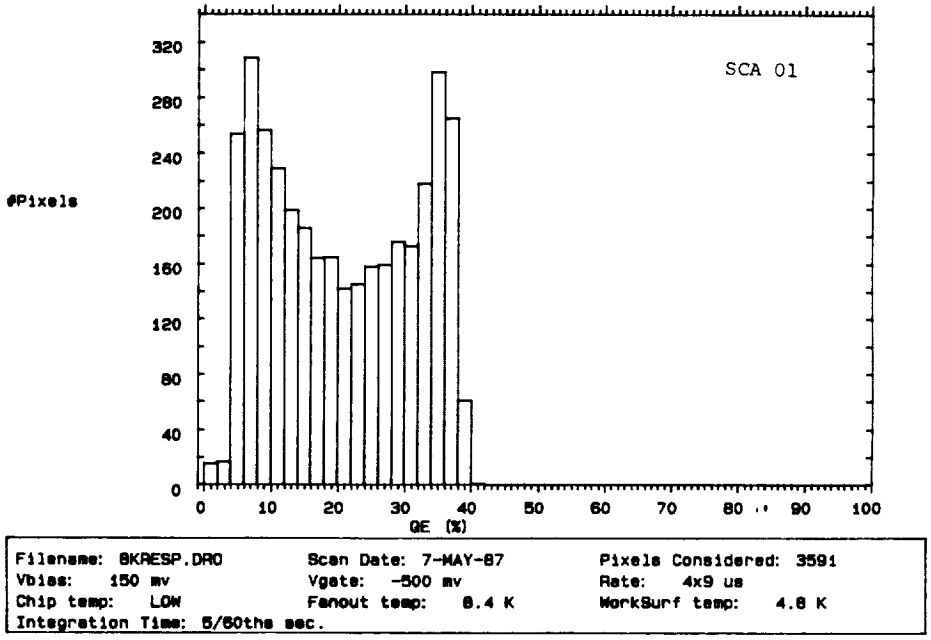

Fig. 2b - Histogram of Quantum Efficiency measurements at 8 K. Other conditions as above.; assumed zero-bias capacitance was 0.55 pF.

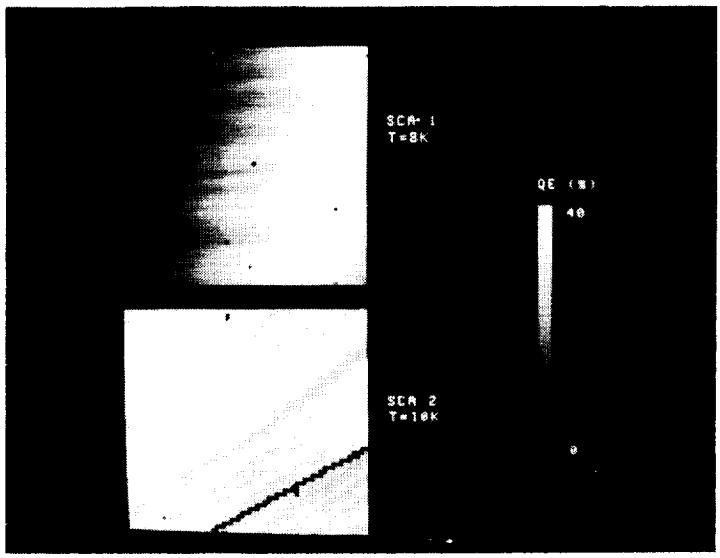

Fig. 3. Gray scale comparison of quantum efficiences of SCA 01 and SCA 02.

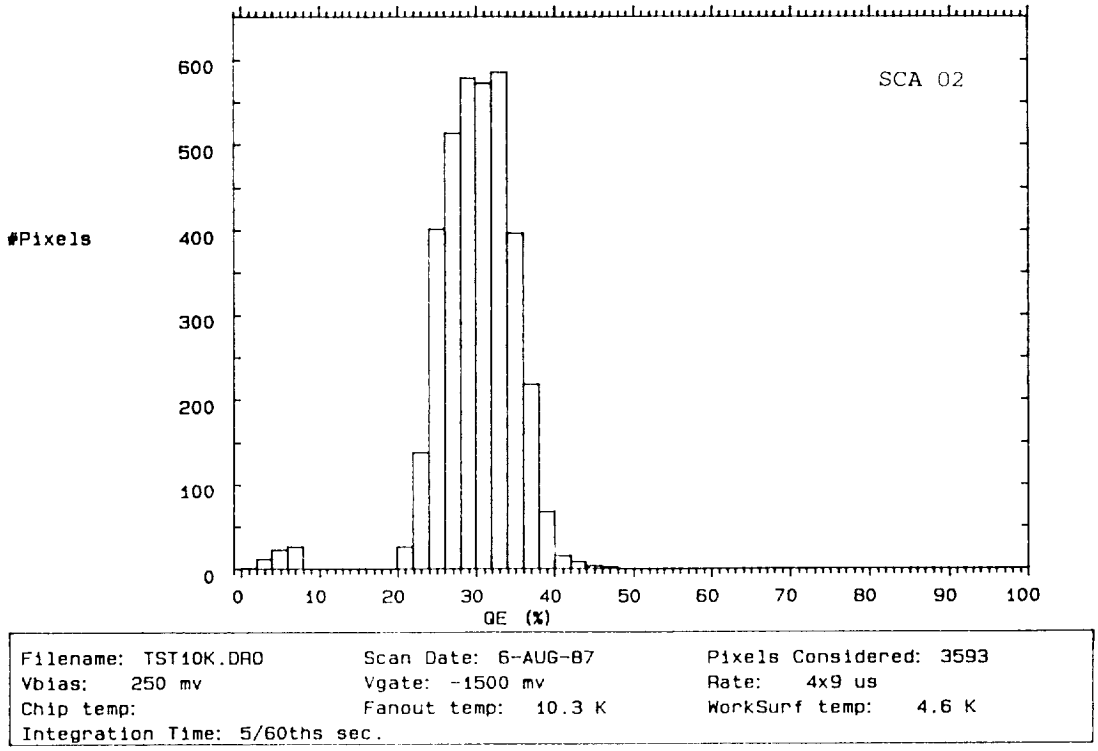

Fig. 4. - Quantum efficiency of SCA 02 at 10 K and 3.3μm.

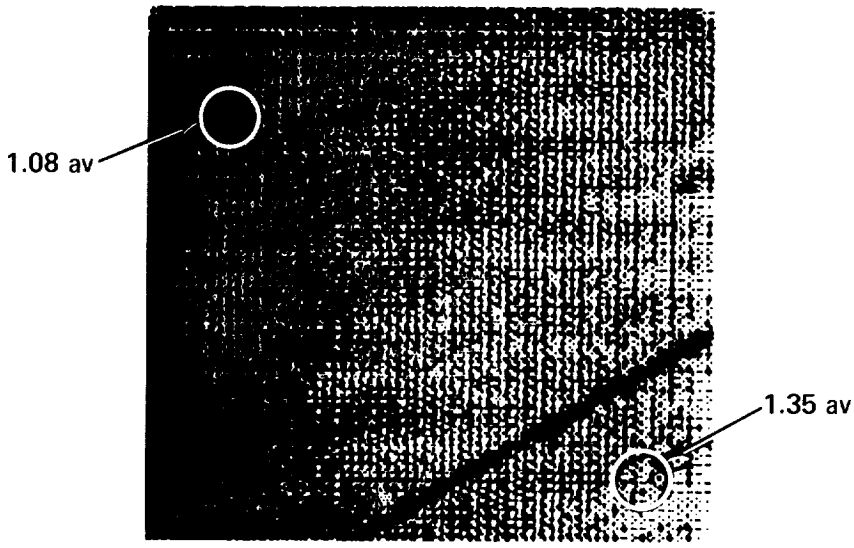

Figure 5. Flat fields for SCA 02 at 3.3 microns. 10 K flat field divided by 7 K flat field showing loss of QE in the lower right corner as the temperature of the InSb is decreased. The QE ratio 10K/8K ranges from 1.35 in the lower right corner to 1.08 in the upper left corner. The dark diagonal line in the lower right is due to approximately 40 permanently dead pixels. They have extremely high dark currents.

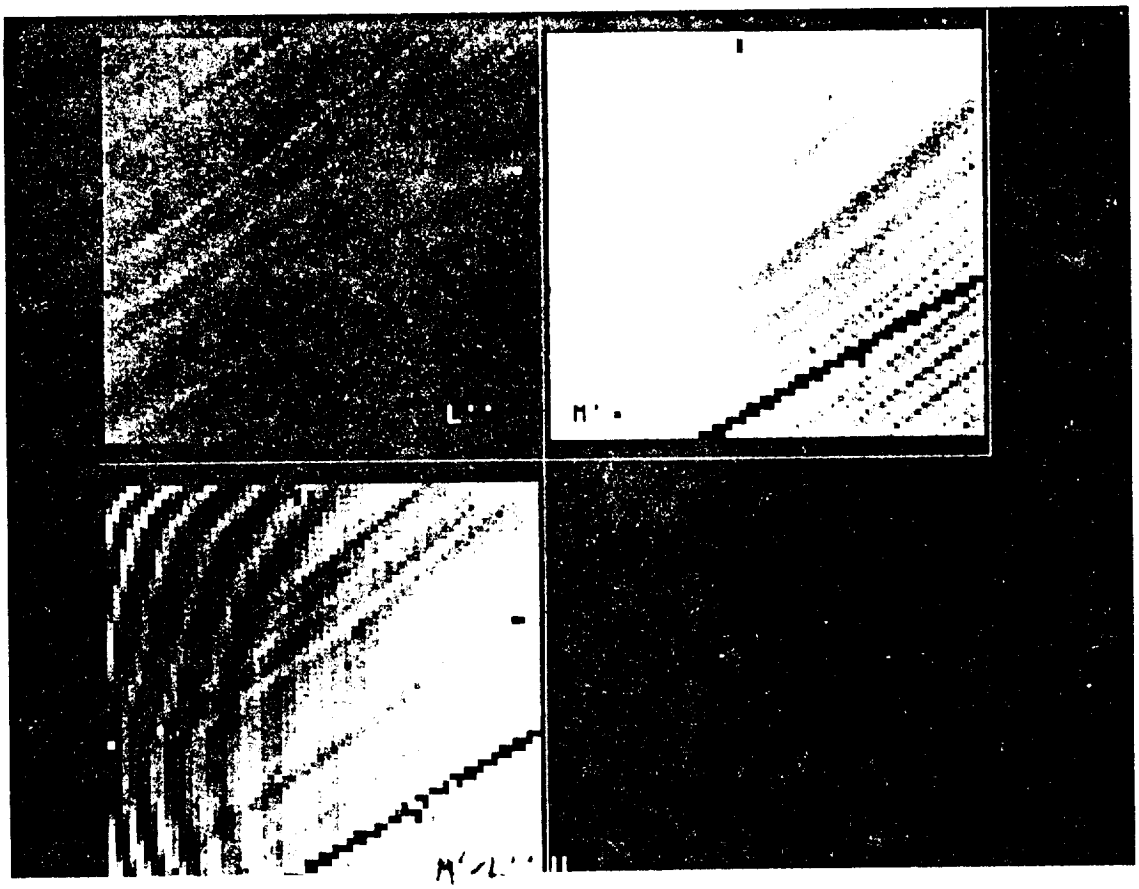

Figure 6. Flat fields for SCA 02. Upper left is at 3.75 μm (L'') through a 22% resolution filter and upper right is through a 4.67 μm (M'), 4% resolution filter. The M' image shows the interference fringes, primarily because of the greater penetration of 4.67 μm photons into InSb. In the lower left, the M'/L'' ratio image shows the interference fringes more clearly. Each fringe corresponds to a change in thickness of 0.6 μm, as described for figure 5a. The greater number of fringes for SCA 02 compared to FPA 72 indicates a greater thickness variation, especially on the left hand side. The more distinct fringes on the left are believed to be from the thinner side. This side also exhibits higher quantum efficiency at these low temperatures, as shown in the upper two images.

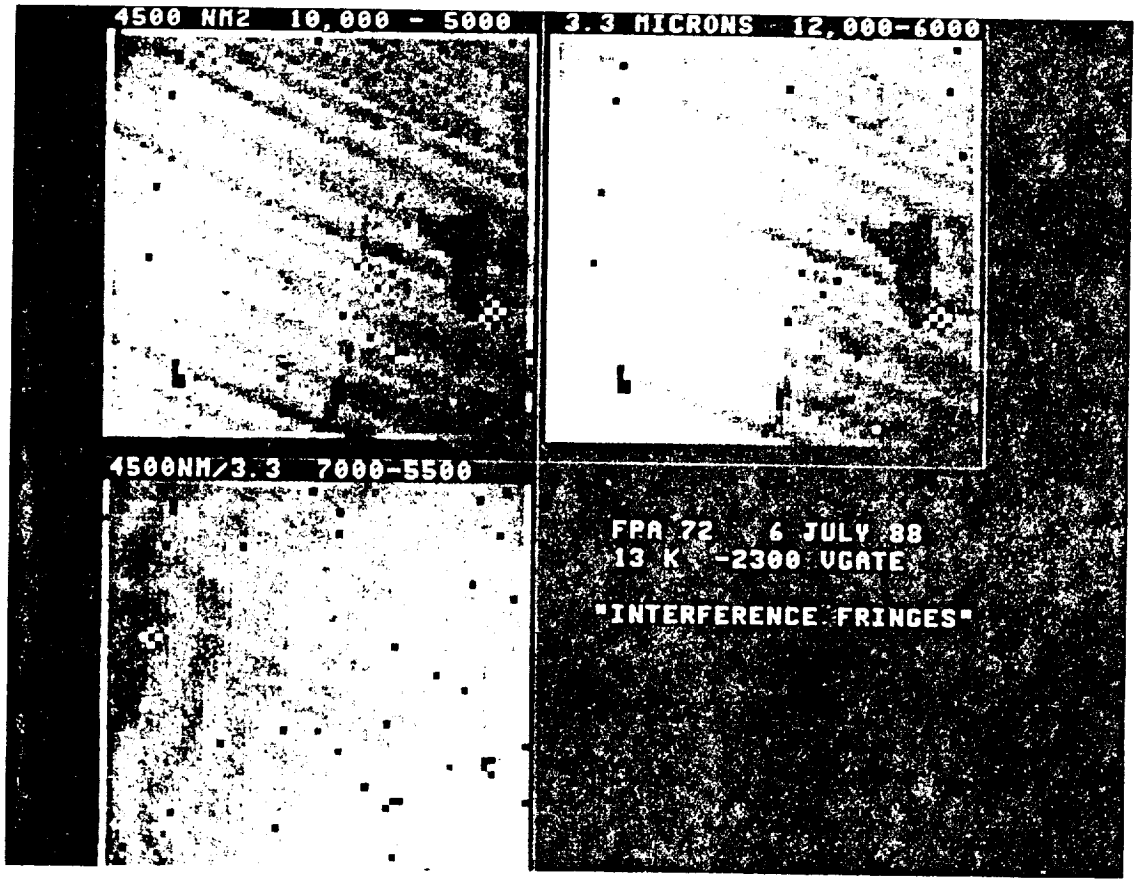

Figure 7. Flat fields for FPA 72. Upper left is at 4.5 microns through a 1% resolution CVF. Upper right is at 3.26 microns through a 7% resolution interference filter. Lower right is the ratio of the 4.5 to 3.26 micron flat fields. We interpret the alternating dark and bright wavy lines as interference fringes in the 4.5 micron radiation. A bright peak is seen whenever the detector thickness equals $m\lambda/2n$, where m is the order, λ is the wavelength, and n=3.8 is the index of refraction of InSb. Adjacent bright lines differ by 1 in m.

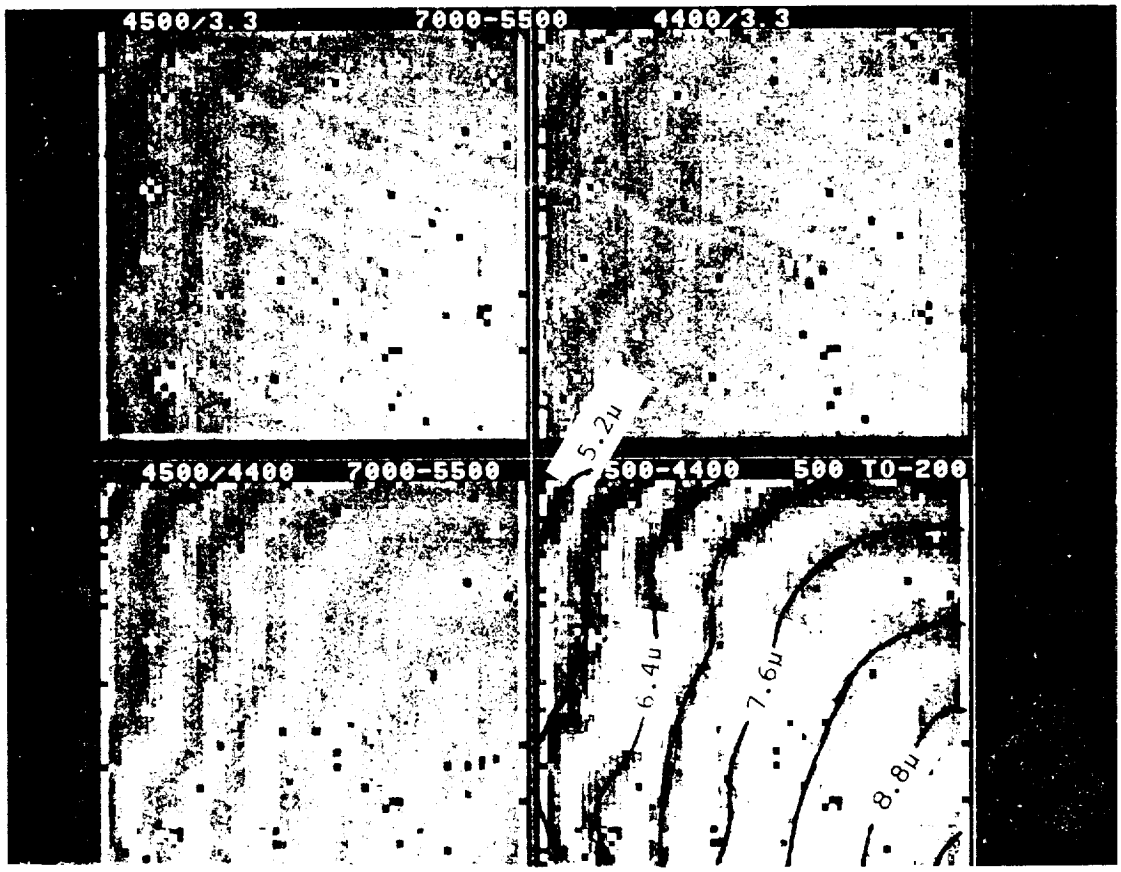

Figure 8 Flat fields for FPA 72. The 4.5μm/3.3μm (upper left) and 4.4μm/3.3μm (upper right) show the interference fringes described for Figure 5a. Note that the fringes are shifted a bit to the right at the longer wavelength, showing that the thickness is increasing in that direction. The lower two images are 4.5μm/4.4μm and 4.5μm - 4.4μm images, which show the fringes more clearly. The detector thickness for selected fringes is indicated on the lower right image.

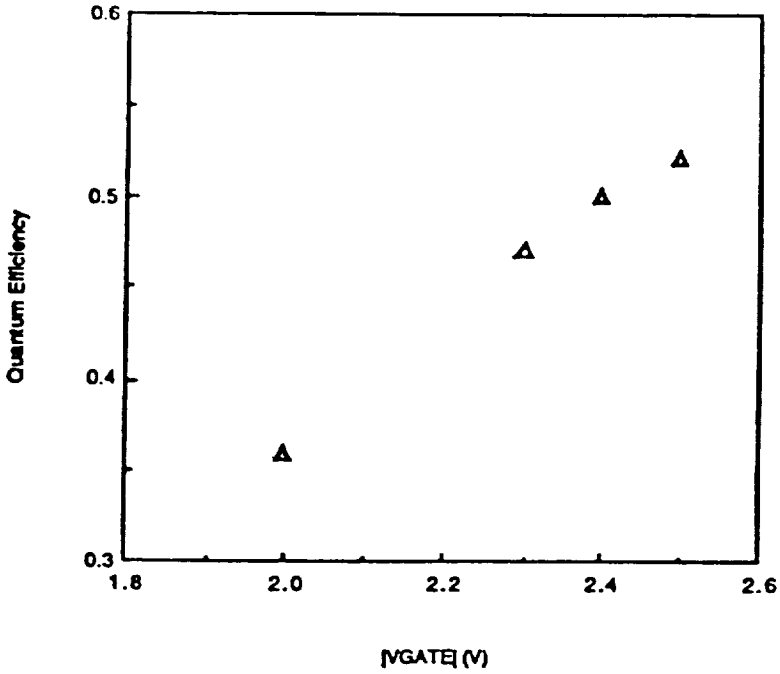

Fig. 9 The effect of gate voltage on average 3.3 μm quantum efficiency. These data were taken on device FPA 72, which was antireflection coated. The temperatures were 9 and 10 K.

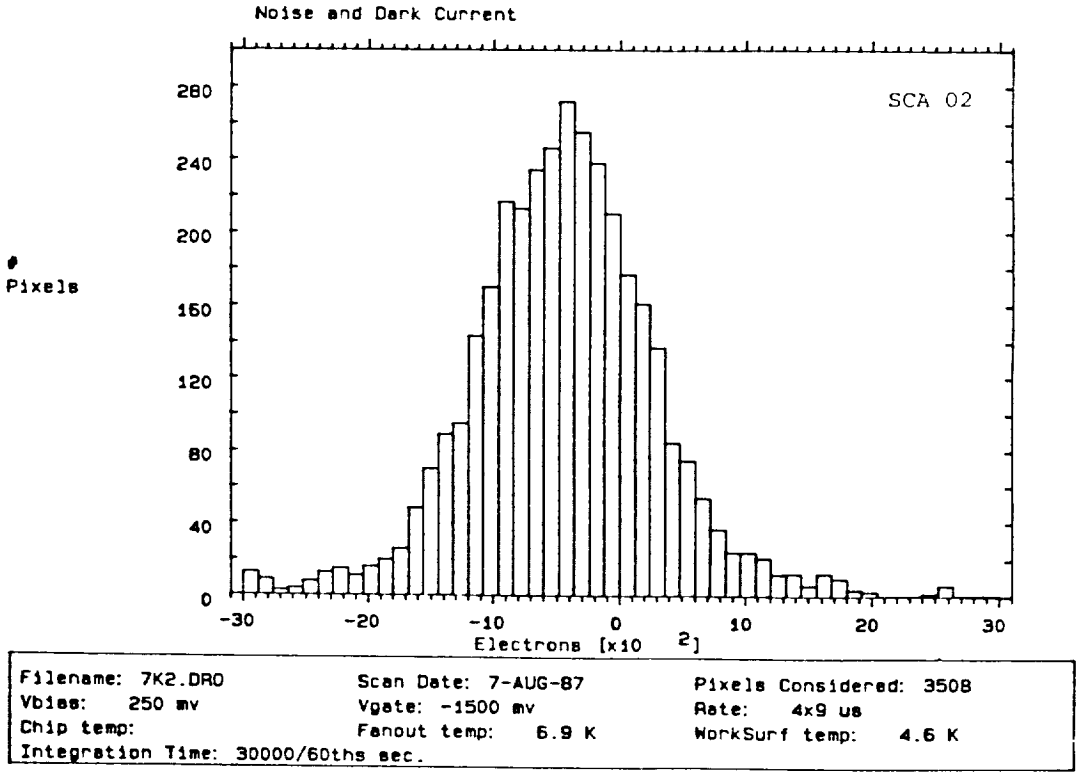

Fig. 10 - Dark charge in SCA 02 after 500 sec. The spread in the measurements corresponds to approximately 300e- RMS noise.

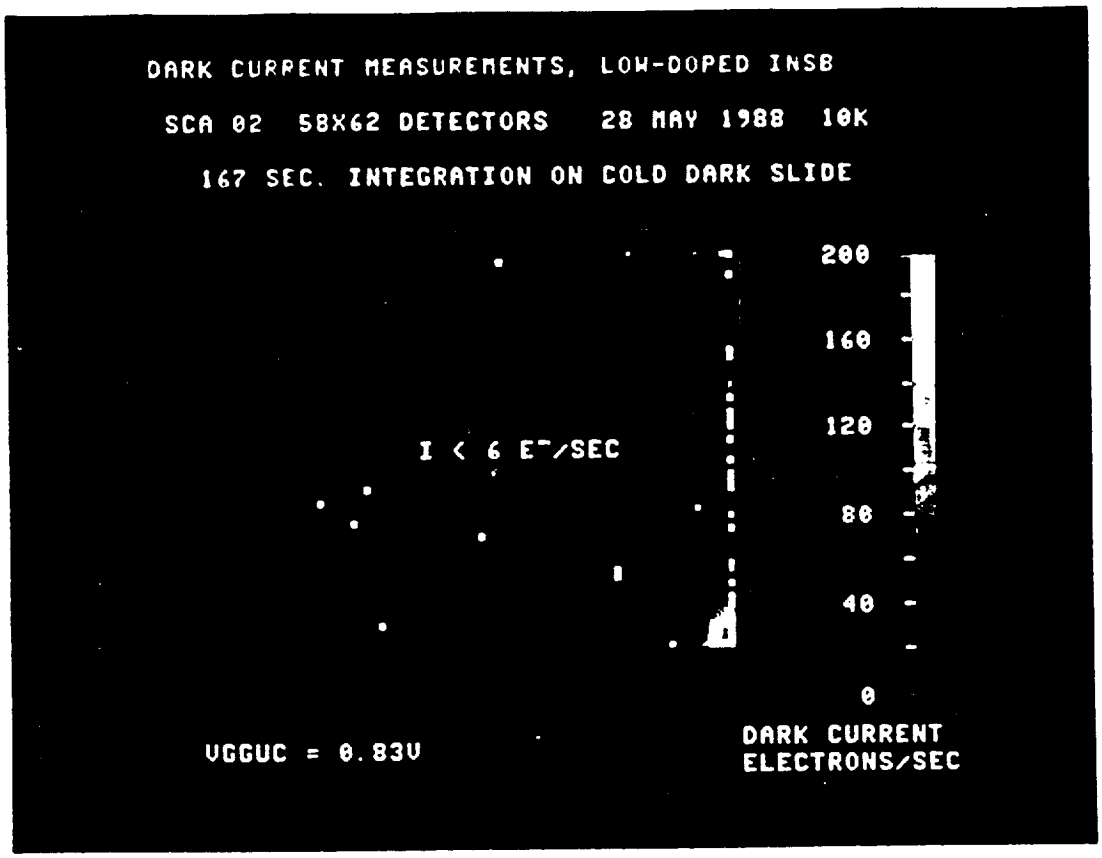

Fig. 11. Dark current in SCA 02 at 10 K. Only an upper limit of less than 6 e-/sec could be established in the central 95% of the array. The glow in the lower right corner may be an LED effect from the output amplifiers, which are located in this vicinity.

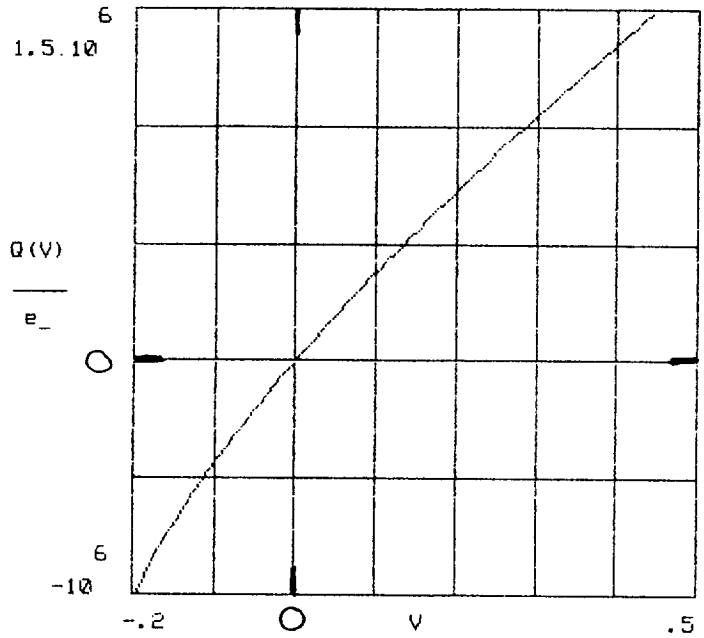

Figure 12. Effective charge stored Q vs. actual detector back-bias V. This plot is a little more linear than the earlier version. Also note the availability of negative back-bias to increase dynamic range.

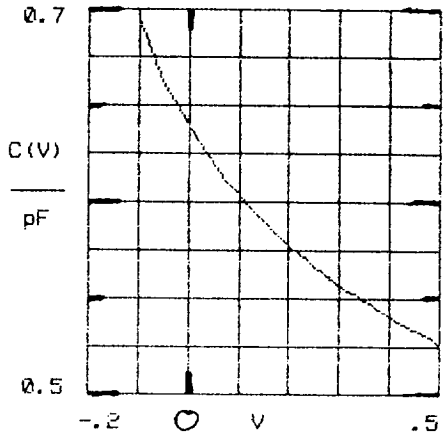

Figure 13. Effective capacitance C vs. detector back bias V. Since Q = CV, this shows the non-linearity more clearly.

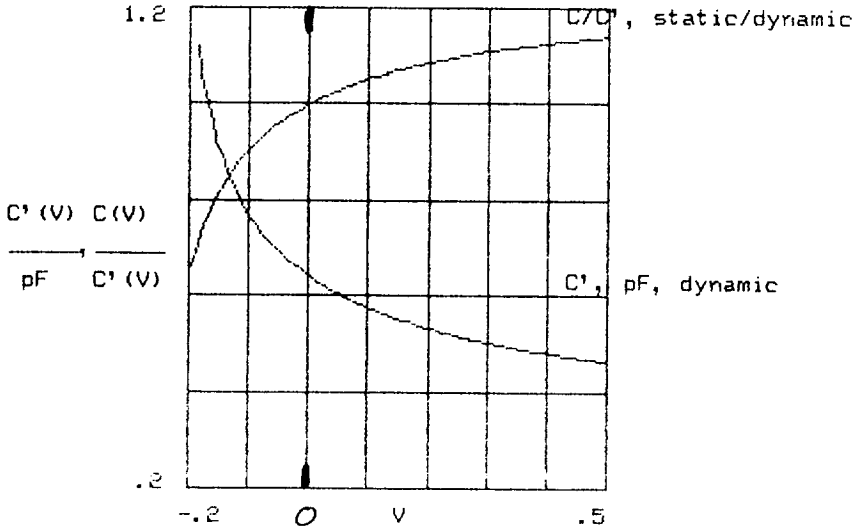

Figure 14. Dynamic capacitance C' vs. back-bias V. Since $\delta Q = \delta V(dQ/dV) = \delta V * C'$, this capacitance determines the electron read noise. Also included is a comparison the static capacitance C to C'.

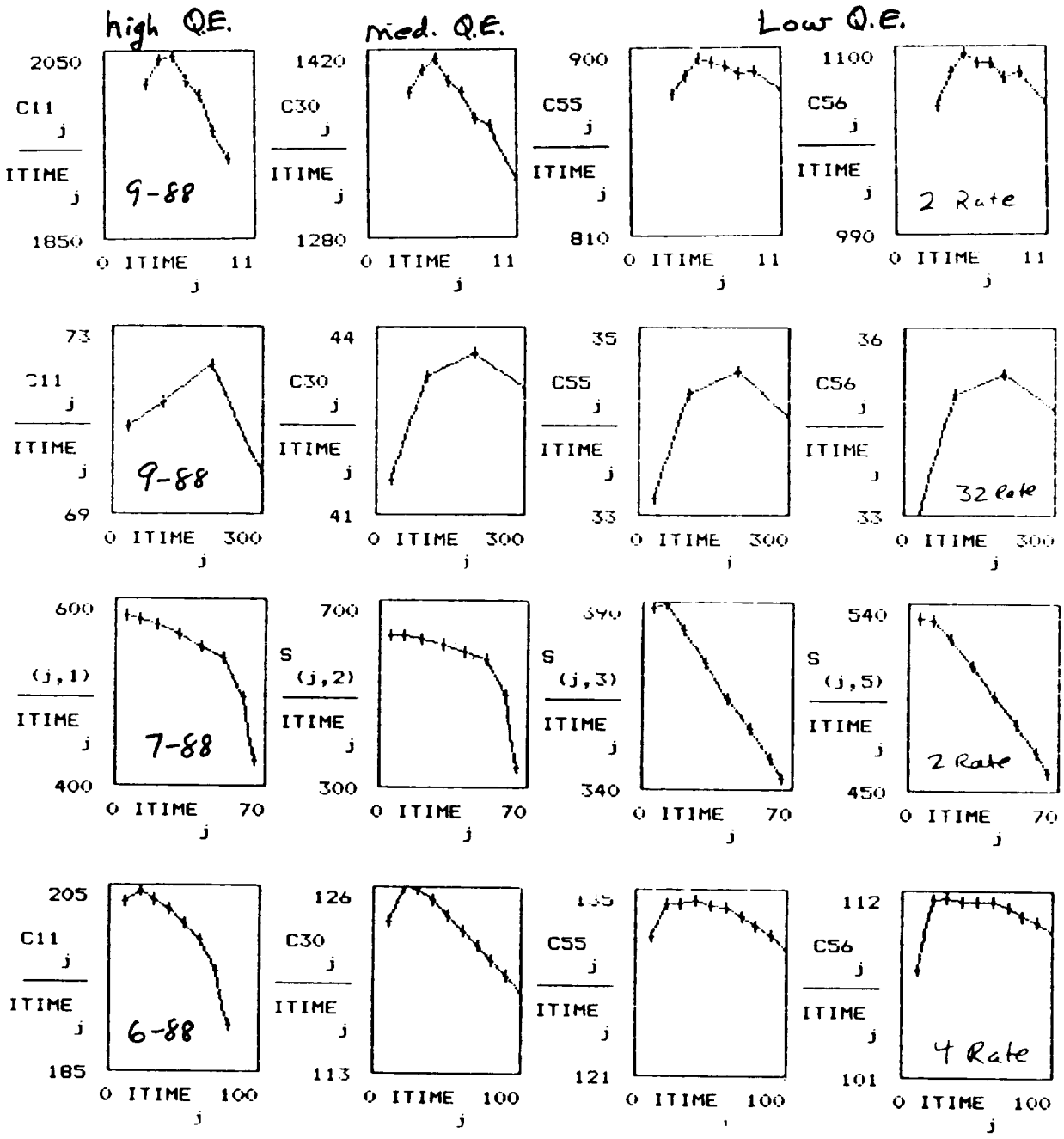

Fig. 15. Signal divided by integration time (ITIME) versus ITIME for pixels 11, 30, 55, and 56 in row 52 of InSb array SCA 02. In all cases, the detector viewed a constant brightness flat field. Data from June, July and September 1988. Detector temperature 10 to 12 K. Pixel read times from 18 μsec (2 Rate) to 288 μsec (32 Rate). The leftmost column is the highest QE pixel and the rightmost column is the lowest QE pixel. The anomalous rise often seen at short ITIMEs is not understood. The droop at longer ITIMEs is analyzed in figs. 16 and 18.

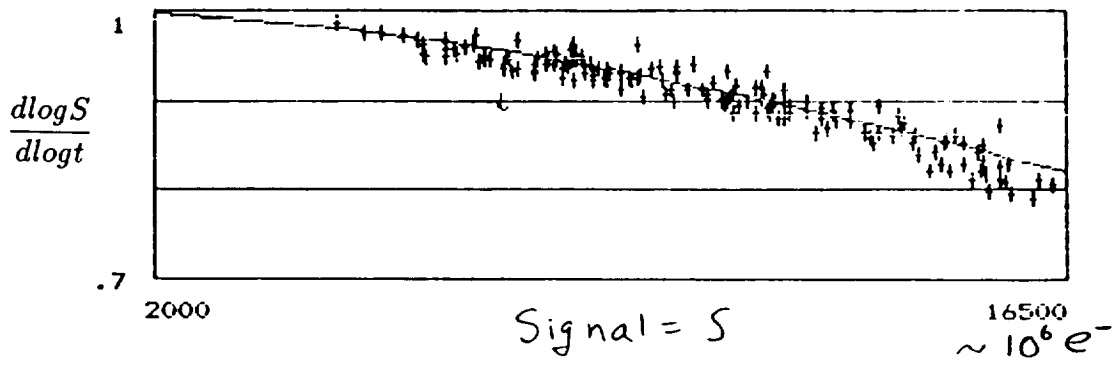

Fig. 16. Logarithmic derivative (see text) versus signal data (crosses) for SCA 02, row 52 pixels. Representative raw data is shown in the first row of fig. 15. The line is a quadratic fit to the data.

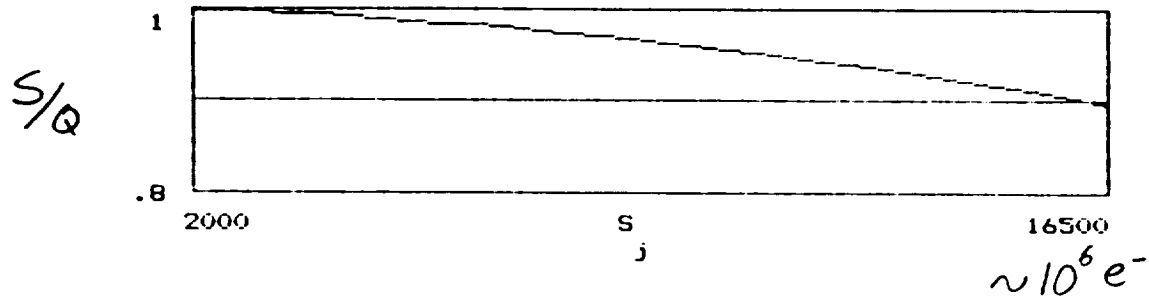

Fig. 17. Linearization factor S/Q versus signal S from the fit to the logarithmic derivative shown in fig. 16 (see text).

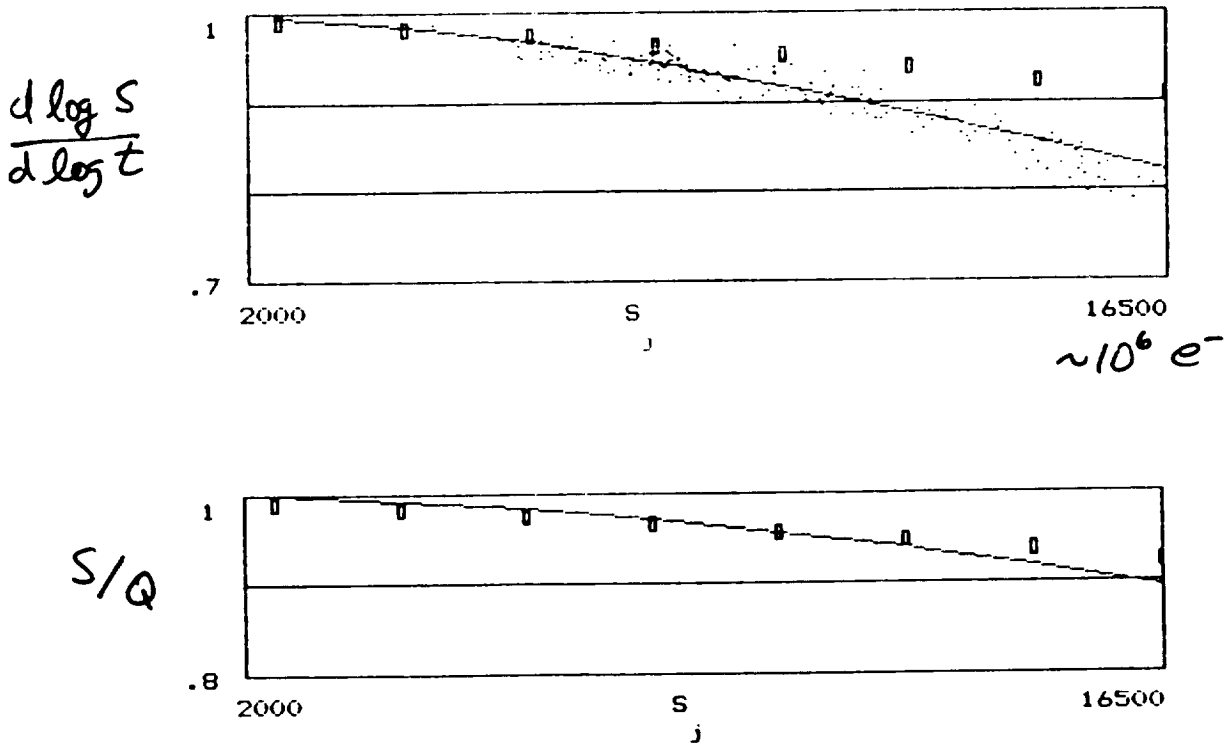

Fig. 18. Capacitance model (boxes) compared to the data (points) and empirical fit (lines) from figs. 16 and 17 (see text).

÷ const.

Key:
X's = low < –4%
+'s = high > +4%
boxes = ave ±4%

σ = 21%

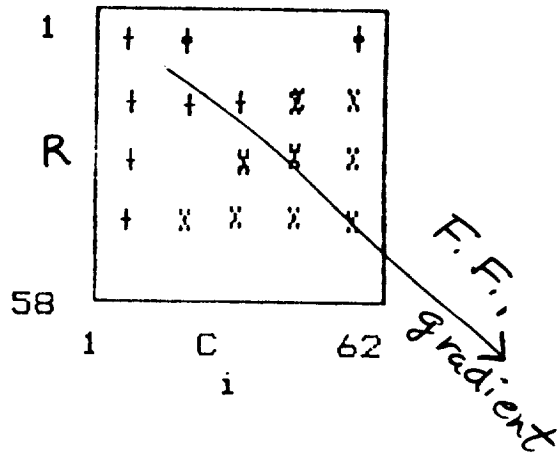

÷ (blue sky + dome)

σ = 4.5%

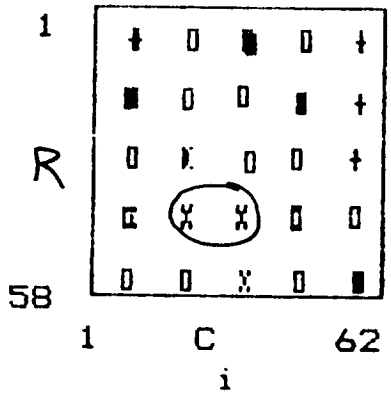

Optics correction (p.s. distortion)
$f = 1 - \epsilon\rho^2$
$\epsilon = \frac{0.1}{41^2}$
Ctr @ Row 42 Col 26

σ = 2.6%

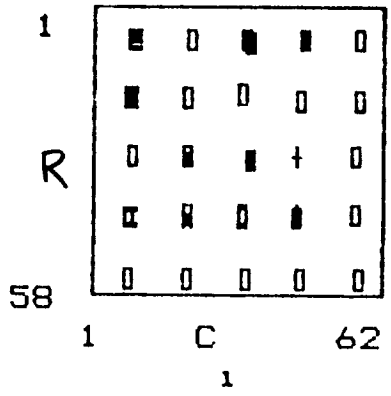

Fig. 19. Tests of photometric accuracy using the infrared standard star HD 40335 in Sept. 1988 at the IRTF. The star was imaged twice at each of 25 positions on the array. The images were divided by a candidate flat field and the signal in a 9 pixel (3.8") octagon was summed to give the total signal. The signal at each position is compared to the average for all positions with the key as shown in the figure. The top figure is with no flat field correction. The standard deviation was 21% of the average. The middle figure used the blue sky and dome as a flat field, improving the standard deviation to 4.5%. The bottom figure includes the optics correction (see text) with further improvement to 2.6% standard deviation.

N90-21327

Experience with the UKIRT InSb Array Camera

Ian S. McLean Mark M. Casali Gillian S. Wright Colin Aspin

Joint Astronomy Centre, 665 Komohana Street, Hilo, Hawaii 96720

Abstract

The cryogenic infrared camera, IRCAM, has been operating routinely on the 3.8 m UK Infrared Tele scope on Mauna Kea, Hawaii for over two years. The camera, which uses a 62×58 element Indium Antimonide array from Santa Barbara Research Center, was designed and built at the Royal Observatory, Edinburgh which operates UKIRT on behalf of the UK Science and Engineering Research Council. Over the past two years at least 60% of the available time on UKIRT has been allocated for IRCAM observations. In this paper we describe some of the properties of this instrument and its detector which influence astronomical performance, discuss observational techniques and illustrate the power of IR arrays with some recent astronomical results.

1 INTRODUCTION

A near infrared imaging system called IRCAM has been in use at the 3.8 m United Kingdom Infrared Telescope since September 1986, and a second camera was introduced toward the end of 1988. Both of these cryogenic imaging systems are "facility" or "common-user" instruments. In competitive scientific proposals, IRCAM has been requested as the instrument of choice for 60–70% of the total telescope time, and is virtually always available as a backup for other instruments. Both cameras use the 62×58 pixel Indium Antimonide (InSb) Direct Readout (DRO) array manufactured by Santa Barbara Research Center (SBRC). In an evolutionary process, several different detectors have been used and evaluated over the past two years in a wide range of ground-based astronomical applications, and a considerable amount of observational experience has been gained.

Naturally, the advent of near infrared imaging systems has led to what might be termed an explosion in *infrared picture-taking*! The ease with which seeing-limited images of a wide range of objects — often invisible at optical wavelengths — could be obtained, especially in non-photometric weather conditions, has led to a huge increase in morphological studies, infrared surveys and studies in which much new insight is gained even if no attempt is made to calibrate the observed brightness levels with high accuracy. Gradually, that situation has been changing to include precise astronomical photometry as more experience is gained on how to calibrate infrared array data. In fact, it is remarkable how quickly infrared arrays have been put to use as precise photometric tools. Undoubtedly, experience carried over from work with optical CCDs has helped considerably.

In this paper we describe some of the properties of the 62×58 InSb detector which influence astronomical performance, describe our observational techniques and illustrate the progress in ground-based IR astronomy with recent results from UKIRT.

2 THE CAMERA SYSTEM

Various aspects of the design and the performance of IRCAM are described in detail elsewhere [1,2,3] so only a summary of major characteristics are given here.

Optically, IRCAM employs un-cooled gold-coated mirrors to collimate the f/36 beam (at 1.53″/mm) from the telescope before it passes through the calcium fluoride window of a vacuum chamber within which is housed the cryogenic camera assembly; the low temperatures are achieved by attaching the vacuum chamber to a large Oxford Instruments LHe/LN_2 dewar. Four liters of liquid helium provide a hold-time of well over two days. (More recently, lab tests with a closed-cycle cooler have demonstrated that this approach is also viable.) Optical re-imaging is performed by one of three cold (77 K) lenses of AR-coated zinc selenide, selected prior to cool-down, which transfer the telescope focal plane image onto the detector array at approximately f/7.2, f/3.6 or f/1.8. Filters are placed in the collimated beam near the position of the Lyot-stop (an image of the entrance pupil). The instrument is a side-looking construction fed by a 45-degree inclined dichroic mirror near the UKIRT f/36 focus, and is one of a cluster of four semi-permanently mounted instruments.

Drive electronics (clock drivers, bias supplies and signal processing circuits), a temperature controller and a two-channel 15 bit A/D unit are located alongside the dewar; clock and bias/signal lines are separated. There is an internal preamp with a gain of 5. A hardware sequencer/computer interface employing Programmable Logic Arrays is located nearby on the mirror cell. The sequencer and an array timing logic unit (supplied by SBRC) are controlled by an LSI 11/23+ microprocessor running DEC MicroPower Pascal software. Also on the mirror cell is a motor-control unit with an IEEE 488 bus to drive the three 5-phase stepper motors used in IRCAM. Digital data from the A/D unit is transferred by a parallel link to a remote LSI 11/73 which acts as a buffer computer capable of "coadding" many frames or exposures before transferring the final image to the UKIRT MicroVax II.

At present, three image scales are available with IRCAM 1 and 2 namely, 0.63, 1.25 and 2.4″/pixel, giving fields-of-view of 39×36.5″, 77.5×72.5″ and about 135″ diameter; the wide field mode is limited by the size of the collimator mirror and the desire to minimise its tilt angle. IRCAM 2 contains a 10% oversized cold-stop, whereas IRCAM 1 is fitted with a special slightly undersized Lyot-stop mask. A choice of broad and narrow bandpass filters are contained in IRCAM's two 10-position filter wheels. In addition to the standard JHKL filters there are 1% bandwidth filters for the Brackett alpha and Brackett gamma lines of hydrogen, the v=1-0 S(1) transition of molecular hydrogen, CO bands at 2.30 μm, ice band at 3.08 μm and the emission feature at 3.28 μm associated with very small grains. Also available is a filter for the 1.644 μm [FeII] line and several regions of continuum.

Other instrumentation can also be used with IRCAM. For example, a piezoelectrically scanned Fabry-Perot etalon, manufactured by Queensgate Instruments, can be placed in the collimated beam immediately outside the dewar window to give an imaging mode with spectral resolving powers in excess of 3500. There is also an infrared polarimeter option (IRPOL) employing a rotatable halfwave plate above the UKIRT dichroic mirror and cold polarizers internal to IRCAM. Recently a slitless "grism" mode providing about 1% spectral resolution across the K-band has been installed, and in addition, a coronagraph mode — developed in collaboration with Ben Zuckerman at UCLA — has been used successfully.

IRCAM is a highly-automated, computer-driven instrument with a very extensive suite of software. Control is from a console/workstation in the UKIRT Control Room either by use of a simple menu or by typing a few keywords which represent command procedures; each procedure prompts the user for required input. For example,

OBS(erve) will request all parameters necessary to set up an observation and store the data;

GO will initiate a simple STARE or CHOP observation;

GODARK will obtain a dark/bias pair and return to the original setup;

GOJHK will carry out a sequence of observations in each passband;

SHOW will enable the resulting image to be displayed;

MAG will return zeropoints/magnitudes of a star;

FINISH will terminate the observing session.

All high-level software is written in FORTRAN, and a great deal of image processing power is available on-line. Instrument status is shown on a monitor at all times and images can be displayed immediately on a high resolution color image display screen with hardcopy facilities. Complex data reduction, such as median filtering of sky flat-fields, piecing together mosaics or deriving polarization parameters, can be carried out while integrations are in progress. There are on-line "magnitude" programs using mean zeropoints, and there are many "procedures" which can be called to execute a repetitive or tedious sequence, including control of the telescope for mapping. Sky conditions (mean signal level per coadd and noise) can be monitored with selectable pixels on the array and displayed on the status monitor. At the end of the night the data stored on the summit disk are also transferred to the sea-level facility, linearised and two copies backed-up onto magnetic tape. Tapes are provided in FITS format or in Vax backup format.

Despite the complexity of the instrument, visitors need only learn a few commands to take data and assess its quality. In addition, more sophisticated image processing software in Hilo allows the user to leave with publication quality hardcopy from either the Seiko D-Scan colour paper unit or the Matrix instruments colour film unit.

3 DETECTOR CHARACTERISTICS AND PERFORMANCE

The SBRC detector itself has been described in detail elsewhere [4,5]. Briefly, the detector is a thinned backside-illuminated "hybrid" formed from an array of reversed-biased InSb photodiodes bonded by indium "bump" interconnects to an array of silicon MOSFET devices thereby associating a Source Follower amplifier to each detector. The silicon Read Out Integrated Circuit (ROIC) is called the CRC-228 Direct Read Out or "DRO" and was developed by the Hughes Micro-Electronics Center in Carlsbad, California. Each source follower MOSFET or "unit cell" can be (randomly) accessed using an on-chip multiplexing scheme. Hence the term Direct Read Out. Photocharge is accumulated on the combined capacitance (C) of the junction of the reverse-biased diode (quoted as 0.65 picofarads by SBRC for the latest devices; for earlier devices the value was about 1.0 pF), the gate of the source follower FET and the indium bump contact (about 0.1 pF together). The potential on this storage capacitance can be reset through an FET switch to a certain "reset" level although in practice the actual level or "pedestal" after reset is uncertain - the so-called *kTC noise*. Odd and even numbered pixels are read out separately via two output amplifiers. Saturation or "full-well" condition (CV_{bias}/e) of the device corresponds to a fully de-biased detector; the detector is still light sensitive and does not bleed or bloom, but integration ceases.

In IRCAM, the 62×58 InSb detector is typically operated at a temperature of about 35 Kelvin to minimise any loss of quantum efficiency or DRO performance, while achieving acceptably low dark currents over most of the array; below 40 K dark current ceases to decrease exponentially. Operating parameters are given in Table 1.

To date, nine SBRC InSb arrays have been received and operated. Of these, one had a blown gate (used to control surface charge) and was therefore insensitive, three incorporated a batch of high-doped

Parameter	Value
Detector Bias	-250 mV
Gate Voltage (typical)	-1.0 V
V_{DD}	<1.5 V
Clocks	0–5.0 V
Detector Temperature	35 K
System Gain (typical)	30 e^-/ADU
kTC noise	~120 e^-
Readout Rate (normal)	130 ms/frame

Table 1: Operating Conditions for SBRC 62×58 Arrays in IRCAM

InSb which failed to retain quantum efficiency at low operating temperatures, and five were low-doped InSb arrays with generally good performance characteristics. Devices FPA118, FPA175 and FPA180 all operate with gate voltages about 2 V *less* negative than their predecessors. A summary of the characteristics of four of our detectors is given in Table 2.

Parameter	FPA061	FPA118	FPA175	FPA180
QE	all in range 50–70% over 1–5 μm			
Readout Noise	450 e^-	500 e^-	480 e^-	400 e^-
Dark Current	150 e^-/s	120 e^-/s	150 e^-/s	60 e^-/s
Full Well	all about 1 x 10^6 e^-			
Bad pixels	112(3%)	25(0.7%)	15(0.4%)	75(2%)

Table 2: Performance figures for SBRC 62×58 InSb Arrays

The noise values are obtained under actual observing conditions using the *reference-to-reset* or "double-correlated sampling" mode. For FPA118 and earlier devices, an anti-reflection coating with a peak near 3 μm was used on the InSb; later devices have a coating which peaks near 1.7 μm. Bad pixels are usually of two types, "dead" or "hot"; the latter pixels saturate instantly.

In the IRCAM system the detector is maintained in a "standby" mode in which it is continuously read out until an integration or "exposure" is requested. At the end of the timed integration period the photocharge is read out in "burst mode" and digitised to 15 bits. IRCAM may be operated in conjunction with the UKIRT chopping secondary mirror, but in general we opt to use STARE mode.

Detectors are normally baked in a clean vacuum oven at 80–90 C for 24 hours before installation into the camera and every effort is made to avoid subsequent contamination with water vapour. If this is not done an unstable, "ring-like" region of high "dark" current will be observed spreading inwards from the edge of the array. For each device a *gate voltage* is derived which minimises dark current over most of the array; we have generally found that in our cryostats this voltage settles out about (2.0 ± 0.5) Volts more negative than recommended in the SBRC data sheet ;the gate voltage exhibits hysteresis. Some devices show a slight "after-image" effect following exposure to high flux levels. The output FET drain voltage (V_{DD}) must be reduced considerably (less than 1.5 V) to minimise light emission effects in one corner of the array and V_{rstuc} can have a strong influence on linearity performance. Many of the early chips exhibited spurious light-emitting problems associated with multiplexer faults.

4 CAMERA PERFORMANCE

The camera, or more precisely, the system performance — including the telescope — is generally background-limited. The system efficiency, that is the product of QE (η) and total transmission (τ) of all optics, is about 20% and extraneous background entering the dewar is controlled and constrained as much as possible by a series of baffles and cold-stops, and by careful mechanical design. Observed backgrounds are reasonably consistent with detailed models [6] and yield typically 2,000 e^-/s/pixel in the J band and 10,000 e^-/s/pixel in the K band with 0.6″ pixels; the J band filter is from Barr Associates and the K filter is from OCLI. Because of the large collecting aperture of UKIRT and the minimum integration time of 50 ms, we are unable to use the standard L′ filter at 3.8 μm, but various narrower bands are possible. In the Fabry-Perot imaging spectroscopy mode the etalons are external to the cryostat, i.e. at dome temperature, and consequently the background is no less than that expected for the narrow-band blocking filter.

For a readout noise of 500 e^- rms the accumulated photocharge must exceed 250,000 e^- before the system begins to become background-limited. This is equivalent to about 25% of full well capacity. Exposure times "on-chip" are optimised to avoid detector saturation yet give background-limited operation by filling the wells to at least 75% full; values range from 50 ms at the longest wavelengths to ten minutes or more with narrow bands at the shorter wavelengths.

4.1 Calibrations

Several corrections to "raw" images are required including (dark current + bias level) subtraction, flat-fielding and non-linearity. The success of these will depend on the stability of the detector system and on the observing strategy used. It is important to realise that the observing strategy can vary considerably from one case to the next depending on the scientific goal, but it is nevertheless true that it is rare to find anyone spending *too much* time on calibrations.

4.1.1 Non-linearity.

The SBRC InSb DRO array is inherently non-linear in its response to photon illumination due to the dependence of the capacitance (C) on the value of the reverse bias voltage which itself is a decaying function of time due to photocharge and/or dark current (see also ref. 6 and the presentation by M. McCaughrean). In other words, high photon fluxes give smaller output signals (in A/D units) than would be expected from a linear extrapolation from signal outputs associated with much lower illumination levels. The magnitude of the effect in all practical circumstances is less than 10% (typically around 8% at 75% of full well) and easily calibrated as shown in Figure 1. A fifth-order polynomial fit to the linearity curve is used to correct "bias-subtracted" images as a first step in data-processing; linearity is restored to an accuracy of about 0.1%.

4.1.2 Dark current and bias.

The "bias" level is the electronic offset or signal obtained for an extremely short exposure with no incident illumination whatsoever. The latter condition is achieved with a "dark slide" at 77 K. Some devices show a large-scale gradient in the bias level along rows, others are largely random. Since the SBRC array is a two-channel output device, odd and even numbered columns may have slightly different levels. This effect can be trimmed-out but is in anycase removed by bias subtraction. A "dark current" frame is obtained in the same way but with a much longer exposure. Dark current is spatially non-uniform and a non-linear function of the reverse bias applied to the detector, therefore it must be carefully determined when it is an appreciable fraction of the background signal — *e.g.* narrow band

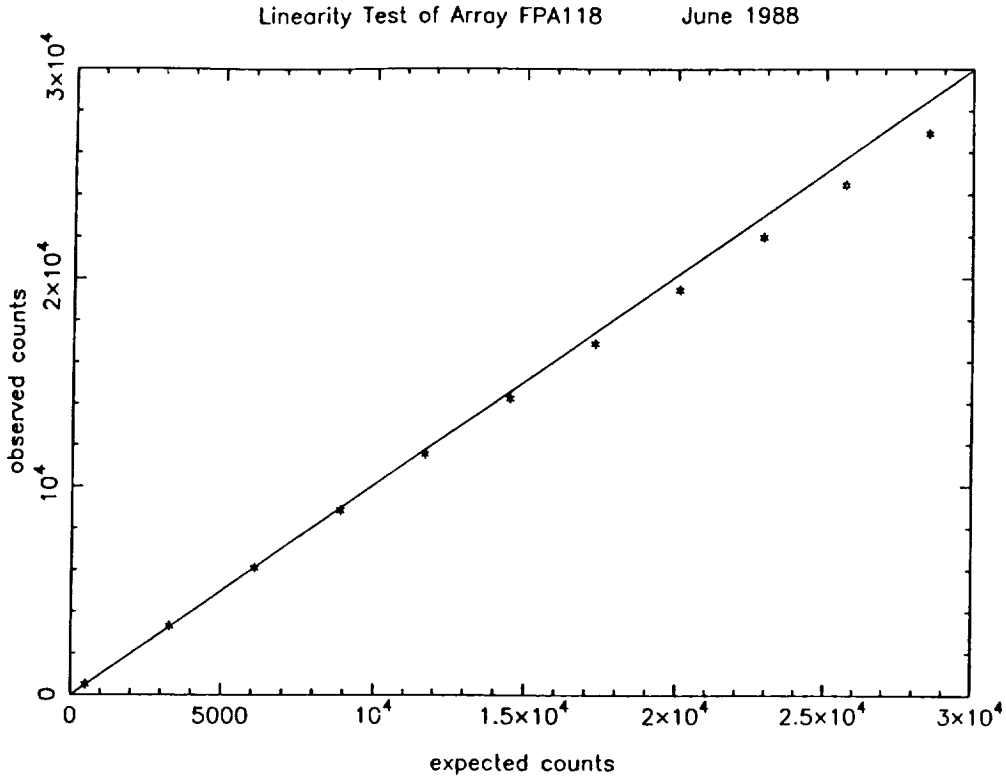

Figure 1: A plot of the output signal counts versus the true input signal counts for the SBRC 62×58 array. The departure from linearity is easily calibrated.

imaging at short wavelengths. At temperatures around 35K the dark current is relatively small and only weakly temperature-sensitive. Near the edges of an array however, the dark current can rise sharply and is very sensitive to gate voltage; small drifts can then lead to "edge-effects" in the image.

4.1.3 Flat-fielding.

Spatial variations in the response of the detector to light are calibrated by dividing by a uniformly illuminated scene — a "flat-field" — of the same color, after dark subtraction (see also more detailed discussion by McCaughrean). That is, the basic algorithmn most often used is

$$\frac{\text{Object frame - dark frame}}{\text{Flatfield frame - dark frame}}$$

The *same* dark frame should be used for object frame and flat-field frame since, to first order, this suppresses the effect of a small drift in dark current level and the signal-to-noise is barely affected if the dark current exhibits good uniformity. We have found that flat-fields are best derived from multiple observations of relatively "blank" sky. Since at some level there will always be sources in the blank sky area, the best technique is to take many images (>5) with the telescope pointing to a slightly different place (by $\sim 5''$ typically), normalise these and calculate the median value for every pixel. This procedure produces a very clean "master" flat-field. For almost empty fields the object frames and the skyflats are one-and-the-same. It is also advantageous to use a running-median flat-field when coadding an extensive data set obtained over many hours; the particular object frame being flattened by the median of the other frames should not be included in the median. With this technique the spatial

non-uniformities, of order 10–20%, can be easily reduced to much better than 0.1% and in an extended survey to very faint levels at 2.2 μm IRCAM has achieved a flat-field precision of 0.007%, by which we mean the *noise* on the mean sky level in the flat-fielded image.

Typical bias, dark and skyflat frames are shown in Figure 2. Regular off-setting to the sky to obtain flat-fields in cases where the primary frame is too crowded does, of course, double the observation time — making it the same as conventional IR photometry — but, for a given total observation time a 50:50 split gives the best signal-to-noise. Also, subtle shifts in the color of the skyflat with time, for instance, make this technique preferable to obtaining all the flats at the end of the night. Taking of such regular sky frames has a convenient and practical side-effect in that it becomes very easy to display (object - sky) differences for a quick-look and provides a means of estimating the temporal stability of the background.

4.1.4 Lamp calibrations.

Since IRCAM is used quite often with a Fabry-Perot interferometer, and now also with a grism, calibrations against an arc-lamp are required. These are basically of two types; wavelength calibration and phase shift. For the former the arc lamp is in focus in the focal plane and for the latter the lamp emission is uniformly diffused to produce a monochromatic flat field.

4.1.5 Polarization calibrations.

Instrumental polarization can be checked against unpolarized stars and position angle offsets from the equatorial system are calibrated against a reference polarizer and against highly polarized sources. There is a one magnitude loss in sensitivity in the IRPOL mode due almost entirely to the polarizer. Since the precision in the measurement of the percentage polarization is $\sigma_P \approx 70\% \times$ *photometric precision/frame* in the photon-noise-limited case, then very high signal-to-noise ratios in photometry are required for good polarimetry, typically 200:1. Good image registration is crucial in the calculation of accurate and reliable polarization. Users should also be aware of the need to remove polarized sky emission from their data (at the shorter near-IR wavelength) when the moon is bright especially if conditions are hazy.

4.2 Astronomical performance

In Table 3 we summarise the sensitivity or "limiting-magnitude" performance of IRCAM 1 in its high-resolution mode of 0.63″ per pixel which is well-matched to typical seeing conditions.

Scale	J	H	K	nbL
0.6″/pix	21.5	21.0	20.3	14.6 mags
	(3.82)	(3.89)	(4.70)	(419) μJy

Table 3: Sensitivity of IRCAM 1

The values are 3 sigma detections in 30 minutes expressed in equivalent magnitudes per square ″ and in μ Jansky. The center wavelengths of the JHKnbL set are respectively 1.26, 1.65, 2.2 and 3.6 μm; passbands are about 20% of the wavelength except for nbL which is 2%. For an object subtending 25 pixels (5×5) in the background-limited case the 3 sigma, 30 minute detection level is 19.1 at K.

Astronomical photometry with IR arrays is now a reality provided the same degree of care is taken as with single-channel photometers (software apertures of sufficient size, psf fitting, airmass corrections).

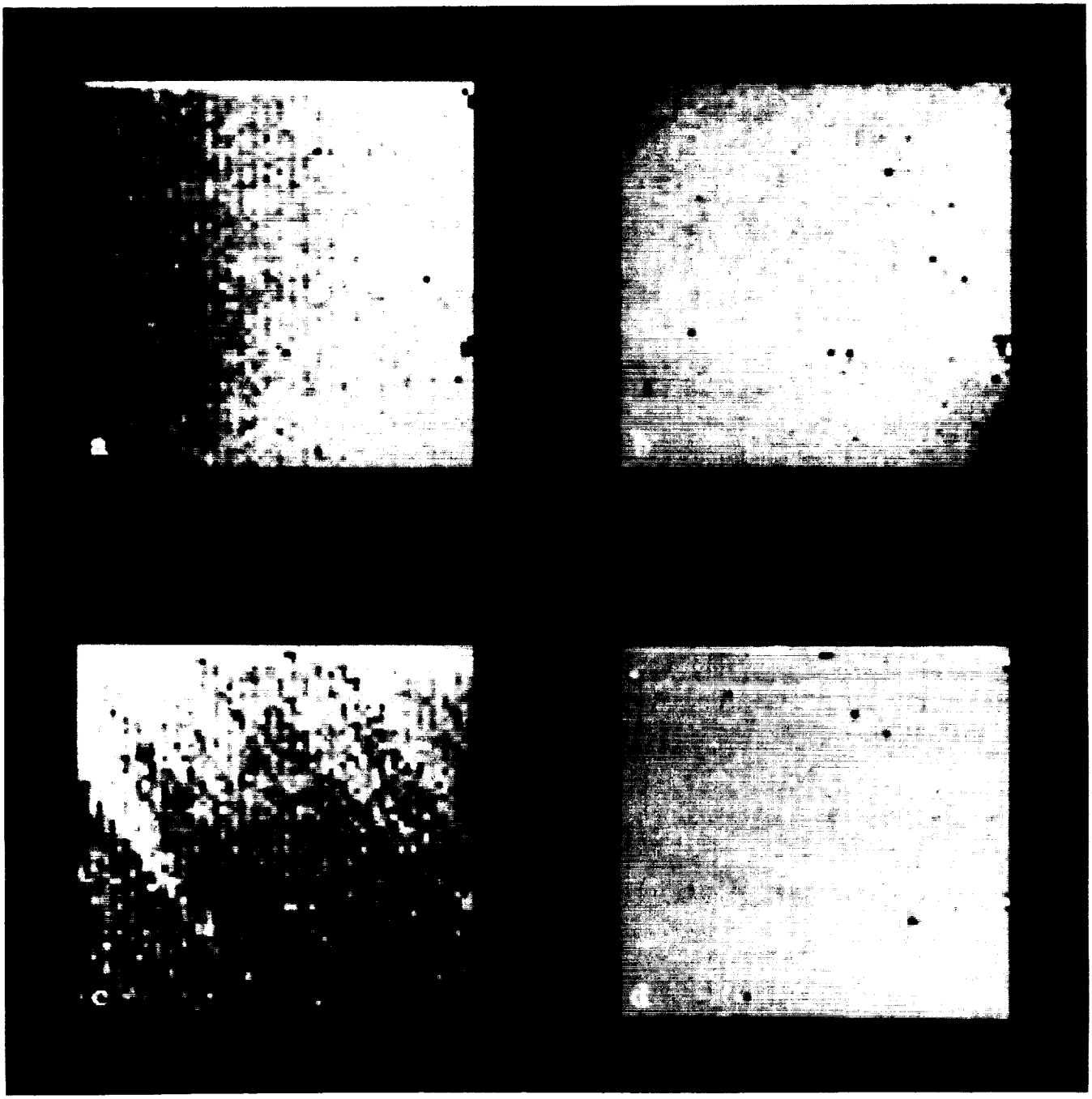

Figure 2: Four frames from a 62×58 InSb array from SBRC showing (a) Bias; (b) dark current; (c) flat-field response at K (2.2 μm); (d) the ratio of two flat-fields.

In a study of bright (K = 7) standard stars we achieved relative photometry between objects on the *same* frame to 0.003 mag (0.3%) and between objects on different frames the agreement was rarely worse than 0.03 mag (3%). Color corrections relative to the UKIRT InSb photometers seem to be small, as expected. For fainter objects and extended sources it becomes essential to have "sky on the frame". Observations of white dwarf stars at K=12–15 have given good agreement (3–5%) with the UKIRT photometers and faint sequences are currently being established as a side-effect of an extensive study of globular clusters.

5 RECENT RESULTS

Infrared imaging systems like IRCAM are now being used widely, in both hemispheres, and in diverse applications. Popular reviews have been given by McLean [7,8] and by Gatley et al. [9]. Progress has been very rapid since the pivotal workshop on *Infrared Astronomy with Arrays* held in Hilo, Hawaii in March 1987 [10]. A selection of some of the highlights from the UKIRT camera over the past two years are listed below.

5.1 Star forming regions

A complete, high resolution (seeing-limited) image of the high-mass star forming cluster in the Orion Nebula was obtained during commissioning of IRCAM 1 leading firstly to a Luminosity Function at 2.2 μm— a plot of the number of stars per unit magnitude interval — (see Figure 3)and then to a full, multi-color photometric study of over five hundred embedded stars [2,6]. The latest results, using Point Spread Function fitting with the DAOPHOT package, are described in the paper following this one.

Many other star forming regions have also been observed. A good example is the object Mon R2 IRS [24]. Figure 7c shows a composite J, H and K image of the region where the J-flux has been colour coded blue, the H-flux coded green and the K-flux coded red. This gives an immediate picture of the colour variations over the object which in this case are interpreted as a combination of emission, absorption and scattering.

In several cases the linear polarization of scattered light from deeply embedded sources has been used to locate the source and to distinguish it from a bright knots of nebulosity. An excellent example is the source GGD-27 [23] shown in Figure 4. The vector plot indicates that the brightest near-infrared source is *not* the illumination source for the nebula.

Many images have been obtained in the light of molecular hydrogen (H_2) emission of regions such as HH7-11 and DR21 which show clear evidence of "bow" shocks [11], and in S106 where the disruption of a placental cloud is observed [12].

5.2 Galaxies

Infrared images of a great many IRAS galaxies, AGNs and known interacting galaxies have been obtained with sufficient resolution to reveal the detailed morphology such as, multiple compact sources, bar-like features, connecting "arms" *etc.*, as well as provide surface brightness profiles.

We have also obtained the first high-resolution, completely-sampled infrared image of the giant spiral galaxy M51 at 2.2 μm (see Figure 5). Because the K light from a galaxy is dominated by light from red giant stars, which trace the distribution of the oldest and most massive stellar component, and because it is significantly less affected by dust than optical emission, such near-infrared images are ideal for the study of structure in nearby galaxies and for comparision with images at wavelengths dominated by other processes (*e.g.* HI, CO, HII, etc). Notice the absence of the striking dust lanes and obscuration in front of the companion galaxy which are seen in optical images. In the IR the companion is clearly seen

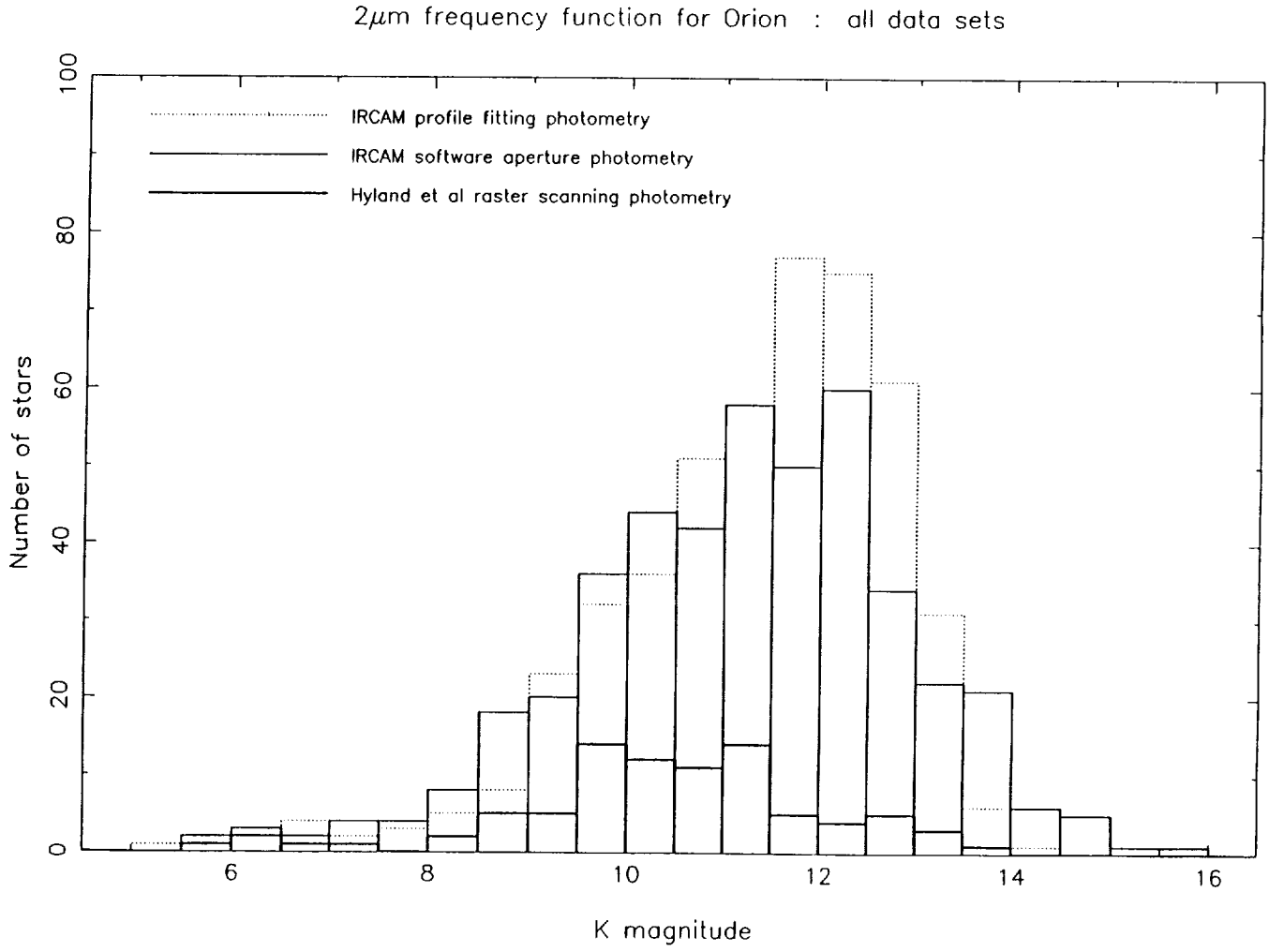

Figure 3: The frequency distribution of K magnitudes in the Orion Trapezium star cluster. If the sun were located at the distance of this cluster its K magnitude would be about 13. (Adapted from McCaughrean 1988).

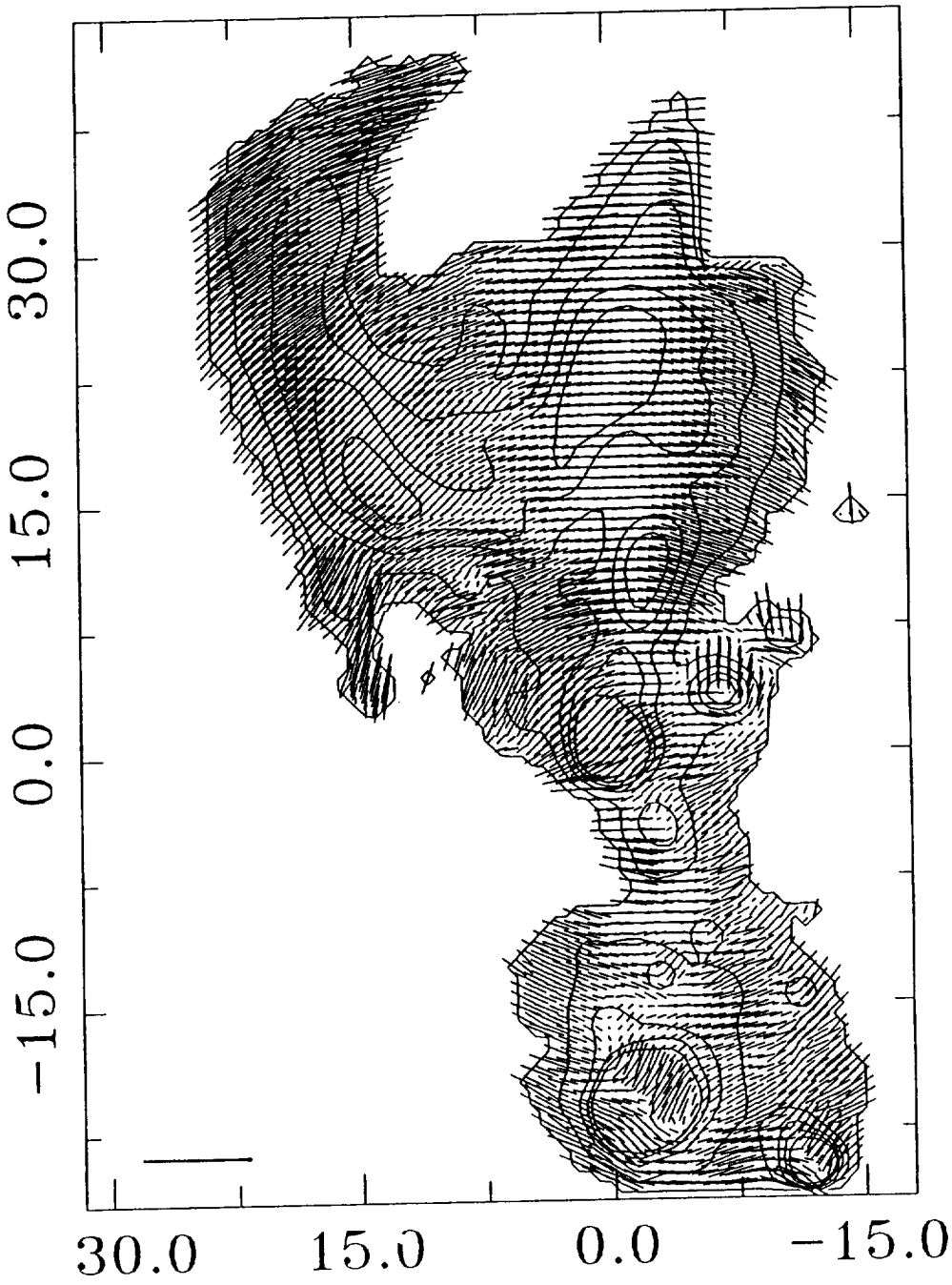

Figure 4: The pattern of linear polarization in the K band for GGD-27. Each line segment represents the percentage linear polarization and the orientation of the electric vector. Note the centro-symmetric pattern.

to be a barred spiral galaxy and there are also clear indications of a non-axisymmetric component in the bulge of M51 itself. The bridge to the companion is much fainter in the IR (relative to the spiral arms) than in the optical suggesting that most of the bridge must be composed of young stars. The contrast in the spiral arms, which should show only the linear response of the stars to the density wave, is (as predicted) less in the IR than the optical, and the arms are smoother and broader than the optical.

5.3 The Galactic Center

Continuous infrared imaging at 2.2 μm at a rate of about 4 frames per second was obtained of the Galactic Center during a unique opportunity when the Moon occulted the source on three occasions visible from Mauna Kea [13,14]. Light curves have been obtained and the imaging photometry data have made it possible to re-interpret aperture photometry observations enabling the components of IRS16 to be distinguished (see the paper by Becklin *et al.*).

In another unique study, the first "velocity-resolved" images of the Galactic Center were obtained using a near-infrared imaging Fabry-Perot interferometer tuned to the Brackett gamma line of hydrogen at 2.166 μm and with a velocity resolution of about 90 km/s; the spatial resolution was seeing-limited at about 1 $\hat{''}$ [15,16]. The FP was scanned over a velocity range of 1045 km/s in steps of 55 km/s and an IRCAM image of 100s on-chip integration time obtained at each setting. The narrow band Brγ filter isolated one order of the FP and the central step of the scan was tuned to the velocity of Brγ from IRS16. When the individual frames have been calibrated and registered, spectra for each spatial location are generated from cuts through the data cube. This technique can generate 3600 spectra of the Galactic Center region in only 30 minutes. Figure 6 shows a contour plot of the peak Brγ emission over the entire field and some sample spectra from a region 10.5 $\hat{''}$S and 2.5 $\hat{''}$W of IRS7. The lower intensity level is 0 on all the spectra while the upper level is self-scaled to the maximum value. The spectra show widely varying line profiles. For example in column 41 the lines display a "red wing" which appears to die away as we move towards row 34 where the lines are narrow (<200km/s) and then re-emerges in the south. Such evidence for multiple kinematic components is found throughout the data.

5.4 Planetary nebulae

Images of a shock-heated toroidal ring of molecular hydrogen have been obtained [17] of the planetary nebula NGC7027 which contrasts dramatically with the optical and radio appearance of this object. The radio maps show a shell structure and the optical image is peculiar and irregular due to extinction by dust. McLean et al. re-classify NGC7027 as a "butterfly" or "bow-tie" planetary nebula most probably in a fairly early stage of formation. A multicolor study of an even younger or "proto-planetary nebula" called M2–9 reveals very clearly a large circumstellar disk [18]. Both these objects are shown in Fig. 7a,b.

5.5 Supernova remnants

Using narrow band filters and the wide-field mode of IRCAM (2.4 $\hat{''}$ pixel) spectacular molecular hydrogen emission in supernova remnants, such as the Cygnus Loop and the Crab Nebula, has been observed with unexpected results which may indicate the occurrence of non-radiative precursor shocks [19,20]. For the Cygnus Loop, a mosaic of 20 frames covering an area of about 7×7 $\hat{'}$ of the bright filaments in the north eastern segment of the loop revealed unexpectedly strong H_2 emission; the bright optical lines indicate that the shocks are fast (> 100 km/s) and in gas of moderate density (n $\sim$ 10 cm^{-3}). The H_2 emission is associated with the bright optical emission and shows the same filamentary structure but is generally *displaced* in front of the edge of the optical emission. Most of the H_2 emission comes

ORIGINAL PAGE
COLOR PHOTOGRAPH

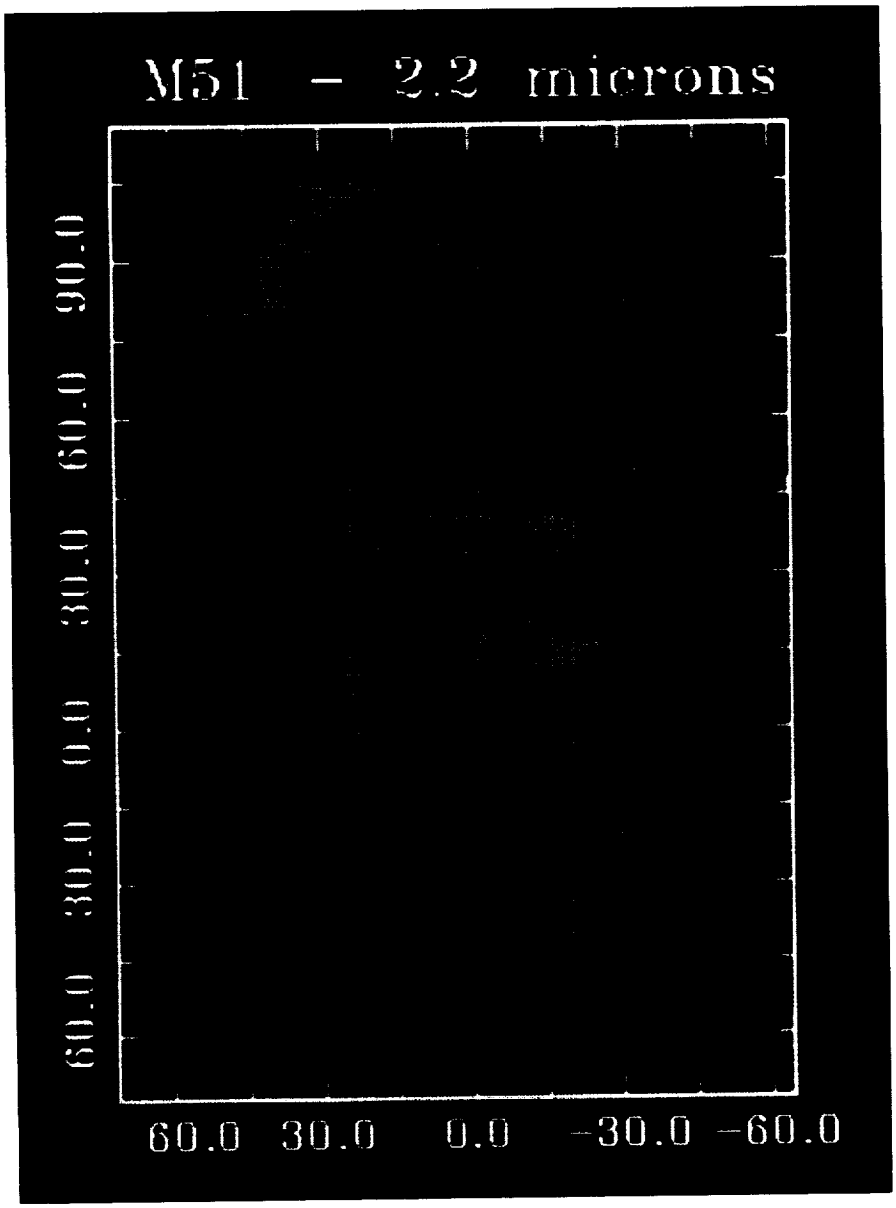

Figure 5: A 2.2 μm (K band) image of the spiral galaxy M51 and its companion. This image is a photometrically-calibrated mosaic of 88 overlapping frames in the 1.2$''$ mode.

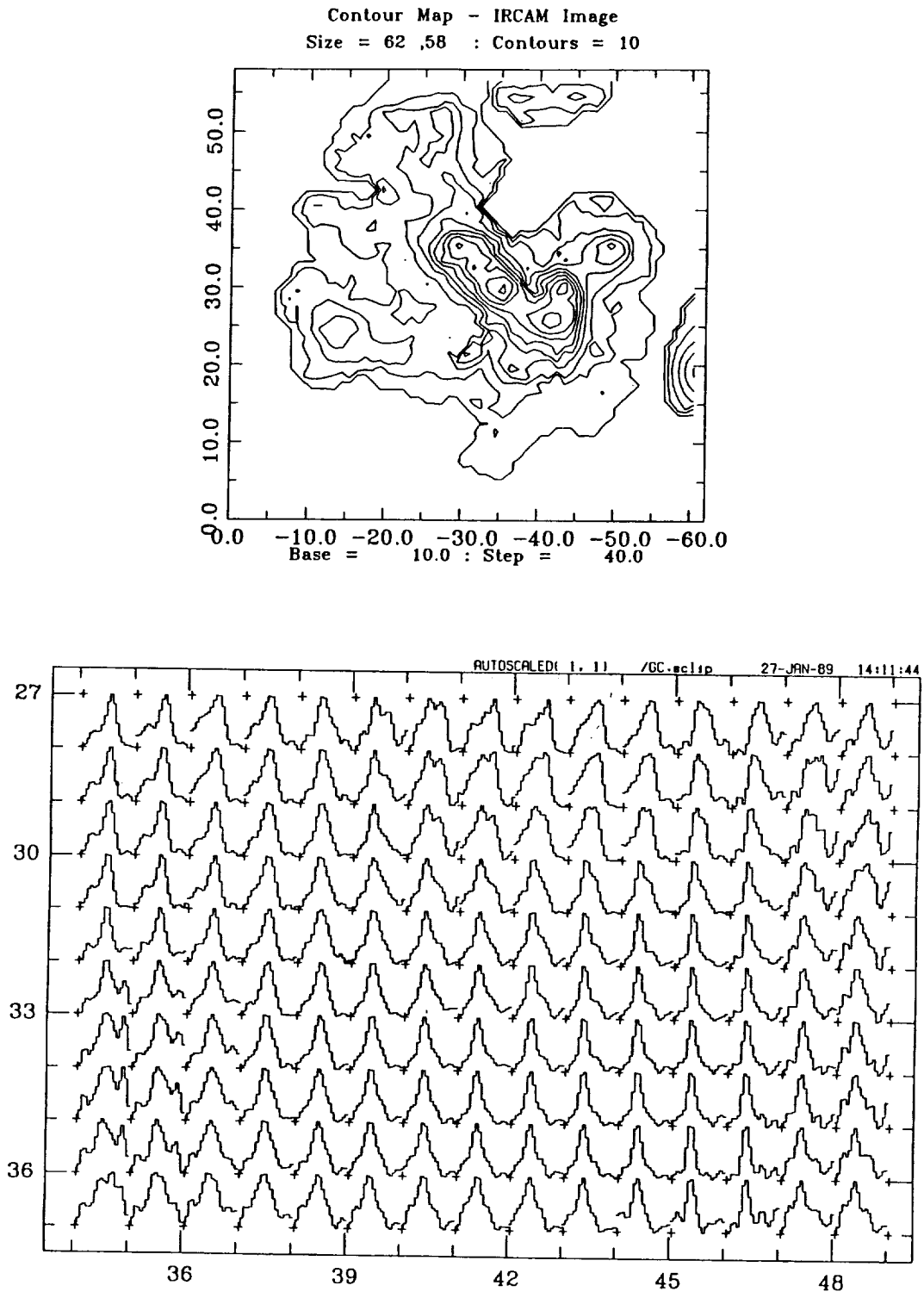

Figure 6: (a) Contour plot of peak Brγ emission in the Galactic Center. (b) A region of the Galactic Center showing the spatial variation of the Brackett gamma line at 2.166 μm with 0.6 arcsecond pixels in 1.0$''$ seeing.

ORIGINAL PAGE
COLOR PHOTOGRAPH

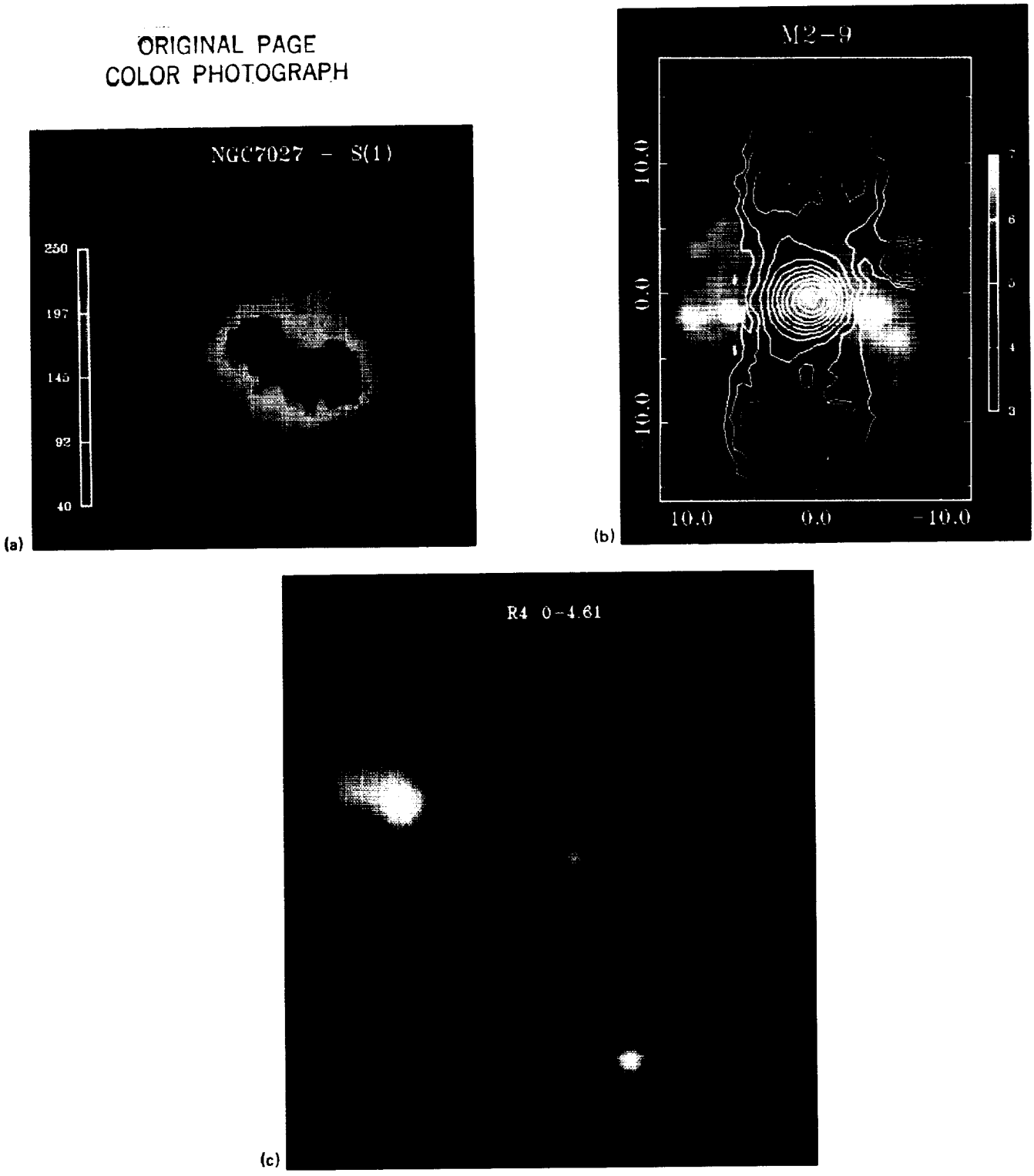

Figure 7: (a) The S(1) v=1-0 emission from the planetary nebula NGC7027. The peak flux in the lobes is about 5×10^{-21}W cm^{-2}; (b) the J-K color map of the proto-planetary object M2-9. The color bar indicates J-K colors in the range 3-7 magnitudes. Overlaid on the map are contours of the J surface brightness; (c) a composite J, H and K image of the star forming region Mon R2 IRS

from a region dominated in the optical by faint, collisionally-excited Balmer emission behind fast (200 km/s) non-radiative shocks propagating into a partially neutral medium. If the pre-shock gas contains a substantial fraction of H_2 rather than HI then the H_2 emission could also be excited in fast adiabatic shocks. Alternatively the H_2 could be excited by UV fluorescence powered by the bright optical shocks.

5.6 Globular clusters

A deep infrared survey of part of the globular cluster M71 was obtained and analysed using the DAOPHOT software package [21]. One strip in the southern part of the cluster has been thoroughly analysed to yield K magnitudes for almost 300 stars using optimised fitting and iterating routines. The best published optical photometry (photographic) does not go as deep and has only 70 stars in the same area. Preliminary V,V-K color-magnitude and B-V,V-K color-color diagrams based on the photographic photometry look very encouraging. Initial experience with the DAOPHOT package suggested that the K zeropoint can be uncertain at the 10% level because of systematic differences in the PSF of the (bright) standard stars used for calibration.

5.7 Deep cosmological surveys

Using a cumulative observation time of almost 12 hours and very careful median-filtering techniques for flat-fielding, the deepest ever infrared images of faint, distant galaxies have been obtained. The limiting magnitude (1 sigma noise) in these studies is around K = 23; the brightness of the infrared background at 2.2μm is approximately equivalent to K = 13 per square $\widehat{''}$ - a factor of 10,000! Combined with deep optical CCD images, a population of galaxies at high redshift (z$\sim$3.0) has been discovered with extremely flat spectral energy distributions characteristic of vigorous star formation suggesting that these objects may be "protogalaxies" or galaxies formed earlier but now undergoing a rejuvenation phase [22]. An example of one such object is shown in Figure 8.

6 CONCLUSIONS AND PROSPECTS

These and many other studies barely scratch the surface of what is possible with photometrically calibrated infrared imaging systems. Despite certain limitations, we have been successful in demonstrating flat-fielding accuracies to better than 1 part in 10,000 and relative photometry to better than about 0.01 mag or 1%.

There is no doubt that the 62×58 InSb array from SBRC has been an astoundingly successful device and that it has catapulted infrared astronomy forward at an incredible pace. Even so, the need for larger format detector arrays with lower readout noise and the highest possible quantum efficiency are already urgent.

Acknowledgements It is a pleasure to acknowledge our many colleagues at the Joint Astronomy Centre and at the Royal Observatory, Edinburgh whose efforts have helped to make IRCAM a success. We especially thank Alan Hoffman and David Randall of SBRC, and Mark McCaughrean, John Rayner, Simon Lilly, Andy Longmore, Eric Becklin, James Graham and Joss Bland for many fruitful discussions and suggestions on all aspects of the design, construction and usage of IRCAM at UKIRT.

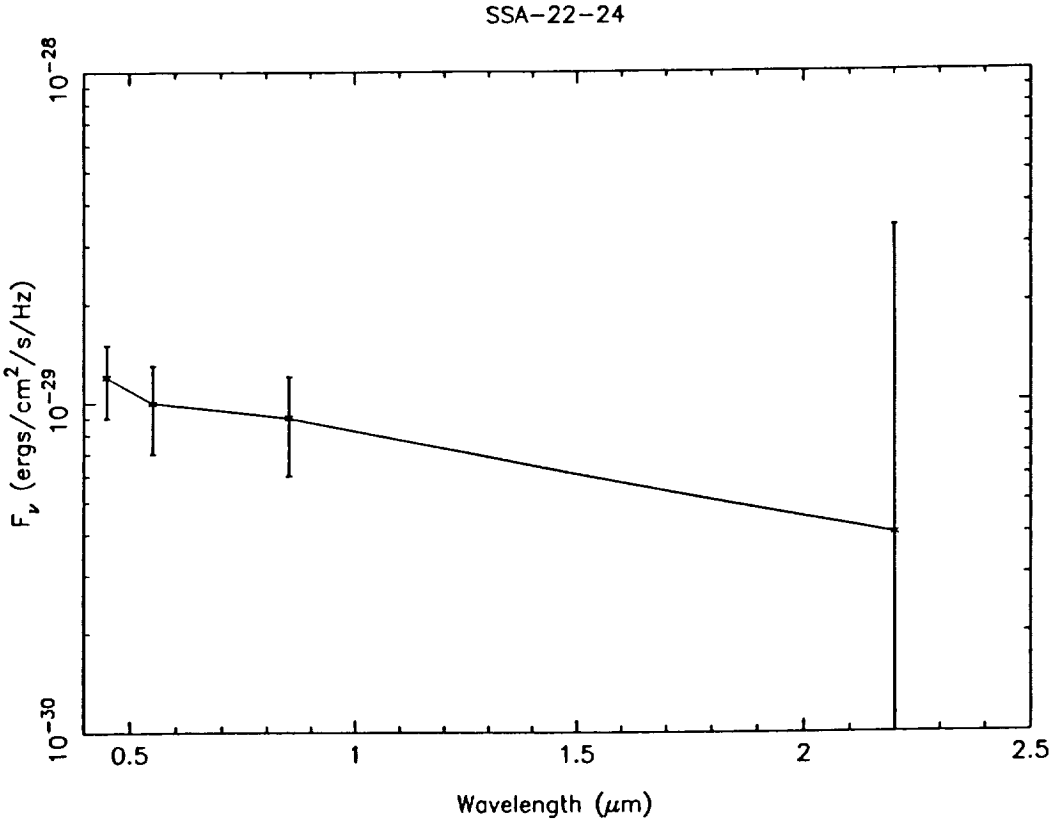

Figure 8: The spectral energy distribution of SSA-22-24 which is a faint galaxy (V=23) at a redshift of about z~3.5.

REFERENCES AND NOTES

1. I.S. McLean, T.C. Chuter, M.J. McCaughrean and J.T. Rayner, *System Design of a 1-5 μm Infrared Camera*, Proc. SPIE **627**, 430-437 (1986).

2. I.S. McLean, *Results with the UKIRT Camera*, in Infrared Astronomy with Arrays, C.G. Wynn-Williams and E.E. Becklin, eds., Institute for Astronomy, University of Hawaii, 180–192, (1987).

3. I.S. McLean, *Optical or Infrared — the Elusive Boundary*, in Instrumentation for Astronomy; present and future, Proc. Santa Cruz Summer Workshop, Lloyd Robinson, ed., Springer-Verlag, (1988).

4. G. Orias, A.W. Hoffman and M. Casselman, *58×62 InSb focal plane array for infrared astronomy*, in Instrumentation for Astronomy VI, Proc. SPIE, **627**, 408–417, (1986).

5. A.M. Fowler, R.G. Probst, J.P. Britt, R.R. Joyce and F.C. Gillett, *Evaluation of an indium antimonide hybrid focal plane array for ground-based astronomy*, Optical Eng., **26**, 232–240, (1987).

6. M.J. McCaughrean, *The astronomical applications of infrared array detectors*, PhD Thesis, University of Edinburgh, Scotland, (1988).

7. I.S. McLean, *Infrared Astronomy's New Image*, in SKY and TELESCOPE, Vol. **75**, No. 3, 254–258, March (1988).

8. I.S. McLean, *Infrared Astronomy:A New Beginning*, in ASTRONOMY NOW, August (1988).

9. I. Gatley, D.L. Depoy, and A.M. Fowler, *Astronomical Imaging with Infrared Array Detectors*, in SCIENCE, Vol. **242**, 1217–1348, (1988).

10. C.G. Wynn-Williams and E.E. Becklin, Infrared Astronomy with Arrays, Institute for Astronomy, University of Hawaii, Honolulu (1987).

11. R. Garden and A. Russell, in prep. (1989).

12. S. Suzuki-Hayashi, T. Hasagawa, C. Aspin and I.S. McLean, *S106: dispersal of a placental cloud*, submitted Ap. J. (1989).

13. I.S. McLean, C. Aspin, A.J. Longmore and R.I. Dixon, *The January 1987 Galactic Center occultation observed with the UKIRT IR camera, IRCAM*, in Infrared Astronomy with Arrays, C.G. Wynn-Williams and E.E. Becklin eds., Institute for Astronomy, University of Hawaii, 321–325, (1987).
14. Longmore *et al.* in prep (1989).
15. D.L. Depoy, I. Gatley and I.S. McLean, in The Galactic Center, Proc. of UCLA conference (1989).
16. G.S. Wright, J. Bland and I.S. McLean, *An infrared imaging Fabry-Perot study of the Galactic Centre*, in 22nd ESLAB Symposium on Infrared Spectroscopy, Salamanca, (1989).
17. I.S. McLean, I. Gatley, P.W. Brand, S. Hayashi, T. Hasegawa and M. Tanaka, *A molecular toroid in NGC7027*, submitted to Ap.J. (1989)
18. C. Aspin, I.S. McLean and M.G. Smith, *The proto-planetary nebula M2–9*, Astron. Astrophys., **196**, 227-232, (1988).
19. J. Graham, G.S. Wright and A.J. Longmore, *Infrared spectroscopy and imaging of supernova remnants*, in 22nd ESLAB Symposium on Infrared Spectroscopy, (1989).
20. J. Graham, G.S. Wright, J.J. Hester and A.J. Longmore Ap. J. (1989). in preparation
21. A.J. Longmore private communication.
22. L. Cowie, S.J. Lilly, J. Gardner, and I.S. McLean, *A cosmologically significant population of galaxies dominated by very young star formation*, Ap. J Letters, **332**, L29 (1988).
23. C. Aspin, M.J. McCaughrean, I.S. McLean and J.T. Rayner Astron. Astrophys. (1989) in preparation
24. C. Aspin, D.M. Walther and T.G. Geballe, Astron. Astrophys. (1989) in preparation

Reduction and Analysis Techniques for Infrared Imaging Data

Mark McCaughrean

NRC Resident Research Associate
NASA Goddard Space Flight Center, Code 685, Greenbelt, MD 20771

1 Introduction

Infrared detector arrays are becoming increasingly available to the astronomy community, with a number of array cameras already in use at national observatories, and others under development at many institutions. As the detector technology and imaging instruments grow more sophisticated, more attention is focussed on the business of turning raw data into scientifically significant information.

Turning pictures into papers, or equivalently, astronomy into astrophysics, both accurately and efficiently, is the subject of this paper. I shall discuss some of the factors that can be considered at each of three major stages; acquisition, reduction, and analysis, concentrating in particular on several of the questions most relevant to the techniques currently applied to near infrared imaging.

2 Data Acquisition

Effective reduction and analysis begin with effective data acquisition. As infrared cameras have become available, observing techniques have been developed that combine features of conventional infrared photometry and raster scanning, optical CCD imaging, as well as new procedures to account for unique problems presented by imaging with small detector arrays at infrared wavelengths.

2.1 Source

Due to the bright sky background, broad band near infrared images become background limited quickly, on the order of a minute. Only very shallow survey projects will require less time on a given field. For deeper experiments, the telescope can be moved a few arcseconds after each background limited exposure is read out, before starting the next—this makes it easier to replace bad pixels, and reduce noise due to fixed, time-independent noise sources such as flat fielding errors. If the source fields are mainly blank, and sky images are being used as flat fields, this method also makes it possible create flat fields from the source data itself. This eliminates the need for separate sky measurements, and effectively increases the on-source integration time by a factor of two (see section 3.2).

2.2 Sky

Classical AC-coupled infrared photometry involves spending half the time measuring the sky; how important is it to measure the sky when using an imaging camera? Sky images have two main uses—measuring the sky brightness as in conventional photometry, and to provide a flat field. The infrared sky background can be roughly divided into three regimes:

- $\lambda < 2.5\,\mu$m : dominated by emission from the hydroxyl molecule OH*—highly structured, both spatially and spectrally, with peak-to-trough intensity variations of up to 50%, on time scales of less than an hour [1].
- $2.5\,\mu\text{m} < \lambda < 10\,\mu$m : thermal emission from telescope/warm optics dominates—thermally stable, so background is relatively stable.

- $\lambda > 10\,\mu$m : thermal emission from telescope/warm optics and atmosphere roughly equal—fairly rapid variations in atmospheric temperature and opacity make for less stable background.

Sky intensity monitoring

The near infrared sky background can change by up to 50% on a time scale of about half an hour—therefore the sky brightness should be measured every 10–30 minutes. This may or may not require separate sky images:

- Blank field experiments—if any given source image is more or less empty, there is enough sky information in the source data alone: the median value in the image provides an accurate estimate of the sky brightness at the time it was obtained. Small time scale sky variations are almost irrelevant; all pixels in the array integrate simultaneously, and the total sky background contribution should be the same for each.

- Filled field experiments—if the source fills the field of view, or you are making a mosaic of a large region filled with low level nebulosity, some measurement of the sky away from the region is required. Current array detectors are small—it is usually possible to find a blank patch of sky near to most sources. In some places (e.g. the Galactic Centre), it may be harder to find a blank patch of sky—as array detectors get bigger, it will be hard to find blank sky anywhere. As long as a patch of sky can be found that fills less than one third of the array pixels with sources, the median value will provide a good estimate of the sky brightness. Time interpolate between adjacent sky measurements to calculate the brightness at the time when a given source frame was taken. However, sensitivity to any short time scale variability will remain function of the time elapsed between sky measurements. If short time scale sky variations dominate the experimental errors, a modified form of chopping can be used. The alternating sequence of source and sky images is co-added in separate sections of the instrument computer. Reading out and storing both co-added images once every few minutes, the effects of short time scale variations are reduced—both images contain a similar cumulative record of background variations at speeds up to the chopping frequency.

Taking skies for flat fielding

Using sky images for flat fielding is an effective way of obtaining very low residual noise. In blank field experiments, where objects are rare, each image is mostly filled with sky, and median stacking techniques will filter out the sources to provide a high accuracy flat field. No separate sky measurements are required. For filled field experiments, separate skies will be required. If no completely blank field can be found, images taken at slightly offset positions can be median stacked to remove sources.

In principle, the actual intensity of the sky background should not be important, and sky images taken many hours before or after a source image could be used to flat field it. In practice, changes in the near infrared sky brightness can seriously affect the quality of flat fielding—the changes in brightness are accompanied by changes in the OH* emission line ratios. Integrated across a broad band filter, the effective 'colour' of the sky background is changed on time scales of an hour or so. If separate sky images are being used to flat field source images at broad band near infrared wavelengths, they are best obtained at least once every half hour. This variability is of even greater concern in higher spectral resolution.

2.3 Additional considerations

As well as imaging the source and the sky, several other factors should be considered at the telescope:

- Instrumental offsets—measurements of system offsets may be required, including dark current and bias. The frequency of measurement will depend on the stability of the detector system. If a dark current image is used in the reduction procedure, the on-chip integration time should be the same as used for source and sky measurements, but a larger number of dark frames should be co-added, to minimise its contribution to the noise. Dark current frames can often be taken in twilight.

- Flat fields—to remove pixel to pixel variations in quantum efficiency and gain, a flat field image is needed. Typical flat fields include images of the sky close in time and space to the source frame; images of the sky at high and low airmass; images of the Moon; images of the inside of the dome; images of the twilight sky. The signal to noise in the flat field images should be significantly greater than in the source images, so that

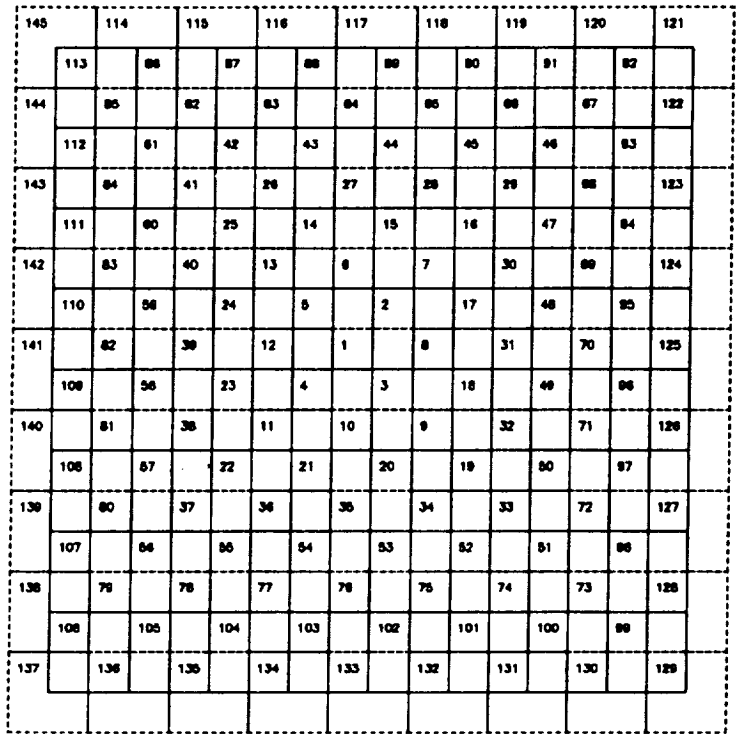

Figure 1: A mosaic scheme

the flat fielding process does not degrade the signal to noise in the reduced data. This is easy for flat fields which can be obtained during daylight or twilight hours, but the time spent on those that must be obtained 'on line', i.e. during observing hours, must be carefully examined. The flat fielding process is discussed in section 3.2.

- Standards—to flux calibrate the data, images of standard sources will be required. The frequency of measurement will depend on the required accuracy. A range of standards is required to measure atmospheric extinction as a function of airmass, and photometric zero-points and colour terms. Standards can also be used to check system linearity. Standards are discussed further in section 4.2.

- Linearity calibrations—if the detector is known to exhibit non-linear behaviour, calibration data may be required to measure and remove it. Usually done for only once for a given detector—however, non-linearity can be quite sensitive to operating conditions such as gate voltage. For the highest precision work, linearity calibration data can be obtained in twilight each night. Non-linearity is discussed in more detail in section 3.1.

- Mosaic scheme—if a large scale view of a region is required, a mosaic scheme is needed. For example, figure 1 shows a fully overlapping grid of image positions, in which every point on the sky is imaged twice. This scheme has many advantages, as discussed in section 3.3.

  If a mosaic is made through two or more filters, it may be worth imaging each mosaic position through each filter before moving to the next position: relative differences in seeing, airmass, and sky background are minimised. In the case of bad weather, some fraction of the mosaic will be complete in all filters, rather than all of the mosaic in just one. If the results of the experiment rely on multi-colour photometry, this is the preferred outcome.

3 Data Reduction

There are many subtleties to the process of reducing infrared imaging data, and more will undoubtedly be uncovered as the data are subjected to increasing scrutiny. Following are some key points.

3.1 Linearisation

The so-called Direct Read-Out (DRO) type multiplexer is common amongst the current generation of devices. The DRO uses a single source-follower for each detector, and the whole array is addressed sequentially via X and Y shift registers. This is simpler to fabricate and quieter to operate than a surface channel CCD, but exhibits a a drawback, namely non-linearity.

The DRO works as follows: the unit cell is reverse biased, to charge up the cell capacitance. Dark current and photo-electrons formed in the detector substrate discharge the cell—measuring the voltage on the cell at the beginning and the end of an integration period, the total voltage discharge can be determined. The instantaneous rate of voltage discharge is determined by the current flow and the cell capacitance—but, a large fraction of the cell capacitance is junction capacitance, which changes as a function of the bias across the diode. Thus, as the cell discharges, the voltage discharge achieved by a unit of input current changes. This makes it difficult to relate the total voltage discharge to the total current integrated. Also, the amount of dark current generated depends on the changing bias across the diode junction, adding to the problem.

A simple analogy

The explicit semiconductor physics behind the operation of a DRO-type detector is covered in detail elsewhere [2, 3,4,1]. In practice however, we are less concerned about *why* the DRO is non-linear, than *how* the non-linearity appears in practice—a simple analogy may be drawn as follows. Figure 2 shows an optical CCD operating as a bucket, with current represented by water. Exposed to light, photo-current is collected in the bucket, as is dark current. At the end of an integration period, we measure the depth to which the bucket is filled, i.e. the voltage change. Because the bucket has straight sides, the depth is directly proportional to the amount of current collected. To determine the dark current contribution, a 'lid' is placed over the bucket. The rate of dark current flow is the same as it was with the lid off—therefore it is easy to calculate the dark current contribution by an appropriate linear scaling.

Figure 3 shows the equivalent bucket model for a DRO detector. Things are more complex—the the bucket is immersed in water, and it has sloping sides and a hole in its bottom. Again, dark and photo-current fill the bucket, the former flowing in through the hole in the bottom of the bucket, and latter coming in from above. However, the final depth to which the bucket is filled (i.e. the voltage change) is not linearly proportional to the amount of current collected, due to the sloping sides. As the bucket is filled, it takes more and more current to increase the depth of the water by a unit amount. This non-linearity is equivalent to that caused by the change in the junction capacitance as the diode discharges.

The non-linearity in dark current generation is seen when the bucket is covered. The dark current flows in through the hole in the bottom of the bucket—it flows fastest when the bucket is empty; as the bucket fills, the dark current flow decreases, stopping completely when the level of the water in the bucket reaches the level of the water surrounding it. As the rate of dark current flow depends on the depth to which the bucket is filled, it is not easy to relate the amount of current collected during a dark integration to the amount collected when photo-current is also filling up the bucket.

This simple analogy can also explain another useful characteristic of the DRO circuit. When the optical CCD bucket fills up, it overflows, and current spills over into adjacent buckets, the process known as blooming or column bleeding. However, with the DRO, there is no blooming. When the bucket fills up, and passes the saturation point (where the level of the water is the same inside and outside the bucket), the photo-current tries to fill the bucket further. The dark current, however, now flows *out* through the hole in the bottom of the bucket, effectively stopping the bucket from overflowing.

How bad is the non-linearity?

The device that has drawn most attention to the problem of DRO non-linearity is the SBRC 62 x 58 pixel InSb+CRC228 DRO array. Figure 4 shows the measured non-linearity of an SBRC InSb+DRO device: the array

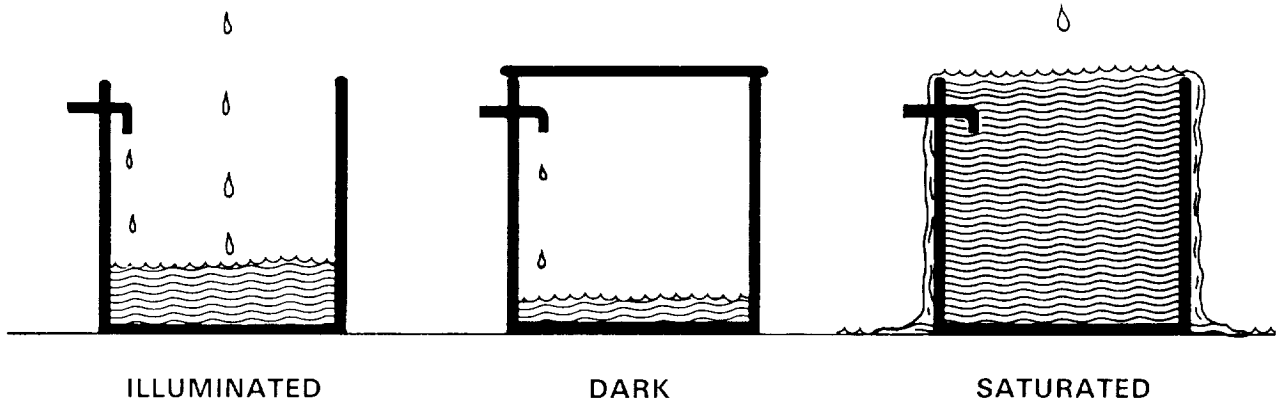

Figure 2: Optical CCD as a bucket

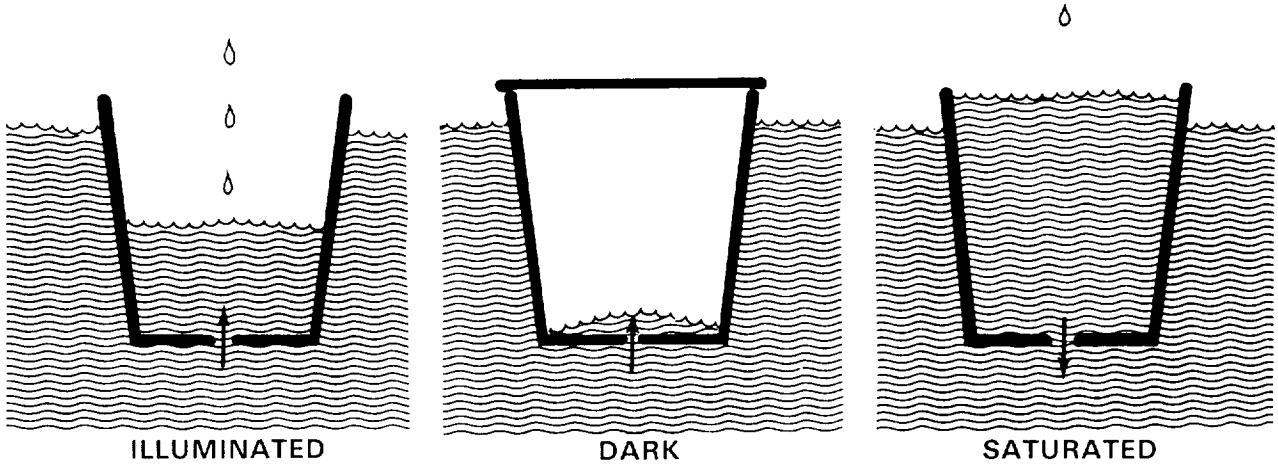

Figure 3: DRO as a bucket

was illuminated with a constant thermal background, by placing a piece of cardboard over the camera window and imaging through the K ($2.2\,\mu$m) filter. The mean output signal over a clean section of the detector is shown as a function of on-chip integration time. The non-linearity of the device is seen to be small and well behaved—a quadratic provides an accurate fit to the measured data. In fact, the measured non-linearity is a little less than predicted for the SBRC array [1]. This is probably due to parasitic capacitances in the actual device, unaccounted for in the modelling. These are independent of detector bias, and thus reduce the non-linearity.

The practical effect of the non-linearity depends on the dynamic range in the data, rather than how deeply the buckets are filled. The further apart in relative brightness two sources are *in the same image*, the larger the error in their measured relative brightnesses. In the worst possible case, with very little sky background, a very bright pixel close to saturation, and a very faint pixel close to zero, the ratio of the measured pixel brightnesses can be wrong by up to 10%, i.e. the bright pixel will appear about 10% fainter than it should when compared to a linear extrapolation of the faint pixel. Conversely, for two sources both close to a bright sky background, the non-linearity will be slight. An extensive discussion of the quantitative effect of DRO non-linearity under a range of typical observing conditions can be found elsewhere [1].

Removing the non-linearity

Removing the non-linearity of a DRO type device is not very difficult, and has been addressed in detail elsewhere, by Alan Hoffman of SBRC [4], and myself [1]—the non-linearity can easily be reduced to less than 1% across the whole dynamic range of the detector. There are some points worth noting about practical implementations of linearisation procedures:

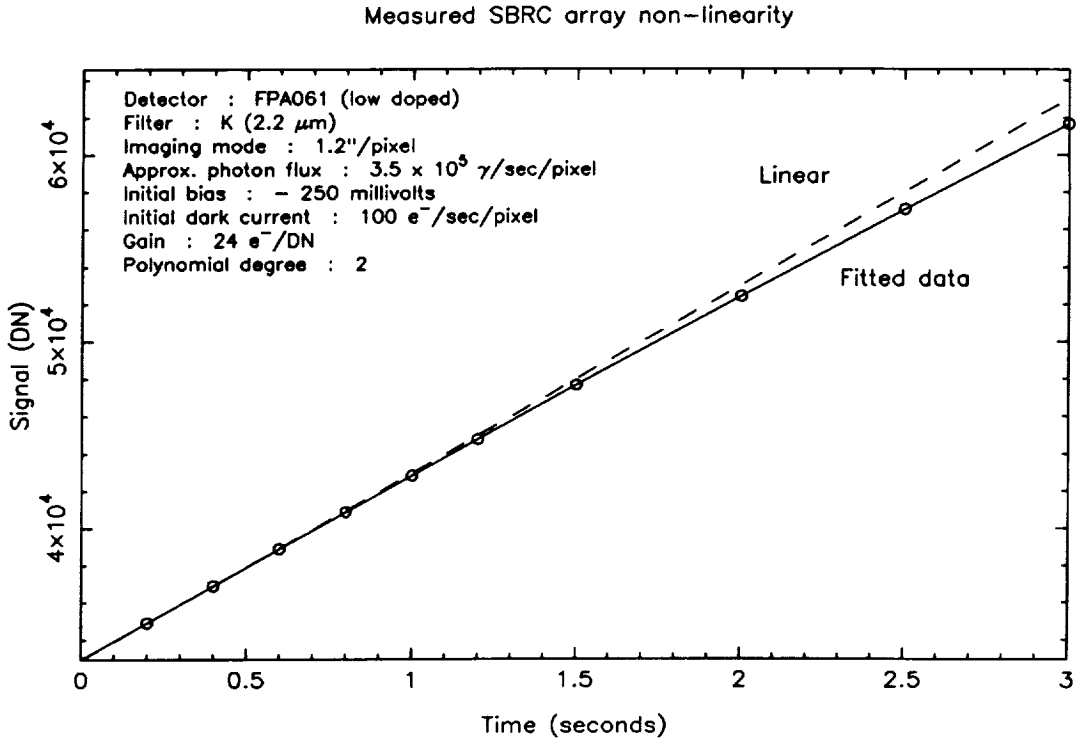

Figure 4: Measured non-linearity of the SBRC InSb+CRC228 DRO

- A numerical approach—make no *a priori* assumptions about the physics of the device, and measure the non-linearity in a controlled experiment involving constant brightness sources across a wide range of parameter space.

  The dark current is commonly assumed to be very small, that its non-linear behaviour can be ignored, and that subtracting a dark current image will remove it completely. This simplifies matters considerably. Only the shape of the curve as shown in figure 4 needs to be determined, i.e. the deviation from direct proportionality between the integration time and the output signal. Each pixel is linearised by applying a polynomial correction as a function of well depth.

  If the dark current is not negligible (e.g. in low background spectroscopic experiments), the independent dark current non-linearity should be accounted for. This can be done by taking a series of blanked-off exposures with increasing integration time, as well as the corresponding set of illuminated exposures. The two curves are combined to remove the effects of both non-linearities [4,1].

- An analytical approach—assume that the device physics can be modelled, and that the non-linear behaviour of the device can be predicted from a few key measurements of the parameters of a given device.

  There is often considerable uncertainty in parameters such as the doping levels and the fixed capacitances. Also, simplifying assumptions about the nature and temperature dependence of the dark current, and whether the p-n junction has a step or graded profile, may be required. These assumptions can lower the accuracy of the resulting linearisation algorithm.

- A "don't" approach—assume the non-linearity is negligible and ignore it; this technique involves the least work. Frequently, sources being measured are faint and close to the sky background, and therefore non-linearity *is* negligible. However, standard stars measured to photometrically calibrate the images might be bright enough that non-linearity in *their* measurement becomes a factor.

- One curve or many?—a single calibration curve is often used to linearise an entire array. Deriving a curve for each individual pixel is seen to be a more accurate technique, resulting in slightly improved signal to noise after flat fielding.

3.2 Flat fielding

Of all the reduction steps applied to imaging data, the flat fielding process remains the most arcane. Optical CCD users have been tackling this question for more than a decade, with no 'standard' methodology yet agreed on. The steps taken to flat field data can depend heavily on the goals of the experiment—one project might require obtaining the lowest possible noise across limited blank patches of sky in a search for extremely faint sources; another might be concerned with photometric repeatability across the whole detector for accurate crowded field point source photometry. The techniques used to achieve these disparate goals might not be the same.

Some possible flat fielding techniques

We can use simple algebraic representation of the factors determining how source photons arriving above the atmosphere are turned into raw numbers in our computer, to examine a few of the flat fielding techniques currently 'in vogue' in the infrared imaging community. First the definition of some variables, noting that the majority, except (hopefully) the on-chip integration time, will differ from pixel to pixel:

S	—	the extra-atmospheric source flux
σ	—	the sky flux at the position of the source
σ_1	—	the sky flux at a low airmass (e.g. the zenith)
σ_2	—	the sky flux at a high airmass (e.g. sec z = 2)
T	—	the total warm optical throughput (including sky and telescope transmission)
τ	—	the telescope and warm optics background (independent of airmass)
η	—	the total cold optical throughput (including transmission losses and detector QE)
I_d	—	the detector dark current
t	—	the on-chip integration time
G	—	the electronic gain
O	—	the electronic offset

Next generate some 'images' by combining the variables appropriately. Note, we are considering a linear system, or at least one in which the data can be made linear, following one of the prescriptions described in the previous section:

$$\begin{aligned}
\text{Source frame} &= ((((S+\sigma)T+\tau)\eta + I_d)tG) + O \\
\text{Sky frame} &= (((\sigma T+\tau)\eta + I_d)tG) + O \\
\text{Low airmass frame} &= (((\sigma_1 T+\tau)\eta + I_d)tG) + O \\
\text{High airmass frame} &= (((\sigma_2 T+\tau)\eta + I_d)tG) + O \\
\text{Dark current frame} &= I_d tG + O
\end{aligned}$$

Next consider some of the ways to retrieve the source flux S from some combination of these images. Implicit in the algebra is the fact that we are manipulating the images on an individual pixel basis.

- Optical reduction: A simple version of the technique used for optical CCD data. First, the additive dark current and electronic components are subtracted from the source and flat field frame. Then the source frame is divided by the flat field frame, in this case, an image of blank sky. The critical assumption made here is that the flat field (i.e. the sky) is indeed flat across the field of view (FOV) of the detector:

$$\frac{(\text{Source} - \text{Dark})}{(\text{Sky} - \text{Dark})} = \frac{(S+\sigma)T+\tau}{\sigma T+\tau} \tag{1}$$

  At $\lambda < 2\,\mu$m, $\tau \sim 0$, i.e. there is no flux from the telescope and other warm optics (~ 300 K)—the result reduces to :

$$\frac{(\text{Source} - \text{Dark})}{(\text{Sky} - \text{Dark})} = \frac{S+\sigma}{\sigma} \tag{2}$$

  Usually the flat fielded image is normalised. Multiplying by the mean of a clean area of the (Sky − Dark) image, i.e. $\overline{\sigma T \eta t G}$, images flat fielded by different sky frames can be compared. Noting that σ and $\overline{\sigma}$ cancel

because we have assumed the sky to be flat across the FOV, we obtain:

$$\frac{(\text{Source} - \text{Dark})}{(\text{Sky} - \text{Dark})} \times \overline{(\text{Sky} - \text{Dark})} = \overline{ST\eta tG} + \overline{\sigma T\eta tG} \tag{3}$$

Finally, the sky background is removed. We assumed the sky was flat across the detector FOV, thus we can subtract a mean value, determined either from the source frame itself (if it is not crowded and does not contain low level nebulosity), or from the blank sky frame, if it was taken nearby in space and time. In either case, the mean sky value is algebraically equivalent to $\overline{\sigma T\eta tG}$

$$\frac{(\text{Source} - \text{Dark})}{(\text{Sky} - \text{Dark})} \times \overline{(\text{Sky} - \text{Dark})} - \overline{(\text{Sky} - \text{Dark})}\;\overline{} = \overline{ST\eta tG} \tag{4}$$

For each pixel we have the source flux falling on it multiplied by the mean system throughput and the integration time. The integration time is trivially removed by division, while the system throughput is 'removed' by comparing a given source measurement with that for a standard source, whose absolute brightness is known.

At $\lambda > 2\,\mu$m however, the telescope and warm optical emission τ is *not* zero. Returning to equation 1, the flat field component of the equation becomes $(\sigma T + \tau)$. If τ is flat across the FOV, then the algebra can be retraced to arrive back at equation 4. But, if the telescope and warm optical emission is *not* flat across the FOV, the process is invalidated. As these components are not in the same focal plane as the source, effects such as vignetting can lead to changes in thermal illumination across the FOV.

- Thermal reduction: Used at longer wavelengths, where the telescope and warm optical emission τ is the dominant component of the background, and where τ may well not be flat across the detector FOV. The atmospheric part of the thermal background is a function of airmass, and the telescope/warm optics part τ should not be. Therefore, a flat field is made by subtracting one sky frame taken at low airmass from another sky frame taken at high airmass, removing τ from the problem. The resulting flat field should be flat, if the *a priori* assumption that the sky is flat holds true. The source frame has its sky, τ, and other system offsets removed by subtracting a nearby sky frame; the result is divided by the flat field frame:

$$\frac{(\text{Source} - \text{Sky})}{(\text{High Airmass} - \text{Low Airmass})} = \frac{S}{\sigma_2 - \sigma_1} \tag{5}$$

This is normalised, multiplying by the mean of the flat field, $\overline{(\sigma_2 - \sigma_1)T\eta tG}$. This leads back to equation 4, again with the proviso that $(\sigma_2 - \sigma_1)$ for any given pixel is equal to $\overline{(\sigma_2 - \sigma_1)}$, i.e. that the sky is flat.

This technique is 'more correct' when the warm optical thermal background is a factor. However, the use of four images rather than three will result in slightly higher noise. Also, there may be large enough differences in the emission at low and high airmass (e.g. colour) that the whole technique might fail. Finally, if the thermal emission background structure *is* a function of airmass (e.g. due to flexure), the technique is further invalidated.

- Raw reduction : This technique is fast and easy—a sky frame is subtracted from the source frame:

$$(\text{Source} - \text{Sky}) = ST\eta tG \tag{6}$$

The technique is incorrect, as it does not divide out any multiplicative pixel to pixel differences. However, it is a useful way of obtaining a quick look at the source data. In the limit of a blank field with no source flux, one sky frame is being subtracted from another; all the multiplicative factors and additive factors cancel out. All that is left is noise (shot, read-out, etc.)—thus it is an effective way of looking for minor perturbations near the background, i.e. very faint sources. It should not be used for photometric work, where the source flux is not close to zero.

This list of techniques by no means covers the whole range of possible approaches. For example, a modified version of the 'thermal reduction' can be used at non-thermal wavelengths: a raw sky frame is subtracted from the raw source frame, effectively removing the additive components, such as system offset, dark current, and sky background. The result is divided by a flat field constructed from images of (say) the Moon or the dome, in order to correct for colour dependent effects in the detector quantum efficiency.

Some practical considerations

There are additional subtleties in the flat fielding process. For example:

- The flat field 'colour'—not only will the quantum efficiency be variable from pixel to pixel across the detector, it is also likely to be wavelength dependent. The two effects will probably be correlated if quantum efficiency is related to thickness of the detector material, i.e. the spatial structure of the flat field may be wavelength dependent.

  Therefore, an accurate flat field should not only be flat, but should also be the same 'colour' as the source: a very red source should be divided by a very red flat field, while conversely, a blue source should be divided by a blue flat field. 'Coloured' flat fields are created in the optical by imaging the inside of the dome, illuminated by tungsten lamps covered with a range of colour modifying filters. Also, the twilight sky is observed at different times relative to sunset and sunrise, as the colour of the sky changes [5]. Similarly, 'coloured' flat fields can be achieved in the near infrared: an out of focus image of a lunar mare provides a flat field with approximately solar colours [6], and illuminating the dome with fairly dim tungsten lamps (T$\sim$ 2000–3000 K) will provide an analogue for late type stars. It is more difficult to create a flat field with an equivalent colour of $J-K\sim5\overset{m}{.}0$, or one that matches the colour of the sky seen through narrow band filters, or a Fabry-Pérot étalon: flat fielding these very narrow band images can be tricky. Note that the nighttime sky background from 1–2.5 μm is virtually all line emission, with an effective integrated broad band 'colour' unlike any black-body or dust reddened source [1]. There is a certain circularity in choosing the colour of the flat field source to match the colour of your program objects—there will always be some colour related errors in flat fielding process.

- Stacking sky flats—if a number of sky images are obtained during the night for use as flat fields, they can be stacked to create a master flat, with higher signal to noise. At broad band near infrared wavelengths (J,H,K), making a master flat out of sky images taken up to an hour either side of the source frame can yield the expected reduction in residual noise after flat fielding. However, adding in data from outside this time frame, the residual noise starts to increase again. This is not unexpected—the the OH* emission component of the sky background can change by 50% on time scales of a half hour, and in addition, changes in sky background will occur as the telescope changes in airmass. Intensity changes are usually accompanied by colour changes, reducing the effectiveness of the stacked flat field. Long term drifts in instrumental parameters such as electronic gain, dark current, and detector temperature, can also make it undesirable to stack a whole night's sky flats. Little is gained by combining more than ~ 5 individual skies to create a master flat—beyond that, only about another 10% reduction in residual noise will be obtained.

How accurately can we flat field?

The accuracy that can be achieved in the flat fielding process depends largely on the definition of "accuracy", and to illustrate this we shall examine two extreme cases:

- Residual background noise—in the case of deep searches for very faint sources, the aim is to reduce the pixel to pixel noise over relatively limited regions of the array, in order to spot small enhancements above the noise. Gross structures across the field are not important if they have a much larger scale size than the faint objects being sought. The limiting case is blank field, which is just an image of the sky background. The best flat field in this case is an image of another piece of blank sky, taken nearby in both space and time. In the limit, source frames can be used to flat field themselves. After each image is read out, the array is moved on the sky by an amount somewhat larger than the objects being searched for. Provided real sources fill no more than about one third of each image, a master flat field can formed by taking the median for each pixel through the images stacked directly on top of one another. Each source frame is divided by the master flat, registered up on common objects, and co-added to provide a master image. This approach has been used to locate very faint galaxy populations, both with optical CCDs [7], and near infrared arrays (McLean, private communication). A residual noise of less than 0.01% of the sky background can be achieved.

- Photometric uniformity—program sources and standard stars may fall on different parts of the detector array, and accurate measurement of their relative brightnesses will depend on the large scale uniformity, including vignetting, image ghosting, and colour sensitivity differences across the array. Intra-pixel variations

may also be important. Taking a large number of images of a standard star, each time moving the star to a slightly new position on the array, the total flux can be measured at each new position, and the degree of photometric uniformity across the array can be derived. Using a number of flat fielding techniques involving coloured dome flats and images of the twilight sky, uniformities on the order of 3% have been measured using this technique (Forrest, private communication).

Flat fielding techniques used to achieve the very lowest small scale pixel to pixel noise might not result in the best photometric uniformity, and conversely, the technique that best corrects for photometric non-uniformities might result in increased pixel to pixel noise in the background. Different techniques may be applicable depending on the experimental goal.

3.3 Mosaic making

Making large scale mosaics out of many smaller images is an effective way of showing the large scale structures in a region at seeing limited spatial resolution, previously almost impossible in the infrared. Although mosaic making should be reduced in importance with the advent of much larger format arrays, the use of $\sim 64 \times 64$ pixel arrays is likely to continue for a few years yet. Also with no equivalent to the combination of Schmidt telescope and photographic plate, the infrared astronomer will still want to make mosaics even when 256×256 pixel arrays are common.

Positional offsets

Few telescopes can offset with an accuracy equal to one seeing limited pixel ($\sim 0.5''$), and therefore, for accurate mosaicing, there should be overlap between adjacent images to allow registration on common objects. Point sources are most effective—centroids can be defined to better than 1/10th of a pixel if fully sampled. In the absence of point sources, extended regions of nebulosity can be used, but will result in lower accuracy registration.

The calculation of positional offsets is trivial: common sources can be manually identified on an image display, their centroids found, and offsets derived. Alternatively, more sophisticated automatic cross correlation procedures can be used, searching for the best fit offset around a box centred on the nominal offset position.

Sky background and transparency changes

These effects can be difficult to remove; one is additive, the other multiplicative. One possible approach is as follows: once the positional offset between a pair of images has been calculated, two intensities for any given point on the sky in the overlap region can be obtained, one from each image. By plotting pairs of values as x and y, a straight line should result (see figure 5). The intercept on the y-axis determines the difference in additive sky background, and the slope determines the relative change in the multiplicative transparency.

To produce a well defined straight line, a large dynamic range is needed, i.e. pairs of points measuring both faint and bright sources in the overlap region. If there *are* bright sources in the overlap region, they will usually be stars. Unless images are accurately registered to significantly less than one FWHM, stars will not exactly overlap, and the plotted value pairs will not be well correlated. Registering fully sampled images to less than one FWHM requires shifting to a fraction of a pixel—the interpolation required will propagate bad pixels. In many situations, only faint sources and nebulosity close to the sky background will be imaged, resulting in a much less correlated plot—see figure 6. Making an accurate linear fit in this situation is more difficult.

A less direct approach can be taken. Regular measurements of a nearby blank field for flat fielding purposes will also monitor changes in the sky background. Time interpolating, the background component of each source image is calculated and subtracted. Regular measurement of a nearby isolated standard star monitors transparency changes, removed by multiplication. Applying these externally calculated corrections, mosaic images usually are reasonably well matched—any small residual offset is assumed (perhaps erroneously) to be additive and is calculated from the mean difference between overlapping pixel pairs.

It is hard to write infallible automated software to perform these tasks alone. Once the first order corrections have been automatically applied, the resulting mosaic should be manually inspected for joins, and the necessary corrections applied to remove them. The human eye is very sensitive to edges—in practice, intensity offsets as small as 0.5σ can be spotted when mosaicing fields with gaussian noise distributions, standard deviation σ.

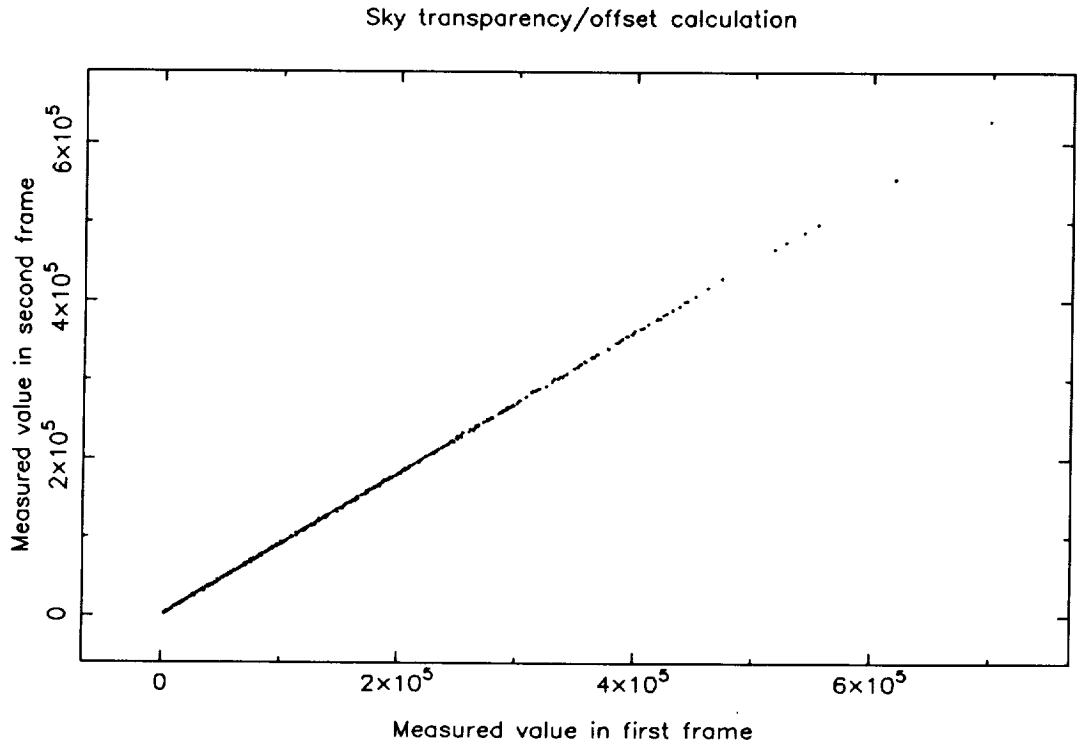

Figure 5: Background and transparency matching--the ideal case

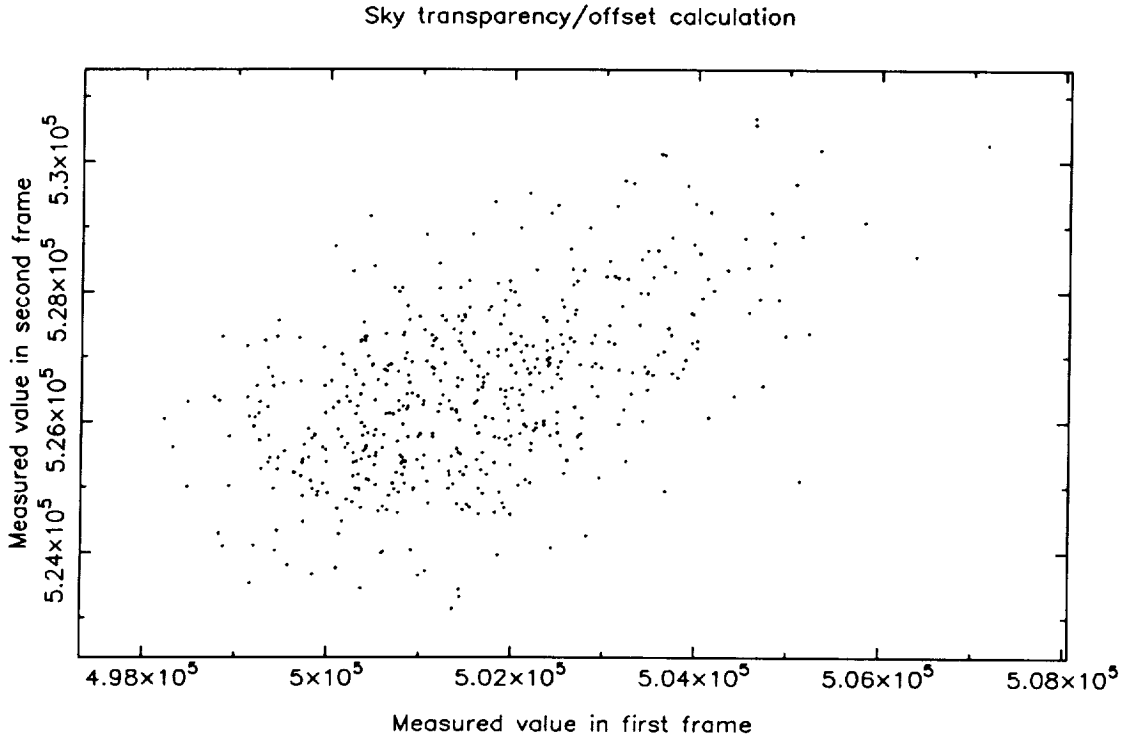

Figure 6: Background and transparency matching—a more typical case

Combining pixel values

To calculate the intensity of each point on the sky, the mosaic can be considered as a series of photographs laid down on top of each other, the value for each point just being the value of the corresponding pixel in the last image laid down. However, this wastes the information in any pixels 'covered up' by images laid on top of them.

A better method is to take the mean in the z-direction, i.e. for any given point on the sky, take the mean of the values in the corresponding pixels in all the images that cover that point. If two images both cover a given region, a $\sqrt{2}$ signal to noise gain would be expected; three overlapping images should yield a gain of $\sqrt{3}$, and so on.

If there is incomplete overlap, taking the mean and increasing signal to noise in the areas that *are* covered more than once may result in a patchy looking mosaic, some areas having higher signal to noise than others—a factor of $\sqrt{2}$ difference is readily discernable. A fully overlapping mosaic scheme as shown in figure 1 will avoid this problem.

The mean can be skewed by bad pixels, of which there are two kinds: fixed ones, which are always bad; and sporadic ones, which can crop up anywhere at any time. The former might be 'leaky', 'dead', or might not flat field properly: they can be catalogued, and a 'bad mask' or 'bad pixel list' used to flag them, and exclude them when calculating the mean. A sporadic bad pixel might be due to a cosmic ray hit or electronic glitch, and are less easily dealt with. If they are infrequent, they can be ignored, included in the mean, detected in the final mosaic, and then suitably replaced. This works well if the image scale fully samples the seeing—single pixel events are easily identified as bad. In undersampled modes where stars may appear as single pixels, this approach can be dangerous.

Taking the median rather than the mean of the pixel values in the z-direction will remove sporadic bad pixels. However, for a gaussian distribution, the mean is a better estimator of the true value than the median, and for small numbers of overlapping frames (< 10), the mean will result in a greater improvement in signal to noise.

Another form of 'bad data' can occur, more insidious than the isolated single pixel event. Infrared cameras have relatively complex optics, and there is a possibility of ghost images and other diffuse features being generated, perhaps near to a bright source, or perhaps far from it, depending on the optical scattering paths. Although these spurious 'sources' are often easily recognised by their peculiar shape, sometimes they are not. A fully overlapping mosaic scheme proves invaluable in detecting and replacing them—any any source that only appears in one frame of an overlapping pair can be considered spurious. Flagging the pixels containing the spurious 'source' as bad, good data from the overlapping image can be used to 'patch' the final mosaic. Mosaic schemes using only a small overlap make it more difficult to detect and remove these undesirable features.

An example

The best scheme will depend on the data being combined. Compromise approaches may be appropriate, with bad masks used to identify fixed bad pixels, a median technique to identify sporadic ones, and flagging to identify spurious 'sources'; after all types are rejected, the mean of the remaining pixels can be used to calculate the final value.

As an example, take a mosaic of 145 2.2μm images of the Trapezium cluster in the Orion Nebula, obtained using the mosaic scheme shown in figure 1. Further details are given in section 3.4. Figure 7 shows the result of taking the mean at every pixel, with no regard to bad pixels. Even the fairly clean SBRC InSb+DRO array used for the experiment results in quite a mess when mosaiced. However, figure 8 shows the result of throwing a switch in the mosaic making software, telling it to account for known bad pixels. Bad data in one image was replaced with good data from another overlapping one; no replacement by artificial data has taken place. The effect is dramatic, with only a few bad pixels remaining, some scattered, and some near the edge of the mosaic, where each point on the sky was imaged once only—the effectiveness of a fully overlapping mosaic scheme is well demonstrated.

3.4 Overlaying multiple images

A 'true-colour' composite image can be created by superimposing three images taken through different filters, representing one each as blue, green, and red, usually in increasing wavelength order. The technique has been extensively applied in the optical, to both photographs [8] and CCD images [9], and has already found popularity

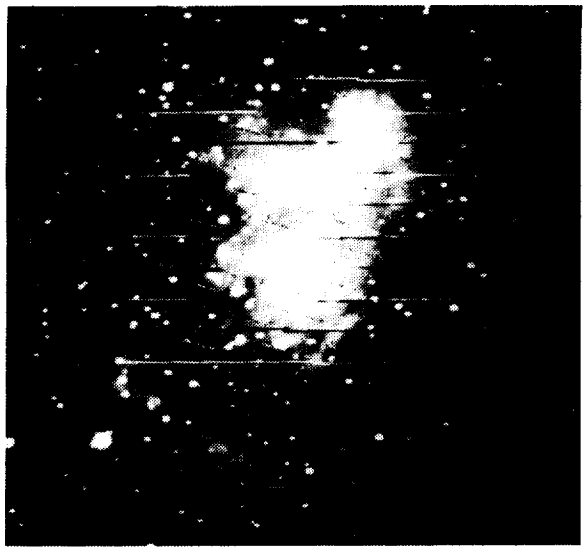

Figure 7: No bad pixel handling

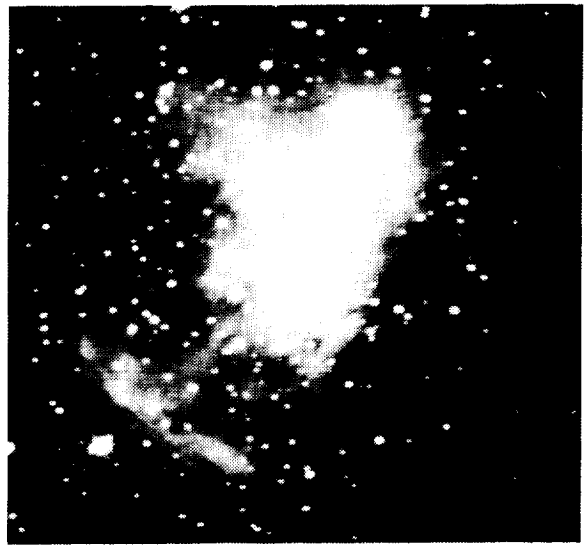

Figure 8: Automatic bad pixel handling

in the infrared imaging community, as it can graphically reveal cool and reddened sources, and regions of increased extinction.

- Pixel scale—the pixel scale may be wavelength dependent if transmissive reimaging optics are used, and images taken at different wavelengths should be resampled on to a common pixel scale. With a number of bright point sources common to each image, the relative pixel scales can easily be determined—otherwise, a large scale mosaic can be used. At longer infrared wavelengths, few point sources are visible at all—the problem of determining absolute and/or relative pixel scales is harder.

  The relative difference in pixel scales may only be $\sim$ a few percent and is often overlooked, particularly if a image contains only one point source and some diffuse emission. Ignoring the pixel scale difference could lead to systematic errors when deriving the radial dependence of the nebular $J-K$ colour, for example—the images should be resampled to a common pixel scale first.

- Dynamic range compression—the dynamic range in infrared images can be very large, and effectively displaying bright point sources and faint nebulosity in a single image sometimes requires non-linear compression. Logarithmic compression is often used, although square, cube, and higher roots of the data have been found empirically to give the necessary compression without reducing contrast quite as much. In some cases, techniques such as histogram equalisation may be useful—these account for the actual numerical distribution of bright and faint data points in a given image, redistributing them across the dynamic range more evenly.

- Intensity scaling—choosing the relative intensity scaling levels for the multiple images is as much an aesthetic issue as scientific. In the visible, the 'true-colour' technique is usually used to create a colour image of a source as it would be seen by the human eye if the retina was more sensitive to low flux levels, while maintaining the same general colour balance it has at high flux levels [8]. However, extrapolating the technique to the infrared, there is no point of reference for how an infrared sensitive eye might perceive 'colours'. For example, what should be forced to come out looking white in a composite? An object with equal flux in detected photo-electron units through each filter, or one with equal extra-atmospheric photon units, i.e. accounting for the total system throughput at each wavelength? Many regions imaged in the infrared have a large amount of dust extinction towards them—the dust could be effectively 'stripped away' by skewing the intensity scaling according to how much each filter is affected by extinction. The flux from stars is predominantly black-body continuum, and the 'colour' of a star in a composite can be physically meaningful. However, extended emission is often due to a complex combination of continuum and line,

reflected and intrinsic, molecular and atomic, and the amount of extended emission seen through each filter will have more to do with which lines happen lie within its bandpass, rather than some simpler diagnostic, e.g. the gas temperature.

An example

Each case must be treated separately. As an example of how a reasonable compromise may be reached, take the colour composite image of the Orion Nebula shown in figure 9.

The data were obtained by myself and Colin Aspin using the common-user 1–5 μm camera IRCAM on the 3.8 m United Kingdom Infrared Telescope, during the week 24–31 December 1987. IRCAM uses 62 x 58 pixel SBRC InSb+DRO array—additional details of this instrument are given elsewhere [10]. A 145 position mosaic scheme was used, as shown in figure 1: the image scale was $\sim$ 0.62 arcseconds per pixel, and the total mosaic covers a 5 x 5 arcminute region centred on the Trapezium OB association. Each position was observed at J, H, and K before moving to the next. Nearby sky frames were taken after every third mosaic position, and standard stars were monitored frequently.

The data were reduced using the 'optical' technique described in section 3.2, with stacked sky images used as flat fields. Positional and intensity offsets were calculated from the image overlaps, and the sky and standard images. The full reduction procedure will be discussed elsewhere, as will the results of imaging photometry of the almost 500 members of the Trapezium cluster [11].

The three raw mosaics were overlaid on a 24-bit colour image display, one each in the red, green, and blue planes. They were registered at the mosaic centre (the brightest Trapezium star, θ^1 Ori C), and the relative pixel scales were calculated from positions of a number of stars around the edge of the mosaic. The three images were bilinearly interpolated to a common pixel scale.

Each image has a dynamic range of about 4000—displayed linearly to show the structure in the nebulosity, the region surrounding the Trapezium OB stars becomes completely saturated, and displayed to show detail in the Trapezium, the nebulosity is almost invisible. Taking the $\sqrt{}$ of each pixel intensity shows the Trapezium and nebular structure simultaneously, while retaining a reasonable amount of contrast in the fainter nebular structure.

To give a wide colour differentiation among the stars, the high intensity scaling levels were chosen such that a star came out white if its $J-H$ and $H-K$ colours were equal to the mean stellar colours of normal cluster members. These mean colours are roughly $1^m.1$ and $0^m.7$ respectively. The low intensity scaling levels were set to make the south-west corner of the composite come out black. While somewhat arbitrary, it has the effect of giving most of the nebulosity a bluish tinge, consistent with much of the emission in the region being hot thermal continuum from the ionised hydrogen gas, at an electron temperature around 10^4 K, and brightest through the J filter.

The chosen display levels give the desired effect—there is a reasonable spread in stellar colours; the hot OB stars appear blue-white; most of the optically visible stars, known to be mostly young late types with some reddening towards them appear white; and the 'infrared' stars (i.e. those not seen at optical wavelengths) appear various shades of yellow, orange and red, depending on stellar type, extinction, and evolutionary status. The HII region nebulosity appears bluish, while reflection nebulosity around the embedded BN-KL complex, and molecular hydrogen emission from beyond the bar and outside the HII region are seen as reddish.

4 Data Analysis

Having arrived at the 'final' image, the next stage is to determine the brightness of sources, point-like and diffuse, within the image. There are two distinct components to this process—the measurement of the 'instrumental' flux from the source, and the conversion of those units to a standard system.

4.1 Measurement of source flux

The technique required to measure the flux from a 'source' in instrumental units such as ADUs or electrons, will depend on the type of source, its surroundings, and the desired accuracy. Sources might be point-like (e.g. stars), or extended (e.g. reflection nebulae, galaxies); they might be isolated, or confused, in a crowded cluster; there might be just sky beneath the source, or it might be embedded in structured nebulosity. Much of the following discussion will concentrate on point source measurement—this is the hardest to do accurately. In this context,

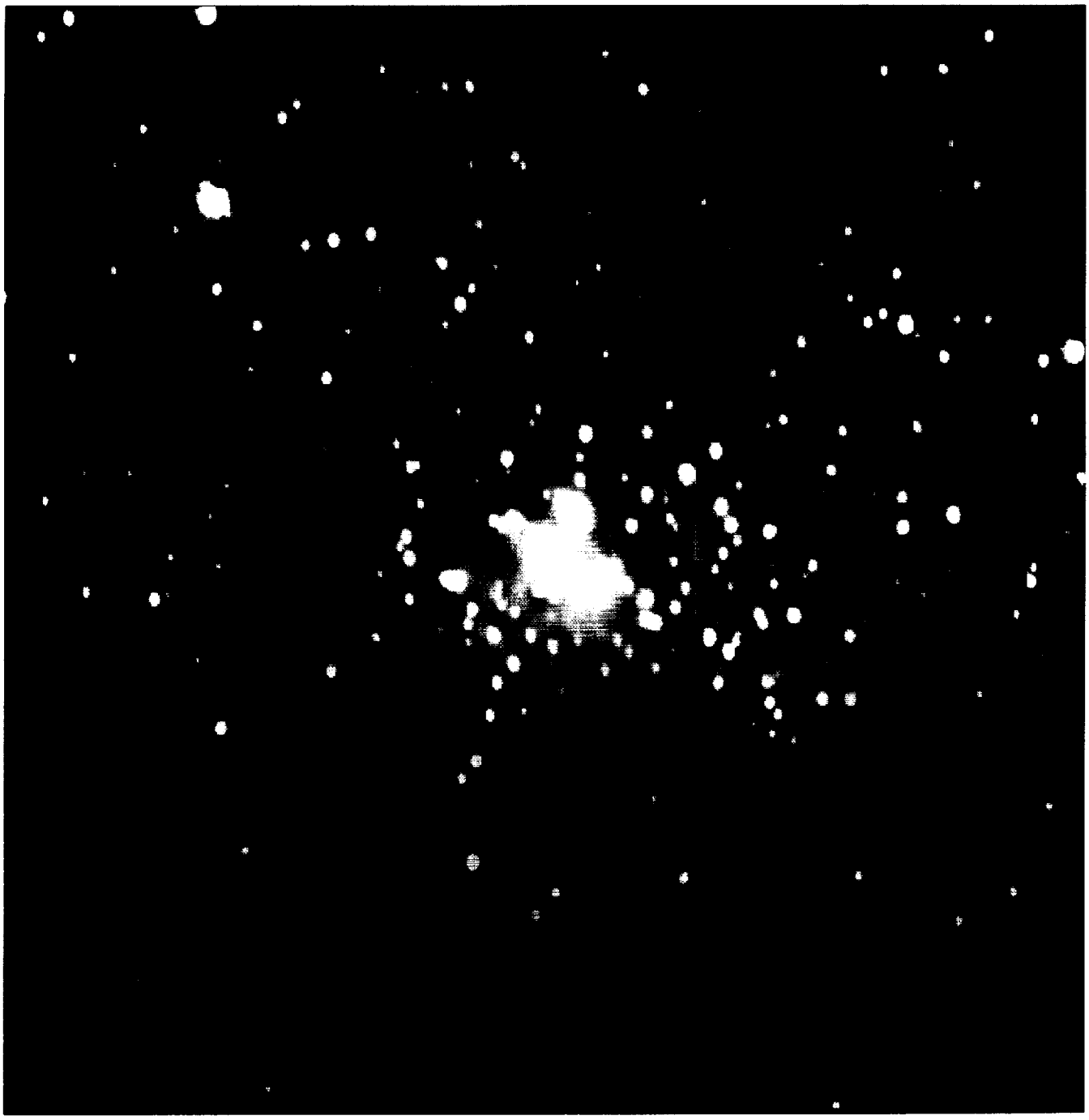

Figure 9: The Orion Nebula in the Near Infrared

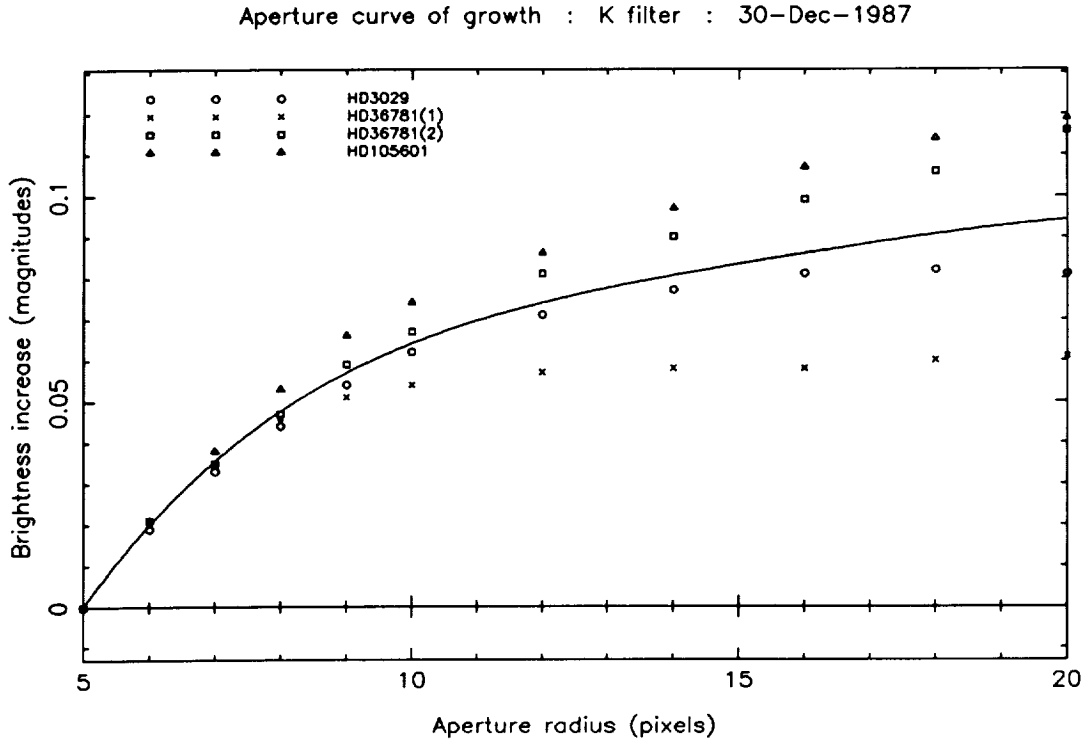

Figure 10: An example aperture curve of growth

'accurate measurement' implies errors $\sim$ a few percent, the best routinely achieved by conventional photometry, and the level at which many subtle systematic and random errors can crop up.

Software aperture

This technique simulates a single element photometer system, in which all the flux falling within a given aperture is added together. A software aperture can take a variety of shapes and sizes, and can be carefully chosen to avoid contamination by fainter nearby objects. Another software aperture placed elsewhere in the image is used to calculate the sky and/or nebular component—this necessarily assumes that these latter components are the same at both the on-source and off-source positions.

For extended emission, this technique can be very useful—the only real alternatives are contour maps or calibrated grey scale images. Software apertures are also often used to measure point sources, and there the technique must be more critically regarded.

Some finite sized aperture is used to measure the flux from a point source. However, for any reasonably small radius aperture ($\leq$ 5 arcseconds), some flux will remain unmeasured outside the aperture. The difference between the flux measured through the finite sized aperture and the 'total flux' from the point source as would be measured through an infinite diameter aperture is derived from the aperture 'curve of growth' (COG).

Unfortunately, changes in the seeing can badly affect the COG. Seeing profiles measured with solid state imaging devices can be well represented analytically by a Lorentzian, with a narrower core yet more extended wings than given by the more usually assumed gaussian profile—as the seeing gets worse, more flux is seen in the wings of the profile [12].

Figure 10 shows COGs derived from measurements of standard stars during one night of observing. The wavelength and camera focus were the same for all measurements, and none of the standards have faint companions. All the curves have been normalised to pass through zero at an aperture radius of 5 pixels—the diagram only shows the increase in flux beyond that point, not the amount contained in the core. The data marked by crosses and squares represent two measurements made of the same star some four hours apart in time. The cross data show an increase in measured magnitude out to an aperture radius of about 12 pixels ($\sim 7.5''$), beyond which

not much increase is seen. The square data however, show a continuing increase out beyond a radius of 20 pixels ($\sim 12.5\hat{''}$). At this point, the difference between the two curves is about $0^m.07$, i.e. about 7% in flux terms. For reference, the conventional seeing parameter, the FWHM of the point source profile, was $\sim 1.45\hat{''}$ for the cross data, and $\sim 1.55\hat{''}$ for the square data, a small change.

Therefore, if a small aperture is used to measure program stars, the correction to an infinite diameter aperture could easily be several percent out, if calculated from a COG derived from a standard star measured under only slightly different seeing conditions.

The larger the arrays become, the lesser this problem. If all the program stars can be measured on one image, seeing changes will matter less—all stars will need the same aperture correction, and any error in the COG derived from a standard star measurement taken at another time will only result in a systematic shift in the program star magnitudes. With small arrays, only a limited number of sources can be measured at any one time, and seeing variations from image to image will create random errors, a worse situation.

In a crowded field, the measurement aperture for any given star will occasionally also include flux from nearby stars. The error for any given star is random—some stars will have nearby companions, some will not. The overall effect is systematic however—flux from another source included in the aperture can only increase the calculated brightness, and averaged over a whole crowded field, the stellar frequency function will appear systematically bright.

Point spread function (PSF) fitting

The technique of choice for crowded field point source photometry is PSF fitting, the best known example of which is Peter Stetson's DAOPHOT package [13]. The technique assumes that all point sources within an image have the same PSF, and that bright and faint stars only differ by a linear intensity scaling of the same profile.

The PSF is defined from the mean profile of a few fairly bright, well isolated stars in the image. All other point-like sources in the image are identified, either automatically or by hand—aperture photometry provides a first approximation to the stellar brightnesses. A model of the point sources in the image is generated from a series of overlapping PSFs, and the brightness and position of each model star is varied until the resulting structure converges in its similarity to the original image. All but a few bright stars are subtracted from the image—aperture photometry performed on the latter provides a normalisation between the profile magnitudes and large diameter aperture photometry. At that point, comments applied to software aperture photometry become relevant again.

Well tried and tested on optical CCD data, the PSF fitting technique has been applied to infrared imaging data with limited success. The main pit falls are as follows:

- One of the underlying assumptions of PSF fitting photometry is that the PSF is the same for all stars being fitted. Due again to the limited size of the current detectors, only a small number of stars can be seen in any one image, and at least one of those stars must be used as a template PSF. Combined with the effects of bad pixels, this makes it likely that a large scale mosaic will be used. However, as the individual mosaic images are taken sequentially, the PSF will not be the same across the mosaic. Also, making a mosaic where multiple images of the same star are co-added in an overlap region, the resulting stellar profile will be further distorted. Even if every individual field had one isolated bright PSF template star and a small group of crowded program stars, problems with the final aperture corrections still apply, as standard stars will have been measured at a different time, with a different curve of growth.

- Another assumption made when PSF fitting is that the background underneath the stars is flat, or at the very worst, uniformly varying on a large scale. Due to the very nature of infrared astronomy, many regions have bright emission and reflection nebulosity associated with point sources—the nebulosity can seriously affect the point source PSF fitting. Modified procedures are needed to account for both the stellar PSF and a structured background beneath the star.

- The limited size of current arrays, and the desire to image very faint low surface brightness sources often leads to the use of images scales of $1\text{–}2\hat{''}$/pixel, undersampling the seeing. For PSF fitting photometry the seeing must be fully sampled, and pixel sizes in the range $0.2\text{–}0.5\hat{''}$ are optimum. In the background limit, which is almost always achievable by on-chip integration, the only thing that large pixel scales buy is field of view. With the current generation of detectors, field of view *is* at a premium, but the use of heavily undersampled pixel scales will probably decrease as infrared arrays grow in size.

Contour maps and grey scale images

For regions of extended emission, contour maps are the most effective way of showing the calibrated intensity in terms of flux per unit surface area. By comparing the total measured signal from a standard star with its known flux, it is easy to convert an image from instrumental units to flux units on a per pixel basis. However, contour maps can be difficult to 'read' if there is small scale structure (e.g. stars) in the extended emission, and a grey scale image can show these details more effectively, and still provide a reasonable indication of the surface brightness, with an accompanying calibrated intensity wedge.

4.2 Conversion to a standard system

To make meaningful astrophysical deductions about sources in the images (e.g. equivalent black-body temperature, stellar type, evolutionary status, dust extinction), fluxes measured in instrumental units must be converted to a 'standard system'.

As well as using standards as zero-points, colour terms should be considered. These terms can be quite large even for transformations between single element photometers: a highly reddened object with a $J-K$ of $\sim 5^{\rm m}.0$ on the AAO system would have a colour of $\sim 4^{\rm m}.5$ on the CTIO system, a significant difference [14]. Infrared imaging systems are quite different to their predecessors, the single element photometers—re-imaging mirrors may be used; new large diameter infrared filters are being used; the detector material may be anti-reflection coated, or made of a material such as HgCdTe, little used in single element photometers. Thus, the 'colour equations' for infrared imaging systems might be quite different to those determined for the single element detector systems.

Correspondingly, measurements of a number of standard sources, both bright and faint, and both blue and red will be required to accurately calibrate infrared imaging data. Bright sources can be found in the usual lists of photometric standards, such as those of Elias *et al.* [15]. These stars are typically $\sim 7^{\rm m}.0$ at K, and rapidly saturate array cameras on large telescopes. If instrument systematics such as non-linearity are taken seriously, standards much closer in brightness to the program objects are required, certainly as faint as $K=10^{\rm m}.0$–$12^{\rm m}.0$, and perhaps even as faint $K=15^{\rm m}.0$–$17^{\rm m}.0$. Some limited work has been done using faint white dwarfs, but it would be extremely useful if a consortium of faint standards could be developed, perhaps based on a homogenised system (e.g. [16]).

4.3 Measurement errors

There are a number of ways in which systematic and random errors can creep into the measurement of a point source before it is finally placed on the HR diagram, for example. Considering the number of steps involved in reducing and analysing infrared imaging data, some of which have been discussed in this paper, cumulative errors $\sim 10\%$ in the magnitude of a star, and errors $\sim 15\%$ in its position on an HR diagram seem likely at this time. In addition, it is likely that imaging photometry with the current generation of detector arrays will involve mosaic making, and errors due to changes in seeing and aperture curves of growth, and residual errors in additive and multiplicative intensity corrections, should also be considered.

As an object lesson in quite how hard imaging photometry can be, it is worth reading the recent paper on optical CCD photometry of the globular cluster M92 by Stetson and Harris [5], in which they painstakingly analyse the errors that arise in converting raw images into calibrated luminosity functions, quoting a final accuracy in their tie in to a standard system of $\pm 1\%$. Bearing in mind that optical CCDs have been in serious astronomical use for over a decade, there are undoubtedly many lessons yet to be learned about obtaining accurate calibrated photometry with infrared imaging arrays.

5 Conclusions

In this paper, I have drawn on my own experiences in infrared imaging, mainly using the UKIRT 1–5 μm camera, IRCAM, and its 62 × 58 pixel SBRC InSb+DRO array. I have only covered some of the possible approaches to acquisition, reduction, and analysis, those most suited to the kinds of data I myself have obtained. Hopefully, I have made some points of a general enough nature to provoke deeper thought about the techniques currently being developed throughout the field.

The most important point to reinforce is that obtaining accurate data from infrared arrays is not easy, and that we must be prepared to expend considerable energy in extracting the undoubtedly exciting new information that will result from the introduction of imaging into infrared astronomy.

Acknowledgements

I would like to thank Craig McCreight for allowing me to insert this talk into the busy workshop schedule at such late notice, and for allowing me to expand considerably in print on the topics I tried to cover at breakneck speed in ten minutes at the meeting itself.

I would also like to thank the staff of the Royal Observatory Edinburgh and the United Kingdom Infrared Telescope for building such a versatile near infrared camera, IRCAM. Discussions with numerous members of the infrared astronomy and detector manufacturing communities have proved invaluable in revealing many of the subtler aspects of infrared image reduction and analysis, and I would particularly like to thank Ian McLean and Colin Aspin for their comments on this paper.

REFERENCES AND NOTES

[1] M. J. McCaughrean. PhD thesis, University of Edinburgh, 1988.

[2] J. L. Vampola. Internal Memorandum 2118-244, Santa Barbara Research Center, September 1982.

[3] M. H. Minshull and S. E. Botts. Internal Memorandum 2113-020, Santa Barbara Research Center, November 1984.

[4] A. W. Hoffman. In C. G. Wynn-Williams and E. E. Becklin, editors, *Infrared Astronomy with Arrays*, pages 29-35, Institute for Astronomy, University of Hawaii, 1987.

[5] P. B. Stetson and W. E. Harris. *Astron. J.*, 96:909-975, 1988.

[6] W. J. Forrest, A. Moneti, C. E. Woodward, J. L. Pipher, and A. W. Hoffman. *Pub. A. S. P.*, 97:183-198, 1985.

[7] J. A. Tyson. *J. Opt. Soc. Am. A*, 3:2131-2138, 1986.

[8] D. F. Malin and P. Murdin. *Colours of the Stars*. Cambridge University Press, 1984.

[9] R. E. Schild. *Sky and Telescope*, 75:144-147, February 1988.

[10] I. S. McLean, T. C. Chuter, M. J. McCaughrean, and J. T. Rayner. In D. L. Crawford, editor, *Instrumentation in Astronomy VI*, pages 430-437, Proc. SPIE vol. 627, 1986.

[11] M. J. McCaughrean, C. Aspin, H. Zinnecker, and I. S. McLean. *Ap. J.*, 1989. In preparation.

[12] F. Diego. *Pub. A. S. P.*, 97:1209-1214, 1985.

[13] P. B. Stetson. *Pub. A. S. P.*, 99:191-222, 1987.

[14] M. S. Bessell and J. M. Brett. *Pub. A. S. P.*, 100:1134-1151, 1988.

[15] J. H. Elias, J. A. Frogel, K. Matthews, and G. Neugebauer. *Astron. J.*, 87:1029-1034, 1982.

[16] J. Koornneef. *Astron. Astrophys. Suppl. Ser.*, 51:489-503, 1983.

Discovery of Low Mass Objects in Taurus

W. J. Forrest, Z. Ninkov, J. D. Garnett
University of Rochester
M. F. Skrutskie
University of Massachusetts
M. Shure
University of Hawaii

Abstract: An infrared (2.2μm, K-band) search of small regions (25″ square) near 26 members of the Taurus star-forming association has revealed 20 dim (K = 13-16 mag) stellar objects near 13 of them. Of these 20 objects, 9 are exceptionally red. It is argued that these 9 are probably also Taurus members. From the luminosities ($0.8 - 4 \times 10^{-3} L_{\odot}$) and ages (estimated at 10^6 years), masses can be determined by reference to theoretical low-mass cooling curves. The masses are in the range 0.005-0.015 $M_{\odot}$, i.e. low-mass brown dwarfs. Proper motion studies of 7 of the objects visible on the POSS plates conducted by Burton Jones establish that 4 are highly probable Taurus members while 1 is a possible member.

I. Introduction

The theory of self-gravitating gaseous bodies predicts that below a mass of about 0.08 $M_{\odot}$, the central temperatures will never be high enough to initiate stable nuclear burning. These sub-stellar objects, which subsist on gravitational energy and cool eternally, have been dubbed brown dwarfs (Tarter, 1986). To date, there are no unambiguous indentifications of a bona-fide brown dwarf, though there are several candidates which are either low mass stars or high mass brown dwarfs, depending on their precise ages. It is of great interest to know if brown dwarfs do exist in the galaxy and, if so, how many there are and what are their masses. A sufficient population of brown dwarfs could represent a large mass which is dim visually. This would have enormous implications for the "missing mass" problem in our galaxy and perhaps others.

Previous searches for brown dwarfs have concentrated on objects ranging in age from $\sim 10^8$ to 10^{10} years. At these advanced ages, brown dwarfs will be cool and dim, especially low mass brown dwarfs. Therefore such searches require high sensitivity to cool objects and will be most sensitive to higher mass brown dwarfs. At very young ages, however, even relatively low mass brown dwarfs of 0.01 $M_{\odot}$, will be relatively luminous. Furthermore, because of the nature of the Hayashi evolutionary tracks, dominated by convection internally and H^- radiative opacity at the surface, the effective temperatures will be relatively high, around 2500 -3500 K in the early stages of evolution. For instance, a 0.01 $M_{\odot}$ brown dwarf 10^6 years old will have a luminosity of $\sim 1.6 - 1.8 \times 10^{-3} L_{\odot}$ and an effective

temperature $\sim 2300 - 2600$K (Nelson *et al.* 1986, Lunine *et al.* 1989).

Based on these ideas, we searched in the vicinities of 26 T-Tauri stars in the Taurus star-forming association. A total of 20 dim (apparent K magnitude 13-16) objects were discovered near 13 of the T-Tauri stars. Of these 20, at least 9 were exceptionally red. We argue that it is extremely unlikely that the red objects could be foreground or background stars and are therefore probably also members of Taurus. Assuming ages equal to the average age of Taurus members (10^6 years) and using the above theoretical evolutionary curves, we estimate masses of $0.005 - 0.015 M_\odot$ based on the observed luminosities.

The key question of true Taurus membership has received strong support from the proper motion studies of Burton Jones (1989, private communication). Of the seven objects visible on the mid-1950's POSS red plates, he has found 4 to have proper motions which indicate Taurus membership and rule out a background star. We conclude that the bulk of the red stars really are Taurus members and therefore low mass brown dwarfs as calculated above.

II. Observations

Infrared observations of 26 T-Tauri stars in Taurus were made at the NASA 3.0m Infrared Telescope Facility on Mauna Kea on 6 nights in September, 1988 using the Rochester 58×62 InSb infrared camera. (This project had not been granted offcial observing time, so a small amount of time, amounting to one night total, was borrowed from other approved projects for this run.) Our procedure was to place the T-Tauri star in the center of the $25''$ square field-of-view of the camera. Then the telescope was nodded to presumed blank sky, usually 100-200″ S, to acquire a background frame. The telescope was then nodded back to the T-Tauri star and 2 exposures of 33 seconds each in the photometric K-band ($\lambda_o = 2.23\mu$m, $\Delta\lambda = 0.41\mu$m) were acquired. The images were inspected by subtracting the background frame and displaying them on a video monitor with display levels set to reveal the dimmest possible object. A stellar object near the T-Tauri star was seen as a bright (positive) image, while a stellar object in the sky frame was seen as a dark (negative) image. We estimate a limiting magnitude of circa 16 for definite detection of positive stars and somewhat brighter for negative stars.

If a positive star was seen, measurements in the H ($\lambda_o = 1.65\mu$m, $\Delta\lambda = 0.32\mu$m) and J ($\lambda_o \cong 1.25\mu$m, $\Delta\lambda \cong 0.21\mu$m) bands were also acquired. In addition, if the original telescope position placed the newly discovered object in a bad part of the array, either near the edge or near the crack in the southeast corner, the telescope was moved to re-position the source more optimally. In most cases, a negative star, i.e. one present in the distant sky beam, was not followed up with J and H photometry unless a positive star was also present. On some occasions, our sky beams were positioned only $24''$ from the main beam. In these cases, negative stars were measured in all bands.

A typical 2.23μm image is shown in figure 1. The $K \sim 13$ mag stellar object $8''$ S of LkCa 4 was first seen. Moving the telescope for better viewing revealed the second $K \sim 14$ mag stellar object $13''$ W of LkCa 4. In this case, a $75''$ square region surrounding LkCa 4 was also surveyed, to a limit of $K = 15 - 16$ mag. No further stellar objects were found.

The images were processed as follows to derive photometric magnitudes. First, as discussed by Forrest *et al.* (1989, this conference), the output of the array is inherently non-linear. Data, both source and background images, were therefore first linearized as described in Forrest *et al.* (1989). After background subtraction, the pixel-to-pixel nonuniformities were eliminated through division by a flat field. We considered candidate flat fields (linearized) from the blue morning or evening sky and the inside of the dome illuminated by five $1000W$ incandescent light bulbs. There was very little difference between any of the flat fields taken throughout the run. We tested the photometric performance of the flat fields by imaging standard stars at 25 grid positions on the array. Using a combination of dome and blue sky flat fields, the best photometric performance was a standard deviation of 4.5% of the average. As discussed in Forrest *et al.* (1989), we attribute a large component of the variation to pincushion distortion in our reimaging optics. After correcting the flat field for this effect, the variation improved to 2.6% at K. The uncertainty due to flat fielding will be somewhat higher at J and H.

Standard stars were observed throughout each night for calibration purposes. Measurements in a synthetic octagonal aperture 4.6″ in diameter indicated quite stable values in the J, H, and K bands. The companions were often very faint, ranging down to a J magnitude of 17. For accurate photometry, a method of estimating the total signal from the star without contribution from nearby sky signal was developed. An octagonal aperture 3.8″ in diameter was centered on the companion. The outer annulus 0.42″ (one pixel) wide was used to estimate the sky level. This surface brightness level (counts per pixel) was subtracted from the inner octagon, 2.9″ in diameter, to give the total star signal. This method of differential photometry is dependent on the seeing, which will smear true star signal into the sky annulus. Measurements on the standard stars indicated a ±2% uncertainty at H and K and ±5% uncertainty at J due to this effect.

We estimate a net uncertainty ±10% in the K, H, J fluxes and colors. To this must be added uncertainty due to detector noise for the fainter sources. Tests of the accuracy of the photometry and colors were generally favorable. For a red standard, we used Giclas 77-31 (Elias *et al.* 1982) with $K = 7.84$, $J - H = 0.58$ and $H - K = 0.32$. Calibrating this in the same manner as the companion stars gave $K = 7.90$, $H - K = 0.26$ and $J - H = 0.56$, well within our quoted 10% uncertainties. For dim standards we observed the white dwarfs H 27 and VR 16 from Zuckerman and Becklin (1987,ZB). For H 27 we got $J = 14.68 \pm 0.15, H = 14.71 \pm 0.1, K = 14.72 \pm .14$ while ZB quote $J = 14.70, K = 14.90$. The J magnitude is satisfactory but the K magnitudes differ by 0.18, which is somewhat larger than our estimated uncertainty of 0.14 mag. This may indicate a slight problem in our photometry, or it could indicate that H 27 has an infrared excess similar to the white dwarf LB 1497 studied by ZB. For VR 16, we found the white dwarf had a dim companion 4.4″ to the W (as well as a star comparable in brightness to the white dwarf 6″ W in our 100″ S sky beam). For the white dwarf we derive $J = 14.58, H = 14.61$ and $K = 14.74$, somewhat brighter than ZB's $J = 14.64$, $K = 14.85$. The 4.4″ W companion was $J = 16.14$, $H = 15.97$, $K = 15.86$. ZB used 12″ diameter aperature, which should have included the 4″ W companion. However, the sum of the white dwarf and the 4″ W companion is brighter than ZB's measurements by 0.3-0.4 magnitudes, which is well outside the uncertainties. (We conclude that ZB probably missed this companion.) If the

4″ W companion is also in the Hyades, its absolute K magnitude would be $M_K = 12.6$, which would be the dimmest known main sequence star. Since it is not outstandingly red, we suggest it may be a cool white dwarf. A typical background star would be a K1 main sequence star reddened by $A_K = 0.22$. This appears incompatible with the observed colors of the 4″ W companion.

We conclude there is no systematic inaccuracies in our J, H, K photometry of dim, red objects exceeding 0.1 in the magnitudes or colors. The photometric results for our objects are given in Table 1. In Table 2 we list the T-Tauri stars without any nearby objects.

The plate scale, orientation, and optics distortion of our camera were determined by measuring the star pairs γ Ari and γ Del and the stars Θ^1 A, B, C, and D in the Trapezium. The average plate scale at K was 0.42″ /pixel and the columns of the array were tilted 0.3° from north. By modeling the pincushion distortion, an accuracy of 0.5% in plate scale and rotation was achieved over the whole array. The position of the companions relative to the T-Tauri stars were measured by calculating the centroid in the same aperature used for photometry. The resulting offsets, appropriate for the 1988.8 epoch are given in Table 1.

III. Discussion

We don't expect that all of the 20 objects discovered here are members of the Taurus star-forming association. To predict the number of background stars expected, a star count model based on the method of Elias (1978 a & b) was developed. The star densities given by Elias (1987a) were used. These were supplemented for main sequence spectral types later than K3 using the V luminosity function of D'Antona and Mazzitelli (1986). This was transformed to a K luminosity function using the relationship $M_K = 0.521 M_V + 0.80$, which was found to fit the range $M_V = 4.4$ to 17. This relationship is derived from Liebert and Probst's (1987) fig. 2 for low mass stars and Allen (1973) for higher mass stars. A further extension of the Elias model was the inclusion of a screen of extinction $A_K = 0.2$ mag. at 140 pc to account for the average extinction through Taurus of $A_V \simeq 2$. The model was normalized to the K star count data of Elias (1978 b) in Taurus by variation of the radial scale length α (Elias 1978 a). The resulting value of $\alpha = 3$ kpc gave a predicted value of 10.7 stars per square degree for $K < 7.5$, in adequate agreement with the actual counts of 11. The cumulative number of stars brighter than $K = 15.5$ from this model is 3033 stars/square degree. For the observed counts, we have taken only the companions seen at the initial telescope setting, with the T-Tauri star centered on the array. (We do not include additional stars revealed when the telescope was moved or stars appearing in our sky beams). We found 9 such objects brighter than $K = 15.5$ in our search of 26, $(25'')^2$ fields. The model predicts 3.7, a factor of 2.4 lower. Therefore, we anticipate that somewhat less than half of our objects may be field stars, while the rest are likely Taurus members, based on the star counts alone.

To select the likely Taurus members, we consider the infrared colors $J-H$ and $H-K$. The colors from table 1 are plotted in figure 2. Also shown are the colors of main sequence stars, the colors generated by interstellar extinction of $A_V = 2$ mag., and the colors of

2000-3500 K black bodies. The star count model predicts that the average field star will be a K1 main sequence star 1.3 kpc distant with $A_K = 0.32$ (corresponding to $A_V = 3.2$ mag.). Such a star would have colors $J - H = 0.75$ and $H - K = 0.33$. Nine of our objects have red colors, which differ significantly from these predicted colors, suggestive of low mass objects in Taurus. We suggest these objects are likely Taurus members, based on their colors and the large number found.

Red giant stars have colors similar to our objects, but a red giant would have to be $\sim$ 200 kpc away to appear at $K = 15$ magnitude. Reddened late M dwarfs would have colors similar to our companions. However, from the star count model described above we expect only 1 M-dwarf in our survey. Reddening in Taurus which exceeded the 0.2 mag. A_K (2 mag. A_V), which we have already included, could cause a G to K background star to appear as red as our objects. However detailed star counts in Taurus by Cernicharo and Bachiller (1984) show a maximum of $A_V = 4$ at the LkCa 5 position and considerably less for the other objects. Therefore, this is not plausible either, since a value of $A_V > 4$ in Taurus would be necessary to account for the observed colors.

A very strong test of Taurus membership is proper motion. Members of the Taurus star forming region have typical proper motions of 2.3″ /century in P.A. 164° east of north. (Jones and Herbig 1979). A typical background star 1.3 kpc distant will have very small proper motion, $\sim$ .26″ /century. Burton Jones (1989) has inspected the POSS plates from the mid 1950's and finds about half of our objects can be seen on the red plate. The others are either not visible or too close to the primary to be seen. For 7 of the objects with proper motion data, 4 definitely have a proper motion characteristic of Taurus members and inconsistent with background stars. These are almost certainly Taurus members. Of the others, one is indeterminate, one has high proper motion ($\sim$ 20″ /century) and one has a low proper motion consistent with a background star (table 1). We conclude that a large fraction of our 11 most likely candidates actually are members of the Taurus star forming association.

In order to estimate the masses of the dim, red Taurus members, we compare the observed luminosities to those predicted by the theoretical evolutionary models of Nelson *et al.* (1986) and Lunine *et al.* (1989). Using the distance to Taurus of 140 pc, the luminosities are $0.8 - 4 \times 10^{-3} L_\odot$. For an age of 10^6 years, which is the average age of the previously known Taurus members, the inferred masses are $0.005 - 0.015 M_\odot$, i.e. low mass brown dwarfs. The ages would have to exceed 10^8 years for these objects to be stars ($M > 0.075 M_\odot$). This is counter to experience in Taurus, where the average age is only 10^6 years and star formation apparently began in earnest only 10^7 years ago (Jones and Herbig, 1979, Hartmann *et al*, 1987). Furthermore, the lifetime of star-forming molecular clouds is believed to be only $10^7 - 10^8$ years.

IV Conclusions

We conclude that Taurus harbors a considerable number of low-mass objects, typically 0.01 $M_\odot$ or 10 $M_{Jupiter}$, which could be described as low mass brown dwarfs or high mass planets. Detailed studies of the low mass objects identified here are necessary to better

understand this new type of object.

Spectroscopic studies can lead to an understanding of the atmospheric structure. This will allow determination of the effective temperatures which are needed to place them on the Hertzsprung-Russell diagram and to compare them with theoretical evolutionary models of such objects. It may also be possible to determine the surface gravities, which will give a direct estimate of the masses. For the objects which can't be seen on the POSS plates for proper motion studies, the spectra will be needed to definitely establish Taurus membership. K-band spectra will reveal the CO absorption ($> 2.3\mu$m) and H_2O absorption (1.9μm and 2.7μm) if the object is actually a 2000-3000K substellar object on its Hayashi convective track, rather than a reddened G-K background star.

Further survey observations are necessary to establish how widespread this phenomenon is. If such objects are found throughout the extensive star-forming regions in Taurus, they could represent a heretofore unknown but dynamically important mass component of our galaxy.

References

Allen, C. W. 1073 "Astrophysical Quantities" (The Athlone Press, London).

Cernicharo, J. and Bachiller, R. 1984 A & A Supp, **58**, 327

D'Antona, F. and Mazzitelli, I. 1986 Astron. Ap., **162**, 80.

Elias, J. H. 1978a Ap J, **223**, 859.

Elias, J. H. 1978b Ap J, **224**, 857.

Elias, J. H., Frogel, J. A., Matthews, K. and Neugebauer, G. 1982 AJ, **87**, 1029.

Forrest, W. J., Pipher, J. L., Ninkov, Z. and Garnett, J. D. 1989 (This conference prodeeding).

Hartmann, L. W., Soderblom, D. R., and Stauffer, J. R. 1987 AJ, **93** , 907.

Herbig, G. H. and Bell, K. R., 1988 "Third Catalog of Emission-Line Stars of the Orion Population", Lick Obs. Bull. No. 1111 (U. Calif.)

Jones, B. F. 1989 private communication.

Jones, B. F. and Herbig, G. H. 1979, AJ, **84**, 1872.

Liebert, J. and Probst, R. G. 1987 Am. Rev. Astron. Ap, **25**, 473.

Lunine, J. I., Hubbard, W. B., Burrows, A. S., Wang, Y.-P., and Garlow, K. 1989 ApJ, **338**, 314.

Nelson, L. A., Rappaport, S. A. and Joss, P. C. 1986 ApJ, **311**, 226.

Tarter, J. C. 1986 in "Astrophysics of Brown Dwarfs" ed. Kafatos, Harrington and Maran (Cambridge U. Press, Cambridge) p. 121.

Zuckerman, B. and Becklin, EE 1987 ApJ (Letters), **319**, L 99 (ZB).

Table 1. Stellar Objects Discovered Near 13 T Tauri Stars

Object	T Tauri Star	HBC#[c]	Offset from T-Tauri(arcsec)[b]		K	H-K (mag)	J-H	Proper Motion, Notes[a]
			a. Red Objects					
1	LkCa 4	370	3.82E	8.28S	13.44	0.45	1.1	too close
2	LkCa 4	370	13.52W	4.75S	14.25	0.41	1.0	YES
3	FP Tau	26	(9.4W)	(7.9S)	15.96	0.50	0.8	NO, background p.m.
4	LkCa 7	379	13.39W	4.34S	15.25	0.34	0.46	YES
5	LkCa 7	379	3.37E	17.08S	15.81	0.0	0.7	YES
6	LkCa 7	379	1.64E	29.68S	14.38	0.4	0.6	not visible, tel. offset
7	LkCa 5	371	12.33E	7.81S	14.54	0.64	1.07	not visible
8	LkCa 8	385	12.65E	0.39N	14.10	0.39	–	MAYBE
9	LkCa 8	385	11.03E	10.10N	13.24	0.43	–	NO, high p.m.
10	NTTS 35120 NE	353	19.35E	4.48S	15.26	0.33	1.2	
11	NTTS 35120 NE	353	11.75E	9.91N	14.14	0.05	0.43	not red
12	NTTS 35120 NE	353	21.84E	17.14N	12.38	–	–	tel. offset
13	NTTS 35120 NE	353	9.27W	13.18N	13.73	–	–	tel.offset
			b. Others					
14	V836 Tau	429	(12.6W)	(6.1S)	16.3	0.9	–	not visible, low lat. (−10°)
15	LkCa 3	386	9.94W	11.40N	15.9(H)	–	0.7	only J, H measured
16	NTTS 45251+3016	427	9.04E	0.23S	15.24	0.08	1.3	too close, v. bright obj. 13″ SSE
17	NTTS 41559+1716	376	4.50E	9.97N	14.14	0.02	0.76	YES
18	NTTS 40234+2143	362	3.27W	4.94S	14.55	-0.01	0.27	too close
19	LkCa 21		(7.7 W)	(6.8N)	(16.4)	(0.1)	–	through clouds
20	V819 Tau		1.24E	10.44S	12.04	–	–	

Meaning Key:

[a] YES: proper motion indicates Taurus membership.
NO: proper motion rules out Taurus Membership.
MAYBE: proper motion indeterminate between a background star and a Taurus member.
too close: Object too close to T-Tauri star to be seen on the POSS red plate.
not visible: object not visible on POSS red plate.
through clouds: observations made through thin clouds, photometry highly uncertain.
tel. offset: offset position derived using telescope motion, somewhat more uncertainty.

[b] Offset uncertaintly ±0.15 arcsec. Offsets in parenthesis and those derived using telescope motion somewhat more certain.

[c] Herbig, Bell (1988) Catalog number

Table 2. 13 T Tauri Stars Lacking Nearby Objects

V410 Tau, V827 Tau, HDE 283572, LkCa 1, V826 Tau,
SAO 76428, LkCa 16, Hubble 4, NTTS 42417+1744,
NTTS 42950+1757 (may be very faint object 10″N)
NTTS 4283+1700, NTTS 34903+2431, NTTS 43220+1815

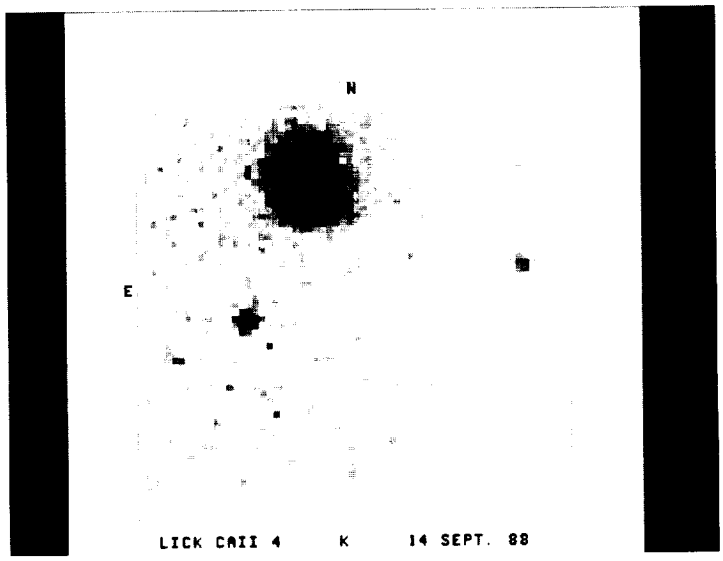

Figure 1 2.2μm (K) image of a 24″ × 26″ region near the T Tauri star LkCa 4 made on 14 September 1988. North is up and East is to the left . The T Tauri star is the bright object near the top. The dim object to the right (west) can also be seen on the POSS red plate no. 1454 from 23 October 1955. Its proper motion (2.7″ /century E and 2.2″ /century S (Jones, 1989) is consistent with that of LkCa 4 and other Taurus members but inconsistent with a distant background star. It is therefore a highly probable Taurus member. Its luminosity derived from the measured infrared fluxes is $2 \times 10^{-3} L_{\odot}$. Its mass is inferred to be $\simeq 0.01 M_{\odot}$ based on an estimated age of 10^6 years. The brighter object to the left and below LkCa 4 is too close to be seen on the POSS plates and, therefore, its proper motion is unavailable at this time. Its red colors indicate probable Taurus membership. If this is confirmed spectroscopically, its luminosity would be $4 \times 10^{-3} L_{\odot}$ and its inferred mass about $0.015 M_{\odot}$.

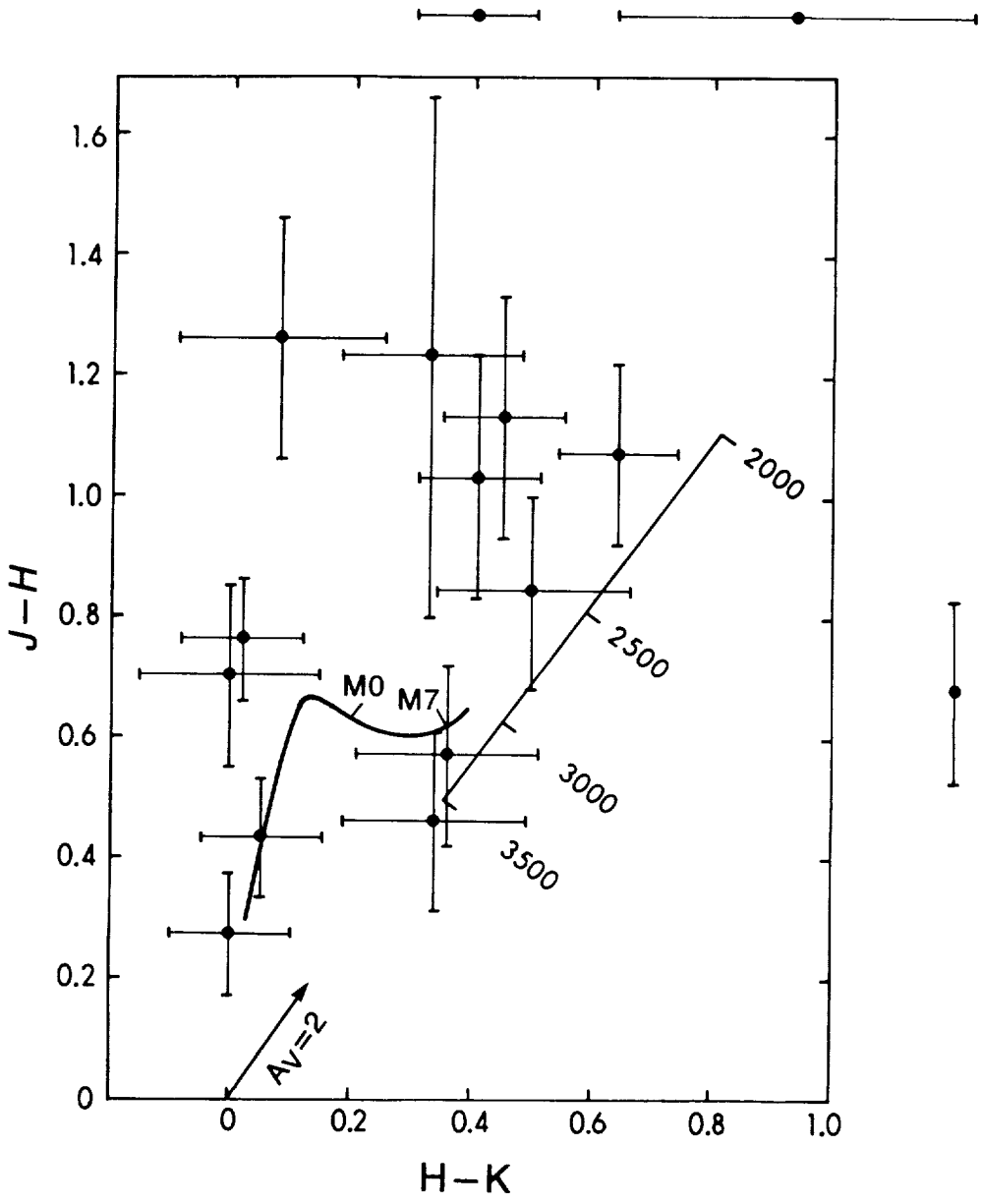

Figure 2 Near infrared color-color plot of the objects (data points with error bars) found in our Taurus survey. The data is from table 1. A 10,000 K star such as Vega (α Lyr) define the zero point of H-K and J-H colors. Also shown is a vector corresponding to A_V=2 mag of interstellar reddening in H-K and J-H. The curve with a J-H peak near H-K = 0.15 represents the average colors of main sequence stars from Probst and Liebert (1983 ApJ, **274**, 245) with the approximate positions of MO and M7 spectral types indicated. The straight line with tick marks shows the infrared colors of black bodies with temperatures of 2000 to 3500 K as indicated. The points outside the box represent stars with only H-K (top) or J-H (right side) measurements. Exceptionally red objects, toward the top right in this figure, are suggested to be possible low mass brown dwarfs in the Taurus association.

High Resolution Imaging of the Venus Night Side Using a Rockwell 128x128 HgCdTe Array

K.-W. Hodapp, W. Sinton
Institute for Astronomy, University of Hawaii

B. Ragent
NASA Ames

D. Allen
Anglo Australian Observatory

Abstract

The University of Hawaii operates an infrared camera with a 128x128 HgCdTe detector array on loan from JPL's HIRIS project. The characteristics of this camera system will be discussed. The infrared camera has been used to obtain images of the night side of Venus prior to and after inferior conjunction in 1988. The images confirm Allen and Crawford's (1984) discovery of bright features on the dark hemisphere of Venus visible in the H and K bands. Our images of these features are the best obtained to date. We derive a pseudo rotation period of 6.5 days for these features and 1.74 μm brightness temperatures between 425 K and 480 K. The features are produced by nonuniform absorption in the middle cloud layer (47-57 Km altitude) of thermal radiation from the lower Venus atmosphere (20-30 Km altitude). A more detailed analysis of the data is in progress.

I. INTRODUCTION

Allen and Crawford (1984) discovered bright features on the dark side of Venus at short infrared wavelengths, where thermal emission from the upper cloud layers of Venus would be too faint to be detected. Spectroscopic observations confirmed that this radiation is seen in two relatively narrow features at 1.74 μm and 2.3 μm wavelength, which are gaps in the absorption of CO_2 and H_2SO_4, the main absorbers in Venus atmosphere. In these spectral features, we see deeper into the hot atmosphere of Venus and the spatial structure arises from patchy absorption in optically thin clouds in the middle cloud layer (47-57 Km altitude) of Venus atmosphere. From measurements of the pseudo rotation period of these features, their association with the middle cloud layer can be confirmed. The features visible in the near-infrared are different from the structure seen in the UV from spacecraft, which is associated with the upper cloud level at 70 Km altitude. Groundbased near infrared observations can therefore make important contributions to our understanding of the dynamics of Venus atmosphere.

II. Infrared Array Characteristics

We were using a 128x128 HgCdTe Detector Array with a cutoff wavelength of 2.5μm, manufactured by the Rockwell International Science Center. The Detector Array is Indium bump bonded to a Reticon readout structure. This Detector array was made available to us by JPL's HIRIS project and, for HIRIS, was optimized for high read-out rates and high flux levels of an earth observing instrument in low earth orbit. Further, this device was optimized for the 150 K operating temperature expected in the passively cooled HIRIS instrument. For astronomical imaging, we use the device at a read-out rate of 4μs per pixel and achieve a read-noise of 2000 electrons. The peak quantum efficiency of the device itself is about 30 % in K, 20% in H and less than 10% in J at an operating temperature of 100 K. At lower temperatures, the Q.E. drops further, higher temperatures give a prohibitively large darkcurrent. The device shows large scale variations of the quantum efficiency of a factor 2 peak to peak across the chip. The dark current is dominated by luminescence in the multiplexer, reaching values as high as 4000 electrons per second near the output amplifier of the multiplexer and 500 electrons per second near the center of the device. The full well capacity is 800000 electrons, so that operation is always read noise limited. The device works linearly up to 70% of full well, above which a smooth transition to saturation occurs. The sensitivity of this detector array is clearly inferior to the performance achieved by other IR-arrays currently in use for astronomy. Its strength is the large format, allowing imaging of large fields of view without the need for extensive mosaicing.

III. The Infrared Camera System

The 128x128 array is mounted in an uplooking liquid nitrogen dewar for use at the 2.2 m and 0.6 m telescopes of the University of Hawaii (Fig. 1).

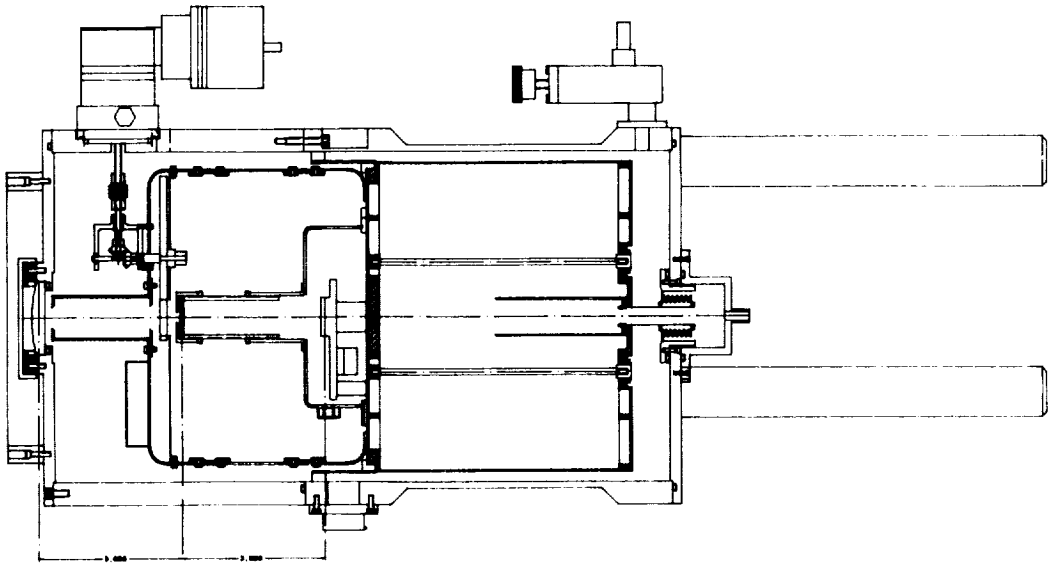

Fig. 1: Cross section through the UH Infrared Camera dewar. The dewar is an uplooking design with one LN_2 can. The optics are a straight refractive system with 1:1 reimaging.

The dewar is currently equipped with 1:1 reimaging optics consisting of a CaF_2 field lens and a biconvex ZnSe reimaging lens. The cold stop can easily be exchanged for use of the camera at different f-ratios ranging from f/5 (0.6 m) to f/35 (2.2 m). Up to now, the camera has only been used at the f/10 focus of the UH 2.2 m telescope with a plate scale of 0.55 "/pixel. The read-out electronics, developed by JPL (Kaki, Bailey, and Hagood, 1988), are mounted on the dewar. The 12 bit data words are transmitted via a high speed data link to a buffer board in a 12 MHz Compac 286 computer which contains sufficient memory to store a complete frame. This buffer board also controls the timing of the integrations. After reading the data from the buffer, the computer than handles data display, subtraction of sky frames, preliminary analysis and mass storage on disk and tape.

IV. Venus observations

As part of a collaboration lead by D. Crisp from JPL, involving UH, NOAO, and JPL's Table Mountain Observatory, we obtained images of the dark hemisphere of Venus approximately 2 weeks before and after inferior conjunction. A narrow band interference filter centered on the 1.74μm feature was custom made by Barr Associates and distributed to all participating observatories. This narrow band filter was used for most of the imaging work. However, we also obtained some images in broad band K, where these atmospheric features are also visible, and, for comparison, a few images at a wavelength of 1.57 μm, where no radiation can escape through the middle cloud layer. We stopped the UH 2.2 m telescope down to 0.55 m by an excentric full aperture mask mostly to keep sunlight from hitting the primary mirror of the telescope. As a positive side effect, we thereby created an unobstructed round telescope pupil eliminating the diffraction spikes of the secondary support and thus enhancing the image contrast. The excentric aperture was oriented such that sunlight would not reach the primary mirror during the daytime observations with Venus being only 20 degrees away from the sun. To further reduce straylight levels from the sunlit crescent of Venus, we placed a neutral density filter in the focal plane, covering the brightest parts of the crescent while leaving the dark side of Venus unobscured. In the end of May 1988, prior to inferior conjunction, with Venus east of the sun, we only obtained images under poor seeing conditions (2 arcsec or worse). In the end of June 1988, after inferior conjunction, with Venus in the morning sky, we obtained data of very high quality on five consecutive days. Each morning, the image quality was best in the first hour after sunrise (0.5 to 0.7 arcsec seeing), resulting in diffraction limited image quality (0.8 arcsec), and later deteriorated to typical mid-day seeing of 2 arcsec. The integration time in the narrow band filter was 30 sec and 2 sec in broad band K. Sky frames were taken 2 arcmin away from Venus and subtracted from the object frames. Skyflats were used for flatfield correction. Between individual images, the telescope was deliberately moved by a few arcseconds, in order to eliminate systematically bad pixels later. We typically took 20 frames per hour and coadded the individual images in 30 min bins, which is a short enough time interval to neglect motion of atmospheric features. For coaddition, the images were interpolated to 256x256 format, registered with a precision of one half the original pixel size, and coadded with the systematically bad pixels masked off.

V. Preliminary Results

The images, Fig. 2, show different atmospheric features on each day. Feature tracking gave a pseudo-rotation period of 6.5 +/- 0.5 days, corresponding to equatorial wind speeds of 68 m/s westwards. These wind speeds are consistent with Pioneer Venus and VEGA Balloon measurements for the middle cloud region at altitudes of 47-57 Km (Preston et al. 1986). It should be noted that the IR cloud features are not identical to those seen on the bright side of Venus in the UV. The UV features have a pseudo rotation period of 4 days and are associated with the highest cloud layer at about 70 Km altitude. At 1.74 μm, the brightness temperature of the brightest features is 480 K while the darkest features have brightness temperatures of 425 K. We do not interpret this as temperature nonuniformities in the middle cloud layer. Temperature nonuniformities of this magnitude in the middle cloud layer have never been observed by in situ measurements and would be difficult to understand theoretically. The brightness variations are interpreted as patchy, optically thin absorption in relatively cold clouds (300-320 K, Sagdeev et al., 1986) against the background of thermal radiation from lower layers of the atmosphere.

We plan to repeat observations of this kind during the next inferior conjunction of Venus, which fortunately coincides closely with the flyby of the Galileo probe at Venus. We hope to provide long time coverage of the atmospheric features on Venus while the spacecraft is expected to obtain images with much better resolution for a relatively short time.

We thank the staff of the UH 2.2 m telescope for their support during these observations. We thank E. Irwin, M. Wagner, and S. Massey for their help in designing and operating the UH Infrared Camera and G. Bailey and S. Kaki for providing the drive electronics for this device. The 128x128 infrared array is the result of work by the JPL Infrared Technology Group in support of the Spaceborne Imaging Spectrometer Project Office at JPL under funding by the NASA Office of Space Science and Application.

References:

Allen, D. A., and Crawford, J. W. 1984, Nature 307, 19

Bailey, G. C. 1987, Infrared Astronomy with Arrays, ed. C. G. Wynn-Williams and E. E. Becklin, University of Hawaii, p. 52

Kaki, S. A., Bailey, G. C., and Hagood, R. W. 1988, preprint

Preston, R. A., et al. 1986, Science 231, 1414

Sagdeev, R. Z., et al. 1986, Science 231, 1411

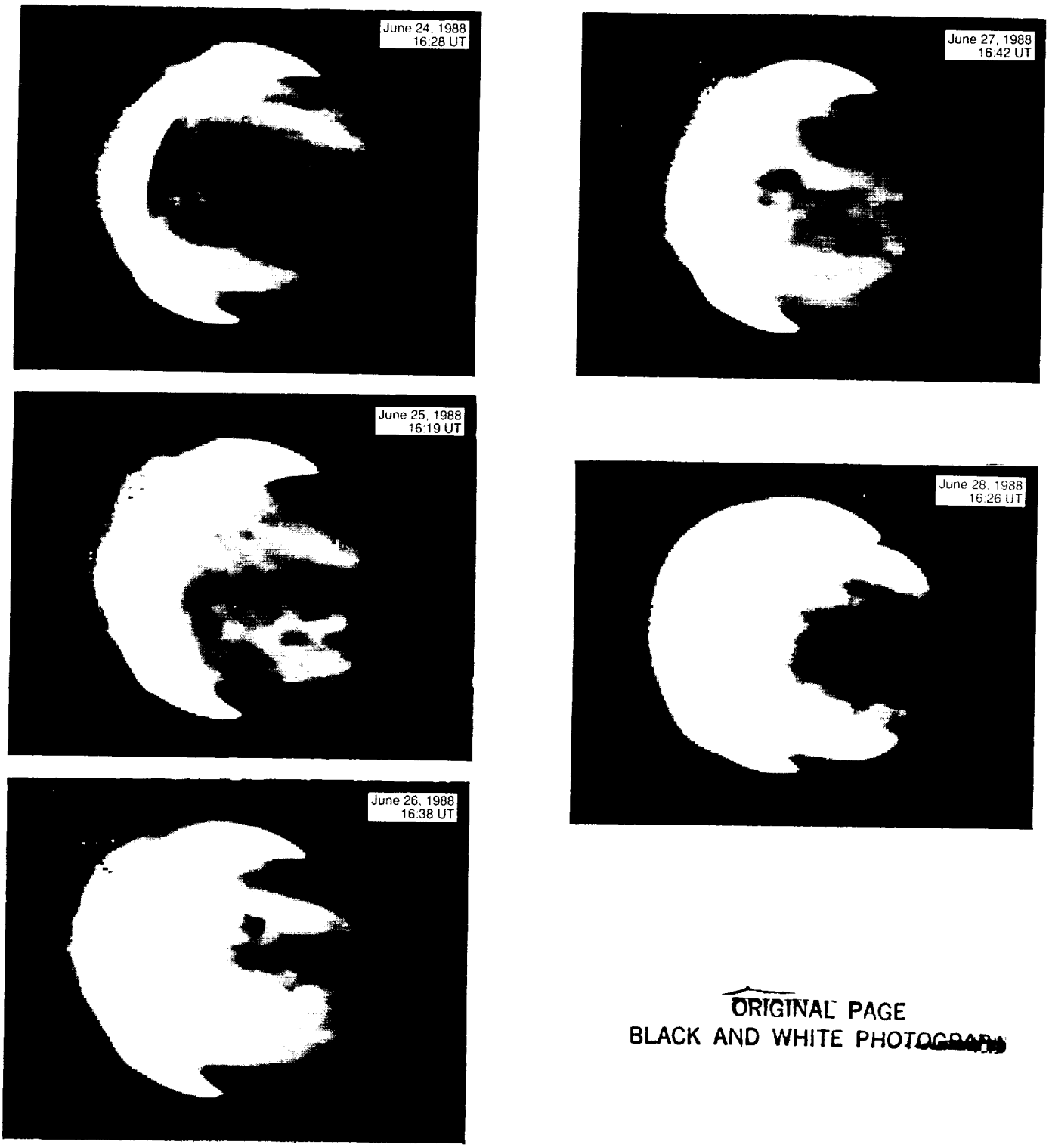

Fig. 2 Images of the night hemisphere of Venus on five consecutive days. The images are the result of coadding up to 12 individual 30 sec exposures, sky subtracted and flatfielded images taken in a half hour interval. In the coaddition process, the images were individually aligned and systematically bad pixels have been removed. The observation dates given in Fig. 2 are the averages of the exposure dates of the individual frames coadded to produce the images.

Infrared Ground-Based Astronomy with the Hughes 256 X 256 PtSi Array

A. Fowler, R. Joyce, and I. Gatley

National Optical Astronomy Observatories††
Tucson, Arizona 85726

J. Gates and J. Herring

Hughes Aircraft Company
Carlsbad, California

ABSTRACT

This paper will show that large format PtSi Schottky diode infrared arrays, the Hughes 256 X 256 hybrid Schottky array in particular, are competitive alternatives to the smaller format photovoltaic arrays for ground-based astronomy. The modest quantum efficiency of the PtSi compared to the photovoltaic devices is more than compensated for by the larger format. The use of hybrid technology yields effective fill factors of nearly 100%, and the low dark current, noise, excellent imaging characteristics, cost, and solid nitrogen operating temperature add to the effectiveness of this array for ground-based imaging. In addition to discussing the characteristics of this array, we will present laboratory test data and astronomical results achieved at Kitt Peak.

1. INTRODUCTION

Two dimensional platinum silicide (PtSi) Schottky barrier diode arrays have been utilized since the late 1970's. The early arrays[1-4] were burdened by poor fill factors due to their monolithic structure, in addition to the poor quantum efficiency of thick film PtSi. Since that time, very thin silicides utilizing optically reflective cavities, hybrid bump interconnect technology, and improved processing have dramatically improved the effective quantum efficiency, decreased the dark current, and increased the yield, making the present generation of arrays useful for ground-based astronomical applications.

This advance in technology has provided us with high performance arrays in the 256 X 256 format, with expectations of even larger formats in the future. This paper discusses the performance of the Hughes 256 X 256 PtSi array, which was tested by NOAO in cooperation with Hughes Aircraft Co. to evaluate its astronomical capabilities. The exciting characteristics of this array for astronomy are the large format, very low dark current, low noise, and ease of operation. Additional positive features are the cosmetic quality, stability of performance, and commercial availability.

2. DEVICE DESCRIPTION

Unlike most PtSi arrays, which are monolithic CCD's, this array utilizes hybrid technology. In this technique, the readout (ROIC) is fabricated using well-developed MOS technology and is tested separately before being mated with the detector. The detector array is also fabricated and tested independently. Indium bumps are defined on both the detector and readout, and those devices which pass the initial screening are then hybridized. Figure 1 is a cross section of a complete array, showing the hybrid structure. Besides the obvious benefits of increased yield and lower cost (since only good devices make it to the hybridization process), the fill factor is large because the readout does not reduce the detection area. This is very important in the case of Schottky devices because of their inherently lower quantum efficiency, and is crucial in any event for

††Operated by the Association of Universities for Research in Astronomy, Inc. under contract with the National Science Foundation.

astronomical use.

The ROIC uses a dual shift register addressing technique and a source follower per detector unit cell. The shift register is a two-phase non-overlapping clock design. Although the devices were designed to run at video rates, the shift registers will run as slow as 1 Hz when cooled to 60 K. This approach has the advantage of requiring fewer clocks, but the disadvantage of losing the ability to randomly access the pixels. This is not much of a practical loss, since the random access feature in other arrays has rarely been utilized.

The detector array, shown in cross-section in Figure 2, is a thin film PtSi structure. The array we evaluated incorporated a SiO dielectric optical cavity tuned to enhance the quantum efficiency at 4 microns, which unfortunately resulted in an optical null at 2 microns. This is not an intrinsic problem and is easily overcome by tuning the cavity differently, as shown later. Elabd and Kosonocky[5] provide a readable treatment of the use of optical cavities in thin film PtSi.

The principle of Schottky diode detection is the internal photoemission of hot holes created by the absorption of a photon. The incoming photon excites electrons in the valence band to energies above the Fermi level, creating holes below the Fermi level. A hot hole, one whose energy is above the Schottky barrier level, can tunnel into the detector substrate. An additional constraint for hot hole tunneling is that its momentum normal to the silicide-silicon surface correspond to an energy greater than the Schottky potential. The use of a dielectric on the backside of the silicide increases the probability of hot hole injection by scattering at this surface and significantly improves the quantum efficiency of these devices.

The fabrication of an extremely uniform silicide layer, as well as the lack of differential thermal contraction between the detector and ROIC, make possible physically large arrays with excellent cosmetic quality. Figure 3 is a ratio of two dome flats (4 s and 2 s integration time), displayed over the range 1.9 - 2.1. With the exception of the upper left corner, where the bonding to the detector substrate is made, only a few pixels were non-operative.

3. ASTRONOMICAL PERFORMANCE

The arrays described here were evaluated in the laboratory, with emphasis on those characteristics important for astronomical applications. Critical factors include (but are not limited to) dark current, read noise, quantum efficiency, linearity, and stability. One of the arrays was used on several occasions at Kitt Peak National Observatory to evaluate its performance under actual observing conditions; these results are discussed in the following section. The characterization and telescope tests were all at a detector temperature of approximately 60K, a temperature attained by pumping on LN_2, obviating the need for LHe and reducing the cost and complexity of operation.

After optimization for slow scan operation, the conversion gain (volts/electron) was determined using the "mean-variance" technique of Fowler and Joyce[6]. Following this, we determined the electrical gain by varying the reset voltage on the detector, obtaining a value of 14 electrons/ADU at the detector node. We could then calculate the capacitance of the detector and the system readout noise in electrons. The physical and derived detector characteristics are given in Table 1. Although the node capacitance is small, we were able to use a large reset level (3 V) to obtain a theoretical well capacity of ~ 10^6 electrons. In practice, the high conversion gain and the 16-bit A/D limited the practical capacity to about 3 X 10^5 electrons, which nonetheless gave excellent dynamic range due to the low read noise. The low node capacitance is largely repsonsible for the very low read noise, although this array, like others we have tested, appears to generate considerable noise in the addressing operation itself.

Table 1 -- Detector Characteristics

• HFPA Structure	
Number of Pixels	256 X 256; 65536 elements
Pixel Size	30 μm X 30 μm
Detector Active Area	28 μm X 28 μm
Readout Type	Direct Readout
Sensor Type	PtSi Schottky Barrier (C_1 = 0.29 / eV; Ψ_{ms} = 0.22 eV)
• HFPA Performance	
Operating Temperature	60 K
Dark Current	< 10 electron/s
Noise	40 electrons
Node Capacitance	0.06 pF
Full Well (3 V reset)	~ 1 X 10^6 electrons

The specific readout technique used presently deserves mention at this point. A common method, which we have used in the past, is to perform the address cycle (read signal, reset detector, read bias) on a sequential pixel-by-pixel basis, as illustrated in Figure 4a. With this data, the user can perform delta-reset, correlated double sampling, or correlated triple sampling operations[7]. Each of these techniques addresses different fundamental noise sources. However, our experience has indicated that the limiting performance is determined not by fundamental noise processes, but by excess noise associated with the addressing cycle. An alternative technique, illustrated in Figure 4b, is to perform a detector reset (only) on the entire array, followed by a readout of the entire array, without resetting (initial detector bias). After a delay for the desired integration time, the array is read out again (signal). The difference between the two values is the measured signal. This is a form of non-destructive double correlated sampling, but its most important feature is the elimination of excess noise associated with the resetting process. Using this technique, we have routinely achieved a read noise of 40 electrons with these PtSi arrays. The use of triple correlation to remove some of the 1/f noise may lead to further improvement, but we have not investigated this at present.

The dark current in this array, measured over time periods from 0.4 to 4000 seconds, is slightly higher for integration times less than 100 s (approximately 10 electrons/s), decreasing to about 3 electrons/s at longer integration times. Since these values are much lower than the background radiation flux for broadband imaging applications, little additional testing was done. We point out that due to the lower quantum efficiency of Schottky diodes, the dark current must be proportionally lower to avoid degrading the performance.

A key parameter for all detectors is the quantum efficiency. Two different arrays were tested in this effort. The first was optimized for thermal imaging with an anti-reflection coating and optical cavity tuned for 4 microns. This had the unfortunate consequence of severely reducing the quantum efficiency at 2 microns. The second array, with a different optical cavity, had a quantum efficiency almost 10 times higher at 2 microns. The measured quantum efficiencies of the two detectors as a function of wavelength are plotted in Figure 5, along with the theoretical performance predicted by a modified "Fowler" equation[7]. The theoretical response utilizes parameters determined from behavior in the 3 - 5 micron range and does not include the effects of transmission through the Si substrate, and thus overestimates the quantum efficiency at shorter wavelengths.

The effective optical fill factor of an array (which may be greater than the geometrical fill factor) is of paramount importance to astronomy. It determines the effective quantum efficiency for an array, which is the measured flux divided by the incident flux per area defined by the pixel center- to-center spacing. More importantly, a near 100% fill factor is necessary for stellar imaging, or signal variations due to the image centroid position relative to the centroid of the pixel point spread function (PSF) cannot be corrected. Pixel-to-pixel gain variations may be calibrated by uniform illumination of the array (flatfielding). The pixel PSF was evaluated in the laboratory by scanning a spot image (~ 20 microns) along a row of the array. The measured response for each of three adjacent pixels as a function of the spot position is plotted in Figure 6, along with the sum of the response. The lack of a statistically measurable dip at the interstitial positions leads us to conclude that the fill factor of this array is essentially 100%.

It is instructive to compare the performance of the PtSi array with that of the SBRC InSb array on a pixel basis. Figure 7a shows the calculated signal and noise, using typical values for InSb (η = 0.6, N_R = 300 electrons) and PtSi (η = 0.05, N_R = 40 electrons), for a photon flux = 1000 /s at a wavelength of 2.2 microns, as a function of the integration time. Complete linearity is assumed. The solid lines represent the measured signal (electrons) for the two detectors. The dashed lines represent the measured noise (electrons), under the assumption that the only noise sources are the read noise N_R and the shot noise of the radiation signal. The arrows indicate equal contributions from these two noise sources and mark the transition from "read noise limited" to "background limited" operation. The ratio of the signal/noise for InSb to that of PtSi, which may be considered the relative performance, is plotted in Figure 7b. The read noise limited regime corresponds to observations through very narrow spectral filters or applications such as speckle, where the integration time must be limited. The signal/noise is directly proportional to integration time and the ratio η/N_R. The much lower read noise of PtSi almost compensates for its lower quantum efficiency. Almost all astronomical imaging falls in the other, background limited, category. The signal/noise in this regime is independent of read noise, depending only on $(\eta)^{0.5}$, giving the InSb an advantage of 3.5, or about 1.4 magnitudes in sensitivity for a given integration time. Alternatively, the PtSi will require a factor of 12 greater integration time to reach the same signal/noise as the InSb. For applications requiring coverage of a large spatial area, this is more than compensated for by the pixel ratio of 18 between the 256 X 256 and 58 X 62 arrays.

An interesting parameter derived from Figure 7a, the integration time to background limited performance (shown by arrows), scales as $(N_R)^2/(\eta)$, and is more than a factor of 4 less for the PtSi than for the InSb. In the background limited regime, no theoretical advantage distinguishes a small number of long integrations from a large number of short integrations, as long as the total integration time is the same. Under the time-dependent sky background conditions encountered in actual observing, the ability to reach background limited conditions quickly may permit greater suppression of systematic effects, more than compensating for the slight increase in overhead associated with shorter integrations.

4. OBSERVATIONAL RESULTS

For the astronomical tests, input optics were installed in the cryostat to convert it to an uplooking camera very similar to that used at KPNO with the 58 X 62 SBRC InSb array.[8] To exploit fully the wide field capabilities of the PtSi array, the telescope focal plane was reduced in scale by a factor of 4, using AR-coated ZnSe lenses. The optical path was similar to that illustrated in Figure 8 of Fowler *et al.*[8] The optics consisted of a field lens near the telescope focal plane to reimage the exit pupil on a cold stop and a triplet in front of the array to achieve the focal reduction. The resulting plate scale on the KPNO 1.3m telescope was 1.36 arcsec/pixel, yielding a field of view 350 arcsec square. At the KPNO 2.1m telescope, the corresponding numbers are 0.78 arcsec/pixel and a 200 arcsec field.

Initial linearity observations were very encouraging. Figure 8 plots the integrated signal in a 5 pixel radius aperture for three stars at integration times ranging from 0.4 to 500 s. The dashed lines have a slope of 1.0. No significant deviation from linearity was seen for the two fainter stars; the deviation in the case of HR 5447 results from saturation of the electronics for the brightest pixels in the stellar image. The calculated intensity differences for the three stars are equal, within the quoted uncertainty, to published values.

A striking example of the performance of this device is shown in Figure 9, a K band image of the galactic center. This image is a mosaic of 25 exposures, each of 3 minutes, taken on 5 arcmin centers, and required approximately 1.5 hours of observing time at the 1.3m telescope. In this and succeeding images, north is up and east is to the left. The field of Figure 9 is approximately 27 arcmin on a side, or 70 pc at the distance of the galactic center. The nucleus is prominent in the center, and thousands of stars, as faint as K = 14, are detected. In addition, the plane of the galaxy, which runs from upper left to lower right, is evident, as is the patch of extinction running parallel to and slightly below the plane, which indicates that our solar system actually lies somewhat above the galactic plane. The patch of extinction about 10 arcmin NW of the center is almost devoid of stars even at this wavelength, suggesting that it is both very thick optically and nearby. Since the visual extinction to the galactic center is estimated to be 15 - 20 mag, almost none of the thousands of stars in this image is detectable at visual wavelengths.

The linear artifact seen on the left side of Figure 9 results from a bright star falling on the edge of the detector-ROIC hybrid interface. Some of this radiation channels across the array within the optical cavity. This effect can easily be prevented by optical masking of the array.

A similar artifact, resembling diffraction spikes along the row and column directions, can be seen surrounding very bright stars. This effect was seen only at K with the array tuned for 4 micron operation and probably is a result of the detuned optical cavity acting as a waveguide and channelling some of the light from the stellar image down the rows and columns of the array. This should not be a significant effect in an array with a properly tuned optical cavity.

Figure 10 is a single frame image (24 coadded 10s integrations) of the Orion Nebula through a 3.28 micron narrowband ($\Delta\lambda$ = 0.1 micron) filter, which isolates the "PAH" emission feature[9,10], a tracer of "hot" dust near sources of ultraviolet radiation. This image prominently illustrates the concentration of this feature along the ionization front of the nebula,[11,12] and shows that PtSi is adequate for many observations longward of 3 microns. Although the theoretical advantage of the much higher quantum efficiency of InSb is considerable in this region, the practical advantage in this "saturation limited" regime is constrained by the finite readout time for the array. The 58 X 62 InSb array in use at NOAO will saturate in the L band filter in approximately 0.1s; a hypothetical 256 X 256 array in this material would require operation at much higher detector bias and clock rate, or through a narrowband filter, to avoid saturation in the minimum integration time. Except for scientific applications requiring narrowband imaging, the low quantum efficiency of PtSi in the L and M bands is compensated for by the ability to use broadband filters.

Figure 11 is a large mosaic image of the region of the Orion Nebula in the H band. The field of view is approximately 27 by 37 arcmin. The familiar shape of the Orion Nebula in the visible, largely the result of dust obscuration, is modified in the infrared to a more symmetrical form. In addition to the Trapezium and the OMC1 complex, one may trace a distribution of stars clusters extending to the north, including the OMC2 complex and a previously unknown bipolar outflow object. This type of image gives a global view of the large and small scale details of star formation in a way impossible before the advent of large-format sensitive infrared arrays.

The construction of mosaic images such as these requires a detector with excellent long-term stability in its spatial sensitivity characteristics, since the effects of temporally varying sky emission must be removed from the individual images prior to coalescence. This is accomplished by using median-averaged frames of off-object "sky", or the object frames themselves, if the star density is low enough, to generate a flatfield frame, essentially a spatial gain map of the array using the sky background emission as a uniform illumination source. Dividing the object frames by this flatfield reduces the sky background in each frame to a constant, which can be subtracted in the mosaic operation. Any variation in the spatial gain over the array during the observations will be manifested as discontinuities in the mosaic, since it will be impossible to match the levels at more than one border. The lack of such features in Figures 9 and 11 attests to the excellent stability of the PtSi array.

An additional consideration for mosaic observations is the need to overlap adjacent frames to obtain a common area for spatial registration and sky level matching. The area of this overlap region will depend on star density and telescope pointing errors, and will be a smaller fraction of the field of view for a larger format array. In addition, covering a given sky area with a small field of view requires that a greater fraction of time be spent in overhead operations, such as moving the telescope. The net result is that for actual mapping operations, the advantage of a large format array is considerably greater than the numerical pixel ratio.

5. SUMMARY

In this paper we have shown the capabilities and utility of PtSi large format arrays. Although their ultimate sensitivity is a factor of 3 to 4 less than the most sensitive photovoltaic arrays, the larger format, stable characteristics, and lower cost make them very attractive, competitive devices for ground-based astronomy.

The comparisons we have made between the 256 X 256 PtSi and the 58 X 62 InSb arrays indicate that they may play complementary roles in astronomy. Certainly, for deep limit observations of distant galaxies or faint stars, the sensitivity advantage of the InSb is of paramount importance. One cannot realistically overcome this fact by a 12-fold increase in observing time, especially on 4 meter class telescopes. However, as pointed

out above, the numerical pixel advantage can more than compensate for the sensitivity factor in observations of extended fields. In addition, our experience indicates that it is very difficult to accurately mosaic extended objects with a limited field of view that does not include "sky", without significant spatial oversampling. A final point lies in the value of large format arrays on moderate aperture telescopes for serendipitous discovery and the necessary survey work prior to deep imaging or spectroscopy on existing 4m and future 8m and 10m class telescopes.

6. ACKNOWLEDGEMENTS

We wish to acknowledge the efforts of K. M. Merrill and M. Tamura in generating the composite image of the Orion Nebula, H. Chen for performing the spot scan tests, and Kate McKennon for the drawings. We thank J. Mooney of RADC for permission to publish his quantum efficiency measurements of one of the arrays. L. Davis generated the IRAF routines which made possible the mosaic images presented here.

REFERENCES

1. F. D. Shepherd, A. C. Yang, S. A. Roosild, J. H. Bloom, B. R. Capone, C. E. Ludington, and R. W. Taylor 1976, "Silicon Schottky Barrier Monolithic IRTV Focal Planes," *Advances in Electronics and Electron Physics,* **40B**, pp. 981-992.
2. F. D. Shepherd, R. W. Taylor, L. H. Taylor, L. H. Skolnik, B. R. Capone, S. A. Roosild, W. F. Kosonocky, and E. S. Kohn 1979, "Schottky IRCCD Thermal Imaging ," *Advances in Electronics and Electron Physics,* **52**, pp. 495-512.
3. W. F. Kosonocky, H. Elabd, H. G. Erhardt, F. V. Shallcross, G. M. Meray, R. Miller, T. S. Villani, J. V. Groppe, V. L. Frantz, and F. J. Tams, "Schottky-barrier Infrared Image Sensors," *RCA Engineer* **27-3**, (May/June 1982).
4. B. R. Capone, R. W. Taylor, and W. F. Kosonocky 1982, "Design and Characterization of a Schottky Infrared Charge Coupled Device (IRCCD) Focal Plane Array," *Optical Engineering,* **21,** 945.
5. H. Elabd and W. F. Kosonocky, "Theory and Measurements of Photoresponse for Thin Film Pd_2Si and PtSi Infrared Schottky-Barrier Detectors with Optical Cavity," *RCA Review* **43** (Dec 1982).
6. A. Fowler and R. Joyce, "Status of the NOAO Evaluation of the Hughes 20 X 64 Si:As Impurity Band Conduction Array," this proceedings (Feb 1989).
7. A. Fowler, R. Joyce, I. Gatley, J. Gates, and J. Herring 1989, "Evaluation of a 256 X 256 PtSi Array for Infrared Ground-Based Astronomy," *SPIE Infrared Detectors, Focal Plane Arrays, and Imaging Sensors,* **1107-06**.
8. A. M. Fowler, Ian Gatley, F. Stuart, R. R. Joyce, and R. G. Probst 1988, "National Optical Astronomy Observatories 1-5 Micron Imaging Camera: A New National Resource," *SPIE Infrared Technology XIV,* **972,** 107.
9. R. W. Russell, B. T. Soifer, and S. P. Willner 1977, *Ap. J. (Letters),* **217,** L149.
10. L. J. Allamandola, A. G. G. M. Tielens, and J. R. Barker 1985, *Ap. J. (Letters),* **290,** L25.
11. K. Sellgren 1981, *Ap. J.*, **245,** 138.
12. I. Gatley and N. Kaifu 1985, "Infrared Observations of Interstellar Molecular Hydrogen," *IAU Symposium No. 120,* ed. Vardya and Tarafdar, p. 153.

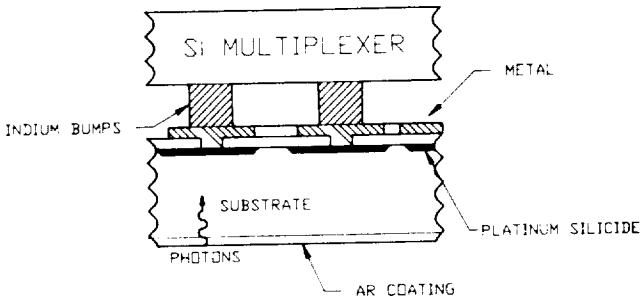

HYBRID ARRAY CROSS SECTION

Figure 1.

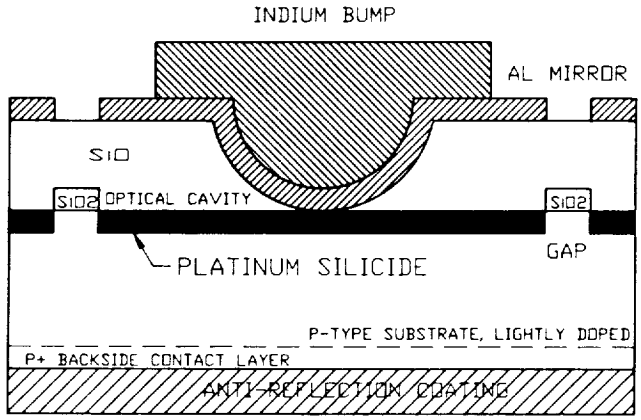

Pt Si ARRAY PIXEL CROSS SECTION

Figure 2.

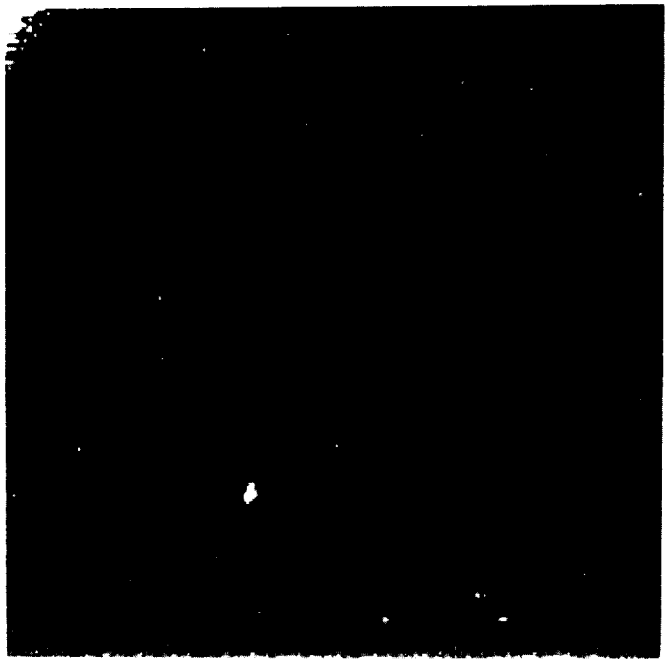

Figure 3. Ratio of 4s, 2s dome flats, displayed over range 1.9-2.1.

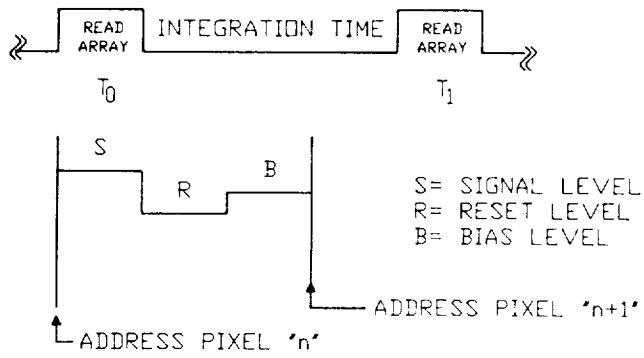

Figure 4a. Combined Readout

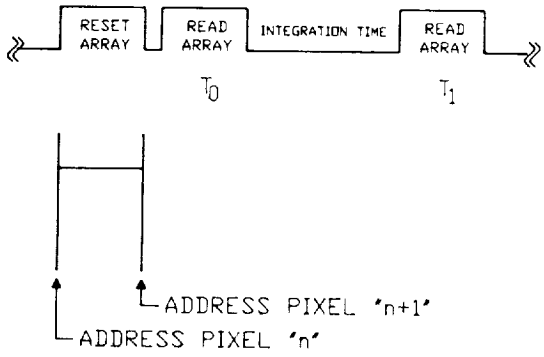

Figure 4b. Serial Readout

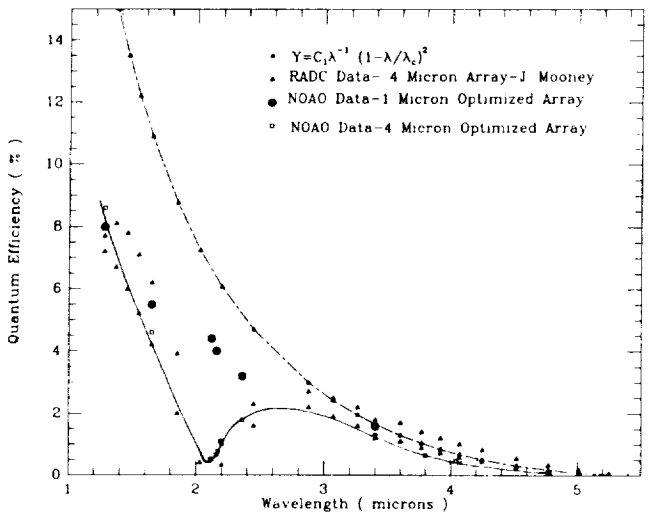

Figure 5. Quantum Efficiency

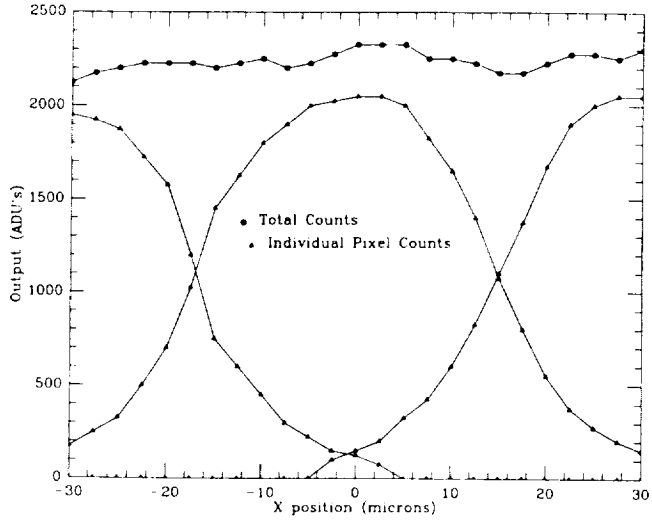

Figure 6. Spot Scan

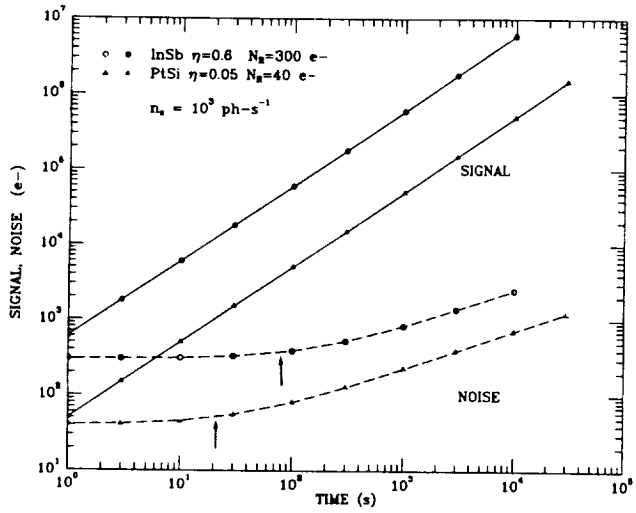

Figure 7a. Signal and Noise for InSb and PtSi

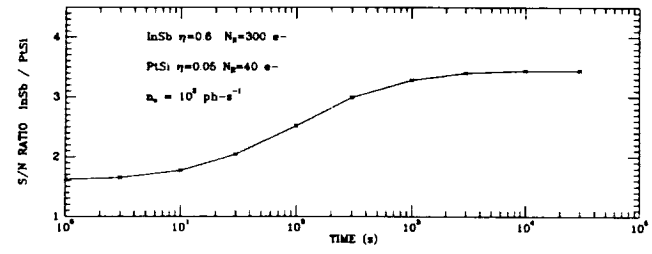

Figure 7b. Performance Ratio InSb/PtSi

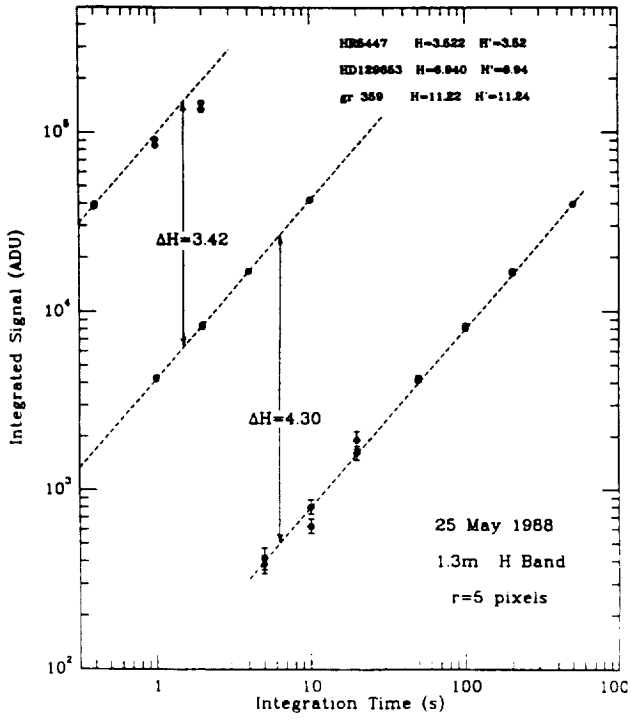

Figure 8. PtSi Linearity Observations

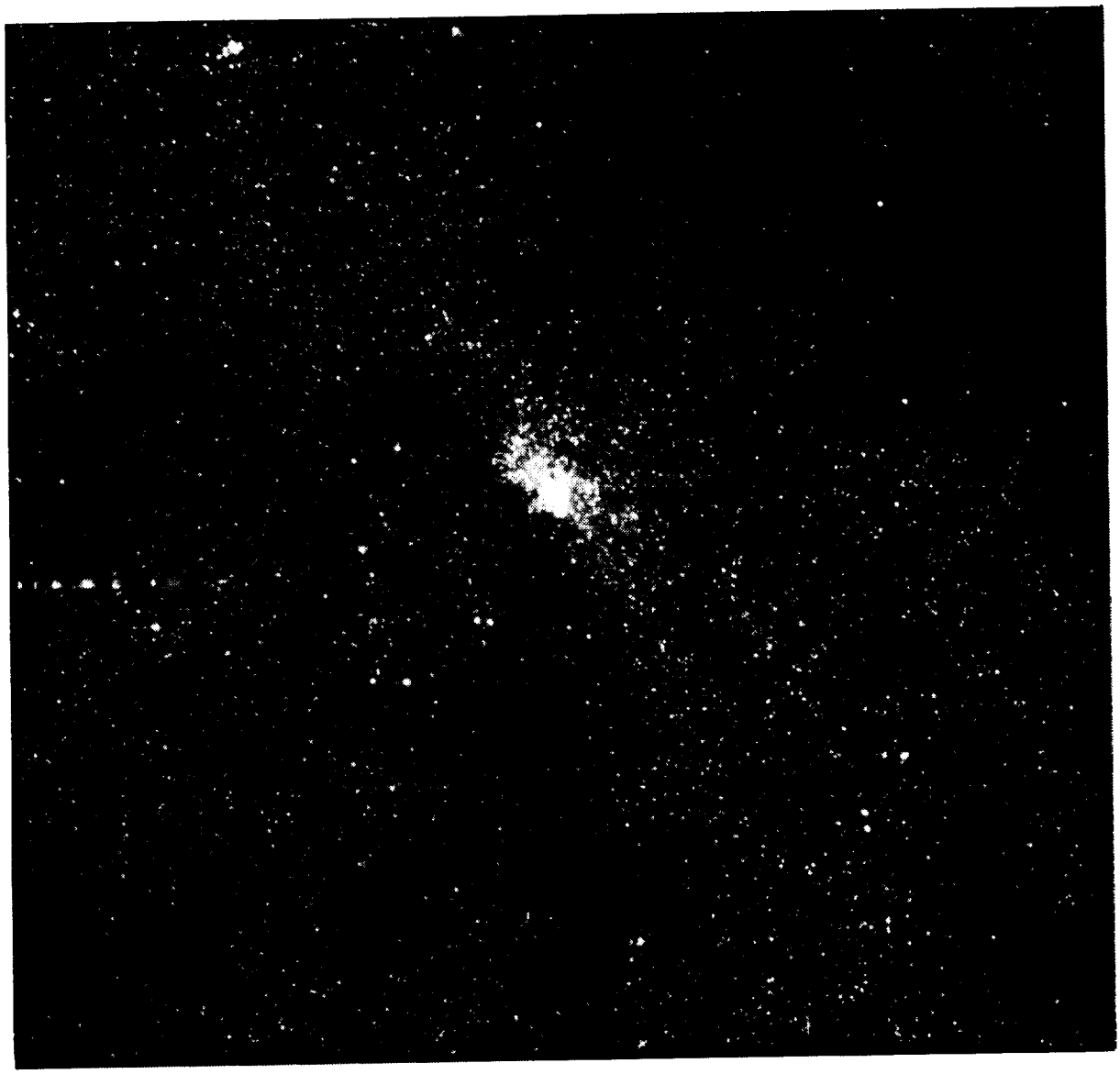

Figure 9 (above). K band mosaic of the galactic center. Field of view 27 arcmin square.

Figure 10 (left). Single frame image (6 arcmin square) of Orion Nebula, through a 3.28 micron ($\Delta\lambda$ = 0.1 micron) filter.

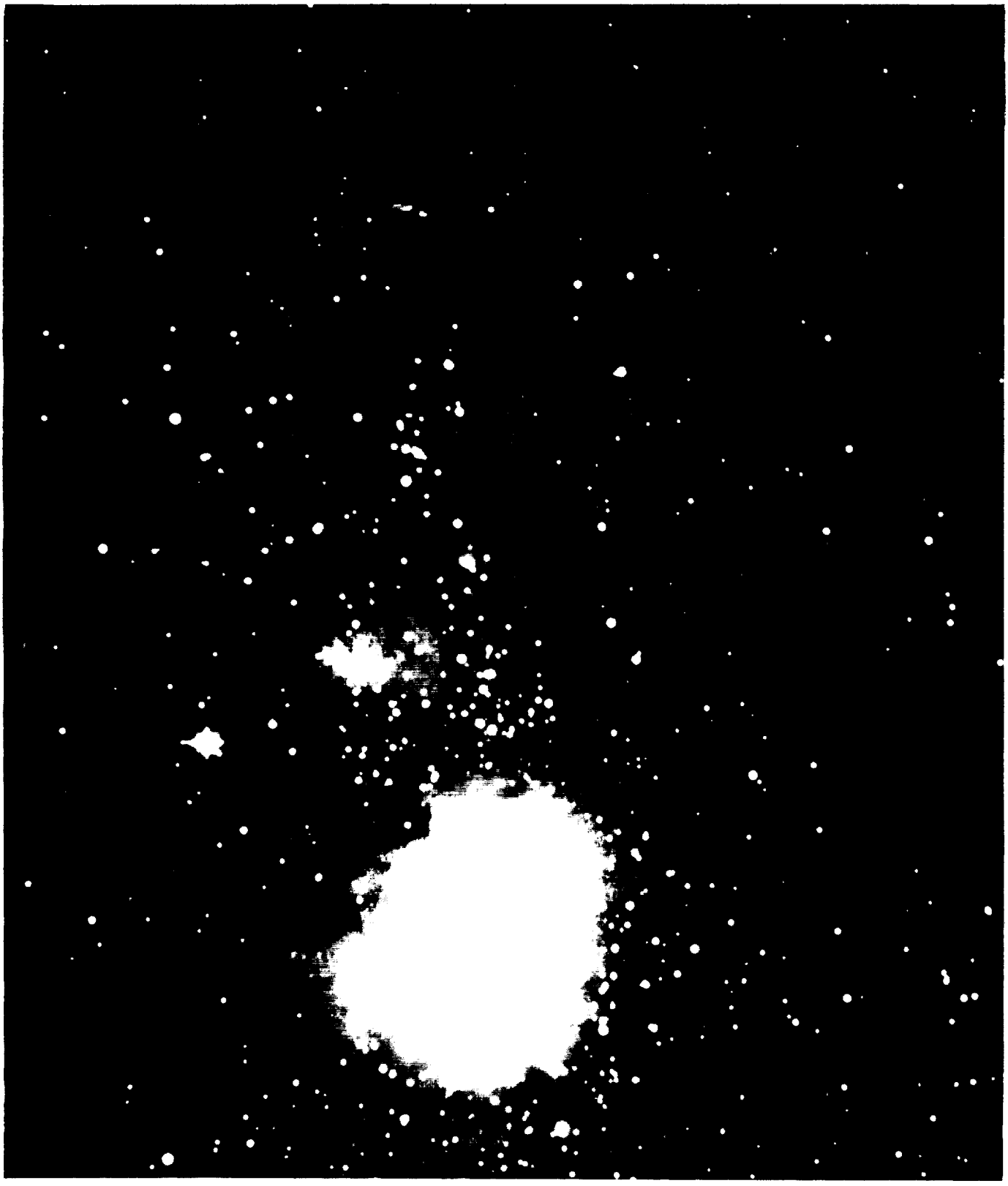

Figure 11. H band mosaic of the Orion Nebula. The field of view is approximately 27 x 37 aremin.

N90-21332

Stressed Detector Arrays for Airborne Astronomy

G.J. Stacey, J.W. Beeman, E.E. Haller
UC Berkeley
and N. Geis, A. Poglitsch, and M. Rumitz
Max-Planck Institut für Physik und Astrophysik

ABSTRACT. We report on the development of stressed Ge:Ga detector arrays for far-infrared astronomy from the Kuiper Airborne Observatory (KAO). We successfully constructed and used a three channel detector array on five flights from the KAO, and have conducted laboratory tests of a two dimensional, 25 element (5×5) detector array. Each element of the three element array performs as well as our best single channel detector, as do the tested elements of the 25 channel system. Some of the exciting new science possible with far-infrared detector arrays is also discussed.

I. Introduction.

Impurity doped germanium photoconductors have been the primary detective devices for far-infrared (FIR) astronomy for many years. The first FIR line detected from an astronomical source was the 88 μm line of doubly ionized oxygen detected from the M17 HII region in 1975 (Ward et al. 1975). The instrument used was a grating spectrometer with a single Ge:Ga photoconductor as the detector. Haller, Heuschen and Richards (1979) demonstrated that the application of 60 kgf mm^{-2} of stress along the [100] crystalographic axis of these Ge:Ga photoconductors lowers the binding levels of the Gallium impurity sites to about 6 meV, shifting the cutoff wavelength of the detectors from ~120 μm to longward of 200 μm.

Stressed Ge:Ga photoconductors were first used for astronomical spectroscopy by Martin Harwit's group at Cornell in 1979. They reported the first astronomical detection of the important fine structure line of singly ionized carbon at 158 μm the following year (Russell et al. 1980). Stressed detectors have now been used successfully by several groups for astronomical research including efforts at Cornell and NASA Ames in the US, in Japan (c.f. Okuda et al. 1989), at MPA in West Germany and our continuing efforts at UC Berkeley and MPE. The detectors and J-FET transimpedance amplifiers have sufficiently low intrinsic noise figures to insure background limited performance from spectrometers on the airborne and balloon borne observatories for even the highest spectral resolutions employed to date (~20 km s^{-1}). Further improvements in the data rate for these spectrometers then requires the implementation of detector arrays.

More than a dozen FIR molecular rotational lines and atomic fine structure lines have been detected by several research groups with stressed detectors. Several other important lines remain undetected. Of special interest are the several rotational lines of H_2O which lie in the wavelength range between 130 and 220 μm. These lines are inaccessible even at aircraft altitudes due to obscuration by terrestrial water vapor lines. Their detection awaits the introduction of space based FIR spectrometers such as SIRTF and ISO.

We report the design and use of a three element linear array for the UCB tandem Fabry Perot on the KAO, and the design and preliminary laboratory testing of a two dimensional stressed detector array to be used on the KAO in a new very high spectral resolution Fabry Perot system in the summer of 1989.

II. A Very Compact Three Channel Stressed Detector.

In order to improve the data taking efficiency of our tandem Fabry Perot system, we replaced our single channel system with a three element detector array.

A. Design Considerations.

The diffraction limited beam size at 158 μm for the 91.4 cm telescope on the KAO is approximately 45". The plate scale at the detector in the UCB Tandem Fabry Perot is 45" per mm. Therefore, the optimal entrance aperture for our detectors (assuming a point source) is 1 mm. It is easy to demonstrate (c.f. Lugten 1987) that the maximum attainable resolution of a Fabry Perot is limited by the angular divergence of the beam in that Fabry Perot. This divergence rapidly worsens as one goes off axis in the system. To minimize this effect, the off-axis channel must be kept as close as possible to the central ray. It is clearly advantageous to keep the beams as close as possible to one another for sampling purposes as well.

This constraint presents a problem. The detectors themselves are typically 1 mm cubes. The probability for single pass absorption for these size detectors is roughly 5 - 10%. Integrating cavities are therefore required for good quantum efficiency. Furthermore, each detector must be stressed nearly to the breaking point along the [100] axis. To achieve high quantum efficiency for a given wavelength (we choose to optimize for 158 μm operation), this stress must be applied uniformly. This insures the response curve in all parts of the detector peaks at the same wavelength.

We achieved this by stacking individual detectors of the array along the stress axis to form a linear array, enabling stress to be applied along a single axis with a single set screw. Figure 1 illustrates our design. The detector is composed of several simple pieces. Each Ge:Ga crystal, (e), (1 mm cube) is mounted in its own integrating cavity whose walls are a 4.5 mm hole drilled through a 1 mm thick wafer of aluminum. The bottom of the cavity is formed by a 50 μm thick piece of stainless shimstock, (a). The aluminum wafers are then stacked such that the bottom of one detector cavity forms the top of the cavity below. The top cavity is capped by the stainless steel top of the detector housing. The aluminum wafers are copper plated, then soldered to the copper plated stainless steel shim stock. The 32 μm copper plating serves as a cushioning pad for the Ge:Ga detectors along the stress axis. This prevents Ge:Ga breakage due to unavoidable small imperfections in the Ge:Ga crystal and stainless surfaces. Each detector is placed within about 50 μm of the center of its cavity and fixed with indium solder. The corners of the detectors are centered with respect to the entrance pinholes to ensure the first pass of reflected radiation is trapped by the integrating cavity and not reflected directly out through the entrance aperture. The detector housing itself is maintained at constant voltage bias, while the signal end of the detector is electrically isolated from the housing by a 75 μm thick sheet of mica, (c). The electrical connection is obtained with a 25 μm thick sheet of brass, (d), which also serves as a stress pad for the detector. Brass pads have an advantage over copper pads in that they cushion adequately but will not extrude under stress nearly as much as copper pads (Beeman et al. 1989). The brass pad has a 75 μm diameter high thermal impedance (Constantan) wire indium soldered at one corner to complete the electrical circuit. A 100 μm thick, 2 mm diameter disk of stainless steel, (b), is fixed to the bottom of each detector wafer, which prevents "drumhead" distortions of the 50 μm stainless plate as the stress is applied. These distortions would result in non-uniform stress, manifested as a slow responsivity onset at long wavelengths, and non-optimal response over a broad band. Stress is applied through the entire stack of three

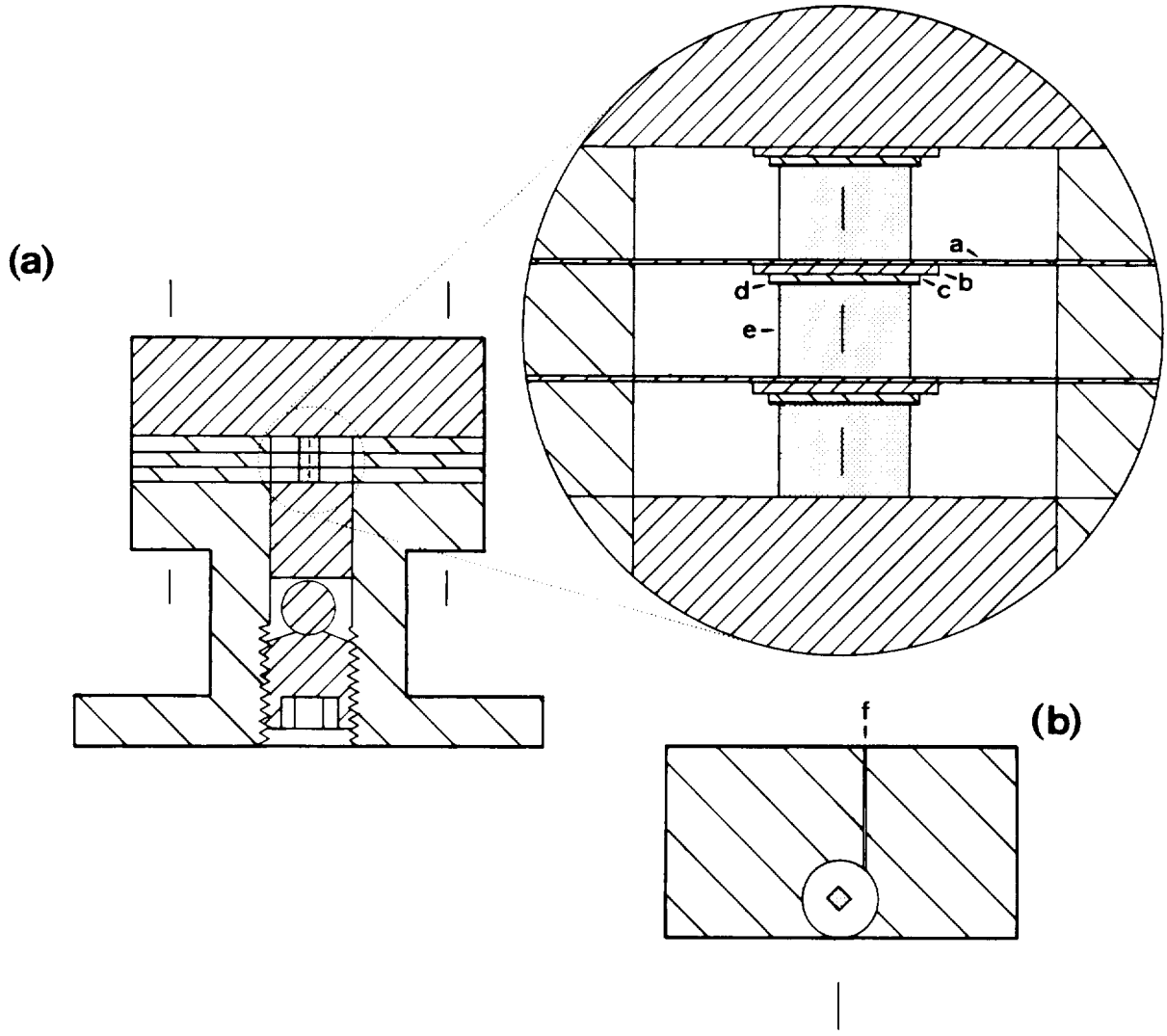

Figure 1. (a) Cutaway drawing of three channel stressed detector array. The inset is an enlarged view of the detector cavities themselves. (b) Top view of a single detector "wafer" shown with the detector installed. (f) is a 250 μm wide, 250 μm deep groove which retains the signal wire.

detectors with a single 1/4" -28 thread set screw. Screw torque is decoupled in the standard manner, a 1/8" stainless steel ball bearing, and stress is delivered through a 4.5 mm diameter piston 5 mm long. The body of the detector is constructed of aluminum alloy which both ensures good thermal conductivity, and results in a large amount of differential thermal contraction between the housing and the stainless steel set screw, ball bearing, plunger and germanium crystal stack. Thus, cooling the detector increases the stress along the detector array axis. The completed detector is shown in Figure 2.

The initial stress on the detector is set at room temperature by measuring the DC impedance of the detector as the screw is tightened. We have found that lowering the impedance to about 85% of its unstressed value results in a responsivity curve which peaks at about 158 μm for this type of detector housing. The differential contraction in the detector housing during cooling will then result in a stress of about 50 kgf mm^2 at 2 K.

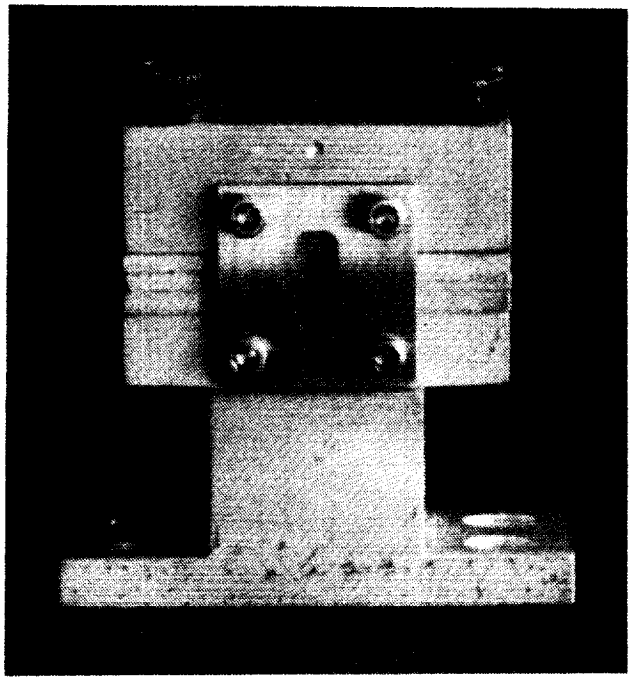

Figure 2. Photograph of the three element linear array. 1 mm pinholes are installed.

TABLE 1

Detector	Cutoff λ	Optimal Bias	Response[1,3]	Noise Equivalent Power[2] Unvignetted[3]	Inflight[4]	
	(microns)	(mV)	(Amp/Watt)	(100 km s^{-1})	(100 km s^{-1})	(40 km s^{-1})
Single Channel	210	15	4.6	3.9	3.9	2.5
Three Channel						
1	215	10	4.1	4.0	5.6	-
2 (central)	220	10	4.9	3.6	3.6	2.3
3	205	10	4.0	3.9	4.6	-
5 x 1 Linear Arrays	212	8	8.5	3.9	-	-

[1] At optimal bias.
[2] In units of 10^{-15} W-$Hz^{-1/2}$, at 158 μm, at the quoted spectral resolutions (FWHM).
[3] For a direct pass through the system; i.e. taking into account known vignetting in the system for the side channels of the three channel detector, but not correcting for walk-off in the Fabry Perot.
[4] Referred to the sky, i.e. including all loses.

B. Three-Element Array Performance

The operating characteristics of the three channel system are similar to the single channel system previously used in the spectrometer (Table 1). At 158 μm, the detector response is ~4 amps/Watt for each channel at the optimal bias voltage (10 mV across the 1mm interelectrode distance). As the detector sensitivity as a function of bias is nearly flat near the optimal bias point, all detectors may be operated at their optimal sensitivity with a common detector bias. The transmission of the entire optical path in the Fabry Perot spectrometer is of the order 16% (Lugten, 1987). With this transmission, and given the background limited performance of the spectrometer, we calculate a quantum efficiency of the order 20% for all of the detectors. Electrical crosstalk has been determined through laboratory measurements at about 1%. Through in flight measurements of Jupiter (42.5" diameter) we have determined the optical crosstalk between detectors, i.e. that percentage of the signal from a point source in one channel which shows up as a edge of the beam signal in the next adjacent channel. The beam overlap is 11% for immediately adjacent channels, and 6% for channels two beams away. The former value is precisely that predicted for a 55" Gaussian beam convolved with the a disk the size of Jupiter (Harris, 1988), while the later number is somewhat larger, consistent with the known extended (non-Gaussian) wings of our FIR beam.

The cutoff wavelengths for each of the three detectors is nearly identical to that of a single stressed detector (~210 μm), the onset is consistent with good uniform stress across the three channels. We measure a system NEP at 158 μm for the central channel of our array which is fully as good as our best single channel NEP (~2-3x10^{-15}W $Hz^{-1/2}$ at 40 km s^{-1} resolution). The side channels have a somewhat higher NEP due to walkoff of the FIR radiation through the FP (c.f. Poglitsch et al. 1989). This problem is not severe at 100 km s^{-1} resolution (factor of 1.3) but rapidly worsens as the divergence limit of the side channel resolution (32 km s^{-1}) is approached.

The detectors are kept at ~2.2 K by pumping on the liquid helium bath. At these temperatures, the dark current is ~3x$10^{6}e^{-1}s^{-1}$. Due to the high background environment on the KAO telescope (equivalent to a 240 K greybody of emissivity 25%) this dark current is an insignificant effect (~10% of the KAO background). We use a standard matched dual J-FET (2N6484) transimpedance amplifier and 2 x 10^{9} Ω ELTEC model 104 load resistors. The silicon J-FETs are mechanically coupled to the helium work surface with thin wall fiberglass tube, and heated to an 80 K operating temperature with a 1kΩ carbon resistor. The detector is shielded from radiation emitted by the heated J-FET assembly with a He temperature copper house around the J-FET "tower". The transimpedance amplifier is essentially microphonic free.

III. A 5x5 Stressed Detector Array.

A. The Triple Fabry Perot Imaging Spectrometer.

As part of a new triple Fabry Perot imaging spectrometer, we have developed a 5x5 stressed detector array. The new Fabry-Perot is a collaborative effort between our laboratories in Berkeley and Munich. The new spectrometer employs several improvements over the tandem Fabry Perot system.

1. We now have a much larger diameter (4 cm vs. 1.6 cm) collimated beam through the scanning Fabry Perot. As the angular divergence of rays in the Fabry Perot goes roughly as the square of the physical size of the collimated beam (assuming diffraction limited beams with the same f-ratio for both systems), the divergence

limit of our new system is approximately eight times better for a given beam size than for the old system. At 158 μm, the divergence limit for the central 40" pixel is of the order 1.5 km s^{-1}. We thus expect to achieve resolutions as high as 2 to 3 km s^{-1} at the [CII] line frequency. At shorter wavelengths, the diffraction limited beam is correspondingly smaller, permitting, for example spectral resolutions as high as 0.5 km s^{-1} at the bright 63.2 μm [OI] line. As with the three channel system, at the highest resolutions the side channels will suffer much more due to off axis rays than the central pixel. The "first ring" of eight pixels has a divergence limit of about 8 km s^{-1}, and the "second ring" of 16 pixels will have a divergence limit of roughly 32 km s^{-1}.

2. We now employ three Fabry Perot interferometers in series to ensure the minimum background radiation on the detectors even at the highest spectral resolution, permitting significant (factor of three to six) improvements in system sensitivity.

3. The focal plane plate scale has been expanded to 4 mm per 40" beam. This expanded scale permits the introduction for the first time of two dimensional detector arrays. These two dimensional spatial arrays offer the advantage over spectral arrays or spatial/spectral arrays of absolute plate scale registry between adjacent pixels in a map.

4. The new spectrometer also features several other new features including: a) Inflight selection of focal plane plate scale, adjustable from 40" to 20" in a few seconds during flight; b) Precise in flight flat fielding with high and low temperature blackbody calibration cells; c) Frequency switched operation of the high order Fabry Perot which permitting accurate mapping of astronomical sources of angular extent larger than the KAO chopper throw.

B. The 5×5 Detector Array Design.

The new 5×5 detector array is essentially an extension of the three detector system. The array is constructed in a stacked manner as with the three channel system, so that the finished detector array consists of five separate 5×1 channel linear arrays. A cutaway of the 5×1 design is illustrated in Figure 3.

The housing is constructed of aluminum alloy. Each detector element, (c), is 1mm × 1mm in cross section and has a 1.5 mm interelectrode distance. Stress is applied by a single torque decoupled set screw through a stainless plunger. The elements in the stack are separated by 3 mm tall close fitting stainless steel plungers which also deliver the stress through the stack. Electrical connection and stress application are achieved in precisely the same manner as with the three element detector array. For all of the detectors in a stack, it is essential that each element have roughly the same cross section through the stress axis, ensuring the uniformity of stress in a stack. It is also important that the plunger walls be both smooth and perpendicular to the stress axis. The detectors themselves must also be cut perpendicular to the stress axis to ensure even application of the stress across the detector face and minimize the probability of breakage.

The focal plane plate scale in the new Fabry Perot is 10" per millimeter. At 158 μm, a diffraction limited beam is therefore ~4 mm in diameter. We use light cones to condense this beam size to a reasonable size entrance pinhole (1 mm) for the detector integrating cavity. The back side of the cone array mates with the detector array and forms a light tight integrating cavity. As with the three element array, all optical elements of the array are plated with a layer of gold 5 μm thick to ensure a corrosion resistant surface of very high reflectivity in the FIR.

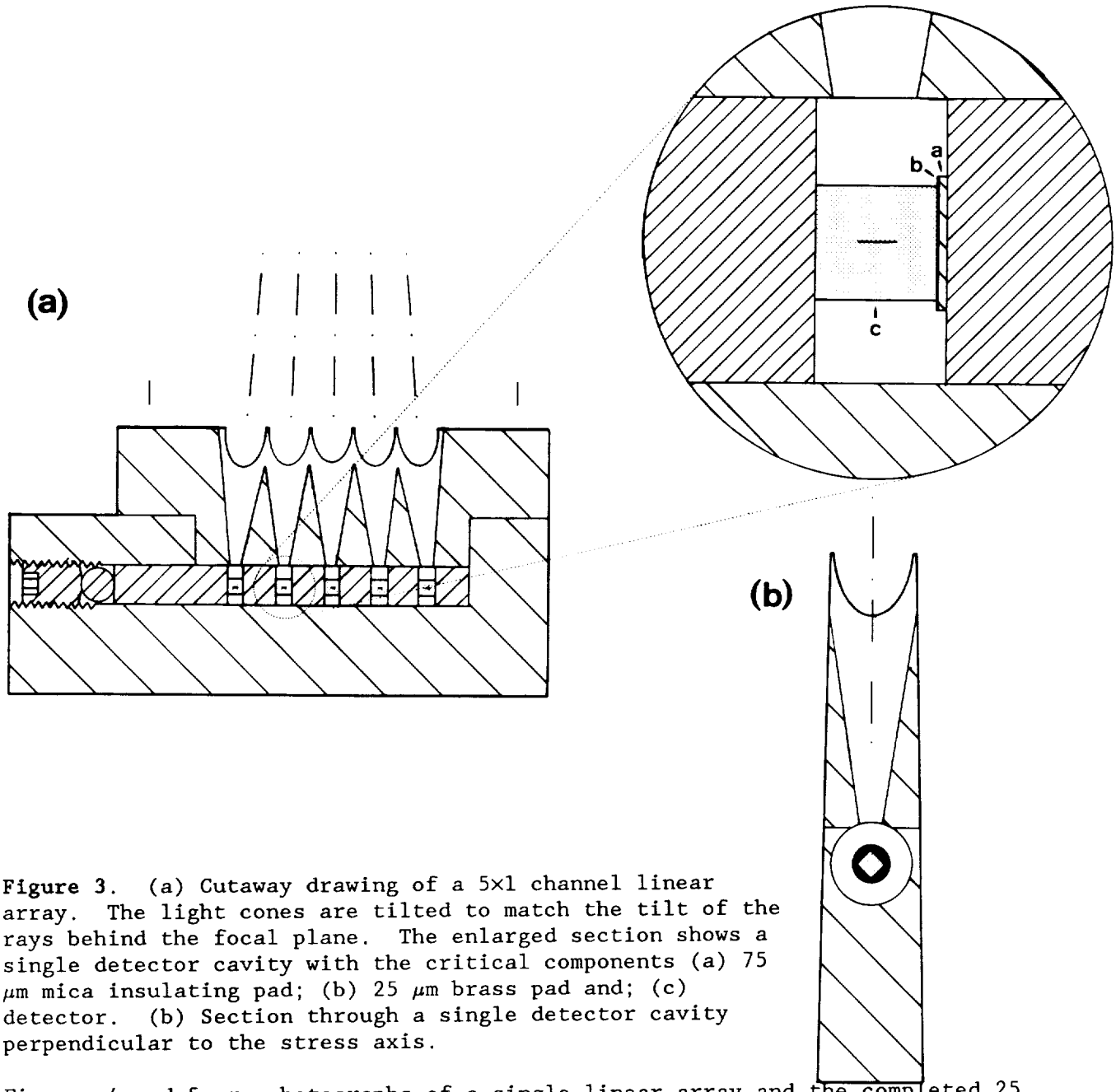

Figure 3. (a) Cutaway drawing of a 5×1 channel linear array. The light cones are tilted to match the tilt of the rays behind the focal plane. The enlarged section shows a single detector cavity with the critical components (a) 75 μm mica insulating pad; (b) 25 μm brass pad and; (c) detector. (b) Section through a single detector cavity perpendicular to the stress axis.

Figures 4 and 5 are photographs of a single linear array and the completed 25 element array respectively. Each array element is identical, and has been designed to be stacked side to side with the adjacent elements. The entire unit makes a reasonably compact unit 8 cm tall and 5 cm wide at the base.

Each linear array is has proven to be easy to assemble. The entire process from cutting the brass pads to stressing the stack takes about two hours per array element. Five stacks have been constructed, each element of which has been thermally cycled to helium temperature at least six times to date with no mechanical failures. The stress on a stack stays constant after about three thermal cycles. Two detectors have been thoroughly tested with respect to sensitivity. Both detectors, the central channel of an array, have 100% of the response and sensitivity of our best single channel detector at both 158 μm and 186 μm, consistent with good uniform stress and high quantum efficiency (Table 1).

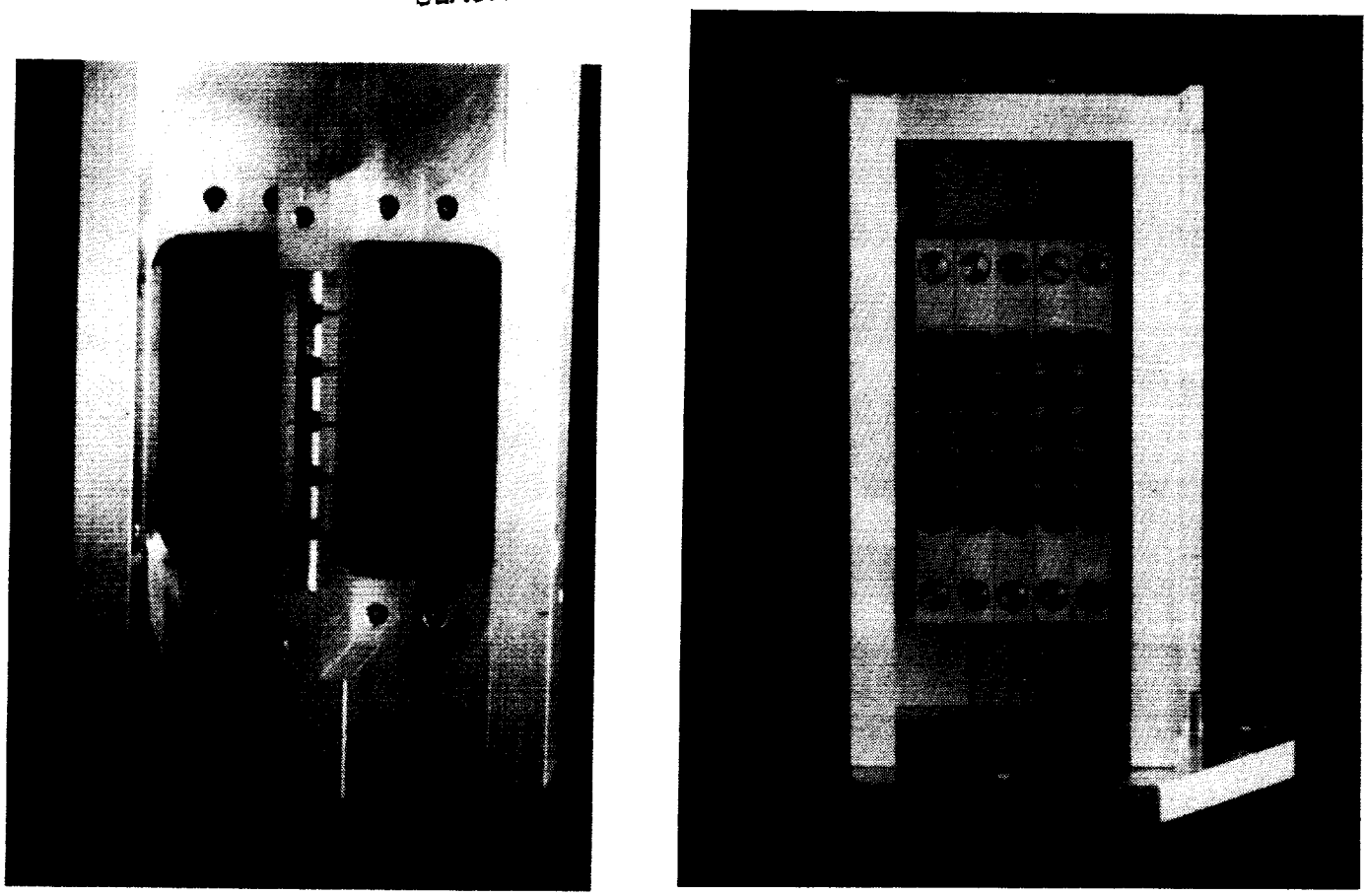

Figure 4. (left) Photograph of a single 5x1 element linear array with the light cone removed.

Figure 5. (right) Completed 5x1 element stressed array with light cones.

IV. Transimpedance Amplifier Arrays

Low noise transimpedance amplifiers (TIA's) which operate at liquid helium temperatures are an important development for detector array technology. Together with the twenty five channel array, a new set of liquid helium temperature transimpedance amplifier arrays has been developed. Each five by one element detector stack has a five channel MESFET transimpedance amplifier securely mounted to its back. These arrays of transimpedance amplifiers consist of five Mitsubishi model 1402 GaAs FET's and five $3 \times 10^9 \Omega$ ELTEC model 112 feedback resistors bonded to a ceramic substrate. These integrated circuits are encased in an aluminum housing which is mechanically attached to the back of each detector array element. The entire assembly makes for a very compact and rugged design. With high input impedance ($>10^{11}\Omega$) and small input noise figures (typically less than 150 nV $Hz^{-1/2}$ at 20 Hz), these transimpedance amplifiers promise to give us background limited performance at even the highest spectral resolutions. As the TIA's are directly mounted to the detector housing, the lengths of the high impedance wires in the TIA circuit are dramatically reduced therefore minimizing microphonics. Further information on the GaAs FET transimpedance amplifiers may be found in a forthcoming publication (Rumitz et al. 1989).

The entire detector block/GaAs transimpedance amplifier stage and spectrometer are in the final stages of testing at present in preparation for a July 1989 KAO flight series.

V. Science with Stressed Detector Arrays.

The three element stressed detector array was flown successfully in flight series during January and June 1988. During these five flights, we have detected six new galaxies in the [CII] line (four of which we have partially mapped), constructed large scale maps of nine galactic molecular clouds in their [CII] line radiation, made the first FIR detection of a rotational line of ^{13}CO and detected FIR ^{12}CO rotational line emission in two galactic sources.

Figure 6 is a 1000 point map of the inner 8' x 10' regions of the Orion Nebula in the [CII] line. We obtained this map in about one hour of observing time on the KAO during the first flight with the new array (Stacey et al. 1989b). The map is fully sampled for each of the three detectors. We have calibrated each channel separately, and combined the maps to achieve the composite image. The side channels serve to improve the signal to noise ratio in the central portions of the map and extend the map borders about 1' in all directions. The least significant contour is about three standard deviations from zero.

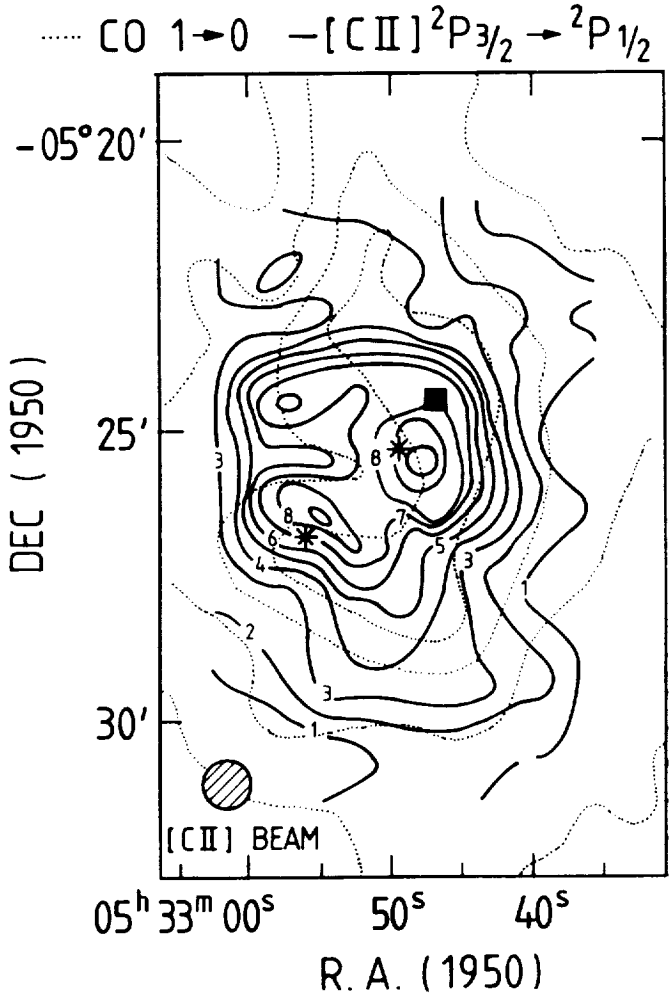

Figure 6. 1000 point [CII] map (dark lines) of the Orion HII/molecular cloud interface region obtained with our 3 detector array in January 1988. The $^{12}CO(J = 1 \rightarrow 0)$ contours (light lines) are from Schloerb et al. 1983).

We have superposed our map on the ^{12}CO (J = 1 - 0) map taken with a similar sized beam by Schloerb et al. 1983. There is excellent agreement between the two maps. The [CII] radiation has been demonstrated to arise in warm (T~500 K) dense ($n_{H2} \sim 2 \times 10^5$ cm^{-3}) photodissociated gas between the visible HII region and the background molecular cloud. The CO line emission traces the molecular gas component. The good spectral and spatial correlation between the two lines indicates that the interface region (traced through its [CII] emission) is physically associated with the "spike" emission seen in the CO line. This supports the contention that this CO emission arises from UV heated warm (T~ 100 K) molecular gas associated with the interface region between the Orion HII region and the bulk of the Orion molecular cloud.

Figure 7 displays a spatially multiplexed spectrum of the starburst galaxy NGC 2146 taken with our three element detector array on its first flight in January 12, 1988 (Stacey et al., 1989b). The array axis was well aligned with the major axis of this highly inclined galaxy: strong [CII] emission is evident from both the nuclear regions (central channel) and regions removed 2.4 kpc away along the galactic major axis (side channels). Strong [CII] line radiation is only consistent with vigorous star formation activity. The large spatial extent of the [CII] radiation in this galaxy indicates that the starburst here is probably not confined to just the galactic nucleus. We have superposed for comparison the $^{12}CO(J = 1 - 0)$ line from this galaxy sampled from the same regions with a similarly sized beam. There is

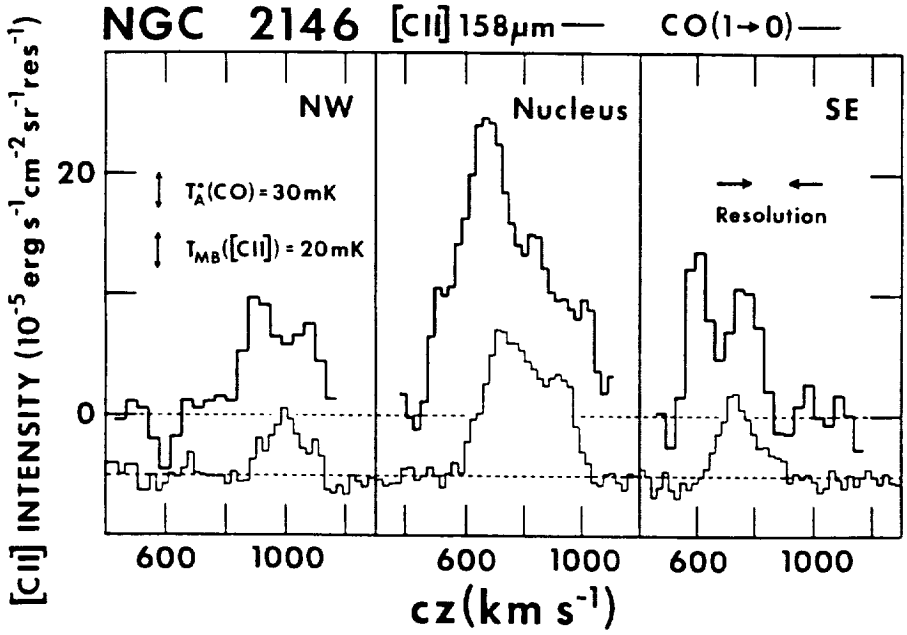

Figure 7. Spatially multiplexed [CII] spectrum (dark lines) of the starburst galaxy NGC 2146 obtained with 22 minutes of integration time with the three channel array. The superposed CO(J = 1 → 0) spectra (light lines) are from Young et al. 1988).

excellent spectral and spatial correlation between the two lines demonstrating that on a galaxy wide scale, the two lines are emitted from similar regions in the galaxy. Notice also that the two lines have a nearly constant line intensity ratio across this galaxy. The line intensity ratio is precisely the same as that obtained for galactic HII regions (e.g. Orion, above).

This result is surprising. The CO line emission from external galaxies is presumed to be dominated by the emission from cold (T~10 K), dark clouds of the galactic "disk". This is the basis for the CO luminosity to mass conversion ratio used for external galaxies. Since there is little UV radiation near these clouds to

photoionize CO and CI to form CII, one would expect very little [CII] line radiation from these cold clouds. This is in fact what we have find for molecular clouds exposed to small UV fields in the Galaxy (Stacey et al. 1989a). On a galaxy wide scale, one would therefore expect a significantly smaller amount of [CII] radiation per unit CO line radiation than for galactic star formation regions. The fact that the line ratio is the same for NGC 2146 (and the nuclei of several other starburst galaxies) as for the Orion HII region indicates that the bulk of the CO line emission from these starburst nuclei may arise in the warm molecular gas associated with star formation regions and not from the cold disk molecular clouds. Thus, for starburst nuclei, the high [CII] to CO line intensity ratio may indicate that the CO line does not purely trace mass but rather traces a combination of mass and molecular gas excitation.

The advantages in a large format detector array for the science described above are evident. The [CII] line radiation from galactic molecular clouds like Orion often extends for substantial fractions of a degree on the sky. Detailed maps of such sources clearly requires a large format array, with its inherent increased data rate (in this case, a factor of 25 over a single channel spectrometer). A 2-dimensional spatial array such as the one described here has the further advantage of absolute registry between pixels in a map. This feature facilitates significantly improved registry between the FIR maps and those obtained with other telescopes in other spectral lines.

Acknowledgements.

We are indebted to the skills of the UC Berkeley machine shop whose talented personnel have made these detectors possible. G.J.S., N.G., A.P., and M.R. thank R. Genzel and C.H. Townes for their enthusiasm and support. We also thank the staff of the Kuiper Airborne Observatory for their usual enthusiasm and especially to W. Whiting for the new programming which allowed us to run with three channels for the first time with minimal pain. We are indebted to A.I. Harris for critical readings of this manuscript. This work was supported by NASA grant NAG2-208.

References

Beeman, J.W., Haller, E.E., Hansen, W.L., Luke, P.N. and Richards, P.L. 1989, this conference.

Lugten, J.B. 1987, Ph.D. thesis, University of California, Berkeley.

Haller, E.E., Hueschen, M.R., and Richards, P.L. 1979, **Appl. Phys. Lett.** 34, 495.

Harris, A.I. 1988, **Intl. J. IR and mm Waves 9**, 231.

Poglitsch, A., Geis, N., Genzel, Haggerty, M.R., Rumitz, M., Stacey, G.J., and Townes, C.H. 1989, in prep.

Okuda, H. et al. 1988, **IAU Symposium NO. 136, The Galactic Center**, M. Morris ed., Springer Verlag.

Rumitz, M. et al. 1989, in prep.

Russell, R.W., Melnick, G., Gull, G.E., and Harwit, M. 1980, **Ap. J. (Letters)** 240, L99.

Schloerb, P.F., Friberg, P., Hjalmarson, A., Hoglund, B., and Irvine, W M. 1983, **Ap.J. 264**, 161.

Stacey, G.J., Genzel, R., Graf, U., Harris, A.I., Stutzki, J., and Townes, C.H. 1989a, in prep.

Stacey, G.J., Genzel, R., Lugten, J.B., and Townes, C.H. 1989b in prep.

Ward, D.B., Dennison, B., Gull, G., and Harwit, M. 1975, **Ap. J. (Letters) 202**, L31.

Young, J.S., Clausen, M.J., Kleinmann, S.G., Rubin, V.C., and Scoville, N. 1988, **Ap.J. (Letters) 331**, L81.

N90-21333

AFGL Ten Micron Mosaic Array Spectrometer - Recent Results

Paul D. LeVan

Air Force Geophysics Laboratory
Hanscom AFB, MA 01731

Abstract

Recent measurements have been made with a novel mosaic array prism spectrometer on long period variable stars of carbon and oxygen-rich atmospheres. These stars have generally large IR excesses and show strong SiC and silicate emission features, respectively. A comparison is provided by published spectra obtained with the IRAS Low Resolution Spectrometer. Emission feature equivalent widths are independent of the absolute photometric level of the spectra and provide information on the relative variation of the feature and continuum fluxes between the epochs of the space and groundbased observations.

1. Introduction

The AFGL mosaic array spectrometer has been discussed previously (LeVan and Tandy 1987); we review the instrument briefly and report here on the more recent characterizations of its performance and on spectra of long period variable stars obtained with the instrument.

a. History The mosaic array is a 58 by 62 pixel Si:Ga detector array hybridized to a CRC-228 Direct Readout (DRO) multiplexer. It was lent to us by Santa Barbara Research Center in summer of 1984. A substantial electronics design effort was undertaken at AFGL to allow the high frame rates expected for such an array operated as a slit spectrometer in the 8 to 14 μm region at resolving powers of approximately 50. The electronics includes both the array address subsystem for operation of the array at frame rates as high as 185 Hz, and the hardware coadder circuitry that allows for real-time accumulation of digitized frames. By September of 1985, the electronics had been built and the array could undergo characterization for high speed operation in a testbed dewar. Concurrent with this, the optics, which consists of a NaCl prism slit spectrometer, was under construction by Sensor Systems Group, Waltham, MA, using our optical design. By summer of 1986, the optics and the array characterization had been completed, and the two assemblies were then integrated into an IR Laboratories Inc. dual flask dewar (an extended Model HD-8). First light was October of 1986 on the University of Wyoming 2.3 m telescope.

2. The Instrument - Electronics

a. The Mosaic Array The SBRC schematic of one of the 1798 total "unit cell" structures is shown in Figure 1. Note that the Si:Ga photoconductors have a bias voltage equal to the difference of the

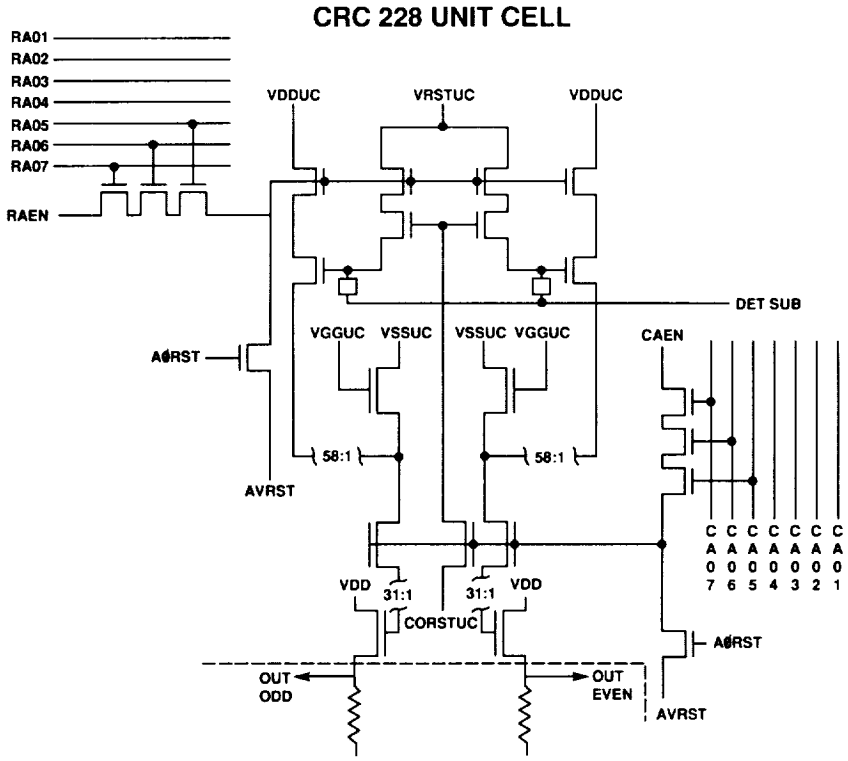

Figure 1. One of 1798 total mosaic array unit cell structures.

"detector substrate" and reset (VRSTUC) voltages immediately after reset; this voltage difference decreases as signal charge is integrated onto the capacitance formed at the detector array and multiplexer interface. The bias and clock voltages may be controlled externally; these were chosen for high speed operation as discussed in **b**, below. Finally, the pair of source followers that comprises the last stage of the multiplexer has associated load resistors that are external (shown below dashed line in Figure 1) and therefore selectable.

b. Operating Bias Voltage and Load Resistor Values The values of bias and clock voltage are in general those determined by NASA/GSFC during testing of a similar mosaic array under low background conditions (Lamb et al. 1986). Several deviations from these values were found by us to permit high speed operation of the array: 1) The source follower gate voltage (VGGUC in Figure 1) was increased from 0.7 to 0.85 volts, and 2) the load resistance was decreased from 100 KΩ to 10 KΩ. These settings resulted in a decrease of the reset time for a one volt source follower signal from approximately 10 to 1 μsec. The reset speed is set by the charging rate of the dewar wire capacitance, which is increased for the higher source follower drain currents. The higher currents are made possible with larger values of VGGUC and smaller load resistances. (For extreme values of either, the gain of this stage suffers).

MODE	ALU	RAM	DATA SELECT
COADD	F = A+B	R/W	ADC
OUTPUT	F = A-B	R	BUS

Figure 2. Hardware Coadder schematic. The inserted table shows component states for data acquisition (= coadd) and data output.

c. Hardware Coadder A schematic of the co-addition electronics shown in Figure 2 illustrates its function for data acquistion (= coadd) and data output. A key component is the Arithmetic Logic Unit (ALU), the mode of which changes from sum to difference between coadd and output modes. In coadd mode, the B input to the ALU is the digitized signal from a mosaic array pixel, the A input is the accumulation of previous signals for the same pixel fetched from RAM in read mode, and the output is the sum of these. This output is latched and rewritten to RAM at the same pixel address. In output mode, the A and B inputs are the accumulation of previous signals for a given pixel in separate telescope secondary mirror chopping positions, and the output of the ALU is the difference of these. The difference is transferred to the data acquisition computer. The table shown in Figure 2 summarizes several of the state changes between data acquistion and data output modes.

d. Electronics Overall Timing An attempt to summarize the timing of the more important clock controls may be helpful: The pixel clock rate of 333 KHz corresponds to 3 μsec pixel "windows" during which we clamp the signal, reset the signal charge, and sample and convert the difference between the clamped and reset levels (= Correlated Double Sampling). The frame rate is 185 Hz and the pixel integration time is 5.4 msec as a consequence of the continuous (as opposed to burst mode) frame reads. After every 32 frames, we

command the telescope secondary mirror to chop. Although the array continues to be scanned after the chop command, coaddition is suppressed during a selectable number of frames to allow for the settling of the secondary mirror. After 5 full chop cycles, the coadded frames of the plus and minus telescope beams are differenced and transferred to the computer. This transfer takes place at a rate of about 25 μsec per pixel, keeping the duty cycle high (96% , or 48% if one considers only the source frames).

3. The Instrument - Optics Characterization

The optical ray trace and assembled optics bench are illustrated in a prior publication (LeVan and Tandy 1987). Here, we discuss spectra of polystyrene film acquired to assess the wavelength calibration of the instrument. Spectral features of polystyrene near 9.35, 9.73, 11.0, 11.9, and 13.3 μm are clearly visible for three spectral rows of a single exposure with the mosaic array spectrometer (See Figure 3). These features are seen to be broadened by the instrumental response over the reference spectrum also shown in Figure 3. By using the Image Reduction and Analysis Facility (IRAF) Onedspec package, a wavelength solution was obtained that is in excellent agreement with published values of $dn/d\lambda$ for NaCl. IRAF was subsequently used to interpolate program object spectra onto an equally spaced wavelength grid.

4. Observing Setup

The dewar is mounted on a down-looking interface to the telescope cassegrain focus. All analog electronics and the analog to digital converters are enclosed in a metal box mounted to the dewar. Four commercial pulse generators (Berkeley Nucleonics Corp. Model 8010) are mounted to the telescope backplane, as is the hardware coaddition electronics. The power supplies reside on the floor of the dome, and the data acquistion computer in the control room at a distance of roughly 20 meters.

5. Recent Results - Long Period Variable Star Spectra

a. Motivation

We now discuss recent results of an ongoing measurement program on the University of Wyoming 2.3 m telescope using the mosaic array spectrometer. Eight sources have been measured during two observing runs reported here. These stars, with the exception of the calibration standard, are long period variables with generally large IR excesses. Three stars have carbon rich atmospheres, and an accompanying SiC emission feature near 11.3 μm. Three others have oxygen rich atmospheres and show pronounced silicate feature emission. We seek to address the possiblity of variation of the feature flux as the continuum varies. An additional observational epoch is provided by the IRAS Low Resolution Spectrometer (LRS) whose published spectra are contained in the Atlas of Low Resolution Spectra (Olnon and Raimond 1986). Since neither the LRS or AFGL instrument is strictly photometric, we may compare equivalent widths of the emission features for the purpose of determining relative variability of feature and continuum fluxes.

b. Spectrometer Exposures The observations consist of 4 exposures per star that individually result from telescope beamswitching over an approximate two minute interval. For such an exposure, the instrument obtains spectra of signal to noise greater than 10 for a -2.5 mag point source. Whereas the quoted sensitivity compares unfavorably with single pixel and mosaic array cameras operated with narrow bandpass filters, the spectral multiplex advantage nevertheless allows for observing efficiencies vastly improved over that of CVF systems.

c. Spectra We show representative spectra for each class of star and for each instrument in Figure 4. Blackbody continuum fits are shown that match best the continua on each side of the feature. Note the short wavelength cut-on of the AFGL instrument is approximately 9 μm and does not encompass the continuum point on the blue side of the strong silicate feature - a correction for this is made by setting the continuum such that its ratio to the feature at 9 μm is approximately that of the LRS spectrum. Also shown in Figure 4 is the feature profile that results upon subtraction of the continuum fit. Of the two stars shown, the V Cygni equivalent widths are in good agreement between the two observational epochs. On the other hand, IRC +10420 appears to exhibit a change in equivalent width between the earlier and later epochs. Further details, including the results of comparison for all six long period variable stars with LRS spectra, are contained in a forthcoming publication (LeVan and Sloan 1989, submitted to PASP).

Acknowledgements

We gratefully acknowledge the generous telescope time allotments provided by the Wyoming IR Observatory, as well as the support of WIRO staff, including T. Hayward and J. Benson. Peter Tandy is acknowledged in his role as the AFGL electronics engineer on this project. Finally, G. Sloan, a coauthor on the manuscript describing in detail the more recent observational work, is thanked for his implicit contributions.

References

Lamb, G.M., Shu, P.S., Lockerson, D.C., Gezari, D.Y., and Bowser, J. 1986 in Proceedings of the Second IR Detector Technology Workshop, (C. McCreight, ed.), NASA Tech. Memo. 88213, pg. 25-1.

LeVan, P.D. and Tandy, P.C. 1987, in Infrared Astronomy with Arrays, (Wynn-Williams and Becklin, eds.), University of Hawaii at Hilo, 411.

Olnon, F.M. and Raimond, E. 1986, Astron. and Astrophys. (Supp.), **65**, 607.

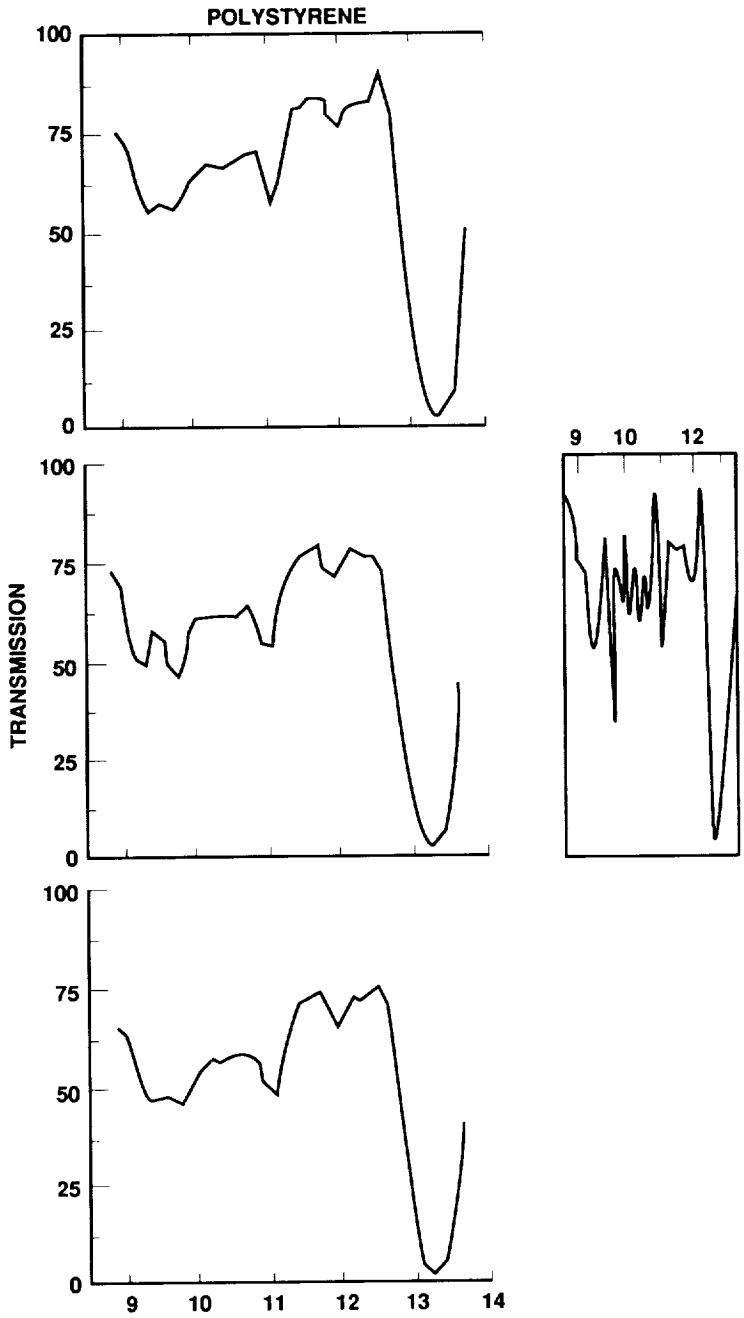

Figure 3. Spectra of polystyrene film. Shown are three spectra from a single mosaic array exposure along with the reference spectrum.

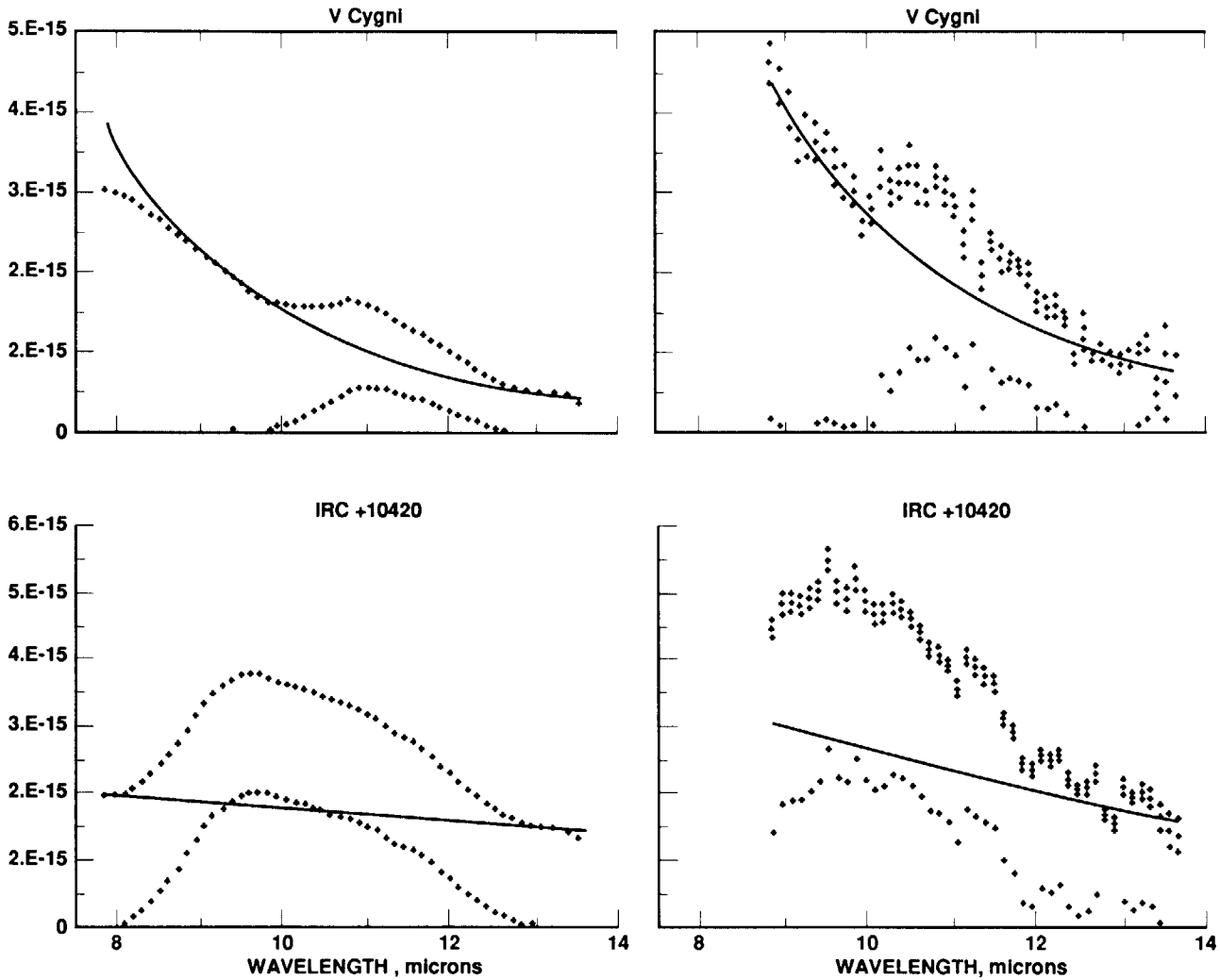

Figure 4. Spectra from the LRS (Left) and AFGL (Right) instruments, before and after subtracting an (approximate) blackbody continuum fit. The units of the vertical axis are W /cm² /μm.

Initial Astronomical Results with a New 5 - 14 μm Si:Ga 58 X 62 DRO Array Camera

Dan Gezari, Walter Folz, and Larry Woods

NASA/Goddard Space Flight Center
Infrared Astrophysics Branch, Code 685, Greenbelt, MD 20771

A new array camera system has been developed using a 58 x 62 pixel Si:Ga (gallium doped silicon) DRO (direct readout) photoconductor array detector manufactured by Hughes/ Santa Barbara Research Center (SBRC). The camera system is a broad band photometer designed for 5 - 14 μm imaging with large ground-based optical telescopes. In a typical application a 10 μm photon flux of about 10^9 photons $sec^{-1}m^{-2}\mu m^{-1}$ arcsec^{-2} is incident in the telescope focal plane, while the detector well capacity of these arrays is 10^5-10^6 electrons. However, when the real efficiencies and operating conditions are accounted for, the 2-channel 3596 pixel array operates with about 1/2 full wells at 10 μm and 10% bandwidth with high duty cycle and no real experimental compromises.

CAMERA SYSTEM AND PERFORMANCE:

The 58 x 62 Si:Ga DRO Array:

The SBRC DRO array is a hybrid device, assembled from an optimized Si:Ga detector wafer bump-bonded to a CRC-228 multiplexer, with stable electronic and photometric characteristics (c. f. Hoffman 1987). The same 58 x 62 CRC-228 multiplexer is used in the SBRC 1 - 5 μm photovoltaic InSb (indium antimonide) arrays, and has been characterized for astronomical applications by several groups (McLean et al. 1986; Fowler et al. 1987a, 1987b; Ninkov, Forrest and Pipher 1987; McCaughrean 1988). The 15 - 30 μm Si:Sb (antimony doped silicon) version in this family of SBRC arrays has been described by McKelvey et al. (1987).

This Si:Ga DRO array (operating at 12 Kelvin) has a detector capacitance = 0.07 pF with a net bias of 10 volts, based on a measured full well capacity = 7 x 10^5 electrons, an ηG_{pc} product ~ 0.2, read noise < 200 electrons/read, dark current < 630 electrons/sec (light leak limited), gain variation among pixels ~ 15% correctable to < 0.1% by flat fielding, active pixels > 99%, and crosstalk < 5%.

Camera Electronics and Data System:

The camera electronics system (Figure 1) is divided into three sub-systems: 1) analog front-end electronics (Folz 1988), including low noise 2-channel preamp modules, high-speed A/D converters, regulated low-noise bias power supplies, timing generator, timing signal buffer, and detector temperature monitor/regulator, 2) digital data acquisition section based on a Q-bus Mercury ZIP 3216 arithmetic array processor and 3) DEC LSI 11/73 host computer for camera control and data analysis. A detailed description of the camera system analog and digital electronics is given by Gezari et al. (1988).

In low background applications correlated triple sampling is used to achieve detector-limited noise performance (<100 electrons/read) by suppressing 1/f noise, kTC reset

noise, and similar small effects. However, at high-backgrounds the measured noise is limited by fluctuations in the thermal photon background at the ~1000 electron level, and detector noise sources are negligible. For applications requiring a faster frame rate, carefully calibrated single sampling is used to operate at 60 Hz without sacrificing noise performance. The full 16 bit resolution of the A/D converters is not required for high-background applications, but would be used for low- background experiments with large dynamic range.

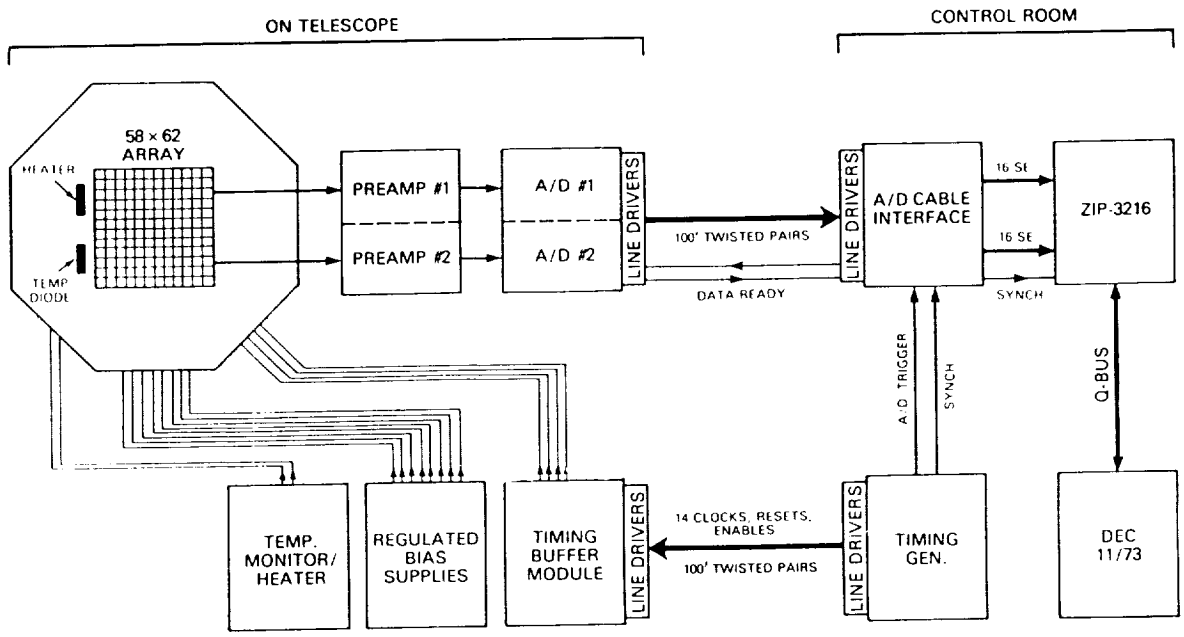

Figure 1: The electronic design of the 58 x 62 Si:Ga DRO camera system.

Cryogenic Optical System Design:

The array camera uses an off-axis reflective optical design (Gezari 1988a) which produces diffraction-limited images with good background radiation suppression. A single off-axis 3.0-inch focal length parabolic mirror, 0.7-inch square, is the only focusing element. The telescope optical axis is located 0.75 inches off the axis of the parabola (figure 2). The parabola re-images the telescope focal plane (located 1 inch outside the dewar) on the array with a de-magnification of 2:1, resulting in an array plate scale on the f/35 3-meter IRTF telescope of 0.26 arcsec per pixel. This permits for rigorous sampling of diffraction-limited image information (two pixels per airy FWHM at 8 μm) and gives a field-of-view on the IRTF of 14.9 x 16.3 ($\pm$ 0.1) arcsec. The parabola also makes an image of the f/35 secondary mirror at a 0.09 inch diameter cold aperture stop on the parabola axis. The cold stop defines the spectral bandwidth of the circular variable filter (CVF) to be 0.4 μm at 10 microns. Another filter wheel contains set of 10% bandwidth OCLI fixed interference filters at 7.9, 8.7, 9.8, 10.3, 11.6 and 12.4 μm. The net optical efficiency (telescope, photometer dichroic and dewar optics) is about 10% (dominated by ~ 50% transmission CVF filter). The camera is diffraction-limited at wavelengths $\lambda > 5$ μm and typically produces seeing-limited 1.0 $\pm$ 0.1 arcsecond stellar images in long integrations

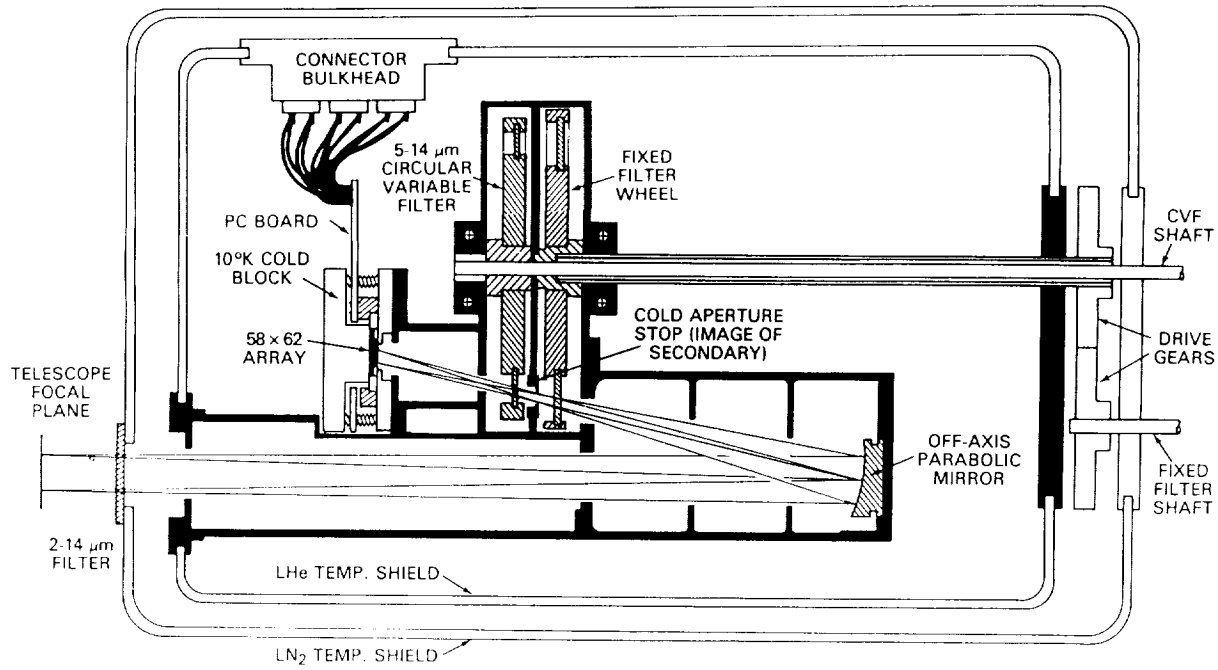

Figure 2: Optical design and mechanical layout of the cryogenic dewar optical bench, showing the arrangement of the off-axis parabola, cold aperture stop at the image of the telescope secondary mirror, 5 - 14 μm circular variable filter (CVF) and fixed filter wheels, and the array at the de-magnified image of the focal plane. The cold optics are contained in a baffle system within the LHe temperature radiation shield to minimize light leaks.

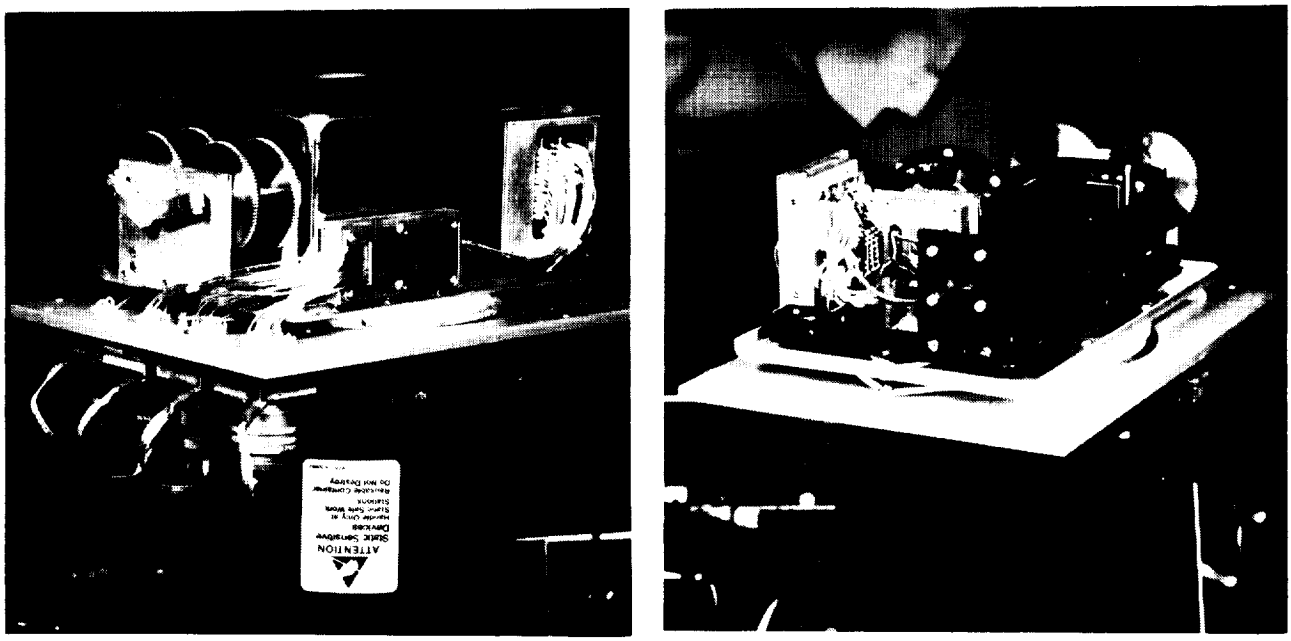

Figure 3: Two views of the cryogenic optical bench assembly with the dewar inverted and vacuum housing and LN_2 shield removed. Left: The LHe temperature cold shield housing, individual stainless steel micro-coax wiring feeding through a heat-sink maze at the LN_2 shield, the LN_2 temperature bulkhead and drive gears for the two filter wheel shafts, connector bulkhead at the LHe shield, and connectors on the warm vacuum housing cover. Right: View from the opposite side with LHe housing removed, showing the square off-axis parabolic mirror segment (right) in front of the filter drive gears, the fixed and circular variable filter wheels (center) behind the cold array mounting block, and the micro-coax cold connector bulkhead (left).

on the IRTF. Aberrations are negligible and field rotation and distortion (pin cushion, etc.) across the array are less than 1/2 pixel across the full field of the detector (<0.5 degrees). The cryogenic optical assembly is shown in Figure 3.

Sensitivity and Noise Performance:

On the telescope the detector is background-limited; electronic system noise, detector read noise and dark current noise are negligible (<200 electrons) compared to total background and sky noise of roughly 1000 electrons (depending on telescope temperature and weather conditions) per 30 msec integration. The array camera NEFD (noise equivalent flux density) at 10 μm on the IRTF is NEFD = 0.05 Jy pixel^{-1}min$^{-1/2}$ (1σ) for extended sources, a source surface brightness of 0.7 Jy arcsec^{-2}. The NEFD for point sources is about 0.7 Jy min$^{-1/2}$ since the diffraction/seeing limit is typically about 1 arcsec and the point source flux is spread among a number of pixels. (*Note added in proof:* The effective well capacity was recently trippled by reducing the net bias to 4 volts, thus reducing G_{pc}, to permit the use of 10% bandwidth interference filters. This resulted in a S/N improvement of about 2 due primarily to improved photon statistics).

ASTRONOMICAL RESULTS:

The Galactic Center - Arcsecond Scale Structure and Dust/Gas Ratio:

Seeing-limited images of the central 16 arcsec (0.8 parsec) field of the Galactic Center obtained at 7.8, 9.8, 11.6 (Figure 4a) and 12.4 μm with the DRO array camera reveal new structural details in the infrared dust distribution on the 1 arcsec scale. In addition, a mosiac image with the same resolution of the 50 x 90 arcsec field in the vicinity of the Sgr A West complex has been developed from 20 individual 1 min integrations at 12.4 μm (Figure 4b). These results are discussed in detail by Gezari (1989b).

The new array results show structure which is strikingly similar to the ionized gas emission features seen in VLA maps (Yusef-Zadeh 1988), and in the Br α and Br γ near infrared array images (Forrest et al. 1986). However, the warm dust and ionized gas distributions show significant discrepancies in the positions of several of the bright peaks (Gezari 1988b).

A detailed comparison of the 11.6 μm array image (Figures 4a, 5a) and 6-cm continuum VLA image (Figure 5b) with the same (1 arcsec) spatial resolution has been made (Yusef-Zadeh and Gezari 1989). The most pronounced positional shift is seen at the positions of IRS 2 and nearby IRS 13. These two sources lie at the western edge of a 2 arcsec mini-cavity which was recently noted in the sub-arcsecond resolution VLA map of Sgr A West (Yusef-Zadeh et al. 1988). The relative infrared and radio emission intensities may be due to stellar wind which has produced the mini-cavity and which has depleted the dust paricles at the inner edge of the cavity close to the source of outflow.

Figure 5(c) shows the dust-to-gas ratio calculated from the two data sets. Differences between the warm dust and ionized gas distributions along the major source structures in the complex are evident as varaitions in the 11.6-μm/2-cm dust-to-gas ratio calculated from the two data sets. Considering the high relative positional accuracy ($\pm$ 0.1 arcsec) and comparable spatial resolution (1 arcsec), the relative source positions and derived dust-to-gas ratio are significant. The spatial variation of R may be due to a

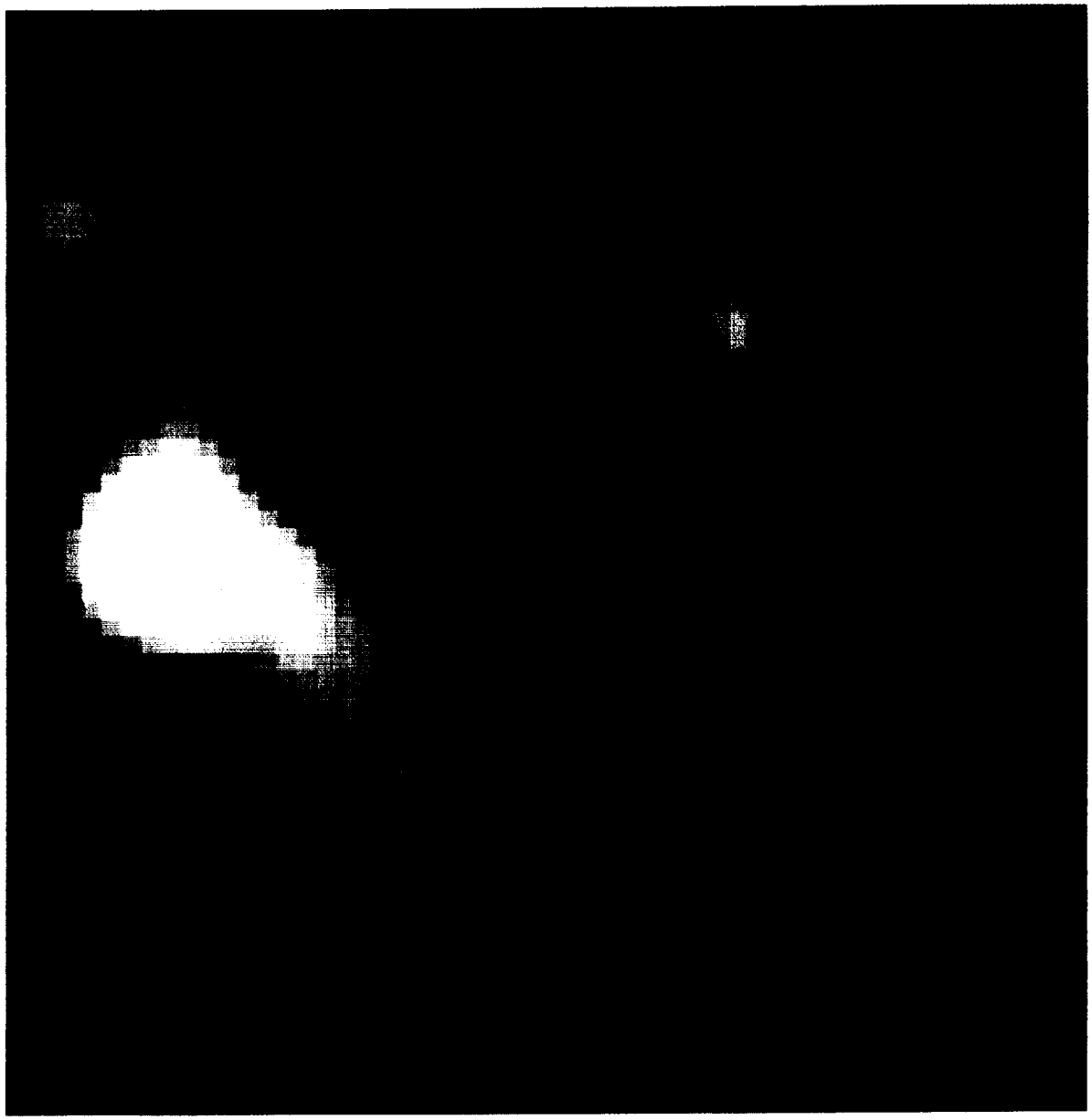

Figure 4a: 11.6 μm array camera image of the central 0.8 parsec (16 arcsec) of the galactic center, coadded from four individual 1 min long integrations on the 3-m IRTF Telescope. This 1 arcsec resolution image shows the curved ridge and bright compact sources surrounding the non-thermal point source Sgr A* (not detected, at the center of the image) and reveals extended infrared source structure similar to the Brackett α and 6-cm continuum VLA distributions, with notable discrepancies in the positions of several bright peaks. The results are discussed in detail by Gezari (1989b).

Figure 4b: A preliminary 12.4 μm mosiac image of the Sgr A West complex assembled from 20 individual 1 min integrations, covering an area of about 50 x 90 arcsec (top 20 arcsec not shown). The brightness scale is logarithmic, from about 1 - 20 Jy arcsec^{-2}. The central field shown in Figure 4a is seen in this large scale image as the saturated ridge at lower-center (approximately 2-inches square). Details in Gezari (1989b).

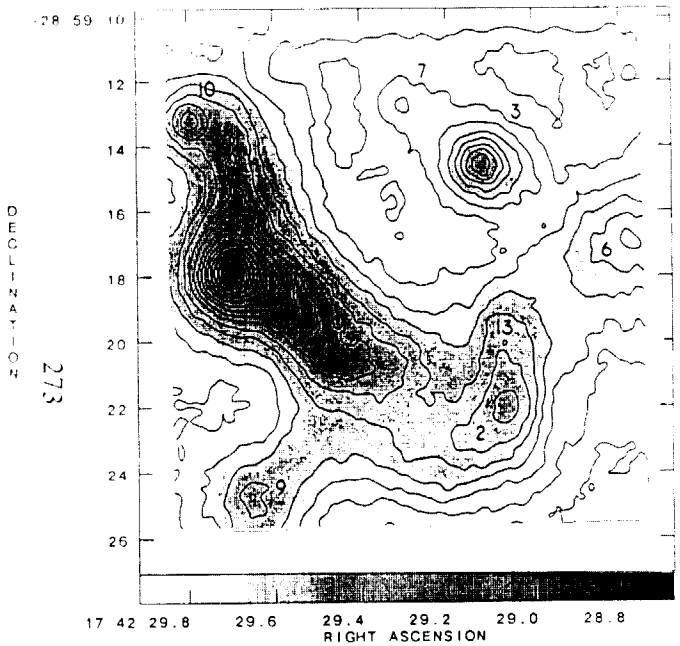

Figure 5(a): Calibrated contour map of 11.6 μm flux density from the central 1 pc of the Galactic Center, corresponding to the seeing-limited (1 arcsec) array image in Figure 4. The contour interval is 1 Jy arcsec^{-2} to the peak brightness of 16 Jy arcsec^{-2} at IRS 1.

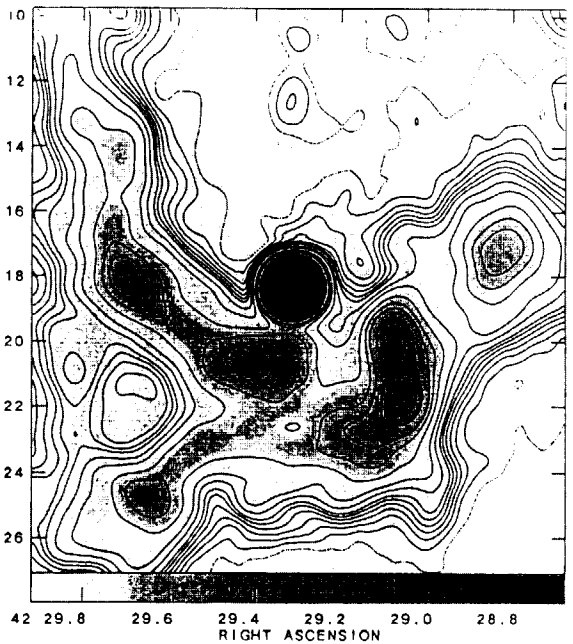

Figure 5(b): VLA map of calibrated 6-cm brightness in the Galactic Center displayed in quasi-logamithmic contours (from about 0 to 200 mJy/ beam) with the saturated peak = 1.2 Jy/beam at Sgr A*.

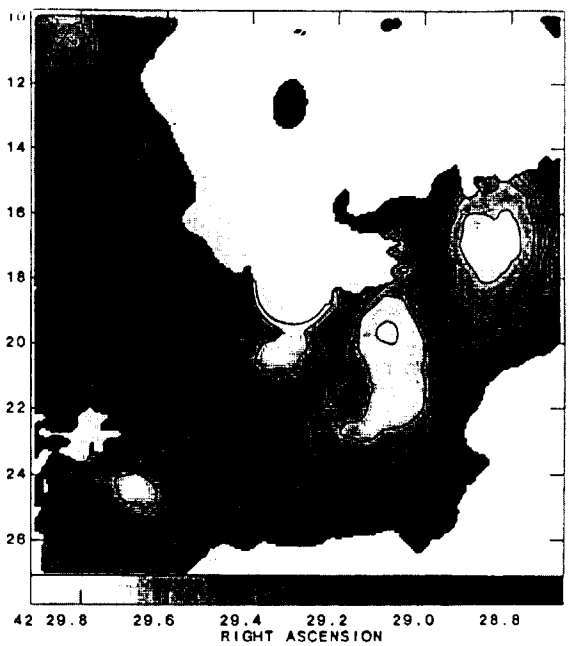

Figure 5(c): The dust-to-gas ratio calculated from the data sets in Figures 5(a) and 5(b). The dust-to-gas brightness ratio ranges from about 50 near IRS 13 to -275 about 2 arcsec west of IRS 10. Darker grey regions richer in dust, lighter grey regions are relatively dust depleated. The ratio in areas away from the ridge and strong sources is reliable in the black regions (300 < R < 700).

non-constant value of dust to gas ratio, or, it may suggest that sources of heating other than a central source at IRS16/Sgr A* may be embedded along the ionized filaments in Sgr A West and contribute to the heating of the intermixed dust. Regarding the question of the luminosity source of the Sgr A West complex, the results suggest that a combination of a central external ionizing luminosity source near Sgr A*/IRS16 and internal heating by imbedded sources with somewhat softer spectra at several of the bright peaks is responsible for the observed infrared and radio contimuum emission. These results are presented in detail by Yusef-Zadeh and Gezari (1989).

5 μm Speckle Interferometry of IRC +10216:

The array camera has been used to make two-dimensional 5 micron speckle interferometry observations of IRC+10216, which resolve sub-arcsec source structure in the presence of seeing and telescope aberations. Fifty separate 5 μm short exposure (1/30 sec) narrow band $\Delta\lambda/\lambda = 0.02$) images of IRC+10216 were taken (Figure 6a) as well as fifty images of reference star R Leo obtained under the same conditions (Figure 6b). The individual exposures in each set were separated by about 15 seconds.

The data were obtained at the Mauna Kea 3-m IRTF telescope in March 1988. Pixel size = 0.26 arcsec square, and the diffraction limit of the 3-meter IRTF telescope is $\theta = 0.35$ arcsec (FWHM) at 5 μm, thus the diffraction-limited speckle image detail was not fully sampled. Seeing was excellent (estimated at about 1/2 arcsec). Therefore only the central few speckles in each image were illuminated and differences between the images appear primarily as seeing-induced image wobble.

The two sets of speckle images images were processed (Gezari, Nisenson and Stachnik 1989) using four techniques: 1) centered direct sums (shift-and-add) of the images, 2) two-dimensional speckle interferometry (power spectrum analysis), 3) iterative deconvolution of one data set by the other, and 4) Knox-Thompson speckle imaging processing. R Leo was used as a reference star because of its proximity to IRC+10216 and comparable brightness at 5μm (ratio about 3:4), minimizing instrumental effects. The spatial structure results obtained by all methods are generally consistent with a slightly asymmetric resolved source of average diameter ~0.65 arcsec (FWHM). The Knox-Thompson speckle imaging reconstruction, the iterative convolution of IRC+10216 by R Leo, and the ratio of their power spectra all show a spatial asymmetry in IRC+10216.

The corrected diameter of IRC+10216 vs. position angle on the sky (north = 0^o) derived from fits of an Airy function to cuts through the ratio of the power spectra at 10^o intervals. A maximum asymmetry of about 20% is evident at a position angle of about 25^o with maximum diameter of about 0.75 arcsec. The apparent 5 μm source assymetry detected here is consistent with the 4.6 μm measurements of Mariotti et al. (1983), but not as large as the effects reported by McCarthy, Howell and Low (1980), Dyck et al. (1984), and Ridgeway and Keady (1988). As these authors point out, the observed infrared fringe visibility of IRC+10216 is complex, wavelength and possibly time dependent, and more extensive two-dimensional speckle observations on a larger telescope are planned. This work is presented in detail by Gezari, Nisenson and Stachnik (1989).

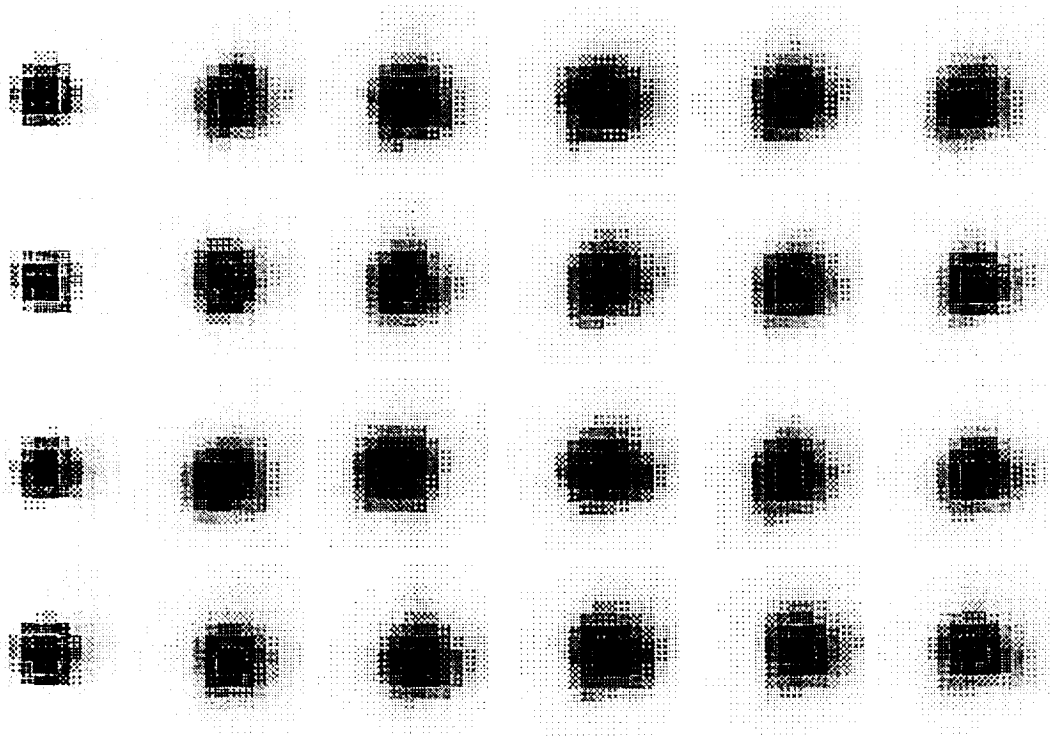

Figure 6(a): Individual short exposure (1/30 sec) narrow band ($\Delta\lambda/\lambda = 0.02$) speckle interferometry observations of IRC+10216 taken at 5 μm in March 1988 (Gezari et al. 1988). The pixel size = 0.26 arcsec, and the diffraction limit of the 3-meter IRTF telescope is θ = 0.35 arcsec at 5 μm. Seeing was excellent (estimated at <1/2 arcsec).

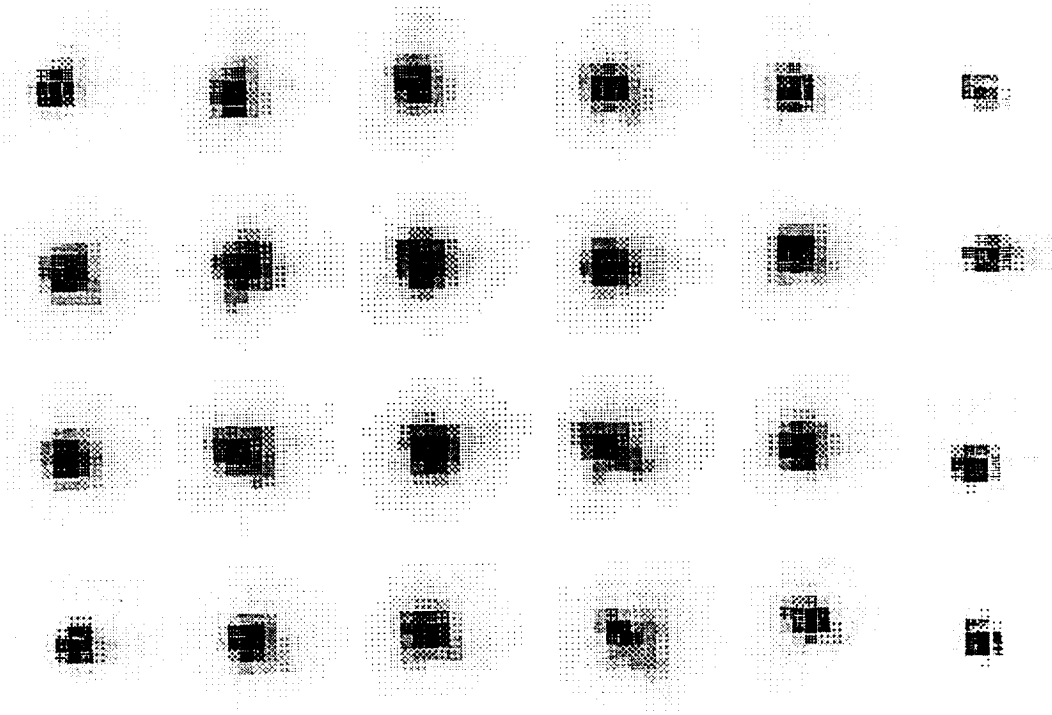

Figure 6(b): Reference star R Leo, obtained under the same conditions as in 6(a). R Leo and IRC+10216 are at the same airmass and are of of comparable brightness at 5μm. The two sets of images are displayed normalized to the peak brightness in each image.

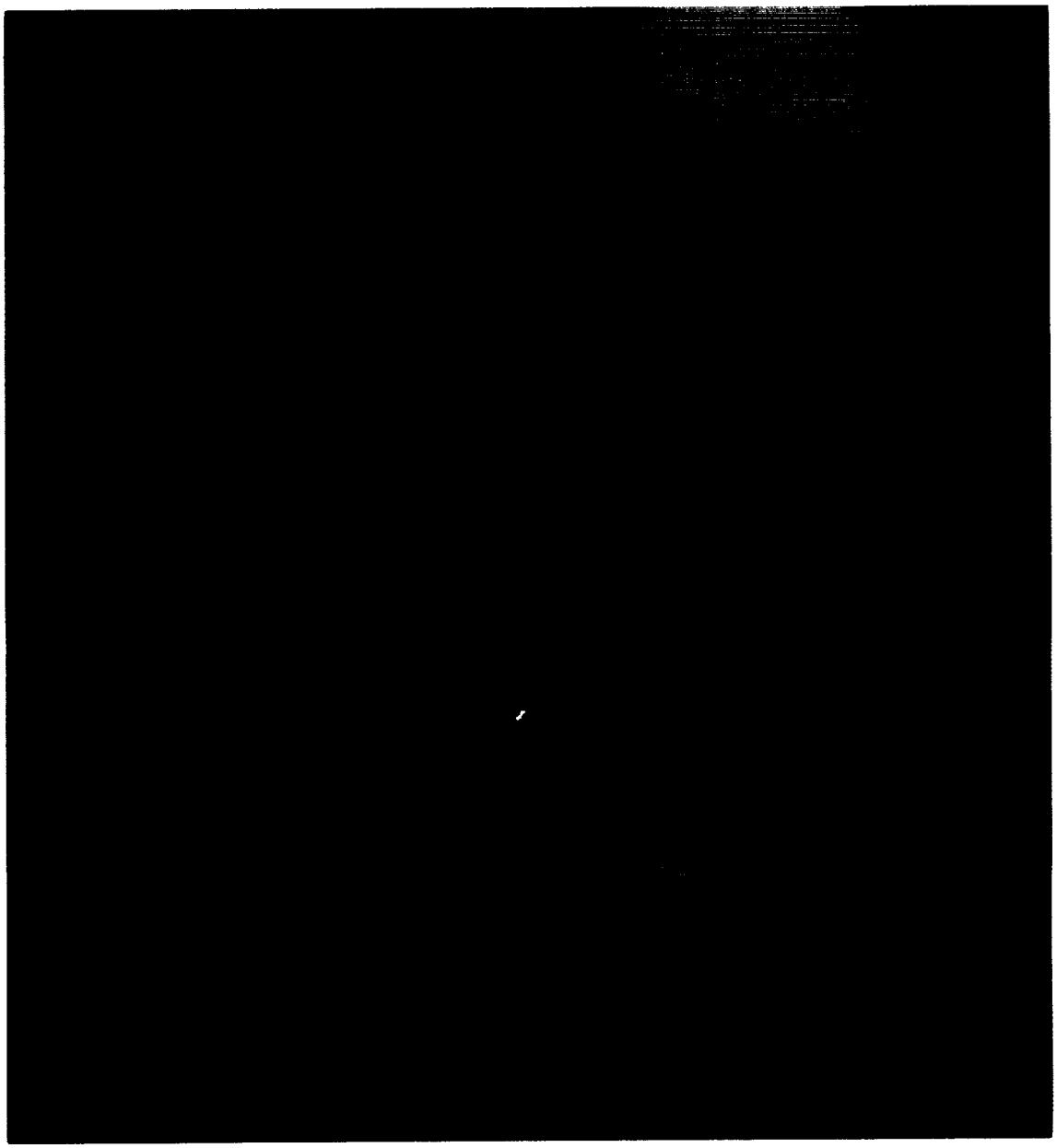

Figure 10: 12.4 μm array camera image of Orion BN/KL. BN is at top, IRc4 (KL) is at bottom, IRc7 is at center, IRc2 is left of center, and the IRc2 ridge source, identified with the SiO maser and the H_2O maser cluster, connects them. The array pixels are 0.26 arcsec and the image size on the 3-m IRTF was 1.0 arcsec (FWHM).

New 12.4 μm Source Structure in Orion BN/KL "IRc2":

Orion "IRc2" was proposed to be the primary luminosity source in the detailed model for the energetics of the Orion BN/KL infrared nebula (Wynn-Williams et al. 1984) based on 2 arcsec aperture photometry. Seeing-limited array imaging at 12.4 μm has resolved complex 1 arcsec scale structure in "IRc2", showing two equally bright compact objects connected by a narrow ridge of emission (Figures 10, 12, 14). One of these is IRc7 (previously thought of only as a significant source at 20 μm) and the other is the true IRc2 (3.2 arcsec to the east). A new, partially resolved ridge source extends from IRc2 toward IRc7. The Orion SiO maser is located at the end of the ridge and the surrounding elongated cluster of H_2O masers is aligned along the ridge, to within the present radio and infrared array positional errors. The small-scale structure of IRc2 ridge source can not be attributed to the effects of "bad pixels" or other array gain defects. Considering the high intrinsic accuracy of the relative array astrometry presented here, the detailed structure of the 12 μm sources and the coincidence of the IRc2 ridge with the SiO/H_2O maser cluster are significant. The SiO maser does not coincide with IRc2, but with the ridge source; thus the SiO maser is not directly identifiable with a high luminosity infrared source. Conversely, it appears that IRc7 is more luminous than previously thought.

Three other new infrared objects have been detected in the complex. One of these is an 8.7 point source 2 arcsec south of IRc7 at the position of the 3.8 μm object "n" (see Figure 11). Careful inspection shows evidence of this object in the 12.4 μm map as well. Two additional new compact 12.4 μm sources are found about 3 arcsec east of IRc2 (see Figure 12). These three new sources are somewhat fainter than IRc3 and IRc6, but are unambiguously detected. The image of IRc4 (KL) is elongated in the N-S direction and resolves considerably more structure than previous results. IRc4 is comparable in peak brightness to but somewhat more extended than IRc2 and IRc7.

There are other indications that the luminosity of the region is not attributable to a single powerful object. The center of outflow low-velocity masers (Genzel et al. 1981) is midway between IRc7 and IRc4 (KL), a significant displacement from the compact IRc2 array source on the scale of the present astrometry. Further, inspection of the 3.8 μm polarization observations by Werner, Dinerstein and Capps (1983) suggests that the vectors point back to at least three equally likely positions near BN, IRc7, and a point east of IRc2. The new array results as well as these factors suggest that a number of sources contribute to the total luminosity of the region, including IRc7, IRc2, IRc4 (KL), several new objects, and BN itself. Complete details of the photometry and astrometry of the BN/KL IRc2 complex, including exact placement of the maser cluster (to within the $\pm$ 0.1 arcsec achievable error), will be presented by Gezari (1989a).

OBSERVATIONAL CONSIDERATIONS:

Calibration:

The reduction of 10μm astronomical array data involves a particuliar set of concerns which arise from observing in a high background, low signal-to-background regime. Drifts in the array gain matrix and the thermal background from the sky or telescope on time scales comparable to the integration or calibration intervals can result in increased noise and image defects. The remedy in many cases is real-time chopping with the telescope secondary mirror. In general, several kinds of array image data must be obtained to produce a final calibrated image set at each wavelength. These include: source data frames, blank sky

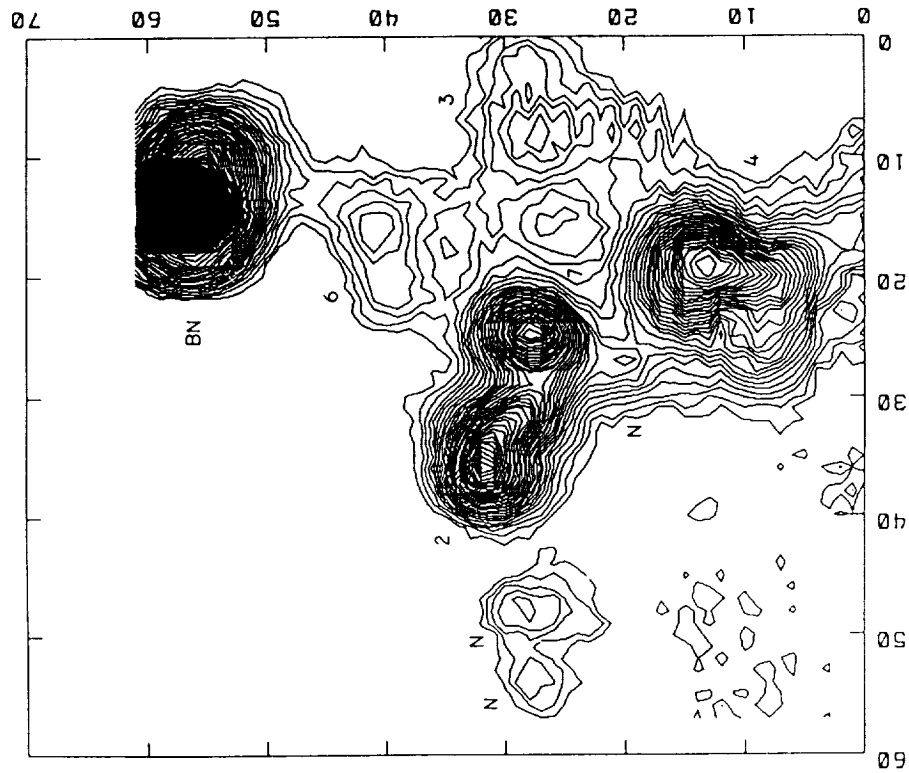

Figure 12: Contour plot of Orion BN/KL at 12.4 μm. The IRc source numbers are indicated. New sources are seen to the east of IRc2, and there is evidence of the new 8.7 source south of IRc7. Structure in the ridge extending from IRc2 toward IRc7 is slightly smoothed as result of mosiacing four shifted 1 min integration images. The axes are labled in pixel numbers.

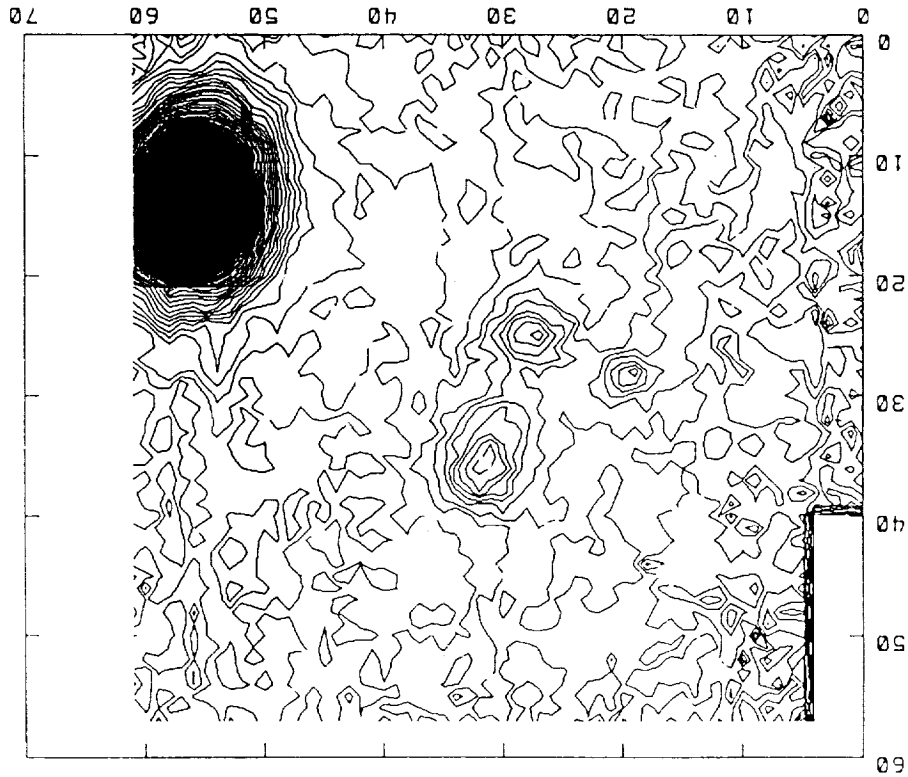

Figure 11: Contour plot of Orion BN/KL at 8.7 μm. The new 8.7 μm source is 2 arcsec south and slightly east of IRc7.

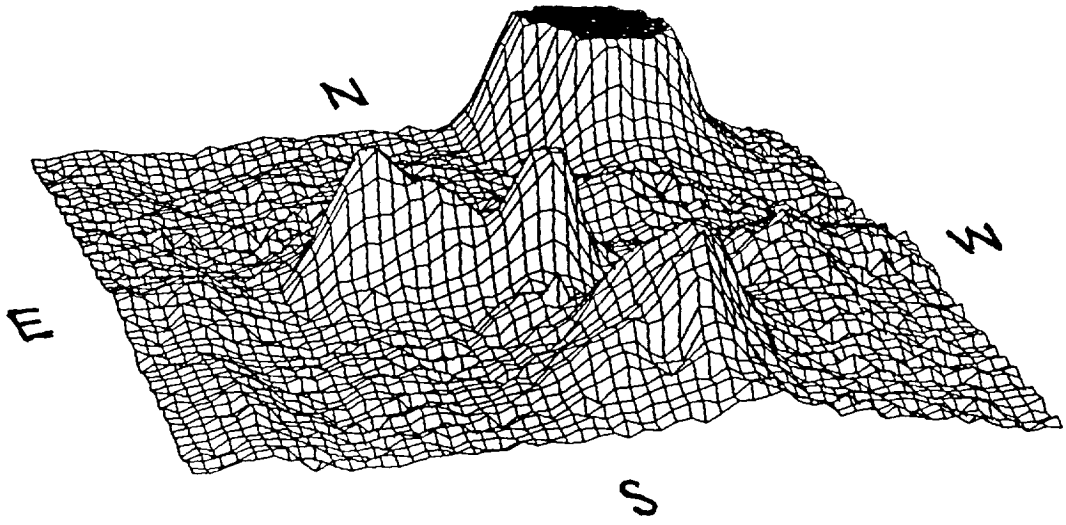

Figure 13: Plot of 12.4 μm Orion BN/KL intensity in one array field as viewed from the "southeast". BN is truncated at the top, IRc7 is the sharp peak south of it, IRc2 is to the east, and the ridge extending from IRc2 toward IRc7 is associated with the cloud of SiO and H_2O masers. IRc4 (KL) at the south, and IRc6 and IRc3 are evident north and west of it.

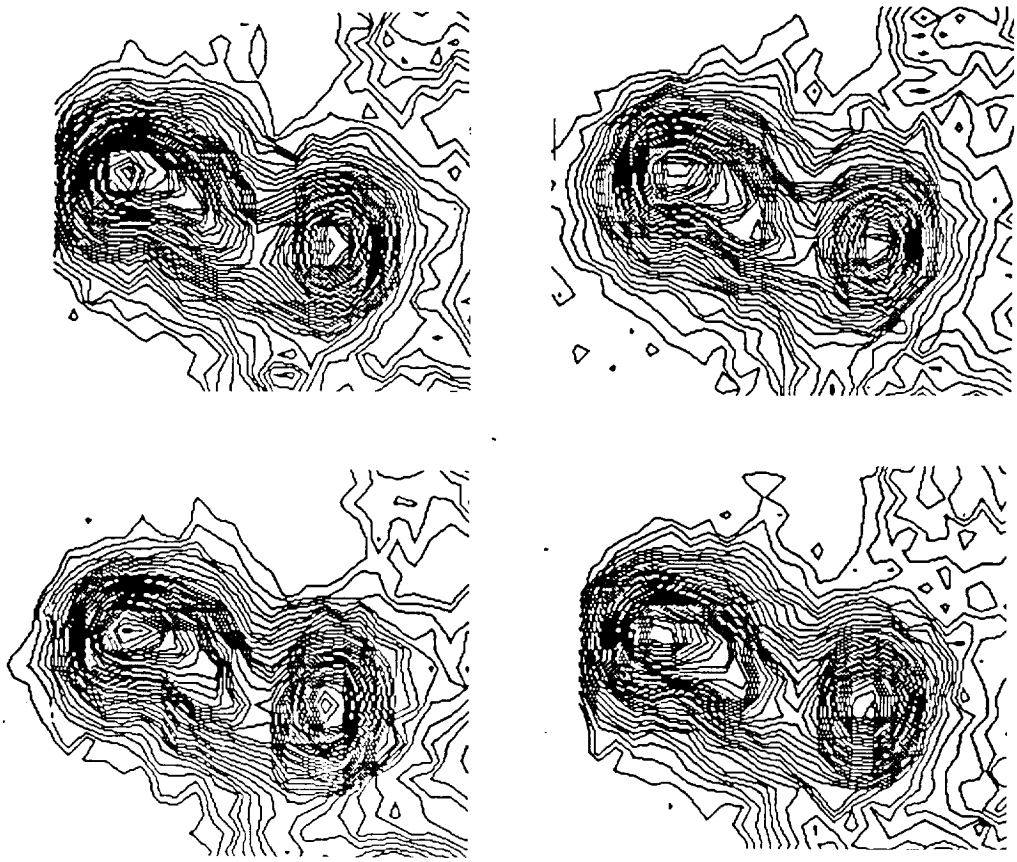

Figure 14: Four individual 1-min integrations of IRc2-IRc7 taken on different parts of the array to illustrate the flat-field uniformity and reproducibility of the array data. These unsmoothed images suggest some additional detail in the IRc2 ridge source.

frame(s) for sky/telescope backround subtraction and removal of residual spatial offsets, additional sky frames at high and low airmasses for flat-fielding, standard star frames for flux calibration and atmospheric extinction correction, and a (cold shutter) dark frame for some detector sampling schemes. The calibration images must have the same noise characteristics (usually equal integration time) as each of the individual data images to be corrected. In single sampling, images used individually are also corrected by subtracting a dark (cold shutter) frame.

Flat-Fielding:

Flat-fielding (gain matrix correction) of a source images requires the image of a a uniform field (usually blank sky) as a map of the net instrumental gain effects due to two-dimensional array, system, and telescope offsets. The basic approach to flat-fielding high-background array image data (after sky subtraction) is to divide the sky subtracted image by a normalized blank sky frame. The blank field image used for the division can be the sky image obtained while chopping, or another sky frame obtained under the same system gain and sky background conditions. A gain matrix constructed by subtracting high and low airmass sky images provides a more rigorous flat field correction. In practice, one or the other of these approaches will occasionally and inexplicably fail, resulting in defects in the image. Under good conditions *in principle* the same flat-field frame could be used for many different data images. However, the temperatures of the sky, telescope and detector, the sky opacity, and the gain of the electronic system must be stable on the time scale of the individual observations. In practice, flat fielding is most successful using nearly symultaneous chopped sky data. Flat-fielding of high-background array data can be the single most demanding calibration requirement.

Plate Scale Calibration:

To take full advantage of the potential intrinsic astrometric precision of the array, the plate scale of the array on the telescope (including linear scale in both dimensions, rotation, and distortion) must be accurately calibrated. This seemingly straightforward task is frustrated by a lack of two or more visual position standard stars in a single array field of view which are also easily detected at 10 μm. Measurements of a star moved around the array (once confidence in the telescope position encoders has been established), combined with lab tests using grid targets, are the basic calibration methods. Considerable effort was put into obtaining an accurate array plate scale, and one should be forewarded that an array camera optical system with variable magnification (zoom) capability (Gezari 1988a) could present a plate scale calibration burden which might outweigh any advantage of flexibility.

Is Chopping Necessary with 10 μm Array Detectors?

In principle chopping is not required for sky background subtraction or flat-fielding of high-background array image data. The ability to make infrared array observations without a chopping secondary would provide significant practical advantages. No telescope chopper mechanism would be needed (a real concern in the design of large next-generation telescopes), and improvement in observational duty cycle of more than a factor of 2 could be achieved over continuous chopping (since the array is on the source only half the time, data is not taken while the chopper switches position and stabilizes). Image quality and astrometric accuracy can become limited by chopper positional stability errors, rather than by optical aberration, focus, or atmospheric seeing, although we have not seen this problem on the IRTF except when attempting chopper rates slower than 1 Hz.

Sky subtraction could be done without chopping if a single pixel in the source image was known to contain blank sky *and* an accurate gain matrix existed for the array system for those observing conditions. The two could be used to create a synthetic sky frame for background subtraction. Sky and offset subtraction can also done by shifting the position of the source on the array, subtracting shifted frames, and deconvolving the source data. System gain stability is critical in these schemes. In practice, sky subtraction using these alternate methods is not routinely accomplished, but it is actively being pursued. Because of the sensitivity of the photon image and system gain matrix to environmental factors, slow (1 Hz) chopping against blank sky remains the least risky approach since it provides real-time sky subtraction and gain matrix data at what is a reasonable cost in observing time. Eventually, with additional experience and system improvements, chopping will probably not be necessary for high-background array observations.

Putting the Array Camera Performance in Perspective:

The signal-to-noise performance of the photoconductor array camera on the IRTF at 10-μm can be compared to the IRTF broad-band single germanium bolometer system (2 arcsec circular aperture, $\Delta\lambda$ = 5μm, and η = 1, NEFD ~ 23 mJy min$^{-1/2}$) by scaling instrumental parameters. If the array pixels were binned up to equal the bolometer aperture, the single bolometer would have a S/N advantage of a factor of about 5 over the synthetic binned photoconductor array "pixel", which is accounted for by the differing $\eta^{-1/2}$ and $\Delta\lambda^{-1/2}$ factors. Scaled to the parameters of the IRTF bolometer, the observationally measured array NEFD would be about 40 mJy min^{-1}pixel^{-1}, compared to the claimed 23 mJy min^{-1}pixel^{-1} for the bolometer. This factor of 2 discrepancy can be accounted for in part by uncertainty in scaling parameters and the likelihood that the IRTF bolometer noise performance is somewhat worse than the 3 mJy hr$^{-1/2}$ claimed.

Arrays have significant advantages over single detectors for high resolution mapping of extended sources. In general, the main advantage of arrays is their increased detector area per unit integration time. Symultaneous photometry and astrometry over 3596 points on the sky, with small pixels to sample diffraction-limited information, and bandwidth narrow enough to do photometry in the standard infrared bands is extremely attractive. But arrays present no advantage in observing compact sources (where most of the array is not utilized) except for problems involving small scale structure or a search for new objects.

The array performance numbers can be somewhat misleading. Consider that a 5σ detection takes 25 times longer than the stated 1σ NEFD figure, that NEFD per pixel numbers can seem deceptively low simply because array pixels are small, that diffraction and seeing spread the flux from a point source over at least 10 pixels and, and that chopping more than doubles the elapsed time. Calibration sources and flat fields generally have to be observed to the same noise level as the in the source image data, and multi-color observations further multiply the total observing time. It is relatively "easy" to image a cluster of ~30 Jy sources like Sgr A West in a 1 minute integration with high signal/noise. A cluster of 1 Jy sources could be detected in 1 minute, but getting an image of them with signal-to-noise comparable to the Sgr A West image would take 1,000 times longer, a sobering prospect. However, it is also true that an array can make mapping observations which would be completely impractical to attempt with a single detector. Each device should therefore be applied to the observations for which it is best suited.

ACKNOWLEDGMENTS

We are grateful to Mary Hewitt for her expert guidance on behalf of Hughes/Santa Barbara Research Center, and to Alan Hoffman, Geof Orias and Carol Oania of SBRC for their valuable advice and support of the DRO Camera program. We acknowledge stimulating discussions with Dick Joyce, Bill Hoffmann, Ian Gatley, Nick Scoville, Chas Beichman, Mark McCaughrean, Reinhart Genzel and Eric Becklin. We thank Gordon Chin for advice on the A/D converter concept and opto-isolation techniques, and Katherine E. (Katie) Boone for her skillful system software support. This research is funded by NASA RTOP 188-41-55 and the Goddard Director's Discretionary Fund.

BIBLIOGRAPHY

Deming, L. D., Mumma, M., Espenak, F., and Gezari, D. 1989 (in preparation).
Dyck, H. M., Zuckerman, B., Leinert, C. and Beckwith, S. 1984, Ap. J., 287, 801.
Folz, W. 1988, NASA Technical Memorandum, #TM-(in press).
Fowler, A., Probst, R., Britt, J., Joyce, R., Gillett, F. 1987a, Opt. Engr., 26, 232.
Fowler, A., Gillett, F., Gregory, B., Joyce, R., Probst, R., Smith, R. 1987b, Infrared Astronomy With Arrays (Proc. Hilo Detector Workshop, Univ. of Hawaii), 197.
Forrest, W. J., Shure, M. A., Pipher, J. L. and Woodward, C. E. 1986, Proc. Townes Symposium on the Galactic Center, (American Institute of Physics, 155), 127.
Gezari, D. Y. 1988a, NASA Technical Memorandum, # TM-(in press).
Gezari, D. Y. 1988b, Proc. IAU Symposium #136 Galactic Center (UCLA), in press.
Gezari, D. Y. 1989, (in preparation for Ap. J. (Letters)).
Gezari, D. Y. 1989b, (in preparation for Ap.J.).
Gezari, D. Y., Folz, W. C., Woods, L. A., Wooldridge, J. 1988, Proc. S.P.I.E., 973.
Gezari, D. Y., Mumma, M., Espenak, F. and Demming, D. 1989, (submitted to Nature (Letters).
Gezari, D. Y., Nisenson, P. and Stachnik, R. V. 1989, B. A. A. S. (Abstract), Boston 1/89, (in preparation for Ap. J. (Letters))
Hoffman, A. W. 1987, Infrared Astronomy With Arrays (Proc. Hilo Detector Workshop 5/88), Univ. of Hawaii, 29.
McCaughrean, M. J. 1988, Ph.D. Thesis, University of Edinburgh.
McKelvey, M. E., Goebel, J. H., McCreight, C. R., Moss, N. N. 1987, Infrared Astronomy With Arrays (Proc. Hilo Detector Workshop 5/88), Univ. of Hawaii, 140.
McLean, I., Chuter, T., McCaughrean, M., Rayner, J. 1986, Proc. S.P.I.E., 627, 430.
Ninkov, Z., Forrest, W. J., Pipher, J. L. 1987, Infrared Astronomy With Arrays (Proc. Hilo Detector Workshop 5/88), Univ. of Hawaii, 37.
Mariotti, J., Chelli, A., Foy, R., Lena, P., Sebille, F., and Tchountonov, G. 1983, Astron. Astrophys., 120, 237.
McCarthy, D., Howell R. and Low, F. 1980, Ap. J. (Letters), 235, L27.
Ridgeway S. and Keady J. 1988, Ap. J., 326, 843.
Werner, M. W., Dinerstein, H. L., and Capps, R. W. 1983, Ap. J. Letters, 265, L13.
Wynn-Williams, C. G., Genzel, R., Becklin, E. E., and Downes, D. 1984, Ap. J., 281, 172.
Yusef-Zadeh, F. 1988, private communication.
Yusef-Zadeh, F. and Gezari, D. Y. 1989, B. A. A. S. (Abstract), Boston 1/89 (in preparation for Ap. J. (Letters)).
Yusef-Zadeh, F., Morris, M., and Eckers, R. 1988, Proc. IAU Symposium #136: Galactic Center, (UCLA 8/88), in press.

PRELIMINARY RESULTS ON 2-DIMENSIONAL INTERFEROMETRY OF HL TAU

Eric V. Tollestrup and Paul M. Harvey
University of Texas at Austin

I. Introduction

Sources with directed outflows occur in a diverse set of objects, including young stellar objects (YSOs), evolved stars, active galactic nuclei, and QSOs. Observations ranging from visible to radio wavelengths show that directed outflows occur over a large range of physical scale lengths and are frequently bipolar. However, most of these observations have not resolved the actual region that produces the directed flow and therefore the mechanism is directly unobserved. But direct observations of the mechanism are needed to study the relationship of directed outflows and nearby physical environment.

What causes the directed outflows? A frequently proposed scenario is to impinge a spherically symmetric stellar outflow onto an asymmetric mass distribution such as a disk or toroid. The asymmetric mass distribution then acts as a funnel or a de Laval nozzle and produces a directed outflow or jet. The biggest observational difficulty is that the asymmetric mass densities occur extremely close to the power source. For example, models by Konigl (*ApJ.***261**, 115, 1982) and Shu, Lizano, and Adams (*Star Forming Regions, Proc of IAU Symp 115*, 417, 1985) for young stellar objects with bipolar flows have the directed flows being produced in the 10 to 10**4 AU range. Generally this resolution can not be achieved for most objects because they are too far away. But one class of objects, nearby (i.e. within 1 kpc) YSOs, are close enough to be imaged on the few 10's of AU scale length with very high resolution techniques. Therefore, nearby YSOs provide a unique opportunity to observe in depth a physical mechanism that could explain many other astrophysically important phenomena.

One very high resolution technique, first proposed by Labyrie (*Astron. Ap.*, **6**, 85, 1970), is speckle interferometry. With speckle interferometry, spatial information down to λ/D is possible, where D is the diameter of the telescope and λ is the wavelength. On a 3-m class telescope this corresponds to 0.11 arcsec at 1.6 μm, 0.15 arcsec at 2.2 μm, and 0.25 arcsec at 3.6 μm. To put this into astrophysical terms, an object in the Taurus dark cloud (150 pc) could be resolved down to 16 AU at H, 22 AU at K, and 37 AU at L'; that is, the size of our solar system and with in the scale size of the above bipolar flow models.

One well known YSO that is a good candidate for studying the relationship between any mass distribution near the star and a directed outflow is HL Tau. It has been studied before with 1-D slit scanning IR speckle interferometry techniques (Beckwith, S., Zuckerman, B., Skrutskie, M. F., and Dyke, H. M., *Ap. J.*, **287**, 793, 1984) and maximum entropy techniques (Grasdalen, G. L., Strom, S. E., Strom, K. M., Capps, R. W., Thompson, D., and Castelez, M., *Ap. J. Letters*, **283**, L57, 1984) and was shown to be extended ~1-2 arcsec in the E-W direction. It also has a strong 3.1 μm ice feature (Cohen, M., *M.N.R.A.S.*, **173**, 279, 1975; Rydgren, A. E., Strom, S. E., and Strom, K. M., *Ap. J. Suppl.*, **30**, 307, 1976) and has optical jets (Mundt, R. and Fried, J. W., *Ap. J. Letter*, **274**, L83, 1983). The extended structure and strong ice feature may be indicative of an asymmetric mass distribution, like those proposed in the above models, which in turn would be the constraining mechanism that creates the optical jet. Motivated by these issues, we have been studying HL Tau and other objects with speckle interferometry using a 2-dimensional IR array camera. In the following sections, we present a small sample of preliminary results obtained for HL Tau.

II. The Observations and Equipment

We have been pursuing sub-arcsecond resolution techniques using the UT IR array camera, which uses a SBRC 58 X 62 InSb array (Orias, G., Hoffman, A. W., and Casselman, M. F., *SPIE*, **627**, 408, 1986) mounted in a Infrared Labs cryogenic dewar (see Figure 1). The camera has standard J, H, K, and L' broad band filters as well as a 2% CVF mounted on a filter wheel. The optics consist of cold field and reimaging lenses for regular imaging plus a warm adjustable negative lens used to obtain the appropriate plate scale for speckle interferometry work. The camera can be run using either LHe or pumped LN2 and the detector temperature can be adjusted by means of a heating resistor. Used in the speckle interferometry mode the average read noise is ~300-450 electrons/pixel.

The observing technique is as follows. We obtain 128 very short integration images (35-300 msec) of an object of interest. This is then repeated for the sky and for a nearby point source. These three steps are repeated many (10 to 30) times, depending on the object's brightness and the seeing quality. The 35-300 msec exposures are required to freeze the seeing, while the point sources are used to measure the point spread function of the atmosphere + telescope + camera. The repetition insures that wildly fluctuating conditions in the sky or instrument will not produce false results and also to improve the S/N ratio for faint objects. To calibrate the plate scale at the detector focal plane, a double star with a well-determined separation is observed using the same technique.

III. Results

We have obtained diffraction limited images on the IRTF 3.0-m, the McDonald Observatory 2.7-m, the AAT 3.9-m, and the UH 2.2-m telescopes. As a demonstration that the 2-dimensional speckle interferometry is working, Figures 2 and 3 show some of the typical data which we have obtained at the McDonald 2.7-m and the AAT 3.9-m telescopes, respectively. In Figure 2, the three left-hand frames show single flat-fielded speckle images (out of a 128 image data cube) while the right-hand side show the corresponding average power spectrum obtained from the whole 128 image data cube. The top image is a ~0.25 arcsec double star, the middle image is a ~0.8 arcsec double star, and the bottom image is a 1.8 arcsec double star. The respective power spectra clearly show the interference-like pattern that a double star will produce in Fourier space. Note that the seeing was excellent; in the top and bottom images each star shows not a speckle pattern but diffraction (i.e. Airy) patterns instead, while in the middle image there is only about six major speckles.

Figure 3 shows similar results; the top three frames show single flat-fielded images (out of a 128 image data cube) while the bottom three frames show the corresponding average power spectra of the whole data cube. The left-hand image is the same 1.8 arcsec double star shown in Figure 2, the middle image is a ~0.2 arcsec double, and the right-hand image is a point source (note the lack of the interfence-like pattern in its power spectrum). Once again the seeing was excellent since the diffraction patterns are clearly seen on the left hand image, the middle image has only one major speckle for each double star component, and the point source shows only three major speckles. Obtaining images with only diffraction patterns or a few major speckles has been fairly common and shows that the seeing improves in the infrared as compared to the visible. It also demonstrates that true diffraction limited imaging in the IR is possible.

As a final demonstration that the technique is working, an autocorrelation and a reconstructed real image of the 1.8 arcsec double star is shown as a contour plot in Figure 4. In Figure 4a a trace through the secondary star shows that it is only two pixels wide and is diffraction limited in the Nyquist sense with 2 sample per resolution size. Figure 4b is a Fienup (*Appl. Opt.*, **21**, 2758, 1982) reconstruction of 4a (rotated by 90 deg) and also shows that both the primary and secondary star are diffraction limited with 2 pixels per resolution size.

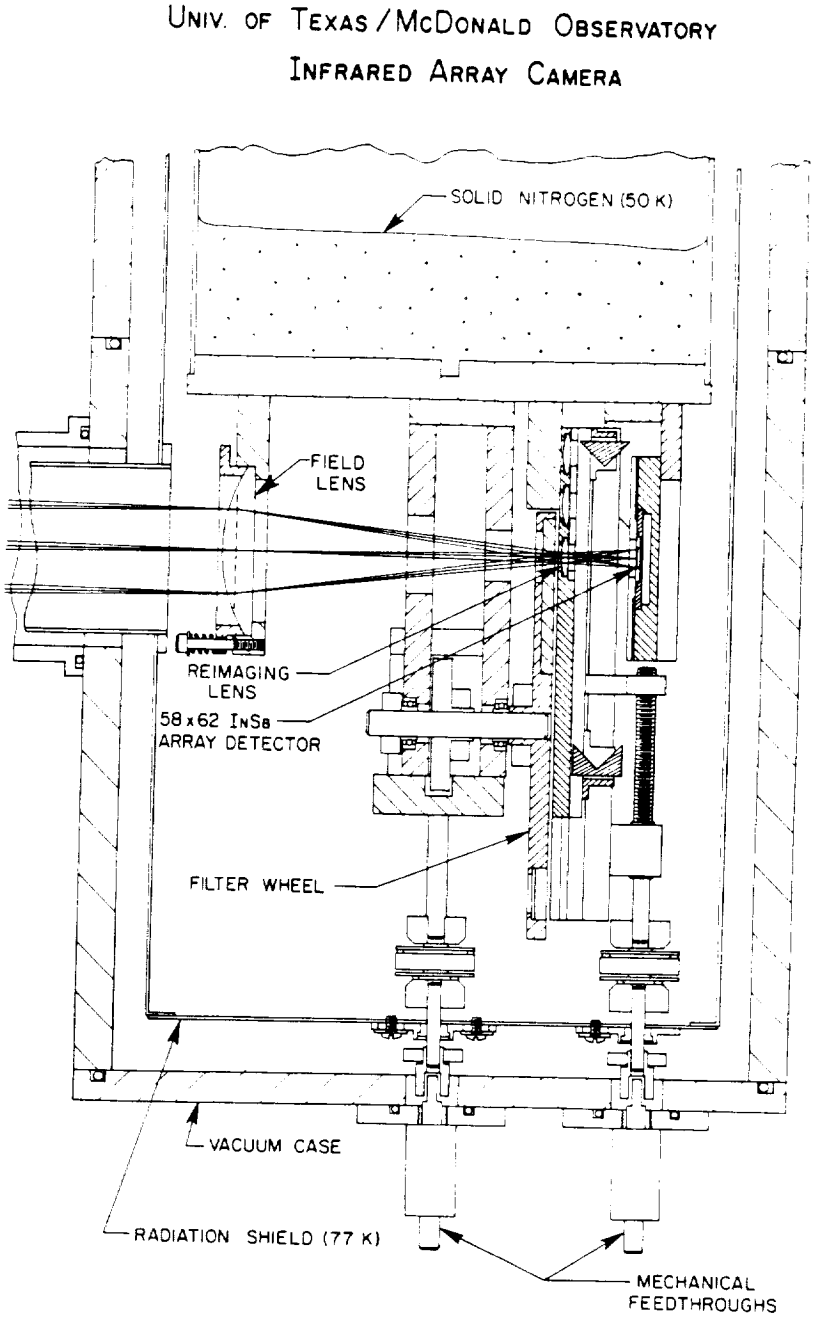

Figure 1. Drawing of UT IR array camera deware.

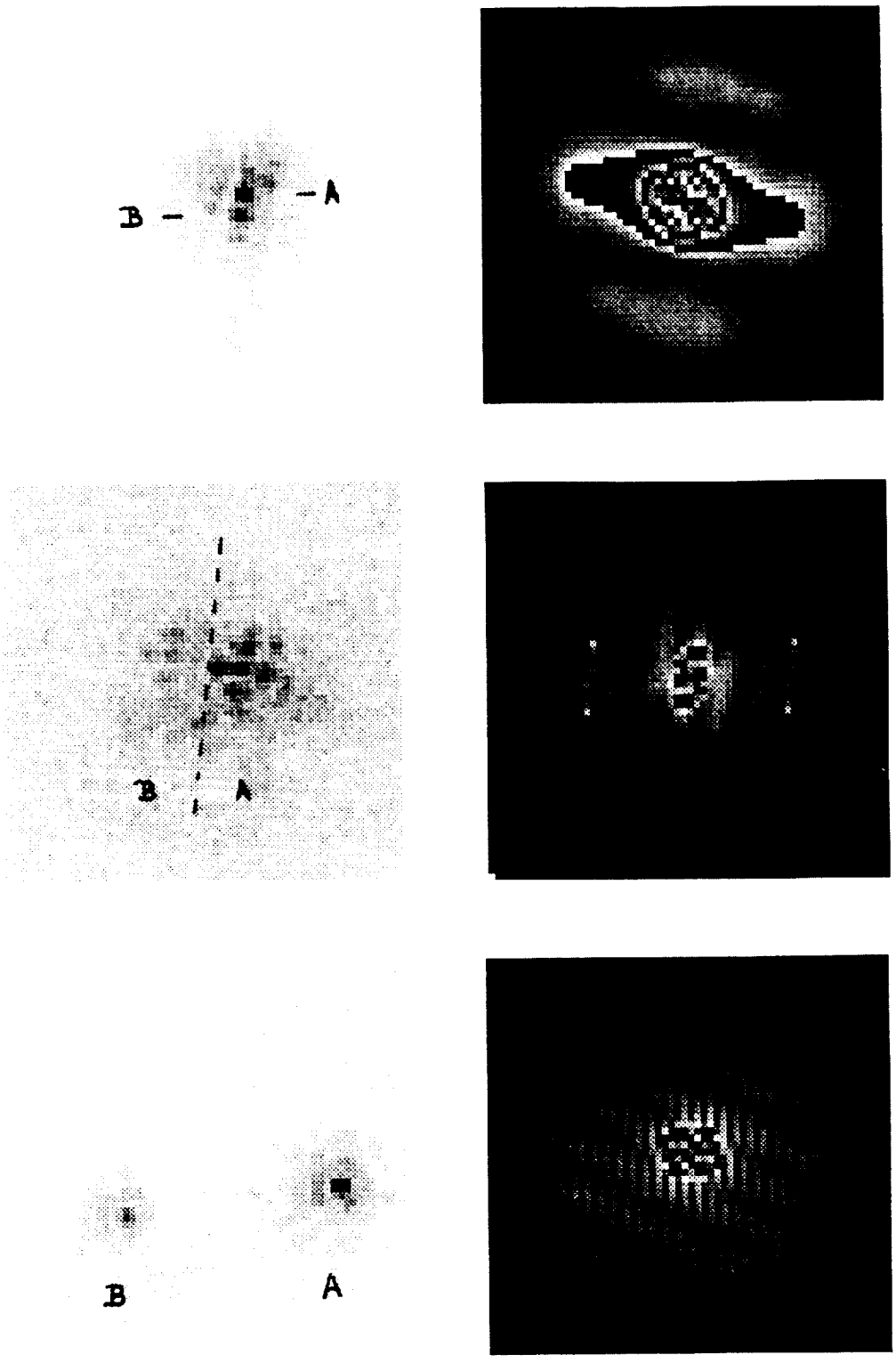

Figure 2. Speckle images (left) and power spectra (right) from McDonald Obs.

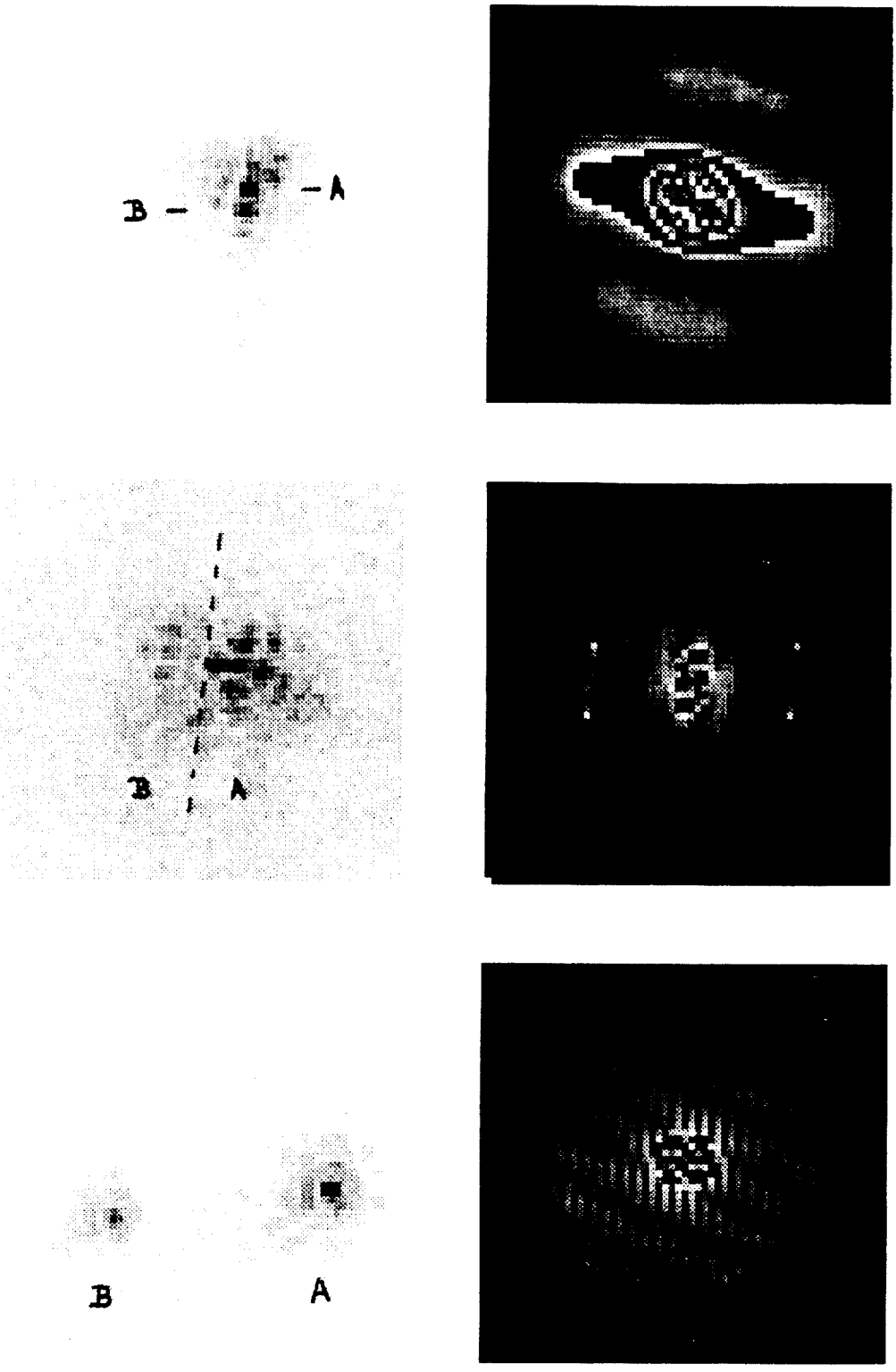

Figure 2. Speckle images (left) and power spectra (right) from McDonald Obs.

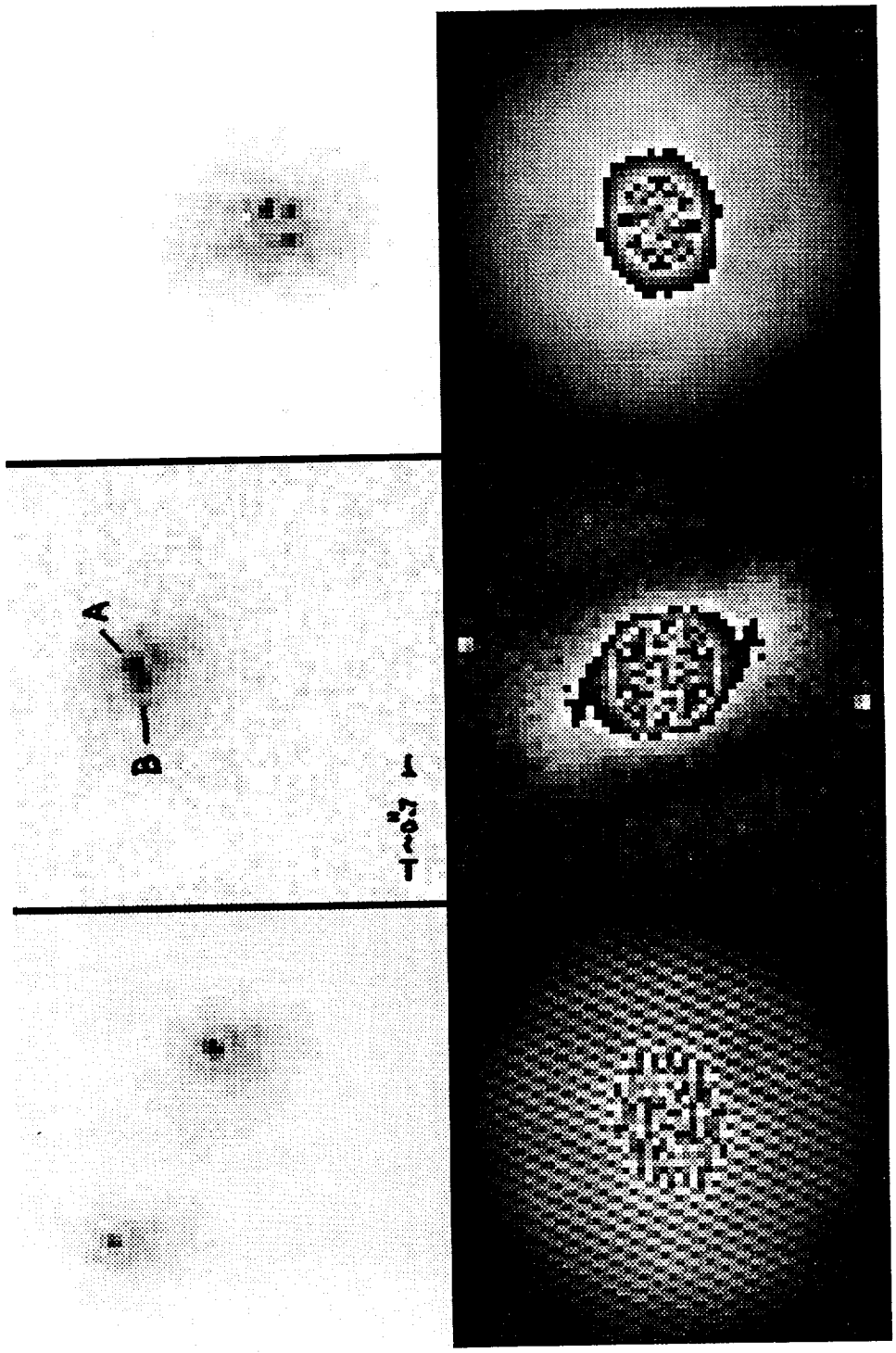

Figure 3. Speckle images (top) and power spectra (bottom) from AAT.

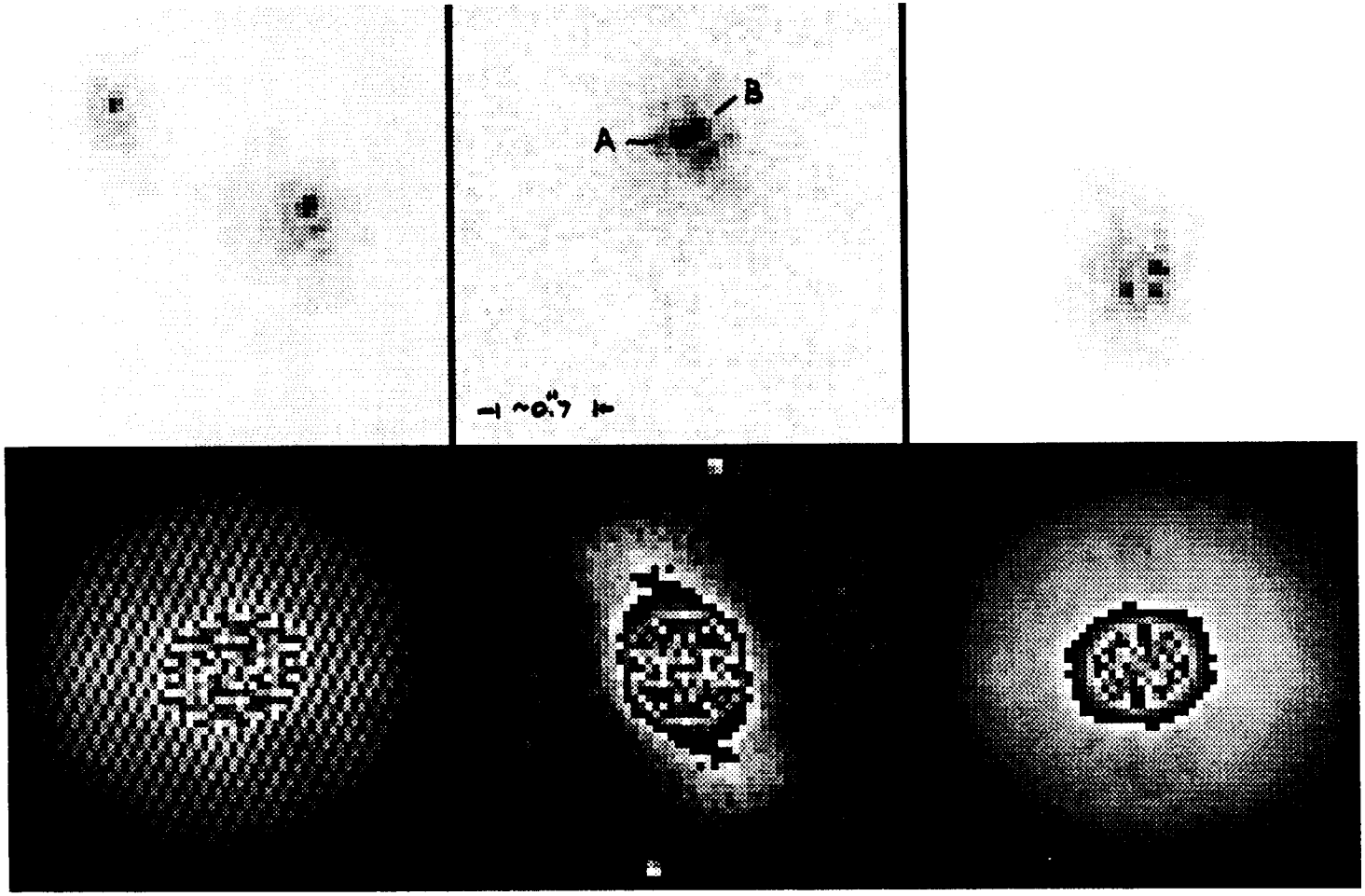

Figure 3. Speckle images (top) and power spectra (bottom) from AAT.

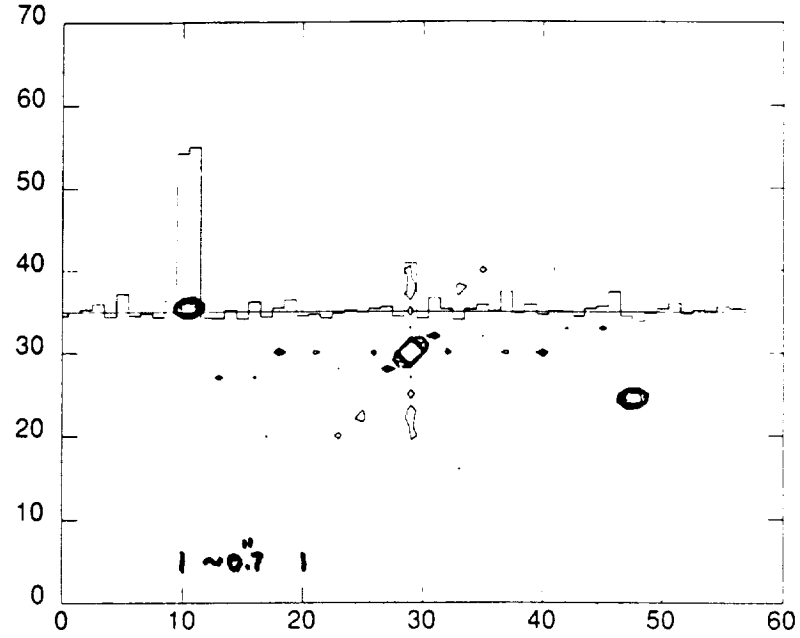

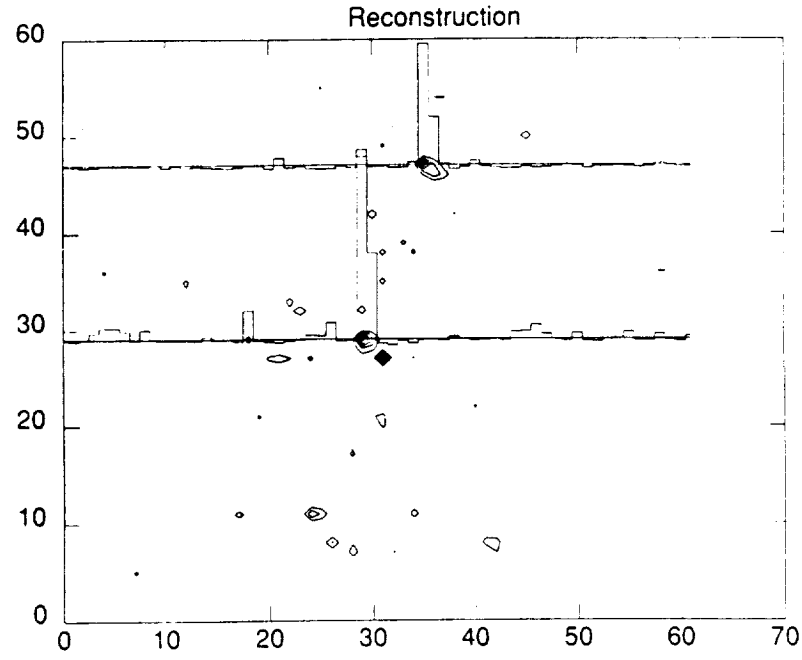

Figure 4. Autocorrelation (a) and Fienup reconstruction (b) of a double star.

IV. HL Tau Results

HL Tau was observed on the McDonald 2.7-m telescope, the IRTF, and the UH 2.2-m telescope in December 1988 and January 1989. Only one night of 2.2μm data from the McDonald run is presented. The data consists of a total of 1792 frames of HL Tau, 1280 frames of the point source SAO 093993 and 1792 frames of the sky. After the average power spectra of HL Tau, the point source, and the sky were calculated, the sky (i.e. noise) power was subtracted from HL Tau and the point source. Then HL Tau was divided by the point source to form the visibility function of HL Tau (see Figure 5). If HL Tau was a point source, then the visibility function would simply be a constant (in this case equal to 1.0) at all spatial frequencies. However, as Figure 5 shows, the visibility functions is not a constant. To get a quantitative examination of the visibility function, a plot of the visibility power versus the magnitude of the spatial frequency is shown in Figure 6 (this is analogous to the visibility functions presented by slit-scanning speckle workers). The telescope cut-off frequency is about 27 units so that the scatter in the data for frequencies above ~27 units is just noise. Two features are evident; the first is the decrease in visibility power from 0 to 10 units, while the second is the flat constant power from 10 to 27 units. The first feature represents a resolved component while the second feature shows that an unresolved component is still present. This is qualitatively the same result that was found by Beckwith *et al* (1984) using slit scanning speckle interferometry. The high frequency noise was filtered and then the visibility function was inverse Fourier transformed to produce an autocorrelation (Figure 7) which shows the unresolved component and the resolved component (Figure 8 shows a blow up of the central 25 X 25 pixel). As Figure 8 shows, the resolved component is about 0.7 arcsec is size. Since this paper is a report on work in progress, a more in depth discussion will be published at a later time.

V. Conclusions

These preliminary 2-dimensional speckle interferometry results of HL Tau are qualitatively similar to those found with 1-dimensional slit scanning techniques; a resolved component (~0.7 arcsec in size) and an unresolved component. We are currently reducing the rest of the data (taken on the three different telescopes and at three different wavelengths) and are also exploring other high resolution methods like the 'shift-and-add' technique and selecting only very best images for processing. The availability of even better 2-dimensional arrays within the next couple of years promises to make speckle interferometry and other high resolution techniques a very powerful and exciting tool for probing a variety of objects in the subarcsec regime.

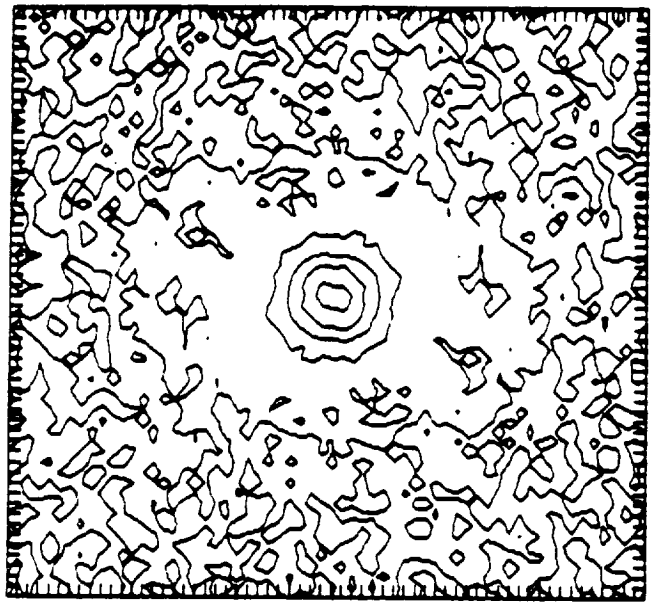

Figure 5. 2-D visibility function of HL Tau.

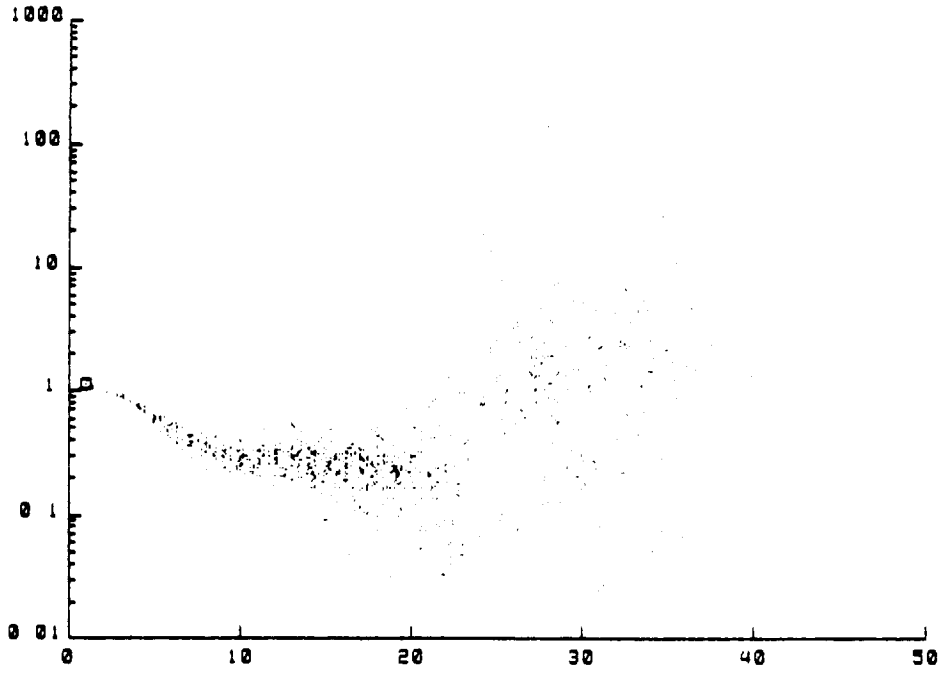

Figure 6. Visibility vs magnitude of spatial frequency of HL Tau.

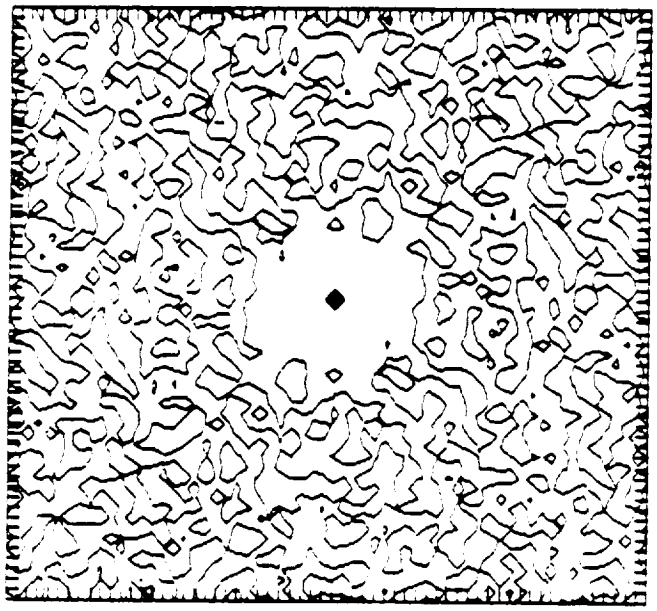

Figure 7. Autocorrelation of HL Tau, point spread function removed.

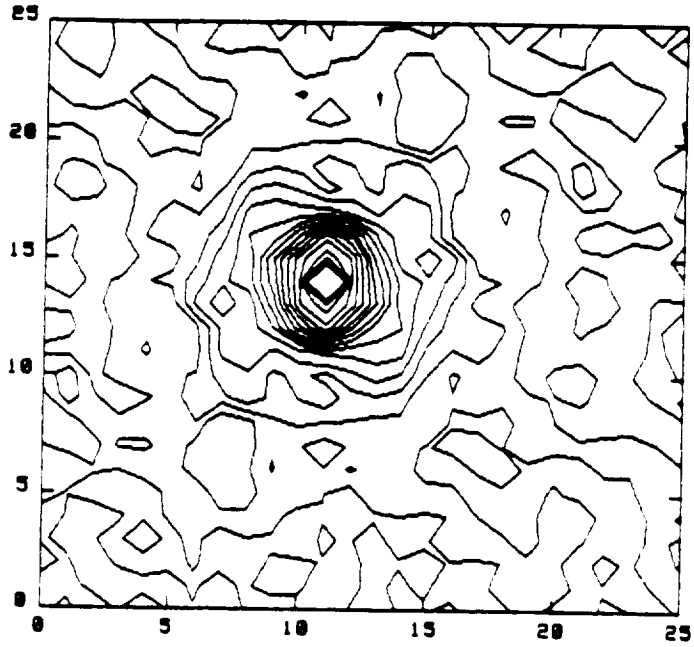

Figure 8. Inner 25 pixels of Figure 7. One pixel is ~0.07 arcsec.

SHORT WAVELENGTH HgCdTe STARING FOCAL PLANE FOR LOW BACKGROUND ASTRONOMY APPLICATIONS*

8 February 1989

J. Stobie, N. Hartle, D. Lacroix, K. Maschhoff
Honeywell Electro-Optics Division
Lexington Massachusetts 02173

ABSTRACT

The design of a 128x128 staring SWIR HgCdTe focal plane incorporating charge integrating transimpedance input preamplifiers is presented. The preamplifiers improve device linearity and uniformity, and provide signal gain ahead of the multiplexer and readout circuitry. Detector's with cutoff wavelength of 2.5 microns and operated at 80 K have demonstrated impedances in excess of 10^{16} ohms with 60 percent quantum efficiency. Focal plane performance using a smaller format device is presented which demonstrates the potential of this approach. Although the design is capable of achieving less than 30 rms electrons with todays technology, initial small format devices demonstrated a read noise of 100 rms electrons and were limited by the atypical high noise performance of the silicon process run. Luminescence from the active silicon circuitry in the multiplexer limits the minimum detector current to a few hundred electrons per second. Approaches to eliminate this excessive source of current is presented which should allow the focal plane to achieve detector background limited performance.

1.0 INTRODUCTION

Infrared astronomy is yielding significant quantities of data to enhance our understanding of the universe. However, unlike the visible spectrum the infrared sensor technology has not matured as rapidly. Sensors which dramatically reduce the exposure time of a two dimensional observation to 1 to 1000 seconds, while achieving zodiacal background limited performance in the short wavelength 1 to 2.5 micron range would significantly advance this branch of astronomy. This implies a large staring sensor format with small diffraction limited elements. The sensor's noise must be less than the shot noise of the collected signal and the detectors dark current, for space based observations, less than the zodiacal background of 10 photons per second near 1.4 microns. The focal plane should be capable of multiple nondestructive reads to support off focal plane signal processing to optimize the sensors sensitivity and to provide immunity to spurious noise, such as events caused by gamma radiation. Additional system requirements emphasize good linearity and system stability for accurate radiometric measurements with minimal system calibration and maintenance.

Short wavelength, 1 to 3 micron, HgCdTe photovoltaic detectors have demonstrated RoA products of 10^{12} ohms-cm^2 at temperatures below 100 K.[1,2] Thus at 80 K the detector's thermal noise should be below the zodiacal background noise. This noise performance coupled with high quantum efficiency, better than 70 percent, provides ample sensitivity. Furthermore imaging requirements can be satisfied using current processing technology to fabricate small 2 mil detectors arranged in a staring format exceeding 100 elements on a side.

The small detector size also yields a device with small capacitance, less than 250 femtofarads, which is beneficial for a low noise coupling scheme. Ideally, the detector

should be operated at or near zero bias to minimize any nonlinear effects introduced by the detector's capacitance-voltage characteristics and to minimize dark current and detector 1/f noise. These requirements lead to an input circuit design using a charge integrating transimpedance differential amplifier. Negative feedback maintains a constant detector bias which is adjustable by the voltage placed on the non-inverting input terminal. Honeywell has completed the design of a SWIR 128 x128 staring multiplexer incorporating this input preamplifier in each unit cell. This preamplifier is designed to boost the signal voltage by a factor of 10 in order to minimize the effects of subsequent signal processing functions, such as the multiplexing and off focal plane data acquisition system, on the signal integrity. This latest design benefits from its predecessor, a small format multiplexer[4], developed specifically to demonstrate the merits of the charge integrating differential preamplifier approach.

The performance of the small format hybrid focal plane is summarized in Table I along with the performance expected for the 128x128 focal plane. The measured performance of this small format device compares very well with the theory and the parameters measured for the detector array and multiplexer. This direct conformation of the performance model has given us the confidence to conservatively predict the performance for the 128x128 SWIR focal plane.

A description of the 128x128 focal plane is given in the following section. The next three section will discuss the performance obtained with the small format focal plane; Section 3 will present the detector performance, Section 4 will discuss the multiplexer, and Section 5 addresses the focal plane performance. Finally section 6 will address approaches adopted to further improve the performance of the 128 x 128 staring focal plane.

2.0 Description of the 128 X128 Focal plane

The 128 x128 focal plane is a hybrid focal plane consisting of a photovoltaic HgCdTe detector array on 2 mil centers bump mounted to a silicon CMOS readout multiplexer. A block diagram of the device is shown in Figure 1. The central 128 x128 detector imaging core is embedded within a 132 x132 hybrid array to greatly reduce edge effects. The multiplexer actually contains a matrix of 136 x136 cell where the outermost input cells do not have corresponding detector elements and are included to monitor the multiplexer performance independent of the detectors. The benefits of these additional cells far outweigh the 13 percent increase in the total readout time.

The backside illuminated detectors are fabricated on LPE grown HgCdTe material on a CdTe substrate. The planar design uses a ground ring around each element to improve detector definition as shown in Figure 2. The design yields a fill factor of 80 percent with an expected crosstalk of 3 percent. The fabrication of these array use standard processing techniques. Based on measurements of 4 mil square detectors the detector resistance should exceed 10^{16} ohms at 80 K and have a backside illuminated quantum efficiency of 70 percent with an AR coating on the CdTe substrate. The detector capacitance, even at zero bias, is expected to be less than 200 femtofarads.

The readout multiplexer uses proven low power X-Y addressable analog multiplexers and proven transimpedance input preamplifiers to achieve a read noise capability of 30 rms electrons. The multiplexer configuration is shown in Figure 3. Each detector element is connected to an input preamplifier which integrates and converts this signal to a voltage. An array of analog switches composed of row and column select switches are addressed to sequentially connect each input to the output buffer. Two low-power CMOS digital shift

registers, located along the periphery of the chip, generate the address pulses for the analog switches.

Each input preamplifier is a charge-integrating high gain differential amplifier as shown in Figure 4. A well-defined feedback capacitor is used to integrate the detector current and maintain constant bias across the detector to insure good linearity. The common V_{bias} line connected to every amplifier is used to maintain near zero bias (3 mv, 1 sigma, about a nominal -10 mv) operation across the entire detector array for uniform gain and to minimize dark current and detector 1/f noise. The reset switch across the feedback capacitor is used to initialize the circuit prior to each integration cycle. Signal gain is obtained by using a feedback capacitance which is less than the detector's capacitance. The design uses a signal gain of order 10 to minimize the effect of any additional noise contribution of the readout circuitry. The charge capacity is 1.6×10^5 electrons.

As a goal the response linearity of the focal plane should be better than 1 percent and is dependent upon the current response characteristics of the photodiode, the charge to voltage linearity of the integrating capacitors, and the voltage linearity of the subsequent buffers ahead of the digitizer. The current response of photodiodes is well documented and shown to be linear over several orders of magnitude, and properly designed voltage followers are also linear to better than 1 percent. The characteristics of the integrating capacitor can be a major contributor to nonlinear response. This is particularly true for direct readout devices which rely on the detectors own capacitance. A typical capacitance versus voltage plot of a SWIR HgCdTe detector at 80 K is shown in Figure 5. For most reasonable ranges of integrated input signal the nonlinearity introduced by the detector's own capacitance remains outside the 1 percent maximum. Postprocessing functions are required to store gain and offset normalization curves for each detector as a function of initial and final voltages during an exposure. Establishment and maintenance of these calibration look-up tables is a important requirement for the system.

A major advantage of the high gain integrating input circuit is its removal of this source of nonlinearity by integrating the detector current across a stable feedback capacitor. This capacitor exhibits very stable charge-voltage characteristics to yield a linear response better than 1 percent over the full range in detector currents. Present photo-lithographic tolerances will maintain a variation in capacitance below 5 percent. Furthermore, the virtues of negative feedback allows the multiplexer to maintain a virtually constant detector voltage (less than 0.5 mv change) across the detector diode, which leads to a significant reduction in detector dark current nonuniformity.

The ultra-low read noise performance of this hybrid FPA is made possible by a design which readily supports multiple non-destructive read cycles, and through the use of simple postprocessing techniques. With a nominal 50 kilopixels/second readout rate the entire array can be readout every 370 milliseconds. Thus the reset level, the initial value at the start of the exposure as well as samples all along the integration cycle can be available for signal processing. Simple correlated sampling techniques are useful to eliminate the reset noise from the signal and bound the input 1/f noise. For long integration times the reset level is used to remove the uncertainties in the measurement due to electronic drift introduced by the buffers on the focal plane as well as in the data acquisition electronics.

The entire multiplexer chip dimension is 350 mils on a side as shown in Figure 6. A standard production 1.2 micron CMOS process allows this advanced input preamplifier to be contained within a 2 mil unit cell. Only three bias supplies and four clocks are required to operate the multiplexer. Under continuous readout operation the entire multiplexer will dissipate only about 80 milliwatts of power.

The present design of the 128 x 128 staring focal plane represents only a small

evolutionary step, clearly within the bound of todays technology, from its predecessor, a small 8 x 8 format feasibility focal plane. This small format device employed detectors on 4 mil centers using a readily available design and a custom built readout multiplexer to demonstrate the potential of this design approach. Even though the detectors in the 128 x 128 design are smaller, their expected performance parameters, including collection current, and impedances, have been conservatively determined by measurements obtained on the 4 mil detectors. The multiplexer performance, however, should be quite similar to those obtained on the small format multiplexer. This correlation is because the 8x8 multiplexer was specifically designed to demonstrate the actual performance potential of small 2 mil square unit cells with only a larger feedback capacitor to accommodate the larger detector current. Excellent overall focal plane performance for the large format design is determined by scaling the multiplexer performance with the electrical parameters of the 2 mil detector. The performance measurements of the small format device is presented below.

3.0 DETECTOR ARRAY PERFORMANCE

Excellent detector array performance has been obtained on both Honeywell bulk[3] and LPE grown HgCdTe SWIR material. Since LPE offered shorter material lead times and the potential for better uniformity it has become our primary approach on this effort.

Detector array impedance measurements at high and moderate temperature (300 - 120K) were performed at Honeywell as a screening test using a ultra low-noise preamplifier with a feedback capacitor to eliminate the Johnson noise typically associated with a feedback resistor. Impedances are typically 10^8 ohms at 200 K and greater than 10^9 ohms at 175 K, following the expected theoretical temperature dependence for generation-recombination limited material as shown in Figure 7. As expected, at the nominal operating temperature of 80 K the detector impedance far exceeds the test capability of standard lab bench test equipment. In fact, the detector impedance can only be evaluated when hybridized to a low capacitance preamplifier similar to those incorporated in the multiplexer. The charge integrating differential amplifier used in the input cell provides a unique capability to directly measure the diode current-voltage characteristics. Typical diode characteristics measured at 80 K are shown in Figure 8 and array impedance uniformity is shown in Figure 9. Except for 3 elements all the detectors are between 0.4 and 4.0 $x10^{16}$ ohms. Scaling these results to 2 mil square detectors predicts impedances ranging from 0.7 to 11.0 x 10^{16} ohms with a corresponding thermal noise well below the zodiacal background shot noise.

High detector quantum efficiencies of 70 percent have been achieved over the 1.6 to 2.45 micron interval as shown in Figure 10. Below 1.4 microns the quantum efficiency may fall off quite dramatically, although their has been a considerable variation between the arrays measured as shown in the figure. The cause of this lower quantum efficiency at shorter wavelengths is still being considered with high back surface recombination velocity being a prime suspect. The data shown in Figure 10 is typical of non-AR coated detectors. An improvement as much as 20 percent can be anticipated with optimal AR coated detectors.

Analysis has shown that the detector capacitance linearly effects the total multiplexer read noise. Hence, capacitance below 250 femtofarads is required to achieve a low read noise for the 128 x 128 focal plane. Measurement of the 4 mil square feasibility detectors has shown a capacitance ranging from 400 to 600 femtofarads as shown in Figure 9. The device capacitance is principally the depletion layer capacitance which scales with the junction area. With the smaller 2 mil square detector a predicted capacitance of less than 180 femtofarads will be obtained.

Detector crosstalk well below 1 percent has been demonstrated on 4 mil square

detectors with a 77 percent fill factor. Since the fill factor and the crosstalk of these planar detectors are both controlled by the implant area and diffusion length, a tradeoff analysis was performed to determine the optimum implant configuration for the 2 mil detectors of the 128 x 128 array. A analysis predicts fill factor of 80 percent with a 3 percent crosstalk for the large format device.

4.0 MULTIPLEXER

Two process runs of small format multiplexers have been successfully completed. A layout oversight in the first run omitted bump vias for the detector common and rendered the multiplexers unusable for hybridization to detectors, but were still valuable in evaluating the performance of the multiplexer. The second run of multiplexers corrected this oversight and were integrated successfully with detectors.

Excellent multiplexer performance has been achieved and reported elsewhere[4], so only the significant results which are pertinent to the performance of the hybrid focal plane well be discussed here. The multiplexer has proven to yield very low dark current, less than 2 electrons per second, low detector input offset variation with a peak to peak variation of less than 15 mv, and gain uniformity less than 1 percent. Linear has been measured to within 2 percent for a nominal 1.0 volt full scale output swing. For the feasibility multiplexer the charge capacity of 3×10^5 electrons. Because smaller detectors will be used used in the 128 x 128 focal plane the charge capacity has been reduced to 1.6×10^5 electrons.

The dominate source of read noise in the focal plane is due to the 1/f noise of the differential input amplifier. This source of noise is minimized by design, such as large p channel drive transistors, and effected by process related parameters such as interface trap density. The first lot of multiplexers exhibited typical values for input referred 1/f noise, $e_{1/f}(1\ Hz)$ less than 1 uv/$\sqrt{Hz}$ at 1 Hz, as shown in Figure 11. Unfortunately the second multiplexer lot exhibited, as a result of process variation, an atypical high 1/f noise of about 6 uv/$\sqrt{Hz}$ which has severely limited the performance of the hybridized device.

With correlated double sampling the input 1/f noise contribution to the total rms noise of the focal plane is approximately given by:

$$Noise_{rms} = 2.13*(C_i+C_f)/q*e_{1/f}(1\ Hz)*(1 + \log(t_i*f_{co}))^{1/2} \quad \text{(rms electrons)}$$

where C_i is the total input capacitance including the detector and any strays, C_f is the feedback capacitance, t_i is the integration time, and f_{co} is the cutoff frequency. The logarithmic term accounts for the additional noise power contributed by the 1/f noise in each decade of frequency above the correlation frequency ($=1/t_i$). Thus for a reasonable multiplexed data rate of 50 kilopixels/second, the last factor in the equation amounts to less than 3. For the feasibility focal plane with a total input plus feedback capacitance is 0.6 pf the predicted input referred read noise is about 20 rms electrons, if the first lot of multiplexers had been used. Actual measurement using the second lot of multiplexer exhibit typical read noise of about 100 to 125 rms electrons, reflecting the significant impact the processing quality has on the focal plane performance.

The reset operation of the input integrating capacitor is not ideal and produces a voltage variation from reset to reset, known as reset noise. In addition the circuit requires a short time following the reset interval before equilibrium is attained. Typical relaxation

time is between 0.1 and 1 second as shown in Figure 12. The total settling response corresponds to a total input referred charge of about 2000 electrons which also varies from reset to reset. Two potential mechanisms for this relaxation time have been identified; circuit settling to pickup from the reset clock, or the relaxation of slow traps initially filled during the reset operation and integrated on the feedback capacitor. Relaxation time measurements which vary for different operating temperatures, could be used to identify the validity of the trap assisted mechanism.

Fortunately, simple correlated sampling techniques which take advantage of the multiple non-destructive readout capability of the multiplexer can be readily used to eliminate this offset variation (noise). In its simplest form two samples can be differenced, one taken at the beginning of an exposure and the other at the end of the integration cycle to remove the common reset offset and leave the integrated detector signal. Allowing for the circuit's settling time (0.1 to 1 second) before acquiring the initial sample will ensure the input has relaxed to equilibrium.

5.0 FOCAL PLANE PERFORMANCE

Performance measurements of the small format SWIR focal plane are in excellent agreement with the theory and performance parameters obtained from both the detector array and multiplexer. Scaling this performance to the 128x128 focal plane indicates that the SWIR focal plane requirements for space astronomy can be satisfied. The only disturbing measurements of the small format device was the presence of a relatively large detector current observable even under 100 percent cold shielding. This excessive current, which ranged from 100 to as high as 500 electrons per second, has been identified to be caused by luminescence photons emanating from the silicon multiplexer and which were not adequately blocked in the small format device from being absorbed by the detector. The performance measurement of the small format device including the luminescence will be presented in this section and the last section will discuss the design modifications implemented in the 128x128 device to reduce the luminescence for zodiacal background observations.

Good focal plane response uniformity has been achieved as shown in Figure 13. The histogram shows that the central 36 elements have a 6 percent, 1 sigma, response variation. This uniformity is typical when the anomalous edge element response is excluded.

The typical read noise for the small format device is shown in Figure 14 as a function of integration time. The upper curve was obtained by a device measured at the University of Hawaii. At short exposure times less than 10 seconds the read noise is about 150 electrons and at longer integration times the noise was limited by the shot noise of the luminescent current. Better measurement with a read noise less than 100 electrons have been obtained at Honeywell as shown in the figure. A Honeywell built low noise clock driver for the input reset clock, which couples directly into the detector signal, has allowed the improved measurement to be achieve. These measurement were obtained on hybrid devices using the multiplexers from the second fabrication lot which exhibited significantly higher 1/f noise which becomes the dominant source of read noise. If focal planes could have been fabricated on the initial multiplexer lot the read noise would be considerably lower as shown by the dotted line in the figure. The contributions due to the preamplifiers 1/f noise and Johnson noise is about 20 and 40 rms electrons, respectively, for a total read noise of 45 rms electrons.

The low detector dark current was not measurable on the small format device because of the stray detector current resulting from the luminescent photons generated by the active silicon devices within the multiplexer. The wavelength of these luminescent photons is near

the bandgap of silicon and are readily absorbed by the SWIR detectors. Their intensity has been shown to be a function of the current passing through the active silicon devices. Figure 15 demonstrates the extent to which the luminescence can be reduce by lowering the operating power of the multiplexer. The three 8x8 two dimensional maps illustrate relative intensity of the luminescence observed by each detector. Note that the left most map illustrates a very bright source in the lower corner which is due to the high power output buffer being continually on. By switching this buffer off except during readout times the bright source is eliminated. Although less than 100 electrons/second have been measured on the small feasibility device the typical luminescent current under optimal operating conditions is typically about 200 electrons/second. In order for this focal plane approach to be useful down to the zodiacal background levels, the luminescent photons must be blocked to prevent the absorption by the detectors. An effective approach to block these photons is presented in the next section.

6.0 IMPROVEMENT TO THE 128X128 DESIGN

The performance evaluation of the small format device has been most valuable in optimizing our approach in the design of the 128x128 focal plane. Scaling down to the smaller 2 mil square detector parameters leads directly to improved performance. The read noise for the device is directly related to the combined detector, input stray, and feedback capacitances which have been reduced 60 percent . Thus with typical 1/f noise for the input preamplifiers of 1 to 2 uv/$\sqrt{Hz}$ the read noise can be expected to be between 25 and 30 rms electrons. The feedback capacitor has been reduce to attain an input signal gain of 10 . This minor modification allows the entire input circuit to readily fit within a 2 mil square cell, with the most critical element, the differential amplifier, retaining the identical configuration as used on the small format multiplexer. The usable charge capacity is 1.6 $x10^5$ electrons over the 1 volt linear region of the amplifier yielding a the dynamic range of 74 dB.

The approach to reduce the luminescent current is several fold. Scaling to the 128x128 device reduces the luminescent sources per detector element by a factor of two. The metal interconnect coverage within the unit cell has been increased from 66 percent in the small format device to 83 percent in the 128x128 design with special attention to cover active regions. Peripheral luminescent sources such as the output buffer and shift registers have been moved as far from the active detectors as possible, and generally masked with a reflecting layer. And because the luminescence is presumed to be emitted isotropically with low reabsorption within the silicon, an absorber placed on the backside of the silicon multiplexer substrate will prevent the photons from being reflected back up to the detectors. With these design approaches the resultant luminescent current is expected to be less than 10 electrons/second. Additional improvements are possible with an absorbing layer placed between the multiplexer and the detector.

In summary, the benefits of the charge integrating differential input preamplifier have been demonstrated on the small format focal plane. The 128x128 design is only a small evolutionary step and incorporates an effective approach to minimize the luminescent current present with this approach. This design provides a very linear output for accurate radiometric measurement placing minimum requirement on system calibration. The input preamplifiers maintain near zero bias across the entire array, minimizing detector dark current and 1/f noise, and to achieve optimal detector uniformity. Signal gain of order 10 eases off focal plane electronic low noise considerations. The non-destructive array reads offered by this approach support signal processing functions to achieve low noise performance and immunity to spurious noise events.

7.0 REFERENCES

1. N. M. Hartle et al., IRIS Detector Specialty Group Meeting, Moffet Field, CA, August 1986.
2. D. L. DePoy et al., Proceedings of the Second Infrared Detector Technology Workshop, Moffet Field, CA, August 13-14, 1985, p.16-1
3. N. Hartle et al., Proceedings of the Workshop on Ground-based Astronomical Observations with Infrared Detectors, Hilo, HA, March 24-26, 1987, p. 21
4. J. A. Stobie et al., IRIS Detector Specialty Group Meeting, Seattle, WA, August 11-13, 1987

*This work has been supported in part by the Jet Propulsion Laboratory, Pasadena CA, under Contract #958095, D. Ritchie technical monitor, and Dr. D. Hall principle investigator from the University of Hawaii.

Table 1. Performance Summary of the Small Format Device and Expected Performance for the 128 x 128 FPA.

	Small Format Device Meas.	128x128 FPA Expectation
Operating Temp (K)	80	80
Detector	LPE HCT	LPE HCT
size (mil square)	4	2
Cutoff Wavelength (um)	2.5	2.5
Quantum Efficiency (%)	70	>70 w/AR
Impedance (10^{16} Ω)	0.4 - 4.0	0.7 - 11.0
Capacitance (pf)	0.4	0.2
Crosstalk (%)	< 2	< 3
Fill Factor (%)	75	80
Dark Current (e/s)	-	< 10
Focal Plane	CIDA x-y	CIDA x-y
Read Noise (rms e)	100*	< 30
Dark Current (e/s)	-	< 10
Luminescence Current (e/s)	100-500	< 10†
Charge Capacity (e)	3.2 x 10^5	1.6 x 10^5
Power Dissipation (mW)	0.3	< 80

* Limited by atypically high noise CMOS process run

†Luminescence Reduction Layers included

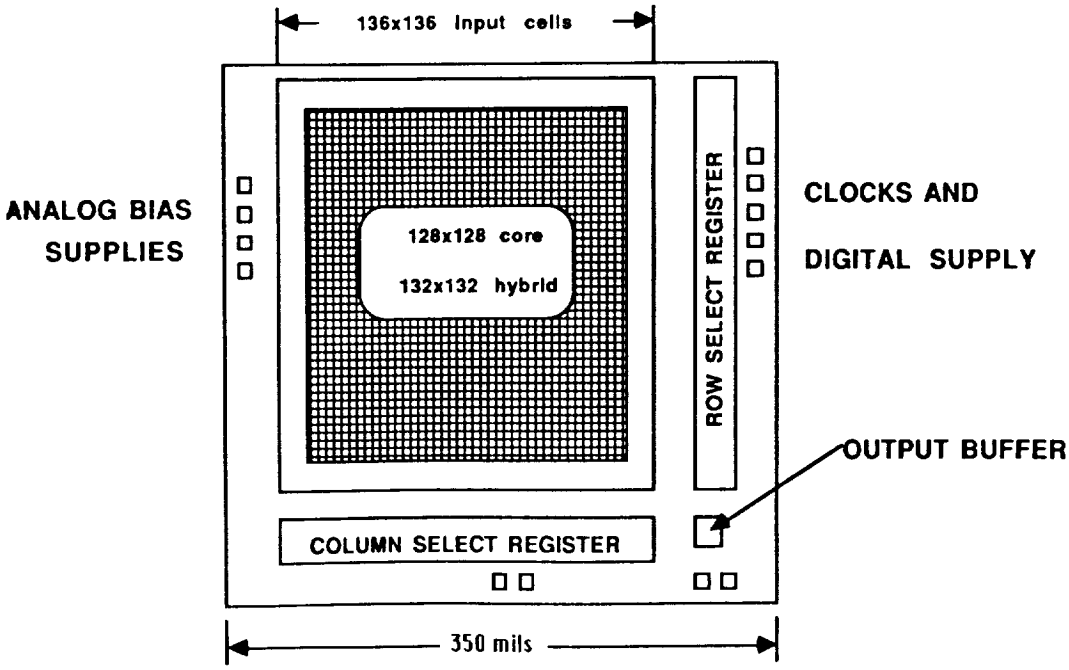

Figure 1. The 128 x 128 SWIR Focal Plane is a Hybrid Structure Consisting of HgCdTe Detectors and a Silicon CMOS Readout Device.

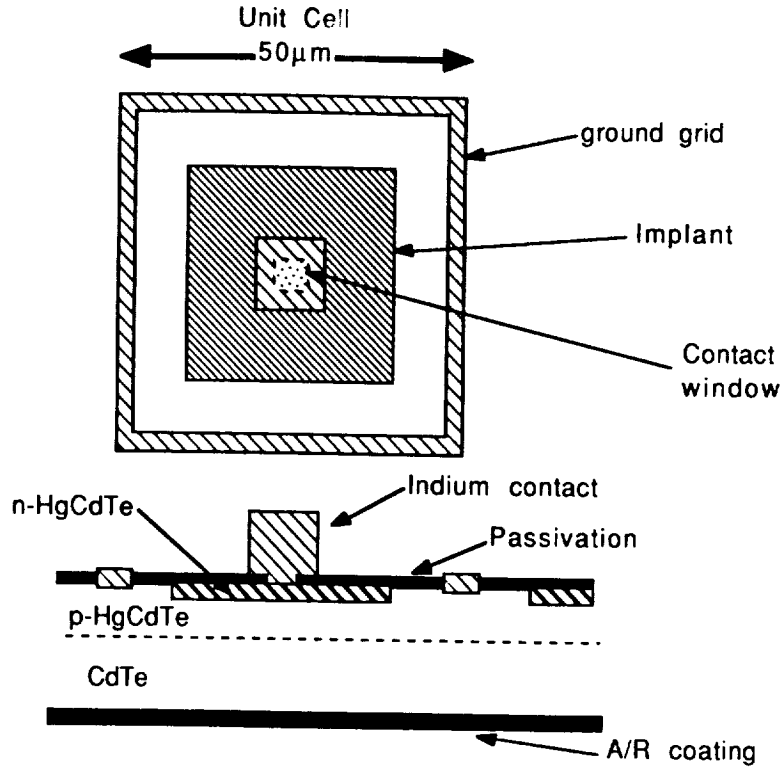

Figure 2. The LPE Grown HgCdTe Detectors are Fabricated Using a Highly Producible Planar Design Approach.

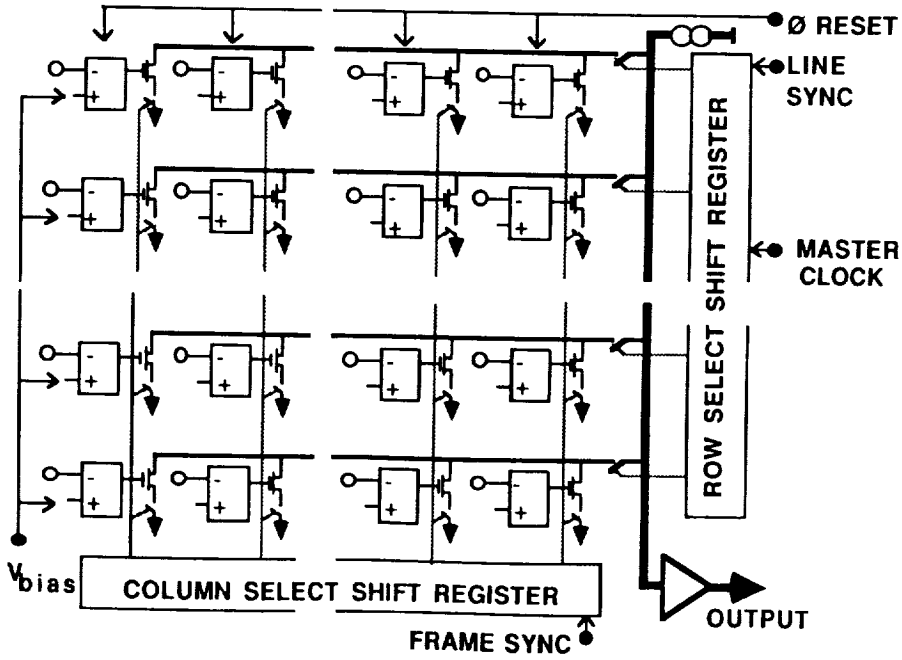

Figure 3. The Readout Multiplexer Uses a Proven Low Noise Non-Destructive x-y Readout Design.

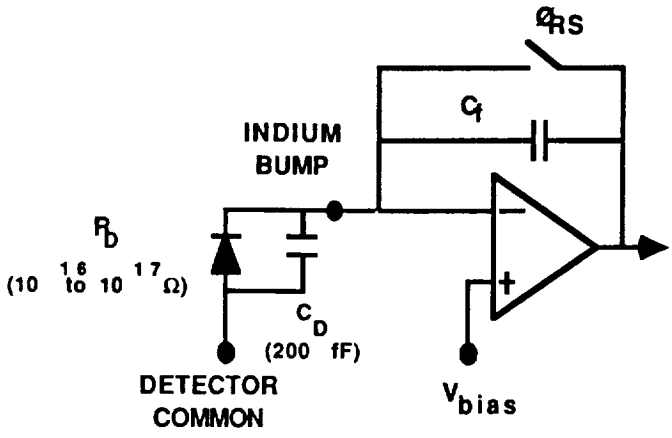

BENEFITS

2 Mil Square Cell

Maintains Near Zero Bias
<3 mv, 1 sigma

Read Noise Contribution to FPA
<30 rms e

Transimpedance Gain 6 uv/e

Dark Current < 2 e/s

Excellent Gain Uniformity
1 sigma variation <1 %

Linearity Deviation <2 %

Charge Capacity 1.6 x 10^5 e

Figure 4. The Charge Integration Differential Amplifier (CIDA) is an Excellent Preamplifier for Low Background SWIR PV Detectors.

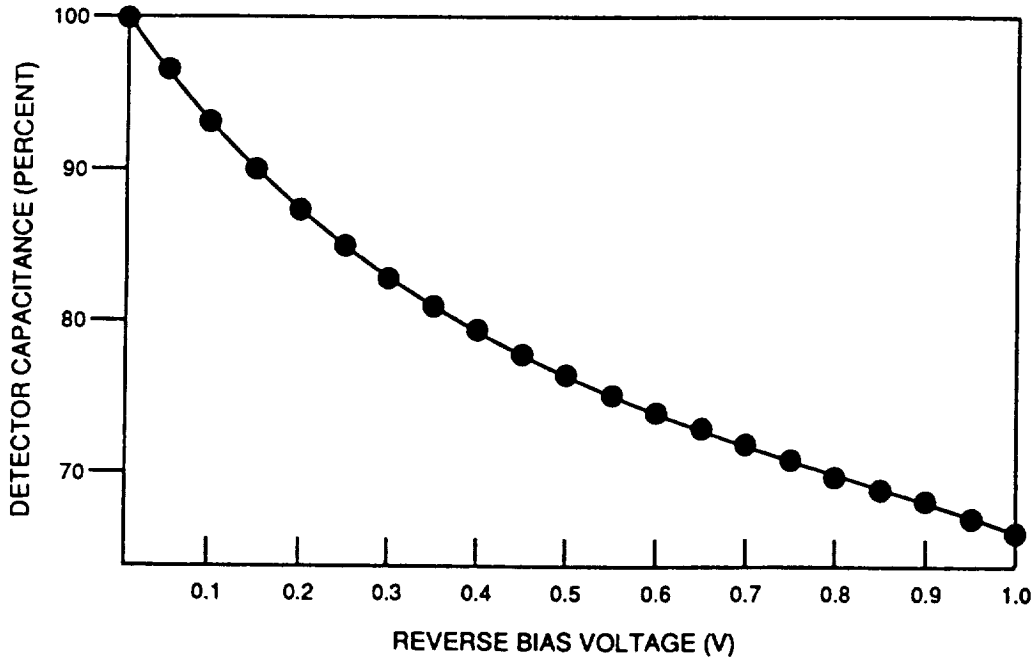

Figure 5. SWIR HgCdTe Detector C-V Characteristics is Clearly Not Constant With Bias Voltage.

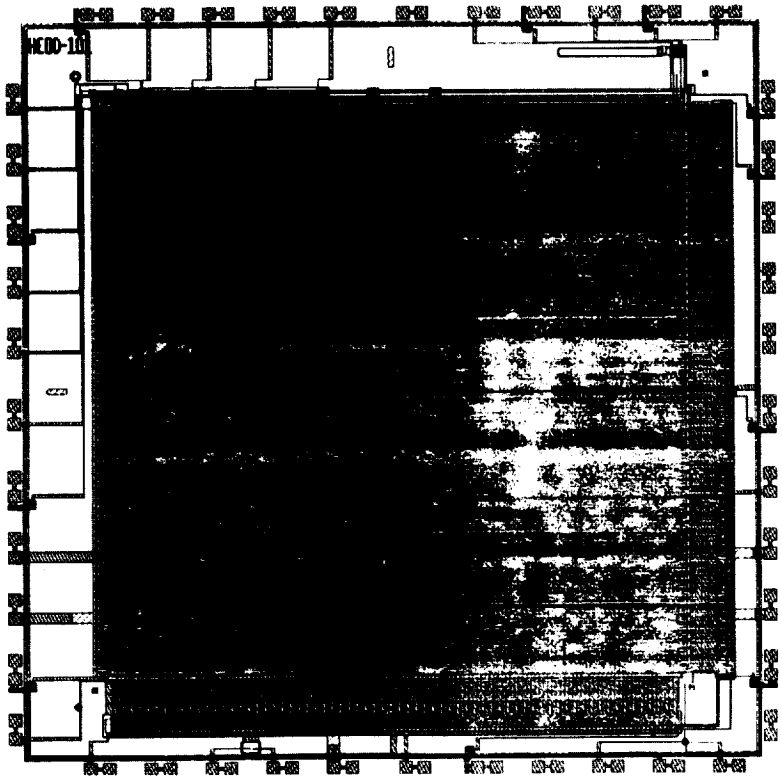

Figure 6. The 128 x 128 SWIR Multiplexer is Fabricated Using a Standard Production 1.2 Micron CMOS Process.

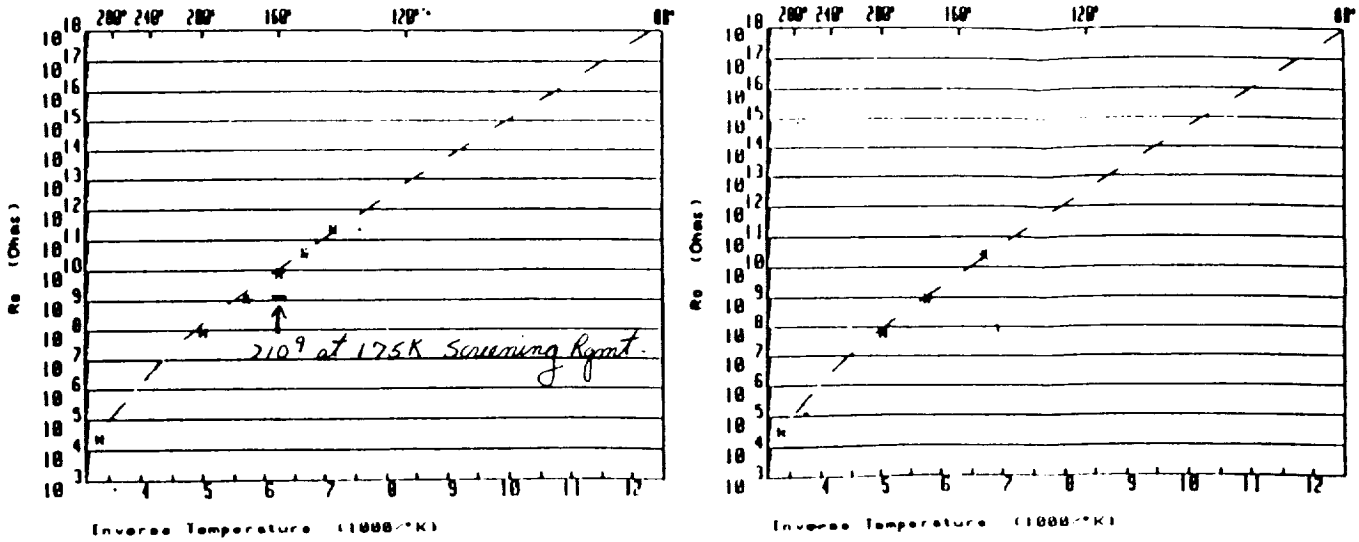

Figure 7. Routine Screening Tests for SWIR Detector are Limited to Impedance Less Than 10^{12} ohms Without Exotic Low Capacitance Coupling Schemes.

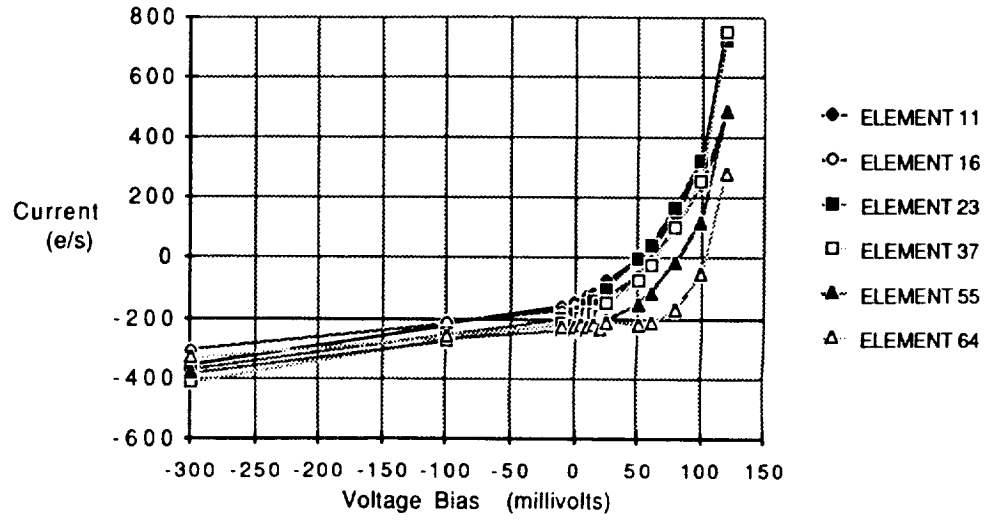

Figure 8. The CIDA Multiplexer is Ideally Suited to Measure the Detectors I-V Characteristics at 80K With dynamic Impedance in Excess of 10^{18} ohms.

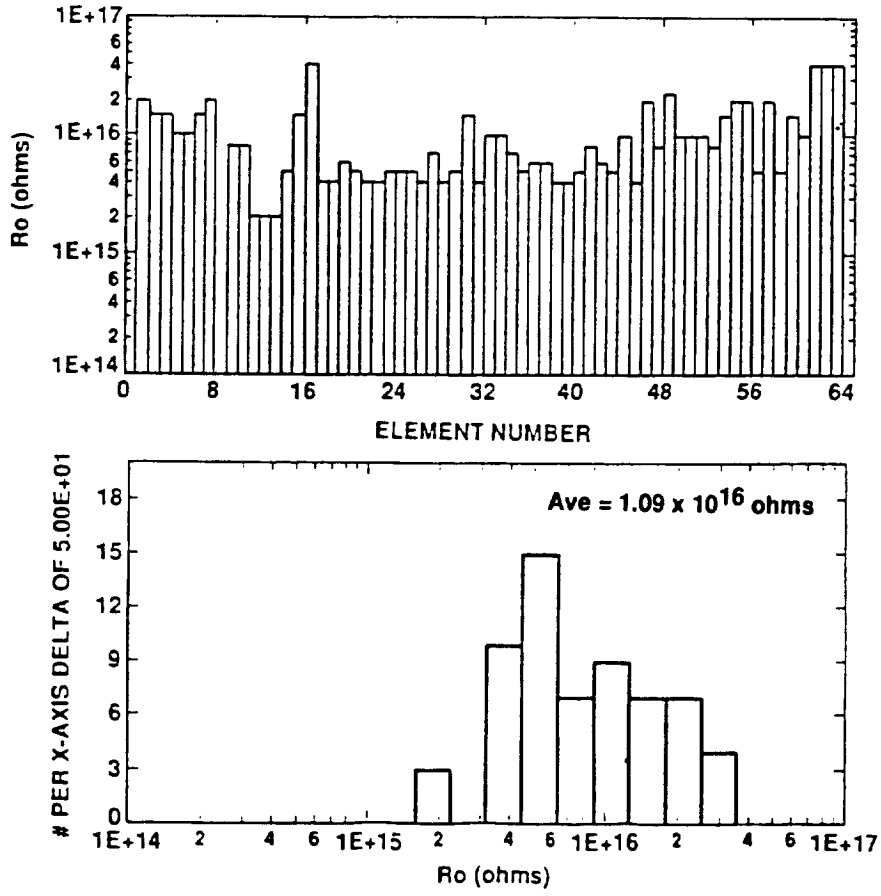

Figure 9. The Uniformity of the Detectors Zero Bias Impedance is Good at 80K.

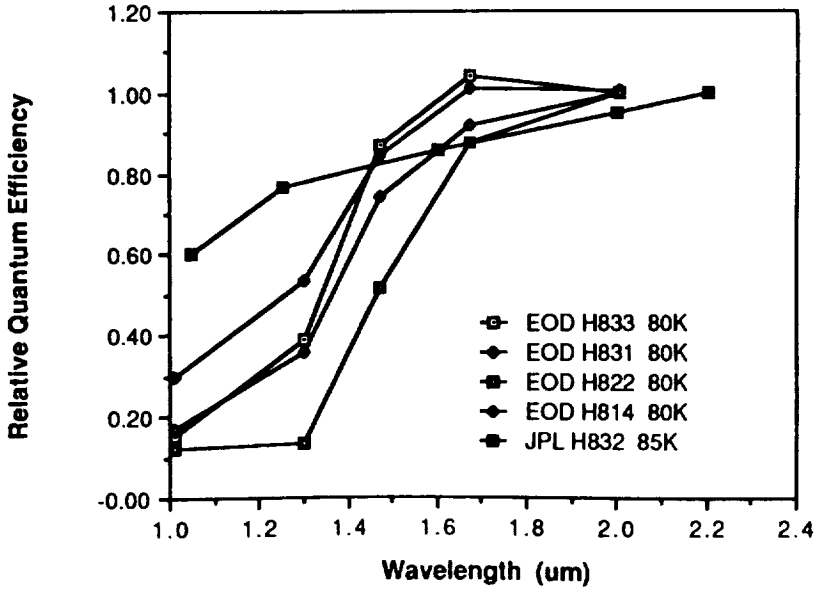

Figure 10. HgCdTe Detectors Achieve 70 Percent Quantum Efficiency Above 1.6 micron at 80K. (No AR Coating)

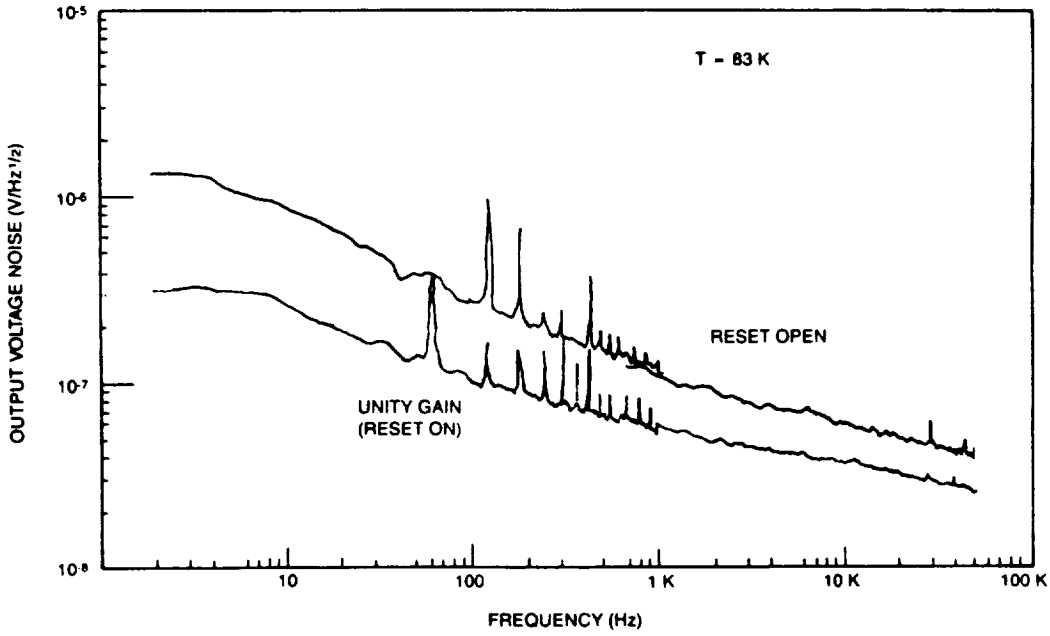

Figure 11. The Initial Lot of Multiplexers Demonstrated the CIDA Input 1/f Noise is Sufficiently Low to Achieve a Read Noise of 20 rms electrons.

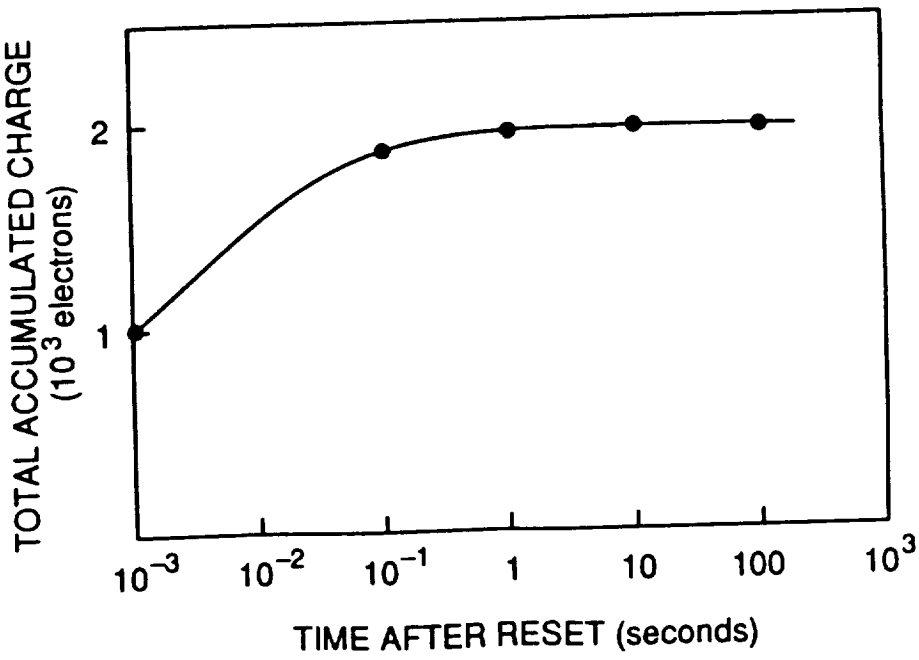

Figure 12. For Optimum Performance a Short Settling Time (0.1 to 1 sec) is Required Following the Reset Operation to let the Circuit Return to Equilibrium.

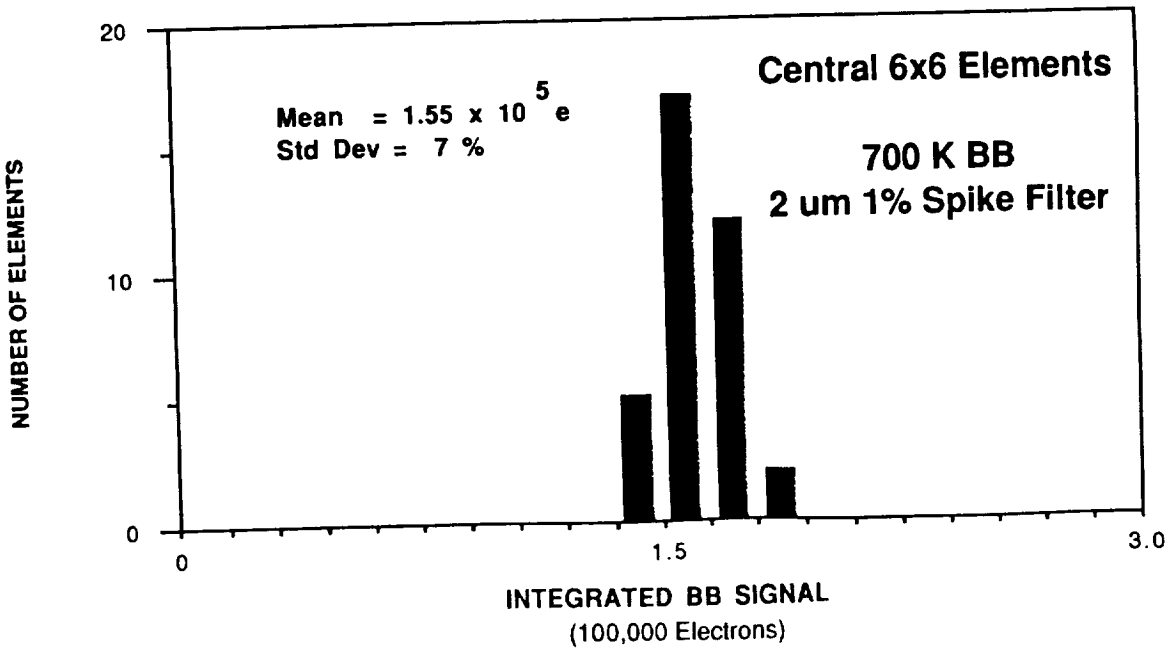

Figure 13. Excellent Response Uniformity is Obtained with a 7 Percent Standard Deviation.

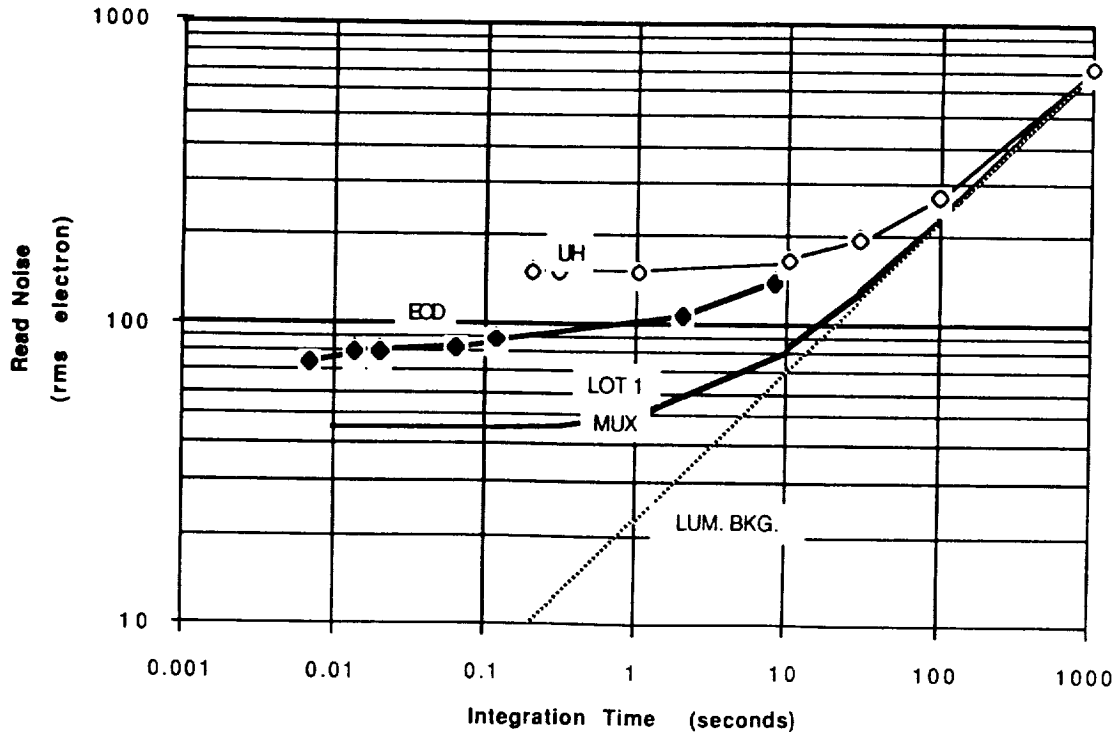

Figure 14. The Measured Read Noise Agrees Well With Theory for Lot 2 Multiplexers with Unusually High 1/f Noise.

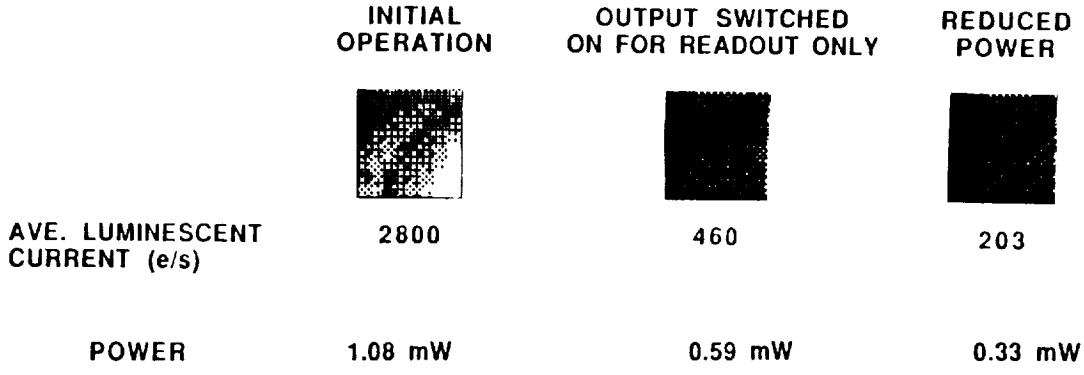

Figure 15. Lowering the Active Power Dissipation on the FPA Substantially Reduces the Luminescence Current.

LOW NOISE HgCdTe 128 X 128 SWIR FPA FOR HUBBLE SPACE TELESCOPE

Michael Blessinger and Kadri Vural
Rockwell International Science Center
Thousand Oaks, CA 91360

William Kleinhans
Valley Oak Semiconductor
Westlake Village, CA 91362

Marcia Rieke, Rodger Thompson and Robert Rasche
University of Arizona
Tucson, AZ 85721

Abstract

Large area focal plane arrays of unprecedented performance have been developed for use in NICMOS, a proposed Hubble Space Telescope refurbishment instrument. These FPAs are 128x128-element, HgCdTe hybrid arrays with a cutoff wavelength of 2.5 μm. The multiplexer consists of a CMOS FET switch array with a typical mean readout noise of less than 30 electrons. The detectors typically have a mean dark current of less than 10 electrons/s at 77K, with currents below 2 electrons/s measured at 60K (both at 0.5 V reverse bias). The mean quantum efficiency is 40-60% at 77K for 1.0-2.4 μm. Functional pixel yield is typically greater than 99%, and the power consumption is approximately 0.2 mW (during readout only).

Focal plane array design

The NICMOS focal plane array (FPA) is a hybrid structure consisting of a silicon multiplexer mated through indium columns to a HgCdTe detector array. The detectors are an array of photodiodes formed by ion implantation in a layer of HgCdTe grown by liquid phase epitaxy on a substrate of sapphire. The bandgap of the detector material is chosen such that it responds to infrared radiation in the 0.8 to 2.5 μm wavelength region. The format of the array is 128 x 128 elements on 60 μm centers.

Each detector is connected to a source follower amplifier in the input cell of the multiplexer through an indium column. This amplifier can be connected to the multiplexer output amplifier through a set of row and column select switches (Figure 1). In normal operation, the reset FETs, M2 and M4, are turned on to reset the voltage at the cathode of the detector, and are then turned off, allowing the cathode to float. Photo and dark current is then integrated into that capacitance which is the sum of the detector capacitance and the input capacitance of the multiplexer. Since the detector substrate voltage is fixed, the cathode voltage (and thus the voltage at the gate of the source follower M1) changes, reflecting the integrated current. Since the integration capacitance is small (approximately 0.1 pf), a small amount of integrated charge produces a significant voltage

change at the source follower gate. When M3 and M5 are turned on, the voltage at the unit cell source follower is sampled at the output amplifier, which is another source follower.

Control of the select and reset switches, M2 through M5, is accomplished by the operation of two shift registers driven by user supplied clocks. Additionally, the reset is gated by an enable line, REN, which allows one to optionally reset or not reset a particular pixel while it is selected. This not only allows monitoring of the reset level at the output, but also allows the pixel to be sampled non-destructively. Consequently, sophisticated sampling schemes can be used to improve the signal-to-noise ratio.

Since the multiplexer is CMOS in design, and because the input cell source folllower only draws power when it is accessed, the design is inherently low power. Turning off the output amplifier when readout is not occurring reduces power consumption to zero. During readout, only the output amplifier and one input cell amplifier are on at any time, so that the power consumed is a minimal 0.2 mW when 5V power supplies are used.

Performance results

Completed focal plane arrays were tested extensively with particular attention paid to their noise and dark current characteristics.

Dark current. The dark current was characterized at a wide variety of reverse biases at 77K. Figure 2 shows a dark current histogram at 79K and 0.5 V reverse bias which has a mean value of 4.3 electrons/s. Figure 3 shows the mean array dark current versus bias at 79K. Even at large biases of several volts, currents less than 100 electrons/s were achieved. At 60K the dark current is even lower as shown in Fig. 4 where it is 1.6 electrons/s (10^{-19} amps).

Noise. The multiplexer readout noise was characterized in a variety of readout schemes. A simple model of the multiplexer circuit based on 1/f and thermal MOSFET noise indicates that the noise level should be about 4 electrons distributed fairly equally between the input cell amplifier and the output amplifier. Since this represents a level of about 3 μV, in practice other sources such as switching transients and crosstalk will in fact dominate.

Three sampling schemes were examined. By sampling the signal, without any multiple sampling, one would expect the noise to be dominated by the reset kTC noise of the integration capacitance, about 60 electrons, which is indeed the case. By sampling both the signal level and the reset pedestal immediately following, one would expect some suppression of low frequency noise, but no removal of the reset noise since the samples are not truly correlated. This results in a noise somewhat worse than the preceding case due to the two samples.

A better sampling scheme is triple correlated sampling where the pixel is sampled immediately before, during, and immediately after reset. By properly correlating samples between frames, a removal of reset kTC noise is accomplished. In this way noise levels below 30 electrons are achieved (Figure 5). From this data a total FPA noise based upon readout noise and dark current can be projected (Figure 6).

Quantum efficiency. The mean FPA quantum efficiency was measured at various wavelengths using bandpass filters, and the results are shown in Figure 7.

Conclusions and future work

The FPAs developed for the NICMOS program have achieved an unprecedented level of performance for a large format array. Readout noises under 30 electrons and dark currents under 10 electrons/s at 77K (<2e-/s at 60K) were achieved using a design which was simple, easy to operate, and easy to produce. Furthermore, the design can be extrapolated to larger sizes (256x256 for example) with low risk and similar performance.

Acknowledgements

The authors thank their colleagues at Rockwell for their work in fabricating the FPAs, particularly Jenkon Chen, Victor Johnson, and Matthias Blume. This work was funded by NASA (NAS5-30008) through the University of Arizona NICMOS project.

NICMOS MULTIPLEXER SCHEMATIC

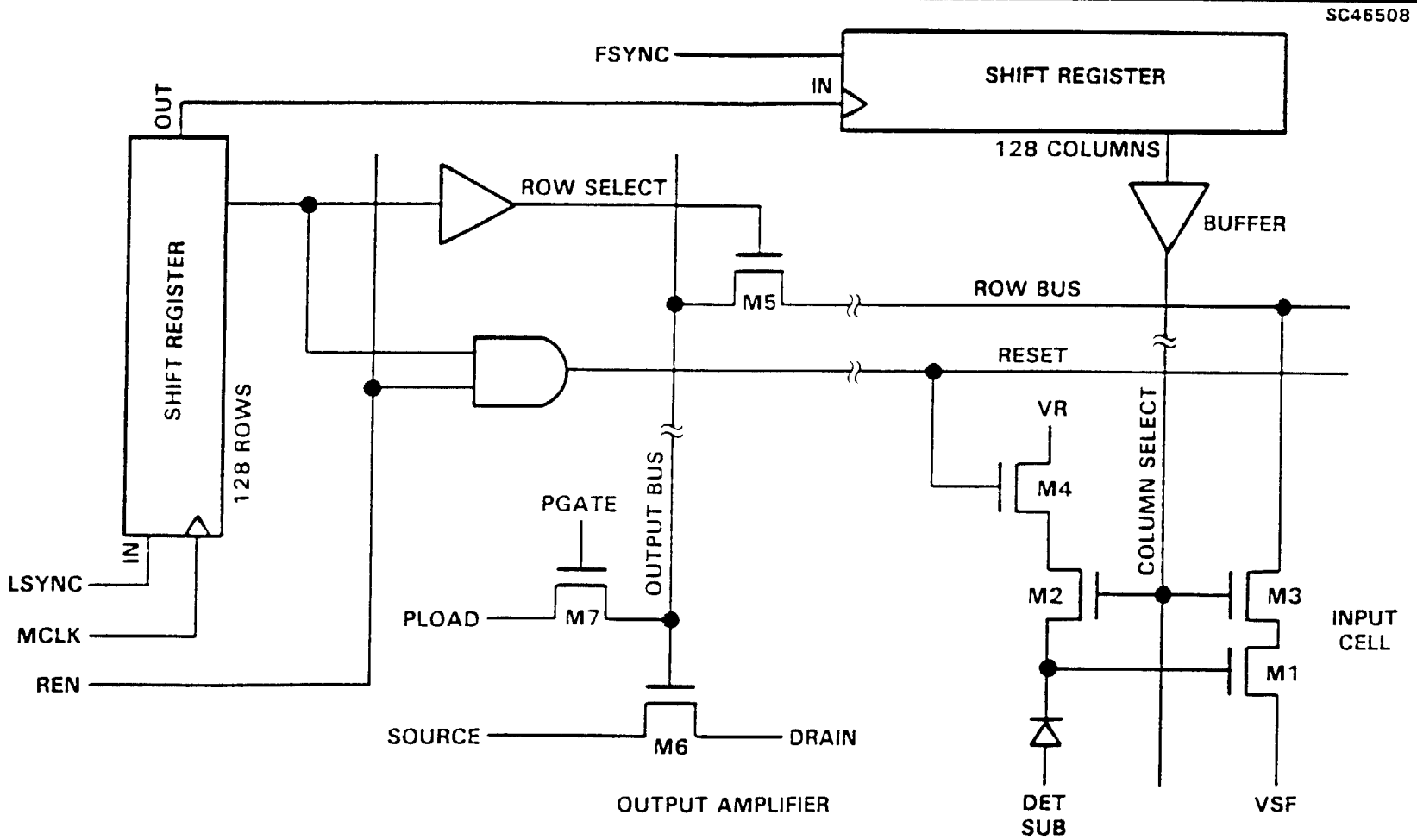

FIGURE 1. NICMOS 128x128 Multiplexer Schematic

NICMOS 128x128 FPA

SC46505

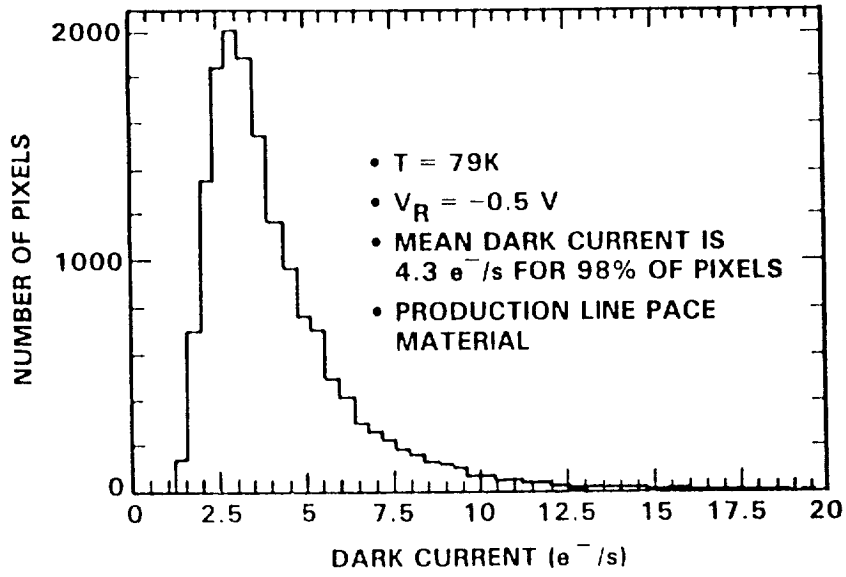

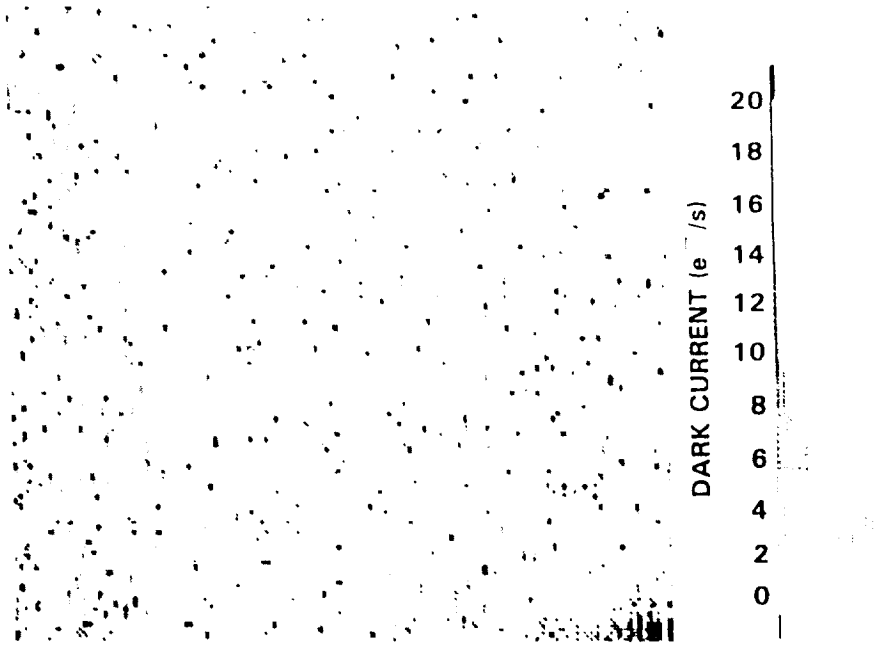

FIGURE 2. Dark current histogram (top) and map (bottom) for NICMOS 128x128 FPA at T = 79K. There is -0.5V bias on the detectors. The PACE-1 material has been grown by our production line at Anaheim (EOC).

NICMOS 128x128 FPA

MEAN DARK CURRENT AS A FUNCTION OF REVERSE BIAS

SC46502

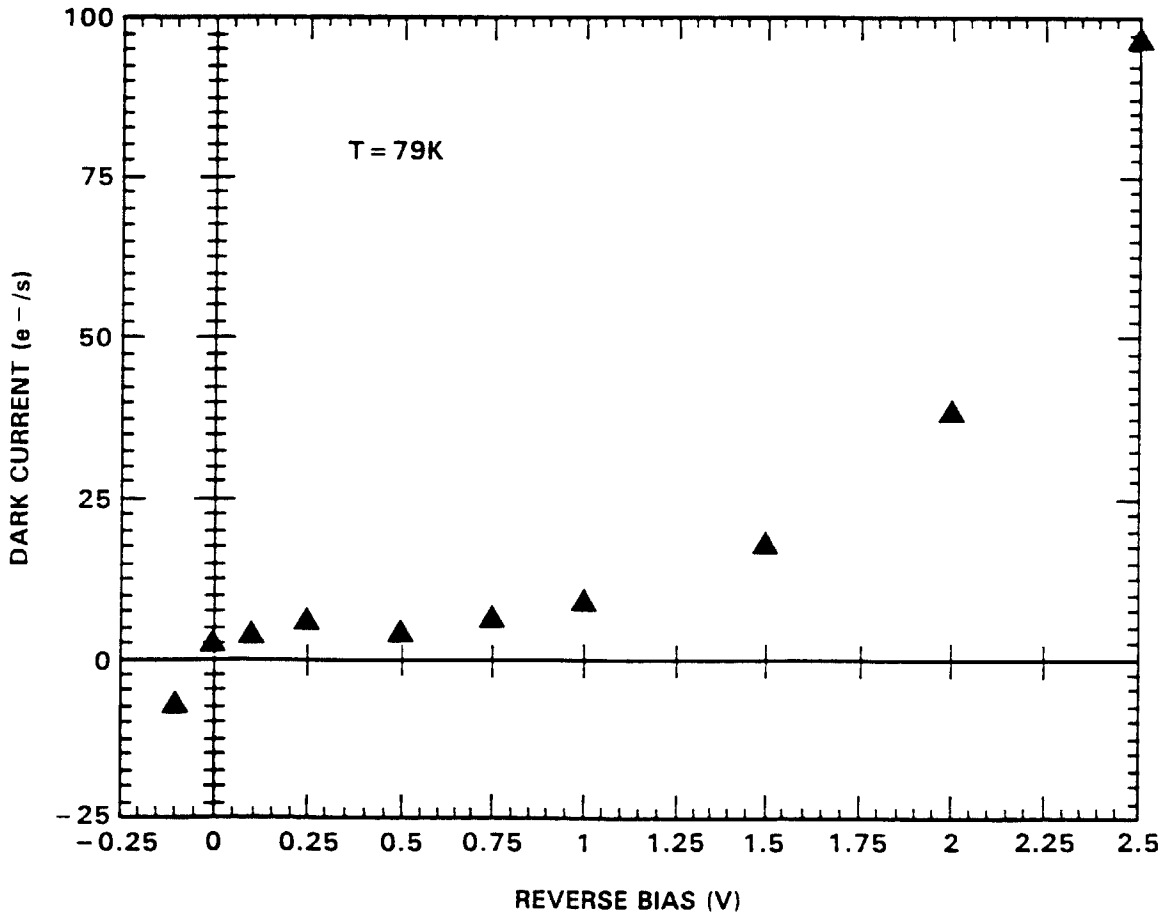

FIGURE 3. NICMOS 128x128 FPA mean dark current as a function of reverse bias at T = 79K.

NICMOS 128x128 FPA

SC46506

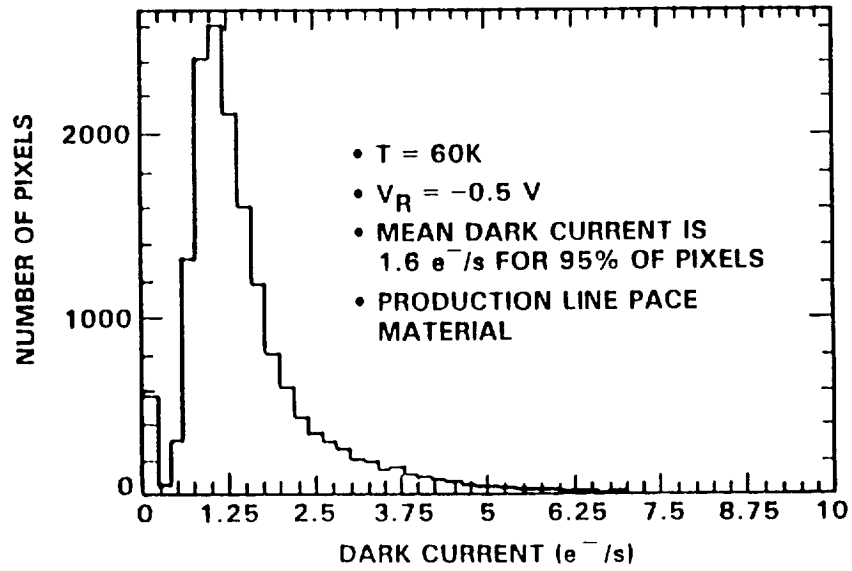

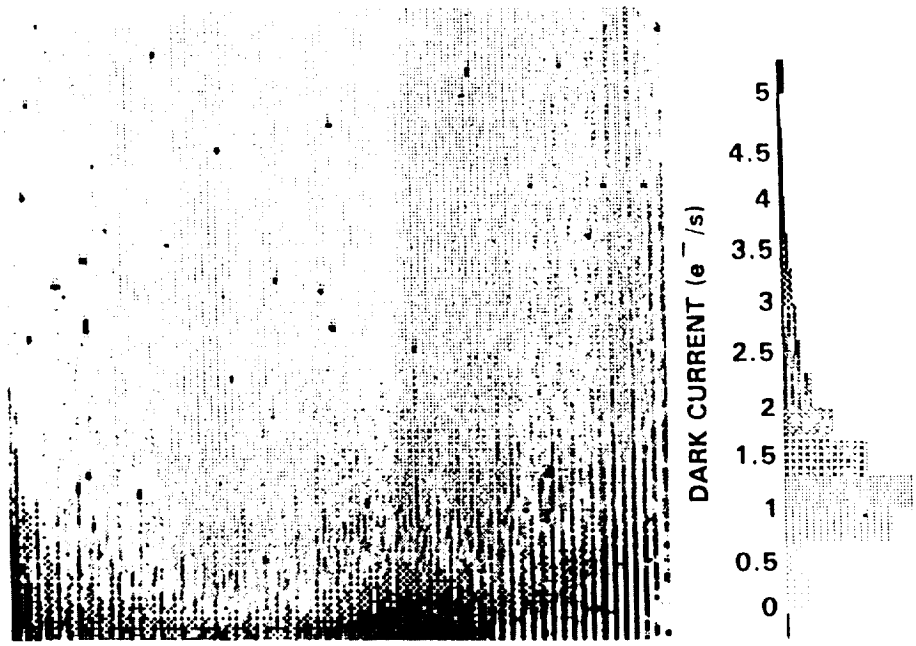

FIGURE 4. Dark current histogram (top) and map (bottom) for the same NICMOS 128x128 FPA of Figure 2 at T = 60K. There is some light leakage in the dewar as seen at the bottom portion of the map.

NICMOS 128x128 FPA

NOISE vs INTEGRATION TIME

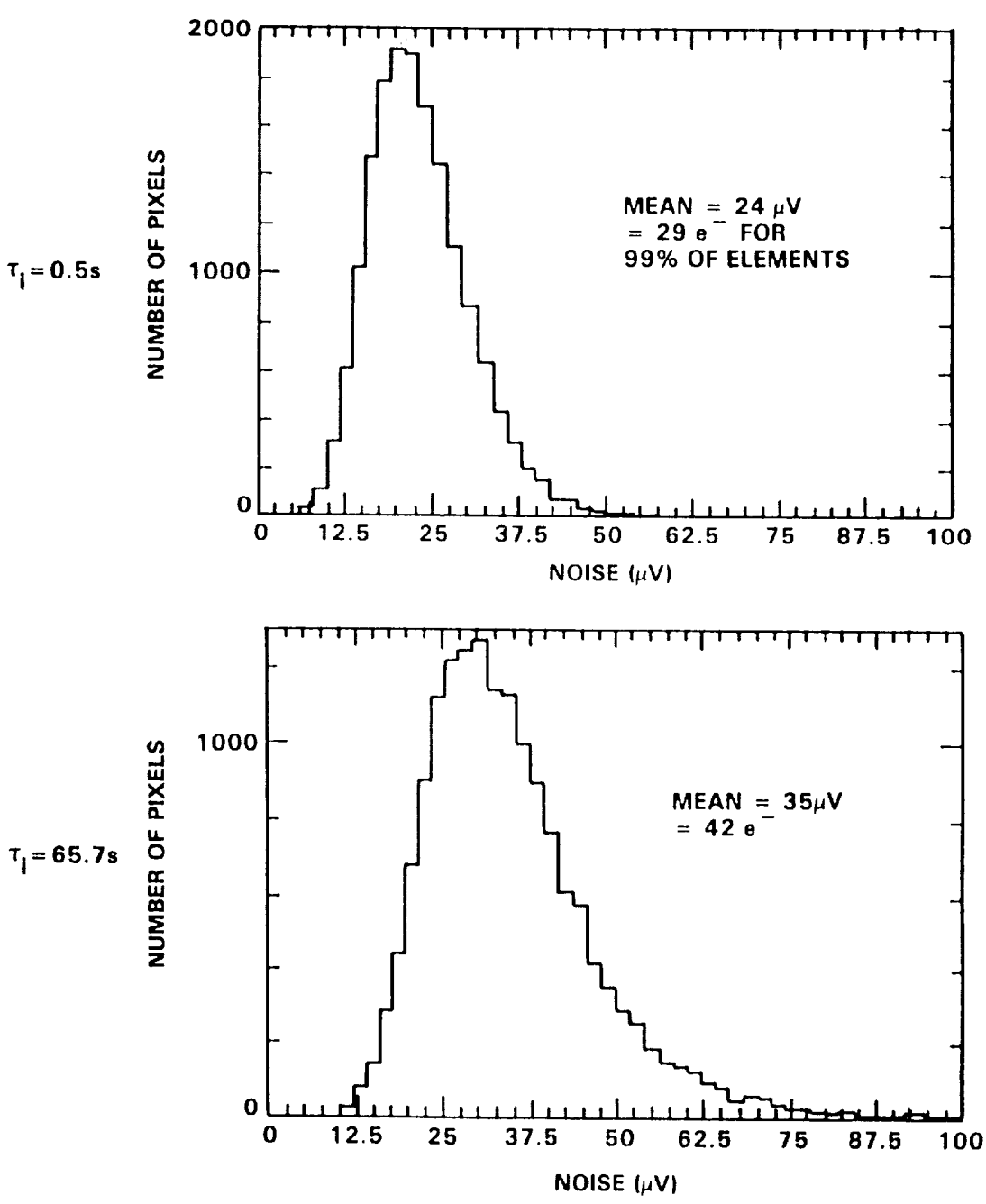

FIGURE 5. Noise histogram for 0.5s and 65.7s integration times.

PROJECTED FPA NOISE

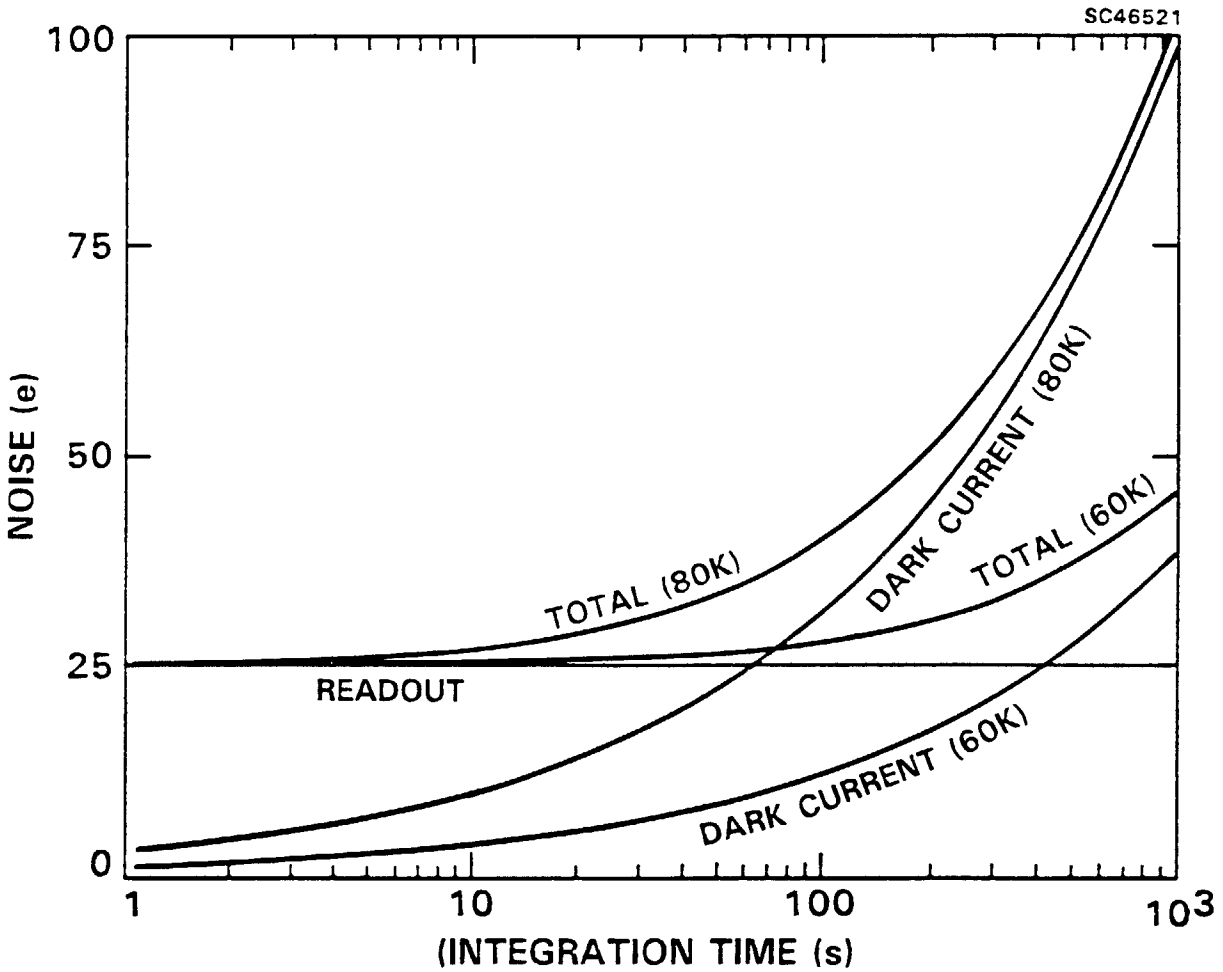

FIGURE 6. Total projected noise (readout plus dark current shot noise) as a function of integration time at 60K and 80K.

DETECTOR QUANTUM EFFICIENCY

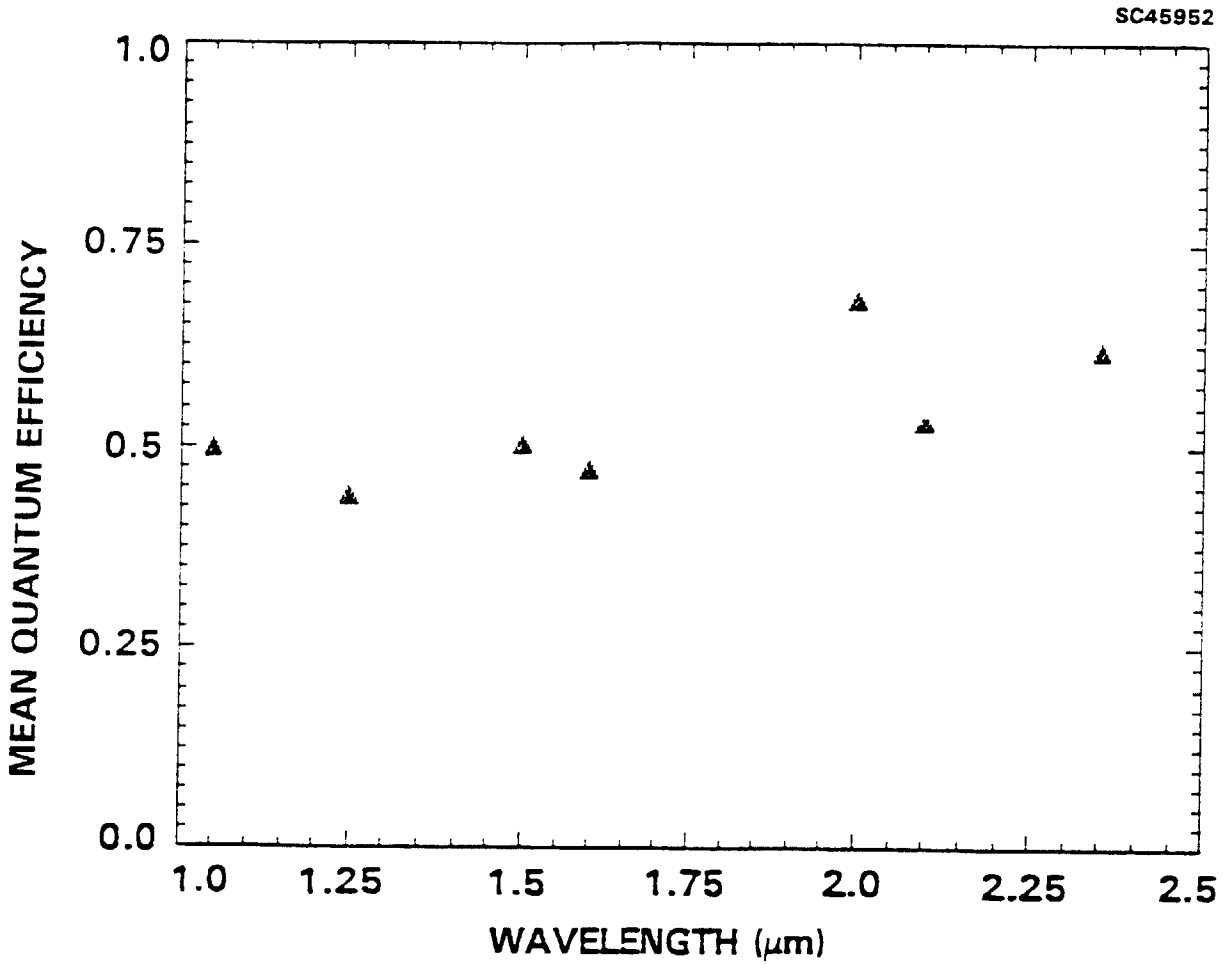

FIGURE 7. Mean quantum efficiency as a function of wavelength for NICMOS 128x128 FPA.

Laboratory and Telescope Use of the NICMOS2 128x128 HgCdTe Array

M.J.Rieke, E.F.Montgomery, G.H.Rieke
Steward Observatory
University of Arizona

K. Vural and M. Blessinger
Rockwell International Science Center

W. Kleinhans
Valley Oaks Semiconductor

I. Overview

The second generation of Hubble Space Telescope instruments will include a near-infrared instrument. This choice has driven the development of near-infrared arrays to larger sizes and lower read noises. Rockwell International has delivered an array for use in the NICMOS instrument; this array has been dubbed "NICMOS2". NICMOS2 is 128x128 array of HgCdTe diodes In-bonded to a switched MOSFET readout (see Blessinger, *et al.*,this volume). The readout was specifically designed for astronomical use with the HST requirement of low read noise a prime goal. These arrays use detector material which is similar to that used by Rockwell in previous arrays (eg. HgCdTe produced on a sapphire substrate), but the NICMOS2 devices differ substantially from other 128x128 arrays produced by Rockwell in having a read noise of only 30 electrons when read out using appropriate correlated sampling. NICMOS2 has now been characterized in the laboratory, and it has been used on groundbased telescopes.

Table 1 summarizes the properties of the NICMOS2 array.

Table 1: NICMOS2 Characteristics

Detector type	PV HgCdTe
Cutoff wavelength	2.5μm
Readout type	switched MOSFET
Unit cell size	60μx60μ
Nominal operating temperature	60-77°K
Read noise	30 electrons
Dark current @ 60°K	1.5 e/sec

II. Laboratory Tests

Arizona has measured the quantum efficiency, linearity, read noise, uniformity, and response to gamma radiation. In tests which duplicated Rockwell data, similar results were obtained. Dark current data were not acquired using a NICMOS2 array but rather were taken

using JFET integrators (see G. Rieke, *et al.* in this volume for a description of the technique); Table 2 summarizes results for a variety of individual diodes with different cutoff wavelengths. In the case of the 2.5-μm cutoff material, Arizona measurements of individual diodes are comparable to the rates measured at Rockwell of 4.5 electron/sec at 77°K and 1.5 electrons/sec at 60°K for NICMOS2 with the output amplifier turned off. Note that the individual diodes have a larger area than the diodes in the array so the lack of a significant drop between the individual diode and array data suggests that a regime is being entered where the dark current is not proportional to diode area. The relatively small drop in dark current between 77°K and 60°K is inconsistent with the dark current being due to generation-recombination and suggests that tunneling may be responsible.

Table 2: Dark Currents for a selection of HgCdTe Diodes

Type	Size	T°K	I_{Dk}(e/sec)
λ_c=1.4μm	160μx160μ	77	6.5
λ_c=2.5μm	130μx130μ	77	9.0
λ_c=2.5μm	130μx130μ	63	2.0
λ_c=3.0μm	50μx50μ	60	6.0
λ_c=4.2μm	60μx60μ	63	200

Of particular interest for NICMOS is the relatively small increase in dark current seen for the 3.0-μm cutoff material as compared to the 2.5-μm cutoff material. This result implies that the NICMOS spectrometer extension to 3.0μm will not exact any large performance penalties.

All of the data reported here were taken using a modified form of correlated sampling. Figure 1 shows this technique where two samples per pixel are taken per readout. One sample is taken at the end of the integration and the second is taken immediately after with the reset enabled. This method also requires that some images (bias frames) with extremely short integration times be taken to calibrate the change in level seen when the reset is released. Bias frames have proven to be very stable over periods of days. The read noise achieved with this sampling technique is 91 electrons; Rockwell saw 80 electrons using a similar method. The 80 electron noise level is what is expected for this technique which is subject to the full kTC noise of the integrating node. A better method which avoids kTC noise and compensates for low frequency drifts is also shown in Figure 1 and is labelled "triple-correlated" sampling. Rockwell has used this method to achieve a readnoise of 30 electrons which is independent of integration time.

Because the read noise as expressed in electrons depends on knowing the integrating node capacitance, this must be measured, and is one of the keys to the good performance of the NICMOS2 array. Rockwell measured the capacitance by measuring the total current flow

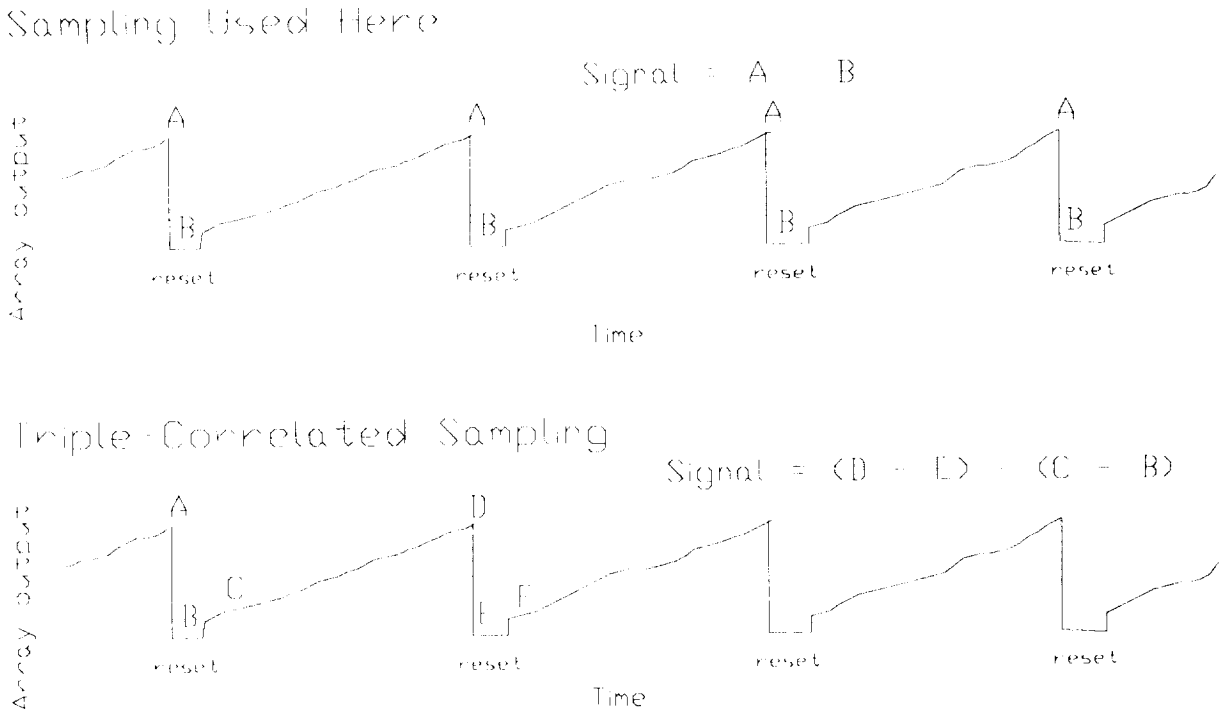

Figure 1: Sampling methods used in reading NICMOS2 arrays.

through the array and obtained a value of 0.10pF with over 80% of the capacitance estimated to be attributable to the HgCdTe diodes. The Arizona measurement took advantage of the fact that signal strength and noise have different dependencies on the capacitance:

$$V_{signal} = ei/C$$
$$V_{noise} = e\sqrt{i}/C$$
$$V_{noise}^2 = e^2 i/C^2$$
$$\frac{V_{signal}}{V_{noise}^2} = C/e$$

$C = capacitance, \quad e = electron\ charge, \quad i = photoelectrons/\sec$

The capacitance of 0.127±.035pF measured at Arizona agrees well with the Rockwell data. For the read noises reported in this paper, a value of 0.10pF has been used.

The quantum efficiency was measured for a central region on the array by imaging a spot onto the array. This spot was illuminated by a blackbody source and a combination of cold and warm filters were used to define the bandpass. Figure 2 shows results from a NICMOS2 array at 77°K and an older 64x64 array (Rieke *et al.* 1987). The newer array does not exhibit as sharp a drop in QE towards 1μm as did the older array. The quantum efficiency of the NICMOS2 array was also measured at 63°K and did not change significantly at the lower temperature.

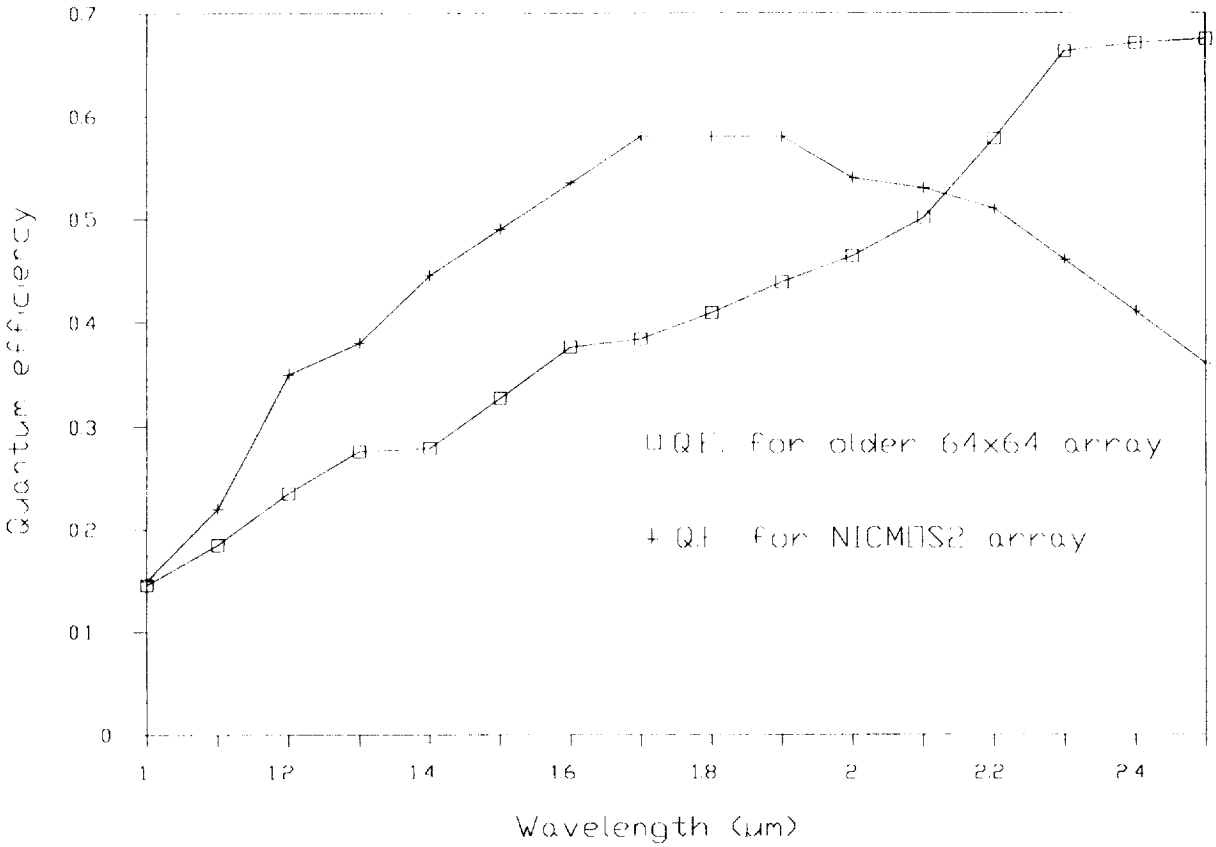

Figure 2: The quantum efficiencies of a NICMOS2 array and an older 64x64 HgCdTe array measured at 77°K.

One problem with the NICMOS2 array which has been used most extensively is its gradient in quantum efficiency from one corner to the diagonally opposite corner. The image in Figure 3 was obtained looking at sky at 2.2μm; no correction procedures of any sort including bias correction have been applied to this image. The gradient in quantum efficiency and "striping" due to column to column variations are apparent. The quantum efficiency ranges from over 70% to about 25% in the worst areas. This gradient is much smaller at 1.6μm and essentially gone at 1.25μm. The "striping" is seen in bare NICMOS2 multiplexers, and is very stable. Flatfielding removes all traces of this column to column structure in the image.

The linearity of the NICMOS2 array has been assessed in two regimes shown in Figures 4 and 5. The array should be subject to an inherent non-linearity because the photocurrent is collected on the combined capacitance of the diode and MOSFET, and the diode capacitance is a function of the bias across the detector and hence depends on how much charge has already been collected (see Hoffman 1987). The degree to which this non-linearity poses a problem depends on how rapidly the diode capacitance varies with bias and on how much effort can be expended on calibrating it and removing it from the data in the image processing steps. HgCdTe diodes have the excellent characteristic that they change in capacitance relatively slowly; from a bias voltage of -0.2 to -0.5 volts, they exhibit a change of only 4% in their capacitance. This voltage range is a typical operating regime for NICMOS2 arrays. Data taken by varying the integration time while viewing a constant source of

Figure 3: An unprocessed image taken of the sky at 2.2μm.

illumination have been used to study the linearity. In the low signal case plotted in Figure 4, NICMOS2 appears very linear with no small signal collection problems seen. In Figure 5, the large signal linearity is examined with no problems apparent until the bias level is approached. The bias used in taking these data was 0.5 volts which yields an effective well-depth of about 300,000 electrons. No linearity corrections are needed if NICMOS2 is operated at less than 85% capacity, and no corrections have been applied to the telescope data reported below.

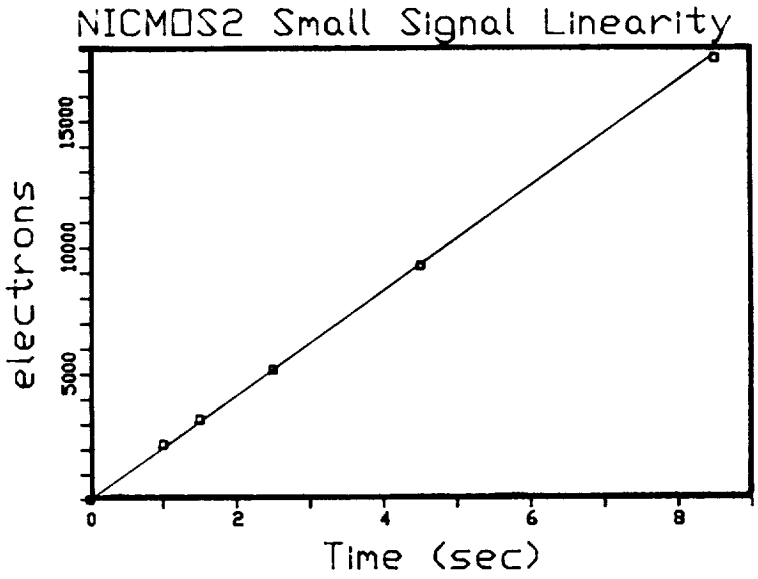

Figure 4: Small signal linearity for a NICMOS2 array.

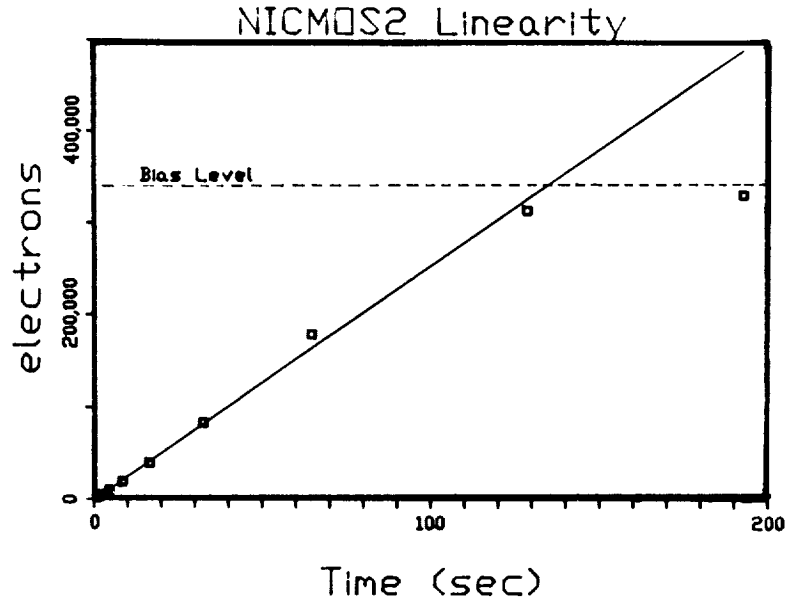

Figure 5: Large signal linearity for a NICMOS2 array. The bias level corresponds to 0.5 volts.

Another important attribute of an array intended for use in space is the ability to withstand charged particle hits. NICMOS2 arrays have not themselves been subjected to radiation testing. A similar readout has been, and limited testing of HgCdTe diodes has been carried

out. In both cases, the testing consisted of exposing the device to a 10 mCurie Am^{241} gamma-radiation source mounted within a few centimeters of the device being tested. In other situations the deposition of energy by gamma rays induces effects similar to those induced by other types of radiation; more extensive testing of NICMOS2 arrays and HgCdTe diodes should be done to verify this assumption. A TCM-1000B switched FET readout with 2.5-μm HgCdTe diodes showed no sensitivity changes when exposed to the Am^{241} source. This test was conducted with the array viewing a relatively high background. The other test consisted of exposing a 3.0-μm diode being read out with a JFET integrator to the radiation source. This diode showed complete recovery to its normal dark current 5 minutes after being irradiated at 20% of an HST South Atlantic Anomaly passage. Recovery may have been faster, but a few minutes are required for an accurate dark current measurement at these levels. Other testing at Rockwell has not revealed any problems, but more radiation testing is needed before certifying the NICMOS2 array for space use.

III. Telescope Use

The NICMOS instrument will operate at wavelengths where observations can be done from groundbased sites. A camera for such use has been built, and the performance of the NICMOS2 in an actual astronomical situation has been characterized. The camera is shown schematically in Figure 6. Note the use of a cold pupil and cold filters to limit the radiation reaching the detector array. The background levels at 2μm from a groundbased telescope are not very different from those expected at this wavelength on HST because the larger pixel scale used on the ground is compensated by the fact that HST is warmed to temperature of 76°F, much warmer than is typical for a groundbased site. At shorter wavelengths the groundbased backgrounds are much higher than will be seen from HST because of the OH-airglow.

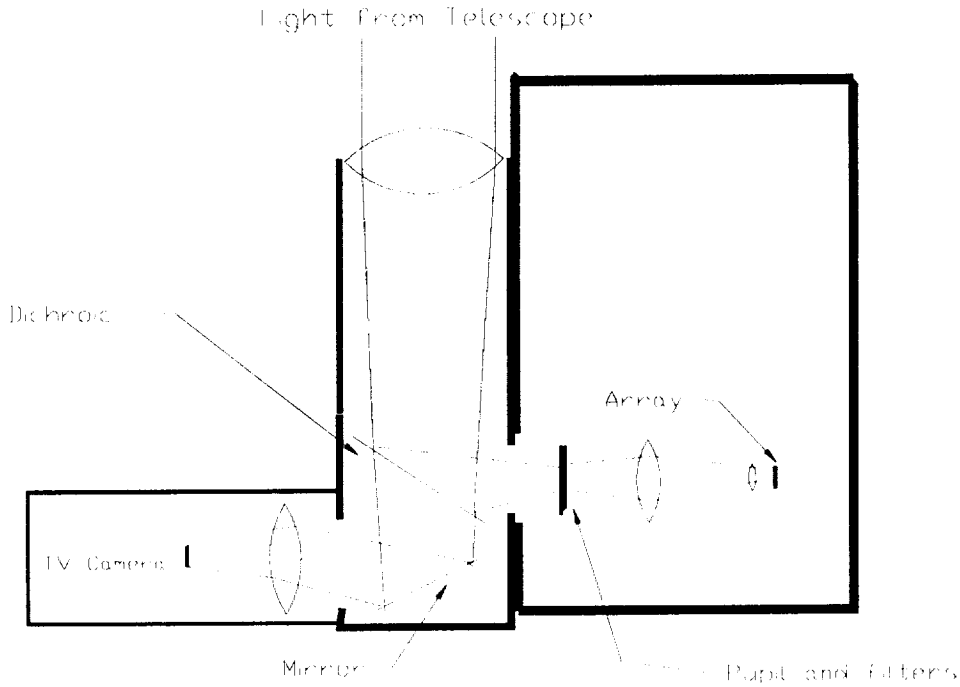

Figure 6: Camera optics schematic

The equipment used to read out the array at the telescope is very compact and is based on clock waveforms being generated using EPROMs. The hardware does not do any of the differencing required by the readout sampling; all differencing is done in the computer controlling the array readout (a 80386-based computer in this case). The readout electronics themselves are very compact and occupy a volume of only .009 cubic meters. These electronics digitize to 16-bits and when used with the NICMOS2 array provide a gain such that one unit of the digitizer corresponds to 19 electrons. The system noise without an array is 40 electrons, and with the array, yielded a read noise of 91 electrons. The electronics also include protection circuits for all lines controlling the array and a real-time video display which is very useful for focussing and alignment.

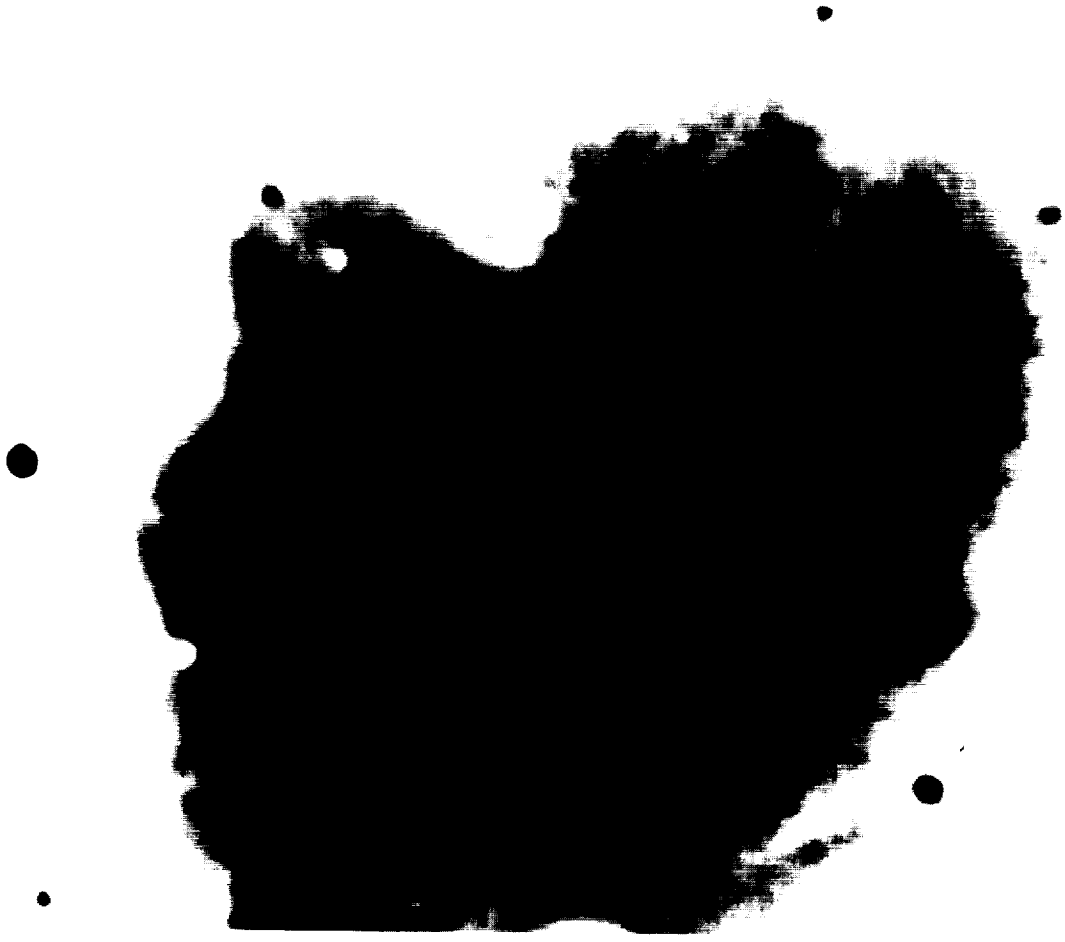

Figure 7: The Crab Nebula at 2.2μm.

Figures 7 and 8 show fully reduced data taken with the NICMOS2 camera using the Steward Observatory 1.5-meter telescope on Mt. Bigelow, AZ. The telescope has an f/45 infrared secondary which was used for these observations. The plate scale of 1.8"/pixel is optimized for studying extended sources. This plate scale yields a total field-of-view of 3.8

arc minutes. These images were produced by beam-switching between the object and adjacent sky every 60 seconds. The 60-second exposures which were recorded for analysis consisted of 6 co-added 10-second exposures which were necessary to avoid overfilling the array. The final pictures were produced by subtracting a bias frame from each of the object and sky frames, ratioing the resulting frames on a pairwise basis, and then averaging all of the ratio frames. This is the same technique that has been used with our previous arrays (Rieke *et al.* 1987), and results in flatfielding to 1 part in 20000. The sensitivity achieved using the NICMOS2 array at K(2.2μm) on the 1.5-meter is 21.5 magnitudes per square arc second (one sigma in one hour of integration composed of co-added frames).

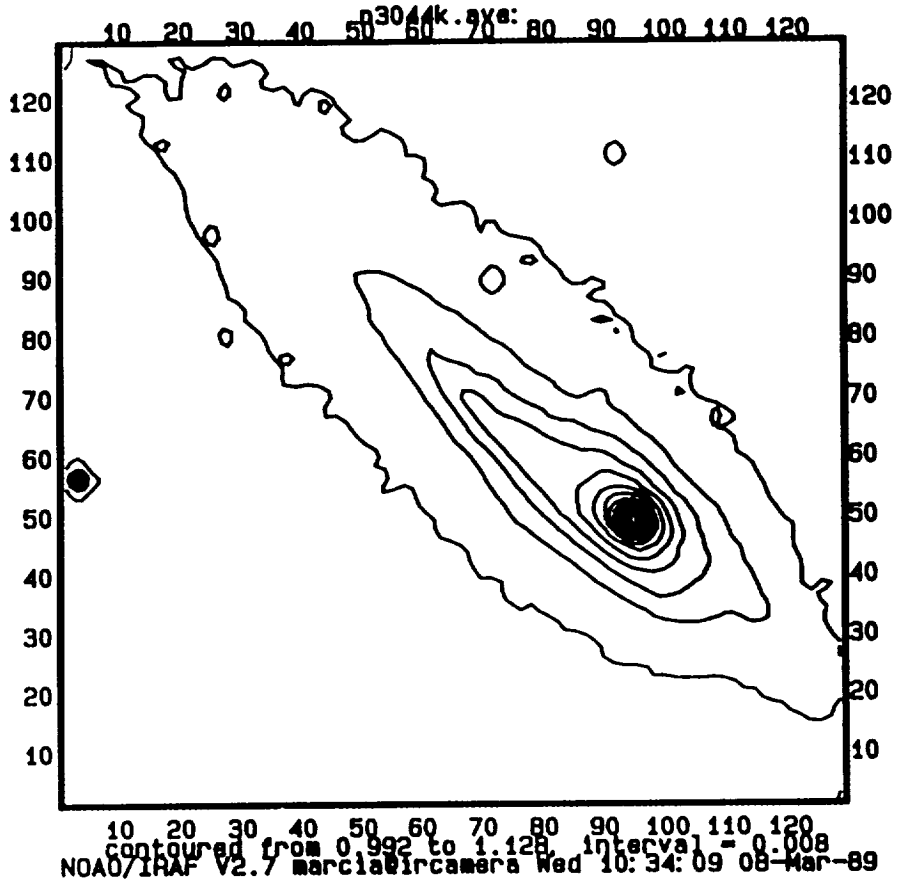

Figure 8: Part of the edge-on galaxy NGC3044 at 2.2μm.

At this point, the full capabilities of the NICMOS2 array have yet to be exploited in groundbased use, but it has already shown that it is capable performer.

IV. Summary

The NICMOS2 128x128 HgCdTe array developed for use on HST is a significant step forward in the technology available to astronomers. Its readout has been designed with astronomical use in mind, and it delivers a level of performance at 30 electrons read noise that will permit full use of HST as well as very interesting investigations from the ground.

V. References

Hoffman, A. W. 1987, in Infrared Astronomy with Arrays, ed. C. G. Wynn-Williams and E. E. Becklin, p. 29.

Rieke, M. J., Rieke. G. H., anf Montgomery, E. F. 1987, in Infrared Astronomy with Arrays, ed. C. G. Wynn-Williams and E. E. Becklin, p. 213.

N90-21339

FUTURE DIRECTIONS FOR NICMOS ARRAYS

by
R. Thompson, M. Rieke, E. Young, D. McCarthy, R. Rasche
Steward Observatory, University of Arizona

M. Blessinger, K. Vural
Rockwell International Science Center

and
W. Kleinhans
Valley Oak Semiconductor

ABSTRACT

The NICMOS project for HST requires focal plane arrays of 256x256 pixels for both its cameras and its spectrometers. The new arrays, developed by the Rockwell Corporation for NICMOS, have 40μm pixels of HgCdTe bump bonded to a switched MOSFET readout. Expected read noise and dark current for the arrays at 60 K are 30 e and 1 e/sec. respectively. The basis for these numbers is previous experience with 128x128 arrays.

1 NICMOS and its Environment

NICMOS (Near Infrared Camera and Multi-Object Spectrometer) is a second generation infrared instrument for the Hubble Space Telescope (HST). It contains both cameras and spectrometers for imaging in the 1-2.5μm range and spectroscopy in the 1-3μm region. There are three cameras with differing spatial resolutions, a warm 1-2μm spectrometer, and two cold spectrometers for the 2-2.5, and 2.5-3μm regions. The NICMOS camera and spectrometer specifications are given in tables 1 and 2.

NICMOS SPECTROMETER SPECIFICATIONS

PARAMETER	MULTI-OBJECT SPECTROMETER	LWS I	LWS II
Wavelength Coverage	1.0-2.0 μm	2.0-2.5 μm	2.5-3.0 μm
Spectral Resolution	100, 1000, 10,000	5000	1000

Table 1.

NICMOS CAMERA OPTICAL SPECIFICATIONS

PARAMETER	CAMERA I	CAMERA II	CAMERA III	LWS CAMERA
$\lambda/2d$ wavelength	1.0 μm	1.75 μm	-	-
Pixel size in arc seconds	0.043	0.075	0.2	0.2
Plate scale in arc sec per mm	1.075	1.875	5.0	5.0
Magnification	3.33	1.91	0.716	.716
f/number	79.9	45.8	17.2	17.2
Total field in arc seconds	11	19.2	51.2	-

Table 2..

All of the detectors are HgCdTe arrays with a 2.5 μm cutoff except for the 2.5-3.0 μm spectrometer array which has a 3.0 μm cutoff. The focal plane for each camera and spectrometer has 256x256 pixels which are currently a mosaic of four 128x128 60 μm pixel arrays. The new arrays are full 256x256 arrays with 40 μm pixels. These new arrays reduce the complexity and cost of the instrument and are expected to improve upon the performance of the 128x128 arrays described in this volume by Rieke et al. and Vural et al.. This presentation will discuss only the improvements in the new arrays. Please refer to the previous articles for the details of the present 128x128 arrays.

Figure 1. shows the expected thermal environment encountered by an infrared instrument on HST. Two emission mechanisms dominate the spectrum. At short wavelengths the scattered Zodiacal light contributes most of the power but at longer wavelengths the emission from the warm HST optical system overwhelms all other emissions. Near the minimum at 1.7 μm the background flux is on the order of 10 (photons/s)/μm. For spectroscopy and small bandwidth observations the background induced current is substantially below 1 e/sec, therefore, low dark current is an important factor in detector selection.

Note that Fig. 1 is for a 0.2" pixel which is the largest angular resolution for a NICMOS camera. The smallest angular resolution is on the order of 0.04".

TYPICAL HST BACKGROUND FLUX

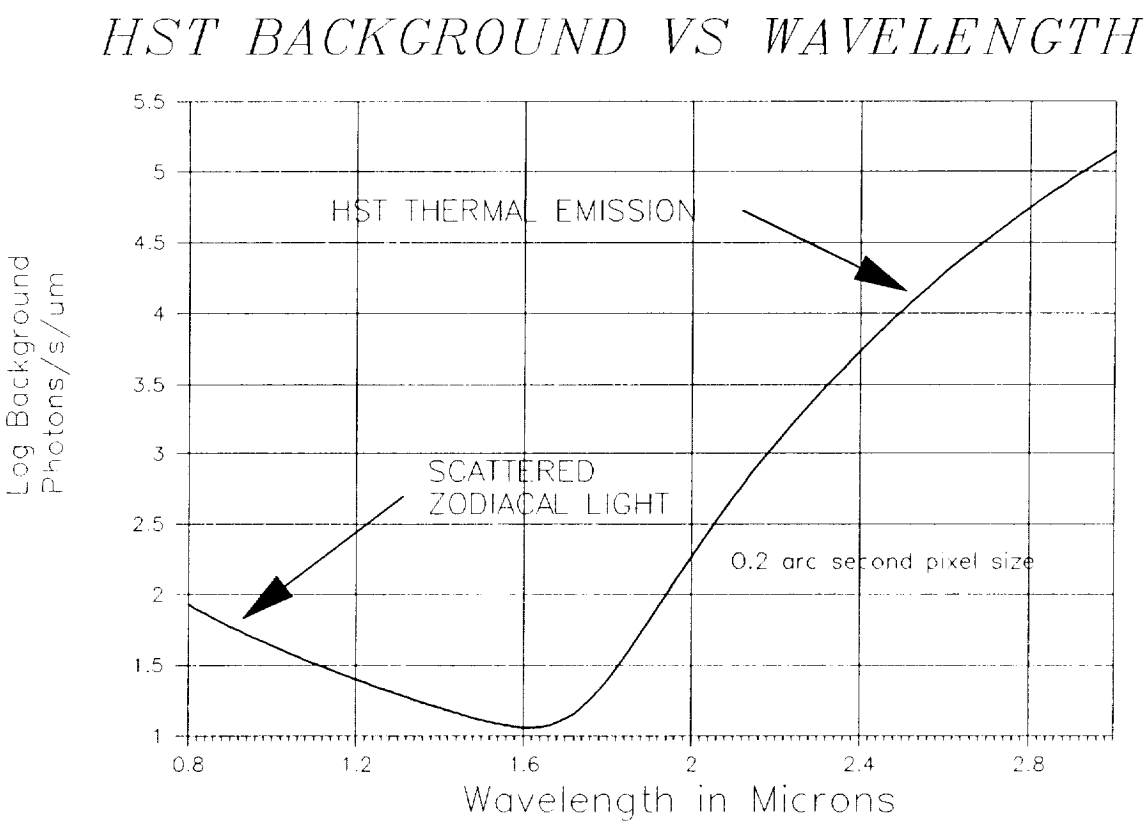

Fig 1.

The three NICMOS cameras and three spectrometers require a total of six independent focal plane arrays. Ease of readout and reduction of associated electronics is therefore an important factor in the array design. At the same time elimination of single point failures in any of the NICMOS instruments is also an important factor. For this reason the NICMOS program is developing two multiplexer designs. The first divides the multiplexer into 4 electrically independent 128x128 quadrants on the same multiplexer chip. The second design reads out the entire 256x256 detector array with a single 256x256 multiplexer. A single readout reduces the associated electronics for each focal plane and the quadrant design has a high degree of redundancy. A decision between the two designs will be made after reliability information is gathered on both designs. Another factor in the decision is the readout time for each array. For a given speed A/D converter the single output array requires 4 times as long to readout. This is an important factor for the observation of bright solar system objects. Except for the division into quadrants or single readout the features of the new arrays are similar therefore in the remainder of this presentation

they will be described without reference to type except when required.

2 NEW MULTIPLEXER FEATURES

Several new features are incorporated into the 256x256 multiplexer design which improve both the signal-to-noise characteristics and the ease of operation. At the same time we have not radically altered the previous design so as to reduce the development risk in the time constrained NICMOS program.

2.1 Electronic and Processing Changes

The new multiplexer process is a P channel - N well process which is expected to produce a lower noise system than the previous P channel - P well process. Both the detector and multiplexer substrates are now at ground and the gain in the switched MOSFET system is now 1 instead of 1/2 in the original system. Since the dominant noise is not in the amplifier system, the gain change is expected to produce a corresponding gain in signal-to-noise. All of the multiplexer test points are now buffered to protect the multiplexer during testing.

2.2 Logic Circuit Changes

In order to facilitate the readout, the shift registers which access each row and column address of a pixel can be reset to zero. Each shift register can also be clocked independently to quickly access a particular pixel. Although during readout the clocking is significantly slower, the shift registers can be run accurately at speeds up to 10 MHz. If only a small portion of the array has useful data, as in target acquisition, the beginning portion can be addressed quickly via independent row and column clocking. The relevant portion is then read out at the appropriate rate and the shift registers reset to zero to restart the process. Figure 2 shows the basic logic for a single pixel in the multiplexer.

As an additional noise reduction procedure the shift registers are now clocked on both the rising and falling edges. This procedure eliminates the possibility of a transition induced glitch on the signal during the time of measurement.

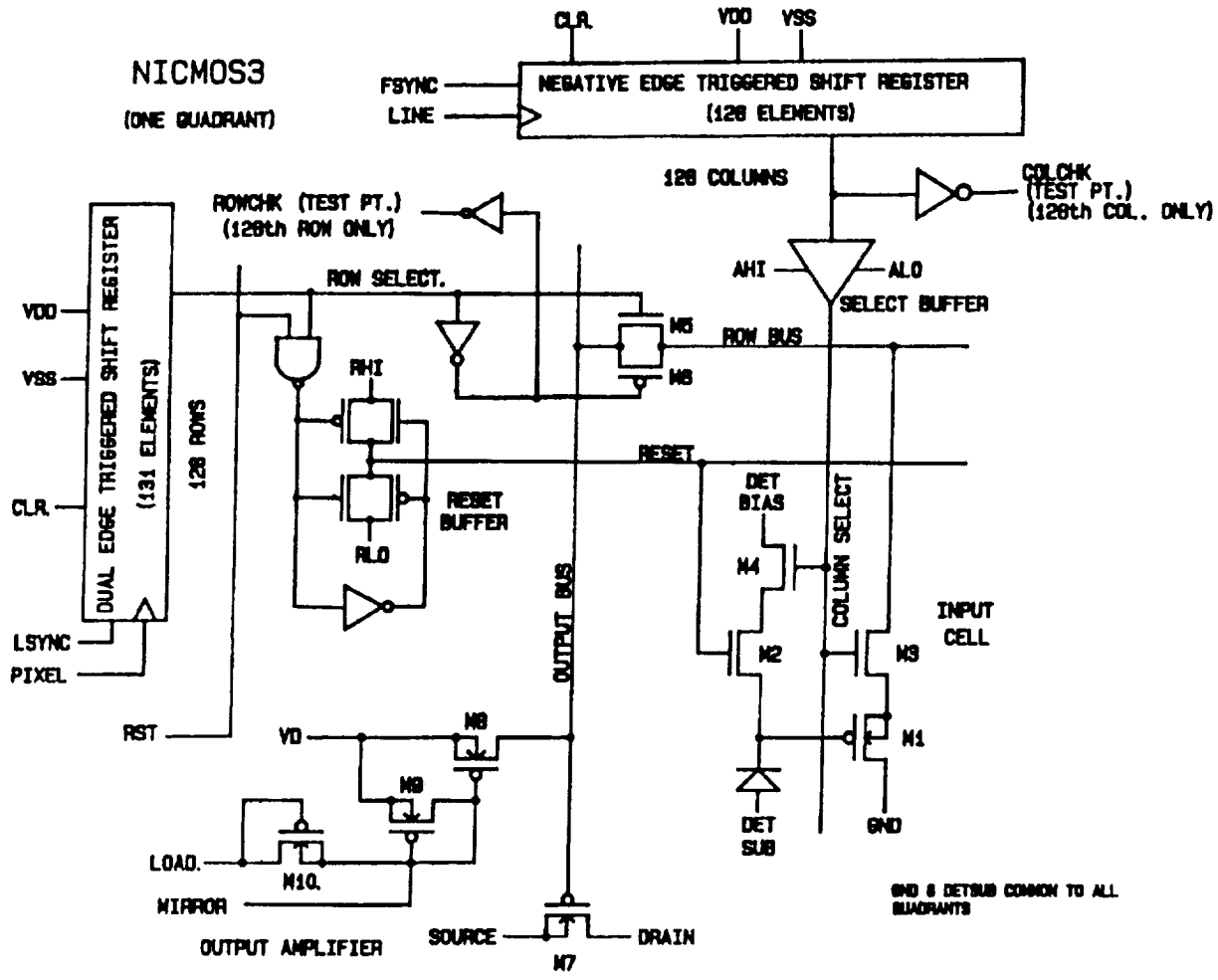

Figure 2

2.3 Geometry Changes

The new multiplexer design contains two major geometry changes. In the first change the pixel cell size is now 40 μm rather than 60. The net size of the bump bonded area is then approximately 1 cm. This size is small enough to ensure that the bump bonds remain secure during cooling. Since the sapphire substrate for the HgCdTe and the silicon multiplexer have slightly different coefficients of expansion, too large a size can break bump bonds during cooling.

The second change entails moving the output amplifier to the far edge of the multiplexer and also photon shielding it so that glow from the amplifier is not detected by the HgCdTe. The original detector arrays detected glow from the output amplifier. This problem was greatly reduced by turning off the output amplifier during

integration, but the geometry solution should entirely eliminate the problem.

3 NEW DETECTOR FEATURES

Except for the smaller pixel size of 40 μm and greater number of pixels, the HgCdTe photodiode array is very similar to the original 128x128 array. The smaller pixel size, however, has three potentially positive effects. First the smaller pixel size reduces its capacitance. A single photo-induced electron therefore produces a higher voltage which improves the signal-to-noise ratio per photon. In a second effect, the smaller pixel size should also have a reduced dark current. This is particularly important in spectroscopy which has a low background per pixel. Finally the smaller size of the pixel reduces the number of cosmic ray hits per pixel by a simple geometrical reduction in the cross section. Reduction of cosmic ray hits is an important factor for space experiments.

A reduction in detector size also carries the possibility of increased cross talk between pixels. Preliminary measurements on the current detectors indicates that the cross talk has an upper limit of less than 1-2 % for 60 μm pixels and therefore is not expected to be a problem in the 40 μm pixels.

A disadvantage of the smaller pixel size is a reduced well depth. Although borrowed from the vernacular of CCDs, well depth in the case of a photodiode is due to a different effect. Since photo induced charge is integrated directly on the photodiode, it alters the bias across the diode. As the bias voltage changes it approaches zero bias where the diode curve is very nonlinear. There is a limit on the accuracy of the correction procedure for the nonlinearity which limits the integrations to less than 300,000 electrons for the 60 μm pixels. This limit is expected to drop to 100,000 for the 40 μm case. Although quite adequate for space instruments, this limit may be troublesome for wide band imaging on ground based telescopes.

4 GENERAL COMMENTS

The new 256x256 detectors have several advantages for the NICMOS program. The factor of 4 reduction in array number reduces the complexity of the instrument and will realize distinct savings in cost and time. In particular it eliminates the need for very accurate alignment of 4 individual arrays to form a 256x256 focal plane and eliminates the 3-6 pixel gap between the arrays required in the mosaic procedure. In future conferences such as these we will report on the results of the detector tests and results gathered with the arrays. We encourage everyone who acquires these arrays for their own use to share their experiences with the NICMOS team. We need to gather as much experience as possible to ensure that the NICMOS instrument is an extremely productive tool for the entire astronomical community.

INTRODUCTION TO THE INFRARED SPACE OBSERVATORY (ISO)

M. F. Kessler[1] and F. Sibille[2]

[1] Space Science Department of ESA, Noordwijk, the Netherlands.
[2] Observatoire de Lyon, Saint Genis Laval, France.

Abstract: The Infrared Space Observatory (ISO) is an astronomical satellite, which will operate at infrared wavelengths (2.5 - 200 μm) for a period of at least 18 months. Imaging, spectroscopic, photometric and polarimetric observations will be obtained by four scientific instruments in the focal plane of its 60-cm diameter, cryogenically-cooled telescope. Two-thirds of ISO's observing time will be available to the astronomical community. ISO is a fully approved and funded project of the European Space Agency (ESA) with a foreseen launch date of May 1993.

1. Introduction

IRAS, during its brief 10-month in-orbit existence, provided astronomers with their first unobscured glimpse of the infrared universe. Such was the wealth of the data – catalogues, sky maps and spectra – of this highly successful mission that now, five years later, they are still being digested, interpreted and producing fresh science. With the end of the IRAS mission, due to depletion of its liquid-helium coolant, observations of the majority of these sources are no longer possible. The Infrared Space Observatory (ISO, shown in figure 1) will give astronomers the capability of routinely making high sensitivity observations at all these wavelengths, but for detailed study of individual objects rather than as a survey mission. Compared to IRAS, ISO will have higher sensitivity – in part from improvements that have been made in detectors since IRAS, wider wavelength coverage, better angular resolution, a longer lifetime and more sophisticated instruments.

ISO results from a mission proposal submitted to ESA in 1979. After various assessments and studies, particularly a phase A study in 1981-2, ISO was chosen in March 1983 to be the next new start in the ESA Scientific Programme. The focal plane instruments were selected in mid-1985 and the industrial phase B study of the spacecraft started in December 1986. Currently, ISO is in its main development phase (C/D).

This paper presents, firstly, an overview of the ISO spacecraft (section 2) and mission operations (section 3) and secondly, a synthesis of the scientific capabilities (section 4) and detector systems of the four instruments (section 5).

2. Overview of Spacecraft

The ISO satellite (5.3 m high, 2.3 m wide and 2400 kg at launch) is dominated by its so-called "Payload Module", the upper cylindrical part seen in figure 1. This module, shown in section in figure 2, is essentially a large cryostat, containing the telescope and the scientific instruments. Inside the vacuum vessel is a toroidal tank filled with about 2300 litres of superfluid helium, which will provide an in-orbit lifetime of at least 18 months. Some of the infrared detectors are directly coupled to this helium tank and are at a temperature of around 2 K. Apart from these, all other units are cooled using the cold boil-off gas from the liquid helium. This gas is first routed through the optical support structure, where it cools the telescope and the scientific instruments to temperatures of 3–4 K. It is then passed along the baffles and radiation shields before being vented to space. A small auxiliary tank, containing about 60 litres of normal liquid helium, fulfils all of ISO's cooling needs for the last 72 hours before launch. Mounted on the outside of the vacuum vessel is a sunshield, which prevents the sun from shining directly on the cryostat. The solar cells are carried by this sunshield.

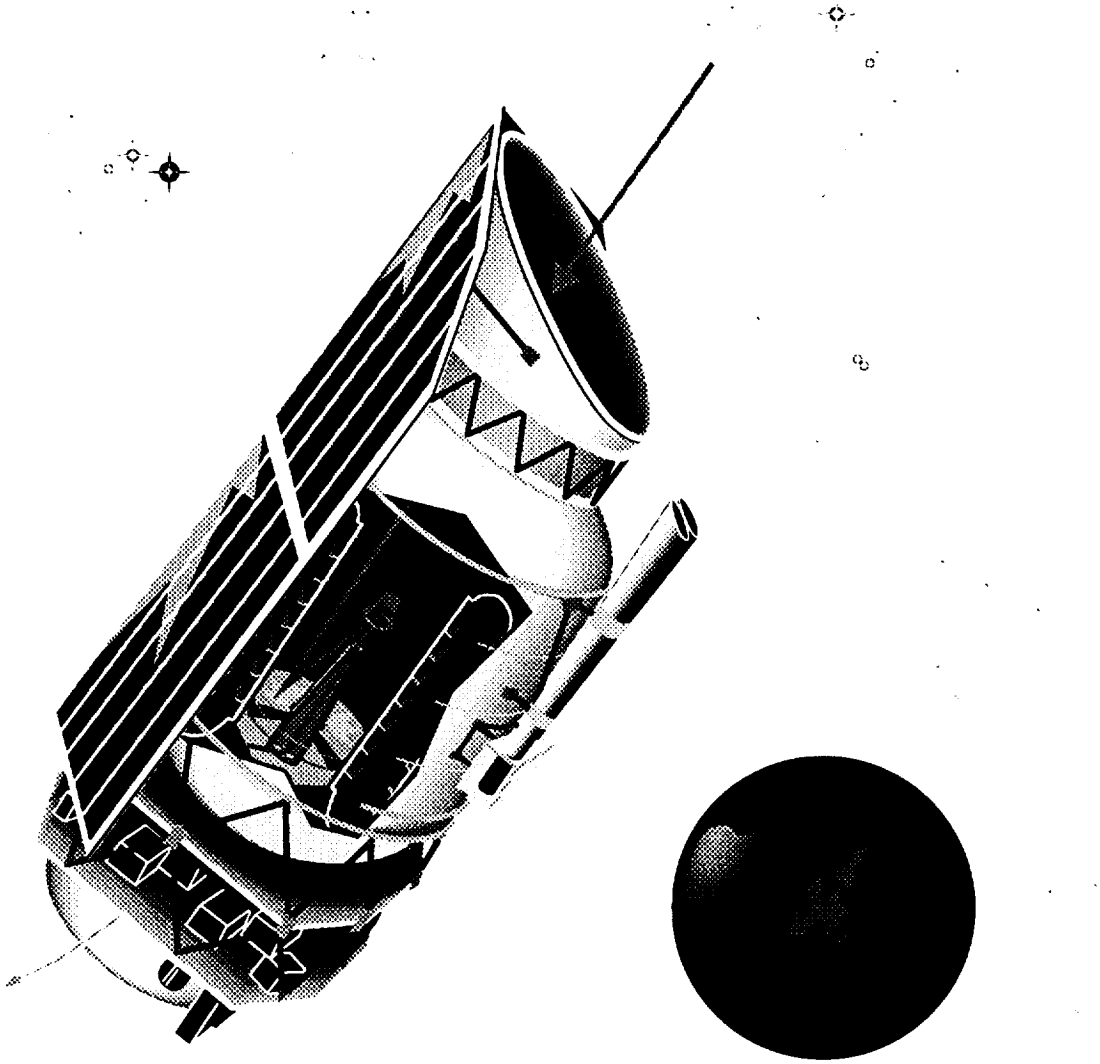

Figure 1: Computer Graphic of ISO in Orbit

The "classical" spacecraft functions are provided by a so-called "Service Module", which can be seen underneath the payload module in figure 1. These functions include the structure and the load path to the launcher, the solar array mounted on the sunshield, and sub-systems for thermal control, data handling, power conditioning, telemetry and telecommand (using two antennas), and attitude and orbit control. The last provides the three-axis stabilisation to an accuracy of a few arc seconds and also the raster pointing facilities needed for the mission. It consists of sun and earth sensors, star trackers, a quadrant star sensor on the telescope axis, gyros, reaction wheels and uses a hydrazine reaction control system. The nominal down-link bit rate is 33 kbps of which about 24 kbps are dedicated to the scientific instruments.

The definition study (phase B) for the ISO spacecraft was sucessfully completed early in 1988. The detailed design, development, integration and test phase (phase C/D) was started on 15 March 1988 by an industrial consortium led by Aerospatiale (F). The structure of this team is shown in figure 3. The next major milestone is the *System Design Review*, to be held in April 1989, with the aim of releasing (i) the structural and thermal model for integration and (ii) the qualification model units for manufacture. The scheduled launch date is May 1993.

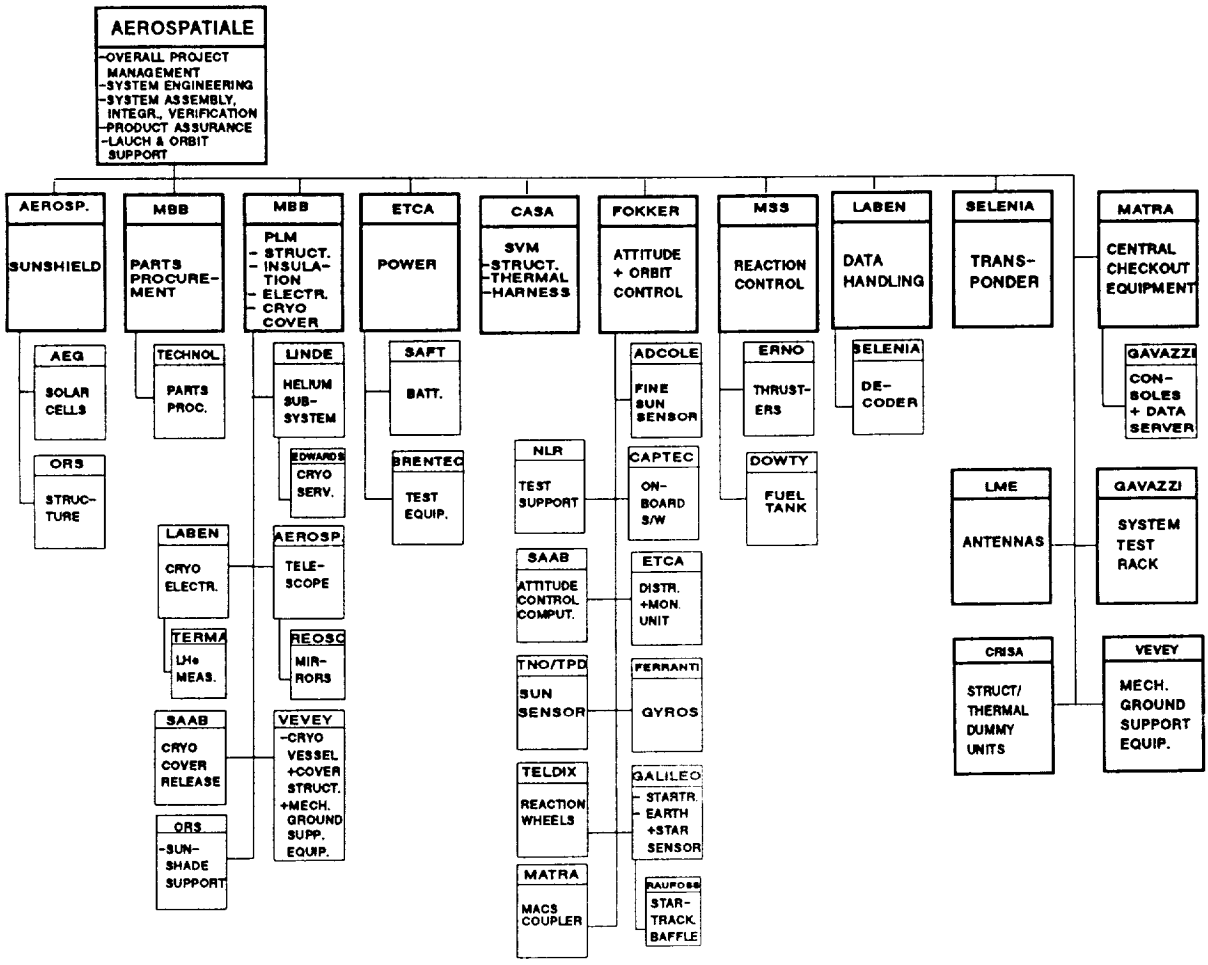

Figure 3: ISO Industrial Organisation

3. Launcher, Orbit and Operations

ISO will be launched into a transfer orbit by an Ariane-4 vehicle. Its hydrazine reaction control system will then be used to attain the operational orbit, which has a 24-hour period, a perigee height of 1000 km and an apogee height of 70000 km. The inclination to the equator will be between 5° and 20° (to be finalised later). ESA plans to supply only one ground station, enabling ISO to make astronomical observations during the best 14 hrs of each orbit. The mission's scientific return could be greatly increased by the addition of a second ground station, which would permit ISO to be operated for the entire time that it spends outside the main part of the Earth's radiation belts. An international collaboration is being sought by ESA to provide this second ground station.

Observing time on ISO will be allocated on a "per object" basis, as was the case for EXOSAT, rather than on a "per shift" basis as is done with IUE. Two-thirds of ISO's observing programme will be determined by the scientific community via the submission and selection (by peer review) of proposals. The remaining time will be reserved for the groups who provide the instruments, for the Mission Scientists and for the Observatory Team who operate the satellite. Details of observations to be carried out in this reserved time will be included in the first Call for Observing Proposals, to be issued to the scientific community 18 months before launch.

The in-orbit operations of the spacecraft and instruments will be carried out by a team of scientists and engineers located at the ISO Control Centre in Villafranca, Spain. During scientific use, the satellite will always be in contact with the ground segment; however, it is planned to minimise real time modifications to the observing programme in order to maximise the overall efficiency of the satellite. A "quick-look" output, adequate for judging the scientific quality of the data, will be produced within a few hours of an observation being completed. A final product with more detailed data reduction and calibration will be supplied later. This product will be the one from which the guest observers make their astronomical analyses.

4. Scientific Capabilities of Instruments

The ISO scientific payload consists of four instruments: a camera (ISOCAM, PI: C.J. Cesarsky), an imaging photo-polarimeter (ISOPHOT, PI: D. Lemke), a long wavelength spectrometer (LWS, PI: P.E. Clegg) and a short wavelength spectrometer (SWS, PI: Th. de Graauw). Each instrument is being developed by a consortium of institutes, using national funding, under the authority of the Principal Investigator (PI). The scientific capabilities, provided jointly by these instruments, can be summarised in three categories: photometry/polarimetry, imaging and spectroscopy.

Photometry and **Polarimetry** will be possible in broad and narrow spectral bands across ISO's entire wavelength range from 2.5 to 200μm. Work using multiple apertures will be possible out to 110μm.

Suspended in the middle of the main helium tank is the telescope, which has a Ritchey-Chrétien configuration with an effective aperture of 60 cm and an overall f/ratio of 15. A weight-relieved fused-silica primary mirror and a solid fused-silica secondary mirror have been selected as the telescope optics. The optical quality of these mirrors is adequate for diffraction-limited performance at a wavelength of 5 μm. Stringent control of stray light, particularly from bright infrared sources outside the telescope's field of view, is necessary in order to ensure that the system sensitivity is not degraded. This control is accomplished by imposition of viewing constraints and by means of the sunshade, the cassegrain and main baffles, and an additional light-tight shield around the instruments.

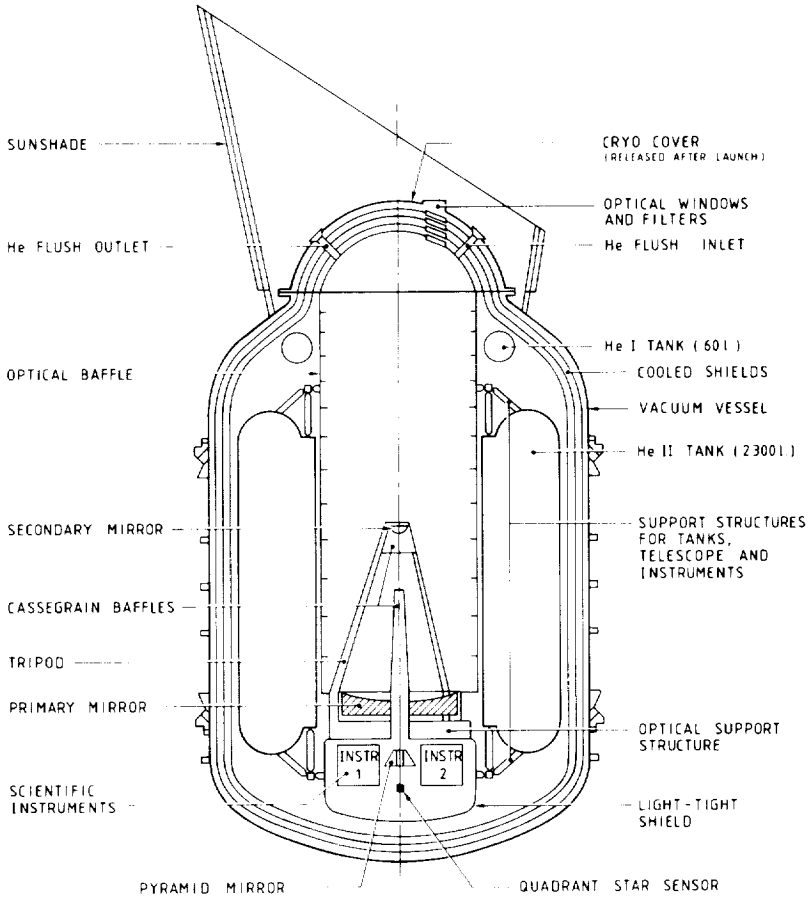

Figure 2: Schematic of the Payload Module

The scientific instruments are mounted on the opposite side of the optical support structure to the primary mirror, each one occupying an 80° segment of the cylindrical volume available. The 20 arc minute total unvignetted field of view of the telescope is split up between the four instruments by a pyramidal mirror. Thus, each instrument simultaneously receives a 3 arc minute unvignetted field centred on an axis at an angle of 8.5 arc minutes to the telescope optical axis. To view the same target with different instruments, the satellite has to be repointed.

ISO will be capable of **imaging** in broad and narrow spectral bands across its entire wavelength range from 2.5 to 200μm. The number of pixels and the pixel field of view vary as a function of wavelength. Details are given in table 1 below.

Wavelength Range (μm)	No. of Pixels	Pixel f.o.v. (arc secs)
2.5–5	32x32	1.5, 3, 6, 12
5–17	32x32	1.5, 3, 6, 12
18–28	8x8	19
30–60	3x5	31
60–120	3x3	44
120–200	2x2	90

Table 1: ISO's Imaging Capability.

For **Spectroscopy**, various resolutions will be available at different wavelengths. Details are given in table 2 below.

Wavelength Range (μm)	Resolution ($\lambda/\Delta\lambda$)	Instrument
2.5–12	90	ISOPHOT-S
2.5–16.5	50	ISOCAM-CVF
2.5–45	2000	SWS-Grating
14–30	20000	SWS-FP
45–180	200	LWS-Grating
45–180	10000	LWS-FP

Table 2: ISO's Spectroscopic Capability.

In principle, only one of the four instruments will be operated at a time; however, when ISOCAM is not the main instrument, it can be used in a so-called "parallel" mode either to gain extra astronomical data or to assist the other instruments in acquiring and tracking their targets. Whenever possible during satellite slews, ISOPHOT will be operated in its normal 200 μm mode so as to make a partial sky survey ("serendipity mode") at these wavelengths which were not covered by IRAS.

5. Outline Description of Scientific Instruments and Detector Systems

The ISOCAM instrument consists of two optical channels, each with a 32 x 32 element detector array, operating, respectively, in the wavelength ranges 2.5–5 μm and 5–17 μm. Each channel contains a wheel for selecting various filters (including circular variable filters, CVF) and a second wheel for choosing a pixel field of view of 1.5, 3, 6, or 12. Polarisers are mounted on an entrance wheel common to both channels. A sixth wheel carries mirrors for selecting between the channels, of which only one is operational at a time.

Material	Manufacturer	Number of Elements and "Read-out"			
		ISOCAM	ISOPHOT	LWS	SWS
InSb	SAT, France	32×32, CID	—	—	—
InSb	Cincinnati, USA	—	—	—	1×12, IA-12
Si:Ga	LETI-LIR, France	32×32, DRO	—	—	—
Si:Ga	Battelle, Germany		1×64, CRE-66		
			1×64, CRE-66	—	1×12, IA-12
			1 individual, CRE-1		
Si:P	Battelle, Germany	—	8×8, CRE-66	—	1×12, IA-12
			1 individual, CRE-1		2 individual, JF-4
Ge:Be	Battelle, Germany	—	3×5, CRE-18	1 individual, JF-4 (non-destructive)	1×12, IA-12 2 individual, JF-4
Ge:Ga	Battelle, Germany	—	3×3, CRE-18 1 individual, CRE-1	5 individual, JF-4 (non-destructive)	—
Ge:Ga (str)	Battelle, Germany	—	2×2, CRE-1/4	4 individual, JF-4 (non-destructive)	—

Table 3: Baseline ISO Detector Systems

The ISOPHOT instrument consists of four sub-systems:
- ISOPHOT-C: a photopolarimeter which also provides imaging capability at close to the diffraction limit in the wavelength range from 30 μm to 200 μm,
- ISOPHOT-P: a multi-band, multi-aperture photopolarimeter for the wavelength range from 30 μm to 110 μm,
- ISOPHOT-A: an multi-band array of 8 x 8 discrete elements for the wavelength range from $\sim$12 μm to 28 μm,
- ISOPHOT-S: a dual grating spectrophotometermeter which simultaneously provides a resolving power of $\sim$90 in two wavelength bands 2.5–5 μm and 6–12 μm.

A focal plane chopper with a beam throw of up to 3′ is also included in ISOPHOT.

The LWS instrument consists of a reflection diffraction grating used in two orders with an array of discrete detectors to provide a spectral resolving power of $\sim$200 over the wavelength range from 45 μm to 180 μm. Either of two Fabry-Pérot interferometers can be rotated into the beam to increase the resolving power to $\sim 10^4$ across the entire wavelength range.

The SWS instrument provides a resolving power of between 1000 and 2000 across the wavelength range from 2.4 μm to 45 μm by means of two reflection diffraction gratings used in 1st, 2nd and 3rd orders. Filters for order-sorting are placed at the instrument's various entrance apertures. Over a part (14–30 μm) of the SWS's operating range, the resolution can be increased to $\sim 2 \times 10^4$ by directing the incident radiation through either of two Fabry-Pérot interferometers.

Each of the instruments contains a variety of detector and read-out systems from various manufacturers. A summary is given in table 3 below; further details may be found in companion papers in this volume.

The first models of all the instruments (alignment, mass and thermal model) have been completed and are either already delivered to ESA or are undergoing final checks (vibration testing at liquid-helium temperatures) prior to delivery. The production of the second instrument models (engineering qulaification model) is well advanced and the due date for delivery to ESA is spring 1990.

6. Conclusion

ISO is a fully-approved and funded mission, which will offer astronomers unique and unprecendented observing opportunities in the infrared spectral region for a period of at least 18 months. Both the spacecraft and its selected complement of instruments are in their main development phase and the scheduled launch date is May 1993.

N90-21341

DESIGN AND STATUS OF THE DETECTOR BLOCK FOR THE ISO-SWS

W. Luinge *, D.A. Beintema *, L. Haser +,
R. Katterloher +, G. Ploeger *.

Introduction

The SWS is one of the two spectrometers for the Infrared Space Observatory ISO. It consists of a pair of grating spectrometers and a Fabry-Pérot interferometer. Together, the grating spectrometers cover the wavelength range 2.4-45 μm, at a resolution between 1000 and 2000. The Fabry-Pérot interferometer, in series with one of the grating spectrometers, provides a resolution of about 20,000 at the wavelengths between 15 and 35 μm [1]. The SWS is being built by the Space Research Organization of the Netherlands and the Max Planck Institute for Extraterrestrial Physics in Garching, Germany.

The spectrometer has 52 discrete detectors, most of which are bulk detectors. In the design of the spectrometer, the main emphasis is on the sensitivity of the individual channels, rather than on the number of detectors. This was one of the main reasons to select non-destructive read-out circuits, with a separate heated-JFET pre-amplifier for each individual detector. The signals are amplified and filtered in parallel.

At the time of writing of this paper, the engineering tests on the SWS detector block have not yet been completed. This paper describes the design of the detector block and indicates the present problem areas.

Detector configuration and detector block design

The spectrometer consists of two sections, each with its own output. One section is a grating spectrometer for the wavelengths below 13 μm, with 12-element InSb and Si:Ga arrays at its output; the second section is a grating spectrometer for the wavelengths above 12 μm, with 12-element Si:P and Ge:Be arrays. A pair of Fabry-Pérot interferometers at the output of the long-wavelength sections has pairs of Si:P and Ge:Be detectors. The detector configuration is described in Table I.

---

* SRON Space Research Laboratory, Groningen, the Netherlands.

+ Max Planck Institut für Extraterrestrische Physik, Garching, FRG.

Type	Range	Dimensions	Spacing	FOV/det
12 x InSb	2.4 - 4 μm	120 x 120 μm	50 μm	7.5" x 20"
12 x Si:Ga	4 - 13 μm	120 x 120 μm	50 μm	7.5" x 20"
12 x Si:P	12 - 28 μm	370 x 280 μm	50 μm	10" x 20"
12 x Ge:Be	28 - 45 μm	450 x 450 μm	100 μm	12" x 32"
2 x Si:P	14 - 26 μm	200 x 700 μm	100 μm	11.4" x 40"
2 x Ge:Be	22 - 38 μm	300 x 700 μm	100 μm	17.2" x 40"

Table I: SWS detector configuration

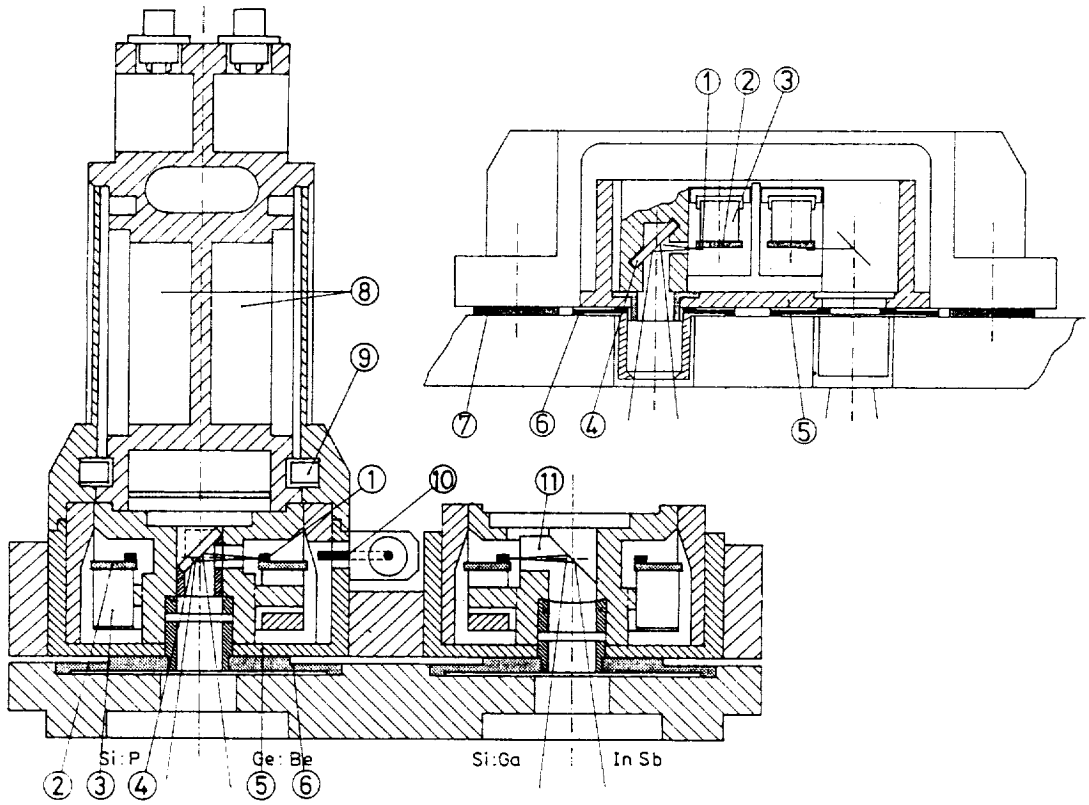

Figure I. Cross sections of the grating detector block and the Fabry-Pérot detector block (upper right). The dispersion is perpendicular to the plane of the drawing.

1 detectors, 2 detector substrate with heater and temperature sensor, 3 stainless-steel leaf springs for thermal insulation, 4 reflection filter, 5 high-Z shield, 6 light baffle, 7 electrically insulating mounting pads, 8 heated-JFET compartment, 9 light barrier, 10 helium tank strap, 11 ZnSe lens with total reflection.

The detector block consists of two different parts. One part stradles the two grating sections and contains all four 12-element arrays. The second part contains the two detector pairs for the Fabry-Pérot exits. Schematic drawings of these different parts of the detector block are given in Fig. 1.

The detector block will be mounted on a structure with a temperature of about 3.5 K. A strap to a 1.8-K heat sink is available for those detectors that need a lower operating temperature, in this case the Ge:Be detectors.

For each array independently the temperature is controlled by means of heaters on the substrates, counteracting the heat flow towards the telescope structure or through the 1.8-K strap (Fig. 1a, item 10, $\approx$ 30 μW/K at 4 K, with sufficient optical stability). The heaters can also be used to give a thermal pulse to anneal detectors after a satellite passage through a radiation zone.

For EMC reasons, the detector block is insulated electrically from the spectrometer and from the telescope structure.

Around the detectors, a shield of 2 mm high-Z material and 1 mm aluminium in all directions minimizes the effect of ionizing particle radiation (mainly trapped high-energy electrons).

A light baffle between the detector and amplifier compartments prevents leakage of IR radiation to the detectors. In the engineering model, the light-tightness of other baffles turned out to be insufficient, so that the baffle design is being improved.

Detector read-out

The arrays are read out with 12-channel units, the Fabry-Pérots with single pre-amplifiers, all procured from Infrared Laboratories in Tucson, Arizona. Some properties are listed in Table II.

	IA-12	JF4
Gain	$\approx$ 0.8	0.8 - 0.9
Input capacitance	3.5 - 4 pF	7.5 - 8 pF
Output impedance	100 - 200 kΩ	80 kΩ
Read noise (1-10sec)	30 - 50 e^-	20 e^-
DC levels	< 40 mV	-
Channels per unit	12	1

Table II. Properties of the heated-JFET pre-amplifiers

The units passed vibration tests at room temperature and at liquid-nitrogen temperature, at the vibration levels specified for the spectrometer.

Modelling, confirmed by testing, indicates that the high output impedances of the pre-amplifiers do not present a problem with the EMC specifications set for ISO.

The on-board signal processing is shown schematically in Fig. 2. An AC amplifier with a cut-on frequency of 0.1 Hz is employed to handle the DC offsets of the pre-amplifiers. The gain of 50 in the first amplifier stage is consistent with the expected magnitude of the offsets. To minimize these offsets, the individual pre-amplifiers used with the Fabry-Pérots have trimming capacitors. The transfer characteristic is consistent with the expected spike rates of one per 10 or 100 sec.

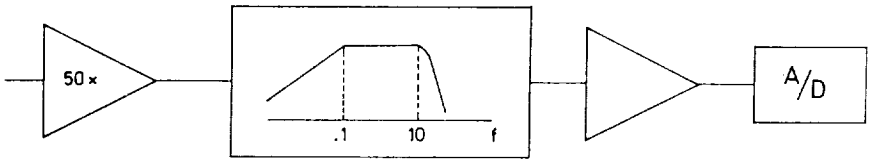

Figure 2. Transfer characteristic of the warm detector-signal amplifiers.

Detector status

A sample of the low-capacitance type InSb detectors from Cincinnati Electronics Corp. showed a responsivity of 1.7 - 2 A/W and a dark current of less than 100 e^-/s. Irradiation with a Co-60 source caused an increase in the dark current, but the responsivity changed only slightly. The capacitance is about 5 pF for the size given in table I. The cross-talk, measured with a trans-impedance amplifier, is about 0.1%.

The other detector types are being supplied by the Battelle Institute in Frankfurt, Germany.

The engineering version of the Si:Ga array has a responsivity of about 3 A/W and a dark current of 100 - 300 e^-/s. Neither of these values depends much on temperature. The observed cross-talk is less than 3%.

The Si:P engineering array has a responsivity of 2 to 3 A/W and a dark current of 10 - 100 e^-/s. Both a thermal pulse and a bias boost resulted in considerable reduction of the dark-current time constant after irradiation with a Co-60 source. In other units spontaneous spiking has been observed, which could be remedied by increasing the operating temperature.

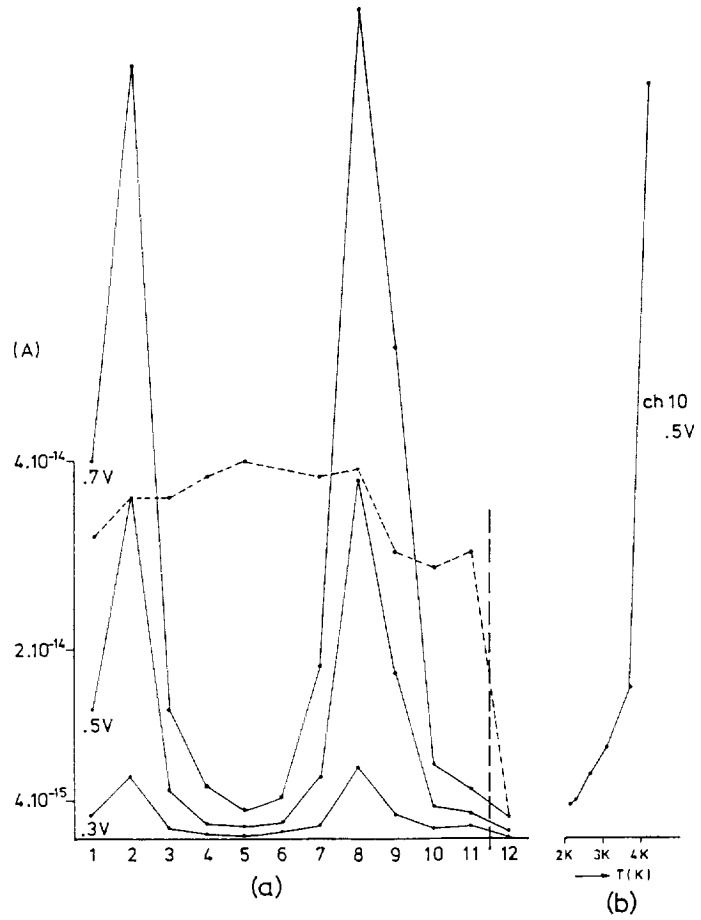

Figure 3. Dark currents in a 12-element Ge:Be array at bias voltages of 0.3, 0.5 and 0.7 V. The dashed line indicates the relative responsivities (channel 12 was not operative). Fig. 3b shows the temperature-dependence of the dark current in one of the detectors.

The main problem comes with the Ge:Be array. A large scatter in dark currents is observed (see Fig. 3). Lowering the temperature to 1.8 K (which would mean a significant thermal re-design) and reducing the bias voltage will help but are not sufficient to solve this problem. Selecting the best parts of the available material, even of manufactured arrays, may solve this problem.

1. De Graauw Th., et al., 1987, Proc. of the Workshop on Groundbased Astronomical Observations with Infrared Array Detectors, p438

STATUS OF THE ISOPHOT DETECTOR DEVELOPMENT

J.Wolf, D.Lemke, M.Burgdorf, U. Grözinger, Ch.Hajduk
Max-Planck-Institut für Astronomie
Heidelberg, Germany

Abstract

ISOPHOT is one of the four focal plane experiments of the European Space Agency's Infrared Space Observatory ISO[1]. Scheduled for a 1993 launch it will operate extrinsic silicon and germanium photoconductors at low temperature and low background during the >18 months mission. These detectors cover the wavelength range from 2.5 to 200 μm and are used both as single elements and in arrays. A cryogenic preamplifier has been developed to read out a total number of 223 detector pixels.

Overview

The ISO observatory comprises four instruments: a camera ISOCAM[2] for $\lambda < 20\,\mu m$, two spectrometers SWS[3] and LWS[4] and ISOPHOT which consists of four subexperiments:

ISOPHOT - P	a photo-polarimeter with selectable apertures and spectral bands, $\lambda = 3 \ldots 120\ \mu m$,
ISOPHOT - A	a camera with selectable spectral bands, $\lambda = 8 \ldots 30\ \mu m$,
ISOPHOT - C	a three channel far infrared camera with selectable spectral bands, $\lambda = 30 \ldots 200\ \mu m$ and polarimetry,
ISOPHOT - S	a dual channel Ebert-Fastie spectrometer, $\lambda = 2.5 \ldots 5\,\mu m$ and $\lambda = 6 \ldots 12\ \mu m$, spectral resolution ~90.

The configuration of the experiment is shown in figure 1. A more detailed description of the experiment and its scientific goals has been given elsewhere[5]. The hardware phase C/D of the project has been started in 1988. The first model is the alignment-mass-thermal-model AMTM, which was delivered to ESA in March 1989. The engineering-qualification model is currently built and is due in March 1990; the flight model follows a year after that. The project is nationally funded in Germany by the Bundesminister für Forschung und Technologie, BMFT. The overall responsibility is with the Max-Planck-Institut für Astronomie, Heidelberg (MPIA), which also leads the scientific consortium including co-investigators of institutes in England, Denmark, Spain, Ireland and the United States. The industrial contract of phase C/D is managed by the Deutsche Forschungsanstalt für Luft- und Raumfahrt, DLR. The project's organisation is shown in figure 2.

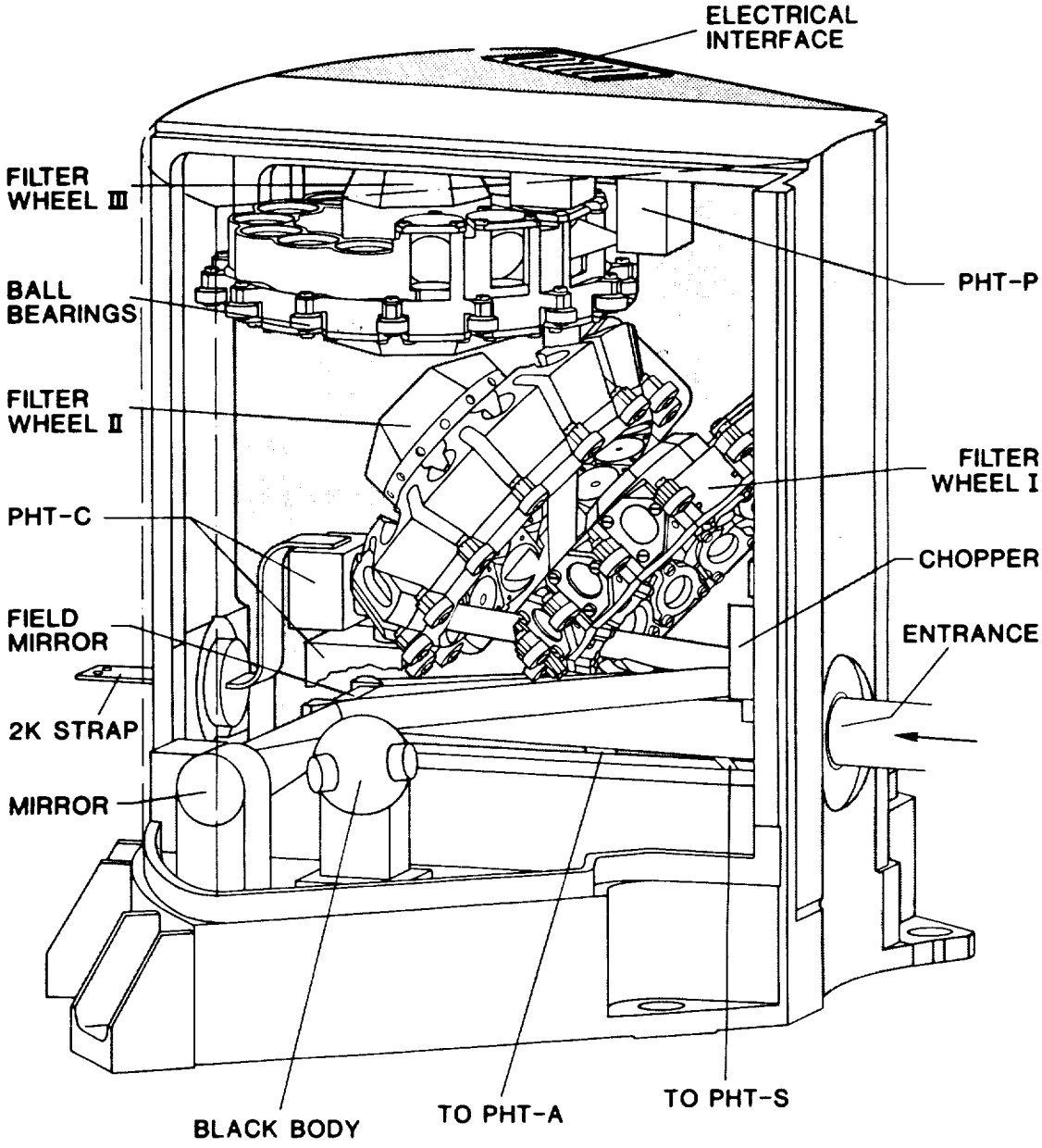

Figure 1 ISOPHOT Configuration

The telescope beam coming from the central pyramid mirror in the instrument chamber is distributed to the four subexperiments by three change wheels carrying mirrors, filters, field stops and polarizers. The germanium detectors of -C and -P are connected directly to the LHe-tank with a 2K–cold strap. A folcal plane chopper is used for differential measurements on the sky and, with larger throw, to deflect the beam of a blackbody radiation sources to the detectors. The calibrated radiation of these sources is used for inflight calibrations.

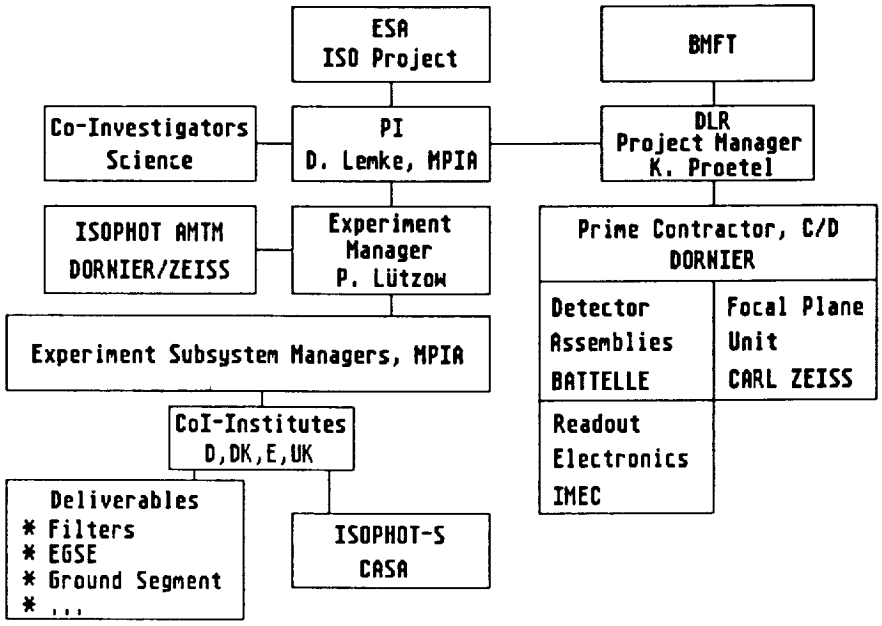

Figure 2 ISOPHOT Project Organization

Detectors

Nine detector assemblies with 223 pixels altogether are used in ISOPHOT. An overview of these assemblies is given in table 1. The -C and -S assemblies are hybrid arrays made of separate detector elements while -A25 is made out of a single piece of Si:P as a monolithic array. The NEP values given are defined as system-NEPs, i.e. measured at the telemetry output of the experiment's electronic box and therefore including all additional noise contributions such as EMI, digitization etc. All detector assemblies are supplied by Battelle, Frankfurt.

Readout Electronics

The cryogenic readout electronics CRE for the experiment was developed during phase B of the project by IMEC, Leuven. It consists of integrating amplifiers followed by a multiplexer. The schematic of the chip is shown in figure 3. Four different detector interface curcuits had been designed and built. In tests the option with a charge feedback loop (figure 4) proved to be most useful and was chosen for further optimisation. With the first generation devices which became available at the end of 1987 a NEP of about $5 \cdot 10^{-17}$ $W \cdot Hz^{-1/2}$ was achieved in the breadboard models of the -S arrays. The CREs were operational down to 2K and the readnoise was about 1300 electrons which could be reduced to about 800 electrons by using correlated double sampling. Although these numbers are quite impressive for a newly developed chip, there were problems with its stability, dynamic range and linearity.

Table 1 ISOPHOT Detector Assemblies

Sub-experiment	Pixel Number	Wavelength Range [μm]	Material	Readout	NEP [W $Hz^{-1/2}$] Goal	Requirement
PHT-P1	1	3 . . . 18	Si : Ga	CRE 1	2.0 10^{-17}	4.0 10^{-17}
PHT-P2	1	15 . . . 30	Si : P	CRE 1	1.5 10^{-17}	3.0 10^{-17}
PHT-P3	1	40 . . .120	Ge : Ga	CRE 1	1.5 10^{-17}	3.0 10^{-17}
PHT-A25	8 x 8	8 . . . 30	Si : P	CRE 66	1.5 10^{-17}	3.0 10^{-17}
PHT-C50	3 x 5	30 . . . 55	Ge : Be	CRE 18	1.5 10^{-17}	6.0 10^{-17}
PHT-C100	3 x 3	60 . . .120	Ge : Ga	CRE 18	1.5 10^{-17}	3.0 10^{-17}
PHT-C200	2 x 2	120 . . .200	str.Ge : Ga	CRE 1/4	1.5 10^{-17}	3.0 10^{-17}
PHT-S1	1 x 64	2.5 . . . 5	Si : Ga	CRE 66	4.5 10^{-17}	1.8 10^{-16}
PHT-S2	1 x 64	6 . . . 12	Si : Ga	CRE 66	2.0 10^{-17}	6.0 10^{-17}

A first redesign of the CREs was done in 1988. These second generation devices are now used for the engineering-qualification models of the detector assemblies. First measurements at Battelle and IMEC indicate that the noise has been reduced considerably - a factor 3 to 8 is expected depending on the sampling method and the readout mode. The dynamic range and linearity are also much improved, as measurements of a CRE1 at MPIA have confirmed. A complete knowledge of the performance will be gathered during the QM tests which are done in the first half of 1989. After these a second redesign is scheduled for the flight models.

ISOPHOT–P

ISOPHOT–P is a multi-band, multi-aperture photometer using single detectors. The telescope beam is deflected by a mirror of wheel I (see fig. 1), passes one of 14 selectable field stops on wheel II and then one of 14 selectable spectral filters on wheel III. Three polarizers on wheel I can also be put into the beam. From measurements of a source at three polarization angles (60°, 120°, 240°) its polarization degree and angle can be deduced. An image of the sky lies in the plane of the apertures (5 arcsec . . . 3 arcmin) on wheel II. These apertures are then imaged onto the -P detectors with a field optics. The filters are choosen to match features of the interstellar matter as well as to cover the entire wavelength range by broad band photometry. In addition the IRAS spectral bands at 12, 25, 60 and 100 μm are reproduced. The detector materials and the element sizes are given in table 2.

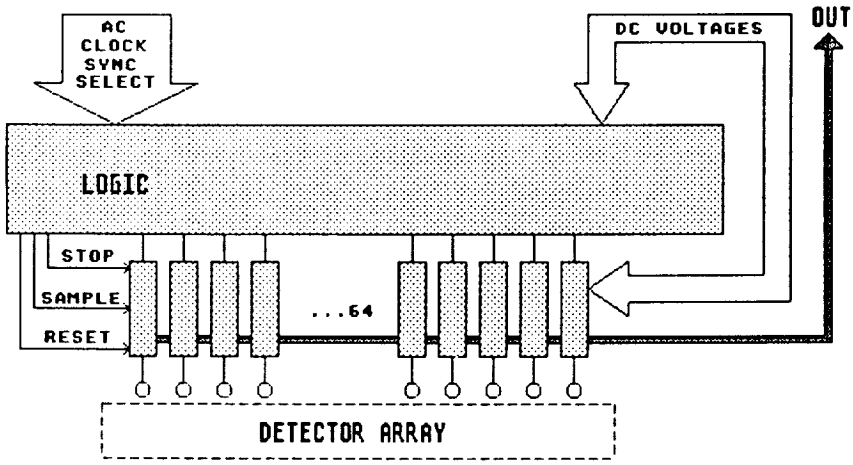

Figure 3 Cryogenic Readout Electronics Chip Schematic

The chip consists of a logic part and analog detector interface circuits. The logic circuit receives a "select"-pulse to enable the device and out of two external AC-lines "clock" and "sync" it forms all pulses to drive the multiplexer internally. The number of detector interfaces is adapted to the number of pixels in the arrays; two additional channels are normally used as monitors for the electronics behaviour and for room temperature checkout. In all assemblies the connection to the detector elements is made by wire bonds with the exception of A25 where a two dimensional bond matrix 8 x 8 is needed. A special connection technique of gold ball bonding combined with conductive epoxy has therefore been developed.

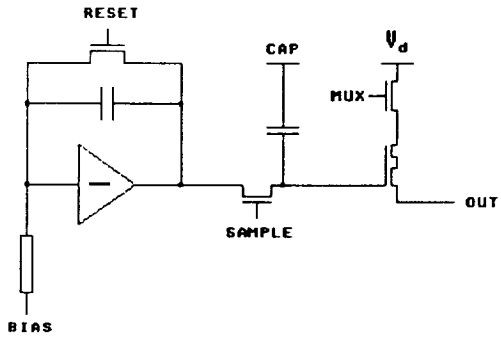

Figure 4 Charge Feedback Detector Interface

The detector is connected to an integrator. The charge accumulated on the feedback capacitor can be transferred to a sample capacitor for all detectors of an array in parallel. If a reset pulse is applied after the sample pulse, the integrator starts over while the charge on the sampler is read out through the multiplexer (destructive readout). Non-destructive readout is realised by applying several sample pulses between resets, so the charging ramp of the integrator is monitored at the output.

Although no special breadboard models of the -P detectors have been built during phase B, there is plenty of experience at MPIA and Battelle with such discrete detectors. Many have been built and tested for various aspects and the performances given in table 2 are results of the GIRL program obtained with trans-impedance-amplifiers (TIA). Currently the engineering- qualification models (EQM) of the -P detectors are manufactured. The readout is the CRE 1 which is a version without logic, sampler and multiplexer. The analog output of the integrator is sampled in the external electronics unit. The -P3 assembly is shown in figure 5.

Table 2 ISOPHOT - P Detectors

	P1	P2	P3
Material	Si : Ga	Si : P	Ge : Ga
Detector Size [mm^3]	1.0 x 1.0 x 1.0	1.0 x 1.0 x 1.0	1.0 x 1.0 x 1.0
Breadboard Model Performance :			
NEP [$W\ Hz^{-1/2}$]	$2.0\ 10^{-17}$	$2.0\ 10^{-17}$	$5.0\ 10^{-17}$
R [$A\ W^{-1}$]	10	8.6	3
Current Activity	Manufacturing Of Engineering-Qualification Models		

ISOPHOT-C

ISOPHOT-C is made up of three far infrared cameras. Their dimensions are fitted to the 3 arcmin unvignetted field of view of the experiment with formats of 3 x 5 pixels in -C50, 3 x 3 in -C100 and 2 x 2 pixels in -C200 (figure 6). Filters and polarizers on wheel I and II are used to define a spectral band and for polarization measurements.

The detector matrix is made up of individual elements placed in integrating cavities. The crystal sizes are optimized for detector performance. The main characteristics of the ISOPHOT-C arrays are shown in table 3.

To achieve a high fill factor, fabry lenses are placed in front of the detector cavities. These lenses are square shaped and made of germanium for -C100 and -C200 and of silicon for -C50. The area of the field lenses defines the pixel's field of view. The lenses are seperated with an opaque material. This and the closed cavities of the detectors guarantee minimal crosstalk between the pixels (figure 7).

The -C200 camera is of special scientific interest as it extends the wavelength range observed by IRAS to beyond 200 μm. Spectra of the breadboard detectors show cut-off wavelengths around 240 μm. In addition to pointed observations of selected sources -C200 will perform a serendipituous sky survey during slews of the ISO satellite. These strip maps will be taken in a broad wavelength band around 200 μm. The sky coverage will strongly depend on the observing program of the observatory and is estimated to 10 . . . 40%. With a limiting sensitivity of about 1 Jy this incomplete 200 μm survey will be a valuable supplement to the IRAS survey.

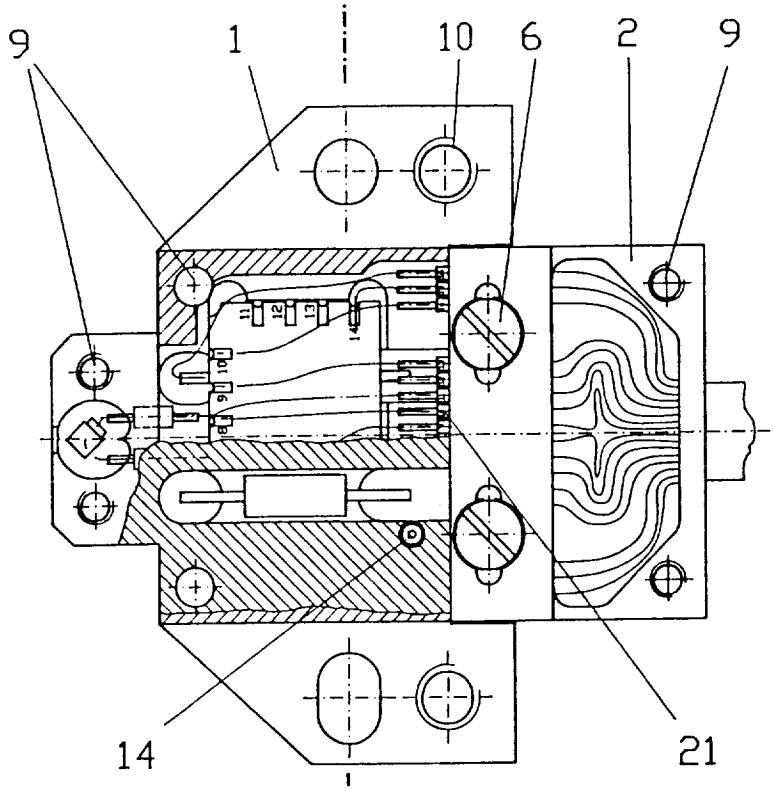

Figure 5 ISOPHOT-P3 EQM-Detector Assembly

The detector element has transverse contacts and is placed in an integrating cavity. Its orientation and the cavity shape have been optimized for maximum light absorption in the crystal. Two electrical feedthroughs connect the detector to the CRE which is mounted on a ceramics substrate. This Ge:Ga detector is mounted to the 2K-cooling strap of the experiment. Slightly higher temperatures can be obtained with a carbon resistor as a heater. A second carbon resistor is used as temperature sensor. To the right a pigtail harness is attached with a strain relief.

Table 3 ISOPHOT-C Arrays

	C50	C100	C200
Material	Ge : Be	Ge : Ga	stressed Ge : Ga
Array Size	3 x 5	3 x 3	2 x 2
Detector Size [mm^3]	0.5 x 0.5 x 1.5	0.7 x 0.7 x 2.0	1.0 x 1.0 x 1.0
	30° Wedge	30° Wedge	30° Wedge
Fabry Lens Area [mm^2]	1.33 x 1.33	1.90 x 1.90	3.90 x 3.90
Array Area [mm^2]	7.05 x 4.19	5.90 x 5.90	7.90 x 7.90
Gaps [mm]	≤ 0.1	≤ 0.1	≤ 0.1
FOV Per Pixel [$arcsec^2$]	30.5 x 30.5	43.5 x 43.5	89.4 x 89.4
Total FOV [$arcmin^2$]	2.69 x 1.60	2.25 x 2.25	3.02 x 3.02
Fill Factor	0.90	0.93	0.97
Breadboard Model Performance			
NEP [W $Hz^{-1/2}$]	$3.0\ 10^{-16}$	$5.0\ 10^{-17}$	$3.0\ 10^{-17}$
R [A W^{-1}]	1 - 2	3 - 4	6.5 - 10
Dark Current [$e\ s^{-1}$]			$< 5\ 10^5$
Current Activity	Manufacturing Of Engineering-Qualification Models		

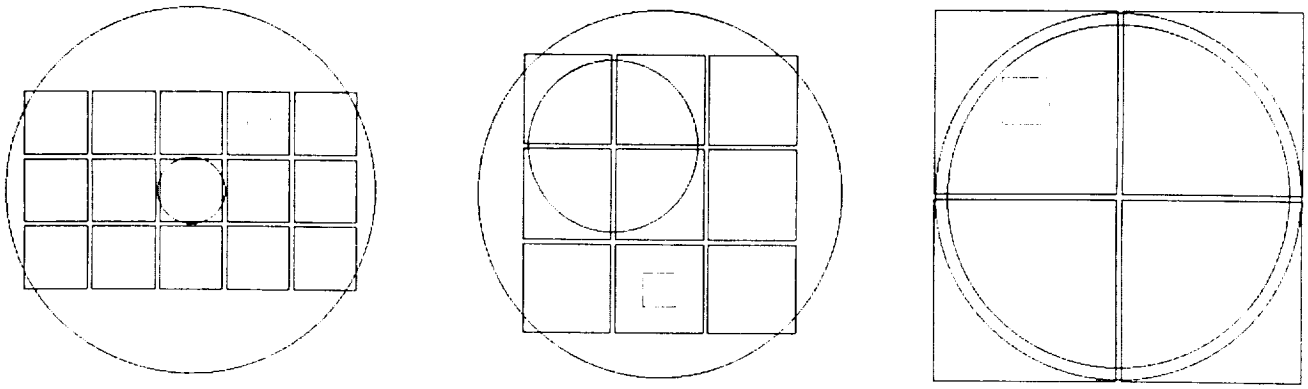

Figure 6 Optical Layout of the ISOPHOT-C Arrays

In -C50 the fabry lens size is matched to the Airy disk at the wavelength of maximal detector response λ = 39μm. The larger Airy disk at 100μm in -C100 is oversampled by four pixels. The big circles denote the 3 arcmin unvignetted field of view of the experiment. In -C200 the Airy disk at 200μm almost fills this field. Each of the four pixels Ge:Ga has its own stressing mechanism, providing important redundancy for this new technology in a space experiment. The dotted squares indicate the size of the detector elements located behind the lenses.

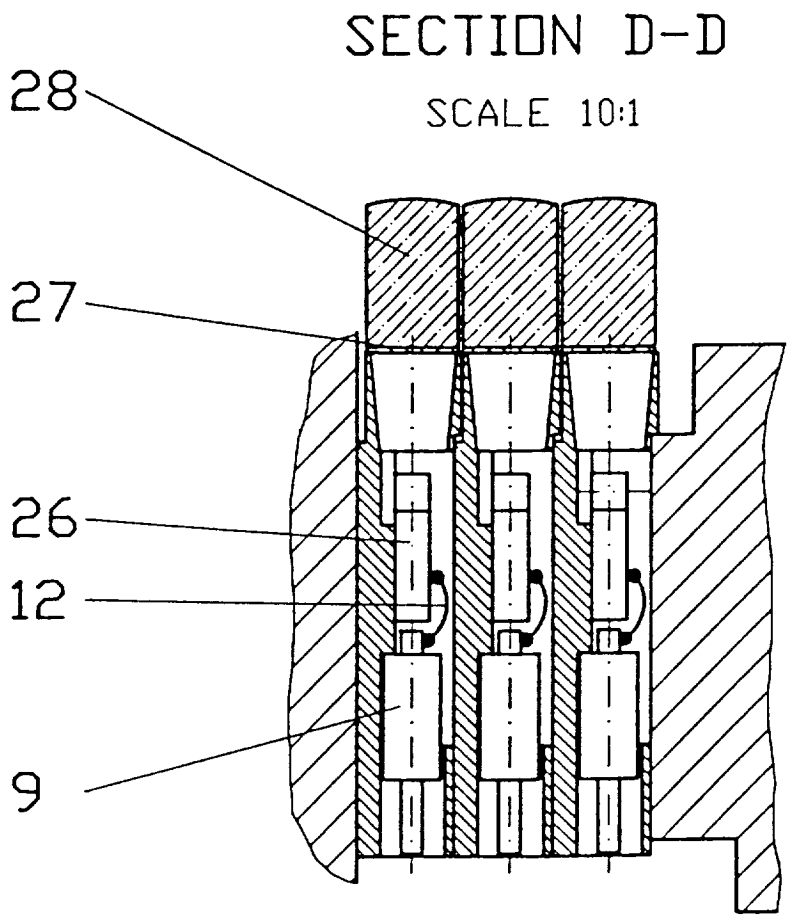

Figure 7 Design of ISOPHOT-C50

This cross section of -C50 shows the fabry lenses that are connected to the integrating cavity of the detectors by a cone. The detector elements are mounted to the metallic sides of the cavity and therefore have a common bias contact. The other contact is connected via a feedthrough to the CRE17 located behind the 15 cavities. The crystals have a 30^{o} wedge at the front end to maximize light absorption by internal reflections. Three rows of 5 such elements each are made and stacked together to form the 2-dimensional array. A similar approach is taken for -C100 with three elements per row, while -C200 has four individual stress-cavities. By using two electrical feedthroughs for each element of the -C100 and -C200 arrays, they can be supplied with individual bias voltages. Some voltage scatter in the detector elements or the CRE input channels can therefore be accommodated.

ISOPHOT-A

ISOPHOT -A is a two dimensional array of 8 x 8 pixels filling the 3 arcmin field of view. Figure 8 shows the optical design. The detector array is monolithically made of Si:P and connected to a two dimensional CRE with matching geometry. For this direct hybrid a new, two dimensional matrix of connection points was needed. As the project's schedule did not allow the development of an indium bump technology, a simpler technique using gold ball bonds combined with silver filled epoxy was choosen.

The decision for that monolithic array was taken late during phase B, so no breadboard model could be built. Instead a test array was made in a pre-C/D phase. To minimize crosstalk between the pixels, the detector chip has sawing grooves at the backside and a metal grid at the front surface. Measurements with the test array showed that very deep grooves (950μm in a 1 mm thick wafer) gave the best performance. The grid size was choosen to 120 μm for the engineering qualification model (table 4). The performance of Si:P has earlier been tested with single elements and TIAs.

Table 4 ISOPHOT–A25 Array

Design Of The Qualification Model			Detector Material Performance	
Material		Si : P	NEP [W $Hz^{-1/2}$]	2.0 10^{-17}
Array Size		8 x 8	R [A W^{-1}]	8.6
Pixel Size	[mm^2]	0.83 x 0.83		
Array Area	[mm^2]	7.48 x 7.48		
Gaps	[mm]	0.12		
FOV Per Pixel	[$arcsec^2$]	19 x 19		
Total FOV	[$arcmin^2$]	2.9 x 2.9		
Fill Factor		0.79		

Current Activity: Manufacturing Of Engineering-Qualification Model

ISOPHOT–S

ISOPHOT–S is the spectro-photometric subexperiment. The flight hardware will be supplied by the Spanish co-investigators. The telescope beam is deflected by a mirror on wheel I into the 24 arcsec aperture of that dual channel Ebert-Fastie spectrometer. The two 64 element linear arrays of Si:Ga cover the wavelength bands 2.5 to 5μm

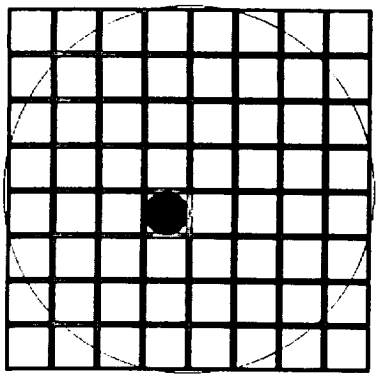

Figure 8
Optical Layout of ISOPHOT–A

The monolithic piece of Si:P covers the 3 arcmin FOV which is indicated by the circle. The pixels are at the front surface defined by a metal grid of 120 μm width. At the backside sawing grooves should minimize crosstalk. The pixel size is matched to the 915 μm Airy disk at 25 μm.

and 6 to 12 μm and are operated simultaneously. The main characteristics of the -S arrays are shown in table 5. While the long wavelength channel is close to the wavelength of the Si:Ga peak response, the short wavelength channel suffers from the short wavelength fall-off of the material's spectral response. Originally Si:In was planned to use, but existing materials all turned out to be very insensitive ($R < 1\ A W^{-1}$). The time schedule of the project did not allow for a new material development or switching to InSb. Two breadboard models of the -S arrays have been built during phase B (figure 9). As readout electronics the first generation CRE 66 was used.

Table 5 ISOPHOT–S Arrays

			Breadboard Model Performance	
Material		Si : Ga	NEP [$W\ Hz^{-1/2}$]	$5.0\ 10^{-17}$
Array Size		1 x 64	R [$A\ W^{-1}$]	10
Detector Size	[mm^3]	0.31 x 0.37 x 1.80		
		30° wedge		
Gaps	[μm]	17.5		
FOV Per Pixel	[$arcsec^2$]	24 x 24		
Current Activity		Manufacturing Of Engineering-Qualification Models		

High Energy Radiation Effects and Calibration

High energy radiation effects in the bulk detectors have been studied[6]. Responsivity increases of up to 35% in Si-detectors have been observed after simulated passages through the electron belt. With similar doses stressed Ge:Ga showed a factor of 32 R-increase. As self-relaxation takes many hours, curing procedures need to be applied. Currently heating and bias boost are planned. However, both concepts are problematic; for all Ge-detectors which are mounted to the 2K cooling strap, heating is almost prohibited due to the restricted power budget of 0.5 mW. Bias boost on the other hand can by itself upset the detectors and the CREs.

For monitoring the detectors' calibration during the mission, an onboard calibration source is foreseen. Thermal radiation sources similar to those used in IRAS are imaged with f/15 on the detectors via the chopper mirror using a large throw. In the ground calibration of the experiment these sources will be calibrated with a standard laboratory blackbody source. Their inflight stability can be checked with celestial standards.

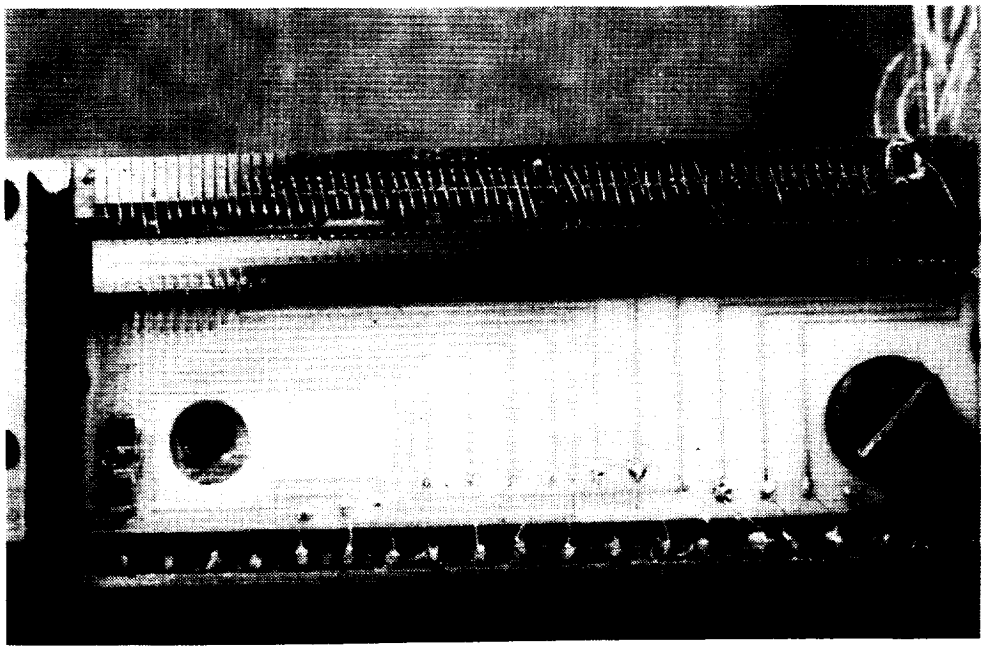

Figure 9 Breadboard Model of the ISOPHOT-S Array

The detectors are fabricated from a strip of Si:Ga material that is glued to a substrate. The individual pixels are then seperated by sawing. While the electrical contacts at the substrate provide the common bias to the detectors, the top contacts are wire bonded to the input pads of the CRE 66 which is mounted alongside the detector array.

Acknowledgement

We appreciate very much the support of Dr. R. Faymonville of Battelle, Frankfurt in compiling this status report.

References

1. Kessler, M.F.: "The Infrared Space Observatory (ISO)", Proc. SPIE, 589, 201 (1985) and
   Kessler, M.F., Sibille, F.: "Introduction to ISO", this conference
2. Sibille, F., Cesarsky, C., Rouan, D., Agnese, P.: "ISO Camera Arrays Development Status", this conference
3. Luinge, W., Beintema, D.A., Haser, L., Katterloher, R., Ploeger, G.: "Design and Status of the SWS Detector Block", this conference
4. LeNaour, C.: "LWS Detectors: Status Report", this conference
5. Lemke, D.: "ISOPHOT-Photometer for the Infrared Space Observatory", Proc. SPIE, 589, 181 (1985)
6. Blum, J., Hajduk, Ch., Lemke, D., Salama, A., Wolf, J.: "High-energy radiation effects on the ISOPHOT far-infrared detectors", submitted to Infrared Physics

ISO/LWS : DETECTOR STATUS

C. Le Naour[1], C. Delettrez[1], M. Griffin[2], P. Ade[2], D. Robinson[2], D. Vickers[2]

[1] Centre d'Etude Spatiale des Rayonnements, 9, avenue du Colonel Roche - BP 4346 - 31029 Toulouse FRANCE

[2] Physics Dept. Queen Mary College, Mile End Road, London E1 4NS ENGLAND

The aim of the long wavelength spectrometer of the Infrared Space Observatory is to perform spectrometry in the wavelength range 45 to 200μm using two resolution modes. The resolution will be around 200 in the medium resolution mode while it will reach 10^4 in the high resolution mode. The sensitivity of this instrument will be close to 10^{-18} W/$\sqrt{}$Hz.

A schematic view of the focal plane unit is presented in figure 1. The input beam comes from the pyramidal mirror. The beam is collimated by a large mirror assembly. However, mirror 2 restricts the field of view to an opening of 1.65 arc minutes. In the medium resolution mode the beam goes directly to the diffraction grating while in the high resolution mode it passes through a Fabry-Perot interferometer mounted on a wheel in front of the grating. The diffracted radiation from the grating is collected by a spherical mirror and brought to a focus along a line matching the surface of the detector assembly. The temperature of the optics will be 3 K while the detectors will be cooled to 1.8 K.

The detectors divide the wavelength range into ten spectral channels. The spectral range and position of each detector will be as indicated in figure 2. Each detector will cover approximately a spectral bandwith sufficient to allow for a 50 % redundancy in the case of detector failure. There are three types of detectors. SW1 is a Ge:Be photoconductor covering the 45-55μm region. LW1, SW2, SW3, SW4, SW5 are unstressed Ge:Ga photoconductors which cover the 50 to 120μm region. LW2, LW3, LW4, LW5 are uniaxially stressed Ge:Ga photoconductors covering the range from 100 to 200μm. The stress applied to each detector will be adjusted in order to get the peak response in the corresponding wavelength range, and to minimize the dark current of the shorter wavelength stressed detectors. Stressed and unstressed detectors are located alternatively in order to receive the first and second

order of the diffracted beam. In the medium resolution mode the ten detectors are used simultaneously while in the high resolution mode only one detector is used. Response curves for prototype stressed and unstressed Ge:Ga photoconductors are shown in figure 3 together with the usable wavelength ranges allowed for each type. In order to limit the spectral range of the incident beam a bandpass filter will be used with each detector. This will be a metal mesh filter consisting of a combination of about five grids made by photolitographic process. Very narrow spectral passbands can be achieved, as illustrated by the 160μm filter profile shown in figure 4. In addition to the bandpass filter, a blocking filter will be used to reject the near IR radiation.

Figure 5 presents a schematic view of an unstressed detector mounting unit. The filter assembly is placed at the aperture of a parabolic light concentrator used to limit the field of view of each detector. The unstressed detector glued on a sapphire support is placed in a spherical integrating cavity in order to increase its effective absorption efficiency. A set of two feedthroughs is used to connect the detector contacts with the external wires. This reduces dramatically the light leakage at the detector.

In figure 6 a schematic drawing of a stressed detector mounting unit is presented. The detector is mounted between two pieces of sapphire and stressed with a screw over a ball. The overall stress system is 9.6 mm long and has a diameter of 3 mm. Detector mount is typically 26.2 mm long, 16.9 mm high and 6.7 mm in width. The detectors are mounted on a bar which is coupled strongly to the superfluid helium tank in order to operate the detectors at a temperature of 1.85 K. The detector assembly is shown in figure 7. To calibrate the detectors during the flight five infrared sources are placed in front of the detector assembly. These sources are mounted on the sidewall of the instrument. Figure 8 shows how they are placed with respect to the principal beam.

The currents from the detectors are collected by ten individual integrating amplifiers (Infrared Labs model JF4) mounted in T05 cans. They are placed in holes built into the detector support frame behind the detector block as shown in figure 7. The JF4 circuit is presented in figure 9. It consists of 3 Si JFETS. The photocurrent is integrated on the 7.5 pF gate capacitance of the JFET1. The resulting voltage is transmitted to the output by the JFET1 mounted in a follower configuration. The input is set to zero by the "reset and compensation process". Figure 10 shows a functional diagram of the warm analogue processing unit for the detector subsystem. The output voltage of the IA is amplified and AC coupled. It is then sampled at around 100 Hz and finally converted into a digital signal.

The integrating amplifier has been chosen to avoid the limitation by Johnson noise of the feedback resistor that is encountered in the transimpedance amplifier configuration. Moreover if the detector is noiseless the signal to noise ratio is improved at a rate $(t)^{3/2}$ faster than $(t)^{1/2}$ obtained in TIA configuration, where t is integration time. The detector dark current is a very critical feature and in the IA configuration must be reduced to a very low level. Originally, it was intended to operate the unstressed detectors at 3 K and the stressed detectors at 2 K, with TIA readout electronics. However, reducing the operating temperature of all the detectors to 1.85 K results in a dramatic reduction in the dark current. In the first base line the unstressed detectors were cooled down to 3 K and the temperature of the stressed detectors was 2 K. Reducing the temperature to 1.85 K for all of the 10 detectors permits to decrease the dark currents by one order of magnitude. This is shown in figure 11 for the unstressed prototype . The prototype is a cube of 1.4 mm base length biased with 350 mV while its breakdown voltage is around 500 mV. At 1.85 K the dark current reaches 300 e/s.

The variation of the dark current with temperature for the stressed prototype is shown in figure 12. The stressed detector is also a cube of 1.4 mm base length. The bias voltage is equal to 100 mV while the breakdown voltage is around 150 mV. At 1.85 K the dark current of the stressed prototype approaches 10^4 e/s.

With the reduction of the temperature no significant difference in sensitivity for the unstressed detector has been measured. On the other hand, the signal to noise ratio of the stressed detector is improved as the temperature decreases. This is shown in figure 13 where the variation of the normalized responsivity and the normalized square root of the dark current are plotted as a function of the temperature. Assuming that the noise is limited by the dark current shot noise, it decreases more rapidly than the responsivity. In these operating conditions the performances of the Gallium doped Germanium detector prototype are as follows : the responsivities reach 3A/W for the unstressed detector and 5A/W for the stressed one. The Noise Equivalent Powers approach 10^{-18} W/$\sqrt{}$Hz for the unstressed detector and a few 10^{-18} W/$\sqrt{}$Hz for the stressed one.

ISO

esa

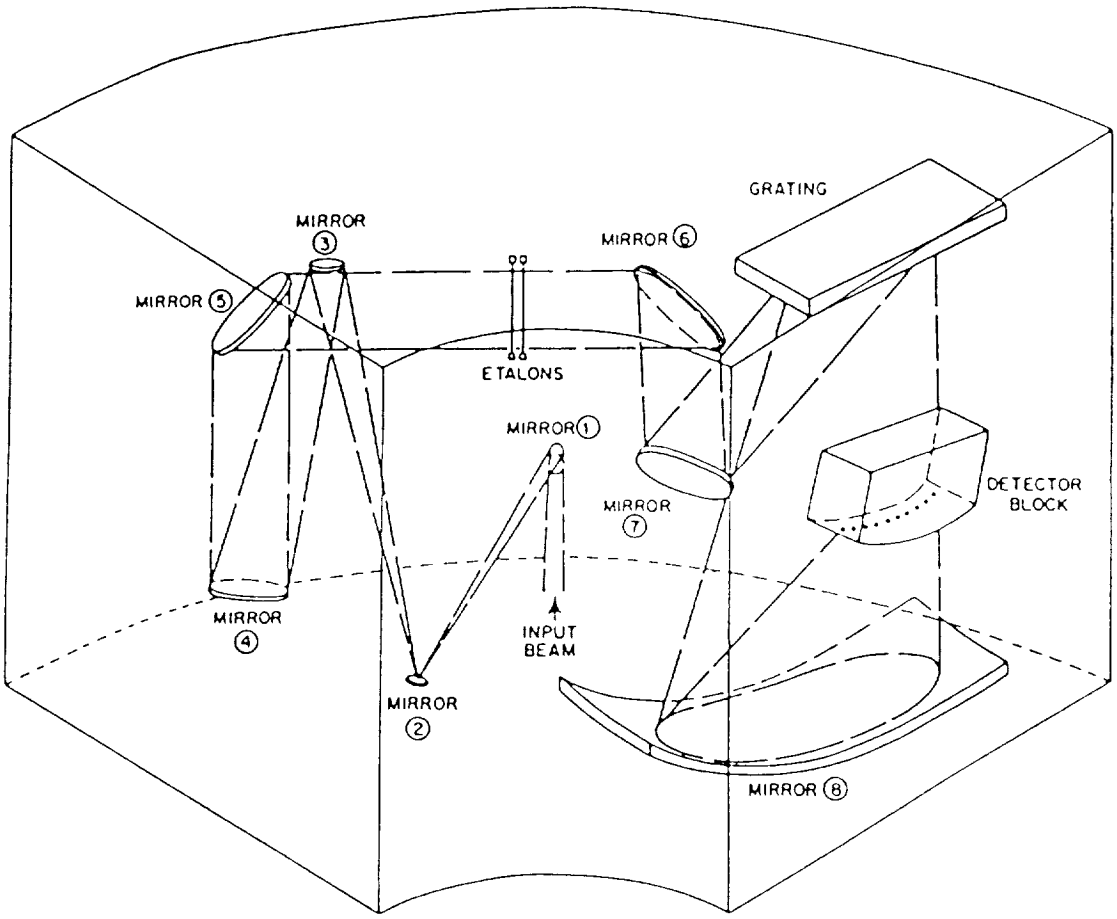

Schematic of LWS

FIGURE 1

DETECTOR	TYPE	NORMAL RANGE	USABLE RANGE
SW1	Ge:Be.u	45 - 50 μm	45 - 55 μm
LW1	Ge:Ga.u	90 - 110 μm	80 - 120 μm
SW2	Ge:Ga.u	50 - 60 μm	50 - 65 μm
LW2	Ge:Ga.s	110 - 130 μm	100 - 140 μm
SW3	Ge:Ga.u	60 - 70 μm	55 - 75 μm
LW3	Ge:Ga.s	130 - 150 μm	120 - 160 μm
SW4	Ge:Ga.u	70 - 80 μm	65 - 85 μm
LW4	Ge:Ga.s	150 - 170 μm	140 - 180 μm
SW5	Ge:Ga.u	80 - 90 μm	75 - 95 μm
LW5	Ge:Ga.s	170 - 180 μm	160 - 200 μm

"U" IS UNSTRESSED AND "S" STRESSED

FIGURE 2

SPECTRAL RANGE AND POSITION OF THE DETECTORS

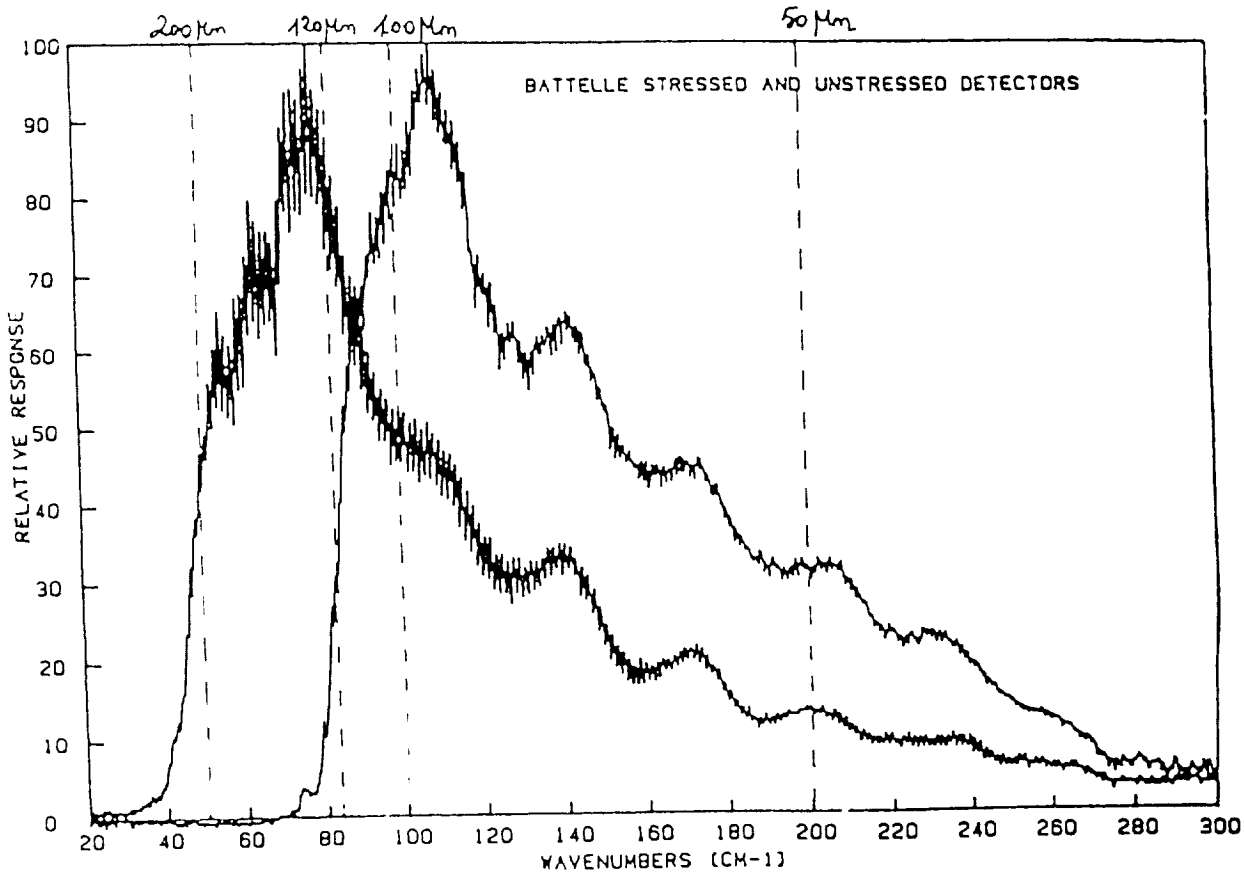

FIGURE 3

SPECTRAL RESPONSES OF STRESSED AND UNSTRESSED Ge:Ga PHOTOCONDUCTORS

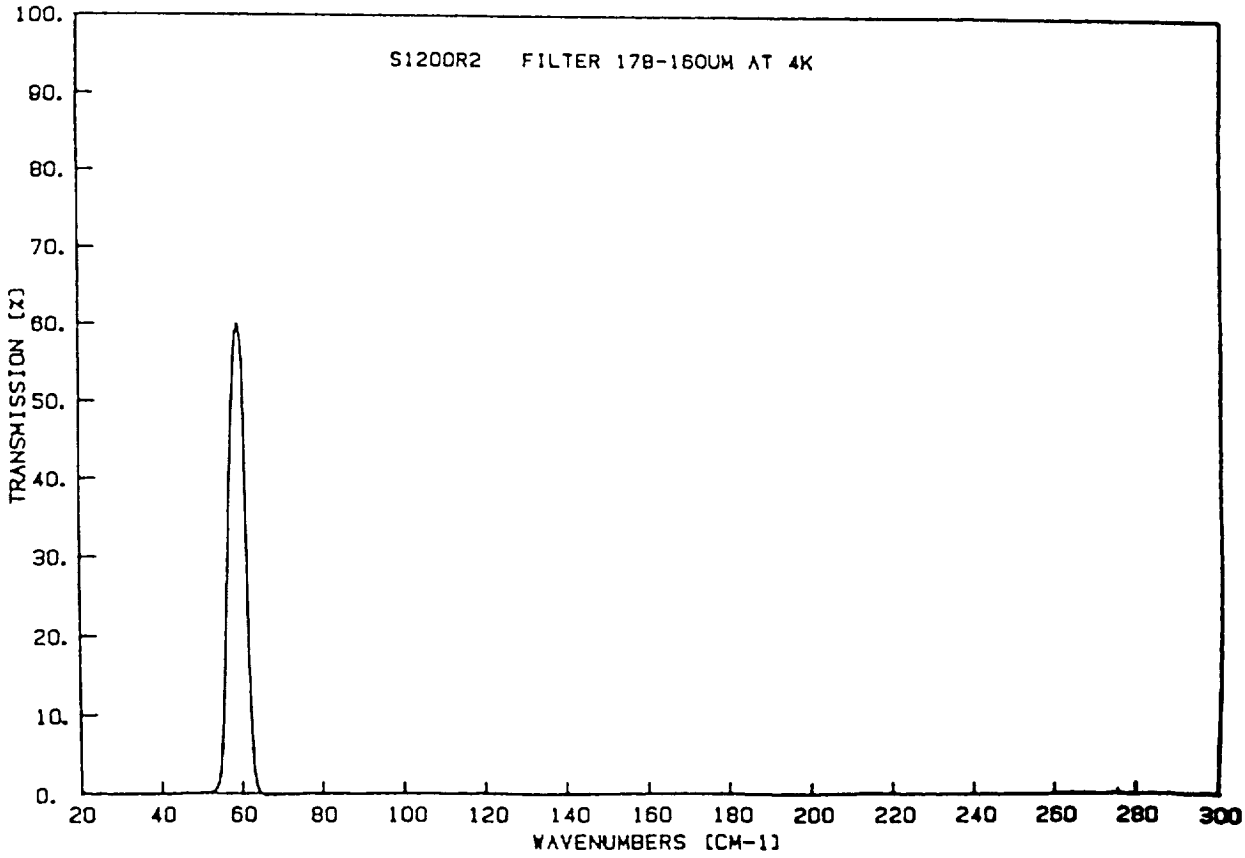

FIGURE 4

MEASURED FILTER RESPONSE

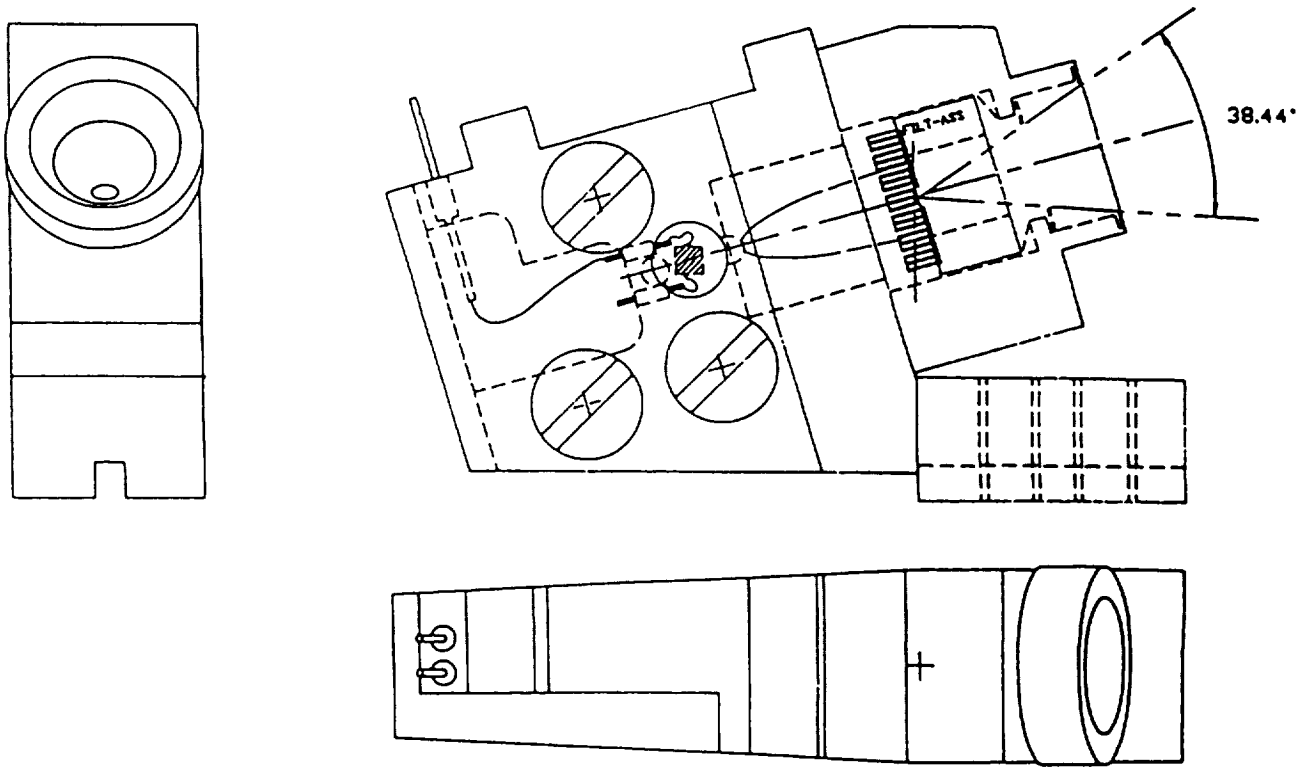

FIGURE 5

UNSTRESSED DETECTOR MOUNTING UNIT

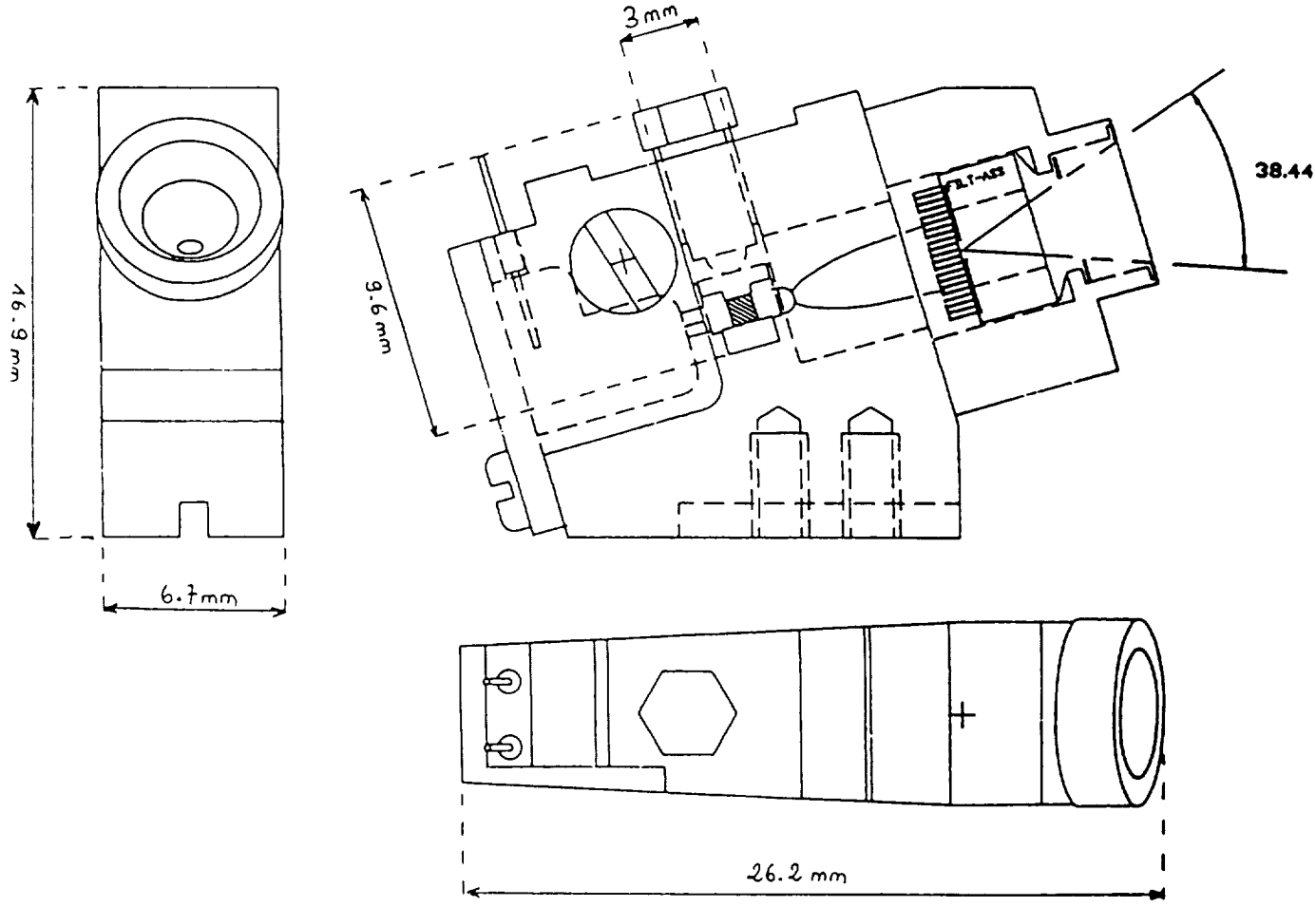

FIGURE 6

STRESSED DETECTOR MOUNTING UNIT

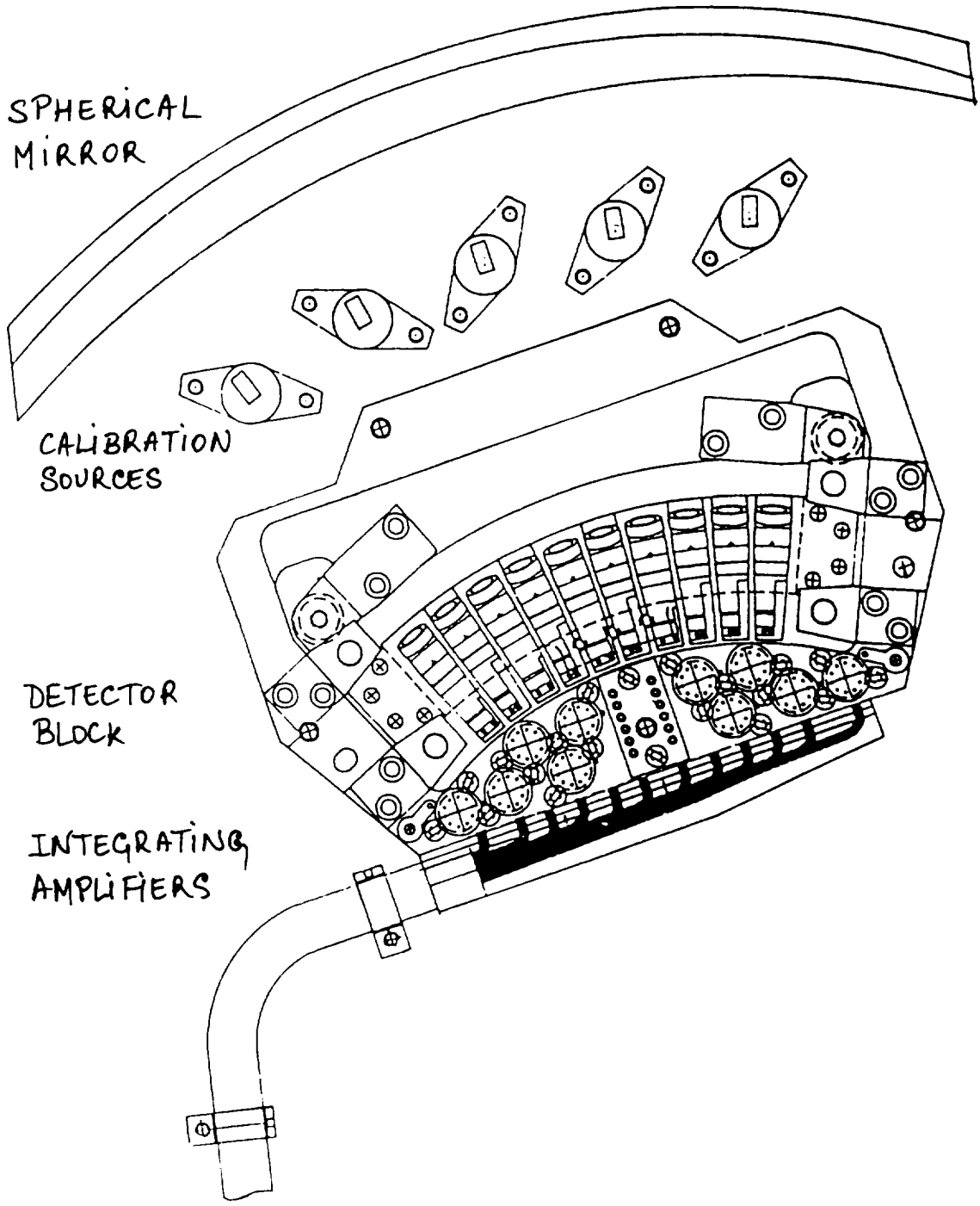
SPHERICAL
MIRROR
CALIBRATION
SOURCES
DETECTOR
BLOCK
INTEGRATING
AMPLIFIERS

FIGURE 7

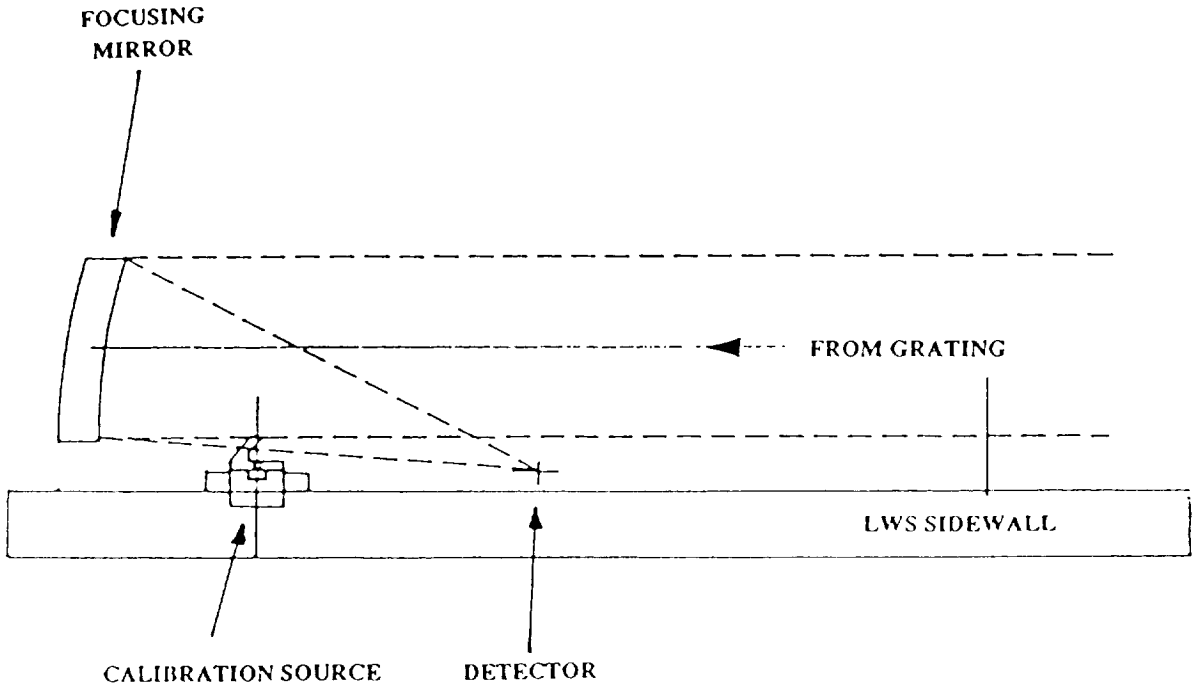

DETECTOR INFRARED CALIBRATION SOURCES (SCHEMATIC)

FIGURE 8

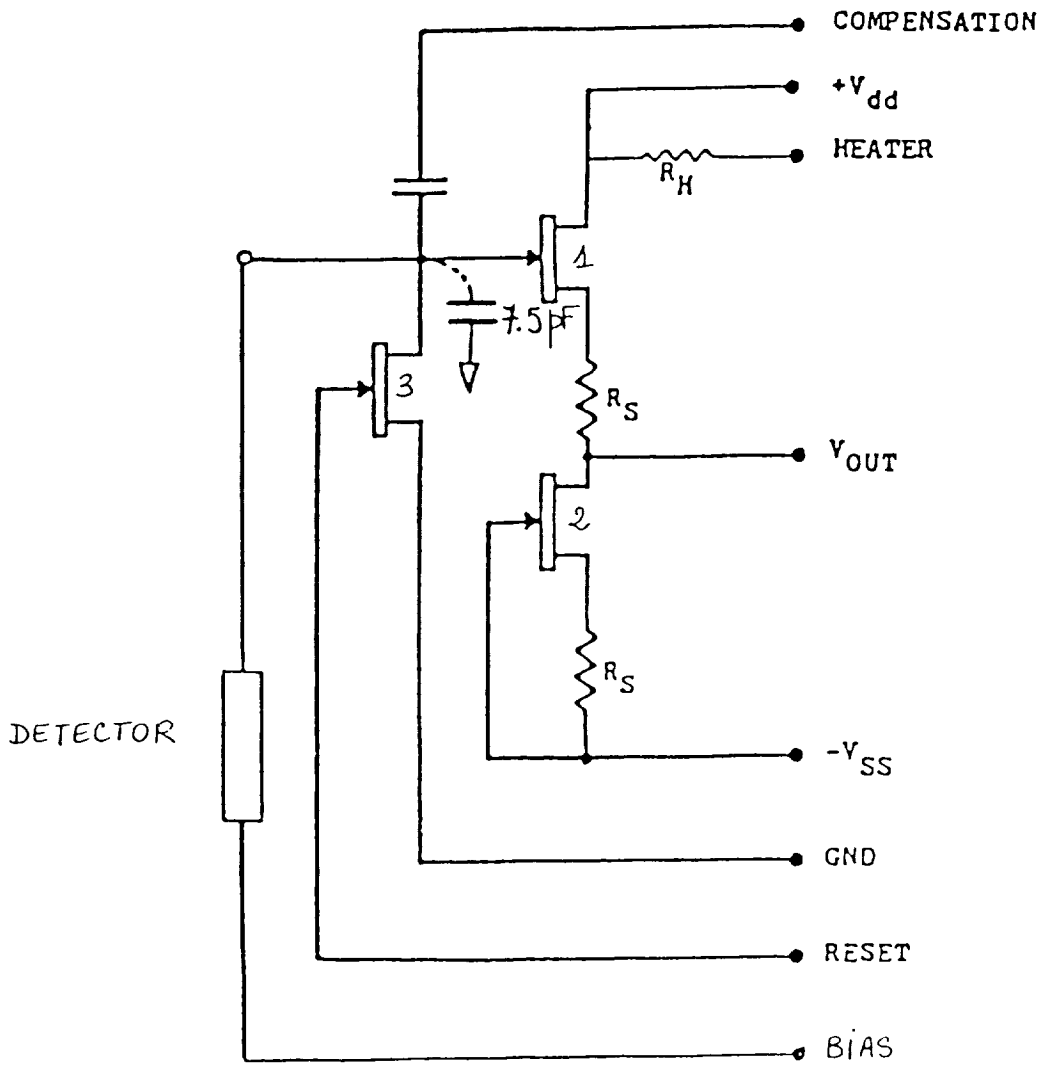

FIGURE 9

JF4 CIRCUIT

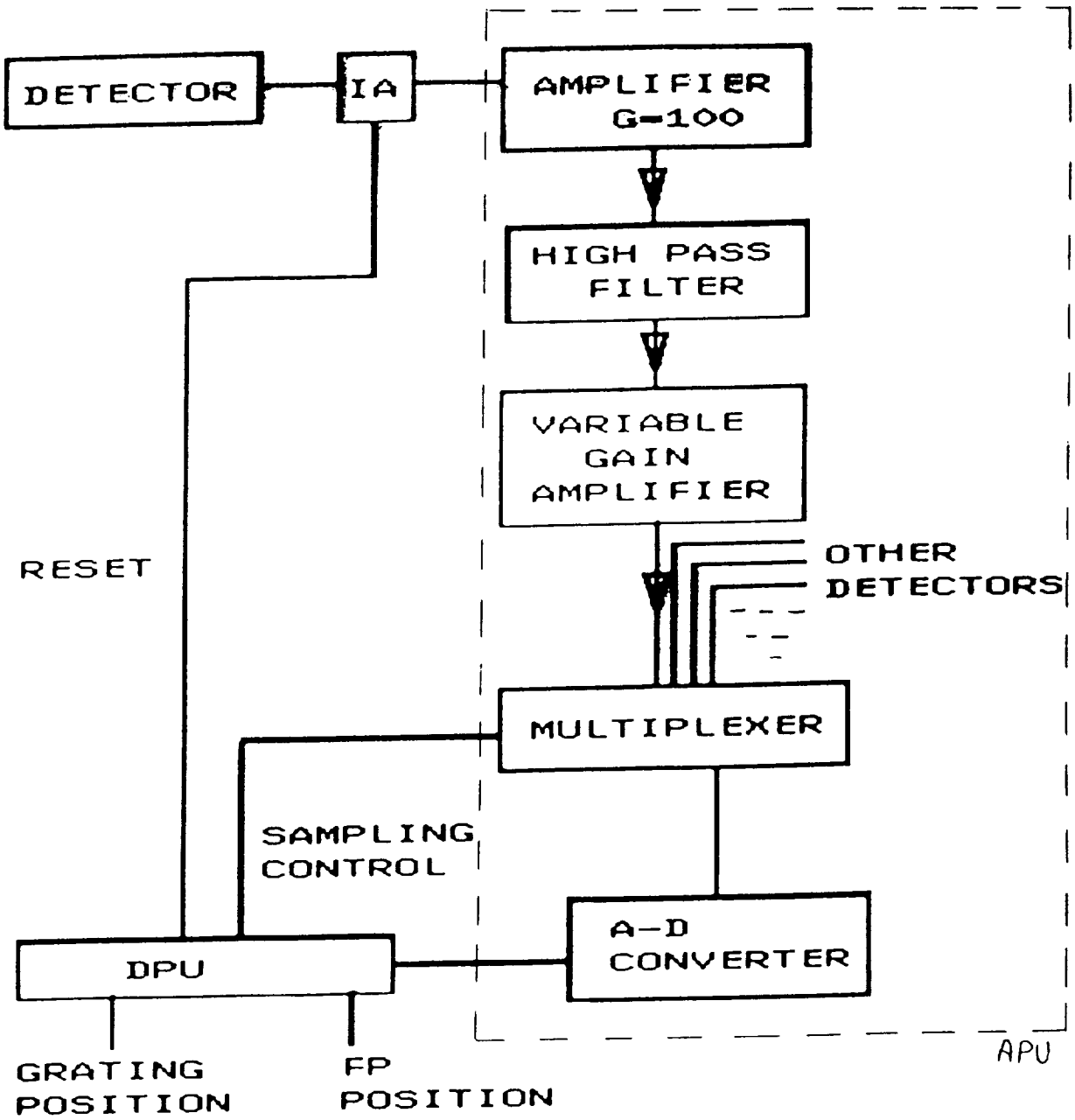

FIGURE 10

SIGNAL PROCESSING

Dark current Versus Temperature for Unstressed Prototype

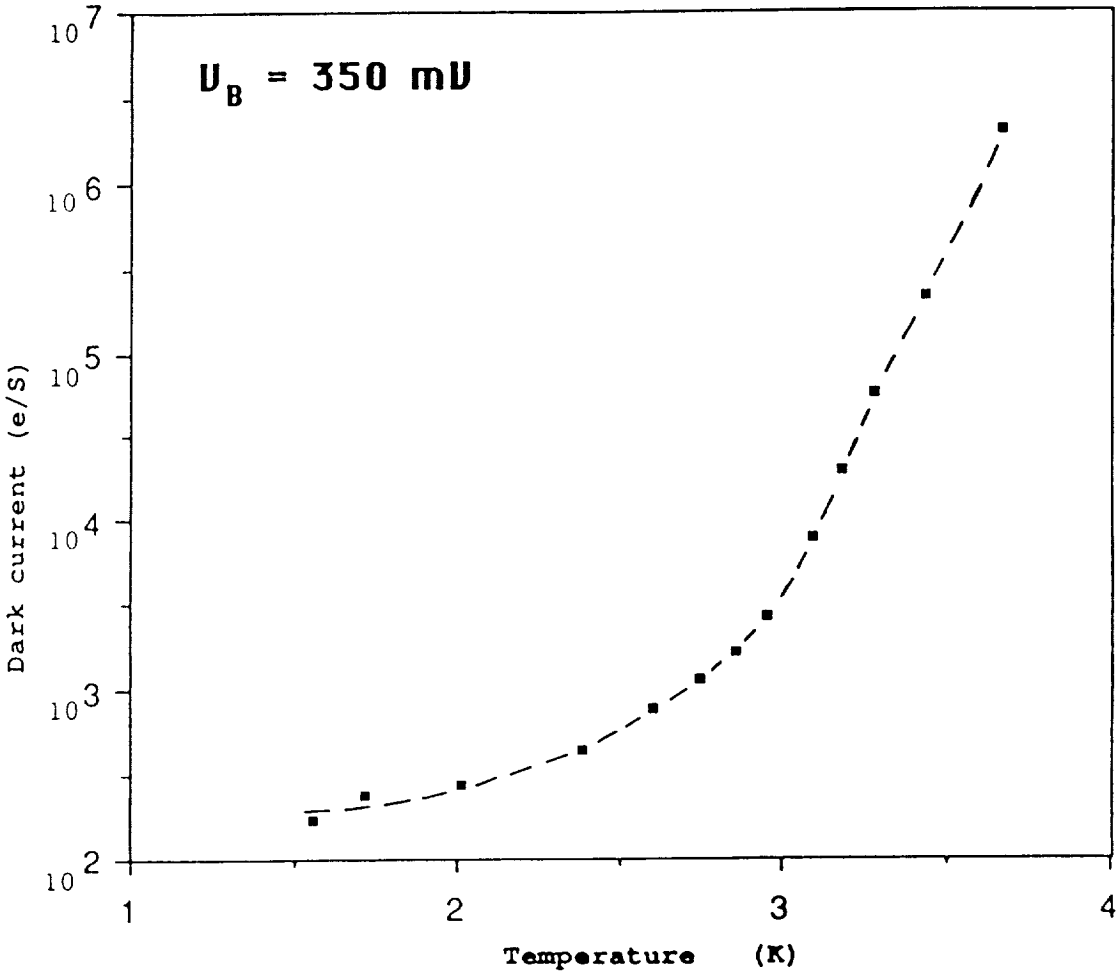

FIGURE 11

Dark current Versus Temperature for 1.4 mm Stressed g_e : g_o Prototype

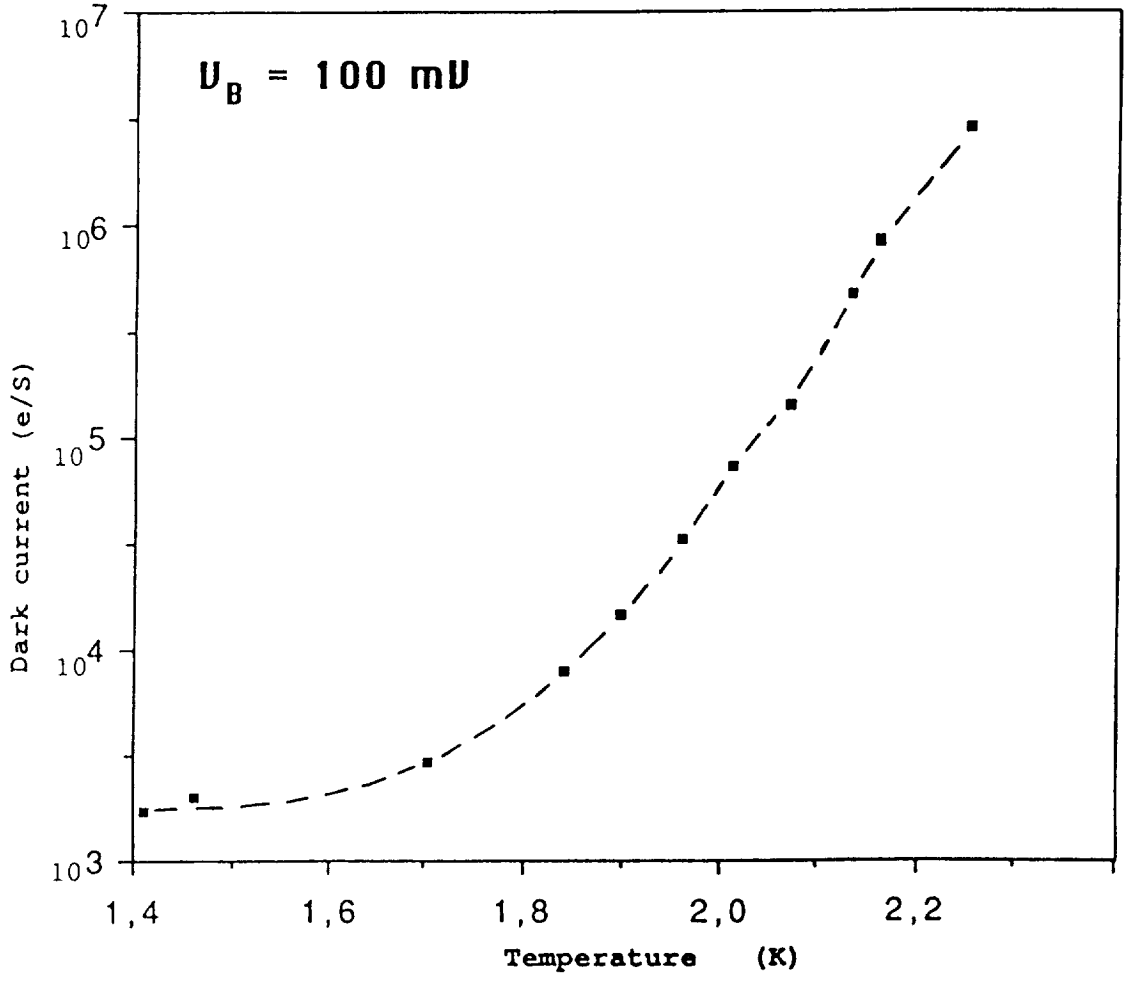

FIGURE 12

Normalised Responsivity and Dark current Versus Temperature for 1.4 mm Stressed Prototype

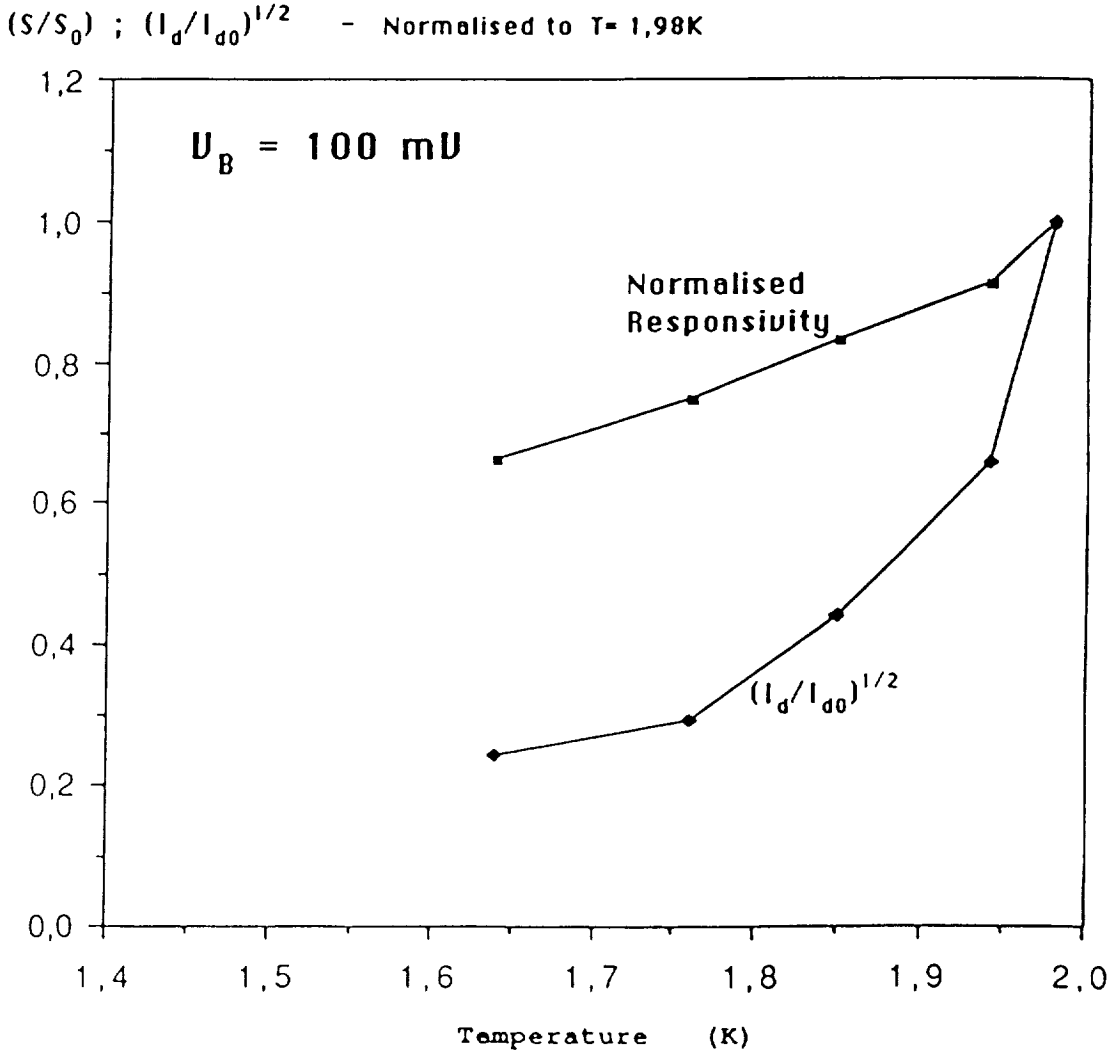

FIGURE 13

N90-21344

ISO CAMERA ARRAY DEVELOPMENT STATUS

F. Sibille, Observatoire de Lyon
C. Cesarsky, P. Agnèse Service d'Astrophysique, DPhG, CEN Saclay
D. Rouan, Obervatoire de Meudon

Abstract

We present a short outline of the camera ISOCAM, one of the 4 instruments onboard ISO, with the current status of its two 32x32 arrays, an InSb CID and a Si:Ga DRO, and the results of the in orbit radiation simulation with gamma ray sources. A tentative technique for the evaluation of the flat fielding accuracy is also proposed.

I Outline of the camera ISOCAM

Amongst the 4 instruments onboard ISO, the task of the camera ISOCAM is to provide 32x32 pixel images in the 2,5 - 17 μm spectral range with the following characteristics :
- 4 different spatial samplings are available : 1.5, 3, 6 and 12 arc sec. per pixel, with respectively a total field of view (FOV) of 48, 96 (array size limited), 180 and 180 arc sec (ISO telescope FOV limited). With 1.5 arc sec./pixel, the spatial resolution will be limited by the spacecraft pointing jitter of 2.7 arc sec. (half cone, 2σ) with a pseudo-period of about 30 seconds.
- 21 bandpass filters, with resolutions $\lambda/\Delta\lambda$ between 2 and 30, and CVF's covering the spectral range 2.5 to 16.5 μm with a resolution of the order of 50.

An optical layout of the instrument is shown in Fig. 1. Two field mirrors mounted on the "selection wheel", at the telescope focal plane, allow to feed the beam into one or the other of the two wavelength channels, covering respectively the 2.5 - 5.5 μm and the 4 - 17 μm range. Both are optically identical, and they operate only one at a time. The filters and CVF's are mounted on a "filter wheel", in the plane of the pupil image provided by the field optics. Four lenses, mounted on a "lense wheel", allow to reimage the focal plane onto the array with a magnification matching the pixel size to the desired pixel FOV. Only 2 lenses are shown in Fig. 1 for each channel. Polarization mapping can be done using three polarizers mounted on the "entrance wheel", otherwise normally used on a free hole position. An integrating sphere mounted on the selection wheel is used as an internal calibration/flat-fielding device. In its operating position, its output port-hole matches the 3 arc min FOV of the camera in the telescope focal plane. It is illuminated through a small hole on its side by an external 1 mm^2 thin film heater element.

II The detector arrays in ISOCAM

Two arrays, with the same 32x32 pixel format and 100x100 μm^2 pixel pitch have been developed for ISOCAM.

II - 1 Short wavelength channel array : InSb CID

This array is a modified version of the CID produced by SAT (Société Annonyme des Télécommunications, France). The area filling factor is 83%, and the overall efficiency, read out electrons per incident photons, is 33 %. Below 10K, the dark current is very low and tunnel effect limited, so that the amount of dark charges is proportional to the logarithm of the integration time. For instance, one has 800 dark electrons per pixel for a 500 sec. exposure, which makes the device suitable for very long integration time. The full well capacity is bias voltage dependant, it

can be adjusted in the 2 to 4 10^6 electrons range, providing an excellent linearity. With an integration time of 60 sec., the NEP(5μm) is of the order of 2.5 10^{-18} W.

A major emphasis has been put on the development of a low noise preamplifier hybrid circuit, operating at 3 K close to the focal plane temperature, located in the nearest possible vicinity of the array in order to reduce noise pick-up and cross-talk. This assembly uses G118 for reset switches and ZK111 for source follower amplifiers. The current noise level is about 1100 electrons rms, close to the design goal of 1000. The cross-talk is below 1 %.

II - 2 Long wavelength channel array : hybrid Si:Ga DRO

This array has been produced in a special development program by LETI-LIR, a division of the Atomic Energy Comission (CEA-CENG, Grenoble France).

The Si:Ga material has a dopant concentration about 6 10^{16} cm^{-3}, and a compensation level in th lower 10^{12} - 10^{13} cm^{-3} range, providing an R.A product above 10^{12} Ω cm^2, and a responsivity larger than 3 $A.W^{-1}$. Taking an input capacitance of .1 pF, which may actually be smaller than that, the full well capacity is 1.2 10^6 elect. with 2 Volt of output voltage range, and the readout noise is below 500 electrons rms. Under low background conditions, the NEP(15μm, 1sec.) is in the 2 - 4 10^{-17} W, with a linearity better than 1% when the flux is between 10 and 1000 NEP, but it shows a marked threshold effect at very low signal level. The uniformity of the response is quite good : several arrays have all their pixels within ± 20 % of the average. Different filling factors have been produced, but the value of 100 % has been selected for the final device. Measured with an f/2 beam, faster than any beam in ISOCAM, the cross-talk is less than 1 % between side by side pixels, and 2 % between corner to corner neighbour pixels.

The readout circuit is a classical DRO made with MOS N-channel technology. The source follower MOSFET is permanently biased, and its output is sampled to a column bus with a switch. The total heat dissipation is below 5 mW. The typical frame readout time is .1 sec. and the the integration time is limited to 800 sec. by the dark current, 2 10^3 elect./pixel/sec, or by the background which depends upon the selected pixel FOV or filter. In orbit, the high energy particles will be the most severe limitation in the integration time : simulations shows that in 30 seconds there will be 8 impacts producing 60 glitched pixels. Above this value the deglitching algorithms loose efficiency, the smallest glitches beeing the most difficult ones to disentangle, and there is little gain, or even loss, in integrating further.

III In orbit radiation effects

The radiation environment along the ISO 24 hours orbit is sketched on Fig 2. So far simulations of the orbital conditions on the arrays have been done only with gamma rays sources with low dose rates representative of the inner and of the outer belt, or with high dose rate to study the cumulated dose effects. Simulations with protons will be performed soon.

The main conclusions are that in most of the outer belt the CID can be operated with slightly degraded, but still acceptable performances, whereas the integration time of the Si:Ga DRO is limited by the glitches to about 1 second, which severely degrades the performances. Cumulated doses did not produce any degradation on both arrays, but only a permanent drift of some MOSFET threshold voltages, still at an acceptable level.

After the perigee passage, the responsivity change of the CID is barely measurable, which makes it ready for use immediately in the outer belt. On the other hand, the Si:Ga DRO responsivity increases by about a factor of 2, and returns to normal during the crossing of the outer belt, so that

it is ready for use during the radiation quiet part of the orbit. It was noticed during these tests that its recovery time is noticeably reduced when the array is exposed to a large photon flux.

IV Flat fielding characterization

This section is an attempt to summarize the approach currently adopted in evaluating the usefulness of an array. Most often, during the operation of ISOCAM, the performances limiting factor will be the accuracy with which one knows the "gain" matrix |Ri| of the array, or the relative response of each pixel with respect to the others. Would it be perfectly stable, one could spend a long time measuring it with a high accuracy, and then just use this calibration. But real life is far from that ideal situation.

We try to characterize the changes of |Ri| occuring with time, the usual temporal drifts, or with the change of a parameter which is a factor of the gain. Instead of |Ri|, we use |xi| = |Ri/<Ri>| where <Ri> is the spatial average of Ri over the array, and we characterize any change in |Ri| by :

$\sigma = \sigma_{xi}/\langle xi \rangle$, where σ_{xi} is the standard deviation of xi.

This approach has been recently implemented in the tests of the Si/Ga DRO at Saclay. For instance, if one performs two measurements of |Ri| at time t and t', σ_t characterizes the differential drifts, pixel to pixel, over the time interval (t'-t). If one changes the integration time Ti, σ_{Ti} characterizes the differential linearity of the signal with respect to Ti. If one changes the flux level, σ_W does the same with respect to the linearity with respect to the flux.

If xi = 1, then $\sigma = 0$, one find the ideal situation of a perfect photometric and imaging device. If xi is not 1 but a constant, $\sigma = 0$ again, the imaging capability is still perfect, and there is a constant bias in the photometric calibration, which is not too difficult to correct. Finally, if σ is large, the photometric calibration does not make any sense, and worse, there is a large potential for false source detection.

The followings are a few preliminary results obtained on the "scientific model" of the array :

t' - t = 4 hr	—> σ_t	= .2 %
.1 sec < Ti < 2 sec	—> σ_{Ti}	= .2 —> .7 %
.1 W_{sat} < W < .8 W_{sat}	—> σ_W	= .2 —> 1 %

ISOCAM SCIENTIFIC CONSORTIUM

Principal Investigator :	C. CESARSKY	SAP
Co-investigators :	S. CAZES	IAS Orsay
	D. CESARSKY	IAP Paris
	A. CHEDIN	LMD Orsay
	M. COMBES	Paris Obs.
	M. GORISSE	SAP Saclay
	T. HAWARDEEN	Edinburgh Obs.
	P. LENA	Paris Obs.
	M.S. LONGAIR	Edinburgh Obs.
	R. MANDOLESI	TESRE Bologna
	L. NORDH	Stockholm Obs.
	P. PERSI	IAS Frascati
	D. ROUAN	Paris Obs.
	A. SARGENT	Caltech
	F. SIBILLE	Lyon Obs. (Proj. Scientist)
	L. VIGROUX	SAP Saclay
	R. WADE	Edinburgh Obs.

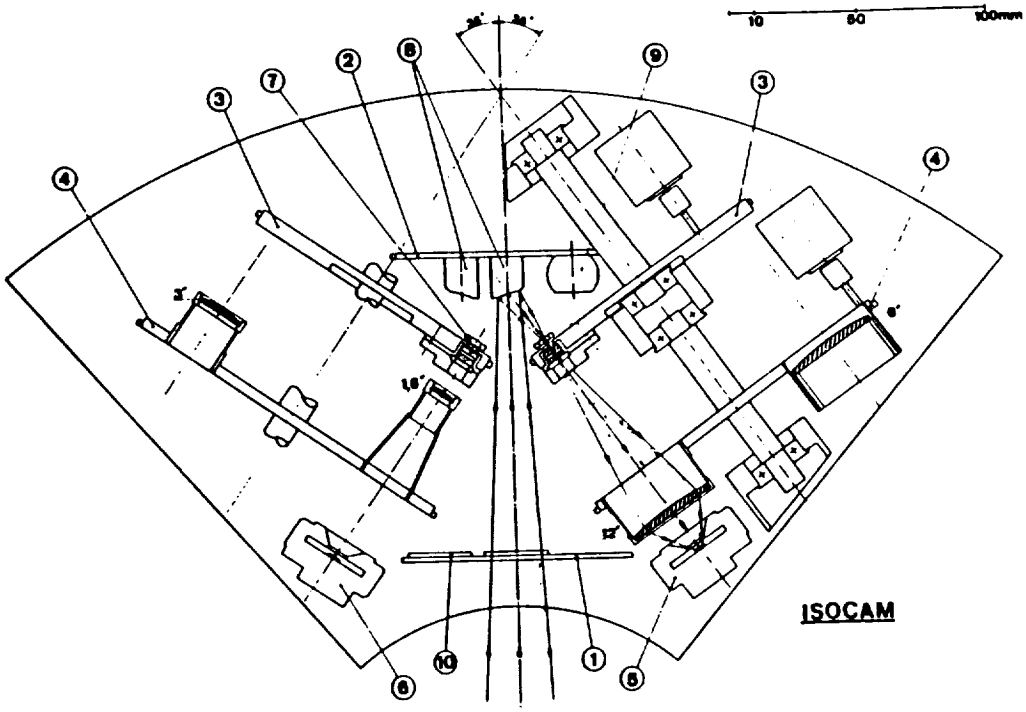

Figure 1 : ISOCAM optical lay out

1. Entrance wheel
2. Selection wheel
3. Filter wheel
4. Lens wheel
5. InSb CID
6. Si:Ga DRO
7. Aperture stop
8. Fabry mirror
9. Calibration source
10. Polarizers

Figure 2

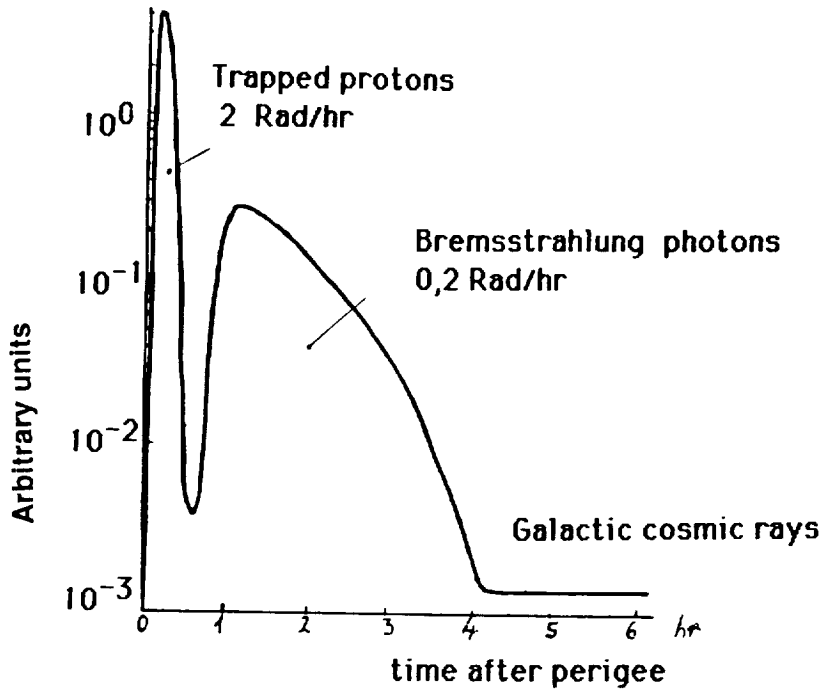

±(0-0,5hr) Trapped protons
Experiment is OFF
dose rate < 2 Rad/hr (integrated : 1.1 Krad)

±(0.5-4hr) Bremsstrahlung photons
Experiment may be ON
dose rate < 0.2 Rad/hr (integrated : .25 Krad)

±(4-12hr) Solar/Galactic Cosmic rays
Best part of the orbit
dose rate < 10^{-3}Rad/hr (integrated : .1 Krad)

TOTAL DOSE (600 days mission) 1,5 Krad

SIRTF in High Earth Orbit

Michael W. Werner, Walter F. Brooks, Larry A. Manning and Peter Eisenhardt*
NASA-Ames Research Center

1 Introduction

The exciting scientific results reported from the first use of large format infrared arrays at ground-based telescopes (Gatley *et al.* 1988) set the stage for the eventual application of this technology on cryogenic telescopes in space. The difference in infrared sky brightness seen by a cryogenic space telescope, versus an ambient temperature ground-based or airborne facility, is comparable to the difference in visible sky brightness at night versus day. This reduction in background brightness places an enormous gain in sensitivity within our grasp. Space telescopes also have a clear view of all infrared wavelengths, unimpeded by atmospheric absorption. The first cryogenic space telescope to take full advantage of the new generation of infrared detector arrays will be the Space Infrared Telescope Facility (SIRTF–Figure 1). Indeed, much of the work reported at this conference on detector arrays for space applications at wavelengths longward of 2.5μm was stimulated and/or supported by the SIRTF detector technology program.

SIRTF will be an observatory class facility for infrared astronomy, carrying three instruments providing a broad range of capabilities. With the Hubble Space Telescope, the Advanced X-Ray Astrophysics Facility, and the Gamma Ray Observatory, SIRTF makes up NASA's family of Great Observatories. Most of the observing time over the SIRTF mission lifetime (currently estimated as 5 years with a substantial safety margin) will be used by general observers drawn from the broad astronomical community.

SIRTF has been under study and development by NASA for over a decade. The SIRTF Science Working Group (Table 1) and instrument teams were selected in 1984. Efforts since then have focussed on validating the system performance requirements, working on key telescope and instrument technology areas, and optimizing all portions of the mission. SIRTF stands second in the queue for major missions within NASA's Office of Space Science and Applications. The current schedule for SIRTF calls for initiation of the final design and fabrication activities (Phase C/D) in 1992/3, leading to launch in 1998.

In the spring of 1989, NASA adopted a new approach to SIRTF, utilizing an expendable vehicle launch into a high earth orbit (HEO – orbital altitude 100,000 km above the Earth's surface). The main purpose of this article is to introduce the HEO mission and the advantages which it will bring over the previous 900 km altitude low earth orbit (LEO) approach. In addition, we emphasize the importance for SIRTF of the continuing developments in infrared array technology. More complete discussions of SIRTF's scientific objectives and potential can be found in Rieke *et al.* (1986) and in a series of articles in Astrophysical Letters and Communications (Vol. **27** No. 2, pp. 97 ff., 1987). The (LEO) SIRTF mission and SIRTF instruments are more fully described in Werner *et al.* (1986) and Ramos *et al.* (1988).

*Department of Astronomy, University of California, Berkeley, CA 94720

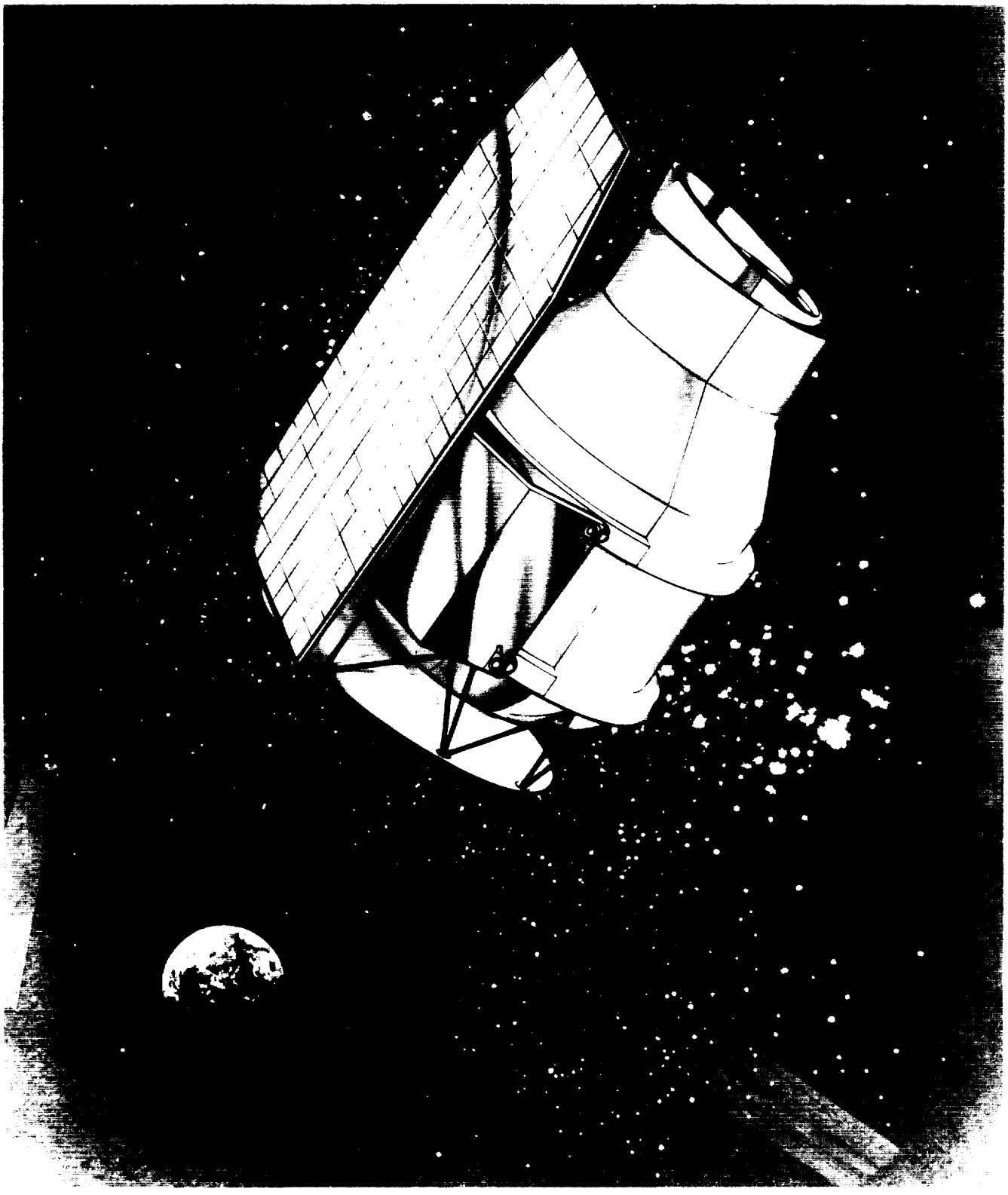

Figure 1: The Space Infrared Telescope Facility (SIRTF), shown in its new high altitude Earth orbit (HEO) configuration.

Table 1: SIRTF Science Working Group.

Giovanni G. Fazio, Smithsonian Astrophysical Observatory	Principal Investigator (PI), Infrared Array Camera (IRAC)
James R. Houck, Cornell University	PI, Infrared Spectrograph (IRS)
George Rieke, University of Arizona	PI, Multiband Imaging Photometer for SIRTF (MIPS)
Michael Jura, UCLA	Interdisciplinary Scientist
Frank Low, University of Arizona	Facility Scientist
Edward L. Wright, UCLA	Interdisciplinary Scientist
Dale Cruikshank, NASA/Ames	Interdisciplinary Scientist
Fred C. Gillett, NASA Headquarters	Program Scientist
Michael W. Werner, NASA/Ames	Project Scientist
Fred C. Witteborn, NASA/Ames	Deputy Project Scientist

2 Rationale and Requirements

The fundamental rationale for a cryogenic telescope in space is shown in Figure 2, which compares the infrared background brightness of the earth's natural astrophysical environment with that encountered by an ambient temperature telscope operating within the atmosphere. The natural astrophysical background radiation includes contributions from the zodiacal dust cloud, diffuse galactic dust, and the 3 K cosmic background. These natural backgrounds are more than a million times lower than those characteristic of Earthbound ambient temperature telescopes. The minima in the natural backgrounds around 3 and 300μm are particularly noteworthy, as sensitive observations in these windows may provide unique views of the distant, early universe. Because the limiting sensitivity improves with the square root of the background brightness, even a modest sized cryogenic space telescope, such as SIRTF, can have a thousand or more times the sensitivity of a large ground based telescope. SIRTF's goal is therefore to reduce both the thermal emission of the telescope and scattered and off-axis radiation sufficiently so that its performance can be "natural-background limited" at wavelengths between 2 and $\gtrsim$ 200μm.

SIRTF's scientific objectives require not only high sensitivity but also excellent performance in many other areas. The resulting system parameters and requirements are listed in Table 2. Also shown for comparison are the parameters for the Infrared Astronomical Satellite (IRAS), the pioneering cryogenic infrared space telescope (Neugebauer *et al.* 1984). IRAS, which flew in 1983 and carried out the first sensitive all-sky survey at infrared wavelengths, established the scientific and technical framework for the development of SIRTF. Although the size difference between the telescopes is not large, SIRTF goes far beyond IRAS in many important scientific dimensions: wavelength coverage, spatial and spectral resolution, sensitivity, and lifetime. The European Space Agency's Infrared Space Observatory (ISO – Kessler 1986), scheduled for launch in 1993, will have capabilities intermediate between those of IRAS and SIRTF. SIRTF's biggest gains result from the fact that its instruments will be equipped with large arrays having up to tens of thousands of detector elements, as is discussed further in section 4. Thus SIRTF will be an extremely powerful observatory, capable not only of following up the discoveries made by IRAS and by ISO, but also of extending our knowledge of the infrared universe still further back in both space and time.

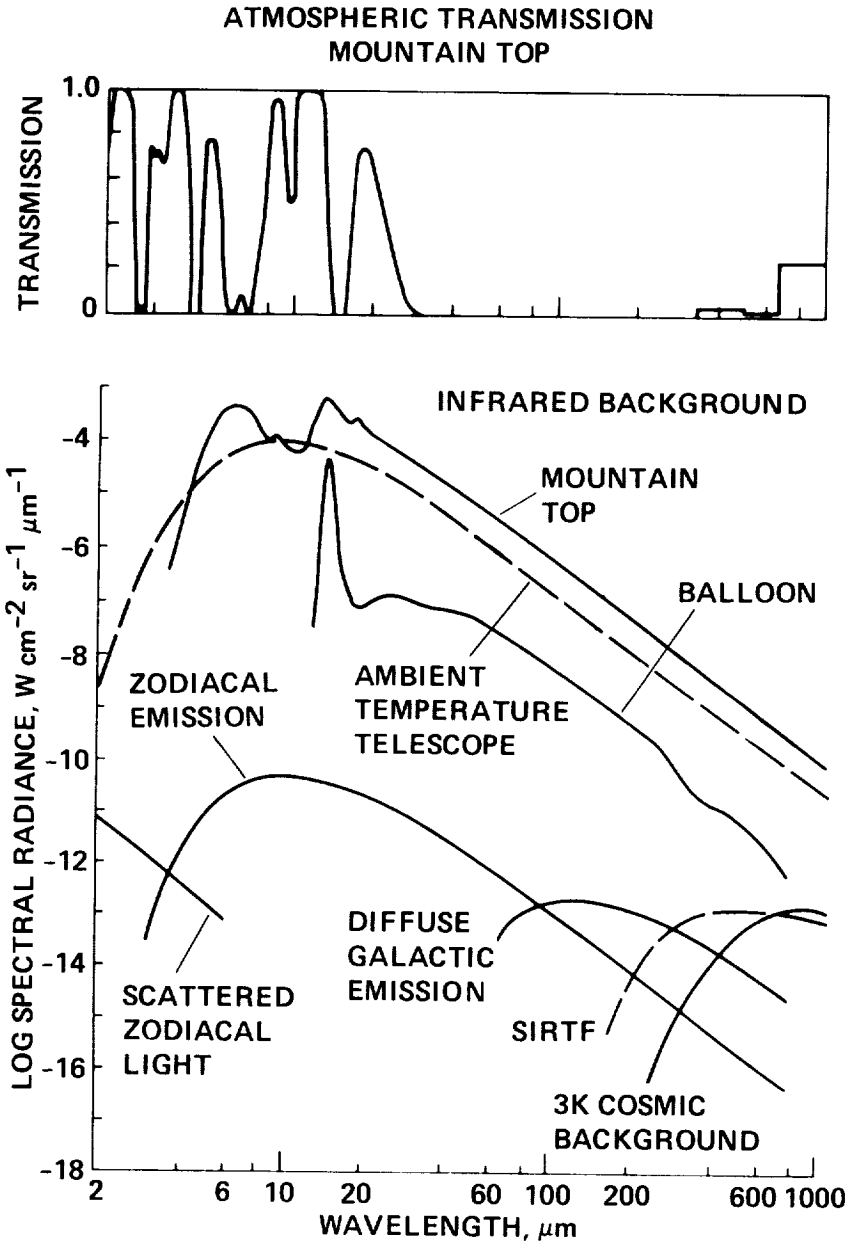

Figure 2: Atmospheric transmission and background fluxes for infrared astronomy. The upper panel shows the atmospheric transmission seen from a good mountain top observatory, illustrating that much of the infrared spectrum is completely inaccessible from the ground. Solid curves in the lower panel show the infrared background flux in three observing environments: a good mountain top observatory, high balloon altitudes, and space. Atmospheric background flux at airplane altitudes is intermediate between the curves for the mountain observatory and the balloon. The natural astrophysical background radiation in space is the sum of scattering and emission by zodiacal dust grains, emission by diffuse galactic dust, and the 3 K cosmic background radiation. Dashed curves show the background contributions from optimized infrared telescopes: an ambient temperature instrument (such as would be used from the ground, airplanes, or balloons) and SIRTF. The total background at the infrared detector is the sum of the natural and telescopic contributions.

Table 2: Comparison of SIRTF and IRAS System Parameters

Parameter	SIRTF	IRAS
Mirror Diameter	95 cm	60 cm
Wavelength Coverage	1.8 – 700μm	8 – 120μm
Diffraction-Limited Wavelength	2.5μm	$\sim$ 15μm
Angular Resolution at Wavelength λ	$\lambda/4\mu$m arcsec	$\gtrsim$ 15 arcsec
Pointing Stability/Accuracy	0.15/0.15 arcsec	2 arcsec
Sensitivity:[1]		
10 μm	6 μJy	70 mJy
60 μm	150 μJy	70 mJy
Number of Detectors	$\gtrsim$ 10,000	62
Spectral Resolving Power	$\gtrsim$ 2000	20
Mode	Observatory	Survey
Lifetime	> 5 years	10 months

[1]One sigma in 500 seconds of integration for SIRTF, and in one survey pass for IRAS.

3 Mission Options Study

NASA's decision following the Challenger accident to employ a mixed fleet of launch vehicles encouraged the SIRTF team to explore alternate mission approaches to achieving SIRTF's science objectives. In an initial study phase concluded in mid-1988, a circular orbit at an altitude of approximately 100,000 km above the Earth was selected for detailed study and comparison with the 900 km altitude baseline mission (Figure 3). These two altitudes are, respectively, just above and just below the Earth's Van Allen belts, whose trapped energetic particles would degrade infrared detector performance. The rules of the comparison stipulated that both missions satisfy the requirements in Table II and that both be capable of supporting the complement of three instruments selected for SIRTF.

The HEO mission concept outlined below is the result of six months of intensive study headed by the Ames Research Center with support from the SIRTF Science Working Group, the Jet Propulsion Laboratory, the Marshall Space Flight Center, and the Lewis Research Center. An alternative HEO option, in which SIRTF is flown at the Earth-Sun L2 Lagrangian point (1.5 million km in the anti-solar direction), was proposed by the Goddard Space Flight Center. Further optimization of the HEO concept will take place during the SIRTF Phase B studies beginning in 1990.

3.1 The HEO Mission

The new mission will use a Titan IV/Centaur to launch a 5 m long, approximately 4,500 kg SIRTF into a 100,000 km altitude, 28.5° inclination orbit with a period of $\approx$ 100 hours. Seen from this altitude, the Earth subtends an angle of less than 7° (vs. 122° in LEO), so it is possible to maintain a flexible viewing strategy while constraining the telescope to point no closer than 80° to the Earth or Sun limb. This orbit allows the use of a fixed solar panel, which shades the telescope and lowers the predicted temperature of the telescope outer shell to 110K. Eclipses are infrequent in this orbit; the time and date of launch can be selected to orient the orbit so that the spacecraft passes through the Earth's shadow only a few days each year. Reaction wheels provide slewing and fine pointing capability. Environmental disturbance torques are small, but momentum control requires the use of cold gas because the Earth's magnetic field is too weak for momentum dumping at 100,000 km. The helium boil off from the cryogen system and a small tank of compressed helium gas will be used for this purpose. Science and engineering data will be stored on-board the spacecraft and downlinked

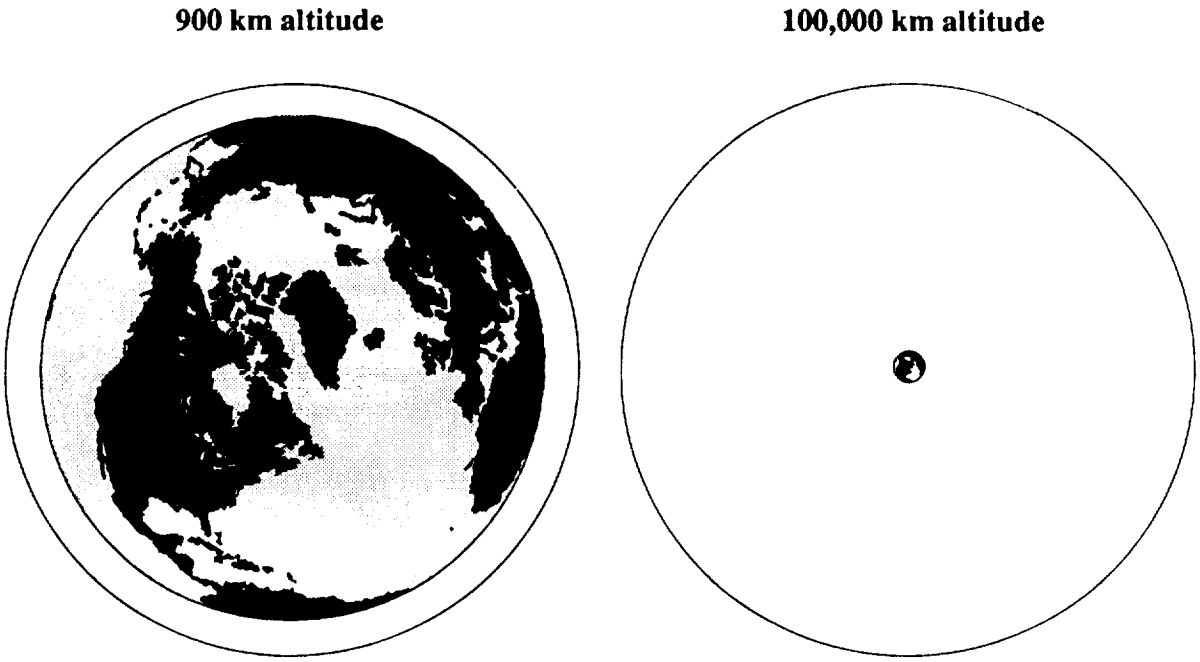

Figure 3: Relative size of the Earth in comparison to the low Earth orbit (LEO – on left) and high Earth orbit (HEO – on right).

8 hours per day via a fixed omnidirectional antenna to the 26 m dishes of the Deep Space Network.

Figure 4 shows a cutaway view of the telescope concept for the HEO mission. The IRAS heritage is shown in the annular cryogen tank, containing 4000 liters of superfluid helium which cools the optics and baffles, and in the truncated "sugar scoop" aperture shade, which allows the telescope to point as close as 80° to the Earth and Sun limb. The optical system is an f/24 Ritchey-Chrêtien design with a 95 cm f/2.3 primary mirror. The secondary mirror will be used for conventional chopping at the longer wavelengths and for flat-fielding and scanning procedures at the shorter wavelengths. Within the multiple instrument chamber, a rotatable dichroic tertiary mirror will direct the entire seven arcminute field of view to whichever instrument is in use, while the optical image is passed to a fine guidance sensor which will be used with the spacecraft gyros to provide pointing and stabilisation.

3.2 Technical Concerns

The two principal technical concerns which arose during the study of the HEO SIRTF option were in the areas of launch vehicle capability and lifetime. The present HEO baseline configuration has a mass of 4370 kg. By comparison, the expected Titan-Centaur launch capability to 100,000 km for a SIRTF-sized payload is at least 5770 kg. It is felt that the 1400 kg difference (36% of the current mass excluding the helium) is adequate margin in this critical area.

The cryogen lifetime is an issue in HEO because on-orbit cryogen refill, which was to be used in LEO to achieve the five year lifetime, will not be available in this option. Preliminary optimisation of the 4000 liter HEO system yields an estimated useful on-orbit cryogen lifetime (exclusive of losses due to launch holds, on-orbit cooldown, etc.) of six years, giving a 20% margin over the requirement. The dramatic increase over the 2.5 year lifetime predicted for the same size dewar and the same instrument complement in LEO reflects:

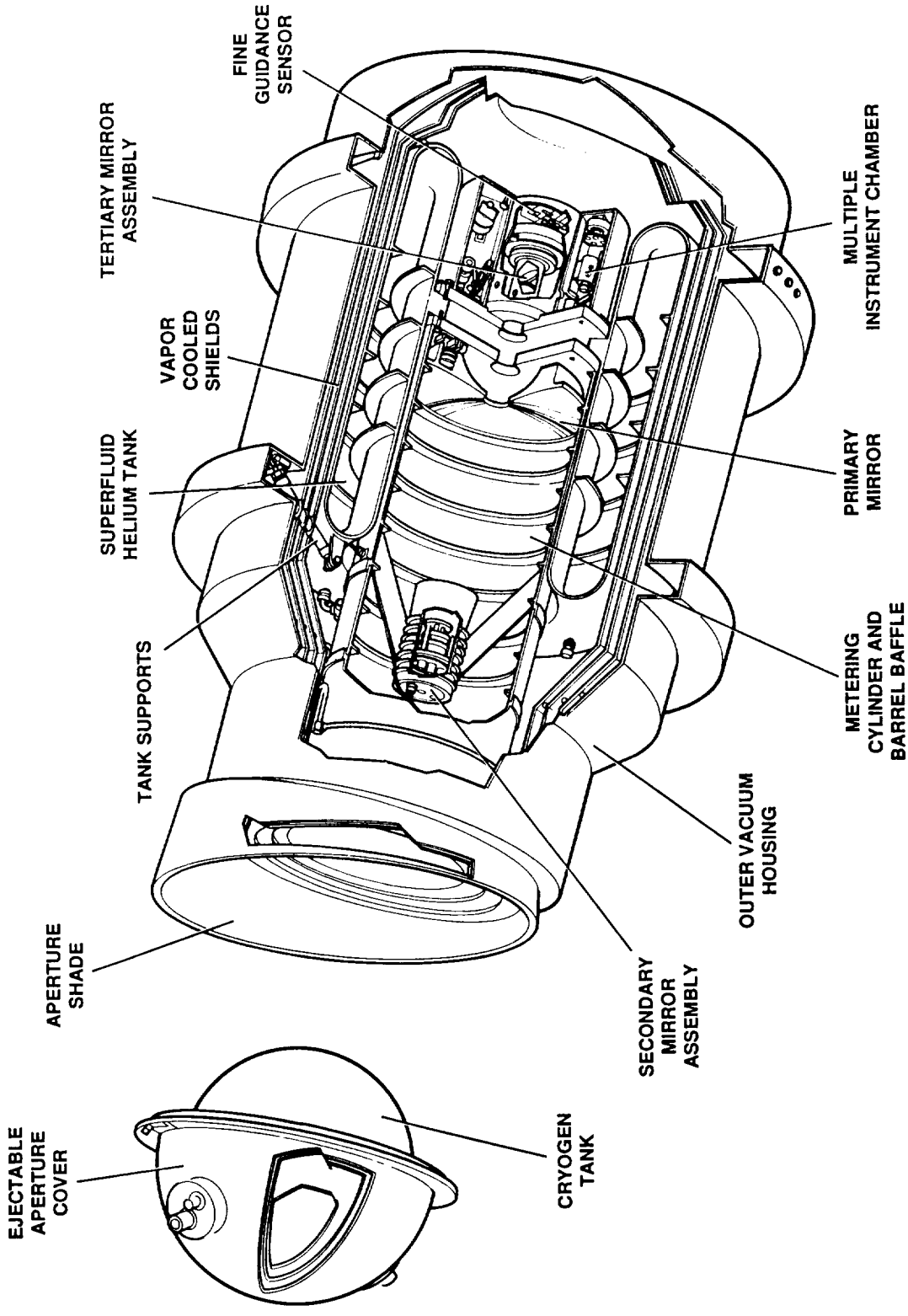

Figure 4: Cutaway view of the SIRTF telescope concept for the HEO mission.

1. the lower outer shell temperature (110K vs. 220K) achievable in HEO due to the greatly reduced heat load from the Earth and to a lesser extent to the shading provided by the fixed solar panel; and
2. reduction by more than an order of magnitude in the "aperture load" - the power radiated into the dewar by the aperture shade - which results from the fact that the aperture shade in HEO is both smaller and colder than in LEO.

3.3 Comparison of HEO and LEO Missions

3.3.1 Overall Configuration

Figure 3 shows the relative sizes of the Earth and SIRTF'S orbit for the HEO and LEO missions, while Figure 5 compares the general configuration of the orbiting observatories in the two missions, with IRAS shown for reference. Both missions have an orbital inclination of 28.5° to maximize the launch capability and to permit servicing in the LEO mission. The 280-fold reduction in solid angle subtended by the Earth in HEO leads to the thermal advantages cited above and also permits more freedom in telescope pointing, even though the solar and terrestrial avoidance angles are larger in HEO. These larger avoidance angles cannot be satisfied when SIRTF passes directly between the Earth and Sun in the LEO mission. The 122° angle subtended by the Earth permits Sun and Earth avoidance angles no greater than 59° at these times, which occur for several orbits approximately every 28 days. The use of the larger avoidance angles (80°) in HEO leads to a smaller aperture shade, which in turn permits the forward portion of the telescope baffle tube to be shortened while maintaing the required rejection of stray radiation. The reduction in aperture shade size and forebaffle length lead to the overall shortening of the system shown in Figure 5. Note also in Figure 5 that the solar arrays and antennas are fixed in the HEO system but must be deployable and steerable in LEO. The dewar, optical system, and instruments are essentially identical in the two concepts. Thus the analysis and technology work done on these system elements for LEO carries over directly into the HEO system.

3.3.2 Operations

On-orbit science operations in HEO will benefit from the reduced Earth solid angle, the long orbital period (100 hours vs. 100 minutes in LEO), and the absence of the South Atlantic Anomaly (SAA - see section 3.3.3 below). In addition, the contamination constraint introduced in LEO that the telescope not point into the "wind" created by the orbital motion of the spacecraft does not apply in HEO, where the atmospheric density is negligible. Depending on the relative location of the Sun, Earth and spacecraft, SIRTF can view instantaneously 14 to 33% of the sky in HEO but only < 1 to 12% in LEO. In HEO, there are zones over the orbit poles ($\approx$ 200 square degrees in total) which can be viewed continuously, and accessible targets elsewhere in the sky can typically be observed for 50 or more consecutive hours. By contrast, there is no direction which can be viewed continuously in LEO, because the combination of Earth limb and "wind" avoidance constraints limit the maximum viewing time per target to 15 minutes. These and similar considerations suggest that the observation planning and scheduling process will be much more straightforward in HEO. Maintaining the Earth avoidance constraint in LEO means that tens of minutes in each 100 minute orbit must be spent in large angle slews. Observing efficiency simulations for LEO including sky visibility, slewing, and time lost to the high proton fluxes in the SAA, indicate that the average efficiency (fraction of time on-target) would be about 45%. The corresponding efficiency in HEO is estimated at 90%.

3.3.3 Ionizing Radiation Environment

In LEO, the main radiation effects are due to the intense fluxes of trapped and highly energetic protons encountered during passages through the SAA, a low lying region of the Van Allen belts. These

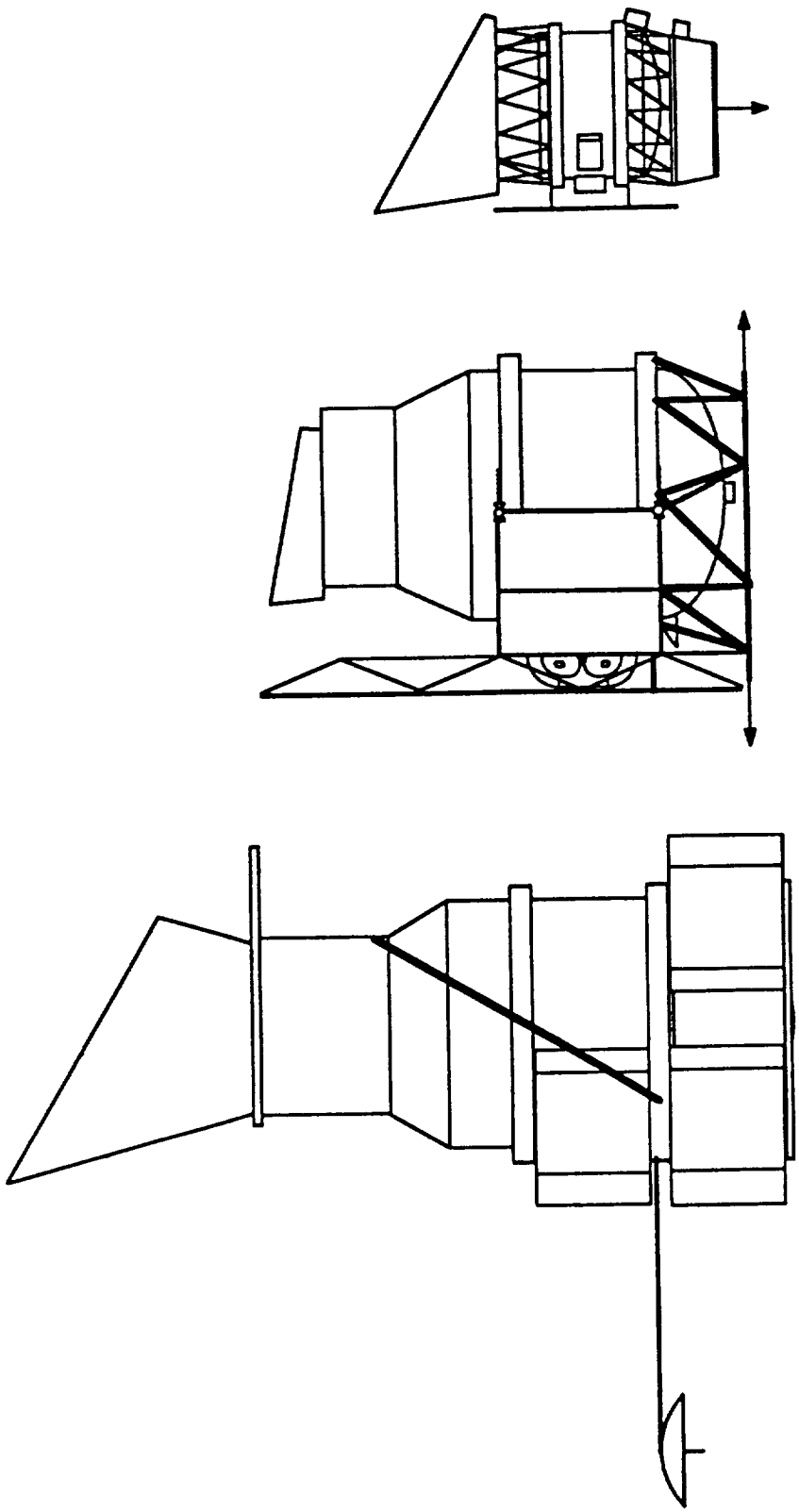

Figure 5: General configuration of the LEO (bottom) and HEO (center) SIRTF concepts, and of IRAS (top). The masses and lengths of the three satellites are 6620 kg, 4370 kg, 1080 kg; and 8 m, 5 m, and 3.7 m respectively.

passages occur almost every orbit and render about 25% of the time unsuitable for observations. Because these high fluxes alter detector response, additional time would be required for post-SAA annealing and recovery. In HEO, analysis of satellite data shows that only a few percent of the time is likely to be lost to quasi-trapped electrons and to solar flares. However, without the shielding effect of the Earth's magnetic field, the *quiescent* (cosmic ray) hit rate is predicted to be a few times higher than that expected for LEO outside of the SAA, leading to a reduction in sensitivity for certain instrument modes. Thus radiation effects would be a concern in either orbit, and radiation testing continues to be an important part of the SIRTF detector technology program.

3.3.4 Risk and Complexity

The HEO mission appears to have lower operational risk than the LEO option. In LEO the performance and system lifetime depend critically on maintaining the cleanliness of the telescope and the aperture shade, which are subject to contamination both by the residual atmosphere and by problems which could occur during a servicing mission. In addition, an emergency safe-hold mode is simply achieved in HEO by pointing at the constant viewing zone, while in LEO a complex series of pointing constraints must be continually satisfied. Finally, the use of fixed solar arrays and antennas in HEO eliminates the risk of failure during deployment or operation of these mechanisms.

3.3.5 Scientific Performance

The features of the HEO mission summarized above improve the scientific performance of SIRTF in many ways, including the following areas of particular importance:

- The doubled on-target efficiency means that the HEO mission will support twice the number of investigations, and produce twice the quantity of data, as the LEO mission.
- The longer on-target times and greater sky accessibility in HEO will allow SIRTF to operate in a true observatory mode, in which a single scientific investigation can be scheduled in an unbroken block of time. Data from the completed observation will be available to the observer more quickly, and will be more uniform and easier to calibrate and reduce, than if it were obtained on many successive orbits in the LEO mission.
- The long wavelength $> 100\mu$m performance will be improved in HEO. SIRTF's sensitivity at these long wavelengths will be influenced by radiation from the telescope itself. To reach natural-background limited performance at 300μm requires a forebaffle temperature of 7K or below; the predicted temperature is 4K in HEO and 8 to 14K in LEO. The longer on-target times and much less frequent eclipses in HEO imply that the temperature will be more stable as well as lower. These effects together should allow the HEO mission to achieve far better performance in the cosmic window at 300μm, where recent results (Matsumoto *et al.* 1988) indicate that many important cosmological questions can be investigated.
- Performance at the 3μm window may also be improved in HEO. The extremely low background photon rate means that observations (especially spectroscopy) near this wavelength are likely to be limited by detector read noise (see section 4) in 15 minutes, the maximum integration time in LEO. Under these circumstances, n^2 15 minute integrations must be combined in LEO to equal the sensitivity of a single $(n \times 15)$ minute integration in HEO. However, the benefits of longer continuous integration times in HEO may be offset by the higher cosmic ray rates.
- The high galactic latitude sky (latitude greater than 60°) can be observed at any time during the HEO mission, but is accessible only about 25% of the time in LEO. This is important because many of SIRTF's most important scientific objectives, including deep cosmological surveys, will require extended access to high latitudes.

Table 3: SIRTF Instrumentation Summary

Instrument	Principal Investigator	Characteristics
Infrared Array Camera (IRAC)	G. Fazio, Smithsonian Astrophysical Observatory	Wide field and diffraction limited imaging, $1.8 - 30\mu$m, using arrays with up to 256×256 pixels. Simultaneous viewing in three wavelength bands, selectable filters. Polarimetric capability.
Infrared Spectrometer (IRS)	J. Houck, Cornell University	Grating spectrometers, $2.5 - 200\mu$m, using two dimensional detector arrays. Resolving power from 100 to 2500. Low and high resolution options at most wavelengths.
Multiband Imaging Photometer for SIRTF (MIPS)	G. Rieke, University of Arizona	Background limited imaging and photometry, $3 - 200\mu$m, using small arrays with pixels sized for complete sampling of Airy disk. Wide field, high resolution imaging, $50 - 120\mu$m. Broadband photometry and mapping, $200 - 700\mu$m. Polarimetric capability.

3.4 Summary

The consensus of the SIRTF Study Office at Ames, the other NASA centers which participated in the Mission Options Study, and the SIRTF Science Working Group is that the high orbit offers significant scientific and engineering advantages for SIRTF. These advantages have been summarized above. As a result, the HEO mission has been adopted by NASA as the new baseline. This selection of an orbit optimized to maximize the scientific productivity of the mission, together with the dramatic advances in detector performance which are the subject of these proceedings, has brought the promise of SIRTF close to realization.

4 Instruments and Arrays

The properties of the three instruments under development for SIRTF are briefly summarized in Table 3. The Multiband Imaging Photometer and the Infrared Array Camera, using arrays with up to 256×256 pixels, will provide wide field and high resolution photometry, imaging, and surveying capabilities. Scientific objectives include imaging of objects ranging from comets to galaxies, mapping of extended regions of star formation, and deep surveys at SIRTF's limiting sensitivity. The Infrared Spectrograph will have low and moderate spectral resolution modes, using arrays to provide spectral imaging with > 10 spatial elements along the slit and > 50 spectral elements in the dispersion direction. Scientific objectives include studies of composition and physical conditions in planetary atmospheres, the interstellar medium, and external galaxies. The spectrograph will also be used to determine the nature of objects discovered in SIRTF's surveys, many of which will be too faint to be studied in detail from other platforms.

While SIRTF's larger size and superior imaging capabilities provide substantial improvements over IRAS and ISO, SIRTF's most dramatic gains will result from improved detector - and hence instrument - performance. Much of the SIRTF resources over the past several years have been devoted to detector and array development and characterization. This program has been carried out in a coordinated way among the instrument teams (Houck 1987), and the success of the activity

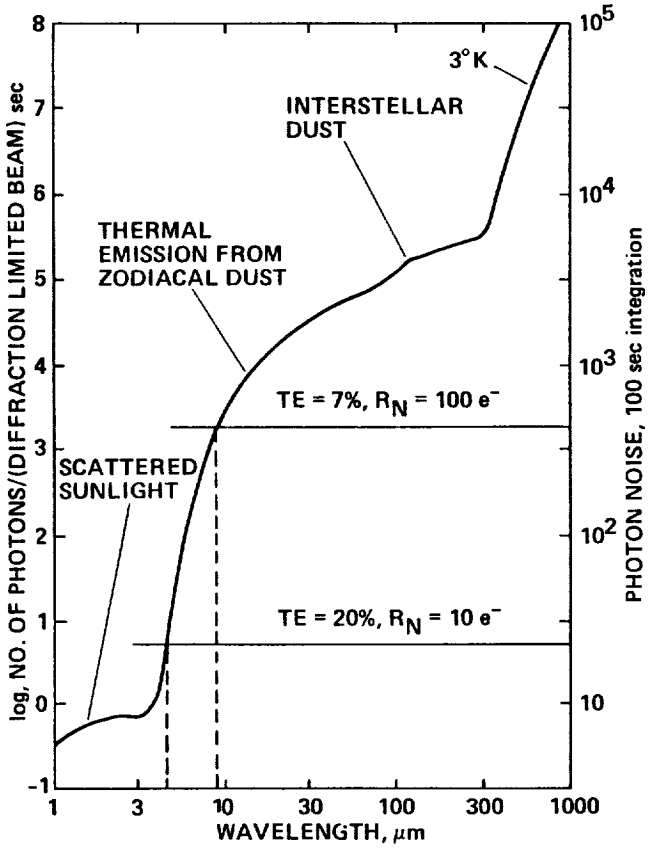

Figure 6: Natural infrared background vs. wavelength. The left vertical axis shows the photon arrival rate for spectral resolution $\lambda/\Delta\lambda = 100$ and pixel solid angle $\Omega = (2.4\lambda/D)^2$, typical for the SIRTF spectrograph, or equivalently for $\lambda/\Delta\lambda = 4.3$ and $\Omega = (\lambda/2D)^2$, typical for SIRTF photometry. The right hand axis gives the corresponding photon noise in 100 seconds of integration. The primary background contributor for each wavelength regime is indicated. Horizontal lines show the effective read noise (R_N) of instruments with stated values of transmission times quantum efficiency (TE). Background and read noise curves intersect at the wavelength where the two noise sources are equal.

is apparent from the many reports on the SIRTF detector work included in this volume. Except at wavelengths beyond 200μm where bolometers will be employed, SIRTF will use arrays of charge integrating detectors, characterized by a read noise, which is determined by the detector itself and by the readout or multiplexing circuit to which it is mated. Figure 6, adapted from Houck (1987), shows the background photon rate for combinations of bandwidth and field of view which represent typical observing conditions for the low spectral resolution spectrograph and high spatial resolution photometer modes. To achieve background limited performance in integration time t requires, approximately, that the read noise be less than the square root of the number of background photons detected during that time. For example, for the parameters relevant to Figure 6 and a 100 second integration, a read noise of 100 electrons will allow background limited operation at all wavelengths longer than 10 μm, as shown by the upper horizontal line.

Table 4 summarizes the materials and current performance of the arrays now under test for the various bands of the SIRTF instruments. The pixel formats shown are those anticipated to be used in flight. The test results are for detectors with non-optimized sizes and formats ranging from single elements to 58 $\times$ 62 arrays. The details of these developments are given elsewhere in this

Table 4: SIRTF Array Performance Status

Material	Format	Pixel Size (μm)	λ (μm)	Q.E.	R_N (e^-)	I_D (e^-/sec)	Responsivity(A/W)
HgCdTe	256×256	40	$1-5$	0.3	90	50	0.8
InSb	256×256	40	$1.8-5.3$	0.5	168	< 2.4	2.0
Si:Ga	128×128	100	$4-18$	0.3	50	90	14
Si:As BIBIB	128×128	100	$4-28$	$0.2-0.5$	77	8	68
Si:Sb	128×128	100	$14-30$	0.3	50	13	3.8
Ge:Be	2×25	500	$30-52$	$0.3-0.4$	75	< 100	12
Ge:Ga	32×32	500	$50-120$	0.2	25	500	39
Ge:Ga BIB	1×20	500	$50-190$	0.04		10^6-10^7	5
Ge:Ga (Stressed)	1×20	500	$120-200$	0.1	75	1000	100

volume. Meeting SIRTF's goals of achieving diffraction limited imaging with sensitivity limited by the natural astrophysical background is particularly challenging at the shortest wavelengths. Large detector arrays are required to fully sample the field of view, and the extremely low background level at the 3μm cosmic "window" demands detectors with correspondingly low read noise and dark current which are capable of long integration times. Basic characterization of detectors for this band is still underway. But the goal of background limited performance is in hand across most of SIRTF's spectral band. The emphasis in the detector development program is shifting to include more specialized issues such as linearity, hysteresis, and susceptibility to charged particles.

The scientific impact of the use of arrays on SIRTF can be illustrated by the following example. An important scientific objective for SIRTF will be to search in various astrophysical environments for "brown dwarf" stars - stars with mass $< 0.08 M_\odot$ which are unable to sustain nuclear burning processes but which may be visible in the infrared through the faint glow of their escaping internal heat. One region to search for brown dwarfs is in a star cluster such as the Pleiades, which contains numerous recently formed low mass stars. Based on the currently projected performance of the baseline 58 x 62 pixel arrays in the 5-15μm region, SIRTF in 3 days can map the entire central square degree of the Pleiades to sufficient depth to identify all brown dwarfs with masses greater than $0.01 M_\odot$. Extrapolation based on the recent results of Stauffer *et al.* suggests that these maps would reveal > 50 such objects. Thus three days of observation would produce definite results illuminating such fundamental questions as: the nature of the "missing mass" in the galactic disk; the formation of low mass stars and the shape of the faint end of the main sequence; and the behavior of helium-hydrogen mixtures at high densities. Even at SIRTF's background-limited sensitivity, this important investigation would take a prohibitively long time without the large number of detectors provided by the large array.

5 Summary and Conclusions

Figure 7 shows the expected performance of SIRTF, compared to that of other facilities for infrared astronomy and to the predicted fluxes of selected astronomical targets. One sigma sensitivity limits are shown for broadband observations with the currently available large groundbased and airborne telescopes and for the IRAS survey. For SIRTF, one sigma sensitivity for a point source is shown for broadband imaging and for moderate resolution (R = 1000) spectroscopy. This figure does not properly reflect the additional quantitative and qualitative gains which will result from the use of large detector arrays on SIRTF, as illustrated in the previous paragraph. Further gains will come from SIRTF's long lifetime, total freedom from atmospheric absorption, high photometric and

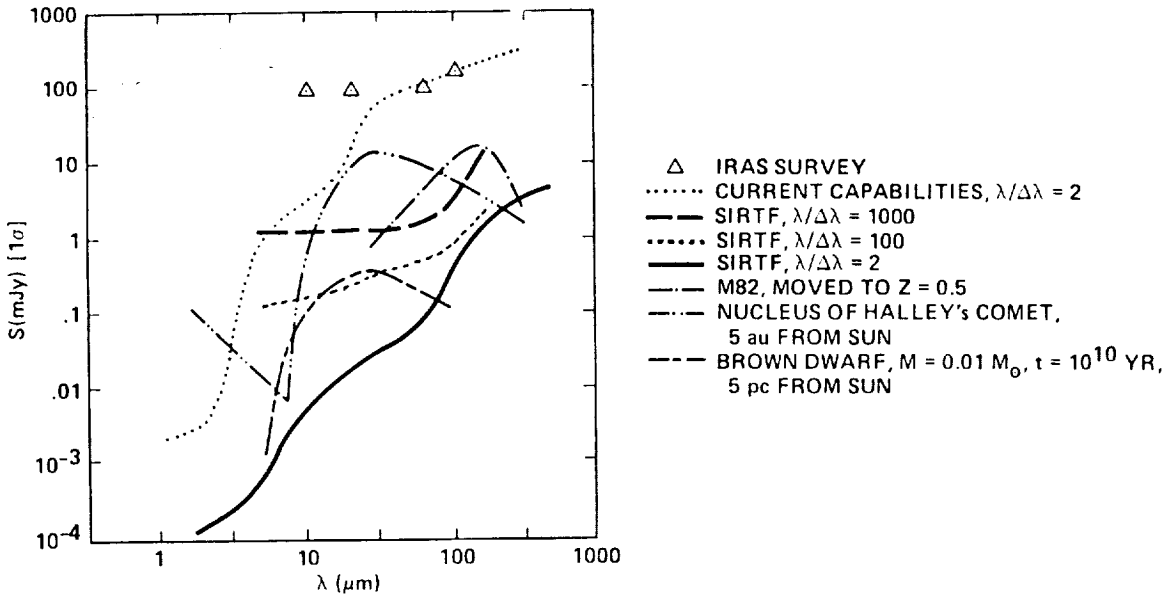

Figure 7: Comparison of background-limited sensitivity limits for SIRTF in imaging and spectroscopic modes (500 sec. integration), IRAS (survey mode), and current groundbased and airborne telescopes (1 hr.). Also shown are expected fluxes for the nucleus of Halley's comet, M82 at a redshift of 0.5, and a 0.01 $M_\odot$ brown dwarf at 5 pc.

radiometric stability, broad and simultaneous wavelength coverage, and speed of data acquisition. Together, these factors will make SIRTF an extremely powerful instrument for the study of a very broad range of solar system, galactic, and extragalactic problems.

Figure 7 illustrates that the faintest IRAS sources cannot even be detected with existing instruments, but that SIRTF will be able to take spectra of them easily. SIRTF will allow the first detailed study of the infrared properties of objects as diverse as cometary nuclei and distant galaxies. Predicted but unseen phenomena such as brown dwarfs will come within the range of SIRTF's capabilities. But the most exciting objects SIRTF will study are not shown in Figure 7, because they will be the unexpected discoveries that inevitably follow such major gains in sensitivity.

References

Gatley, I., DePoy, D.L., and Fowler, A.M. 1988, *Science* **242**, p. 1264.

Houck, J.R. 1987, in *Infrared Astronomy with Arrays*, eds. C.G. Wynn-Williams and E.E. Becklin, (Honolulu: University of Hawaii), p. 108.

Kessler, M.F. 1986, *Proc. SPIE* **589**, p. 201.

Matsumoto, T. *et al.* 1988, *Ap.J.* **329**, p. 567.

Neugebauer, G. *et al.* 1984, *Science* **224**, p. 14.

Ramos, R., Hing, S.M., Leidich, C.A., Fazio, G., Houck, J.R., and Rieke, G. 1988, *Proc. SPIE* **973**, p. 2.

Rieke, G.H., Werner, M.W., Thompson, R.I., Becklin, E.E., Hoffmann, W.F., Houck, J.R., Low, F.J., Stein, W.A., and Witteborn, F.C. 1986, *Science* **231**, 807.

Stauffer, J., Hamilton, D., Probst, R., Rieke, G., and Mateo, M. 1989, *Ap.J.(Letters)*, submitted.

Werner, M.W., Murphy, J.P., Witteborn, F.C., and Wiltsee, C.B. 1986, *Proc. SPIE* **589**, p. 210.

N90-21346

SOFIA

STRATOSPHERIC OBSERVATORY FOR INFRARED ASTRONOMY

E. F. ERICKSON, NASA Ames Research Center

SOFIA will be a three meter class telescope operating in a Boeing 747 astronomers routine access to infrared wavelengths unavailable from the ground, and with the means to observe transient astronomical events from anywhere in the world. The concept is based on 15 years of experience with NASA's Kuiper Airborne Observatory (KAO), which SOFIA will replace in the mid 1990's. SOFIA's wavelength range covers nearly four decades of the electromagnetic spectrum: from the visible, throughout the infrared and submillimeter, to the microwave region. Relative to the KAO, SOFIA will be roughly ten times more sensitive for compact sources, enabling observations of fainter objects and measurements at higher spectral resolution. Also, it will have three times the angular resolving power for wavelengths greater than 30 microns, permitting more detailed imaging at far infrared wavelengths.

The infrared spectral regime encompasses a multitude of rich and varied physical processes and is uniquely suited for study of the cosmic birth on all scales. SOFIA's high spectral and spatial resolution will exploit and extend the scientific legacy left by IRAS (the Infrared Astronomical Satellite) and will complement the enormous sensitivity for imaging and moderate resolution spectroscopy to be furnished by SIRTF, the Space Infrared Telescope Facility. Questions that SOFIA users would address include:

* Interstellar cloud dynamics and star formation in our galaxy: Why and how do galactic clouds form stars? How important are magnetic fields and rotation in this process?

* Proto-planetary disks and planet formation in nearby star systems: How common are solar-systems? Under what conditions are they created?

* Origin and evolution of biogenic materials in the interstellar medium and in proto-planetary disks: What environments are hospitable to pre-biotic molecules and compounds?

* Comets, planet atmospheres and rings in our solar system: How did our solar-system evolve? What was the composition of the solar nebula?

* Star formation, dynamics and chemical content of other galaxies: How different are other galaxies? Why do some exhibit extraordinarily large infrared luminosities? What is the origin of this luminosity?

* The dynamic activity in the center of our own galaxy: What powers the highly luminous phenomena hidden at the center of the Milky Way - a compact star cluster or a black hole? Is this region similar to the "Active Galactic Nuclei" seen in some other galaxies?

SOFIA is currently being studied jointly by NASA and the German Science Ministry (BMFT). NASA would provide and modify the aircraft, and West Germany would develop the telescope assembly. As can be seen from Figure 1, the SOFIA telescope is much larger relative to the B747 than the KAO telescope is to the Lockheed C-141. This means that the new telescope requires considerably more sophisticated technology.

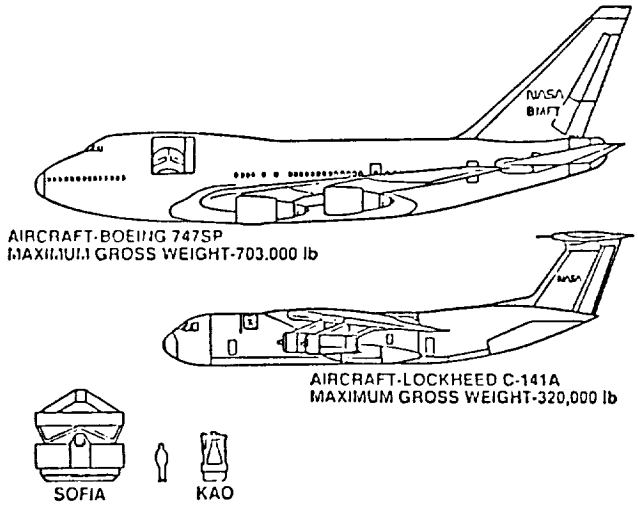

Figure 1: Comparison of SOFIA and KAO.

Nevertheless the SOFIA telescope concept, shown in Figure 2, borrows heavily from the KAO heritage. The optical system is supported on vibration isolators and an air bearing, and is expected to achieve sub-arcsecond pointing stability, as does the similar KAO design. Light weight is achieved by use of a carbon fiber structure and a thin meniscus mirror. The telescope operates in an open port cavity, while the experimenter has continuous access to his focal plane instrument.

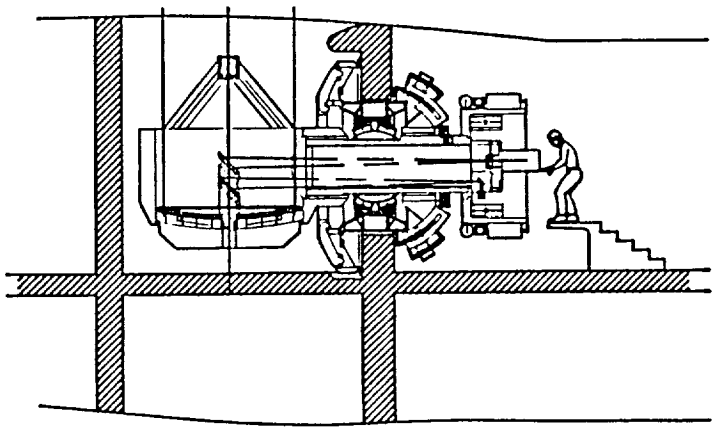

Figure 2: SOFIA Telescope Concept

NASA will operate SOFIA with support from the BMFT as an international facility for astronomy throughout an estimated 20 year lifetime. It will provide 120, 8 hour flight opportunities per year for approximately 40 principal investigator teams, selected by annual peer review.

Evolution of state-of-the-art focal plane instrumentation is a key aspect of the SOFIA concept. Roughly half of the investigator teams will provide the observatory with a wide variety of specialized instruments including array cameras, polarimeters, and several types of spectrometers. Major improvements can be expected in both conventional infrared detectors and heterodyne receivers which will extend the scientific productivity of SOFIA. Far infrared detector array technology, although currently in a primitive state, has excellent potential for airborne astronomy applications. It is imortant to note that the relatively high backgrounds may imply considerably different requirements on detector systems than for space-based cryogenic telescopes. In particular, higher dark currents can often be tolerated, but high quantum efficiencies are extremely desireable.

It is clear that SOFIA, as a unique astronomical observatory, as an educational facility for the science community, and as a stimulus for the development of new focal plane instrument technologies, will have a major influence on astronomy well into the next century.

Laboratory Characterization of Direct Readout Si:Sb and Si:Ga Infrared Detector Arrays

Mark E. McKelvey, Nicolas N. Moss, Robert E. McMurray, Jr.,
John A. Estrada, John H. Goebel, Craig R. McCreight
NASA Ames Research Center, Moffett Field, CA 94035

Maureen L. Savage
Sterling Software Inc., 1121 San Antonio Road, Palo Alto, CA 94303

Frank Junga, Thomas Whittemore
Lockheed Research Laboratory, 3251 Hanover Street, Palo Alto, CA 94304

Abstract

Highlights of recent results obtained at Ames Research Center in performance evaluations of infrared detector arrays are presented. Antimony- and gallium-doped silicon direct readout 58x62 element hybrid devices from Ames' ongoing detector technology development program are described. The observed characteristics meet most of the performance goals specified by the SIRTF instrument teams and compare favorably with the best performance reported for discrete non-integrating extrinsic silicon detectors. Initial results of radiation-environment testing are reported, and non-ideal behavior demonstrated by these test devices is discussed.

Introduction

Space-based infrared (IR) astronomy projects such as NASA's Space Infrared Telescope Facility (SIRTF) and Large Deployable Reflector (LDR) and the European Space Agency's Infrared Space Observatory (ISO) will require significant advances in detector technology if they are to realize the full potential offered by on-orbit observing conditions. A continuing technology development program has been underway at Ames Research Center to help achieve sufficient improvements in the state of the art to allow space telescope IR observations to achieve sensitivity limited only by the natural background flux.

As part of this work, evaluations have been carried out in some detail on two 58x62 element IR detector array types based on the Hughes Aircraft Company's CRC-228 direct readout multiplexer[1,2]. Si:Sb and Si:Ga detector substrates have been indium-bump-bonded to the CRC-228 to produce high performance hybrid arrays. The Infrared Array Camera[3] (IRAC) for SIRTF has specified these devices as baseline candidate technologies for two of its wavelength bands.

A photograph of one of the arrays is shown in Fig. 1, and a schematic of the array unit cell is shown in Fig. 2. Each unit cell contributes one detector element to each of the two parallel output channels when its unique address is sent to the on-chip decoder circuit. The unit cell is repeated 58x31 times to make up the full array of 3596 pixels. A software-selectable reset pulse can be applied during the address period to reset the integration nodes in a unit cell to a known reference level. Alternately, a non-destructive read can be performed, allowing several measurements to be made of the charge packet as it builds up during the integration period.

In the following sections, recent measurements of the basic performance of these devices will be highlighted, radiation testing procedures will be outlined, and limitations of these arrays will be briefly discussed.

Performance

Table 1 contains a summary of the various figures of merit obtained to date on the two array types tested. The read noise figure for the Si:Ga array is superior to that listed for the Si:Sb type, but this is largely an artifact of the more recent (and improved) test methods used in the evaluation of the gallium-doped array. Because the Si:Ga array was loaned to us for a limited time by NASA's Goddard Space Flight Center[4], it was the device most recently tested. Since the return of the Si:Ga array, our attention has shifted back to the Si:Sb device, and upcoming tests are expected to show read noise comparable to that of the Si:Ga array.

ORIGINAL PAGE
BLACK AND WHITE PHOTOGRAPH

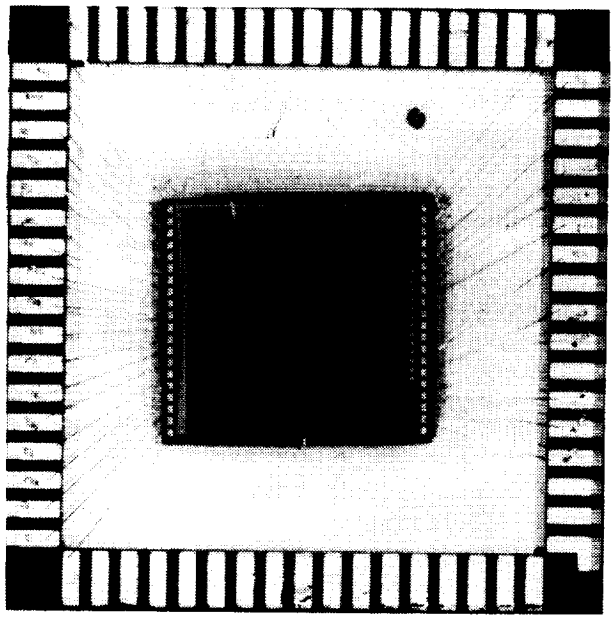

Figure 1. 58x62 DRO infrared detector array.

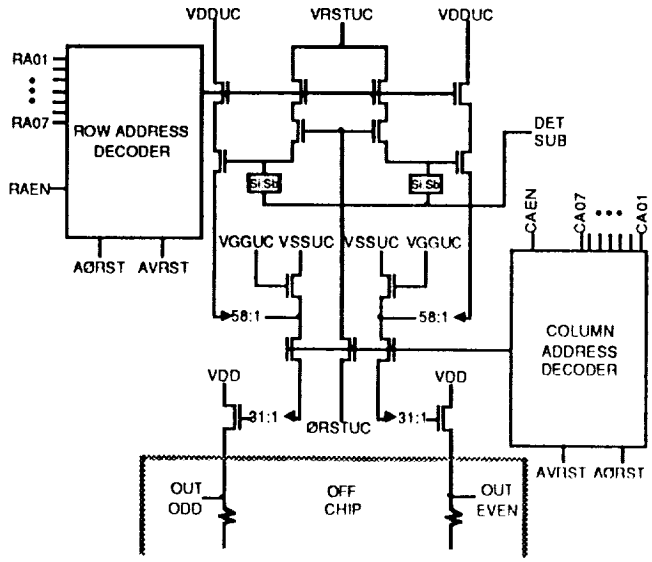

Figure 2. Schematic diagram of multiplexer unit cell.

Characteristic	Si:Sb		Si:Ga	Units	Conditions
General					
Dopant Concentration	4		40(?)	10^{15} atoms/cm^3	
Format		58 x 62		rows x columns	
Pixel size		75		μm	Square
Pixel Spacing		75		μm	Centers
Wavelength range	15 - 31		4 - 18	μm	
Test background	0.17 - 18		0.30 - 28	10^4 ph/s	Corrected to
	0.30 - 32		0.54 - 50	10^8 ph/cm^{2}s	response peak
Performance					
Responsivity	3.8		12	A/W	8 K, 2V bias (70V Si:Ga)
Read noise	220		95	μVrms	q_b=1.8 x 10^5 ph/s
	100		53	rms e$^-$	(2.8 x 10^5 ph/s Si:Ga)
NEP	2.7		0.24	10^{-17} W/√Hz	t_i = .204 s
Gη product	0.17		0.99(?)		"
Dark current	13		450	e$^-$/s	8 K, 1 V bias (7K,70V Si:Ga)
	3.2		75	aA	q_b = zilch
Input Capacitance	0.06		0.07	pF	Measured
Well Capacity	>2		>5	10^5 e$^-$	
Max. integration time	>10^4		>10^3	s	8 K, dark current limited
Operating temperature		5 - 12		K	
Uniformity	15		8	%	1σ/mean

Table 1. 58x62 DRO array test summary.

The performance summarized in Table 1 compares well with IRAC goals in most areas, and indeed with the best reported non-integrating discrete detector performance. The one area shown that is out of the IRAC specification is the dark current measured for the Si:Ga array at 450 e$^-$/s. This is well above the specified 10 e$^-$/s, but still is low enough to give a dark-

current-limited maximum integration time (t_i) of $>10^3$ s. Actually, the cosmic ray background flux, rather than the dark current, is likely to limit t_i on SIRTF.

Pixel-to-pixel uniformity is good in both array types with variations in responsivity of 8% for the Si:Ga array and 15% for the Si:Sb array (defined as standard deviation/mean). These levels produce obvious nonuniformities in the raw signal output, but they can be corrected without difficulty in post-processing.

The dependence of Si:Ga response and noise on the applied bias voltage is shown in Fig. 3. Responsivity is nearly proportional to applied bias between 20 V and 60 V, and becomes superlinear at higher biases. The read noise is essentially independent of bias below 70 V, but noise behavior is erratic at higher applied voltages. A definite impact-ionizing breakdown condition is not achieved in the Si:Ga below 95 V (the maximum available in our test setup), but low noise performance is not repeatably obtainable above 70 V (1400 V/cm). At 70 V applied bias and a temperature of 8 K, peak responsivity in the Si:Ga array is 12 A/W and read noise is 53 e^- rms. This corresponds to a read-noise limited NEP of 2.4 x 10^{-18} W/$\sqrt{\text{Hz}}$ in a 217 ms integration period. The best measured NEP for the Si:Sb array is an order of magnitude higher, but this should improve by a factor of two when its read noise is measured in our improved test set.

An unexpected variation in Si:Ga responsivity with operating temperature was observed and is shown in Fig. 4. A steep decrease in responsivity with increasing temperature above 7 K was noticed near the end of our Si:Ga tests. Improved mobility due to a decrease in charged impurity scattering should occur as temperature is increased, which should create a modest increase in responsivity at higher operating temperatures. This trend is observed for the Si:Sb array to temperatures >12 K, and in the Si:Ga array for temperatures up to 7 K. The curious drop in Si:Ga response above 7 K is not understood, but could be explained by the presence of a very shallow energy level (~ few meV) that contributes long-wavelength photoconductivity at low temperatures but is thermally depopulated as temperature is increased. An attempt was made to

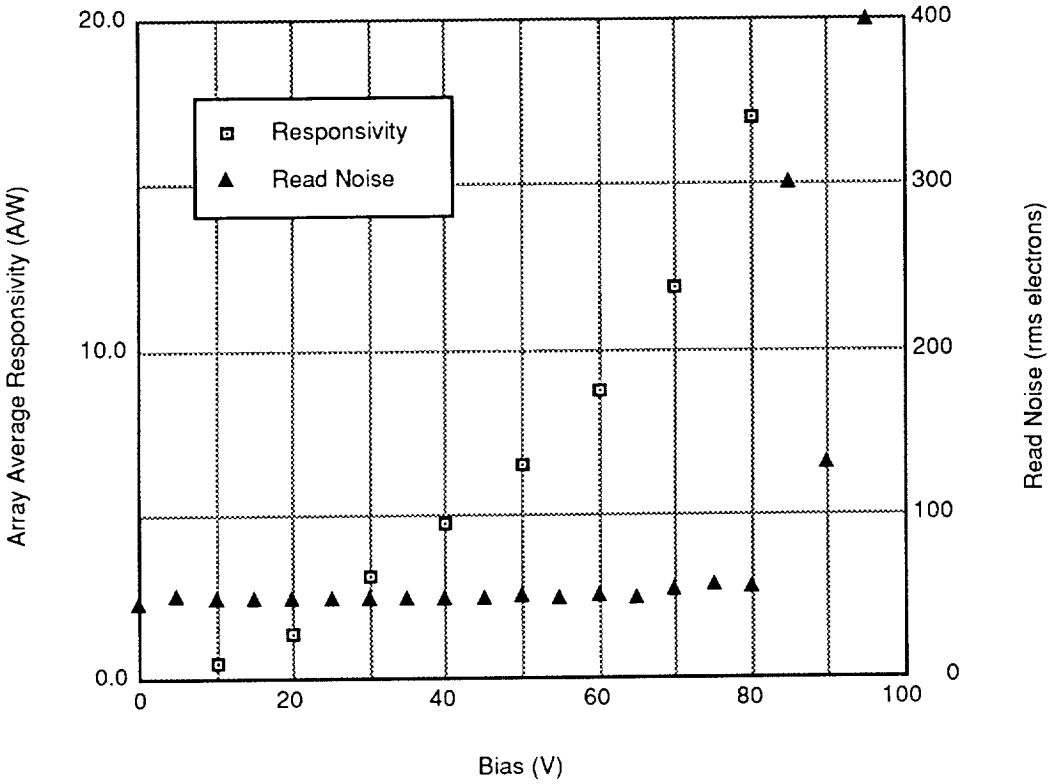

Figure 3. Si:Ga array responsivity and read noise vs. applied bias voltage. Background = 3 x 10^3 ph/pixel-s. T = 8 K. Integration time = 217 ms.

demonstrate long wavelength photoconductivity in the Si:Ga array by blocking wavelengths shorter than 20 μm, but no photoresponse was observed in this test. This does not rule out the shallow levels, since the effect may depend on the spectral quality of the incident radiation (particularly if the supposed level was an excited state of the Ga dopant).

The presence of very shallow levels may also be suggested by the dependence of Si:Ga dark current on temperature, shown in Fig. 5. The activation energy obtained from this Arrhenius plot is on the order of a few meV, much less than the 72 meV expected if thermal activation of the Ga impurity controlled the dark current. The two regimes evident in the plot differ in activation energy by nearly a factor of two. This might be consistent with a single level and a change from diffusion- to generation-recombination-limited carrier transport.

A systematic determination of the cause of the responsivity decrease above 7 K and the small dark current activation energy was not possible within the time available. If long wavelength photoconductivity is contributing to the responsivity below 7 K, the quoted responsivity is in error. A careful measurement of spectral response would be required before detector material displaying this behavior could be used on a space telescope mission.

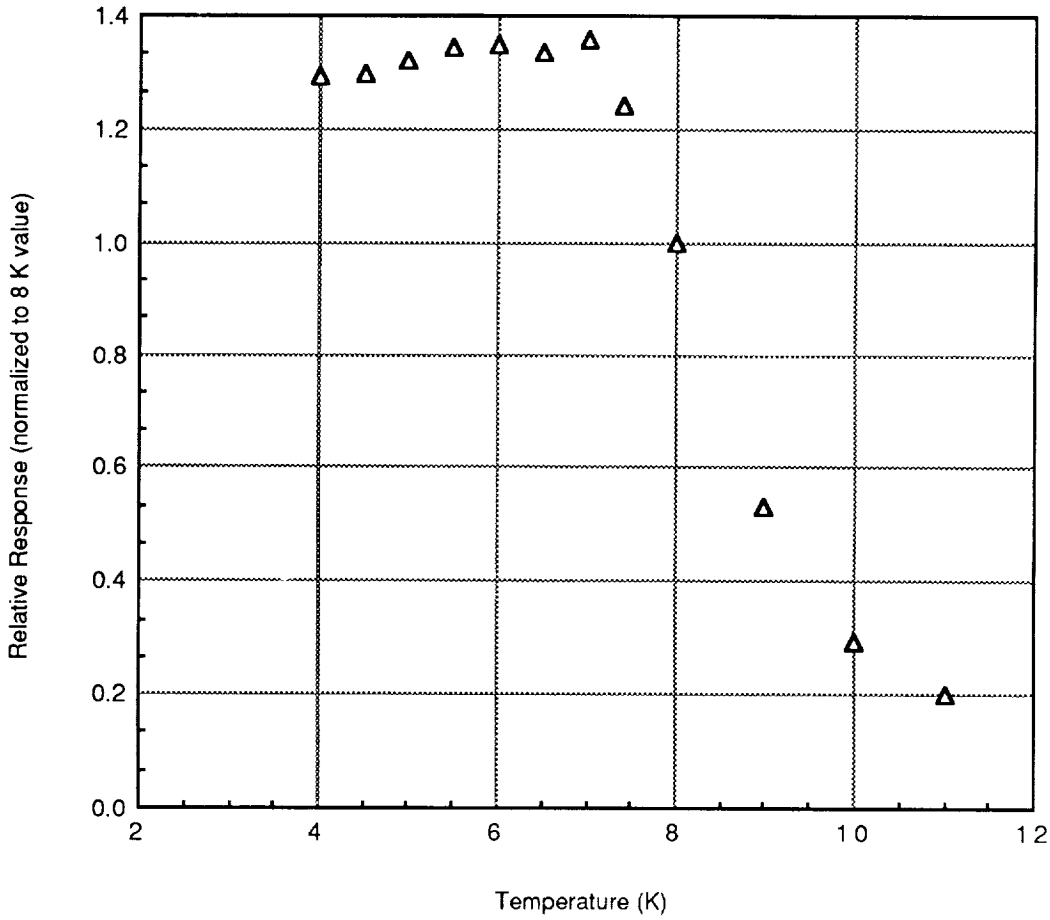

Figure 4. Si:Ga array relative responsivity vs. temperature, normalized to 8 K value (12 A/W). Background = 4 x 10^3 ph/pixel-s. Integration time = 217 ms.

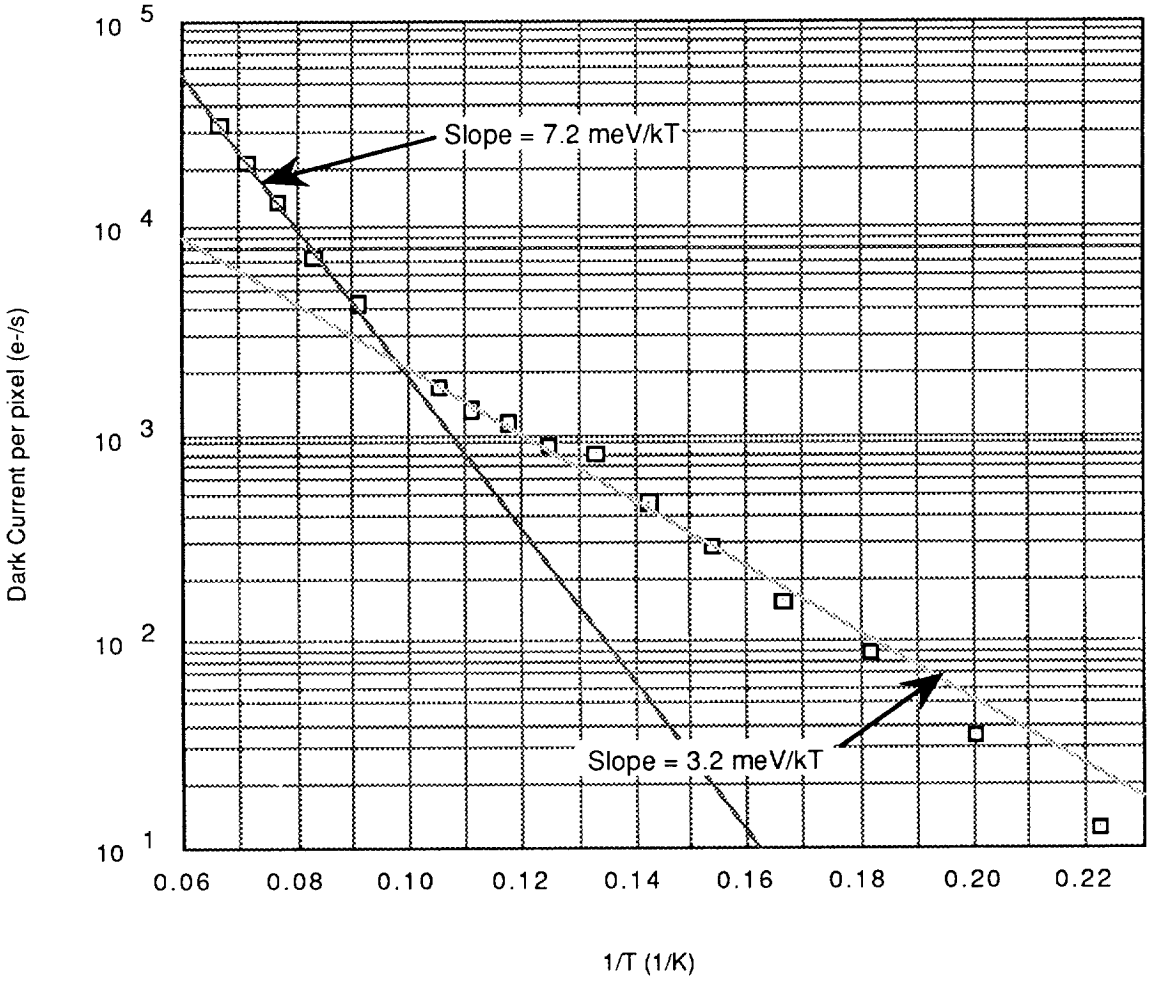

Figure 5. Si:Ga array dark current vs. temperature.

Radiation Testing

Space telescope platforms will experience a cosmic ray background composed primarily of high energy protons. The level of this background will depend on the orbit chosen, but representative predictions are for a proton flux of about 4 p^+/cm^2-s over most of a high (70,000 km) orbit[5]. "Pockets" of higher flux levels will be encountered with rates increased by up to two orders of magnitude.

Laboratory detector testing in an ionizing radiation environment is required to understand what changes in performance characteristics will occur and what strategies can be used to maintain the best possible radiometric calibration. To this end, tests of these detector arrays in γ-ray and proton environments have been initiated and constitute a major focus for near-term testing at Ames.

Although γ-rays constitute only a fraction of the on-orbit ionizing radiation environment, the convenience of small radioactive γ-sources that can be safely used in laboratory tests makes them attractive for preliminary investigations. ^{137}Cs, ^{241}Am, and ^{55}Fe sources of activities up to 10 mCi have been mounted inside our test cryostat to yield dose rates up to 0.3

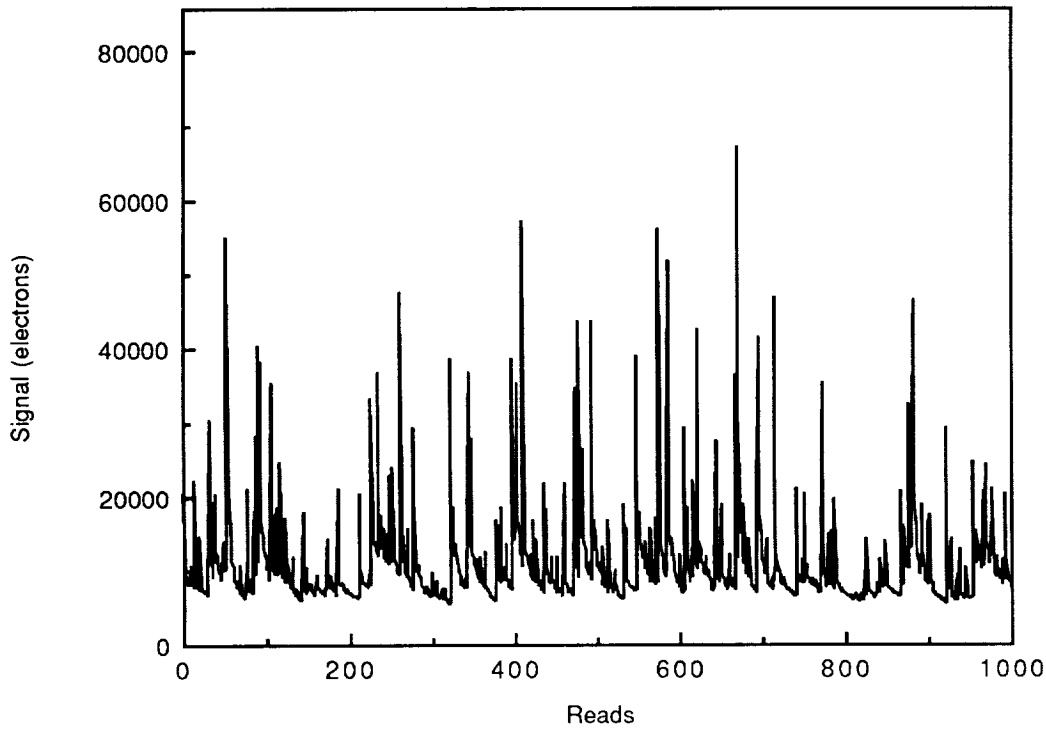

Figure 6. Si:Sb response in γ-environment. ^{137}Cs (660 keV) irradiation. Read rate = 60 Hz. T = 8 K. Bias = 2 V.

rad(Si)/hr in the detector arrays. Although these dose rates are much lower than the worst on-orbit conditions, they do produce doses sufficient to significantly change detector performance characteristics. Experimentation with different annealing schemes to recover the pre-irradiation calibration is also possible in our in-house tests.

Figs. 6 and 7 are representative of data gathered in initial radiation testing of these devices. Fig. 6 is a time series of a single Si:Sb pixel output under ^{137}Cs γ-ray bombardment at a calculated dose rate of 0.2 rad(Si)/hr. Fig. 7 is a pulse height distribution of the same data, showing a peak at about 5,000 carriers/read and a characteristic pseudo-exponential tail. Some hits produce in excess of 60,000 carriers. While these events produce only a fraction of the number of carriers associated with high energy proton interactions, they are sufficient to cause shifts in charge distribution leading to changes in responsivity and perhaps dark current, although the latter has not been demonstrated in these devices.

Such a shift in responsivity is shown in Fig. 8. The lower curve in Fig. 8 shows the change in Si:Ga array average responsivity during the deposition of about 1 rad(Si) at an IR background of about 5 x 10^4 ph pix^{-1} s^{-1} and a temperature of 8 K. After a six-hour irradiation under these conditions responsivity had increased by about 7 %. Once the Cs source was removed, a natural recovery began with a time constant on the order of several hours. Actual astronomical observations would clearly require some kind of intervention to restore the photometric calibration of the device for efficient use of allotted observing time. Boosting the bias level beyond breakdown to flood the material with free carriers has been shown to remove the radiation-induced responsivity shift in other devices. However, this did not occur for the maximum 95 V bias (1900 V/cm) our test system could supply to the Si:Ga array. A short-duration thermal cycle to 20 K did recover the initial performance, and could be reasonably performed on-orbit with a properly designed array mount.

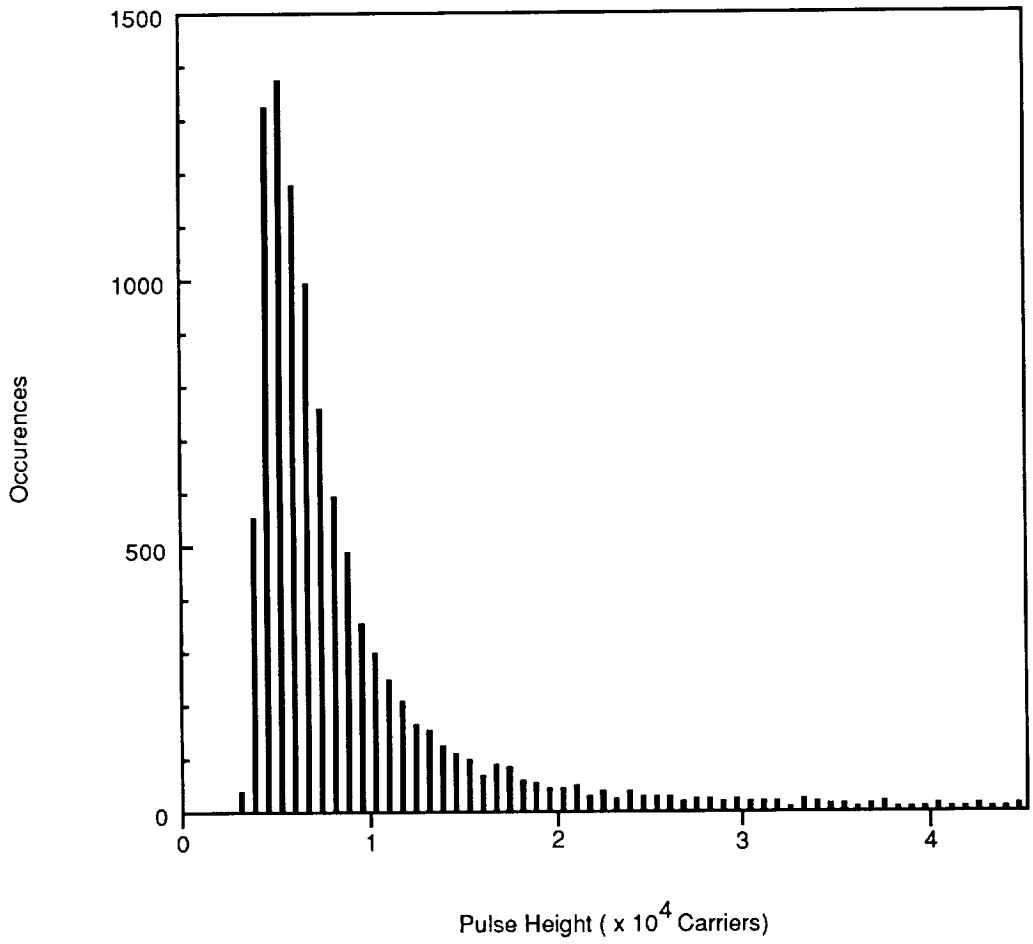

Figure 7. Si:Sb γ-ray pulse height distribution. ^{137}Cs (660 keV) irradiation. T = 8 K. 2k total reads.

The upper curve in Fig. 8 shows results of a similar irradiation of the Si:Sb array. Here the responsivity shift is much larger, showing a near doubling at an accumulated dose of 1 rad(Si) and a similarly long natural recovery period. The difference in the magnitude of responsivity change between the Si:Sb array and its Si:Ga counterpart is likely due to the higher level of impurity compensation (through the unintended presence of boron) in the n-type Sb material. Actual shifts in response depend on dose rate and IR background level, and perhaps on applied bias and operating temperature. Mapping out the effects of these and other factors will be carried out in future work.

Because the on-orbit environment is primarily composed of high energy protons, a better simulation can be made with a proton source such as a particle accelerator. Arrangements have been made in conjunction with Lockheed Research Laboratory to study array performance under proton bombardment at the 74-inch Crocker Cyclotron on the campus of the University of California at Davis. Flux levels down to 5 $p^+cm^{-2}s^{-1}$ at energies up to 67 MeV can be obtained, and tests in various simulated space telescope environments are to begin shortly.

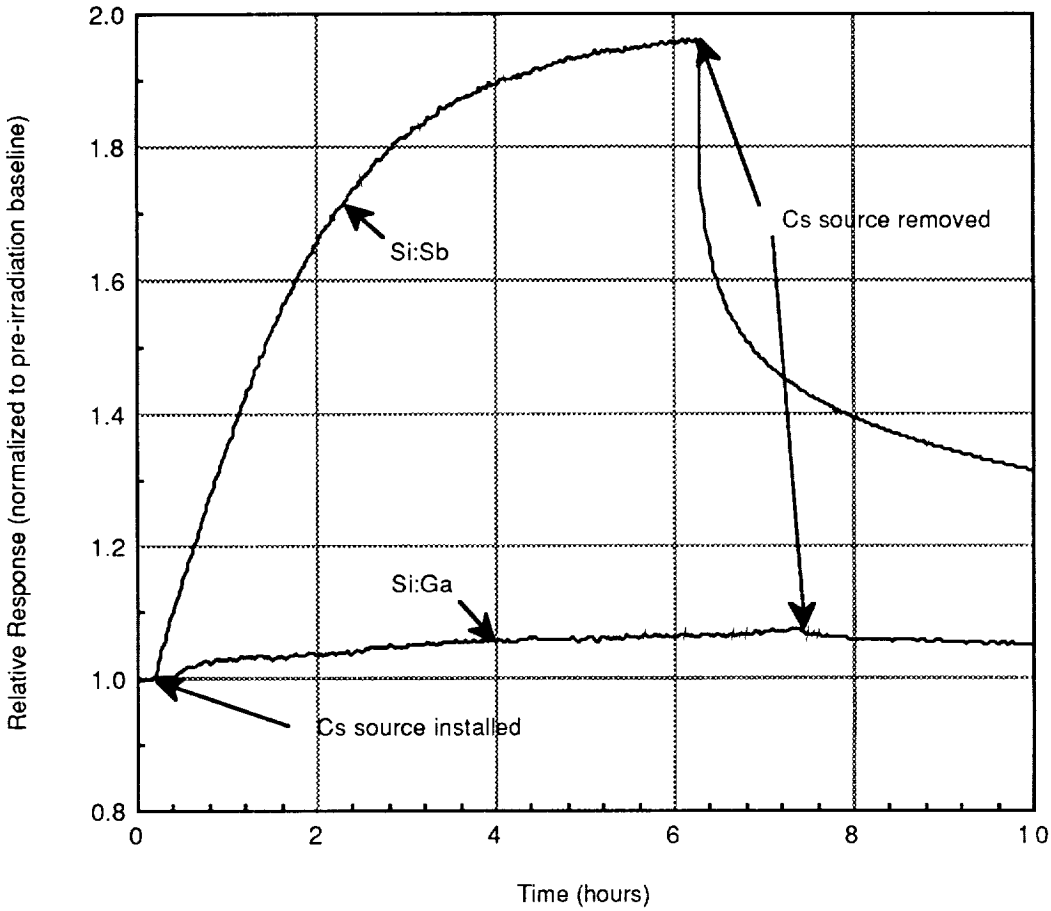

Figure 8. Si:Ga and Si:Sb responsivity under γ-radiation. ^{137}Cs (660 keV) source, 0.183 rad(Si)/hr. T = 8 K. Background = (a) 4.8 x 10^4 and (b) 9.0 x 10^3 ph/pix-s.

Problem Areas

While these arrays have generally delivered a high level of performance, some problem areas have become apparent. As bulk photoconductors, these arrays have shown some of the anomalous behavior characteristics long associated with this type of detector[6]. Multiple time constants, hook anomalies, and memory effects have been observed in these devices and represent serious limitations in astronomical applications. Fig. 9 shows the time development of the output of a single Si:Ga pixel under various step changes in incident IR flux. The time constant problems worsen as the flux level is decreased, and this may be a critical obstacle in the ultra-low background conditions anticipated in space telescope applications. Materials processing, detector design, or other operational improvements may lessen the severity of these non-ideal characteristics. Determining whether such techniques can sufficiently mitigate these concerns is a major objective of the Ames detector development program.

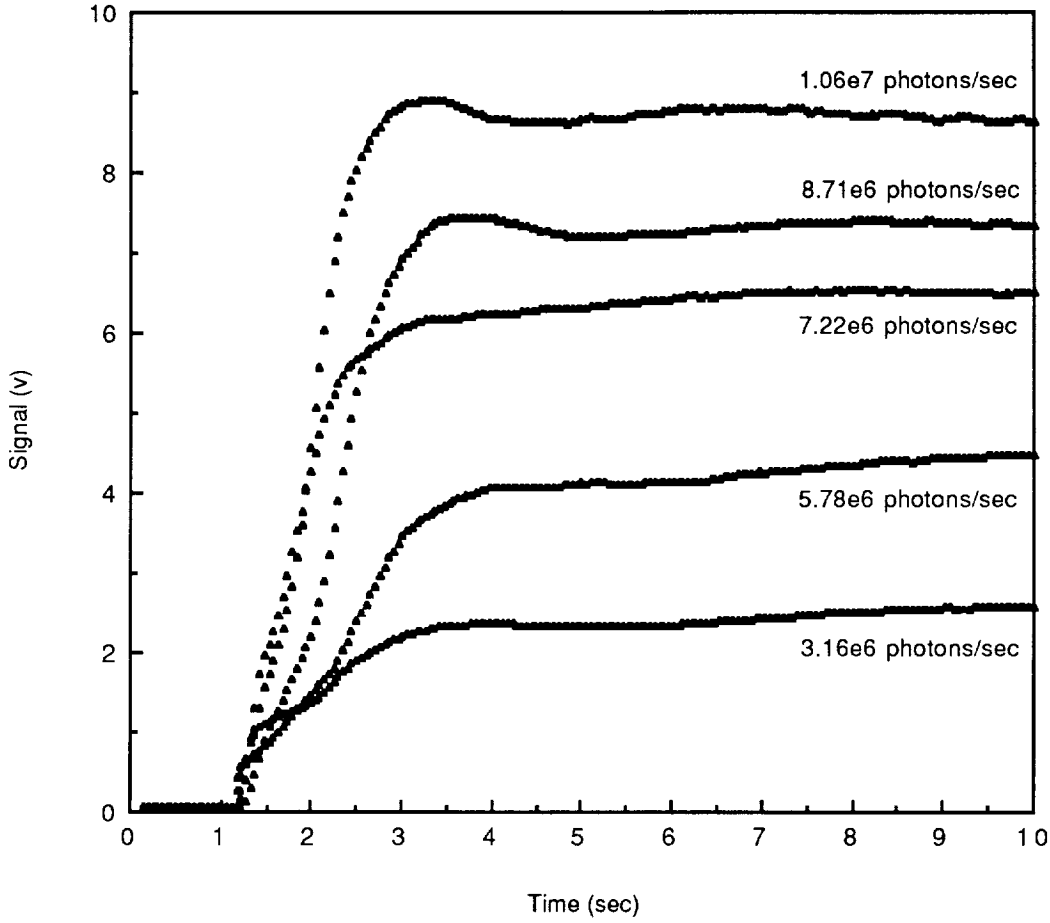

Figure 9. Si:Ga single pixel response to step changes in IR flux level. Gain = 40. Zero signal = cold slide in field of view. T = 8 K.

Summary

Characterization of Si:Sb and Si:Ga 58x62 direct readout IR detector arrays has been carried out in considerable detail. These devices have shown excellent performance characteristics overall. They meet or exceed most IRAC specifications for detector figures of merit, with the exception of certain transient response criteria. The performance demonstrated by these arrays also compares well with discrete detectors in the same wavelength range. Radiation environment testing has shown shifts in responsivity after γ-ray bombardment as expected. These shifts vary in magnitude with incident IR background and other parameters. Thermal annealing has proven effective in restoring pre-irradiation performance levels.

The observed slow transient behavior may prove to be a serious limitation in space astronomical applications. These anomalies are familiar from previous experience with bulk photoconductors. The Infrared Astronomical Satellite (IRAS) successfully used bulk photoconductors at low background, and improvements in materials processing and operating techniques may be able to surmount the present difficulties for applications such as SIRTF. Alternatively, other detector technologies (such as impurity band conduction (IBC) detectors[7]) may prove more suitable for these missions.

Much work remains before a final determination of the suitability of these array types can be made. Future test work is planned to further quantify the transient characteristics of these devices and to add to the (inadequate) existing database on their performance in a radiation environment.

---

[1]McKelvey, M. E. *et al.*, *Proc. Soc. Photo-Opt. Instrum. Eng.* **868**, 73 (1987).
[2]Orias, G. and Campbell, D., NASA Contractor Report 177,446 (1986).
[3]G. G. Fazio *et al.*, *Proc. Soc. Photo-Opt. Instrum. Eng.* **589**, 229 (1986).
[4]G. Lamb *et al.*, in Infrared Astronomy with Arrays (C. G. Wynn-Williams and E. E. Becklin, eds.), University of Hawaii, 144 (1987).
[5]E. G. Stassinopolous, NASA SP-3054 (1970).
[6]Zachor, A. S., and Huppi, E. R., Appl. Opt. **20**, 1000 (1981).
[7]T. Herter, C. E. Fuller, G. E. Gull, and Houck, J. R., in Infrared Astronomy with Arrays (C. G. Wynn-Williams and E. E. Becklin, eds.), University of Hawaii, 128 (1987).

N90-21348

HgCdTe 256x256 MWIR FPA

Kadri Vural, Michael Blessinger and Jenkon Chen
Rockwell International Science Center
Thousand Oaks, CA 91360

William Kleinhans
Valley Oak Semiconductor
Westlake Village, CA 91362

Abstract

We have developed a HgCdTe 256x256 focal plane array (FPA) which operates in the 1-5 μm band. This is presently the largest demonstrated HgCdTe FPA. The detector material is HgCdTe on sapphire (PACE-1 technology) which has a low thermal expansion mismatch with silicon. The multiplexer is a CMOS FET-switch device processed through a commercial silicon foundry. The multiplexer input is direct injection and the charge capacity is about $2x10^7$ electrons. The kTC limited read noise is 400 electrons. We have demonstrated high background imaging using the device. The broadband quantum efficiency is measured to be 59%. Dark currents less than 0.1 pA have been measured at 77K for detectors processed on PACE-1 material with 4.9 μm cutoff. The dark currents decrease as the temperature is lowered and we are presently studying the T<77K characteristics. The interconnect yield is >95%. The devices are available for astronomical applications.

Material

The detector array material is HgCdTe on sapphire called PACE-1 (Producible Alternative to CdTe for Epitaxy). A layer of CdTe is deposited onto the sapphire first using vapor phase epitaxy. The HgCdTe is grown by liquid phase epitaxy. The sapphire substrate is strong, durable and has large area (2 inch diameter wafer) which is crucial for large arrays such as a 256x256. The sapphire is transparent up to 5.5 μm and this technology is used for the 1.0-5.5 μm band. For longer wavelengths (8-12 μm) we are developing HgCdTe on GaAs (PACE-2) technology.

Detector Array

The photovoltaic detectors are planar structures formed by ion implantation. After passivation indium columns are deposited for hybridization to the multiplexer. The detector unit cell size is 40 μm x 40 μm. Typically over 90% fill factor is obtained with less than 2% crosstalk.

We have characterized the detectors at 77K. The R_oA is typically 10^6 to 10^7 Ω-cm^2 and the dark current is less than 0.1 pA for 100 mV reverse bias. The dark currents decrease further as the temperature is lowered. George Rieke, University of Arizona,

measured 30-60 e-/s at 30-35K for detectors with similar cutoff but larger area. These detectors have not been optimized for low temperature (<77K) operation; with further work the dark current can be reduced to lower levels.

Multiplexer

The multiplexer has a CMOS FET-switch architecture and is processed at a commercial silicon foundry. A schematic is shown in Figure 1. The input is direct injection and the charge is integrated on a capacitor. The charge capacity is about $2x10^7$ electrons and the kTC limited read noise is 400 electrons. The dynamic range is about 50,000. The integration time can be varied from 0.5 to 99.5% of frame time. Three clocks and four bias voltages are needed to operate the device.

Focal Plane Array

The FPA is fabricated by mating the detector array and the multiplexer through the indium columns (Figure 2). Interconnect yields of above 95% were obtained and 99% yields similar to the 128x128 FPAs are possible. A concern is the reliability of large area hybrid structures. We have thermally cycled 256x256 test structures (more than 100 times) and MWIR FPAs (more than 20 times) between room temperature and 77K with no mechanical or electrical degradation. The excellent reliability is a result of the PACE-1 material having low thermal expansion mismatch with silicon. A photo of the 256x256 FPA mounted on a 68 pin chip carrier is shown in Figure 3.

Initial characterization tests show that the mean broadband (no filters) quantum efficiency is 59% at 77K (Figure 4). Higher quantum efficiencies (>70%) are possible as evidenced from 128x128 FPA results. At short wavelengths (1 μm), >50% quantum efficiency is observed. We are presently continuing the characterization of the FPA.

Summary

We have developed a HgCdTe 256x256 focal plane array (FPA) which operates in the 1-5 μm band. The detector material is HgCdTe on sapphire (PACE-1 technology) and the multiplexer is a CMOS FET-switch device. The FPA charge capacity is about $2x10^7$ electrons with a read noise of 400 electrons. The mean broadband quantum efficiency is measured to be 59%. Dark currents less than 0.1 pA have been measured at 77K. The dark current can be further lowered by decreasing the temperature of operation. These devices are available for astronomical applications.

Acknowledgments

We thank Shawn Johnston for growing the PACE-1 material and Matthias Blume for the detector array characterization. This work was supported by Rockwell IR&D funds.

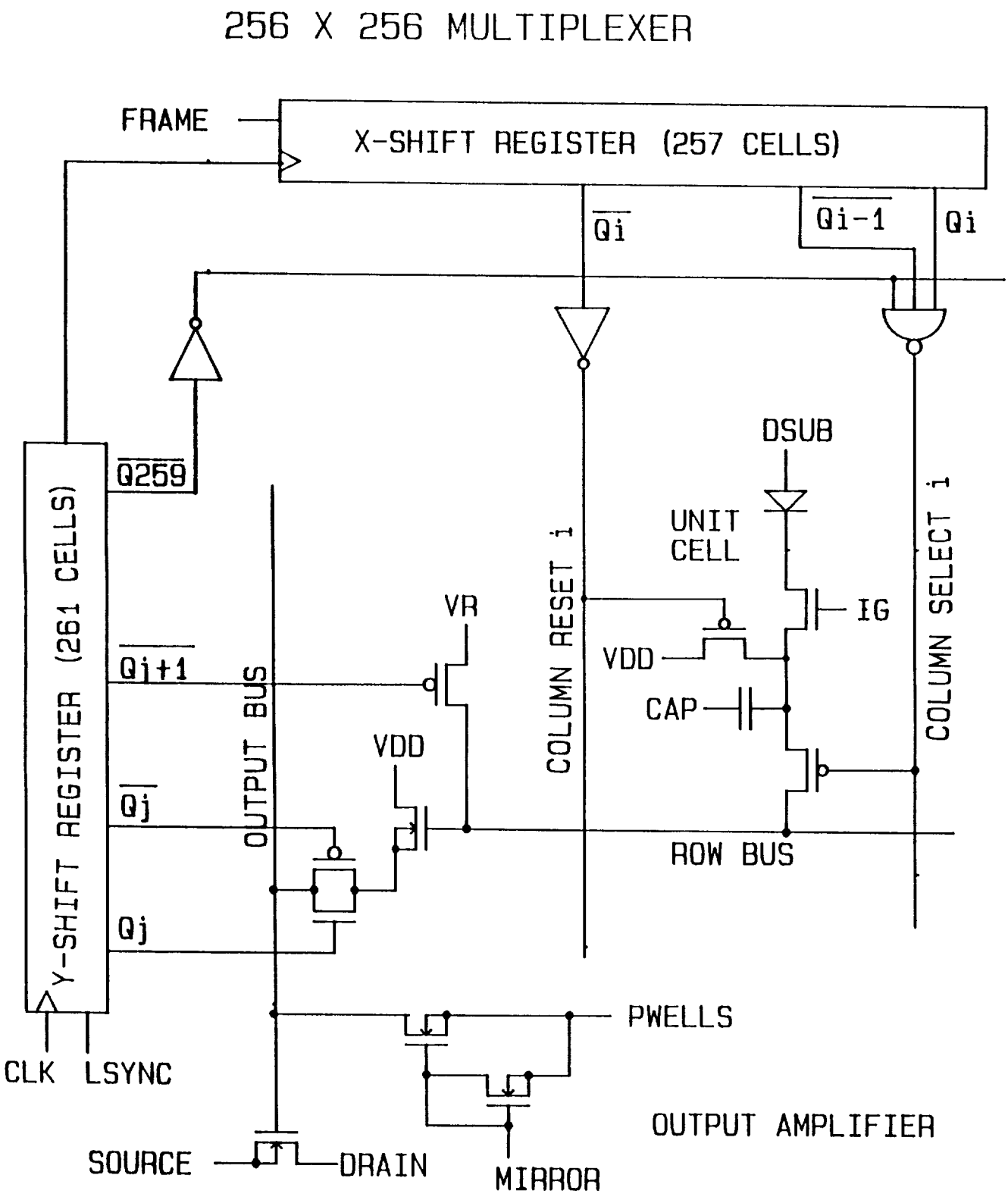

FIGURE 1. 256x256 CMOS Multiplexer Schematic

PACE-1 HYBRID FOCAL PLANE ARRAY

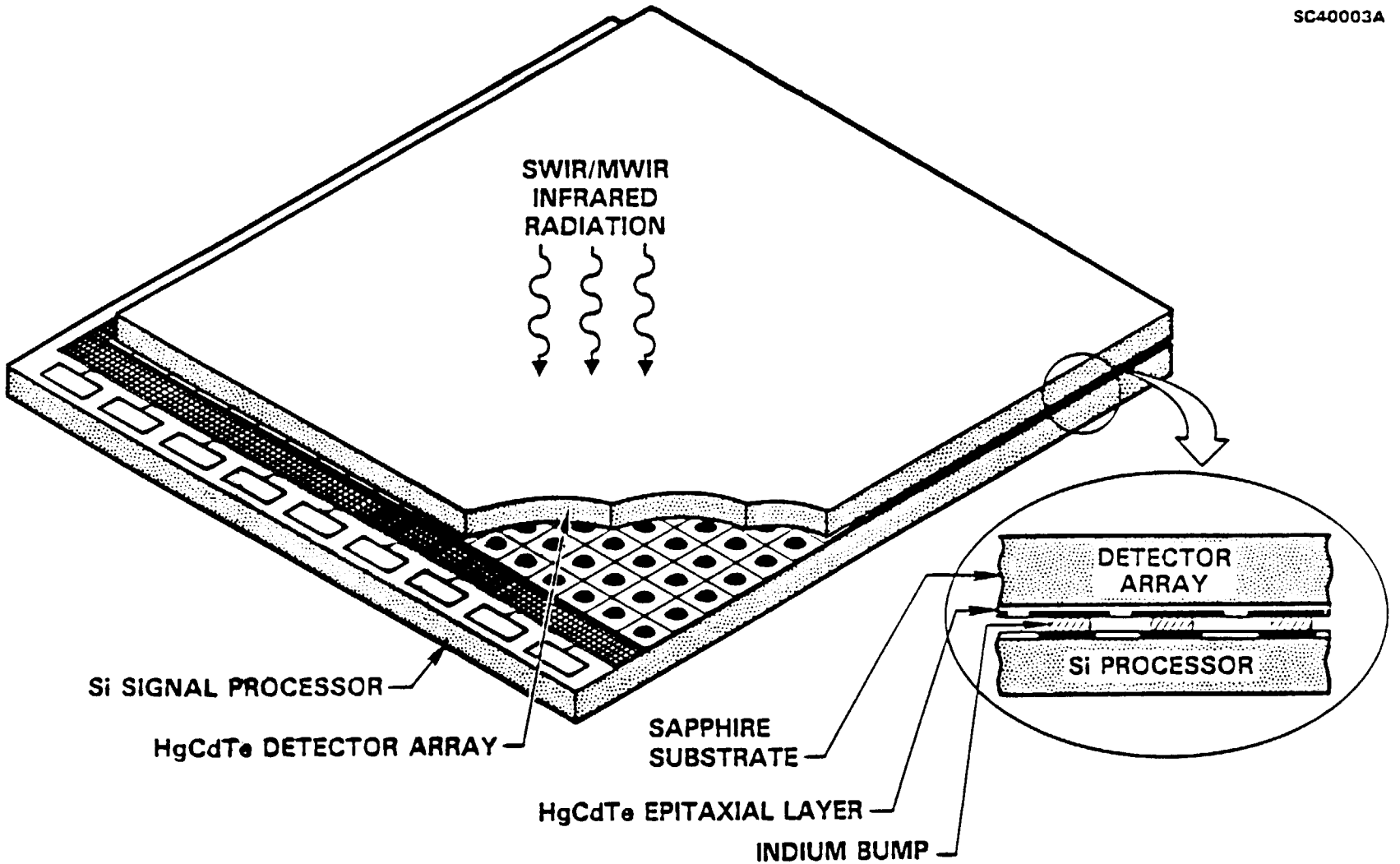

FIGURE 2. Hybrid Focal Plane Array Cross Section

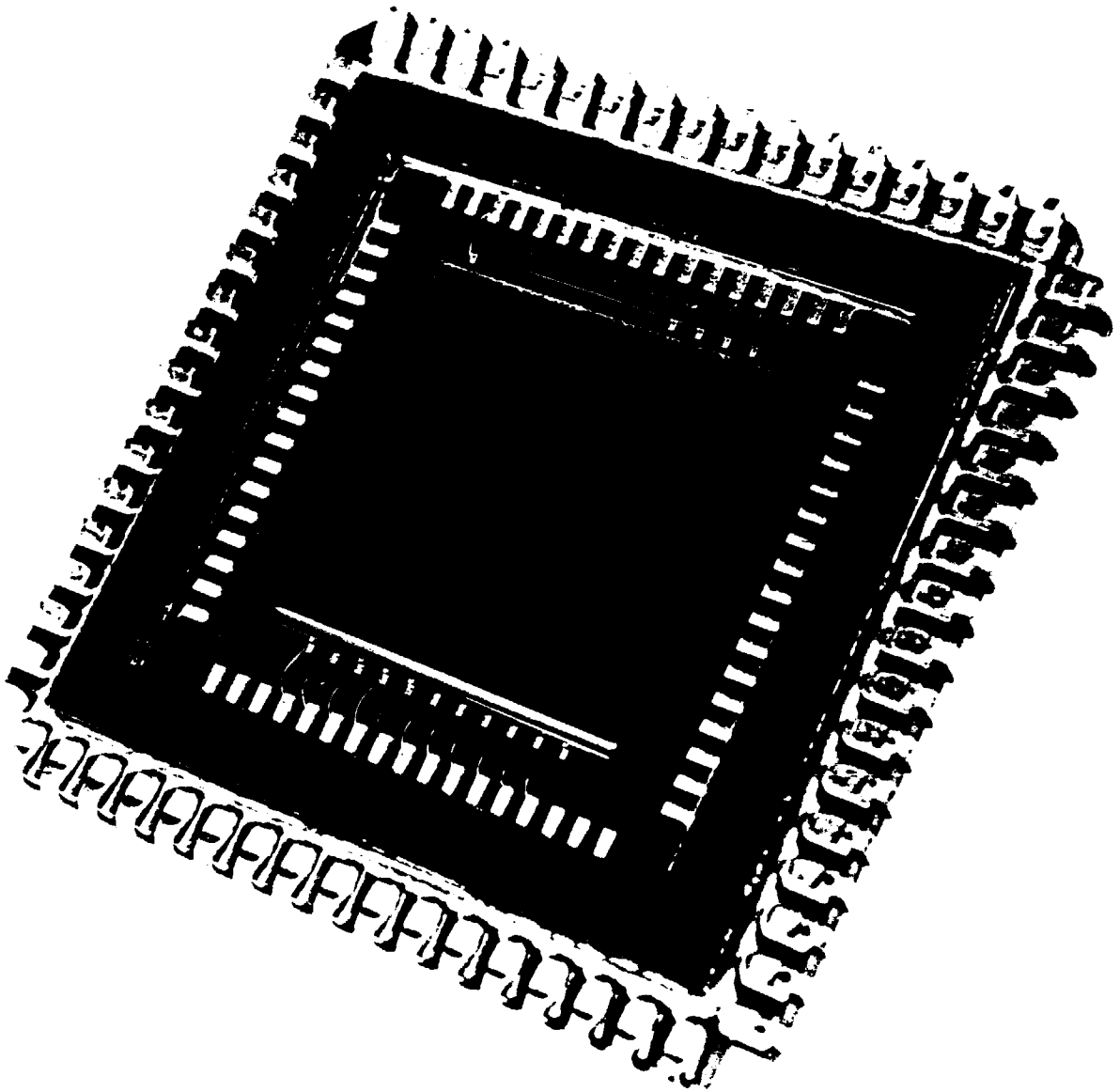

FIGURE 3. 256x256 FPA

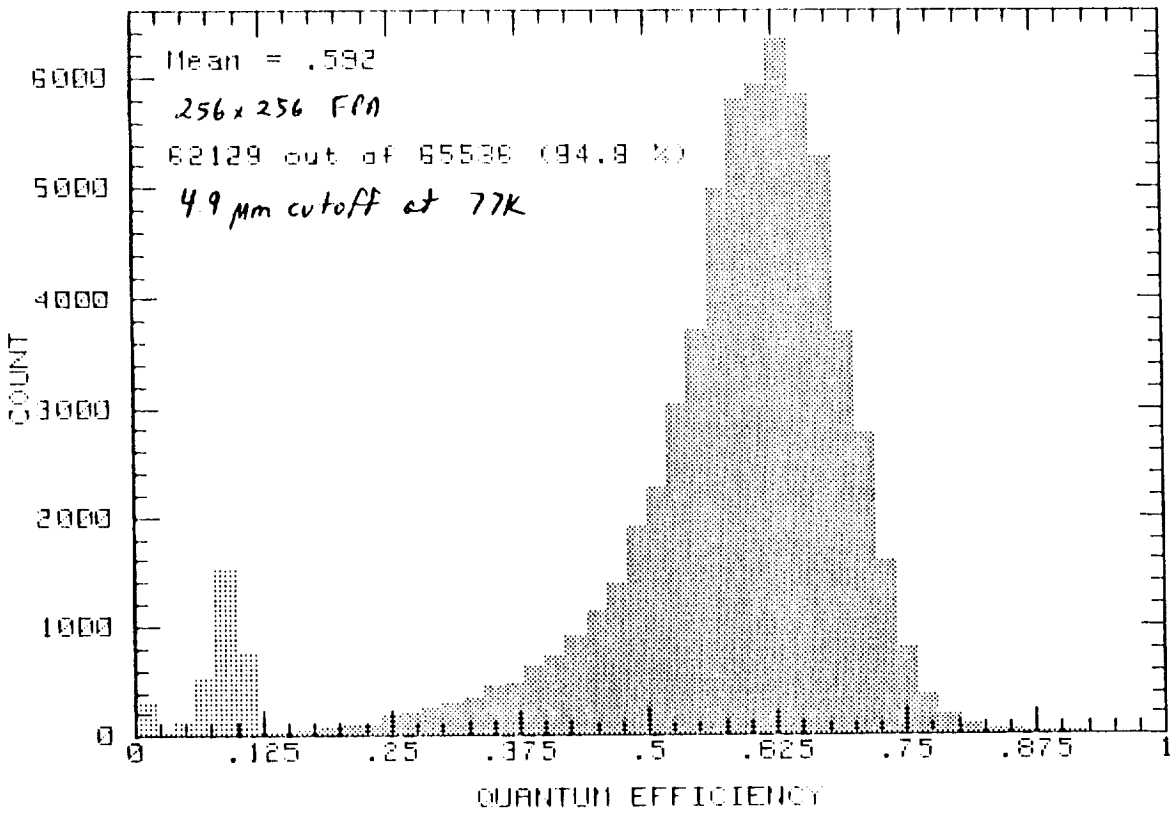

FIGURE 4. Quantum Efficiency of 256x256 FPA

Published in IEEE Transactions on Nuclear Science, Vol. 36, No. 1, Feb. 1989

HIGH SPEED, LOW READ NOISE ELECTRONICS FOR ASTRONOMY DETECTOR ARRAYS

Michael C. Peck, John F. Arens, J. Garrett Jernigan,
Space Sciences Laboratory, University of California, Berkeley, CA 94720

Stephen D. Gaalema
Hughes Aircraft Company, Carlsbad, CA

Abstract

The third generation electronics system of the Berkeley infrared camera has been built with improved frame rate, size, manufacturability, and real-time data processing power. The flexibility to easily operate a variety of detectors and the vast improvement in speed was achieved by using Motorola DSP56001 Digital Signal Processors[1,2] (DSP) to serve as controllers and processing elements throughout the system. The new data acquisition system has one DSP per analog channel, making the system scalable to match the sensor being used. Each channel can run up to 1 MHz sampling rate (A/D limited) using 20% of the DSP's 10-30 MIPS bandwidth for interrupt driven data acquisition, leaving 80% for background processes. The A/D is presently a 1 MHz 12 bit unit. The conversion resolution is enhanced by a pattern subtraction system allowing the removal of the first order signal and digitization of the amplified residual. The analog board is dynamically configurable and is capable of performing self diagnostics and calibration. A DSP56001 is also used in the timing generator, which outputs patterns at a rate up to 10MHz and has a fine timing adjustment of 2 nsec using programmable delays. The computer system hardware and software are layered, supporting real-time interrupt response down to the microsecond level. The system is is the prototype for the electronics for the 1-5 μm and 8-24 μm cameras being designed for the Keck Ten Meter Telescope.

Introduction

High speed electronics is required for the high photon fluxes encountered when observing at wavelengths longward of 2.5 μm. Low read noise is required at shorter wavelengths or

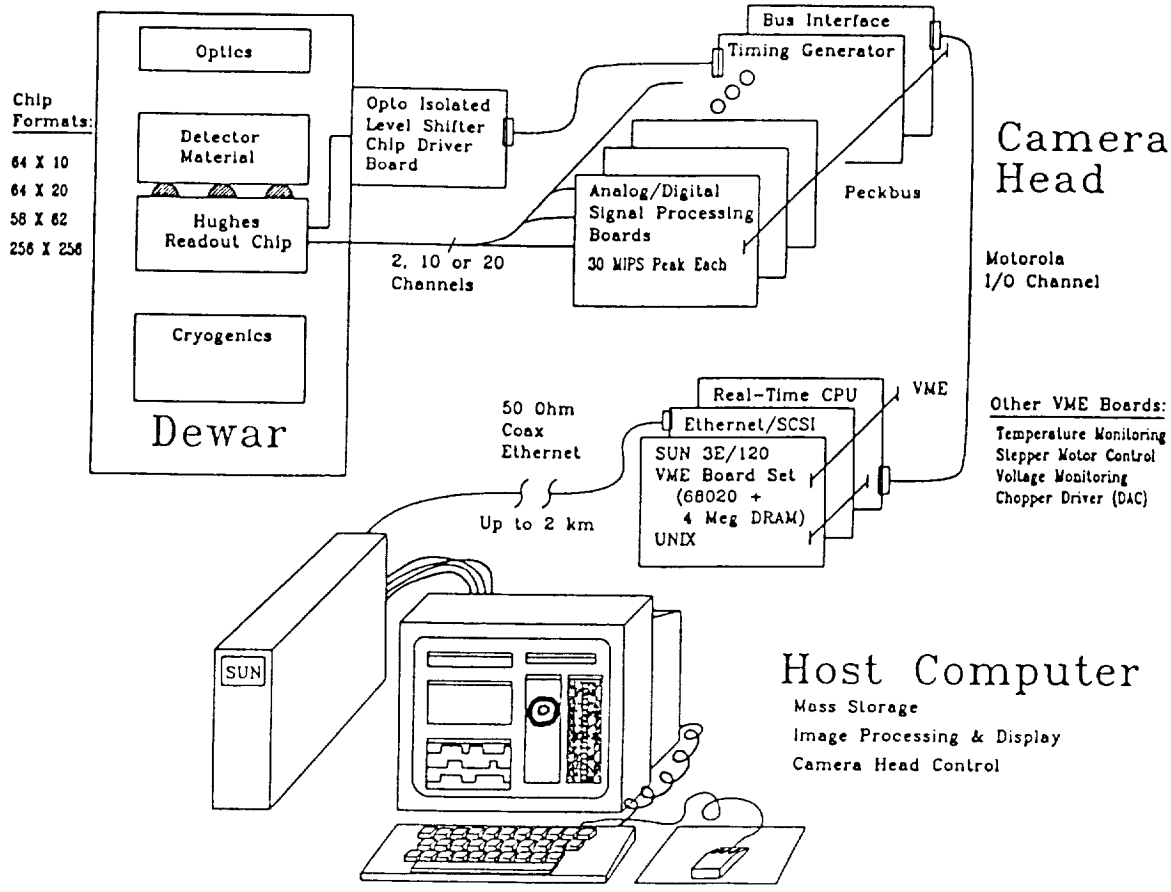

Fig 1 System Block Diagram

narrow bandwidths, where the charge and the statistical variation in the charge collected in a pixel are small. The old Berkeley infrared camera[3,4,5] operated at 10 μsec/pixel/channel peak rate, forcing the use of narrow bandwidths. In the new system, the pixel read time has been decreased to 1 μsec, allowing observations over the full 8 to 13 μm atmospheric window.

The new system's speed is achieved by incorporating high speed, highly integrated single chip computing elements on every analog amplifier chain. The Motorola DSP56001 was chosen for this task.

The camera system, Figure 1, is based on a four level hierarchy. The components are: a Sun workstation in the control room, a Sun 3E/120 VME card set on the camera head running Unix, a Parity Inc. 68020 single board computer in the VME rack running Magic/L[6] , and a bank of DSP56001s in the analog rack running optimized hand coded assembly routines. UNIX gives us the powerful development environment and transparent access to the camera head over Ethernet. The camera control, data acquisition, and DSP monitor software are written in Magic/L, which is an interactive language developed by Loki Engineering Inc. that looks like C or Pascal but works like Forth allowing spontaneous code creation and use. It is most useful for hardware debugging and user interface environments. The DSP assembly code was developed using the Motorola development package and our look-alike debugger running on the targets. The software system breaks new ground in the layering of the application by putting the vast majority of the code on a single host processor and only the core of the application on the front end DSPs.

The use of commercial VME cards and the use of VME sized Eurocards for the timing generator and analog boards allowed for a compact package as shown in Figure 2.

Low Noise on a Mixed Analog and Digital Board

The amplifier board block diagram is shown in Figure 3. It is a highly configurable pulse amplification system with support for diagnostics and self calibration. A feature of the system is variable bandwidth in the analog chain. As the gain is increased and integration time increased for low signal level conditions, the bandwidth of the analog channel is decreased to reduce the noise bandwidth of the system. In the low gain (=5) setting, full scale pulse settling time to 12 bits is 100 nsec from input to A/D. The

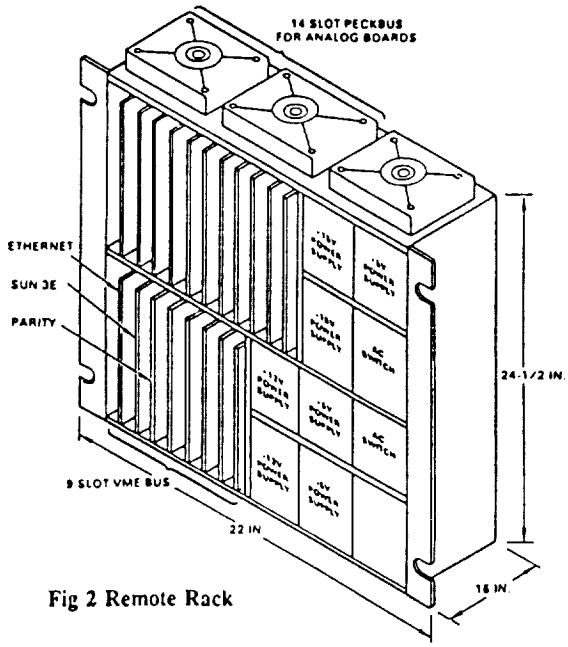

Fig 2 Remote Rack

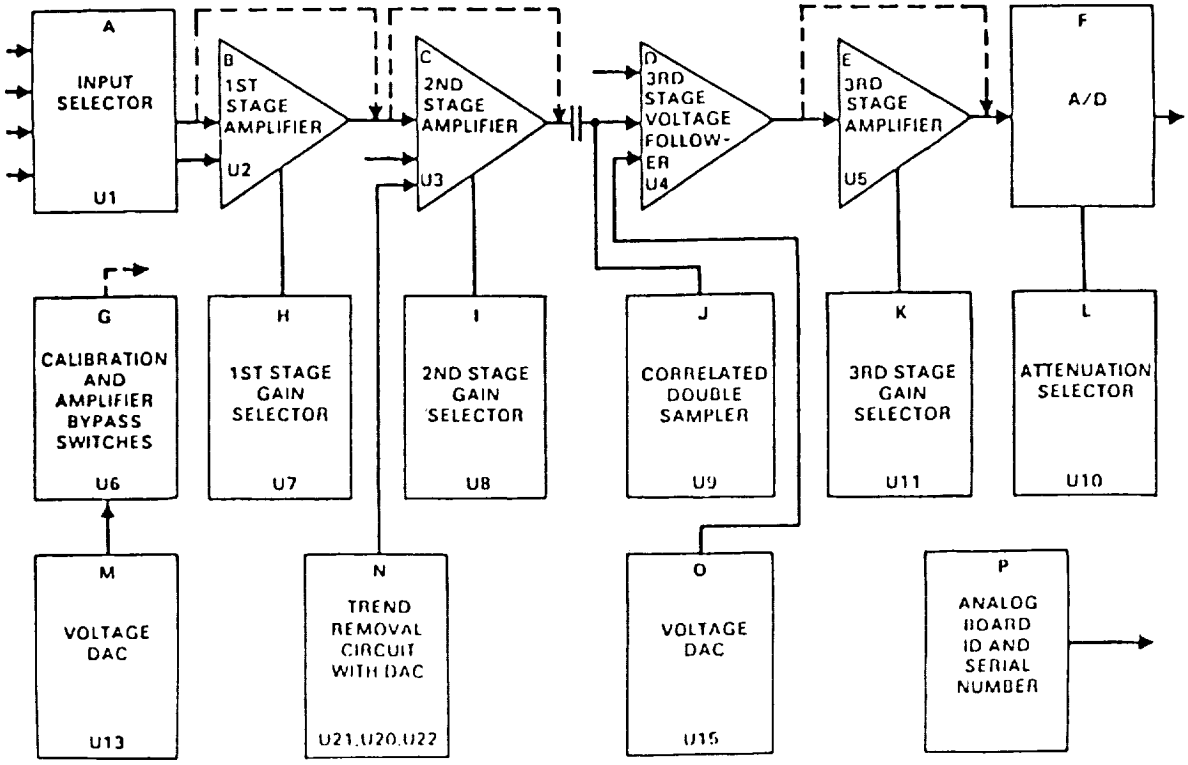

Fig 3 Analog Block Diagram

amplifiers used are the OEI AH0013 JFET preamp and the Harris 5195 high speed fast settling opamp. The system also incorporates a fixed pattern subtraction circuit to remove the first order pattern from the chip, allowing use of higher gains into the A/D and therefore higher resolution. Correlated double sampling is used to eliminate the 1/f noise (DC instability) inherent in the readout MOSFETS as shown in the timing diagram in Figure 4.

In Figure 1, the bus interface logic represented by block "P" was a dozen ICs on the prototype board. In the production run, these ICs were replaced by three CMOS programmable logic devices (PLD) and the DSP56001, using less space on the board and eliminating the separate digital board. The PLDs were the XL78C800[7] from EXEL, an extremely flexible 800 gate equivalent electrically erasable application specific integrated circuit (ERASIC).

All timing and digital clocks are generated from a central 20 MHz clock on the timing generator board. The timing signals are transmitted differentially over the backplane using high speed parts (75ALS194/5). The fine adjustment on the timing signals is in 2 nsec increments so that the noise critical sampling time can be moved to a quiet period between digital transitions. This feature should allow the system to approach the noise performance of the previous generation Berkeley camera electronics which had 20 μvolts rms noise. Low noise measurements on the new system are yet to be completed.

Coadder

The system has a DSP on each of the 20 analog channels that coadds in 700 nsec with interrupt signals, or 200 nsec in bursts with an input FIFO. The old camera had a coadder external to the analog box, requiring 5 μsec to coadd ten pixels. The DSP and PLDs also implement the bus interface logic, reducing the complexity of the analog board.

Timing Generator

The timing generator uses a DSP56001, is situated in the analog rack, and is the source of the clock and timing for all camera functions. The DSP56001 enables the timing generator to be built with a small number of chips. Because its characteristics are determined by software it can be programmed for a variety of observing modes, and it is functionally open-ended to support lab testing.

DSP Operation

16 bit DSPs have been available for many years. Motorola's DSP56001, which became available in 1987, has a 24 bit word size and 56 bit accumulators, which allows processing real data without roundoff. As shown in Figure 5, the chip is massively parallel and incorporates peripheral chip functions making it very easy to use. The Host Port and the Host Command facility made hardware and software design simple. The

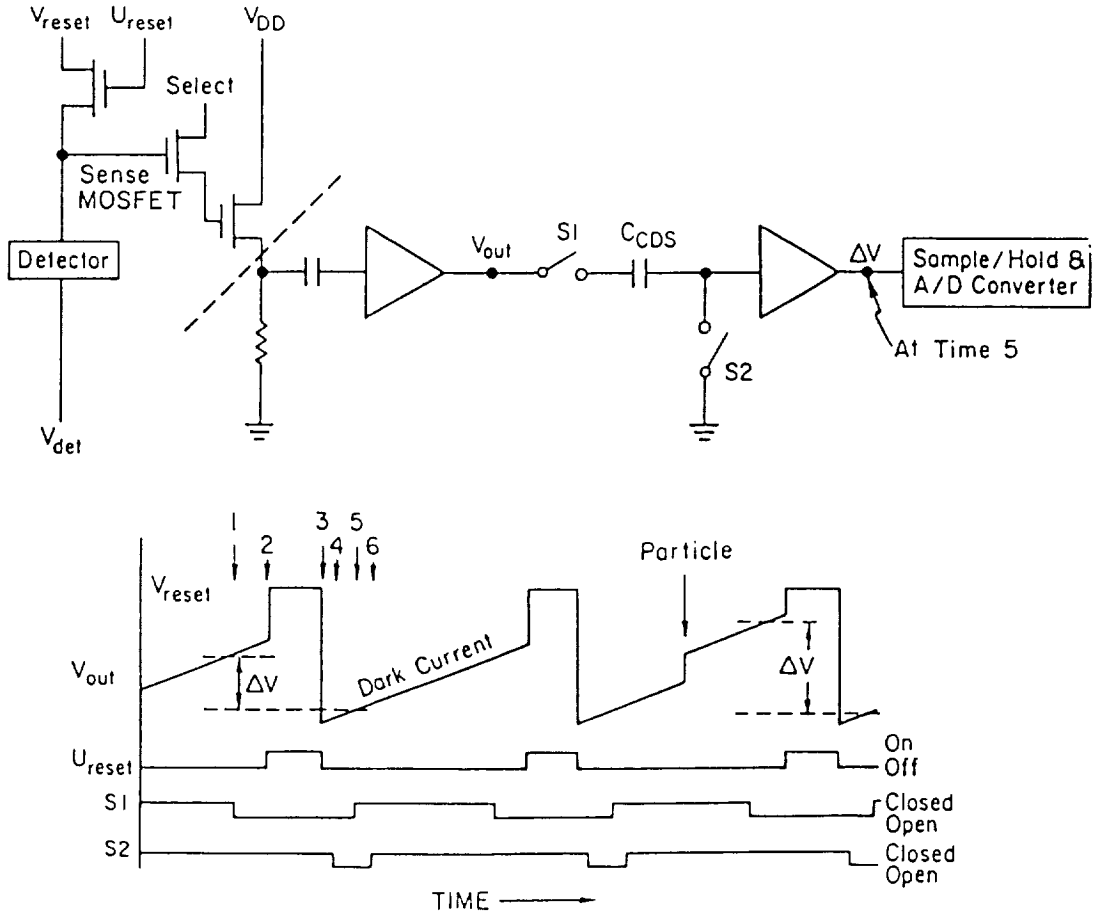

Fig 4 Correlated Double Sampling

DSP host port is interfaced to the Peckbus[8] , a minimal bus using CMOS levels that is trivial to interface to and works with extender cards. The bus consists of 16 data bits, 16 board select lines, 8 address lines for on card selection, and read, write and acknowledge handshake lines. The signals are on the a and c rows of the 96 pin DIN connector, leaving the unbused b row for user definition. A controller card resides in slot one translating the Motorola I/O Channel signals from the Parity CPU board to Peckbus signals.

DSP56001 Characteristics

The DSP56001[2] is a self contained computer on a chip, with program controller, math unit, program and data memories, and peripherals typically associated with computers, and a selection of bootstrap modes[1] The chip executes instructions at a 10 MHz rate, but the instruction fields can contain up to three instructions, giving a peak rate of 30 MIPS at 20 MHz clock. 27 MHz parts are now available, and we have run the 20 MHz parts at up to 40 MHz in the lab with a special clock generator. Tests have been done at Lincoln Labs on radiation hardness. The clock rate was run up to see where the parts stopped, then the parts were radiated and tested again. The test part died between 100krad and 200krad, and ran at 32 MHz up to that point. The chip has a 5 Mbit synchronous serial link, a UART, and a host interface port. The host interface port looks like a set of 8 byte wide registers (50 nsec access time) and can be very simply interfaced into any computer system.

DSP Software

The most unusual aspect of the host port is the host interrupt facility. The host can invoke one of the 32 interrupt service routines by writing the vector number to a register in the host interface. Using 8 of these vectors, we built a complete monitor and development system, supporting memory dump and load, program execution control, and machine state dump.

Monitor

The monitor in the target DSP consists of 16 lines of code:

```
;       MONITOR SERVICE ROUTINES:  300 nsec @ 20 MHz
;       (address,vector)
;       All functions require that r7 be set (via SETr7 call).

; SETr7 (24,12) Transfer the address value to r7
            movep               x:HRX,r7
            nop
; XPEEK (28,14) Read a 24-bit value from X memory
            movep               x:(r7)+,x:HTX
            nop
; XPOKE (2a,15) Write a 24-bit value to X memory
            movep               x:HRX,x:(r7)+
            nop
; YPEEK (2c,16) Read a 24-bit value from Y memory
            movep               y:(r7)+,x:HTX
            nop
; YPOKE (2e,17) Write a 24-bit value to Y memory
```

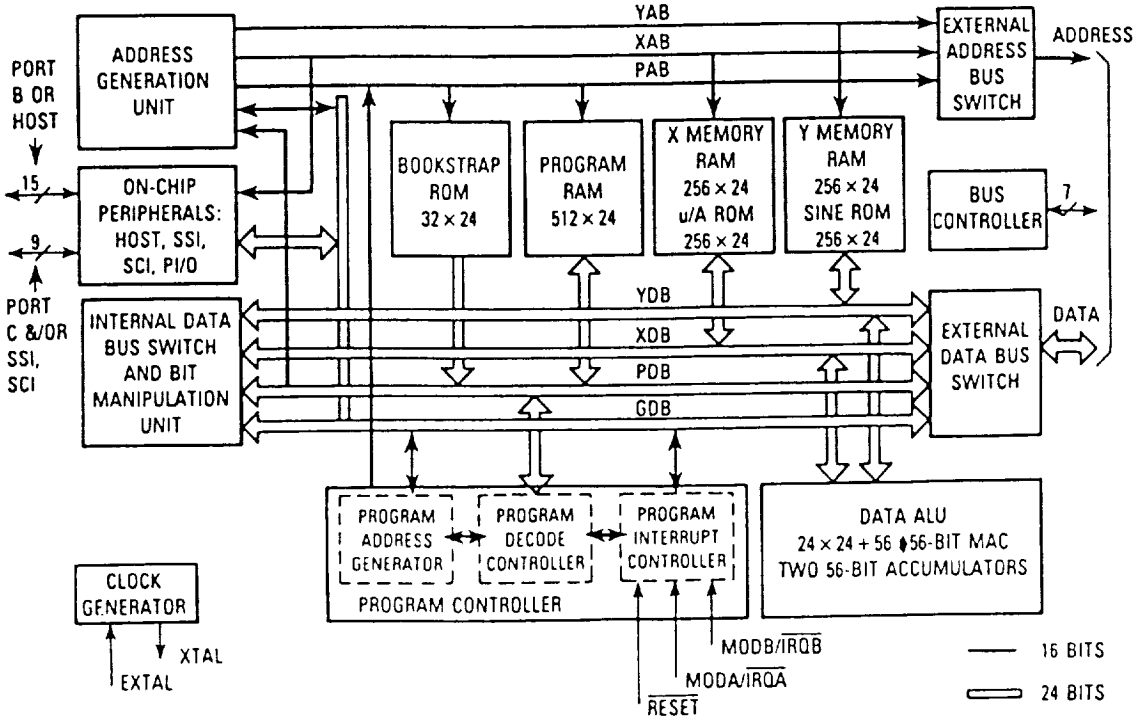

Fig 5 DSP 56001 Block Diagram

```
        movep           x:HRX,y:(r7)+
        nop
; PPEEK {30,18} Read a 24-bit value from program memory
        movep           p:(r7)+,x:HTX
        nop
; PPOKE {32,19} Write a 24-bit value to program memory
        movep           x:HRX,p:(r7)+
        nop
; SOFT  { 6, 3} Code is PPOKEd here for dynamic expansion
        nop
        nop
```

The host computer is used to implement all the higher level code including initialization, data transfer, non time critical operations, and a full development system, monitor and debugger. The functions we implemented were made to duplicate the functions available in Motorola's DSP Development Software package. Using three windows on a workstation, code can be assembled and executed in the simulator, added to the target hardware and experimented with, and added to the source code. This development system allows loading of object files into the simulator and the target from the same load file generated by the Motorola assembler.

Timing Generator Code

An example of application code is the timing generator:

```
; outer loop to address all (aalen=64) rows of the array
AATOP   do      #aalen,AAEND
; inner loop: output 12 bits of CDS pattern at 10MHz
        rep     #cdslen
        move            x:(r1)+,b    b,y:(r4)
;  does:                x(i+1) -> b  & x(i) -> latch

; strobe 24 bits of AAPM and CDSPM
        move            x:(r0)+,a    a,y:(r5)
AAEND

; Frame time code goes here
        rep     #framewait
        nop

        jmp     AATOP
        end
```

Data Acquisition - Coadd Code

An example of interrupt service routines for data acquisition are the coadd short interrupt service routines. These routines are transferred into the low memory vector location at frame time by a frame interrupt routine that counts frames. Each of these routines executes in 200 nsec after a 500 nsec synchronization delay in the DSP. No instruction execution cycles are lost in the process.

```
;               first frame
MOVEX   movep   y:$ffc1,x:(r4)+ ; A/D -> X data buffer
        nop

;               frames 2 to n-1
ADDX    tfr     b,a     x:(r2)+,b       y:(r6),y1
        add     y1,b    a,x:(r4)+

;               last frame: results in y buffer for readout
ADDXY   tfr     b,a     x:(r2)+,b       y:(r6),y1
        add     y1,b    a,y:(r4)+
```

Conclusion

We took a big risk on redesigning the camera's entire digital system based on DSPs. The success of this experiment shows that there is a new generation of programmable logic to bring to bear on difficult design problems. Hardware designs can be greatly simplified and made more flexible. It is yet to be seen wheather or not the necessary software tools also appear to support these chips in general use. We have made initial steps in developing these tools, but they are far from what is needed to make these parts as easy to use as the hardware they replace. The power, simplicity and tremendous flexibility do come at a price for now.

References

1. *56-Bit General Purpose Digital Signal Processor*, document DSP56001/D, Motorola, 1988.
2. *MOTOROLA DSP56000 DIGITAL SIGNAL PROCESSOR USER'S MANUAL*, document DSP56000UM/AD, Motorola, 1986.
3. John F. Arens, J. Garrett Jernigan, Michael C. Peck, Carl A. Dobson, Erik Kilk, John Lacy, and Stephen D. Gaalema, "10 Micrometer Infrared Camera," *Applied Optics*, vol. 26, 1987.
4. J.F. Arens, G.M. Lamb and M.C. Peck, "Infrared Camera for 10 Micron Astronomy," *Optical Engineering*, vol. 22, pp. 267-268, 1983.
5. John F. Arens, Gerald M. Lamb and Michael C. Peck, "Infrared Camera for 10 Micron Astronomy," *Proceedings SPIE*, vol. 280, no. Infrared Astronomy, April, 1981.
6. Arnold Epstein, David M. Jordan and Jeffrey D. Morris, *Magic/L User's Manual*, Loki Engineering, Inc., Cambridge, MA, March 1987.
7. *ERASIC XL78C800, Multi-Level E²* PLDs, EXEL Microelectronics, Inc., San Jose, CA.
8. Peter C. Abrams, William T. Marchant, Michael C. Peck, Carl A. Dobson, and Roger F. Malina, "Real-Time Data Acquisition for the Extreme Ultraviolet Explorer Science Instruments," *Proc. IEEE 1987*, Astronomy Department & Space Sciences Laboratory, University of California, Berkeley.

Improved Si:As BIBIB Hybrid Arrays

T. HERTER, N. ROWLANDS, S. V. W. BECKWITH, AND G. E. GULL

Department of Astronomy, Cornell University

AND

D. B. REYNOLDS, D. H. SEIB, AND M. G. STAPELBROEK

Rockwell International Science Center

ABSTRACT

We present results of a program to increase the short wavelength (< 10 μm) detective quantum efficiency, η/β, of Si:As Impurity Band Conduction arrays. The arrays are epitaxially grown Back-Illuminated Blocked-Impurity-Band 10×50 detectors bonded to switched-FET multiplexers. We show that the 4.7 μm detective quantum efficiency increases proportionately with the thickness of the infrared active layer. A BIB array with a thick active layer, designed for low dark current, exhibits η/β = 7–9% at 4.7 μm for applied bias voltages between 3 and 5 V. The product of quantum efficiency and photoelectric gain, ηG, increases from 0.3 to 2.5 as the voltage increases from 3 to 5 V. Over this voltage range, the dark current increases from 8 to 120 $e^- s^{-1}$ at a device temperature of 4.2 K and is under 70 $e^- s^{-1}$ for all voltages at 2 K. Because of device gain, the *effective* dark current (equivalent photon rate) is less than 3 $e^- s^{-1}$ under all operating conditions. The *effective* read noise (equivalent photon noise) is found to be less than 12 electrons under all operating conditions and for integration times between 0.05 and 100 seconds.

I. INTRODUCTION

Impurity Band Conduction (IBC) detectors and their generic equivalents – Blocked Impurity Band (BIB) and Backside Illuminated Blocked Impurity Band (BIBIB) – were developed to be sensitive to infrared light in the 6–26 μm wavelength range, but with substantially smaller active volumes than the extrinsic photoconductive detectors normally used at these wavelengths. The smaller active volume means a correspondingly smaller sensitivity to high energy radiation and particles. Silicon BIBs employ a thin, undoped, epitaxially grown silicon layer between a heavily doped, infrared-active layer and a planar contact. The undoped layer blocks hopping conduction (dark current) but conducts the current generated by infrared light which photoionizes neutral impurities in the heavily doped layer. When a voltage is applied between the active layer and the planar contact, the blocking layer causes BIB detectors to behave like reverse-biased diodes rather than

photoconductors. Because of the high doping concentration, BIB detectors achieve good quantum efficiency with an infrared-active layer more than an order of magnitude thinner than that of extrinsic Si photoconductors, making BIBs much less susceptible to damage by cosmic rays. Some of the problems inherent in extrinsic photoconductors are not present in BIBs: there appear to be no large, transient currents associated with voltage changes, and the electrical and optical crosstalk between pixels is small. BIBs offer improved uniformity and larger wavelength coverage than possible with extrinsic photoconductors. The theory and operation of BIBs and the characteristics of the Rockwell International Si BIBIB arrays discussed in this paper are described in detail by Petroff and Stapelbroek (1984, 1985) and Stetson *et al.* (1986).

We are developing improved BIB detectors under a program to support the Space Infrared Telescope Facility (SIRTF), a cooled infrared space telescope planned by NASA for launch in 1998. Cornell is building the Infrared Spectrometer (IRS) as one of three instruments for SIRTF. The IRS will provide spectra from 2.5 to 200 μm at resolving powers ($\lambda/\Delta\lambda$) of 100 and 2000. Silicon BIB detectors from Rockwell will cover the 5–27 μm wavelength range for this spectrometer. Because the background radiation from the telescope and celestial sources will be extraordinarily small, the detectors must have good quantum efficiency, low dark current, and low readout noise. A small detector volume is desired to minimize interference from cosmic rays.

Figure 1 shows the background radiation expected at the detector for resolutions of 100 and 2000. The background is dominated by emission from zodiacal dust particles. At the highest resolution, less than one photon per second will reach the detector for wavelengths shorter than 9μm.

It is evident from Figure 1 that if the IRS is to achieve near background-limited-performance, the detectors must be very good and very quiet. It is desirable to simplify the focal plane by using only a few different types of detectors to cover the waveband. The Si:As BIBIB (hereafter simply called BIB) hybrid detector arrays made by Rockwell are the best available to meet these requirements, but the first generation devices have low quantum efficiencies at the short wavelengths, $\lambda \sim 4$ μm. We present here results from a program undertaken to improve the short wavelength quantum efficiency of Si BIB detectors.

II. DETECTOR DESCRIPTION

Detector arrays are produced with 10 rows of 50 pixels. Pixel centers are 150μm apart, and the detector active area is 135×135μm. The detector array is bump-bonded with indium contacts to a MOSFET multiplexer specially designed for low-noise operation at temperatures of less than 10 K. The photocurrent from each detector is collected at the gate of a MOSFET which can be sampled nondestructively. The nodal capacitance is between 0.37 and 0.42 pf, depending on the detector configuration, and the total capacity is about 2×10^6 electrons. The output amplifier of the multiplexer has a gain of 0.7, giving 3.30 to 3.75 electrons per μV.

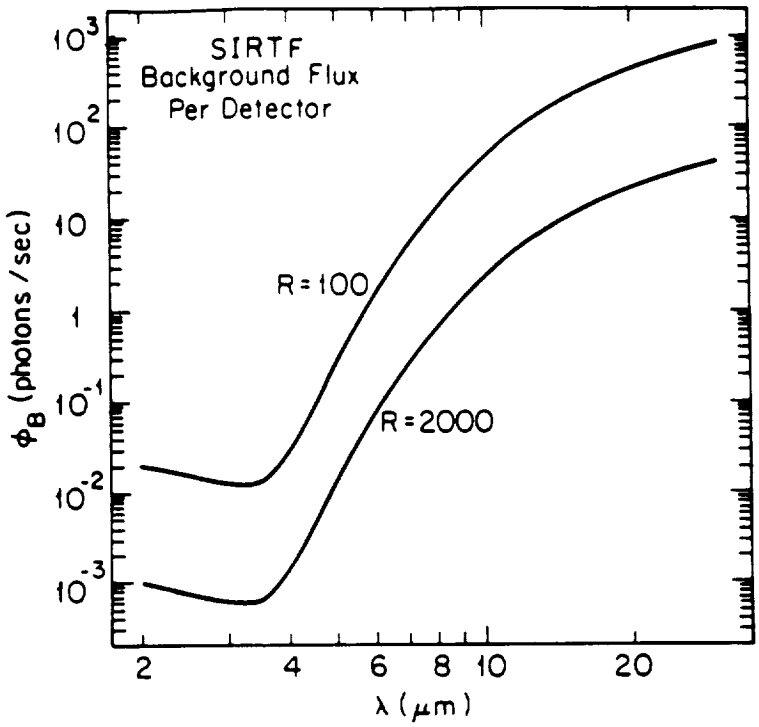

Figure 1: Photon rate on the midband (5–27 μm) detectors for resolving powers of 100 and 2000. The transmission of the optics is assumed to be 0.10; the pixel size is $1.2\lambda/D$, where λ is the wavelength and D is the telescope diameter. The major contributor to the photon rate is zodiacal emission which is assumed to have an emissivity of 2.3×10^{-7} and a temperature of 246 K (Hauser *et al.* 1984).

Test results from the first generation of these arrays are presented by Herter *et al.* (1987). The detectors responded poorly to light near 5 μm ($\eta/\beta \sim 4\%$), but otherwise met the requirements for the IRS. A second generation of detectors was made to improve the short wavelength response. The responsivity can be enhanced by increasing the donor concentration and/or by making the infrared active layer thicker. Increasing the donor concentration may increase dark current. Increasing the thickness of the active layer will only be effective if the layer can be fully depleted of ionized donors (due to impurity acceptors) when a voltage is applied to the detector. It is most important to keep the acceptor concentration low.

Rockwell developed a high purity, epitaxial reactor, making it possible to increase the active layer thickness of BIB detectors. A group of detectors was fabricated with different active layer thicknesses and donor concentrations to determine the optimum characteristics for enhancement of short wavelength quantum efficiency while maintaining low dark current. Discrete detectors were cooled to 10 K and illuminated with a photodiode to test performance prior to bonding. The best material was used to make hybrid arrays. Two detector materials were chosen for further evaluation, both with an infrared active

layer twice the thickness of the first generation devices. One was doped uniformly. The other contained a graded donor concentration which increased linearly from the blocking layer to the contact. The average donor concentration was the same for both materials.

Reynolds *et al.* (1988) present initial test results on the responsivity and detective quantum efficiency at 4.5 and 10.6 μm at an operating temperature of 10 K. These tests show that the short wavelength quantum efficiency is a factor of two greater than that of the thin detectors, the same factor as the increase in thickness of the infrared active layer. They found the graded layer device to have the lowest dark current without a loss of responsivity. We present here test results for the graded layer detector operated at 4.2 and 2.0 K. These lower operating temperatures further reduce dark current and are a better match to the range of focal plane temperatures that will be available on SIRTF.

III. BACKGROUND

a) IBC Performance Characterization

The noise, N, in an IBC device after collecting photons of energy $h\nu$ for a time t is:

$$N^2 = \frac{P_B}{h\nu}\frac{\eta}{\beta}(\beta G)^2 t + \beta_d G_d i_d t + R_N^2, \tag{1}$$

where P_B is the radiant power per 150 μm $\times$ 150 μm area, η is the quantum efficiency, G is the photoconductive gain, β ($\equiv \langle G^2\rangle/\langle G\rangle^2$) is the gain dispersion, R_N is the readout noise which may be a function of the integration time, i_d is the dark current, G_d is the gain of the dark current, and β_d is the gain dispersion of the dark current. In general, we expect $G_d < G$ and $\beta_d < \beta$, since most dark current occurs near the blocking layer. We define the *signal*, S, to be the number of collected electrons generated by radiation:

$$S = \frac{P_B}{h\nu}(\eta G)\, t, \tag{2}$$

$$= \frac{P_B}{h\nu}\frac{\eta}{\beta}(\beta G)\, t. \tag{3}$$

When the fluctuations in the radiation power dominate the last two terms in equation (1), the detective quantum efficiency, η/β, may be measured directly from the signal-to-noise ratio:

$$\frac{\eta}{\beta} = \left(\frac{S}{N}\right)^2 \frac{h\nu}{P_B}\frac{1}{t}. \tag{4}$$

Measurement of η/β does not require knowledge of the amplifier gain of the device or the nodal capacitance, since these terms affect the signal and noise equally, and thus cancel in the ratio. The quantity ηG is determined from the responsivity, S/P_B, using equation 2. Notice that for photoconductors, the gain dispersion, β, is at least 2 because shot noise in the generation and in the recombination of carriers contribute equally. This factor is typically ignored when quoting the quantum efficiency of photoconductors. Thus, for a photoconductor with $\eta = 20\%$, $\eta/\beta = 10\%$ which is the relevant quantity for comparison to IBC devices.

b) Experimental Setup

The detector arrays are cooled in a dual reservoir cryostat filled with liquid helium and nitrogen. By adjusting the pressure over the helium, the detector temperature can be varied between 2 and 4.2 K. The array is illuminated through a 750 μm circular aperture cooled to the detector temperature. A stack of several neutral density and bandpass filters limits the radiation passing through the aperture. For the tests described here, the bandpass filter was centered at 4.7 μm with a width of approximately 0.64 μm. Either an ambient temperature (300 K) metal block with a blackened cavity or a commercial blackbody source was used to illuminate the array through the cooled aperture.

A Stride 460 VMe bus microcomputer controls the array electronics. The Stride microprocessor uses a separate single board computer (SBC) on the VMe bus to provide TTL level clocking signals for the multiplexer. The signals are conditioned with a level-shifter which allows adjustment of both the upper and lower voltages of each clocking pulse. This box also provides steady voltage levels to the array. The array output voltages are amplified through a ten-channel preamplifier with programmable gain and bandwidth. The Stride microprocessor samples the preamplifier output with a multichannel A/D converter which is also on the VMe bus. The level of the output signal from the array is not constant from pixel to pixel. It increases systematically with pixel position across the array, and may saturate the preamplifier or A/D converter. This level change is eliminated by injecting a dynamic offset voltage at the front end of the preamp in synchronization with the array using a D/A converter driven by the SBC.

The array output may be sampled in different sequences to record voltage levels at any time from the beginning to the end of an integration and when the detectors are discharged (reset). We define three sampling schemes which are useful in testing detector characteristics. In the first scheme, called *sequential sampling*, the detectors are read out sequentially at a fixed rate, and the integration time during which charge is collected is proportional to the total time to read the entire array. In the second scheme, called *burst sampling*, all detectors are reset in rapid succession, charge is collected during integration time t, and the detectors are then sampled sequentially, but very rapidly, so the time to read the array is small compared to the integration time. Either doubly- or triply-correlated sampling may be used with either of these schemes, since the multiplexer allows nondestructive sampling. Triply-correlated sampling can, in principle, remove the kTC noise resulting from fluctuations in the amount of charge left on the detector after reset. In the final scheme, called *sampling up-the-ramp*, each detector is sampled many times during integration. A linear regression fit to the samples determines the rate at which charge accumulates (proportional to the photon rate). This technique typically gives better read noise performance than the other two modes.

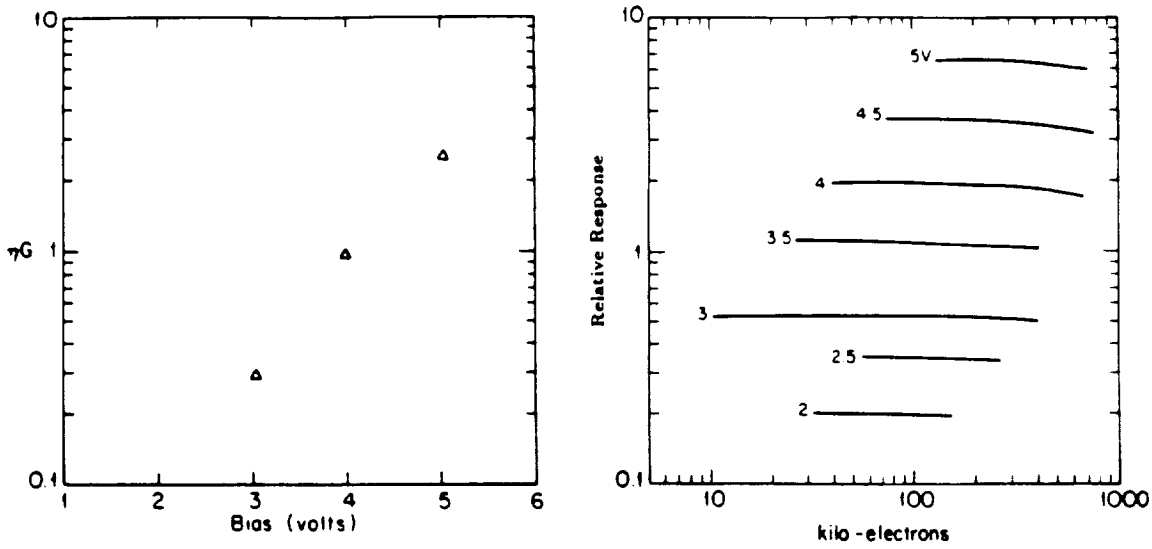

Figure 2: Responsivity (ηG) at 4.7μm for a graded profile detector at 4.2 K. The photon rate is 4000 photons s^{-1} per detector. The responsivity, ηG, is computed assuming a fixed nodal capacitance of 0.37pf independent of detector bias. (a) Responsivity versus bias voltage. (b) Relative responsivities versus collected charge for different bias voltages.

IV. TEST RESULTS

We measured the responsivity, detective quantum efficiency, read noise, dark current, transient response, and response to γ-rays to assess detector performance. Because of our interest in the short wavelength quantum efficiency, only measurements at 4.7 μm are presented here. The peak detector response occurs at about 23μm.

a) *Responsivity*

Measurements of ηG versus bias with the detector operating at 4.2 K are shown in Figure 2a. Figure 2b shows the relative responsivity as a function of collected charge for different bias voltages. The roll-off noted previously by Herter *et al.* (1987) is evident. This effect is likely due to *debiasing* of the detector as charge accumulates.

The responsivity, ηG, decreased by factors of 0.6, 0.8 and 1.0 as the detector temperature decreased from 4.2 to about 2 K for operating biases of 5, 4 and 3 volts respectively. The photon background was relatively large compared to the photon background at this wavelength in the SIRTF environment. However, measurements at a lower photon flux of $\phi_b = 600\ s^{-1}$ show no change in ηG.

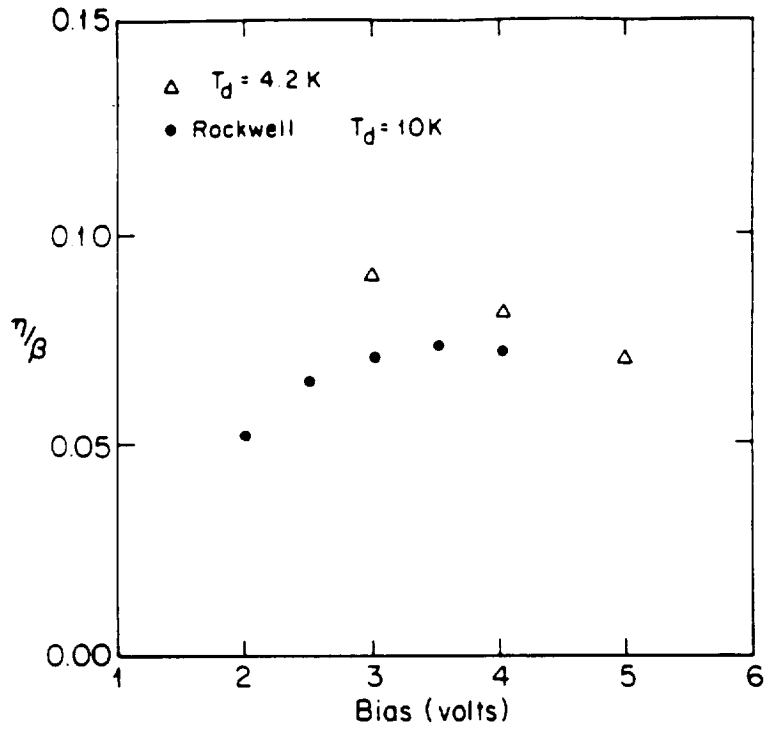

Figure 3: Detective quantum efficiency (η/β) at 4.7μm versus bias for the graded profile detector at 4.2 K. The photon rate is 4000 s^{-1}. Data from Reynolds *et al.* (1988) is also plotted (filled circles).

b) Detective Quantum Efficiency

Figure 3 presents the detective quantum efficiency, η/β, versus bias voltage. Data from Reynolds *et al.* (1988) are also shown. The array has quantum efficiencies between 7 and 9% depending on bias voltage. Our results are fairly consistent with those of Reynolds *et al.* (1988), who find an optimum value of η/β at 3.5 volts. We find that η/β continues to increase at lower bias voltages, though the curve could turn over in the voltage region we did not sample. This data set differs from that of Reynolds *et al.*, who operated the array at 10 K, in that our tests were done at 4.2 K. In fact our data indicates that η/β increases as the operating temperature decreases and that this effect is greater at the smaller bias voltages. This effect is then completely opposite to the temperature dependence of ηG and it would explain the difference between the data in Figure 3. Theoretical modeling (Petroff and Stapelbroek 1984) predicts that at low bias voltages, the active layer will not be fully depleted, and the device quantum efficiency should be low. The quantum efficiency should increase as the depletion of the active layer increases. This is seen in Reynolds *et al.* (1988) data. However, as the device gain increases beyond unity, gain dispersion should cause η/β to decline; this is seen in both data sets.

TABLE 1
READ NOISE PERFORMANCE

Bias (v)	$T_N(e^-)$ 10s	$T_N(e^-)$ 100s	$R_N(e^-)$ 100s	βG	$R_N(e^-)/\beta G$ 100s
3.0	55	109	48	4	12
4.0	64	193	34	12	3
5.0	170	620	150	34	4

c) Read Noise

Table 1 shows the total noise T_N and read noise R_N, of the device at integration times of 10 and 100 seconds for different bias voltages; the results include a contribution from dark current noise (see next section) which has to be accounted for in order to determine the read noise. The detector temperature was 4.2 K, and the sampling up-the-ramp scheme provided a measure of the total noise. For most integration times, sampling up-the-ramp gives noises lower by 30 to 50% than either doubly- or triply-correlated sampling. The noise for an individual pixel is determined as the standard deviation of that pixel's value over a sequence of frames (usually five). The total noise (as shown in Table 1) is then the average of the individual pixel deviations. Another method of determining the noise is by subtracting two successive frames and computing the standard deviation of the differences for all pixels in the array. The noises computed with this latter method are therefore a factor of $\sqrt{2}$ larger than the actual noise for a single frame. This procedure is similar to taking the difference of source and background frames during astronomical observations and might provide a better estimate of the performance during actual use. Also, very low frequency drifts ($\lesssim$1 Hz) in the average output level of the array do not affect the noise measured in this manner.

The total noise increases with integration time and with bias voltage, but the read noise is fairly constant with respect to these two quantities, once the noise due to the dark current (see equation 1) is taken into account. The larger read noise seen at a bias of 5 volts is due to the error in subtracting off the noise due to the dark current. This error is large when the dark current noise contributes the vast majority of total. The increase in read noise with integration time as seen by Herter *et al.* (1987) in the first generation devices can be accounted for by the noise due to the dark current and its gain and gain dispersion. Since the BIB has gain (more than one electron per photon), the read noise expressed in equivalent number of detected photons is less than the number shown in Table 1. Because photovoltaic and extrinsic photoconductor detectors have gains at or near unity, the BIB detectors are intrinsically quieter, even if the read noise at the output is the same.

In order to properly evaluate the performance of these detectors for use on SIRTF the read noise should be compared to the noise in the photon background. Thus we should define an *effective* read noise that is the read noise divided by gain and gain dispersion

TABLE 2
DARK CURRENT PERFORMANCE

Bias	$i_d(e^-/sec)$			$i_d^{eff}(e^-/sec)$	
(v)	2.2°K	4.2°K	βG_d	2.2°K	4.2°K
4	20	30	12	2	3
5	70	120	30	2	3

(βG) seen by the photons, since the photon noise term is proportional to $(\beta G)^2$ (see equation 1). The quantity βG is easily determined from the measurements of η/β and ηG. In fact, when photon noise dominates, βG is given by N^2/S (see equations 1 and 2). Effective read noises using βG as the scale factor appear in the right-hand columns of Table 1. The effective read noise is quite low.

d) Dark Current

Dark currents were measured at both 4.2 and 2 K. Table 2 gives the results. The dark currents are under 120 e^- s^{-1} for all measurements. However, it is the noise contribution of the dark current in comparison to the photon noise contribution that is of interest here. We therefore define an *effective* dark current based on equation 1, which is the dark current multiplied by the βG that applies to the dark current divided by the square of the βG in the photon noise term. The βG for the dark current is determined by evaluating the total noise performance of the darkened array at different integration times. For short integration times the read noise is the major contributor, while at long integration times the dark current term is the major contributor. Then, with value of the dark current known from the acculumated charge, we can determine βG for the dark current. Using our estimates of βG for photons as given in Table 1, and the βG for the dark current given in Table 2, the effective dark current is less than 3 e^- s^{-1} (see Table 2, columns 5 and 6).

e) Transient Response

We investigated the temporal response of the detector to changes in the incident photon flux at a bias voltage of 5 V and temperature of 2.2 K. The array was read every 25 ms, and the collected charge was approximately 90,000 e^- per detector per read. A bright source illuminated the array for several seconds, so that each detector received approximately 800,000 electrons per read. Then the illumination was decreased rapidly to 90,000 e^- per read again. The responsivity of the array decreased after the bright illumination for a period extending over many minutes. The responsivity returned to within 5% of the low-level value after 2.5 minutes, and it was within 1% of its initial value after 8 minutes. This behavior does not appear to depend on temperature, but it could be a function of bias voltage and how the detectors are reset. We are investigating these effects and also the responsivity changes for less extreme changes in detector illumination.

f) Radiation Recovery

The array was irradiated with a ^{241}Am γ-ray source to measure response to high energy radiation. The dominant lines are at 59.54, 17.61, and 13.92 keV which comprise 36, 20 and 13% of the total photon emissions respectively. All other lines are less than 5% of the total. The γ-ray source was about 20 cm from the array illuminating it face-on. In this configuration, a γ-ray is detected by the array every few seconds. The resulting charge on a detector was between a few tens of thousands and a few hundred thousand electrons. The gamma rays do not saturate the detectors. The largest events usually affect three neighboring detectors: the detectors immediately above and below in the same column collect a few times ten thousand electrons, as does the immediately preceding detector in the same row. If there is no infrared illumination on the array, these detectors require about 10 resets to fully recover their response characteristics. The voltage level of the detector in the same row as the pixel primarily affected by the γ-ray actually goes below its normal value when reset immediately after the detection of the γ-ray. The voltage returns to normal after a few more resets.

Since infrared light aided recovery from high energy radiation events, the response was measured using a resistor to illuminate the detector inside the cryostat; no bandpass filter was used. At a frame rate of 10 Hz with a bias voltage of 4 V, the photon background generated 6500 electrons on each detector between resets. The detectors then recovered from radiation events after one reset. At lower photon fluxes, recovery from a radiation hit was similar to that under dark conditions. For 6000 e^- per read and 400 e^- per read, 8 and 12 resets were required, respectively. The low illumination measurements were done at a frame rate of 10 Hz with a 5 volt detector bias. We note that even though the accumulated charge is the same for two of the cases (because of the higher bias), fewer resets are required to recover from an event under high illumination. It is possible that photons anneal the detectors by removing the carriers generated by the γ-hit.

The number of resets after an event appears to determine the recovery time of the detectors. The recovery did not depend on the total time after the event. The radiation response is independent of the detector temperature. We are experimenting with longer integration times (time between resets) and smaller photon fluxes to determine the resulting radiation response under conditions closer to those expected for SIRTF.

V. Projected Performance

Figure 4 shows the projected sensitivity of the SIRTF midband spectrometer using the measured performance characteristics of the Rockwell Si:As BIBIB hybrid array. In this figure we have interpolated our measured η/β values of 0.15 and 0.25 for 10 and 18 μm respectively to calculate the curve at various wavelengths. We underestimate the performance at longer wavelengths, since η/β increases with wavelength; the peak response occurring near 23μm. Included for comparison in Figure 4 are the performance curves for ideal detectors with various quantum efficiencies and read noises. An ideal

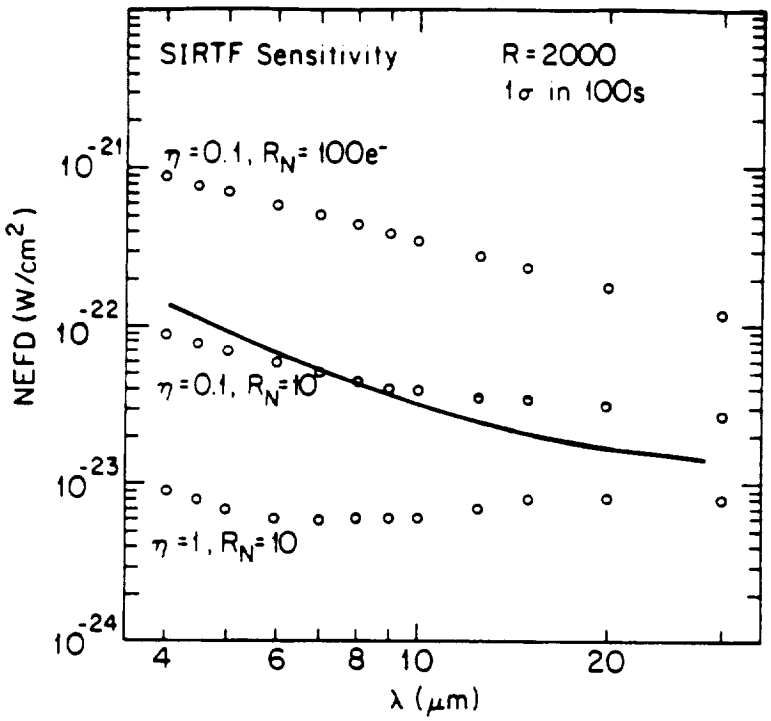

Figure 4: Projected performance of the SIRTF midband spectrometer operating at a resolution of 2000 using the measured η/β, ηG, dark current and read noise of the Rockwell Si:As BIBIB hybrid array. The 1σ sensitivity in 100 s is plotted as a function of wavelength. The array is assumed to be operating at a temperature of 4.2 K and a bias of 4V. Open circles indicate the performance of ideal detectors (no generation–recombination noise and no dark current) with different quantum efficiencies and read noises.

detector here has no dark current, no generation–recombination noise, unity gain, and no gain dispersion. If the measurements obtained here in relatively high backgrounds apply also for the low background conditions of SIRTF, the projected performance using the Si BIBIB array achieves the equivalent performance of an ideal detector with 10% quantum efficiency and a read noise of 10 electrons.

VI. Conclusions

The short wavelength detective quantum efficiency, η/β, of Si BIBIB arrays increases approximately linearly with the thickness of the infrared active layer. The second generation detectors, with twice the active layer thickness, exhibited quantum efficiencies twice those of the first generation detectors. At 4.7 μm, the best detectors have $\eta/\beta \sim 0.10$. Furthermore, the dark current is very small in a graded layer device, allowing high bias voltages to increase detector gain. Responsivities, ηG, larger than two are seen under

some operating conditions. Because of this gain the *effective* read noise (equivalent number of detected photons) is small, less than 10 electrons. The projected performance of the SIRTF midband spectrometer, 5–27μm, using the Si BIBIB hybrid arrays is excellent. Sensitivities better than 10^{-22} W cm^{-2} can be achieved in 100 s.

Further improvements in η/β and ηG are possible. The active layer thickness can probably be increased by 30% and remain fully depleted under bias voltage. In addition, Rockwell has demonstrated that anti-reflection coating can improve the responsivity by 20–25% at peak transmission. By coating for 5–6μm, the responsivity can be improved at the short wavelengths with no degradation or fringing at the longer wavelengths.

On the negative side, the transient performance of the array is not very good. Recovery from changes of state such as background illumination, detector bias, or the detector read out rate require at least 5–10 minutes before stable operation is achieved. This may be a result of the low temperature or low background operating conditions and may only be a characteristic of the graded layer device. In principle, the transient response is not a significant problem for SIRTF conditions because the array can be brought into its required state of operation prior to an exposure. However, recovery from radiation hits could present problems since in the SIRTF high orbit each pixel will be hit about once every 500 seconds. We are currently investigating these issues.

Acknowledgments: We are grateful to Jim Houck for useful discussions and for securing the ^{241}Am source for the radiation testing, and to Justin Schoenwald for providing software support. Financial support for this work was provided by the SIRTF project and Craig McCreight through NASA-Ames contract NAS2-12524 to Cornell University.

REFERENCES

Hauser, M. G. *et al.* 1984, *Astrophysical Journal (Letters)*, **278**, L15.

Herter, T., Fuller, C., Gull, G. E., and Houck, J. R. 1987, "Test Results with Rockwell Si BIBIB Hybrid Arrays," in *Proceedings of Workshop on Ground-based Astronomical Observations with Infrared Arrays*, eds. Wynn-Williams, C. G. and Becklin, E. E., (Univ. of Hawaii, Honolulu), p. 128.

Petroff, M. D. and Stapelbroek, M. G., "Responsivity and Noise Models of Blocked Impurity Band Detectors," in *Proceedings of the IRIS Specialty Group on Infrared Detectors*, August 1984, Seattle, WA.

Petroff, M. D. and Stapelbroek, M. G., "Spectral Response, Gain, and Noise Models for the IBC Detectors," in *Proceedings of the IRIS Specialty Group on Infrared Detectors*, August 1985, Boulder, CO.

Reynolds, D. B., Seib, D. H., Stetson, S. B., Herter, T., Rowlands, N. and Schoenwald, J. 1989, "Blocked Impurity Band Hybrid Infrared Focal Plane Arrays for Astronomy," in *IEEE Transactions on Nuclear Science*, **36**, No. 1, p. 857.

Stetson, S. B., Reynolds, D. B., Stapelbroek, M. G., and Stermer, R. L., "Design and Performance of Blocked-Impurity-Band Detector Focal Plane Arrays," in *Proceedings of 30th Annual International Technical SPIE Symposium on Infrared Detectors, Sensors, and Focal Plane Arrays*, August 1986, San Diego, CA.

TESTS OF THE ROCKWELL Si:As BACK-ILLUMINATED BLOCKED - IMPURITY BAND (BIBIB) DETECTORS

J. Wolf, U. Grözinger, M. Burgdorf, A. Salama[+] and D. Lemke
Max-Planck-Institut für Astronomie
Heidelberg, Germany

Abstract

Two arrays of Rockwell's Si:As back-illuminated blocked-impurity-band detectors have been tested at the Max-Planck-Institut für Astronomie (MPIA) at low background and low temperature for possible use in the astronomical space experiment ISOPHOT[1]. For these measurements a special test equipment was put together. A cryostat was mechanically modified to accommodate the arrays and special peripheral electronics was added to a microprocessor system to drive the cold multiplexer and to acquire the output data. The first device, a 16x50 element array on a fan-out board was used to test individual pixels with a trans-impedance-amplifier at a photon background of 10^8 Ph $s^{-1}cm^{-2}$ and at temperatures of 2.7 to 4.4 K. The noise-equivalent-power NEP is in the range 5 - 7 x 10^{-18} $WHz^{-1/2}$, the responsivity is ≥ 100 AW^{-1} (f = 10 Hz). The second device was a 10x50 array including a cold readout electronics of switched FETs (SWIFET). Measurements of this array were done in a background range of 5 x 10^5 to 5 x 10^{11} Ph $s^{-1}cm^{-2}$ and at operating temperatures between 3.0 and 4.8 K. The NEP ranges from < 10^{-18} $WHz^{-1/2}$ at the lowest background to 2 x 10^{-16} $WHz^{-1/2}$ at the highest flux. On-chip integration times from 1 ms to 4 s were used for these photometric measurements and bias voltages around 4 V proved to be useful. The dark current was measured to be about 64,000 electrons/s and 16,000 electrons/s at 4.2 K and 3.1 K respectively.

Test Equipment

For testing the detector arrays, special test equipment has been built, consisting of a liquid helium cryostat, an infrared radiation source and a computer system with special peripheral electronics to drive the device and for data acquisition. This test set-up is schematically shown in figure 1.

+ Present address: Astrophysics Division, ESTEC-SA, Noordwijk, The Netherlands

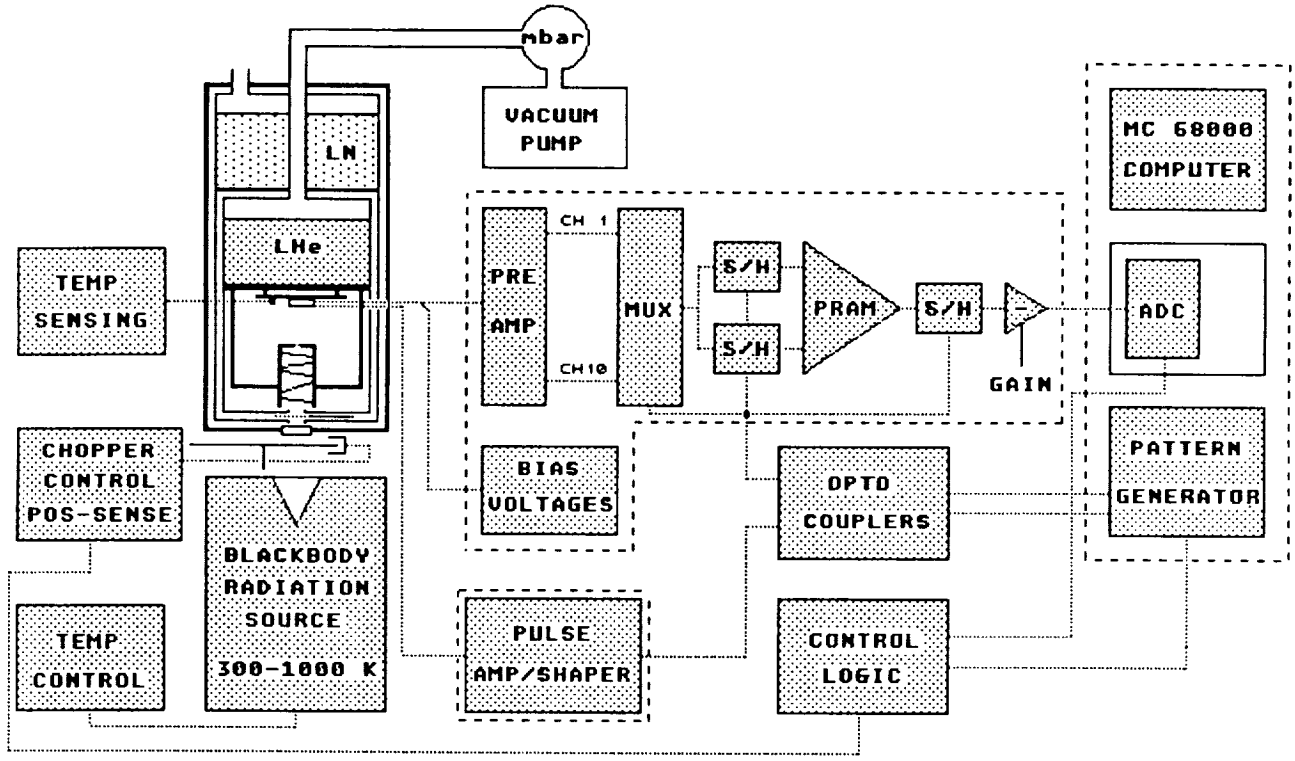

Figure 1 **Test Equipment for Detector Arrays**

Cryogenics and Optics

A commercial liquid helium dewar (HD-3, Infrared Laboratories) has been modified as shown in figure 2. An aluminum base plate is bolted to the LHe-tank and carries a pc-board with a 68-pin chip carrier. The test array fits into this chip carrier and is held in place by an aluminum/glass-fibre frame. This frame presses the contacts of the ceramics array substrate against the spring loaded contacts of the carrier. A cold finger of the baseplate penetrates through the pc-board. At its end there is a copper-berylium spring which provides thermal contact to the ceramics substrate. Additional cooling is provided to the device by the electrical contacts. Copper wires are used from the pc-board to the connectors at the base plate. They are fed through to the bottom of the base plate and are run in milled channels. Thus the wires are in close thermal contact to the helium bath and at the same time light is prevented from leaking into the test housing. The aluminum/glass fibre frame is coupled to the base plate by a strap of braised copper strands. Temperature down to about 2 K can be achieved by pumping on the liquid helium and two carbon resistors are used as temperature sensors at the base plate and the frame.

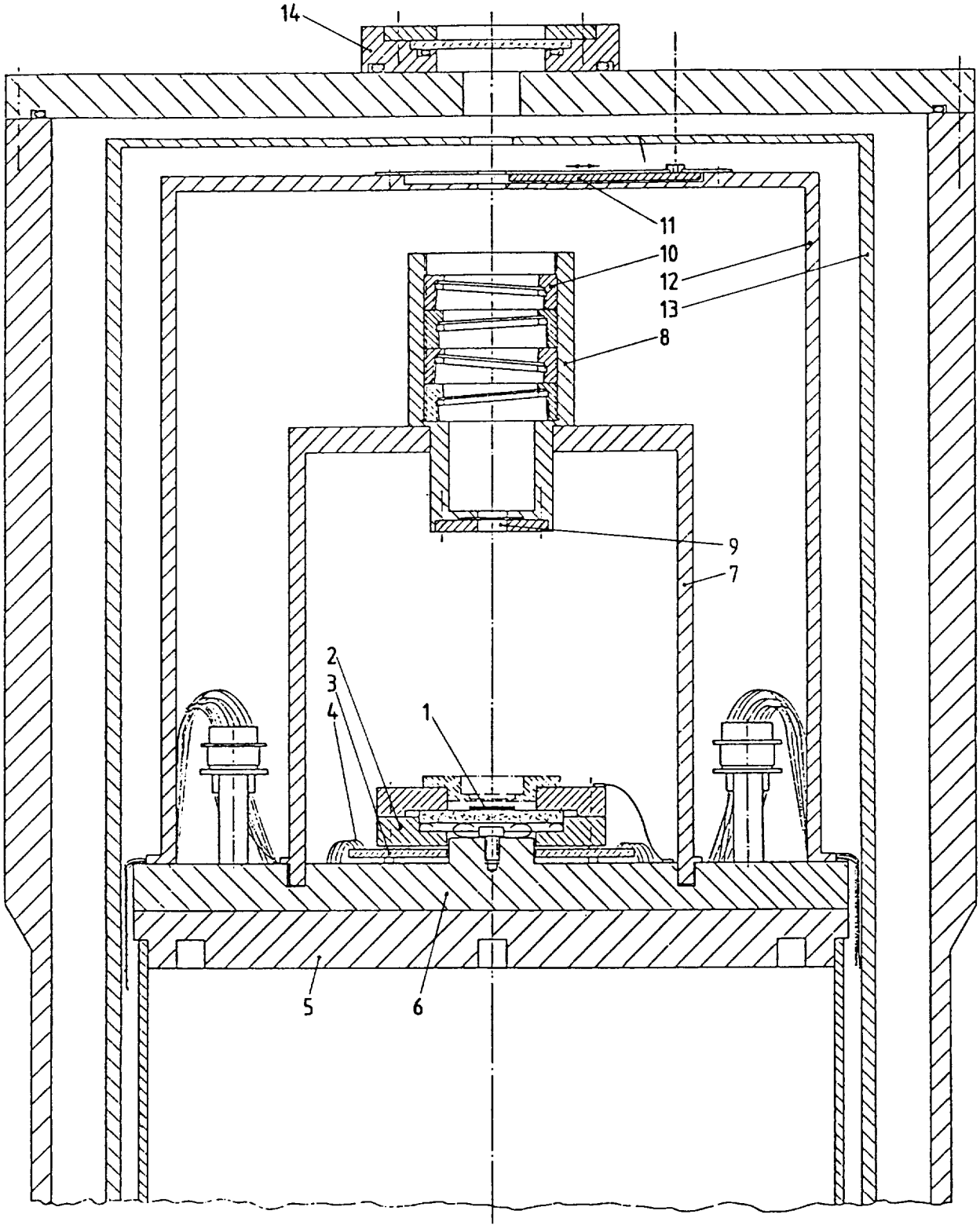

Figure 2 Detector Test Cryostat

A threaded lid covers the base plate light-tight and carries a filter holder. Several spectral and attenuation filters can be mounted into this holder to select the desired infrared flux. The filters are tilt against each other by 3° to avoid multiple reflections between them which could contaminate the beam. A cold aperture of typically 1 mm in diameter in this filter holder defines the field of view of the array.

This test housing is surrounded by a radiation shield at LHe-temperature which contains a shutter to block all light coming into the cryostat. This shutter can be manipulated from outside the dewar with a vacuum feedthrough and is used for dark current measurements or for switching between "0 flux" and radiation entering through the KRS-5 window.

As radiation source a calibrated blackbody with temperature controller is used. Its radiation can be modulated by a rotating chopper wheel at room temperature which can be synchronized to the readout electronics. The fluxes incident on the detectors are calculated using Planck's law and the cold transmission of the filters involved. In chopped operation the signal is the difference of fluxes from the blackbody source and the chopper blade. All numbers of NEP and responsivity given here are calculated at the detector's peak wavelength of 25 μm.

Electronics

The 16x50 element array was mounted on a fan-out board and individual pixels could be accessed with a single channel preamplifier. The well known trans-impedance-amplifier, TIA was used with an IRAS module from Infrared Laboratories as an input stage.

The 10x50 element hybrid came with a cryogenic switched FET readout electronics to which the detector array was directly sandwiched. That multiplexer provides one output line for each of the 10 rows. A special electronics system was built to drive the mux and to acquire the output data. For EMC/EMI reasons the system is separated into three parts: a MC 68000 computer system including an analog to digital converter and a pulse generator and two boxes that are directly connected to the electrical plugs of the test dewar. One contains the amplifiers and shaper circuits for the array drive pulses while the sensitive signal processing electronics is located in the second box (see figure 1).

The pattern generator is programmed by the main computer. Once the pulse pattern needed is stored in its RAM, this memory is continuously read out with a selectable speed. No further interaction with the computer is needed. For galvanic separation between analog and digital grounds, the TTL pulses of the pattern generator are fed to the pulse amplifier via opto-couplers. A control logic synchronizes the chopper and triggers the ADC.

The drive pulses needed by the cryogenic multiplexer are generated in the pulse amplifier/shaper box. The upper and lower level of a pulse are defined by two voltage references. An analog switch that is contolled by the pattern generator feeds one of these voltages to an adjustable lowpass filter which is set to provide the desired pulse shapes. A current amplifier is then used as a buffer to provide a low impedance signal to the array (see figure 3). Five such channels are contained in the box.

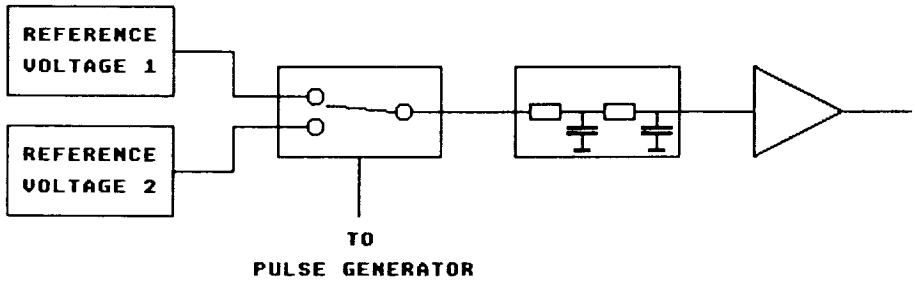

Figure 3 Pulse Shaper and Amplifier

The ten output lines of the hybrid are terminated by 10 kΩ resistors and are then fed into a 10-channel preamplifier of gain 16. To apply that gain without saturating the amplifiers, the offset voltage of the signals must first be compensated. This is done by feeding a well filtered DC voltage of a reference source (2.66V) into the inverting input of the operational amplifiers. One of the ten channels is selected by a multiplexer and fed to the inputs of two sample-and-holds which sample the signal and reset levels. The difference of those is then amplified by an instrumentation amplifier where a gain of ten was normally used. This differential signal can be clamped by a third S/H and be additionally amplified by a programmable inverting amplifier which also provides lowpass filtering. It is then fed to the 14-bit analog-to-digital converter of the MC 68000.

Also contained in this "clean" electronics box is the supply for the DC voltages needed by the hybrid. A 10V reference voltage source feeds a set of adjustable voltage dividers. The voltages then go through a buffer amplifier with an active filter and finally to an lowpass RC-filter to ensure stable and very low noise performance.

TIA Measurements

One pixel of the 16 x 50 element array was connected to a TIA with feedback resistor of $R_f = 1.7 \cdot 10^9\ \Omega$ (at 4.2K). Some results of these tests are shown in figure 4. Figures 4a and 4b show identical NEP and responsivity taken with different blackbody temperatures.

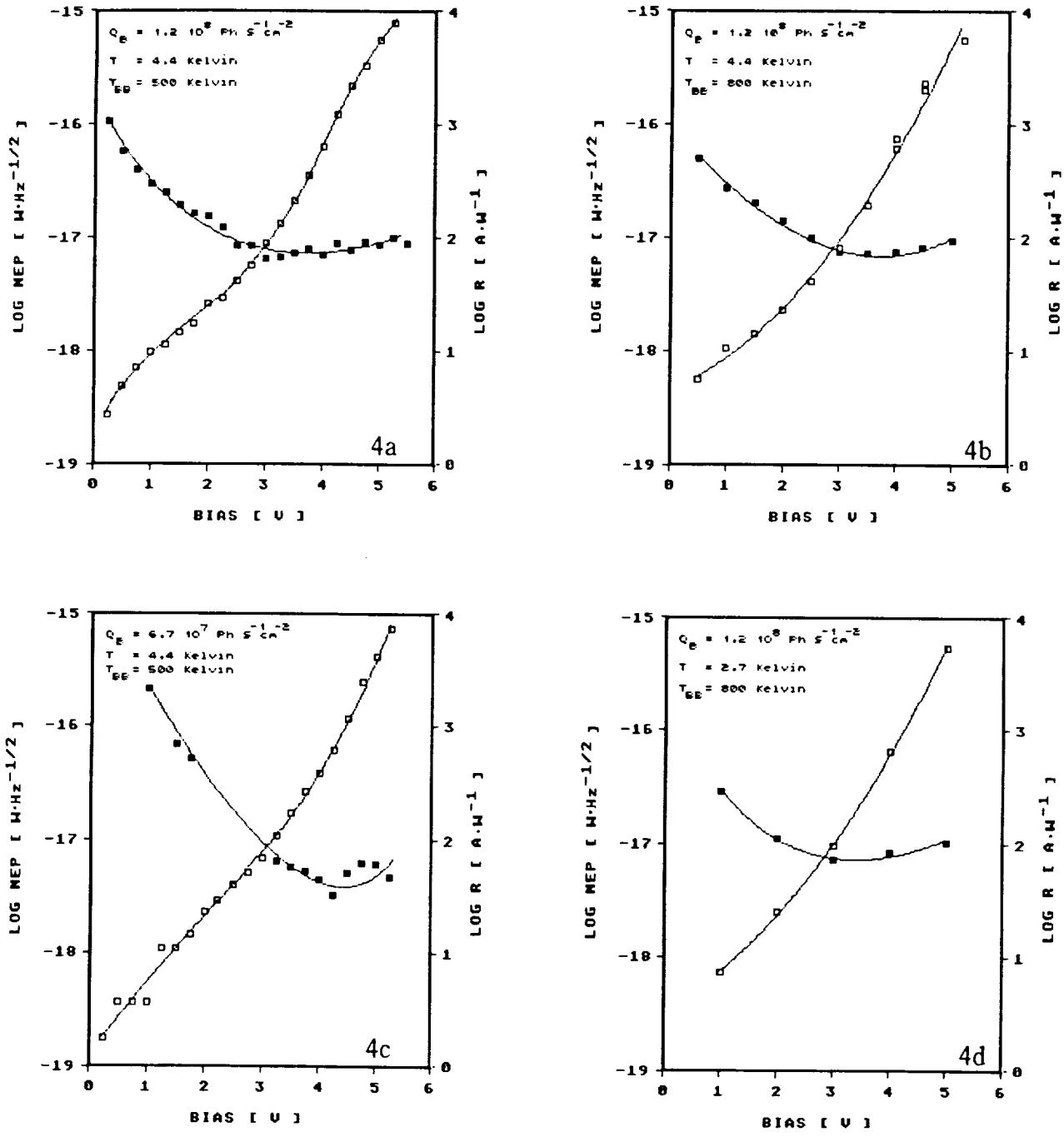

Figure 4 Testresults of TIA Measurements

In the TIA circuit a feedback resistor of 1.7 ·10^9 Ω which has been calibrated for its non-linearity at temperatures down to 2.7 Kelvin. For the tests in figure 4a,b and d a 16 μm cut-on filter was used, for figure 4c a 13μm cut-on was choosen to check the radiometrics. All tests were done with a chopper fequency of 10 Hz.

This is a first indication that the radiometric calculation and the derived results are reliable. An even better test is the comparison of Figures 4a and 4c. Up to bias voltages of 3.5V the responsivities are identical although completely different cold spectral and attenuation filters were used.

Some deviations between these two responsivity measurements at higher bias voltages could be related to signal drifts. Such drifts were observed after bias switch-on above 3.5V. Their amplitude was within a factor of 2 of the starting point and their time constant at the order of 20 to 30 minutes. As no such effect has been observed in the TIA circuit before, the drift is probably due to the detector.

The NEPs of figure 4a and 4c ratio 7/5 which scales closely with the square root of the background flux ratio, indicating that the NEP is background limited at bias voltages 3 to 4V. Assuming a quantum efficiency of 0.5, the measured responsivity of 100 . . . 200 $A \cdot W^{-1}$ (in the bias region of best NEP) gives a photoconductive gain of G = 10 . . . 20. From this the preamplifier-limited NEP of our TIA is calculated to $1.9 \cdot 10^{-18}$ $WHz^{-1/2}$ which is consistent with our results. Using again η = 0.5 background limited NEPs of $4.3 \cdot 10^{-18}$ $WHz^{-1/2}$ for figure 4a and $3.3 \cdot 10^{-18}$ $WHz^{-1/2}$ for figure 4c are found if the photon noise of the background and the signal flux (differential flux blackbody/chopper ~ photon background) are considered. Our results which are about a factor 1.5 higher indicate an additional noise source in the detector, e.g. gain dispersion. Finally figure 4d indicates that the detector's performance is not changing if it is operated at 2.7 Kelvin.

Multiplexed Measurements

The test equipment was normally run with the warm multiplexer scanning all ten detector rows, so the data of all 500 elements were taken. By varying background flux, temperature, bias voltage and integration time over a wide range each, huge amounts of data had to be stored. All this data is still available for detailed evaluation, our heavy involvement in the ISOPHOT program however does not allow for that. For this report we have therefore choosen to summarize our results.

Figure 5 shows an example of the NEP and responsivity averaged over the array. At minimum NEP the responsivity is ~1000 AW^{-1} if an effective node capacitance of 0.6 pF is assumed[2]. Taking η = 0.5 the photoconductive gain is calculated to G ~ 100. Although this gain is very high, no long time constants are seen. During a 10 minute run after opening the cold shutter at a bias voltage of 3.5V no significant signal drift was observed. Figure 6 gives an overview of the NEP results we got in a wide range of background fluxes.

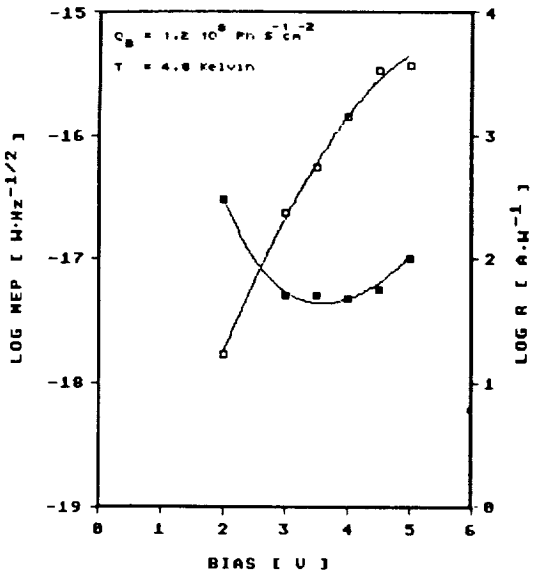

Figure 5
NEP and Responsivity of 10 x 50 Array

NEP and responsivity are averaged over all 500 elements. The signal flux is $1.8 \cdot 10^{-16}$ Watt per pixel and the integration time is 19 msec.

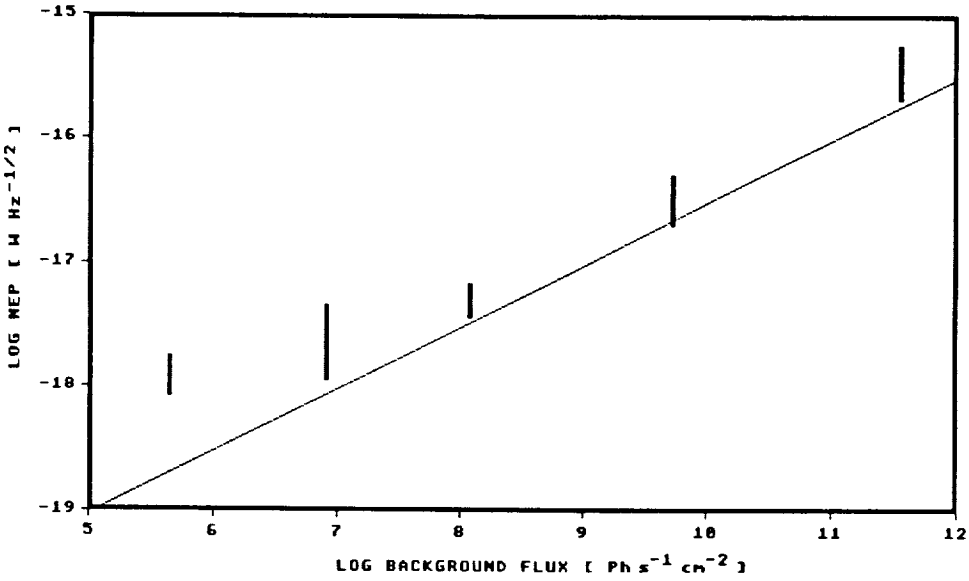

Figure 6 Summary of NEP Measurements of the 10 x 50 Array

By using different sets of cold attenuation filters the background was varied over 6 orders of magnitude. The vertical bars indicate the range of NEP found by using various integration times (1 to 4000 msec) and bias voltages (up to 4.5V). Also different algorithms for data evaluation like statistical analysis and Fourier transformation have been applied. At background fluxes down to about 10^7 Ph s^{-1} cm^{-2} the lower end of these bars where the operating parameters are optimized, coincide well with the BLIP-limit calculated with $\eta = 0.5$. At lower backgrounds the deviation from that limit indicates the influence of the readout noise.

NEP and responsivity were almost independent of temperature below 4 Kelvin as shown in table 1. The dark current was measured at pixel #25 of rows 1,3,5 and 9 at a bias voltage of 4V. The results are shown in table 2. The linearity over integration time and infrared flux is shown in figures 7 and 8. A qualitative test of the crosstalk is shown in figure 9.

Table 1 Temperature Dependence

Q_B [Ph $s^{-1}cm^{-2}$]	V_b[V]	T_D [K]	t_{int}[msec]	NEP [W $Hz^{-1/2}$]	R[A W^{-1}]
$8.2\ 10^6$	4.0	4.7	75	$2.7\ 10^{-18}$	570
	4.0	3.6	75	$2.4\ 10^{-18}$	900
	4.0	3.2	75	$2.2\ 10^{-18}$	920
	4.0	3.0	75	$2.1\ 10^{-18}$	900

Table 2 Dark Current at 4V Bias

Pixel	Dark Current [Electrons / Second] T = 4.2 K	T = 3.1 K
1 , 25	63 700	16 300
3 , 25	64 400	16 800
5 , 25	63 200	15 900
9 , 25	61 000	14 800

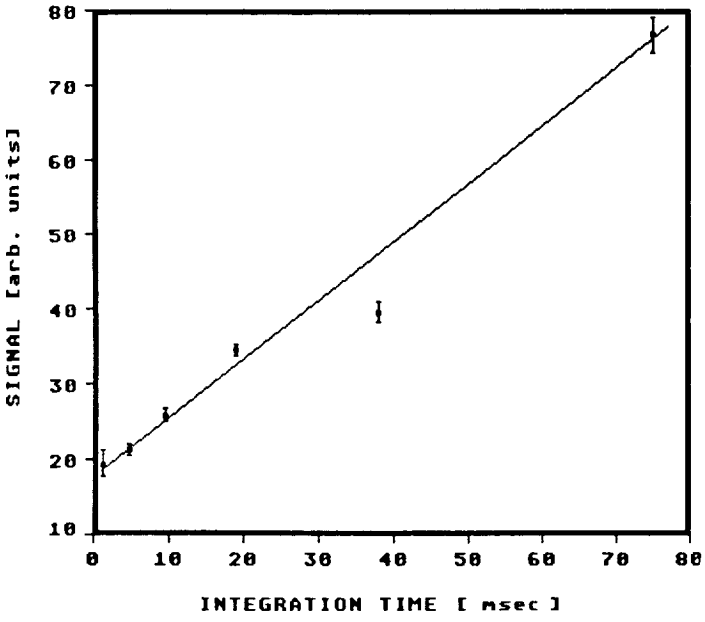

Figure 7
Linearity over Integration Time
Except for the integration at 38msec the signal is linear in time within the measurement's accuracy.

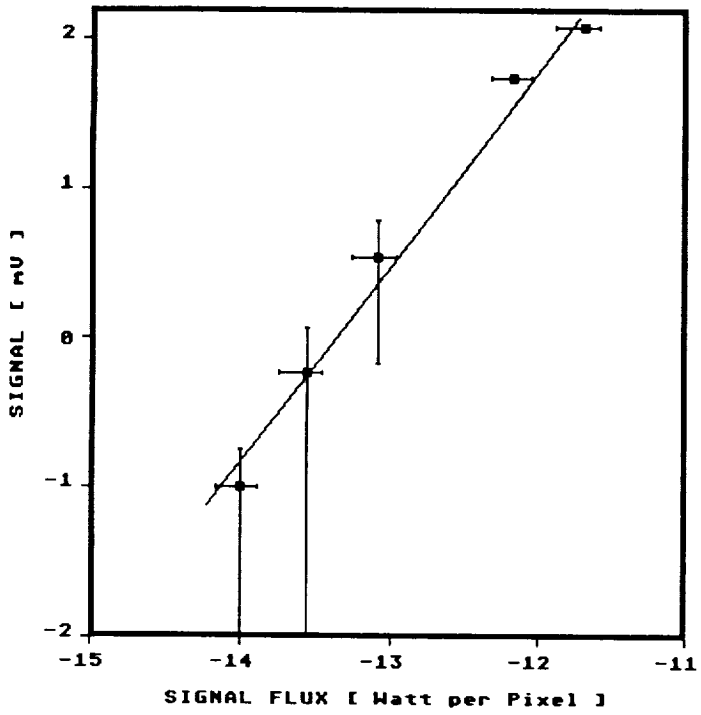

Figure 8
Linearity in Infrared Flux
At low fluxes the noise of the output voltage gives large error bars which disappear at the higher signals. The errors in flux are caused by the uncertainty of the attenuation filter's cold spectral transmission. Within these limits the detector is linear.

Conclusion

Although the data presented here are not a complete investigation of the devices, the excellent suitability of these arrays for space astronomy is obvious. With a NEP of about 10^{-18} $WHz^{-1/2}$ the 10x50 array offers a factor ~10 better sensitivity compared to bulk detectors at photon background fluxes below 10^7 $Phs^{-1}cm^{-2}$. Its very high responsivity of ~1000 AW^{-1} makes the use of a relatively noisy readout circuit possible. Besides these sensitivity advantages, the high energy radiation immunity of these detectors would be a great gain for a space astronomy. We very much regret that this technology could not be made available for the use in our ISOPHOT experiment.

Acknowledgement

The export license for the two detector arrays authorized testing for a 10 months loan period in our lab. We are very grateful to C. D. Lawson of Rockwell International in Anaheim for the big amount of work he put into obtaining that license. During set-up of our tests we got valuable help from the staff of the Rockwell Science Center, Anaheim. We appreciate very much the open discussions of our technical problems and the advices we got. We also thank the staff of the machine shop in our institute for the quick delivery of test equipment. Finally we want to thank C.R. McCreight for his support to include this presentation in his workshop.

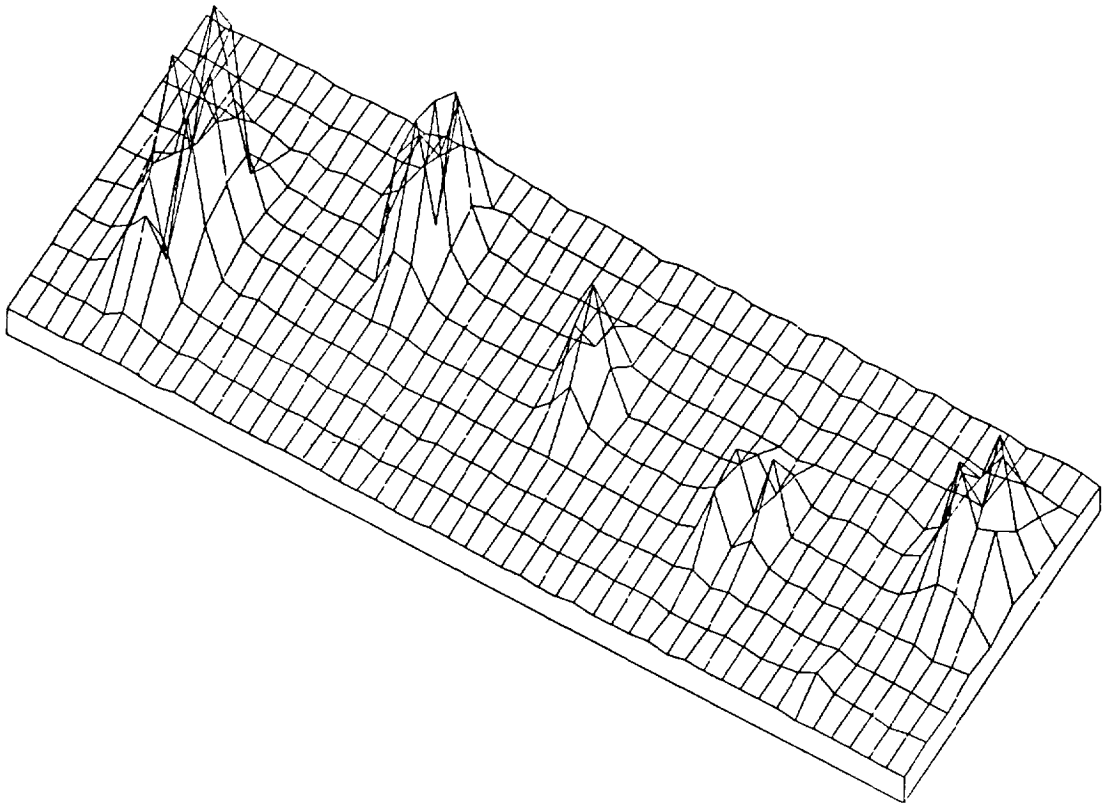

Figure 9 Crosstalk Test

To test the crosstalk of the array a blackened mask was put within 1 mm close to its surface. Through holes ranging from 0.2 to 0.5 mm in diameter small areas of the array were illuminated. We did not attempt a quantitatively evaluate this but the steep slopes of the "light-mountains" indicate low crosstalk. For this plot an integration looking at the cold shutter was used for flat-fielding.

References

1. Wolf, J., Lemke, D., Burgdorf, M., Grözinger, U., Hajduk, Ch.:"Status of the ISOPHOT Detector Development", this conference
2. Stetson, S.B., Reynolds, D.B., Stapelbroek, M.G., Stermer, R.L.:"Design and performance of blocked-impurity-band detector focal plane arrays", Proc. SPIE, 686, 48 (1986)

☆ U.S. GOVERNMENT PRINTING OFFICE: 1989—785—551

NASA
National Aeronautics and Space Administration

Report Documentation Page

1. Report No.	2. Government Accession No.	3. Recipient's Catalog No.
NASA TM-102209		

4. Title and Subtitle	5. Report Date
Proceedings of the Third Infrared Detector Technology Workshop	October 1989
	6. Performing Organization Code
7. Author(s)	8. Performing Organization Report No.
The authors and their affiliations are shown in the list of attendees	A-89200
	10. Work Unit No. 506-45-31
9. Performing Organization Name and Address	11. Contract or Grant No.
Ames Research Center Moffett Field, CA 94035	
	13. Type of Report and Period Covered Technical Memorandum February 7-9, 1989
12. Sponsoring Agency Name and Address	14. Sponsoring Agency Code
National Aeronautics and Space Administration Washington, DC 20546-0001	

15. Supplementary Notes

Point of Contact: Craig R. McCreight, Ames Research Center, MS 244-10, Moffett Field, CA 94035
(415) 694-6549 or FTS 464-6549

16. Abstract

This volume consists of 37 papers which summarize results presented at the Third Infrared Detector Technology Workshop, held February 7 - 9, 1989, at Ames Research Center. The workshop focused on infrared (IR) detector, detector array, and cryogenic electronic technologies relevant to low-background space astronomy. Papers on discrete IR detectors, cryogenic readouts, extrinsic and intrinsic IR arrays, and recent results from ground-based observations with integrated arrays were given. Recent developments in the second-generation Hubble Space Telescope (HST) infrared spectrometer and in detectors and arrays for the European Space Agency's Infrared Space Observatory (ISO) are also included, as are status reports on the Space Infrared Telescope Facility (SIRTF) and the Stratospheric Observatory for Infrared Astronomy (SOFIA) projects.

17. Key Words (Suggested by Author(s))	18. Distribution Statement
Infrared detectors Infrared detector arrays Cryogenic electronics Infrared astronomy	Unclassified-Unlimited Subject Category - 35

19. Security Classif. (of this report)	20. Security Classif. (of this page)	21. No. of Pages	22. Price
Unclassified	Unclassified	474	A20

NASA FORM 1626 OCT 86

For sale by the National Technical Information Service, Springfield, Virginia 22161